Fatigue of Materials and Structures

Fundamentals

Edited by
Claude Bathias
André Pineau

ISTE WILEY

First published 2010 in Great Britain and the United States by ISTE Ltd and John Wiley & Sons, Inc.

ISTE Ltd
27-37 St George's Road
London SW19 4EU
UK

www.iste.co.uk

John Wiley & Sons, Inc.
111 River Street
Hoboken, NJ 07030
USA

www.wiley.com

Library of Congress Cataloging-in-Publication Data

Fatigue of materials and structures / edited by Claude Bathias, André Pineau.
p. cm.
Includes bibliographical references and index.
ISBN 978-1-84821-051-6
1. Materials--Fatigue. 2. Materials--Mechanical properties. 3. Microstructure. I. Bathias, Claude. II. Pineau, A. (André)
TA418.38.F375 2010
620.1'12--dc22

2010002223

British Library Cataloguing-in-Publication Data
A CIP record for this book is available from the British Library
ISBN 978-1-84821-051-6

Printed and bound in Great Britain by CPI Antony Rowe, Chippenham and Eastbourne.

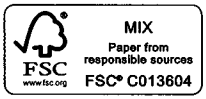

Table of Contents

Chapter 1

Introduction to Fatigue: Fundamentals and Methodology

1.1. Introduction to the fatigue of materials

1.1.1. *Brief history of fatigue: its technical and scientific importance*

Experience shows that fracture of structures or machine parts during regular operating conditions are most often due to fatigue. Structural integrity has always been an obstacle to industrial development. Its consequences could be seen during the development of mechanical industry in the 19th century. The industrial revolution, particularly the development of rail transportation, was affected from the start by a certain number of serious accidents, such as the one in Versailles, 1842, where the rupture of an axle caused the death of 60 people [SMI 90]. This death toll is close to that of the two Comet plane crashes that occurred in 1954.

It is known that fatigue damage costs several percent of the gross domestic product of the engineering industry. For this reason, we can understand the fact that articles and papers about this type of damage are ever increasing. Toth [TOT 01], who recently checked the COMPENDEX data base, found about 10,000 articles on this topic between 1988 and 1993, which comes to 2,000 articles a year.

According to Schütz [SCH 96], Braithwaite [BRA 1854] introduced the term "metal fatigue" in 1854. Despite this, Lemaitre [LEM 01] reckons that Poncelet

---

Chapter written by André PINEAU and Claude BATHIAS.

mentioned this term during an engineering lecture in Metz as early as 1839, and that Rankine used it in 1843. To gain a better understanding of the work carried by Poncelet and Rankine in this field, we can refer to Timoshenko's work dealing with the history of the strength of materials [TIM 53]. As a matter of fact, this term has probably been in use for a long time. For instance, Stendhal used it in one of his pieces "Memoirs of a tourist" published in 1838 [STE 1838]. On his way to Civitavecchia, in Italy (where he had been appointed Consul), while crossing the Loire river in La Charité one of the axles of his carriage broke. What he wrote is as follows:

"La Charité – April 13. I was riding through the small town of La Charité, when, as a reminder of the long thoughts I had in the morning about iron diseases, the axle of my carriage suddenly broke down. I have to be blamed: I swore that if I ever had my own carriage, I would get a nice Fourvoirie axle, with six mild steel rods, forged under my own eyes... I checked the iron grain of my axle; it was larger as it has apparently been used for a long time... ."

We should remember that in those times, and for many years during the 19th century, people thought that iron "crystallized" due to mechanical vibrations. The fact that Stendhal, who lived at the same time as Poncelet, already knew what fatigue was, at least in this form, is not surprising. They both campaigned for Napoleon in Russia in 1812 and we can assume that they would have discussed this subject.

Excellent reviews on the history of fatigue have been written, some of them very recently. We can for instance refer to the work of Schutz [SCH 96] which lists more than 550 references, such as Toth [TOT 01], or Schijve [SCH 03].

It is worth noting that some works on this subject have recently been published:

– Bathias and Baïlon [BAT 97];

– Bathias and Paris [BAT 05];

– Henaff and Morel [HEN 05];

– Murakami [MUR 02, MUR 03];

– Polak [POL 91];

– Reifsnider [REI 91];

– Schijve [SCH 01];

– Shaniavski [SHA 07]; and

– Suresh [SUR 98].

Here we should mention two regularly published journals that explicitly refer to the fatigue phenomenon: *Fatigue and Fracture of Engineering Materials and Structures* and the *International Journal of Fatigue*. In addition to this, in other countries scientific societies organize lectures and conferences on this subject, such as the ASTM (American Society for Testing and Materials) in the USA and the SF2M (French Society of Metallurgy and Materials) in France.

Year	Event
1842	Meudon railway accident
1858	First publication by Wohler
1860-70	Wohler experiments on smooth and notched axles. Bending and torsion tests – Investigation on the effect mean stress
- 1881	Study by Bauschinger which initiated low-cycle fatigue
1910	Basquin law
1913	Stress distribution within notches (Inglis)
1920	Energy balance regarding the propagation of a crack (Griffith)
1930	Stress concentration factor and endurance limit (Peterson)
1937	Neuber concept applied to notches
1939	Statistical approach Weibull law
1945	Miner concept for fatigue damage accumulation
1953-54	Low cycle fatigue. Manson – Coffin law
1954	Comet aircrafts accidents
1956	Introduction of strain energy released rate (Irwin)
1960	Servohydraulic machines
1961	Paris law
1968	Introdcution of effective stress intensity factor (Elber)
1988	Aloha B737 accident
1989	DC 10 Sioux City accident
1996	Pensacola accident
1998	ICE. Eschede railway accident
2006	Los Angeles B767 accident

Table 1.1. *A few stages and main events regarding the history of the fatigue phenomenon*

Some memorable stages and events that have marked the history of fatigue are highlighted in Table 1.1. As mentioned earlier, this type of damage has clearly been of great importance during the development of rail transportation. The various ruptures that Wöhler observed in Germany led him to undertake a systematic study of this type of damage.

Along with trains and many other mechanical structures, aircraft were also readily affected by the fatigue phenomenon. The first serious accidents that occurred are those involving two Comet aircraft in 1954. A more recent example was the Aloha accident in 1988, which involved a Boeing 737. The damage was really serious, as we can see in Figure 1.1. This accident was caused by the formation of cracks due to fatigue and corrosion in the assembly rivets area within the fuselage. As a result, numerous studies have been carried out regarding the issue of multiple site damage.

Figure 1.1. *The Aloha Airlines Boeing 737at Honolulu international airport, Hawaii, following the accident on April 28, 1988*

Another example concerns the MacDonald Douglas DC 10 crash, which occurred in Sioux City in Iowa in 1989 (see Figure 1.2). The explosion of one of the engines led to this tragic accident. Even more recent was the Pensacola crash, when one of the engines broke apart due to cracking initiation caused by a drilling defect within a fan disk (see Figure 1.3).

These three examples from the aeronautical industry should not lead people to think that aircrafts as a means of transportation are dangerous and the only means affected by fatigue phenomenon. If we calculate the distance to passenger ratio, flying remains the safest means of transport. Nevertheless, due to its rapid development and despite the work being done on its design, manufacturing and maintenance, we can predict that in about 10 years' time a major aircraft accident is likely to occur every week (see Figure 1.4). Let us keep in mind that human error is the main cause of accidents involving aircraft. Accidents caused by defects in the materials are still occurring in spite of improved manufacturing processes.

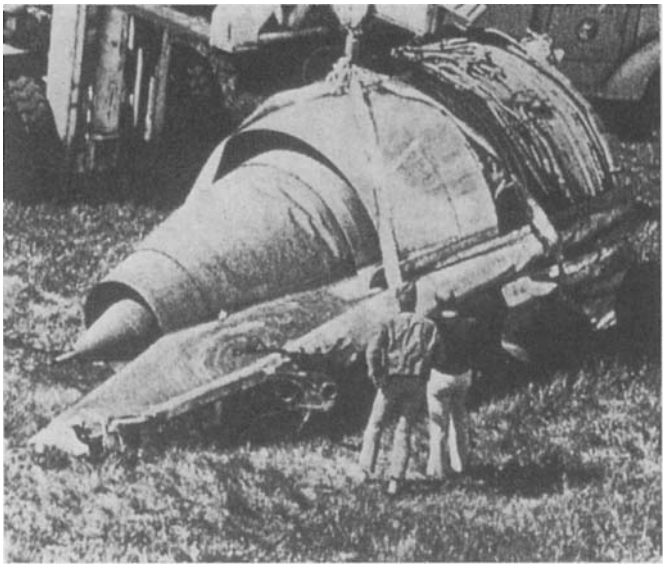

Figure 1.2. *DC 10 aircraft crash. Part of a detached engine. Sioux City Airport, July 19, 1989*

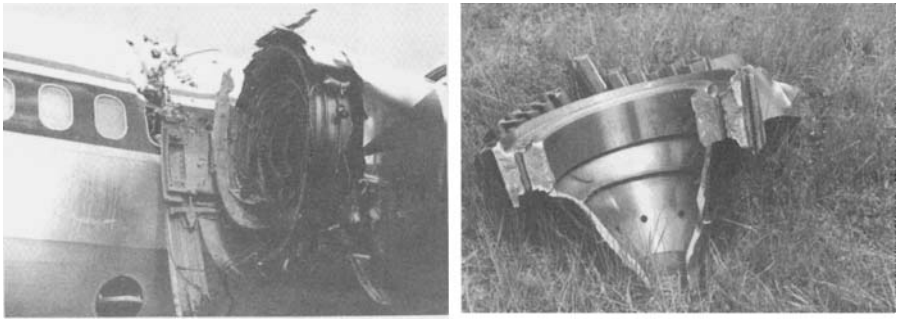

Figure 1.3. *Pensacola Crash (Florida, USA), July 6, 1996, was due to a failure during thetake off of a Delta Airlines MD-88 aircraft*

Fatigue also affects many other fields of transport, as shown in Figure 1.5 where cylinder heads of diesel engines subjected to increasing thermo-mechanical loading can break due to thermal and mechanical fatigue cracking if their design is wrong [SAL 07].

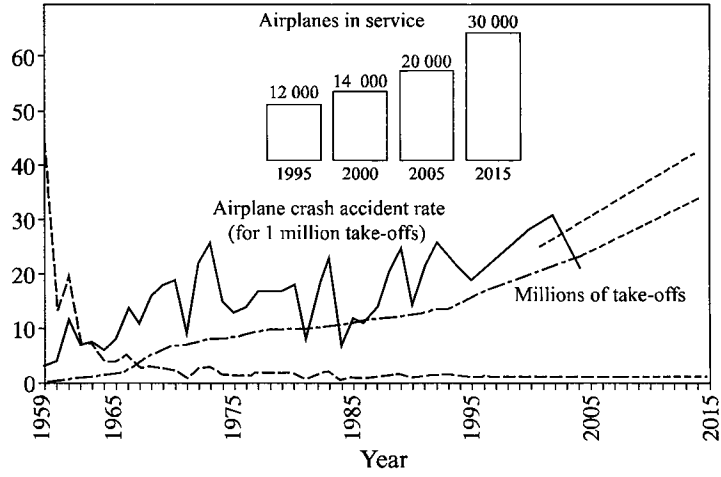

Figure 1.4. *Statistical study of the evolution of air traffic and of the number of crashes (MANHIRP, 2001, see also 1001crash.com)*

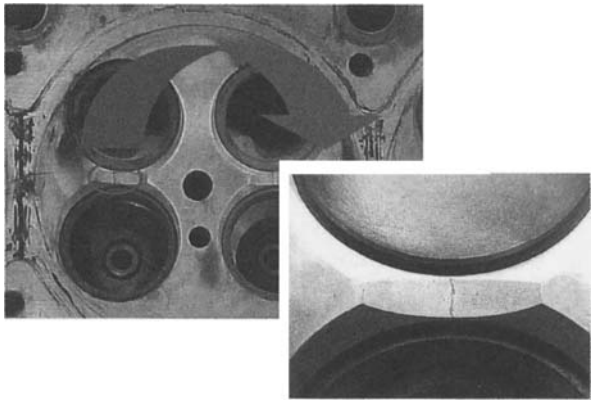

Figure 1.5. *Cracking within the cylinder head of a diesel engine [SAL 07]*

1.1.2. *Definitions*

Fatigue or *fatigue damage* refers to the modification of the properties of materials due to the application of stress cycles whose repetition can lead to fracture.

Uniaxial loading is defined as *the amplitude of the maximum stress* during a cycle σ_{max}. The *stress ratio* R is the ratio between the *minimum stress* σ_{min} and the

maximum stress σ_{max}, that is to say $R = \sigma_{min}/\sigma_{max}$. We sometimes have to distinguish the *alternating component* σ_a from the mean stress σ_m. Thus, depending on the relative values of these two components, we can differentiate the tests under different stresses (see Figure 1.6), such as:

– fully reversed: $\sigma_m = 0$, $R = -1$;

– asymmetrically reversed: $0 < \sigma_m < \sigma_a$, $-1 < R < 0$;

– repeated: $R = 0$;

– alternating tension: $\sigma_m > \sigma_a$, $0 < R < 1$.

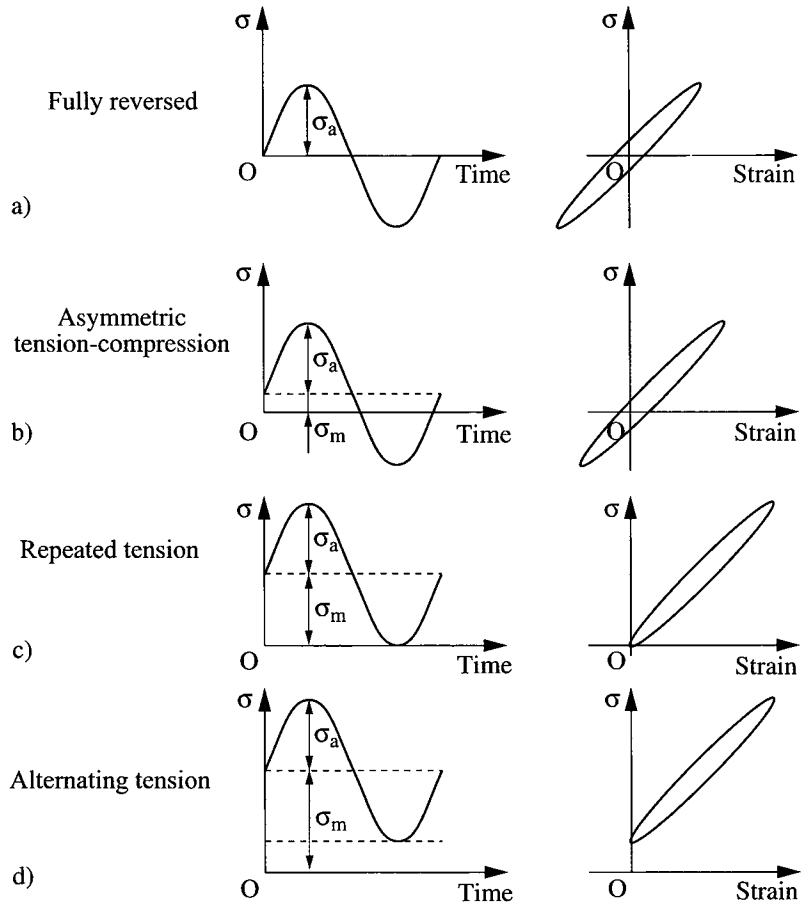

Figure 1.6. *Different cases of fatigue stresses: load-time; force-strain*

Plastic deformations occur with low-cycle fatigue (see Chapter 4). Usually, the fatigue phenomenon occurs without any general plastic deformation, which makes it less likely to be noticed. Nevertheless this phenomenon occurs with a localized plastic deformation around pre-existing defects within the materials, at the notches of the structures, or at the tips of a crack when it has already been initiated.

For multi-axial loading, which will be presented in [BAT 10], the definition of a strain amplitude is much more subtle, especially when loading is not proportional.

Fatigue is rarely perfectly cyclic (of constant amplitude and frequency), as shown in Figure 1.6. In many cases (thermal engines, bridges, etc.), loads have variable amplitudes and frequencies. These kinds of loads are examined in detail in Chapter 12.

Theoretically, fatigue damage only depends on the number of cycles and not on their frequency. As a matter of fact in most cases frequency does have a consequence. This is the case when environmental and visco-plasticity effects at high temperatures are involved (see Chapters 10 and 11).

In general, *lifetime* is measured using the number of cycles to failure, N_F. When N cycles have occurred ($N < N_F$) a given damage is accumulated and has to be evaluated. This allows us to determine the residual lifetime of the structure and the management of its operation, such as the timing between aircraft inspections.

We define *endurance* as the strength capability of components and entire structures before fatigue develops.

Thus, in general, fatigue occurs as soon as time dependent forces are involved. As a consequence, fatigue damage is characterized by its danger, which is basically that fracture can occur at low cycle stresses that in most cases are lower than the tensile strength and even lower than the elastic limit of the material.

1.1.3. *Endurance diagrams*

The easiest fatigue test consists of subjecting each specimen to periodic loading cycles, most frequently sinusoidal, with a maximum amplitude J_a, along with a constant frequency. The number of cycles is measured once rupture starts to occur (N_F). We then obtain a curve which looks like the one plotted in Figure 1.7.

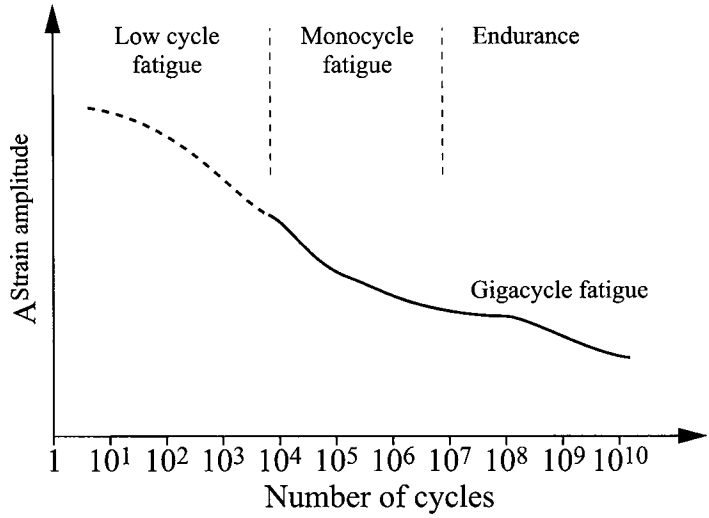

Figure 1.7. *Wöhler curve and definition of the various endurance areas*

With this curve, known as the Wöhler curve, SN curve (*stress-number of cycles*) or endurance curve, we can differentiate four different regions:

– with a high stress, we get *low cycle plastic fatigue*. Within this region, studied later on in Chapter 4, fracture occurs after a relatively low number of cycles (10^2 to 10^4) along with a significant plastic deformation. This type of damage has been studied since the 1950s, following Manson [MAN 52] and Coffin [COF 54] who introduced the Coffin-Manson law;

– with a lower stress there is a fatigue region where endurance is limited. Within this region, fracture occurs for a given number of cycles. The lower the stress amplitude, the higher the number of cycles. The region of limited endurance is presented in Chapter 2;

– an endurance region, which has been considered as an infinite lifetime, or safety region, corresponding to what is called the endurance limit. For steels, this region is reached after 10^6 to 10^7 cycles. In reality metal alloys have no real endurance limit. This has led us to consider the fourth (gigacycle) region in the past 10 years;

– a region corresponding to the *gigacycle* fatigue, which is significant for a given number of applications. Within this region, studied in Chapter 5, we often see that the "endurance limit" still decreases when the number of fracture cycles increases.

1.2. Mechanisms of fatigue damage

1.2.1. *Introduction/background*

On the Wöhler curve (see Chapter 2) we can see four stages, as shown in Figure 1.8, where, in contradiction with what is described in the previous figure, an endurance limit σ_d is highlighted for demonstration purposes. The upper region I corresponds to conditions in which specimens are broken. The lower region IV corresponds to the cases of unbroken specimens, where curve A separates both regions. Within the area directly below curve A, we can see two new regions located above the endurance limit: region III corresponding to the initiation of a crack, and region II associated with the propagation of this crack, the number of corresponding cycles being N_p. We can also see that initiation N_i represents the main part of the lifetime when the number of cycles to failure N_F, is high.

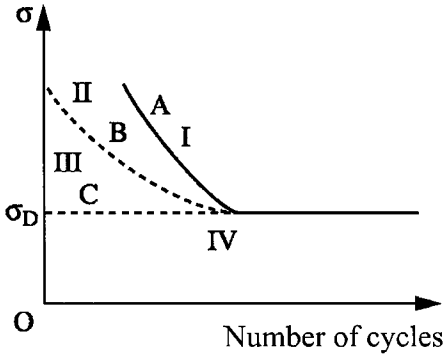

Figure 1.8. *Wöhler SN curve (A) and number of crack initiation cycles (B)*

Numerous fatigue damage indicators, in addition to crack initiation and propagation, have been studied, such as electrical resistivity. For a decade, infrared thermography has been used, providing researchers with encouraging results [DOU 04, LUO 95, LUO 98]. However, it is still too early to know whether this method can provide reliable results, and especially whether it can be used to speed up the determination of endurance curves.

1.2.2. *Initiation of fatigue cracks*

Since the first observations were made using optical microscopy in 1903 by Ewing and Humphrey [EWI 03], the initiation of fatigue cracks has been widely studied. In the mid-1970s the articles published by Thompson and Wadworth [THO

58] and by Laird and Duquette [LAI 71] enabled a review to be written on this subject. Since then, significant efforts have been devoted to this stage of fatigue damage.

Work carried out by Forsyth [FOR 51, FOR 53] showed that fatigue damage is mainly surface related. On the polished surface of the specimens, we can observe steps due to the formation of localized deformation bands, known as *persistent slip bands*. These bands are formed on the sliding planes with a maximum resolved shear stress. The mechanisms by which these bands form are presented in Chapter 4. Topography of the surface reveals the formation of *intrusions* and *extrusions*, as shown in Figure 1.9.

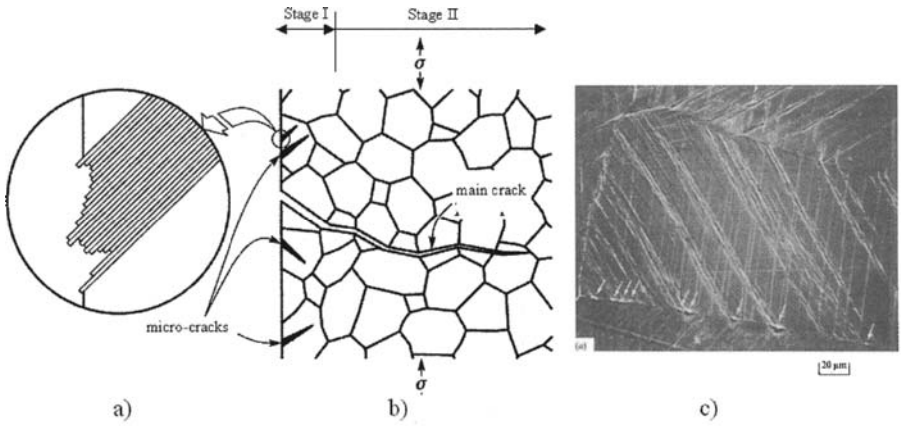

Figure 1.9. *a) Initiation of micro-cracks due to the sliding of alternate planes and to the formation of intrusions and extrusions at the free surface (cross-section); b) formation of a main crack from micro-cracks; c) characteristic formation of stage I intrusions and extrusions at the surface of a fatigue specimen made of copper*

During a uniaxial test on polycrystalline specimens, these bands, which will lead to the formation of *stage I* micro-cracks, appear at a 45 degree angle to the tensile axis. Only a few grains are involved in the formation of these bands. Orientation of the persistent bands and of the stage I cracks is significant not only in the case of a uniaxial loading (tension or torsion), but also in the case of a multi-axial loading where the directional characteristic of fatigue damage is essential. Brown and Miller [BRO 79, MIL 91] have introduced the really useful notion of type A and B facets regarding multi-axial loading, as shown in Figure 1.10. As expected, type B facets, whose slip vector goes into the material, are usually more dangerous than type A facets, whose slip direction is tangent to the free surface of the specimen. Unfortunately, few studies have been carried out regarding this directional

characteristic that occurs at the start of fatigue damage. We can nevertheless list some studies, such as the one carried out by Jacquelin [JAC 85].

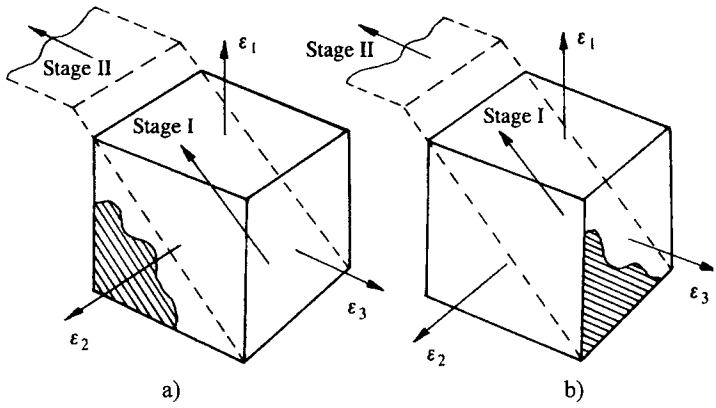

Figure 1.10. *Directional characteristic of fatigue damage. The significance of the orientation of the strain field compared to the surface plane and free surface plane (cross hatched); a) type A facet; b) type B facet*

Intrusions and extrusions, associated with persistent slip bands and the micro-propagation of stage I cracks, extend over a distance of the order of the grain size. Indeed, as soon as this micro-crack of significant crystallographic nature hits the first grain boundary it branches off, following a stage II course and then propagates perpendicularly to the direction of the maximum principal stress.

The definition of initiation remains ambiguous as it depends on the chosen scale. We usually define this damage stage as corresponding to the number of cycles, N_i, that have to be applied before the crack branches to stage II. Here, the corresponding distance is similar to the size of a grain. To the best of our knowledge, this is the most plausible definition. The most commonly accepted definition, which corresponds to the failure of a specimen or to the reduction of the maximum tensile stress by a certain amount (for example 5%), is not accurate enough.

1.2.3. *Propagation of fatigue cracks*

Stage II crack propagation according, that is to say in mode I, has been studied frequently since the early work by Paris and Erdogan in 1963 [PAR 63]. When these cracks are long enough, the rate of crack propagation, as presented in Chapter 4, can be described using Paris' law:

$$\frac{da}{dN} = C(\Delta K)^m \qquad [1.1]$$

where a stands for the length of the crack and ΔK for the variation of the stress intensity factor K, whereas C and m are constants, depending on the material. The loading ratio R is also important. The various laws proposed are listed in Chapter 4.

A region between stage I and the long crack stage is known as the *short crack* stage. It has been extensively studied since Pearson published his work on the topic in 1975 [PEA 75]. He proved that short cracks propagate faster than long cracks at the same apparent value, ΔK. This short-crack phenomenon is significant and is presented in Chapter 7. It increasingly appears that the particular behavior of short cracks, or at least those termed "physically short", can mainly be explained by their tri-dimensional aspect and by the crack closure phenomenon [LIN 95, PIN 86] concept introduced by Elber in 1970 [ELB 70].

Paris' law is purely phenomenological. Since then, some authors have tried to develop and improve this law using the properties of materials. These authors have developed what we call a local approach to fatigue crack. The principle of this approach is to start from the crack tip stress-strain field ahead of the crack-tip (see Chapters 8 and 9) and then introduce a fatigue failure criterion. The first model of this type was proposed by McClintock in 1963 [CLI 63], who assumed that the crack propagates in successive stages under the effect of low-cycle fatigue-type damage. The law thus formulated by McClintock considers that the exponent m in Paris' law [1.1] is equal to four and a non-propagation crack threshold ΔK_{th} is involved. A second model was also suggested by McClintock in 1967 [CLI 67], due to the observations of Pelloux [PEL 64] and McMillan [MIL 67]. These authors showed that fatigue failure surfaces were covered with striations – one striation corresponding to one cycle – at least in a certain region of crack propagation rates (0.01 to 1 μm/cycle). McClintock then related crack growth rate per cycle, being the distance between the striations, to the blunting at the crack tip (see Chapter 6). This model then considers that the slope m of Paris' law is equal to two. In practice, we can observe that the value of this exponent goes from two to six in the case of most materials. Since McClintock developed his models, others have been proposed (see Chapters 6, 8 and 9 for more information).

1.3. Test systems

The most commonly used method to obtain endurance curves is the rotating bending or plane bending test (see Figure 1.11). The machines used for these tests allow for frequencies close to 20 Hz.

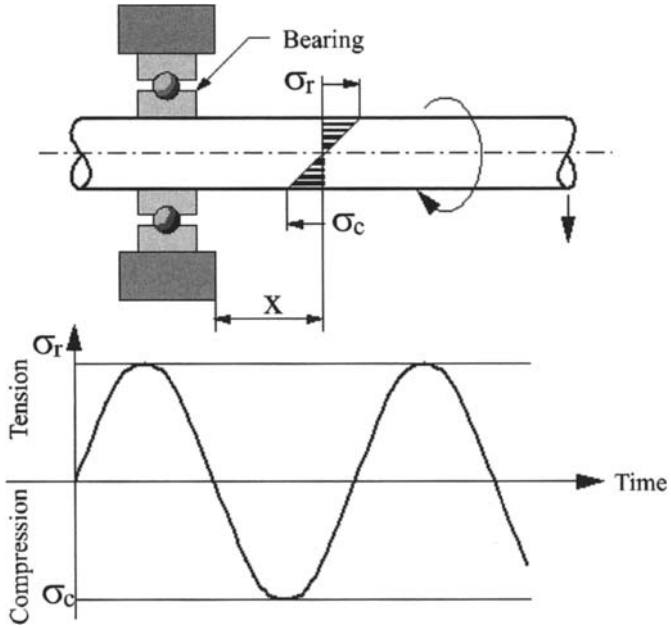

Figure 1.11. *Principle of rotary bending tests*

These machines are simple to use and relatively inexpensive. We can also use these machines to perform some traction/compression tests. The advantage of this is that the effect of a constant stress through the section of the specimen can be observed. The choice of specimen and loading mode is significant because a size effect is involved. Thus, with similar conditions, and especially with a similar cyclic stress, the tension-compression endurance is lower than that calculated in the case of rotary bending, itself being lower than that measured using plane bending.

Determination of an endurance curve takes a long time. A failure test with $N_F = 10^7$ cycles performed at 20 Hz lasts around six days. In addition, the test results are scattered. This is why testing methods were developed very early on to determine the endurance limit of metallic materials at higher frequencies (see Chapter 2). In the case of polymers and elastomers, the frequency has to be further reduced, otherwise significant over-heating is observed.

Resonance machines have been developed in order to perform higher frequency tests on metallic materials. Some specific machines can enable much higher frequency tests (close to 20 KHz) and thus allow us to study the region of gigacycle fatigue (see Figure 1.7). Chapter 5 deals with this particular topic.

All of these tests have been carried out with a load or imposed strain within the elastic region. Low-cycle fatigue tests, however, are performed under strain control, meaning that an extensometer system has to be used. The servo-hydraulic machines were developed in the mid-1960s for that purpose. A description of these tests, specimens and of extensometers can be found in Chapter 4.

More specific and less common machines have to be used in order to carry out multi-axial fatigue tests. Tension-torsion fatigue tests on thin tubes are well developed. The introduction of an internal/external pressure within the traction-torsion stressed tubes allows the degree of multi-axiality to be increased. These machines are less commonly found in practice, especially the ones allowing a range of temperatures to be studied. The downside (or the advantage, depending on the context) of these tests, is that the reference of the main stresses is not fixed. This issue can be overcome if a machine that can exert independent forces along three orthogonal directions (XYZ) is used. Only one machine of this type can be found in France. Biaxial machines (XY), however, are easier to use in order to test relatively thin materials.

1.4. Structural design and fatigue

Since Wöhler, engineers have developed new mechanical parts that are capable of resisting fatigue. The improvement of fatigue tests came hand-in-hand with the improvement in design methods.

The initial idea of an infinite lifetime or a fatigue limit under which a propagating fatigue crack could not form within a metal, has been questioned. At the same time, experiments based on Gauss statistics around the notion of a fatigue limit in order to predict an infinite lifetime related to a quasi-asymptotic SN curve were questioned. Statistics therefore had to be introduced to fatigue test results and the design methods were no longer purely deterministic but probabilistic.

As an example, we can consider a research engineer working in the aeronautical industry. He designed the "Caravelle" aircraft, in the 1950s, as beams put together under bending conditions, using Timoshenko's strength of materials approach. "Concorde" was the first aircraft in which the fracture mechanics was partially applied in 1970. The design of the European supersonic aircraft was first based on the conventional concept of strength of materials but was then improved using the notion of fail safe, which was developed from the application of fracture mechanics. Following this, the "Airbus" was the first aircraft to be built using the *damage tolerance* design in 1980.

In scientific terms, the main stages in the development of mechanical design are listed below chronologically:

– *safe life*: the structure is designed so that the stresses remain lower than the endurance limit. No defect is considered or accepted;

– *fail safe*: the structure is designed in relation to the residual strength of the metal when a planar defect, representing a crack, is involved. Some defects are accepted;

– *safe crack growth*: the failure mechanism allows the crack growth instability to be deterministically predicted.

A fourth approach – the *local approach to failure* – has recently been developed in France to overcome problems in the analysis of the fatigue of metals. In addition to this, the discovery of gigacycle fatigue in the 1990s highlighted the critical role of microscopic defects, such as inclusions, porosities, large grains due to forging, etc.

Micro-cracks remain the most harmful lifetime defects in the region of a few million cycles and micro-defects control billion cycle lifetime, the latter being the lifetime of engines, turbines and bearings. The initiation of distortion bands around the defects is then essential. Control of resistance to fatigue caused by micro-defects has been extensively studied. The notion of infinite lifetime obviously has to be discarded and the failure mechanism along with its *local approach* have to be added to the study of the resistance of materials to fatigue failure.

1.5. Fatigue of polymers, elastomers and composite materials

As modern industry commonly replaces one material with another, the fatigue of non-metallic materials is worth mentioning. Moreover, a global representation of material fatigue is fundamentally worth studying. This topic will be covered in [BAT 10].

All materials are prone to fatigue damage in their own way.

We can basically say that the fatigue of metals arises from:

– plasticity;

– general plasticity during low-cycle fatigue;

– plasticity during mega-cycle fatigue under plane stress; and

– micro-plasticity on a grain-scale during gigacycle fatigue.

In any case, dislocation debris accumulates in permanent slip bands before the first cracks develop (see Figure 1.12).

It would be a mistake to consider the fatigue of non-metallic materials as related to plasticity because there is no dislocation within amorphous or semi-crystalline polymers. Damage mechanisms in polymers are related to the formation of cavities or cavitations, two terms used to differentiate the effects of stress tri-axiality and the hydrostatic tensor. When plane stress prevails, fatigue quasi-cleavages can appear within some polymers. All these mechanisms are related to the progressive degradation of macromolecules and have no physical relationship to the plasticity of metals (see Figures 1.13 and 1.14).

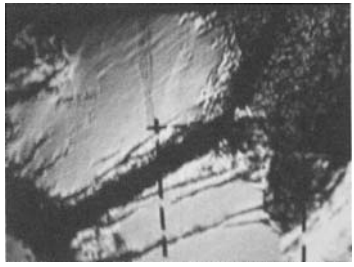

Figure 1.12. *Slip bands within low carbon steel*

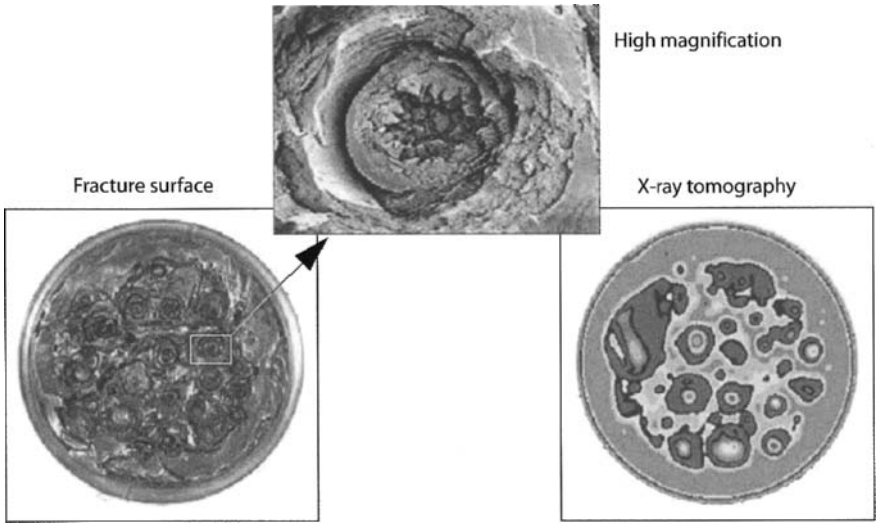

Figure 1.13. *Cavitations due to hydrostatic tension in an NR rubber*

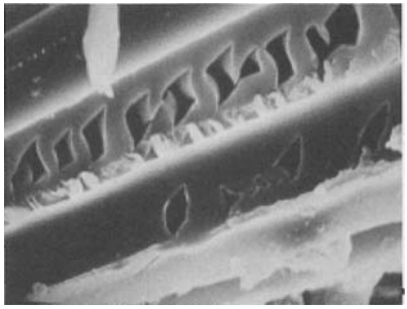

Figure 1.14. *Shear damage in epoxy matrix glass fiber composites*

Basically, fatigue of metals is modeled from von Mises plasticity criteria, based on the stress tensor deviator. This approach is totally justified by solid physics, which confirms that dislocation slip is governed by the shear components of the stress tensor. Experiments have shown that the formation of cavities, cavitations and quasi-cleavages within polymer materials do not just depend on shearing, but also on the principal main strains and the hydrostatic part of the stress tensor. As a consequence, von Mises' criterion and its variations do not apply to the modeling of plastics, rubbers and fibrous composites. This has many important consequences. For instance, an elastomer can crack due to compressive fatigue or under hydrostatic loading, which is not the case with metals. Another example is the substitution of a metallic part with a glass-fiber epoxy matrix in order to overcome the issue of fatigue as fatigue will be increased due to tension but decreased due to compression.

We therefore have to keep in mind that the stress deviator is a main parameter in metal fatigue.

1.6. Conclusion

Fatigue is of major technical and scientific importance. The design of many components is directly related to this type of damage. Fatigue is still the subject of numerous studies at various scales, from dislocations and point defects to macroscopic cracks.

In this book, we have gathered the reviews of experts in this type of loading and damage. The first volume mainly deals with metallic materials whose various damage sequences (initiation of stage I cracks and stage II propagation) are well known. For greater elucidation on the topics covered in this book, we have quoted experts in physical and mechanical metallurgy, fracture mechanisms and the local

approach to failure. Environment and corrosion effects, which are of particular significance, are also discussed.

Finally, a whole chapter has been dedicated to the case of fatigue due to loading of variable amplitudes, which is commonly found in practice.

1.7. Bibliography

[BAT 10] C. Bathias, *Fatigue of Materials and Structures: Application to Damage and Design*, ISTE, London, John Wiley, New York, 2010.

[BAT 05] C. Bathias, P.C. Paris, *Gigacycle Fatigue in Mechanical Practice,* Marcel Dekker, New York, 2005.

[BAT 97] C. Bathias, J.P. Baïlon, *La Fatigue des Matériaux et des Structures,* Hermes, Paris, 1997.

[BRA 1854] F. Braithwaite, "On the fatigue and consequent fracture of metals", *Institution of Civil Engineers, Minutes of Proceedings*, vol. XIII, p. 463-474, London, 1854.

[BRO 73] M.W. Brown, K.J. Miller, "A theory for fatigue failure under multiaxial stress-strain conditions", *Proceedings of the Institution of Mechanical Engineers*, vol. 187, p. 745-755, 1973.

[CLI 63] F.A. McClintock, "On the plasticity of the growth of fatigue cracks", *Fracture of Solids*, John Wiley, New York, 1963.

[CLI 67] F.A. McClintock, "Fatigue crack propagation", *ASTM STP 415*, written discussion, p. 170, 1967.

[COF 54] L.F. Coffin, "A study of the effect of cyclic thermal stresses on a ductile metal", *Trans. ASME*, vol. 76, p. 931-950, 1954.

[DOU 04] C. Doudard, S. Calloch, F. Hild, P. Cugy, A. Galtier, "Identification of the scatter in high cycle fatigue from temperature measurements", *C.R. Mécanique*, vol. 332, p. 795-801, 2004.

[ELB 70] W. Elber, "Fatigue crack closure under cyclic tension", *Eng. Fract. Mech.*, vol. 2, p. 37-45, 1970.

[EWI 03] J.A. Ewing, J.C.W. Humphrey, "The fracture of metals under repeated alternations of stress", *Phil. Trans. Royal Soc. London*, vol A.200, p. 241-250, 1903.

[FOR 51] P.J.E. Forsyth, "Some metallographic observations on the fatigue of metals", *J. Inst. Met.*, vol. 80, p. 181, 1951.

[FOR 53] P.J.E. Forsyth, "Exudation of material form slip bands at the surface of fatigued crystals of an aluminum copper alloy", *Nature*, vol. 171, p. 172-173, 1953.

[HEN 05] G. Henaff, F. Morel, *Fatigue des Structures*, Ellipses, Paris, 2005.

[JAC 85] B. Jacquelin, F. Hourlier, A. Pineau, "Crack initiation under low cycle multiaxial fatigue", *ASTM-STP 853*, p. 285-313, 1985.

[LAI 71] C. Laird, D.J. Duquette, *Proc. 2nd Int. Conf. Corrosion Fatigue*, NACE, Houston, pp. 88-117,1971.

[LEM 01] J. Lemaitre, "Petite histoire de l'expérimentation en mécanique des solides", *Meccanica*, vol. 36, p. 13-51, 2001.

[LIN 95] T. Lindley, A. Pineau, "Short crack effects in fracture and fatigue", *Rev. de Mét.*, vol. 92, p. 187-201, 1995.

[LUO 95] M.P. Luong, "Infrared thermographic scanning of fatigue in metals", *Nucl. Eng. Design*, vol. 158, p. 363-376, 1995.

[LUO 98] M.P. Luong, "Fatigue limit evolution of metals using an infrared thermographic technique", *Mech. Mat.*, vol. 28, p. 155-163, 1998.

[MAN 52] S.S. Manson, "Behavior of materials under conditions of thermal stress", *Heat Transfer Symposium*, University of Michigan Engineering Research Institute, p. 9-71, 1953.

[MIL 63] J.C. Mc Millan, R.M. Pelloux, "Fatigue crack propagation under program and random loads", *ASTM STP 415*, p. 505-535, 1963.

[MIL 91] K.L. Miller, "Metal fatigue-past, current and future", *Proc. Instn. Mech. Engrs.*, vol. 205, p. 1-14, 1991.

[MUR 02] Y. Murakami, *Metal fatigue: Effect of Small Defects and Nonmetallic Inclusions*, Elsevier, Amsterdam, 2002.

[MUR 03] Y. Murakami, "Cyclic loading and fatigue", in Ritchie R.O. (ed.), *Comprehensive Structural Integrity, Fracture of Materials from Nano to Macro*, vol. 4, Elsevier, Amsterdam, 2003.

[PAR 63] P. Paris, F. Erdogan, "A critical analysis of crack growth propagation laws", *J. Basic Eng*, vol. 85, p. 528-534, 1963.

[PEA 75] S. Pearson, "Initiation of fatigue cracks in commercial aluminum alloy and the subsequent propagation of very short cracks", *Eng. Fract. Mech.*, vol. 7, p. 235-247, 1975.

[PEL 64] R.M. Pelloux, "Fractographic analysis of the influence of constituent particles on fatigue crack propagation in aluminum alloys", *ASM Trans. Quart.*, vol. 57, p. 511, 1964.

[PIN 86] A. Pineau, "Short fatigue crack behaviour in relation to three-dimensional aspects and crack closure effects", in Ritchie R.O, Lankford J. (ed.), *Small Fatigue Cracks,* Metallurgical Society of AIME, Warrendale, PA, p. 191-211, 1986.

[POL 91] J. Polak, *Cyclic Plasticity and Low Cycle Fatigue Life of Metals*, 2nd edition, Academia, Prague, 1991.

[REI 91] K.L. Reifsnider, *Fatigue of Composite Materials*, Elsevier, Amsterdam, 1991.

[SAL 07] R. Salapete, PhD thesis, École des Mines, Paris, December 17, 2007.

[SCH 01] J. Schijve, *Fatigue of Structures and Materials*, Kluwer Academic Publishers, Dordrecht, 2001.

[SCH 03] J. Schijve, "Fatigue of structures and materials in the 20th century and the state of the art", *Int. J. Fatigue*, vol. 25, p. 679-702, 2003.

[SCH 96] W. Schutz, "A history of fatigue", *Eng. Fract. Mech.*, vol. 54, p. 263-300, 1996.

[SHA 07] S.A.A. Shaniavski, *Modeling of Fatigue Cracking of Metals, Synergetics for Aviation*, Ufa, Publishing House of Scientific and Technical Literature "Monography", 2007.

[SMI 90] R.A. Smith, "The Versailles railway accident of 1842 and the first research into metal fatigue", *Fatigue'90*, vol. IV, EMAS, Birmingham, p. 2033-2041, 1990.

[STE 1838] Stendhal, *Mémoires d'un Touriste*, Charité-sur-Loire, 13 Avril 1837, Ed Ambroise Dupont, p. 16, 1838.

[SUR 98] S. Suresh, *Fatigue of Materials*, Cambridge University Press, Cambridge, 1998.

[THO 58] N. Thompson, N.J. Wadworth, "Metal fatigue", *Adv. Phys.*, vol. 7, p. 72-169, 1958.

[TIM 53] S. Timoshenko, *History of Strength of Materials*, McGraw-Hill, New York, 1953.

[TOT 01] L. Totoh, "Fatigue crack growth laws and their material parameters", *Zeszyty Naukowe Politechniki Opolskiej. Siria: Mekanika z. 67*, vol. 269, p. 349-368, 2001.

Chapter 2

Modeling of Fatigue Strength and Endurance Curve

2.1. Introduction

Scatter of the results of fatigue tests is now accepted to be an experimental and physical fact. In the past, following a deterministic way of thinking, such scatter was considered to be due to imperfections in the test conditions and, as a consequence, it was assumed that scatter could be reduced *ad libitum*. The scatter is to be considered as a physical aspect of fatigue phenomenon. Moreover, from a practical point of view it is generally far too difficult and/or expensive to entirely remove some of the causes of experimental error, even if it is possible in theory. The simultaneous action of these two kinds of causes, both experimental and physical, leads to a scatter of test results that are rarely negligible with regard to the amounts being measured. On the contrary, in most cases such scatter is often important, and sometimes very significant.

Figure 2.1 gives an example of the scatter observed during some tests performed on a steel specimen.

This is why statistical methods have to be used in order to experimentally determine the characteristics of the fatigue phenomenon. These methods allow us to estimate either the fatigue strength at N cycles along with the corresponding

---

Chapter written by Henri-Paul LIEURADE in collaboration with François BASTENAIRE and Lionel RÉGNIER.

standard deviation or to draw the curve resulting from the amplitude of cyclic stress to the number of cycles to failure.

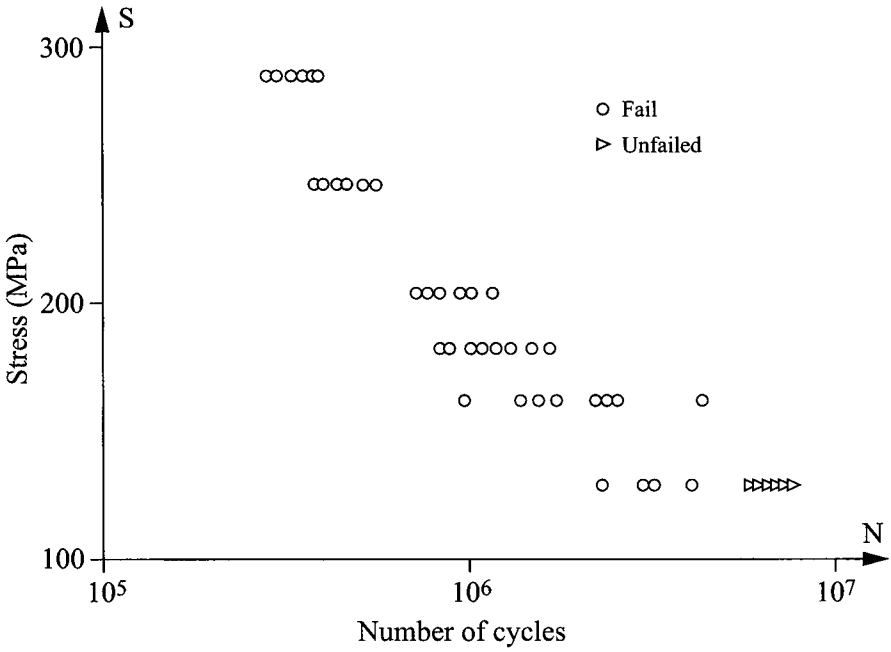

Figure 2.1. *Presentation of the test results using a Wöhler diagram (S-log N)*

Various factors influence fatigue resistance; in particular, the conditions of cyclic stress applications, which can relatively modify the fatigue strength of a piece or an entire structure.

In addition, many studies show that the endurance of a material is related to its ultimate tensile strength and ductility.

This is why, in the case of steels, several authors have suggested a rough estimation of the endurance limit by relating it to the characteristics measured during a tension test.

This chapter aims to present the main statistical methods that can be used to characterize fatigue behavior under simple loading of a material from test results and to specify the influence of the application conditions of cyclic stress.

2.2. Nature and aspect of the scatter of fatigue test results

The scatter we observe results directly from the nature and physiology of a material, which we can split logically into three parts:

– internal to the material;

– due or related to the preparation of the specimens or pieces;

– external to the specimen.

The nature and mode of action relating to the preparation of an environment surrounding the specimen seem to be the most obvious causes of scatter. The setting operations, which include turning, milling and straightening, for instance, relate to preparation of specimens/pieces. The settings are known to influence the endurance of the pieces, as well as the thermal treatments, so the results cannot be rigorously reproduced on other identical specimens from the same batch.

External causes of scatter include, in particular, the uncertainty of the setting within the test machines, and of adjustment of the applied loading, cycle frequency, etc., in addition to the fact that the influence of the surroundings is not negligible.

The causes of scatter, whose mechanisms of action are less well known, are those within the material: inclusions, structure heterogenities, etc. Moreover, these causes are not independent from the influence of preparation settings, which can modify the material and its heterogenity (especially the thermal treatments). Finally, the mechanism of damage itself involves a combination of the various causes of scatter.

Experience has shown us that the result of these combined actions generally leads to the characteristic response shape of SN curves.

If a given number of stress cycles N is set (see Figure 2.2a) and the observed event being the failure or non-failure of the specimen before this cycle number, we define the response to the SN curve – the curve representing the probability of this event – as a function of the amplitude of the cycles.

Various methods have shown that these curves are normal sigmoid shapes that can be represented by the distribution function of a variable with a normal distribution. The failure probability can then be expressed as a function of the amplitude S of the stress using the following equation:

$$P(S) = \frac{1}{\sigma\sqrt{2\pi}} \int_{-\infty}^{s} \exp[-(x - \mu)^2/2\sigma^2]dx \qquad [2.1]$$

where, μ represents the stress amplitude where the failure probability is equal to 0.5 and σ the parameter characteristic of the scatter.

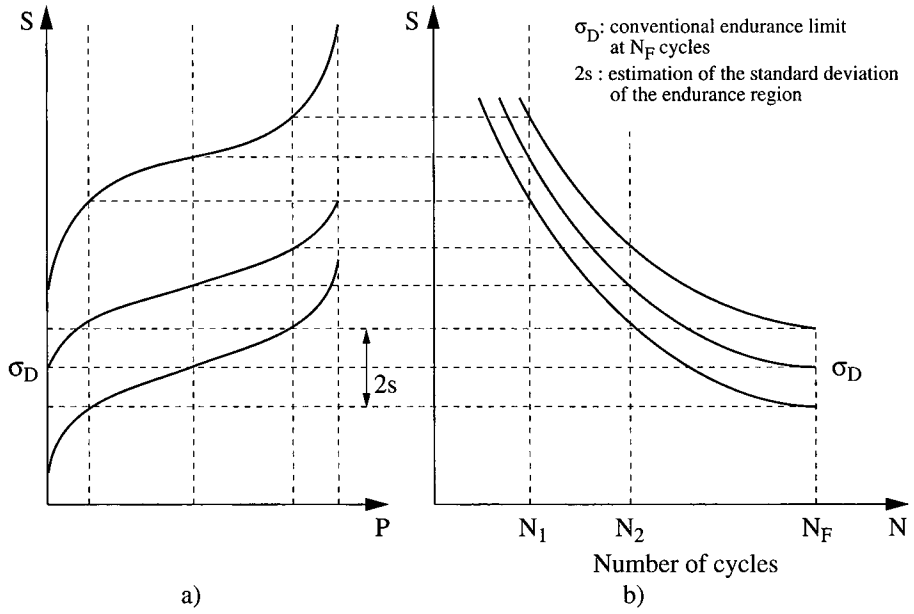

Figure 2.2. *a) Three responses to the stress curves; b) isoprobability curves (p = 0.16; p = 0.50; p = 0.84) using Wöhler's diagram*

The fact that failure probability follows equation [2.1] is similar to the "all or nothing" aspect and allows the application of various statistical techniques to the study of fatigue phenomenon.

Various methods used to deal with fatigue test results aim to estimate the parameters μ and σ of a response to the stress curve for a given number of cycles.

Estimation σ_D of the conventional endurance limit and s of the standard deviation of the endurance region is a particular case (see Figure 2.2a).

Every response to the stress curve allows a value of the amplitude of the stress S_p, whose failure probability is P, to be defined. However, S_p is obviously a function $S_p(N)$, of the number of cycles N and defines the curve of isoprobability of failure corresponding to P.

In Figure 2.2b, three isoprobability curves, respectively corresponding to $p = 0.16$ (average minus standard deviation), $p = 0.50$ (average) and $p = 0.84$ (average plus standard deviation) are shown.

2.3. Determination of the endurance limit

As we just stressed, a normal sigmoid response curve is defined by two parameters: its median and its standard deviation. Figures 2.2a and 2.2b show that these parameters are obviously a function of lifetime N, set for the tests.

In the case of steels, every failure equiprobability curve is supposed to present an asymptote; in particular, the equiprobability curve 0.5, which tends towards a limit called the "endurance limit".

In practice this limit cannot be reached and instead we use a conventional endurance limit σ_D, relative to a significant number of cycles N.

This value σ_D is related to a standard deviation called the "standard deviation of the endurance region" (standard deviation of the response curve, defined by equation [2.1] for the considered number of cycles N). Estimation of the standard deviation of the endurance region is represented by the symbol s.

2.4. Estimation methods of fatigue resistance and standard deviation with N cycles

The previous sections have shown that the estimation of fatigue resistance with N cycles and of its standard deviation or endurance limit, and the standard deviation of the endurance region, are actually the same problem.

The following estimation methods will be described and explained:

– the probit method;

– the staircase method;

– the iteration method;

– the method with K non-failed specimens.

The application of one of these methods, however, means that we need to know in advance the order of magnitude of fatigue resistance we want to study and the standard deviation of its response curve in order to choose the stress levels of the first tests and their spacing.

2.4.1. *Probit method*

2.4.1.1. *Principle*

The probit method is a method of numerical calculation used to estimate response curve parameters. We should make sure we do not confuse this with the test plane, which is supposed to provide the results that are going to be submitted. This confusion is common, however, because of a misuse of language. The test plane is itself really easy to calculate; or at least it seems to be. Its aim is simply to determine the response curve being sought.

As a stress amplitude has been chosen, n specimens are tested until a given number of cycles, N, selected for the tests. In these conditions, the number k of the specimens which, among these n, fail before N cycles, follows binomial probability distribution (the probability law of the number of specimens which, among n, lead to the birth of an event with a given probability).

The properties of the binomial law are well known. If p is the probability of the observed event, k will be, *on average*, equal to np[1]. Nevertheless, k is a random variable presenting a given scatter that we can characterize using either variance or standard deviation k.

Theory shows that the value of this standard deviation $\sigma(k)$ is:

$$\sigma(k) = \sqrt{np(1-p)} \qquad [2.2]$$

The real value p of the failure probability before N cycles under stress amplitude S is obviously unknown and tests are carried out in order to estimate it.

We can show that, using probability calculation, the estimation of p is given by frequency f:

$$f = \frac{k}{n} \qquad [2.3]$$

That is to say, in our case, by the ratio of the number of failed specimens k to the number n of those tested during similar tests.

If k is random, f is also random and the standard deviation of the frequency $\sigma(f)$ is given by:

---

[1] In more precise terms, the mathematical expected value of k is equal to np, which can be written as $E[k] = np$.

$$s(f) = \sqrt{\frac{p(1-p)}{n}} \qquad [2.4]$$

The above equation enables us to measure the uncertainty, which is used to estimate p. For instance, if we have $n = 20$ and $p = 0.25$, we get:

$$\sigma(f) = 0.10$$

If we consider that the distribution of f can be roughly characterized as twice the standard deviation, we can see that f is a poor estimation of p.

On the other hand, we understand that to define the studied response curve we need at least four or five points. For this reason we need to carry out about 100 tests. We will see that, despite the use of a statistical method of estimation allowing us to get the most information from the observations, it is hard to appreciably reduce this figure.

2.4.1.2. *Graphic representation of a response and test result sigmoid curve*

2.4.1.2.1. Galton's anamorphosis

If we define:

$$t = \frac{x - \mu}{\sigma} \qquad [2.5]$$

Equation [2.1], representing a response curve with parameters μ and σ can be written as:

$$P(S) = \frac{1}{\sqrt{2\pi}} \int_{-\infty}^{(S-\mu/\sigma)} e^{-t^2/2} dt \qquad [2.6]$$

The advantage of this representation is that, with the second member of the equation, we can use a function called the reduced Laplace-Gauss integral. This integral only depends on the upper integration end-point $(S - \mu)/\sigma$ and has tables that are known.

To simplify this, we consider:

$$G(u) = \frac{1}{\sqrt{2\pi}} \int_{-\infty}^{u} e^{-t^2/2}\, dt \qquad [2.7]$$

in such a way that equation [2.6] becomes:

$$P(S) = G\left(\frac{S-\mu}{\sigma}\right) \qquad [2.8]$$

Figure 2.3 gives a representation of function $P = G(u)$ and is summarized in Table 2.1, which gives some characteristic points of $G(u)$.

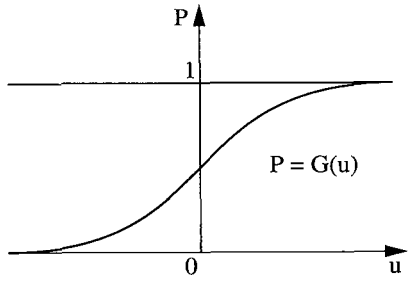

Figure 2.3. *Reduced Gauss integral*

$G(u)$	0.01	0.02	0.05	0.10	0.50	0.90	0.95	0.98	0.99
u	-2.326	-2.054	-1.645	-0.282	0	1.282	1.645	2.054	2.326

Table 2.1. *Characteristic points of G(u)*

We can observe that G is an increasing monotonic function, which enables us to reverse it; that is to say we can match a chosen value to every value p *a priori* given $(0 < p < 1)$ using u_p such as:

$$G(u_p) = p \qquad [2.9]$$

We define u_p as the reduced deviation corresponding to p.

As the value of u_p is unique, equation [2.8] of a response curve with parameters u and σ can also be written as:

$$\frac{S-\mu}{\sigma} = u_p \qquad [2.10]$$

or as:

$$S = \mu + \sigma u_p \qquad [2.11]$$

The above equation is of high practical importance as it enables us, using an appropriate choice of scale for p values, to replace the direct representation of a sigmoid curve (with $p(S)$, S as coordinates) by a line (with u_p, S as coordinates).

It is worth noting that this linear representation of a sigmoid curve can either use linear scales for S and u_p or directly display the value of p on the scale of u_p (see Figure 2.4).

The method dealing with the replacement of p with u_p is called Galton's anamorphosis and is widely used in order to represent response curves.

It is worth noting that, when $p = 0.50$, $u_p = 0$, and then $S = \mu$ according to equation [2.9].

We can also observe that, when the ordinates represent u_p, equation [2.9] can be written as:

$$u_p = \frac{S}{\sigma} - \frac{\mu}{\sigma} \qquad [2.12]$$

The slope of the line representing the response curve then has a value of $1/\sigma$. The higher this slope is, the lower the scatter σ is.

2.4.1.2.2. Plotting of experimental points

We already know (section 2.4.1.1) that failure frequencies with N cycles among n tests (k/n), is an estimation of the basic failure probability p.

Frequencies f_i, observed at different stages S_i of the stress amplitude and plotted within the same graph will then be averaged but a given scatter, on the line will represent the response curve (see Figure 2.4).

2.4.1.3. *Estimation of parameters μ and σ*

We can obviously graphically estimate μ and σ using a line crossing the (S_i, f_i) points, representing our observations. Estimation of μ is the value of S when $p = 0.50$. In order to estimate σ, we can use the fact that when $u_p = -1$, $p = 0.16$ and when $u_p = +1$, $p = 0.84$.

We then have, according to equation [2.11]:

$$S_{0.16} = \mu - \sigma$$

and:

$$S_{0.84} = \mu + \sigma$$

therefore:

$$\sigma = \frac{S_{0.84} - S_{0.16}}{2}$$

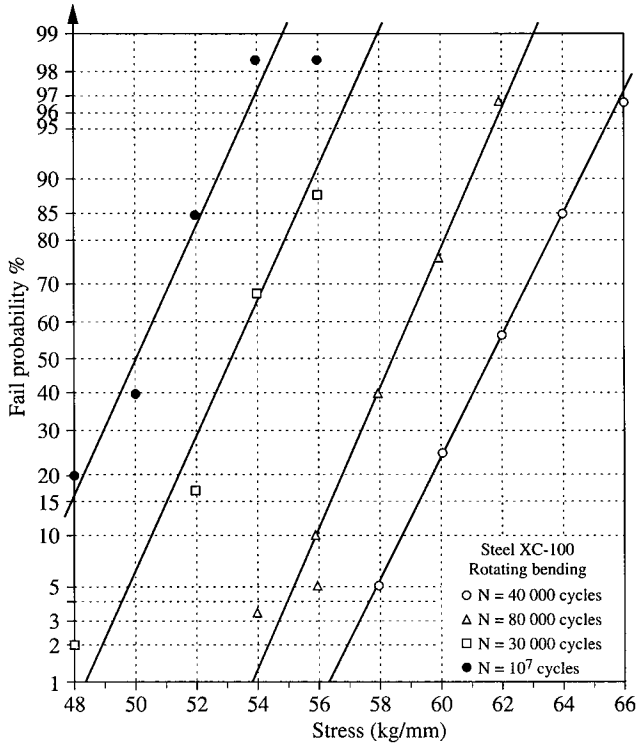

Figure 2.4. *Proportion of failed specimens with fewer N cycles as a function of the stress amplitude. XC100 (N= 30,000 to 10^7 cycles)*

We then determine the values of S that correspond respectively to $p = 0.16$ and $p = 0.84$ and divide their difference by two.

Nevertheless, the graphic estimation of μ and σ is a rough method and we recommend the use of a statistical method for calculating the estimations m and s of μ and σ.

Two of these statistical methods can be found: the "probit" method and the "maximum likelihood" method. The study of these methods is not our goal, however. Useful information about these two methods can be found in application examples in [FIN 72] and [ULM 52].

The observations that have been made above regarding the number of tests needed enable us to understand these methods are not commonly used for the study of fatigue. Nevertheless, we appreciate that when these tests have been performed there can be a genuine reason for the precise estimation of μ and σ and that, as a consequence, we should not stop at the graphic representation but should go further using numerical calculation.

2.4.1.4. *Conclusions*

The "probit" method (wrongly termed as we do not proceed to a numerical operation of the test results using the real "probit" method [FIN 72, ULM 52]) takes a long time to be carried out. It is also expensive as a high number of tests is required and is hard to perform. It will therefore only be used for fundamental studies, when we are seeking sufficiently precise determinations of fatigue resistance and especially the standard deviation of response to the stress curves. It can also be used if we want to test, at the same time, the normal sigmoid shape of these curves (using χ^2 tests) [FIN 72, ULM 52].

In other cases, it is better to apply application methods that are simpler, like ones presented in the next section.

2.4.2. *Staircase method*

The drawbacks of the "probit" method led to the birth of other application methods that are simpler and cheaper.

In 1948, Dixon and Mood [DIX 48] proposed the "staircase" method. The test stress stages can be found much more easily using this method. It can be carried out automatically and gives the user a wide choice of the number of tests required (which can be much lower than the "probit" method). However, if the method can be performed with a low number of tests, we should still bear in mind that the precision (accuracy and fidelity) of the results obtained will strongly depend on it.

2.4.2.1. *Rules of the staircase method*

As was the case regarding the "probit" method, we set a maximum test duration N and define a spacing of the stain amplitudes through arithmetic evolution, whose pitch has a value similar to that of the standard deviation σ, of the response curve.

The first test will be carried out at the level of spacing *a priori* thought to be the closest to the targeted median μ. From the second test, the stress amplitude level can be chosen:

– for the new test, if the previous test did not lead to failure we should choose a higher spacing stresses stage than the one used during the last test;

– if the previous test led to failure, we should choose the stage that is lower.

In other terms, as d stands for the spacing pitch of the stresses and S_i for the accepted value regarding the i-th test, we will consider that:

– $S_{i+1} = S_i + d$ when the i-th tested specimen did not fail;

– $S_{i+1} = S_i - d$ when the i-th specimen failed.

The tests can then be carried out following this rule, one after another, until all n available specimens have been used.

Figure 2.5 gives an example of a batch of this type of test.

2.4.2.2. *Use of the results*

Test results obtained using this method enables us to estimate the median resistance of fatigue with the number of given cycles and, usually, the standard deviation. The calculation to be performed is simple. We first determine the type of event that occurred *less frequently* during the test batch: failure or non-failure. The results of this type are enough for the calculation and are more acceptable compared to other ones. The fact that the results of a given type (failures, for instance) outnumber others is often due to the choice of a starting stage that is a long way from the value to be estimated. The sequence then begins with an uninterrupted test from a batch of the same type whose inclusion would lead to a systematic error.

We count the number N_i of implementations of this event for each test stage, and then number these stages with the attribution of value $i = 0$ to the lowest of those stages observed at least once. As i stands for the number of the test stage, we then have to calculate the following:

$$N = \sum_i N_i; \quad A = \sum_i i.N_i \quad \text{and} \quad B = \sum_i i^2.N_i$$

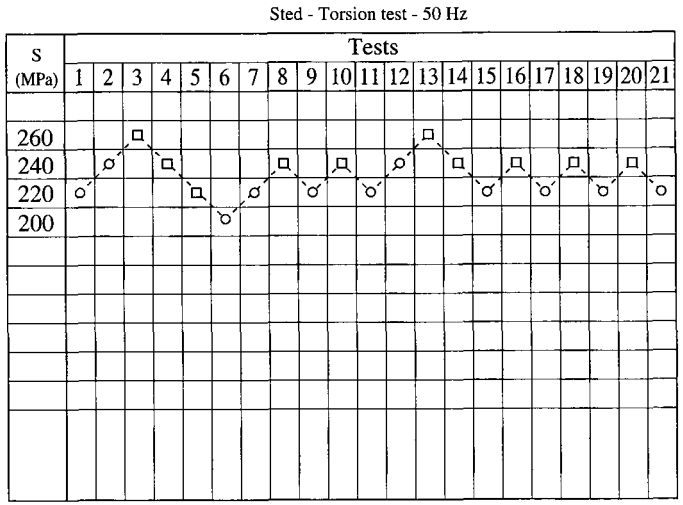

i	N_i	$1N_i$	1^2N_i
4			
3			
2	2	4	8
1	7	7	7
0	1	0	0
Σ	N:10	A:11	B:15

$$\Sigma^* = S_0 + d\left(\frac{11}{10} \pm \frac{1}{2}\right)$$
$$= 232 \text{ MPa}$$

d = 20 MPa
□ : 10 failed
o : 11 unfailed

Figure 2.5. *Staircase method*

The table in Figure 2.5 shows us how to perform these calculations in the case where the results obtained are related to the failures.

Estimation of m and μ is obtained using the following equation:

$$m = S_0 + d\left(\frac{A}{N} \pm \frac{1}{2}\right) \qquad [2.13]$$

where:

– S_0: index 0 stage, as defined above (the lowest stage used allowing us to obtain at least an accepted type of result);

– d: stage spacing:

- +1/2 when calculation is based on the test stresses of the non-broken specimens;

- -1/2 when based on the test stresses of the failed specimens.

The staircase method also enables us to obtain an estimation s of the standard deviation σ of the response to the stress curve:

$$s = 1.62\,d\left(\frac{NB - A^2}{N^2} + 0.029\right) \qquad [2.14]$$

According to Dixon and Mood [DIX 48], equation [2.14] can only be used if the following condition is true:

$$\frac{N B - A^2}{N^2} > 0.3 \qquad [2.15]$$

As a matter of fact, estimation of the standard deviation of the response to the stress curve, using the staircase method, has to be taken cautiously when the number of tests is lower than 50. Estimation of this standard deviation is not any better, for the same number of tests, than estimates obtained using the "probit" method.

2.4.2.3. *Precision of m and s*

The estimation m of μ is usually scattered with a negligible bias and a standard deviation:

$$\sigma_m = \frac{G}{\sqrt{N}} \qquad [2.16]$$

where G is a factor depending on the d/σ ratio:

$$G \approx 1 + \frac{d}{8\sigma} \qquad [2.17]$$

The estimation s of σ presents a significant bias, as a function of d/σ. Scatter of s is also a function of d/σ. When $d = \sigma$, where it is close to its minimum, the accuracy of the estimate of standard deviation σ is almost equivalent to the accuracy based on quantitative data with $N/3.5$ degrees of freedom.

2.4.2.4. *Observation on the practical application of the staircase method*

In section 2.4.2.1, we mentioned that the spacing d should be of the same magnitude as σ. In practice, the estimation m of μ remains satisfying as long as $1.5 < d/\sigma < 2$. The estimation s of σ, already less satisfying in optimum conditions ($1 < d/\sigma < 1.5$), rapidly becomes wrong if we move away from these conditions.

2.4.3. *Iteration method*

This method is applied to cases where the response curve is estimated using an alternative more general method designed by Robbins and Monro [ROB 51].

The probability distribution of a random variable Y is supposed to be a function of a parameter x, so that $E[Y/x]$ (the expected value or average value of Y to x) is a monotonic function of x. Robbins and Monro's method aims to estimate the value of x when $E[Y/x] = Y_0$, with Y_0 being an *a priori* fixed value.

Regarding the application of Robbins-Monro's law to the estimation of fatigue strength, Y is the failure proportion observed and x the stress amplitude. Indeed, the conditions of application of Robbins-Monro law are very wide. Random variable Y can also be distributed according to a discontinuous probability law (which is the case of a proportion, especially when there are few elements) rather than a continuous one.

2.4.3.1. *Rule of the testing method following the iteration method*

As is the case with the staircase method, the iteration method defines for each test (except for the first one) the stress to be applied as a function of the result obtained during the previous test. Nevertheless the stress loading, instead of being constant, varies and is defined by the test order number.

The choice of stress to be applied during the first test is very important. It has to be as close as possible to the stated value. The acceptable deviations between the applied stress during the first test S_1 and the value to be determined will be presented later.

Tests can be carried out in groups of any size, and even separately – that is to say specimen by specimen.

Each group of tests performed with the same stress S_i enables us to determine a failure frequency f_i.

Let p be a randomly chosen failure probability, σ the standard deviation of the response curve and A a properly chosen constant. We can prove that the sequence of the values, defined as:

$$S_{i+1} = S_i + \frac{A\sigma}{i}(p - f_i) \qquad [2.18]$$

converges towards the value $S(p)$, whose failure probability is p. We usually use this method to estimate the median of the response curve and consider that $p = 0.5$, but it is also worth noting we can estimate another point of this curve if we wish. An example of the application of this method is given in Figure 2.6.

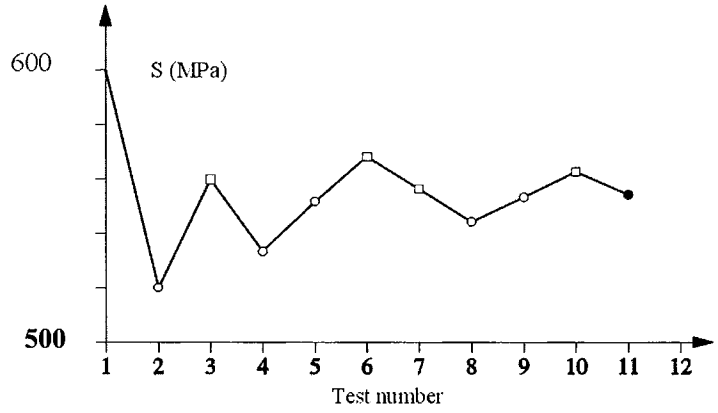

Figure 2.6. *Iteration method: graph of the successive values of a stress test*

2.4.3.2. *Estimation of S(p), stress amplitude with failure probability p*

This estimation requires very little calculation as the sequence of the stress amplitudes applied tends towards *S(p)*. However, if S_n is the last stress stage where tests are performed, the results enable us to calculate a stress S_{n+1}, see equation [2.18], that can be used to perform further tests if the procedure was continued.

In order to take the acquired result with S_n into account, we estimate *S(p)* with S_{n+1}.

2.4.3.3. *Conditions and instructions of the iteration method*

We previously said that the iteration method can be used in many other cases besides $p = 0.5$. Nevertheless, we will avoid looking to determine response curve points that correspond a values of p that are too close to 0 or 1. The reason for this is that the behavior of the method becomes increasingly uncertain the closer we get to these limits.

When $p = 0.5$, the theoretical value of A is [BAS 53]:

$$A = \sqrt{2\pi} = 2.5 \qquad [2.19]$$

Regarding a value of p different to 0.5, the theoretical value $A(p)$ is [BAS 53]:

$$A(p) = \sqrt{2\pi}\ \exp[u_p^2/2] \qquad [2.20]$$

where u_p represents the reduced deviation of Gauss' law corresponding to the probability p.

The estimation of S_{n+1} obtained is characterized by its bias (or systematic deviation) and its scatter (defined by the standard deviation of S_{n+1}).

These two statistical characteristics of S_{n+1} are a function of the deviation of S_1, first test stress level. They have a targeted value and standard deviation σ, *a priori* evaluation of the basic standard deviation, used in equation [2.18].

In the case of S_1, we can show that its effect is dependent on its reduced deviation at the median μ, written as:

$$\frac{S_1 - \mu}{\sigma}$$

Accurate calculation of the bias and standard deviation S_{n+1} for the final estimation are performed as we are trying to estimate the median μ (point $p = 0.5$), with values of A_V ranging from 1.5 to 4, of $\frac{S_1 - \mu}{\sigma}$ ranging from 0 to 3 and $n = 2$, 4 and 6 (Table 2.2), the tests being carried out with a single specimen per stress level. It is actually when n is low that it is worth studying the statistical characteristics of S_{n+1}, as this estimation tends towards the targeted value when n gets much higher.

When the starting error $\frac{S_1 - \mu}{\sigma} = 1$, the systematic error remains unimportant, regardless of n, when compared to the random error $\sigma(S_{n+1})$. In this case, the choice of A is no longer essential, especially when $n \geq 4$.

When $\frac{S_1 - \mu}{\sigma} = 2$, the systematic error regarding $\sigma(S_{n+1})$ becomes higher. This is also the case when the value of A taken is too low, let us say < 2.5.

This trend becomes more significant when $\frac{S_1 - \mu}{\sigma} = 3$. We can see that $\sigma(S_{n+1})$ increases when $n = 4$ or 6, whereas the systematic error decreases.

We can then conclude that, if we are worried of making a significant systematic error right at the start, we should make sure that $A > 2.5$ but that its role decreases as a function of n.

A	$\frac{S_1-\mu}{\sigma_v}$	$E[S_3]$	$\sigma[S_3]$	$E[S_5]$	$\sigma[S_5]$	$E[S_7]$	$\sigma[S_7]$
A = 1.5	0	0	0.629 3	0	0.520 8	0	0.457 1
	1	0.372 5	0.562 9	0.272 1	0.489 7	0.223 2	0.436 3
	2	0.990 6	0.309 3	0.718 8	0.349 4	0.589 1	0.340 1
	3	1.891 1	0.098 0	1.484 9	0.150 4	1.257 7	0.174 7
A = 1.8	0	0	0.707 6	0	0.567 5	0	0.487 2
	1	0.288 1	0.662 5	0.202 5	0.546 3	0.159 6	0.473 7
	2	0.810 3	0.394 4	0.548 5	0.426 0	0.428 8	0.399 0
	3	1.668 5	0.136 0	1.214 6	0.215 3	0.970 8	0.246 5
A = 2.1	0	0	0.775 7	0	0.603 9	0	0.509 6
	1	0.221 5	0.750 9	0.149 9	0.591 0	0.114 4	0.501 5
	2	0.651 7	0.481 8	0.412 2	0.492 7	0.310 9	0.444 4
	3	1.459 4	0.180 9	0.968 7	0.292 6	0.735 3	0.318 5
A = 2.5	0	0	0.851 1	0	0.642 0	0	0.530 9
	1	0.153 7	0.856 3	0.099 2	0.638 5	0.071 8	0.528 3
	2	0.461 5	0.610 7	0.274 1	0.565 6	0.195 7	0.491 0
	3	1.183 0	0.259 1	0.686 3	0.407 1	0.484 9	0.406 0
A = 3.0	0	0	0.929 1	0	0.678 1	0	0.551 6
	1	0.100 1	0.961 9	0.059 7	0.683 8	0.040 4	0.553 4
	2	0.270 5	0.782 5	0.158 7	0.632 9	0.107 6	0.531 7
	3	0.854 1	0.389 1	0.428 6	0.535 4	0.283 1	0.480 7
A = 3.6	0	0	1.021 2	0	0.709 0	0	0.572 5
	1	0.065 5	1.046 1	0.033 6	0.724 2	0.020 6	0.577 1
	2	0.122 0	0.975 4	0.074 9	0.697 1	0.048 9	0.566 7
	3	0.511 7	0.587 4	0.235 8	0.636 1	0.142 7	0.538 0
A = 4.0	0	0	1.087 2	0	0.733 5	0	0.585 7
	1	0.050 8	1.081 2	0.024 5	0.747 3	0.014 1	0.591 5
	2	0.068 2	1.085 1	0.042 1	0.732 3	0.027 2	0.585 1
	3	0.322 3	0.752 6	0.155 6	0.673 9	0.089 3	0.564 0

NB: this table gives the values of the systematic distortion $E[S_{n+1}]$ and standard deviation $\sigma(S_{n+1})$ resulting from application of the iteration method to a normal sigmoid response curve of unit standard deviation and of an average equal to zero.

Both real systematic distortion and standard deviation are obtained by multiplying the values of the above table with σ_V (real standard deviation)

Table 2.2. *Average values and standard deviation of S_{n+1} when n = 2,4 and various values of A and of* $\frac{S_1-\mu}{\sigma}$

We should also mention that the highest value of $\frac{S_1-\mu}{\sigma}$ planned here (3) has to be considered as already high. With the usual value of $\sigma = 0.05\ E$ (representing 5%

of the endurance limit E), 3σ then corresponds to an evaluation error of E ±15%. Some preliminary fatigue tests within the limited endurance region usually allow us to remain within these limits.

2.4.3.4. *Estimation precision*

The values of the bias and standard deviation of S_{n+1} have just been given for low values of n of the stress stages for a single test per stage.

When A = 2.5, a good approximation of $\sigma(S_{n+1})$ is given by the following equation:

$$\sigma(S_{n+1}) = \sqrt{\frac{\pi}{2\,nm}}.\sigma \qquad [2.21]$$

where m is the number of tests carried out at each stage if they are performed by groups.

2.4.3.5. *Application example*

Figure 2.6 provides an example of the iteration method applied to estimate the fatigue limit of steel. The values of A and σ are as follows:

– $A = 2.5$ $\sigma = 32$ MPa;

– $S_{i+1} = S_i + \frac{8}{i}(0.5 - f_i)$;

– $f_i = 1$ when failure occurs, $f_i = 0$ when no failure occurs.

Ten tests have been carried out. The last stress applied in a test was 581.7 MPa. The failure observed during this test allows us to calculate S_{n+1} = 577.7 MPa, which corresponds to the estimation of the targeted conventional fatigue limit, and $\sigma(S_{n+1})$ = 15.4 daN.

2.4.4. *Non-failed specimen method*

2.4.4.1. *Principle*

The K non-failed specimen method is a generic term involving other methods, sometimes known as the "three specimen methods".

Its aim is to basically determine a stage where K tests give K non-failures for successive stress stages, x_1, x_2,..., etc., decreasing due to arithmetic progression.

As the starting stage x_1 is chosen – usually at a sensitivity higher than the endurance limit – the tests are successively carried out with the choice of test stress level being defined by the following rule:

– as the last test has been carried out at stage x_i and the total number of performed tests at this level is n_i:

- if the last of these n_i tests triggered a failure, the following test will be carried out at one stress level lower than the last test;

- if the n_i tests that have been carried out at level x_i just triggered non-failures, the following test will be performed at the same level x_i as the previous ones if and only if $n_i < K$. If $n_i = K$, tests will be stopped.

We can then see that with this rule we move to a stress one level lower than that at which a failure is observed and that we do not carry out any more K tests per level.

The result of this procedure is characterized by the last stress level at which the tests have been carried out.

2.4.4.2. *Statistical properties of the result*

Statistical properties of the result can be determined using calculations when we know the analytical nature of the response to the stress curves. If they are considered sigmoid and normal, we can calculate the statistical behavior of the method during its application to an average response curve μ and we can also calculate the standard deviation σ.

If we choose S_K as the stress level where the procedure stops, S_K is a random variable whose distribution is a function of K (number of non-failures to be obtained), spacing d of the test stress levels and the position of this scale in relation to μ.

We can, however, reduce the study of the corresponding cases to various values of μ and σ only when $\mu = 0$, $\sigma = 1$, if we replace d with d/σ and the values of S_K with those of $(S_K - \mu)/\sigma$.

Regarding a standard sigmoid curve ($\mu = 0$, $\sigma = 1$) and given values of K and d we have then calculated:

– $E(S_K)$: the expected value of S_K or average value of this amount for a high test number;

– $\sigma(S_K)$: standard deviation of S_K (scatter parameter of S_K);

– $M(S_K)$: distribution mode of S_K or level where the halting probability is the highest;

– G_K: fraction percentage at level $E(S_K)$;

– u_K, v_K: limits of the probability interval of S_K at a minimum of 0.95; and

– α%: real probability, expressed in %, where S_K is external to the interval u_K, v_K.

These various values are listed in Table 2.3 as a function of K and of d/σ.

The random nature of the test results enables us to predict the final result using probabilities. The number of stages to be covered is random, as is the total number of tests necessary.

K	$\frac{d}{\sigma}$	$E[S_K]$	$\sigma[S_K]$	$M[S_K]$	G_K	V_K	U_K	α%
K = 1	0.25	0.673	0.661	0.50	75.0	−0.5	+2.0	3.6
	0.50	0.244	0.758	0	59.6	−1.0	+2.0	2.1
	1	−0.273	−0.893	0	39.2	−2.0	+1.0	2.6
	1.5	−0.641	−1.005	0	26.1	−3.0	+1.5	–
K = 2	0.25	−0.115	−0.546	−0.25	45.4	−1.0	+1.0	3.8
	0.50	−0.479	−0.635	−0.50	31.6	−1.5	+1.0	1.8
	1	−0.928	−0.765	−1.00	17.7	−2.0	+1.0	1.0
	1.5	−1.257	−0.871	−1.50	10.4	−3.0	0	–
K = 3	0.25	−0.492	−0.493	−0.50	31.1	−1.5	+0.5	4.2
	0.50	−0.824	−0.580	−1.00	20.5	−2.0	+0.5	0.7
	1	−1.243	−0.710	−1.00	10.7	−2.0	0	2.8
	1.5	−1.555	−0.806	−1.50	6.0	−3.0	0	–
K = 4	0.25	−0.728	−0.462	−0.75	23.3	−1.5	+0.25	–
	0.50	−1.043	−0.548	−1.00	14.9	−2.0	0	–
	1	−1.444	−0.677	−1.00	7.4	−3.0	0	–
	1.5	−1.742	−0.769	−1.50	4.1	−3.5	0	–

d/σ: no gradation of the stress, expressed in multiples of the standard deviation of the response curve

$E[S_K]$: expected value of S_K or average value of this quantity for a high number of tests

$\sigma[S_K]$: standard deviation of S_K (distribution parameter of S_K)

$M[S_K]$:distribution mode of S_K or stage where the halting probability is the highest

G_K: failure percentage at level $E(S_K)$

u_K, v_K: limit of the probability interval of S_K at a minimum of 0.95

α %: real probability in % in order for SK to be external to the interval u_K, v_K

Table 2.3. *Statistical properties of the three specimen/non-failed specimen method*

In addition to the probable region of the halting procedure, however, a probable number of tests necessary to succeed can be found. This number is given as a function of K and of d/σ in Table 2.4, if we consider the stress test to be carried out from three standard values of the targeted average.

K / d/σ	K = 1		K = 2		K = 3		K = 4	
	E(N)	D(N)	E(N)	D(N)	E(N)	D(N)	E(N)	D(N)
0.25	10	3	16	3	20	4	23	4
0.50	7	2	10	2	12	2	15	3
1.00	4	1	6	1	8	2	10	2
1.50	3	1	5	1	7	1	8	2

K: number of non-failures required for the procedure to stop

d/σ: fraction or multiple of the standard deviation of the response curve used as pitch

N: (random) number of specimens required for the procedure

E(N): expected (or average) value of N, rounded to the nearest whole unit

D(N): standard deviation of N, rounded to the nearest whole unit

Table 2.4. *Average value and standard deviation of the necessary number of specimens*

This table enables us to see that regarding the three specimen method, for instance ($K = 3$), and a spacing of the stress stages equal to a standard deviation, we usually have to use eight specimens to complete the procedure, with a characteristic standard deviation of two specimens.

2.4.4.3. *Application example*

Figure 2.7 gives an example of results obtained using this method with $K = 3$, on specimens made of metal sheets bearing a welded clip of the same thickness. The tests have been carried out under repeated bending, welding being loaded in compression up to two million cycles. The results show that the tests have been stopped at a value of 360 MPa – the limit of the standard deviation (twice the value of the stress amplitude) – after using eight specimens.

If we make an assumption on the standard deviation of the response to the stress curve, we can then estimate the conventional fatigue limit at 50% and determine the precision of this estimation.

To do so, let us consider that σ = 20 MPa. As the tests present a spacing of 20 MPa, we have:

$$\frac{d}{\sigma} = \frac{20}{20} = 1$$

In Table 2.3, when $K = 3$ and $d/\sigma = 1$ we have:

– $E(S_K) = -1.24$;

– $\sigma(S_K) = 0.71$;

– $M(S_K) = -1$; and

– $G_K = 10.7$.

The value of $E(S_K)$ shows that, for the considered values of K and d/σ, the halting level is usually 1.24 standard deviations below the median of the response curve, which is 24 MPa.

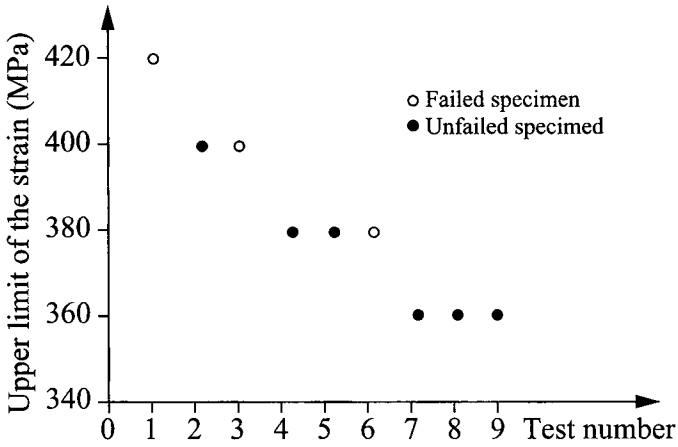

Figure 2.7. *K non-failed specimen method (K=3)*

When we correct the systematic error of S_K, we obtain an estimate of μ:

$$\mu^* = 360 + 24.8 = 384.8 \text{ MPa}$$

In order to obtain the standard deviation of μ^*, we multiply the value $\sigma(S_K)$, given in Table 2.5, which corresponds to a response curve of unit standard deviation, with the standard deviation supposedly equal to 20 MPa: $\sigma(\mu^*) = \sigma(S_K)$ x 20 = 14.2 MPa.

Test number	Stress (MPa)		N_f	Observations
	Lower limit	Upper limit		
1	20	420	1,513	Failed specimen
2	20	400	2,000	Unfailed specimen
	20	400	1,703	Failed specimen
3	20	380	2,000	Unfailed specimen
	20	380	2,000	Unfailed specimen
	20	380	1,429	Failed specimen
4	20	360	2,000	Unfailed specimen
	20	360	2,000	Unfailed specimen
	20	360	2,000	Unfailed specimen

Table 2.5. *Application examples*

2.4.5. *Choice of test method*

To make things easier, we will distinguish three different degrees of precision or demand regarding the estimation of fatigue resistance:

– approximate estimation;

– estimation of average precision; and

– accurate estimation of the median that can also be matched with that of standard deviation.

2.4.5.1. *Methods of approximate estimation*

Estimation methods of fatigue resistance that fit into this category can be performed with fewer than 10 to 15 tests, even if they can be applied to higher numbers of tests.

Methods that therefore fit this category include:

– staircase;

– identical K results; and

– iteration.

2.4.5.2. *Estimation of average precision*

Here we are talking about methods that can be applied when 15 to 40 tests are carried out. The "probit" method remains outside this category as too many tests need to be performed. The *K* identical results method does not fit either because the method would lose its relevance as the standard deviation obtained would be too high due to the number of tests considered.

The methods to be considered in this category are:

– the staircase; and

– the iteration test;

performed in groups from two to four tests at each level.

2.4.5.3. *Accurate estimation methods*

Accurate estimation methods include:

– the staircase, performed in test groups at each stress level;

– the iteration, still performed in test groups at each stress level; and

– the "probit"; applied methods with a test number higher than 40.

The first two are acceptable with random test numbers, whereas we have to be ready to carry out at least 60 to 80 tests if we use the "probit" method.

The staircase method has the advantage of simplicity, but its execution takes time due to the necessity of trying the specimens one after another. The iteration method is more delicate but takes less time as the tests can be performed in groups.

2.5. Mathematical representations and plotting methods of the Wöhler curve

2.5.1. *Introduction*

The general shape of the *S-N* diagram has already been described in section 2.2. We have showed that its description is possible, from the response to the stress curves (see Figure 2.2), or from the response to the failure isoprobability curves (see Figure 2.3).

It then appears that a complete and accurate representation of the *S-N* diagram involves the definition of one or another curve category.

We will first focus on the shape of failure isoprobability curves and then on the adjustment of an "average" curve.

2.5.2. *Mathematical representation of the Wöhler curve*

Dengel [DEN] studied representations of various Wöhler curves. The oldest one introduced was:

$$\text{Log } N = a - bS, \qquad [2.22]$$

where N is the number of cycles at which a failure occurs, S is the amplitude of the applied stress, and two constraints a and b.

Although it cannot reflect a horizontal or asymptotic part of the entire *S-N* curve due to its nature, it usually gives a good representation of the average part of the curve. This is due to the fact that most of the experimental Wöhler curves present within the coordinate system S, log N, a slight inflection point close to which they are almost straight. If we put the low-cycle fatigue domain ($N < 5 \times 10^4$ cycles to get a better idea) and the one with endurances higher than a million cycles aside, the *S-N* curve is really close to a line.

The problem gets more serious when we want to reflect the bend and the almost horizontal branch of the Wöhler curve.

We noted a while ago that the *S-N* curve does not present a pronounced bend, as we can usually expect from a rough representation, but a progressive bend that joins the decreasing branch to the horizontal one.

As early as 1910, Basquin proposed the equation below to highlight this curve:

$$\text{Log } N = a - b \text{ Log } S \qquad [2.23]$$

If we have $A = e^a$ and $c = 1/b$, this equation can also be written as:

$$S = (A/N)^c \qquad [2.24]$$

This equation represents a kind of hyperbole whose branch is asymptotically linked to the N axis. Therefore, this type of curve does not allow us to describe the phenomenon of fatigue limit, even if it is absolute or apparent but sufficiently obvious, unlike the Wöhler line.

As early as 1914, Stromeyer then introduced the equation:

$$\text{Log } N = a - b \text{ Log } (S - E) \qquad [2.25]$$

where three parameters a, b and E are involved, the latter one representing the endurance limit.

The curve obtained is identical to the one described by Basquin's equation where S has been replaced by $S - E$. The curve displays a horizontal asymptote of ordinate E, usually different from the lifetime axis.

Equation [2.25] (where $A = e^a$ and $c = 1/b$) can also be written as:

$$S = E + (A/N)^c \qquad [2.26]$$

The Stromeyer equation is definitely more realistic than the equations proposed by Wöhler and Basquin. Much more data and a serious examination to detect any deficiencies are needed.

This equation has been used by many authors but its adjustment is not that easily done. We will discuss this matter later on, in Chapter 5.

In 1924, Palmgren introduced the following equation:

$$S = E + \left(\frac{A}{N + B}\right)^c \qquad [2.27]$$

which can also be written as:

$$\text{Log } (N + B) = a - b \text{ Log } (S - E) \qquad [2.28]$$

With coordinates S and Log N, and when $B > 0$, the S-N curve then presents an inflection point that allows us to improve the quality of the data adjustment.

Corson [COR 49], using a greatly reduced experimental basis, introduced the equation:

$$N = \frac{A}{(S - E)\, d^{(S-E)}} \qquad [2.29]$$

where A, E and d are constants.

If we have $c = \text{Log } d$, this equation can be expressed as:

$$N = \frac{A \exp\left[-c(S-E)\right]}{(S-E)} \qquad [2.30]$$

whose experimental justification has been established independently on the basis of many test results [BAS 71].

Finally, as a reminder we should quote the Weibull equation:

$$\text{Log } (N+B) = a - b \text{ Log } \frac{S-E}{R-E} \qquad [2.31]$$

where a, b, B and E are constant parameters and R the traction resistance of the material.

As equation [2.31] can be written as:

$$\text{Log } (N+B) = [a + b \text{ Log } (R-E)] - b \text{ Log } (S-E) \qquad [2.32]$$

and as a and b are, *a priori*, unknown, we actually have to assume that:

$$a' = a + b \text{ Log } (R-E) \qquad [2.33]$$

and then estimate B, a, b and E as if to adjust equation [2.31], and use equation [2.33] in order to deduce a, knowing the values of a', b, R and E.

In the end, equation [2.31] does not bring anything more to the shape of the adjusted curve than [2.28] does.

We have seen that the replacement of N in the Stromeyer equation [2.27] with $(N + B)$, which leads to the Palmgren equation [2.28], greatly improved the quality of adjustments that could be made.

The same modification can be made to equation [2.24] and leads to:

$$N + B = \frac{A \exp\left[-c(S-E)\right]}{(S-E)} \qquad [2.34]$$

which allows us, as was the case with equation [2.28], to highlight a possible inflection point of the Wöhler curve.

To compare which of the equations ([2.27], [2.28] and [2.34]) is better, we need a large number of test results. The serious study of several data groups has allowed us to show an increasing adjustment quality when we get from equation [2.25] through to [2.28] and then to [2.34]. With fatigue test results that were performed on a XC-10 steel, used as an example, we can obtain some adjustments of Figures 2.8 to 2.10.

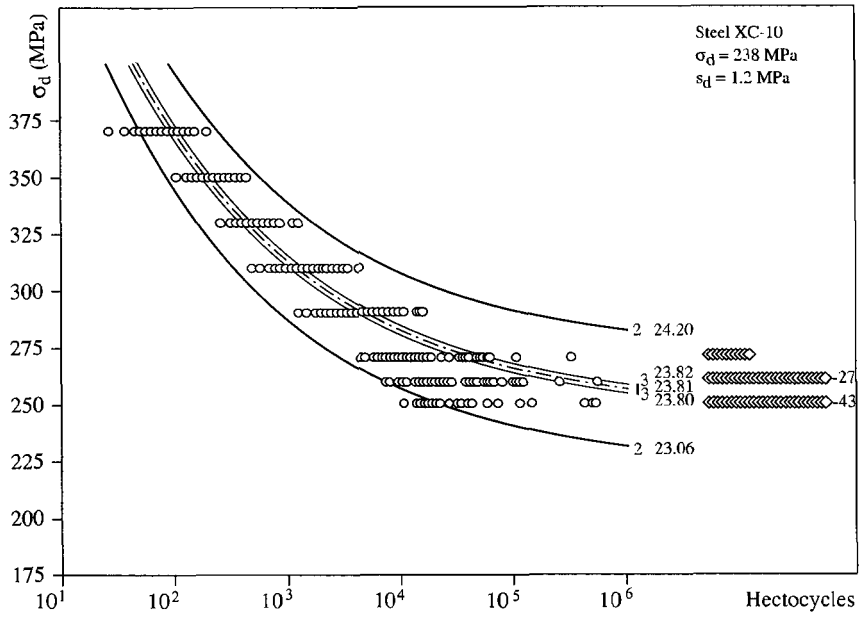

Figure 2.8. *Rotating bending fatigue tests on XC-10 steel*

Figure 2.8 shows the adjustment of equation [2.26] (since $B = 0$). Using the estimation of the value of B, we then obtain the adjustment in Figure 2.9, where the inflection point of the isoprobability curves is obvious.

Finally, Figure 2.10 shows equation [2.34]. In these three figures, the two outer curves are deduced from the median (center) curve using a translation of 2.05 standard deviations parallel to the stress axis. They then correspond to the failure probabilities of 0.02 and 0.98, following the normal law. Circular points show failures and square points non-failures.

We can see that, in Figures 2.9 and 2.10, the endurance limits obtained are close to each other.

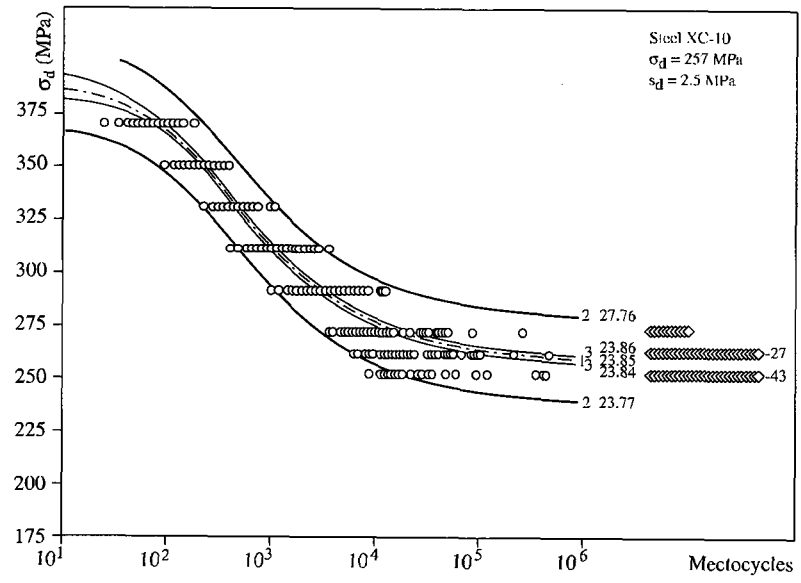

Figure 2.9. *Rotating bending fatigue tests on XC-10 steel*

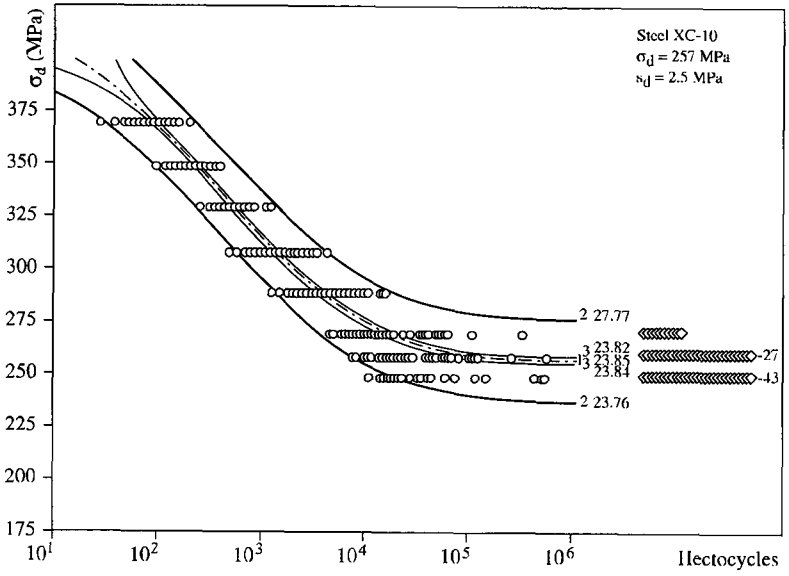

Figure 2.10. *Rotating bending fatigue tests on XC-10 steel*

2.5.3. *Adjustment methods of a Wöhler curve to test results*

Regardless of the adopted shape – [2.19]–[2.22], [2.24] or [2.26] – we have to estimate the unknown constants using the test results.

The only curve whose adjustment is simple is the Wöhler curve (equation [2.19]). As we have already noted, it cannot be applied to the whole Wöhler diagram. It can however, be applied within the intermediate region where the logarithm scatter of lifetimes does not often depend on the stress amplitude. We can then apply the least-squares method in order to adjust a line of equation [2.19] to the test results.

Figure 2.10 allows us to see that, even in the straightest region of the Wöhler curve, the scatter constant of Log N is not completely verified. In addition, within the endurance zone, where we find some non-failing specimens, this scatter grows significantly.

Adjustment of the regression line of Log N with regards to S using the least-squares method has been used by various authors. Many people prefer to apply this method to the values of Log N and Log S, which involves adopting Basquin's equation ([2.20]); see [GUR 92] for instance.

Despite the fact that the validity of Basquin's equation [2.20], like that of Wöhler's line, falls apart within the endurance region and does not really work compared to Wöhler's curve [2.19] within the intermediate zone, it is frequently used. We wonder why this is so.

Adjustment of equations [2.21], [2.22], [2.23] and [2.26] with test data cannot be performed using simple methods. With [2.25] we cannot really estimate E, whereas with the different terms in [2.26] of the same equation, it is c that cannot easily be determined. The same goes for [2.27], where the estimation of B introduces an additional issue. With equations [2.30] and [2.26], estimation of the parameters presents similar issues.

Estimation of E in equations [2.25] or [2.26] can be performed graphically if we try different values of E until we get a linear relationship between Log N and Log $(S - E)$ (which we achieve when we switch N and $(S - E)$ to bi-logarithmic coordinates). We can also optimize this graphic method if, for every value of E, we adjust a second-degree curve to Log N, Log $(S - E)$ values using the least-squares method, and if we study the evolution of the second-degree term that we get as a function of the value of E. We then determine, using interpolation, the value of E whose second-degree term from the Log N, Log $(S - E)$ equation is equal to zero [ROY 73].

We could also work on [2.26] from equation [2.25] and find the value of c when $1/N^c$ linearly depends on S. Other authors give c a value "based on experience" and adjust $1/N^c$ to S using the least-squares method.

Serensen and co-workers [SER 72] set $c = 1$ in Palmgren's equation [2.27]. They performed a regression adjustment of $1/(N + B)$ with regards to S for different values of B that were randomly chosen. Then, using interpolation, they looked for the value of B whose relationship between $1/(N + B)$ and S was the most linear if they considered the correlation coefficient or residual variance.

None of the previous methods is statistically satisfying as the estimations obtained for the targeted parameters cannot be matched with confidence intervals or indications relative to their precision. However, to adjust some functions similar to [2.25], [2.27] or [2.34] to some data, classic statistics does not seem to offer any solution for several reasons.

Usually it appears that the relationship between the number of failure cycles N and the stress amplitude S is related to a regression model, as N is affected by scatter and S is considered to be known. This equation is non-linear when we consider data from the endurance region, the fact that the scatter of N varies greatly and some of the test results lead to non-failures.

From a statistical point of view, these two aspects of the S-N relationship would not be drawbacks if:

– distributions of N, for each value of S, would be normal;

– the scatter of N would be represented by an analytically known function of S (even when depending on unknown parameters).

Even though these conditions are clearly not satisfied, we can still try to achieve them using a known transformation. The most commonly used one, Log N, does not really satisfy these conditions – they roughly match within the decreasing part of the Wöhler curve but are very different within the endurance region (see equation [2.25]).

Actually, no transformation *a priori* given can enable us to satisfy the two previous conditions for the simple reason that the variable depending on N presents an infinite point for a value of S that we can never experimentally consider to be known. On the contrary, it has to be estimated.

If a transformation without any singular point is applied to N, it will not be able to give an infinite value to infinite N.

To overcome this issue, we have to use a transformation that bears a singular point. The $1/N$ transformation [BAS 61] can occasionally be suitable. Usually, however, the transformation that enables us to turn lifetime N into a random and normal scatter variable that is constant or nearly constant, is a function of the unknown parameters of the Wöhler curve, which have to be estimated [BAS 61].

One method proposed for estimating the unknown parameters of a Wöhler curve consists of transforming the curve using approximate values for the unknown parameters. The calculation can then be performed starting with the transformed data and applying a regression method to the corrections to be applied to the temporary parameters. Repetition of this calculation until convergence defines an iterative process of the estimation of the parameters [BAS 53]. Mathematical study of this method using a computer program enables us to calculate the precision of estimations and the accuracy of the adjusted curve. This method, called the ESOPE method, can be applied to the adjustment of any type of function representing the Wöhler curve.

This is how with the same system of test results we could adjust Stromeyer's equation (see Figure 2.8, with $B = 0$), Palmgren's equation (see Figure 2.9, with $B > 0$) and equation [2.26] with four parameters (see Figure 2.10). Calculation involves statistical adjustment tests, that is to say, the validity of the equation used changes depending on the treatment of data.

Figure 2.11 gives an example of the adjustment of a limited number of results using equation [2.34] where $B = 0$. The automatic plotting program enables us to establish curve 2, which corresponds to the estimated curves of failure isoprobability 0.10 and 0.90. The curves numbered 3 are the confidence bounds at the 0.95 stage of the median curve 1. The lower curve 4 is a scatter unilateral limit. For each value of the stress amplitude S, it defines a lower *confidence bound* at stage 0.95 of the estimated lifetime N, for the same value of S, using curve 2. In other words, there is a 95% chance that at the considered level the *real* fraction 0.10 of distribution N is at the right of curve 4.

2.6. Estimation of the cycle number N for a given level of stress amplitude

When strictly applied with limited endurance, this method can also be used in the two following cases:

– determination of the number of cycles, N_p, corresponding to a failure probability equal to p in the case of tests carried out at the same stress level (see Figure 2.12);

– definition of the probabilized Wöhler curve, point-by-point.

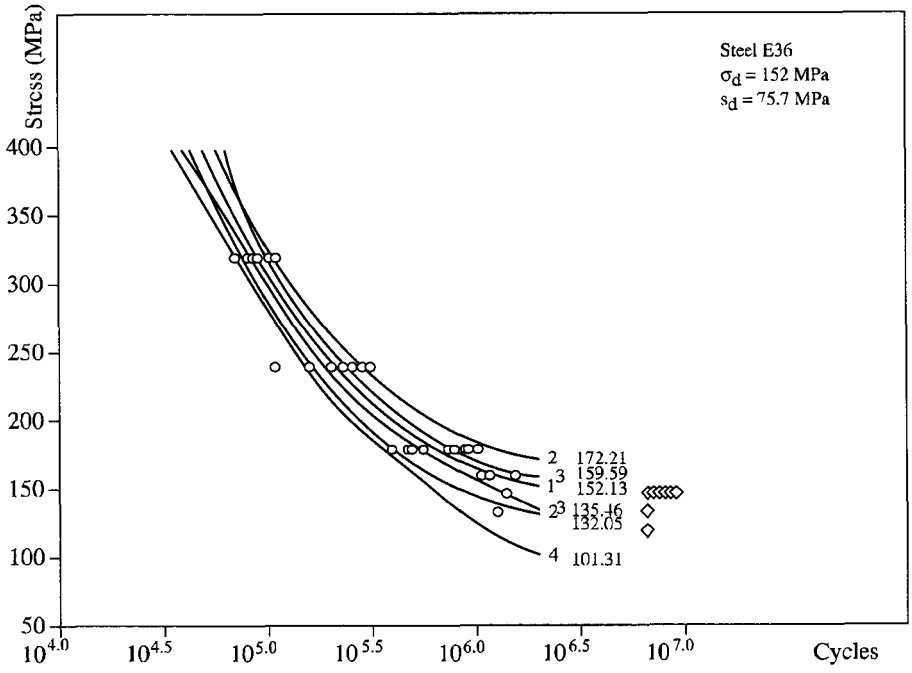

Figure 2.11. *Fatigue tests on a cruciform welded joint – E36 steel*

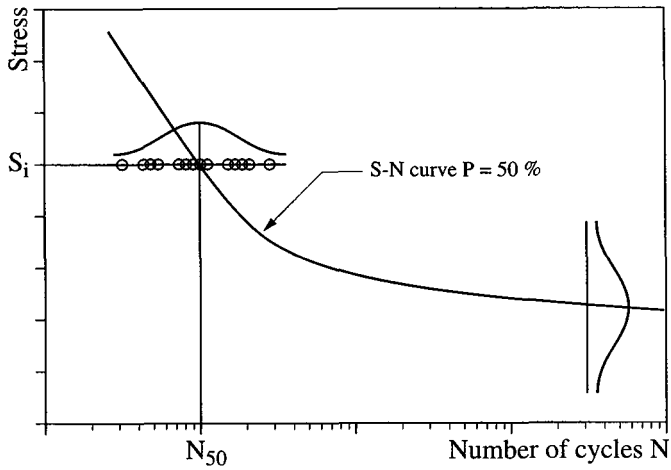

Figure 2.12. *Estimation of the cycle number and scatter within the limited endurance region*

2.6.1. *Principle*

This method is based on the experimental observation that distribution of the numbers of cycles to failure, for a given level of stress amplitude, is normal. It enables us to graphically check this normality using a diagram (Henry diagram) with Gausso-arithmetical coordinates (Gaussian scale as ordinates and arithmetic scale as abscissa).

On this particular diagram (see Figure 2.13), we have the representative points of the test numbers of cycles (expressed as log N) as a function of the proportions of the broken specimens below the considered fatigue lives. Distribution of log N follows a normal law when the experimental points are lined up.

2.6.2. *Set-up*

A minimum of 10 specimens is required. The first time, the n values of N are sorted out following an increasing order: $N_1, N_2, ..., N_i, ..., N_n$.

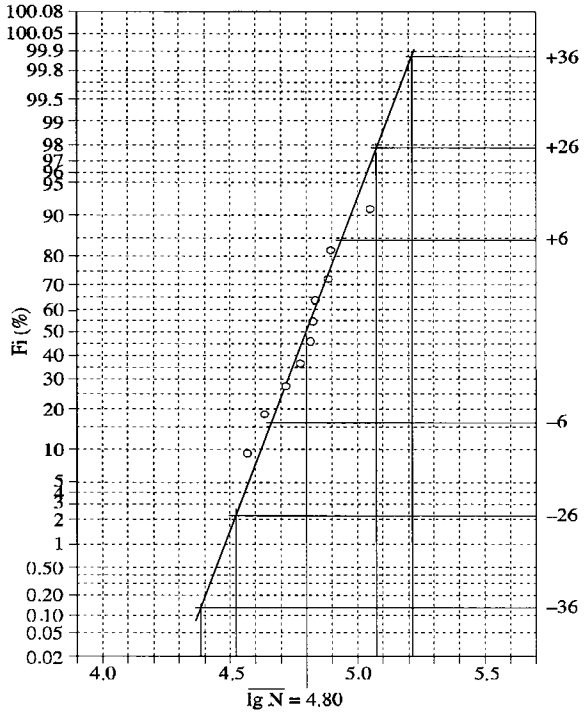

Figure 2.13. *Henry line*

The proportion of broken samples is estimated using the frequency, which can be written as:

$$F_i = i/n+1$$

We then plot the n points with $\log N_i$ as abscissa and F_i as ordinates on a Henry diagram.

In the general case where the points are lined up, we can then estimate the average and standard deviation of $\log N$, using the following expression:

$$s = \sqrt{\frac{\Sigma\left(\log N_i - \overline{\log N}\right)^2}{(n-1)}}$$

The line representing the distribution goes through two points with the following coordinates:

$$\overline{\log N} - s, 16\%; \quad \overline{\log N} - s, 84\%.$$

2.6.3. *Application*

Figure 2.13 shows the experimental results.

In this case, we obtain $\overline{\log N} = 4.803$, which allows us to estimate N_{50}, which is the number of failure cycles corresponding to a failure probability of 50%:

$$N_{50} 10^{\overline{\log N}} = 63{,}500 \text{ cycles}$$

The same goes for the estimation of N_p, the number of failure cycles corresponding to a failure p, which can be obtained if we calculate:

$$N_p = 10^{\left(\overline{\log N} - us\right)}$$

where u is given in Table 2.1.

2.7. Influence of mechanical parameters on endurance

The fatigue resistance of a material is linked to numerous factors, which can be either mechanical or metallurgical. One of the most significant factors deals with the application conditions of the cyclic stresses being applied.

2.7.1. *Influence of the mean stress*

An increase in the mean stress or statistical stress leads to a reduction in the dynamic stress resistance of a material.

If we take a force of the same nature, the stress amplitude σ_a, allowed, which corresponds to a given lifetime, decreases when the mean stress, σ_m, increases.

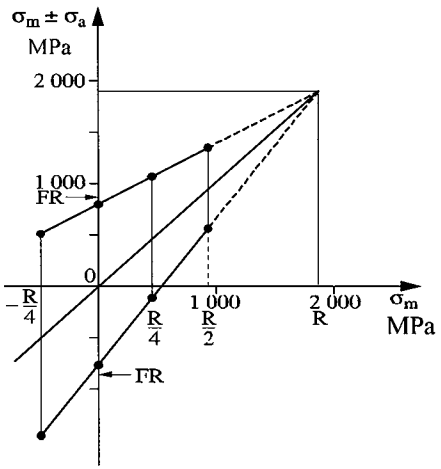

Figure 2.14. *Goodman-Smith diagram (35NCD16 steel)*

If we focus on the fatigue calculation of pieces and entire structures, it is important to know the evolution of σ_a as a function of σ_m. To visualize this evolution, different diagrams have been proposed:

– the Goodman-Smith diagram (see Figure 2.14): $\sigma_{max} - \sigma_m$;

– the Haigh diagram (see Figure 2.15): $\sigma_a - \sigma_m$.

In these diagrams we plot the curves that were previously determined for finite or infinite lifetimes (endurance limit).

2.7.2. *Influence of the nature of forces*

For a given material, fatigue strength varies as a function of the nature of a force. In particular, for a given steel we can find as many endurance limits as types of cycles (alternate, repeated, waved) and stresss of different natures (traction, bending, torsion) that we can imagine.

Comparison of test results usually shows that the endurance limit values decrease when we switch from rotating bending to planar bending and then to compressive traction and finally to torsion. Deviations between the different values depend on the adaptation possibilities of the steel considered. Figure 2.16 shows an example of the type of stress on the endurance limit of two materials [LIE 87].

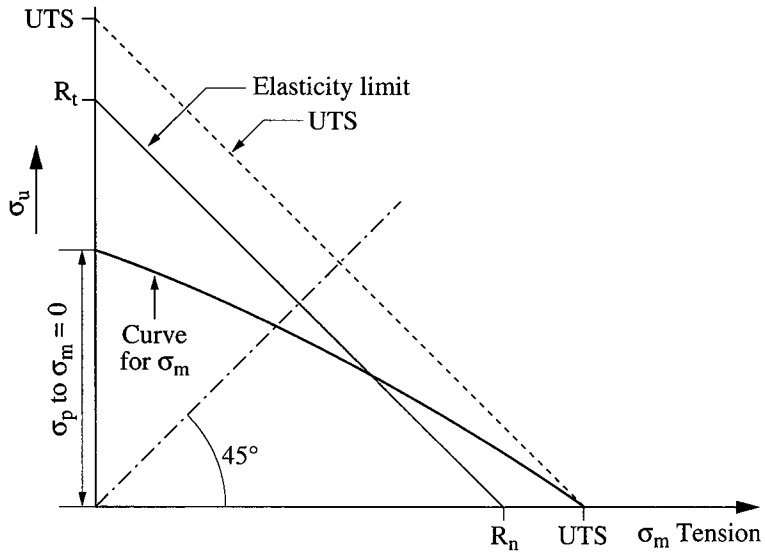

Figure 2.15. *Haigh diagram (simplistic description)*

2.7.2.1. *Alternate traction and alternate planar bending*

In the case of alternate planar bending, stresses are highest for external fibers and close to zero on the axis when there are non-uniform stresses within the sections considered. In the case of compressive traction, however, stresses are homogenous across the whole section.

Experience has shown us that we can find a certain difference between these two types of solicitation. If we take specimens of the same dimension (same section) and same shape within the useful part, planar bending usually gives some endurance

limit values higher than those obtained with compressive traction. This difference can reach 30% depending on the authors but it depends, to some extent, on the dimension of the specimens.

Nevertheless, a component can modify these conclusions: in the case of planar specimens of rectangular section, the edge is not well defined and can lead to some local initiations that can reduce fatigue resistance. This is known as the edge effect. Figure 2.16 shows the possibility of edge effect in the case of a 35CD4 steel [LIE 87].

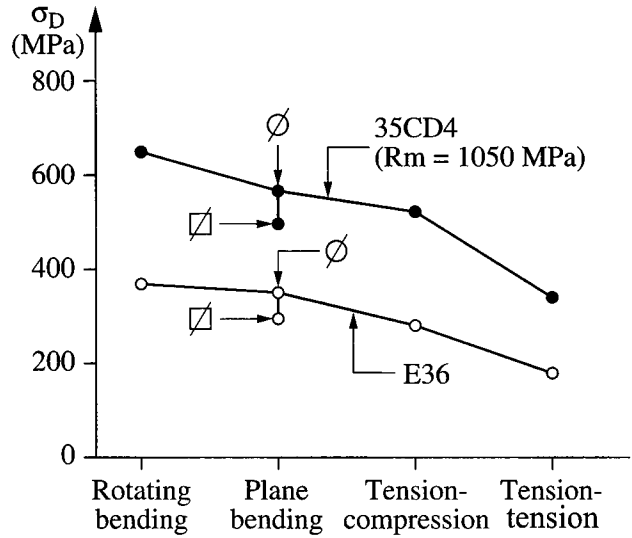

Figure 2.16. *Influence of stress type on the endurance limit (R = -1)*

2.7.2.2. *Alternate traction and rotating bending*

In the case of rotating and planar bending, stresses are not homogenous within the section of the specimen.

When comparative tests are carried out with a specimen of the same dimension and shape, and run at the same frequency, lifetimes within the limited endurance are shorter in the case of alternate traction compared to rotating bending [RAB 67].

The same goes for endurance limits during rotating bending, which are usually higher than during alternate traction: deviation can vary between 0 and 20% [RAB 69].

2.7.2.3. *Alternate planar bending and rotating bending*

Distribution of stresses through a section should lead to a planar bending endurance higher than a rotating bending endurance when specimens of the same circular sections and shapes are used. In these conditions, Roos, Lemmon and Ranson [ROO 49] found that, for a steel treated with nickel-chromium-molybdenum (R_m = 900 MPa), the endurance limit during planar bending is 12% higher than the one during rotating bending.

However, if we try bending specimens with a prismatic section b x h during planar bending and compare them to specimens with a circular section of diameter $d = h$ run during rotary bending, we observe that there is either no significant difference or we get lower values in the case of planar bending. This is due to the edge effect (see Figure 2.16).

2.7.2.4. *Alternate torsion and alternate bending*

Elasticity theory says that there is a constant ratio equal to $\left(1/\sqrt{3}\right)$ between failure strength in the case of torsion and traction.

With alternating loading, we find some variable values relating to the endurance limit ratios of alternate torsion $\sigma_D{}^T$ and alternate bending $\sigma^{FT}{}_D$. We also observe, however, that endurance limits depend on the dimensions of the specimens that were being examined.

According to numerous results, the $\sigma_D{}^T/\sigma^{FP}$ ratio varies between 0.44 and 0.75, with an average value of 0.55.

Moore, Jasper and MacAdam found that for different steels and alloys there was a ratio ranging from 0.44 to 0.71 between the endurance limit during alternate torsion alternate rotating bending. For most of the metals that were used, the ratio ranged from 0.49 to 0.60. According to Föppl, the ratio ranges from 0.48 to 0.75 in the case of steels; and from 0.54 to 0.65 in the case of aluminum alloys.

2.8. Relationship between endurance and mechanical characteristics (of steels)

2.8.1. *Estimations of σ_D*

Many authors [BRA 76, BUC 64, CAZ 34, CAZ 69, HEY 62, POH 64, RAB 54] have tried to link endurance limit to mechanical properties and especially to:

– ultimate tensile strength, UTS or R_m (in MPa);

– yield strength σ_Y or $R_{e0,2}$ (in MPa);

– elongation A (in %); and

– necking Z (in %).

Numerous equations have been proposed [CAZ 69] (σ_D in MPa):

– Mailander $\sigma_D = (0.49 \pm 20\%)$ UTS:

$\sigma_D = (0.65 \pm 30\%)\ \sigma_Y$;

– Strinbeck $\sigma_D = (0.285 \pm 20\%)$ (UTS $+\sigma_Y$);

– Rogers $\sigma_D = 0.4\ \sigma_Y + 0.25$ UTS;

– Houdremont and Mailander $\sigma_D = 0.25(\sigma_Y + \text{UTS}) + 50$;

– Junger $\sigma_D = 0.2\ (\sigma_Y + \text{UTS} + Z)$;

– Lequis, Buchholtz and Schulz $\sigma_D = 0.175$ (UTS + σ_Y - A% + 100);

– Fry, Kessner and Ottel $\sigma_D = \alpha\,\text{UTS} + \beta\sigma_Y$.

Coefficients α and β are not constant: α is proportional to R_m, whereas β is reversely proportional to R_m:

– Heywood $\sigma_D = \text{UTS}/2$;

$\sigma_D = 150 + 0.43\sigma_Y$;

– Brand $\sigma_D = 0.32\ \text{UTS} + 121$.

This last equation deals with 489 endurance limit results of various natures obtained during rotating bending for 10^7 cycles ($300 < \text{UTS} < 2{,}000$ MPa).

These expressions are only applied to specific cases where experiments have already been carried out. As a matter of fact, the characteristics of endurance depend on the number of parameters, such as the metallographic structure, cycle frequency or dimension of the specimens.

Some results obtained with similar test conditions have been gathered by the IRSID (French Research Institute of Steel making) [BUT 86]. Here, endurance limits during rotary bending have been determined for 10^7 cycles at a frequency of 200 Hz on cylindrical specimens with an effective diameter ranging from 5 to 8 mm.

We suggest the following expressions between σ_D, on one hand and *Rm, Re, A* and *Z* on the other hand:

$$\sigma_D \begin{cases} 0.37\,Rm + 77 \\ 0.38\,Re + 160 \\ 0.41\,Rm + 2 \\ 0.39\,Rm + Z \end{cases}$$

where Rm = UTS, Re = σ_Y.

As you can see in the diagrams in Figure 2.17, the expressions where UTS is involved give the best test results. Thanks to these equations, we can now obtain an approximate value of σ_D at ±15%.

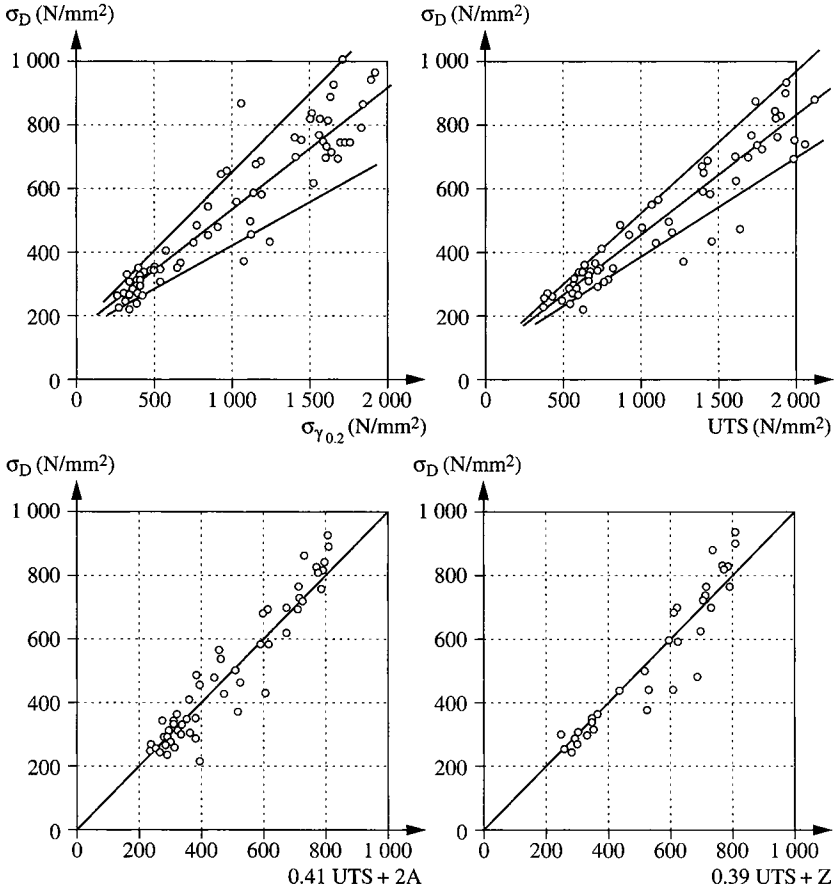

Figure 2.17. *Relationship between endurance limit and characteristics of traction in various steels*

2.8.2. *Estimation of standard deviations*

The values of the standard deviation, s, of the endurance region obtained during the previous study [BUT 86] are widespread. This variation is due, in particular, to the analysis method used.

Results show an average increase in s when UTS increases: we can admit $s = 0.02$ UTS as an indicative value.

2.8.3. *Conclusion*

The distribution of fatigue test results, related to either the nature of the material or the experimental conditions, needs the use of appropriate statistical analysis methods of test results.

In order to estimate the fatigue resistance with N cycles and its standard deviation, several methods are proposed:

– the "probit" method;

– the staircase method;

– the iteration method;

– the K non-failed specimen method.

These methods require a minimum number of specimens and different set-up reactions that enable us to obtain variable estimations that are acceptably accurate.

The same goes for the mathematical representation of the function $\sigma_a = f(N)$, which has led different authors to propose models that are increasingly elaborate. Using a computer, these models now enable us to automatically plot the Wöhler curve as well as some failure iso-probability curves.

Where steels are concerned, a rough estimation of the endurance limit from a simple traction test is often necessary. Different empirical equations are proposed. The best agreement between experimental and calculated values is obtained when we relate endurance limit to traction strength and failure elongation. Moreover, fatigue resistance of a material is modified by mechanical parameters, for a given fatigue life so:

– an increase in the static stress reduces the stress amplitude the sample can endure;

– endurance to stress decreases when we start with bending and then switch to traction and then finally to torsion stress.

It is then worth remembering that we can rely on the French rules regarding statistical analysis of fatigue data obtained on metallic compounds [NOR 91], and that a new ISO TC 164/FDIS 12107 rule has been developed in the same field [ISO 07].

2.9. Bibliography

[BAS 53] F. BASTENAIRE, *Rev. de Stat. Appliquée*, vol. 1, p. 63, 1953.

[BAS 61] F. BASTENAIRE, *Bulletin de l'Inst. Int. de Statistique*, 33rd session, Paris, 1961.

[BAS 61] F. BASTENAIRE, M. BASTIEN, G. POMEY, *Acta Technica Academiae Scientiarium Hungaricae*, vol. XXXV-XXXVI, 1961.

[BAS 71] F.BASTENAIRE, G. POMEY, P. RABBE, "Étude statistique des durées de vie en fatigue et des courbes de Wöhler de cinq nuances d'acier", *Mém. scient. de la Rev. Métallurgie*, vol. LXVIII, pp. 645-664, 1971.

[BAS 72] F. BASTENAIRE, *ASTM STP 511*, 1972.

[BRA 76] A. BRAND, *SFM Document, Commission Fatigue GT2-D25*, SFM, October 1976.

[BUC 64] A. BUCH, *Fatigue Strength of Materials and Structures*, Pergamon Press, London, 1964.

[BUT 86] H. BUTHOD, H.P. LIEURADE, "Influence des propriétés mécaniques sur les caractéristiques d'endurance en flexion d'une gamme étendue d'aciers", *Rev. de Met.*, p. 485-491, 1986.

[CAZ 34] C R.AZAUD, Publication Technique du Ministère de l'Air, 39, 1934.

[CAZ 69] R. CAZAUD, G. POMEY, C.H. JANSSEN, *La Fatigue des Métaux*, Dunod, Paris, p. 241-250, 1969.

[COR 49] M.G. CORSON, *The Iron Age*, p.103, 1949.

[DEN 71] D. DENGEL, *Materialprüfung*, vol. 13, pp. 145-180, 1971.

[DIX 48] W.J. DIXON, A.M. MOOD, "A method for obtaining and analyzing sensitivity data", *J. Am. Stat. Soc.*, vol. 43, p. 109-126, 1948.

[FIN 72] D.J. FINNEY, *Probit Analysis*, Cambridge University Press, Cambridge, 1972.

[GUR 92] T.R. GURNEY, MADDOX, S.J., Report E/44/72, The Welding Institute, January 1992.

[ISO 07] ISO, *Statistical Planning and Analysis of Data, Document ISO/FDIS 12107*, ISO TC 164/SC5, 2007.

[HEY 62] R.B. HEYWOOD, *Designing against Fatigue*, Chapman and Hall, London, p. 16-23, 1962.

[LIE 87] H.P. LIEURADE, *La Rupture par Fatigue*, IRSID-OTUA, 1987.

[NOR 91] Norme Française (French Standard) A 03-405, *Produits Métalliques-Essais de Fatigue (Traitement Statistique des Données)*, September 1991.

[POH 64] D. POHL, "Untersuchungen uber die Wechselfestighkeit unlegierter Vergutungsstahle", *Archiv für das Eisenhüt.*, vol. 35, p. 359-365, 1964.

[RAB 54] P. RABBE, G. POMEY, *Fracture*, MIT Technology Press and John Wiley, New York, p. 524-561, 1954.

[RAB 67] P. RABBE, G. POMEY, *Rev. Met.*, vol. 5, p. 461-473, 1967.

[RAB 69] P. RABBE, G. POMEY, F. BASTENAIRE, "Comparison of fatigue limits by method of determination and type of stressing", *Rev. Met.*, vol. 2, p. 129-145, 1969.

[ROB 51] H. ROBBINS, S. MONRO, "A stochastic approximation method", *Ann. Math. Stat.*, vol. 22, p. 400-407, 1951.

[ROO 49] J. ROOS, J. LEMMON, J.T. RANSON, *ASTM Bulletin*, vol. 63, May 1949.

[ROY 73] A. LE ROY, B. VISEER, Faculté Polytechnique de Mons, 1973.

[SER 72] S.V. SERENSEN, V.I. TROUFIAKOV, V.I. DVORETSKY, *Doc. XIII-GT1-1-72*, International Institute of Welding, 1972.

[ULM 52] J. ULMO, *Annales des Mines*, III-IV, 1952.

Chapter 3

Fatigue Crack Initiation

3.1. Introduction

If we want to accurately estimate the fatigue behavior of mechanical parts we have to evaluate the number of cycles that occur before crack initiation within a region which is highly stressed or containing fabrication defects. In many practical cases, the initiation stage represents a significant part of the fatigue life (by up to 90% of the lifetime), as is highlighted in Chapter 4.

Experience shows us that crack initiation usually results from the concentration of plastic deformations that occur within a small region of finite dimension. From a structural point of view, localized plastic deformations related to extrusion and intrusion mechanisms lead to the development of stage I cracking.

From a practical point of view, we have to relate the number of cycles necessary for the formation of a macroscopic initiation event to the operating conditions (applied loads, design of the components) in order to calculate the total number of cycles to failure.

This chapter examines the two sides of the problem: physical mechanisms and methods of evaluating the number of cycles for crack initiation.

Chapter written by Paul RABBE and Louis ANQUEZ.

3.2. Physical mechanisms of crack initiation

3.2.1. *Three stages of fatigue failure: a reminder*

When a specimen or a component fails due to fatigue, its life can be split into three parts:

– crack initiation;

– slow crack propagation;

– sudden propagation leading to fracture.

3.2.1.1. *Definition of crack initiation*

The definition of crack initiation can be different depending on whether we focus on the microstructural evolution of the material or the formation of a microcrack. We will come back to this definition in Chapter 4.

To evaluate the crack initiation stage within a structure, we usually rely on the notion of microcracking. This notion itself, however, depends directly on the resolution of the means of observation used. Moreover, as there is no general agreement on the definition of crack initiation, different authors have defined the number of cycles to crack initiation, N_i, to create a crack of length a_0 of about 0.1 mm. Actually, this dimension can easily be detected and corresponds to a defect size that we can compare to the grain size of many metallic materials. Finally, experience shows us that in many cases, as soon as a crack reaches a depth close to this dimension, it steadily propagates through the section of the specimen or the component [PIN 76].

3.2.1.2. *Relative significance of crack initiation and crack propagation stages*

Classic fatigue tests (*S-N* curves that give stress as a function of the number of cycles to fatigue N_F) give some global information on the endurance of a material (initiation + propagation + fracture). These particular tests allow us to qualitatively judge the choice of materials, but they can be difficult to apply in a quantitative manner to a structure.

Figures 3.1 and 3.2 show some simplistic representations of:

– the *S-N* curve, with a separation of the initiation N_i and propagation N_p phases;

– the evolution of stress $\Delta\sigma$ as a function of the N_i/N_F ratio of the number of cycles to crack initiation N_i to the number of cycles to failure N_F.

The relative significance of initiation and propagation stages depends on:

– the stress amplitude;

– the component geometry;

– the nature of the material;

– temperature;

– previous loading; and

– environment.

These different factors can interact in such a way that the number of possible parameters is high.

Grosskreutz observed the evolution trends of the ratio N_i/N_F [GRO 71] as a function of these different parameters. These trends can be seen in Table 3.1, where we plotted the N_i/N_F ratio values on smooth and notched specimens for different materials, and for some given values of the number of cycles to fracture N_F.

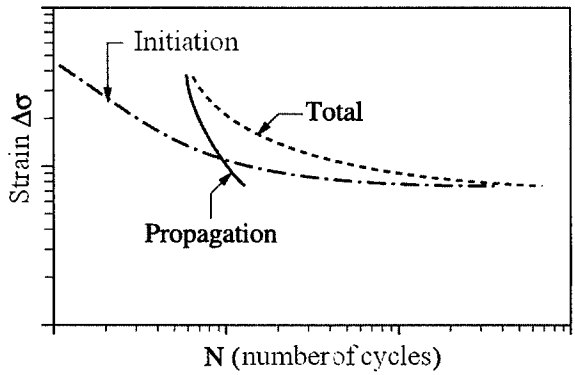

Figure 3.1. *Number of cycles for crack initiation, crack propagation and total fatigue life as a function of the applied stress amplitude*

The ratio N_i/N_F decreases when the alternate stress (or strain) amplitude increases, in such a way that within the region of very low numbers of cycles, the propagation phase represents the main part of the lifetime. In addition, the number of initiation sites increases when the stress (or strain) increases.

When we introduce a stress concentration (notch for example), the N_i/N_F ratio is decreased.

In general, microcracks are more rapidly initiated within ductile materials.

In materials showing a stage I crack initiation within slip bands, the N_i/N_F ratio increases when the temperature decreases.

When a material undergoes a superficial work hardening effect, introducing residual compressive stresses, produces an increase of the initiation phase.

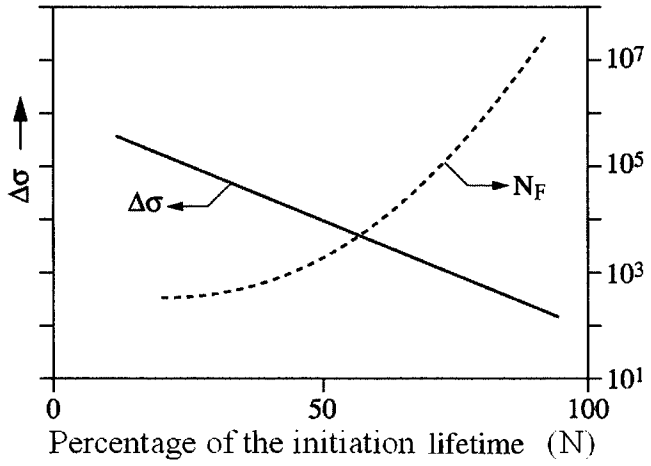

Figure 3.2. *Graph showing the percentage of the fatigue life spent in crack initiation as a function of applied stress amplitude ($\Delta\sigma$) and the total number of cycles to failure (N_F)*

3.2.2. *Influence of stress amplitude*

The evolution of damage phenomenon due to fatigue is generally observed using optical or scanning electron microscopy on a smooth specimen without any significant defect.

Usually, crack initiation occurs at the surface of the specimen. More rarely, crack initiation can occur within bulk, for example within welds (fish-eye), cast steels (microshrinkage cavity), or under the skin (when large inclusions modify the local strain distribution), see Chapter 5.

Forsyth [FOR 72] explains that the three reasons why fatigue cracks develop at the free surface of the specimens are:

– dislocations are more mobile at the free surface compared to the bulk;

– surface is a preferential site of the nucleation of dislocations;

– surface is subjected to the aggression of the environment.

Material	Shape of the specimen	Initiation localization	N_F cycles	Length of the crack for N_i	N_i/N_F
Pure Cu	Smooth	Slip	2.10^6	$0.203.10^{-2}$ mm	0.05
Pure Al	–	Grain Boundary	3.10^5	$0.127.10^{-1}$ mm	0.10
2024-73	–		4.10^4	0.101 mm	0.40
			10^6	0.101 mm	0.70
2024-T4	–		150	0.254 mm	0.60
			10^3	0.254 mm	0.72
			5.10^3	0.254 mm	0.88
4130	–		10^3	0.254 mm	0.72
Pure Al	Notched ($K_t = 2$)	Slip	2.10^6	$0.254.10^{-3}$ mm	0.005
2024-T4	–	Inclusion	10^5	$0.203.10^{-1}$ mm	0.05
			3.10^6	$0.101.10^{-1}$ mm	0.07
2014-T6	–		2.10^3	$0.635.10^{-1}$ mm	0.015
			2.10^4	$0.635.10^{-1}$ mm	0.02
			10^6	$0.635.10^{-1}$ mm	0.05
7075-T6	–	Inclusion	2.10^5	0.508 mm	0.64
7075-T6	–		5.10^3	$0.762.10^{-1}$ mm	0.20
			10^5	$0.762.10^{-1}$ mm	0.40
4340	–		10^3	$0.762.10^{-1}$ mm	0.25
			2.10^4	$0.762.10^{-1}$ mm	0.30

Table 3.1. *Number of cycles to crack initiation as a function of the ratio N_i/N_f and nature of crack initiation sites [GRO 71]*

3.2.2.1. *Very low stress region*

Loadings that are lower than the so-called endurance limit are characterized by dislocation and glide movements that are perfectly reversible: there is no blocking or rearrangement of the dislocations, and the structure is not irreversibly modified.

3.2.2.2. *Endurance region*

The application of cyclic strains (or stress) close to the endurance limit, the application of a certain number of cycles, produces slip bands (within some grains) that can easily be observed on polished surfaces (see Figure 3.3).

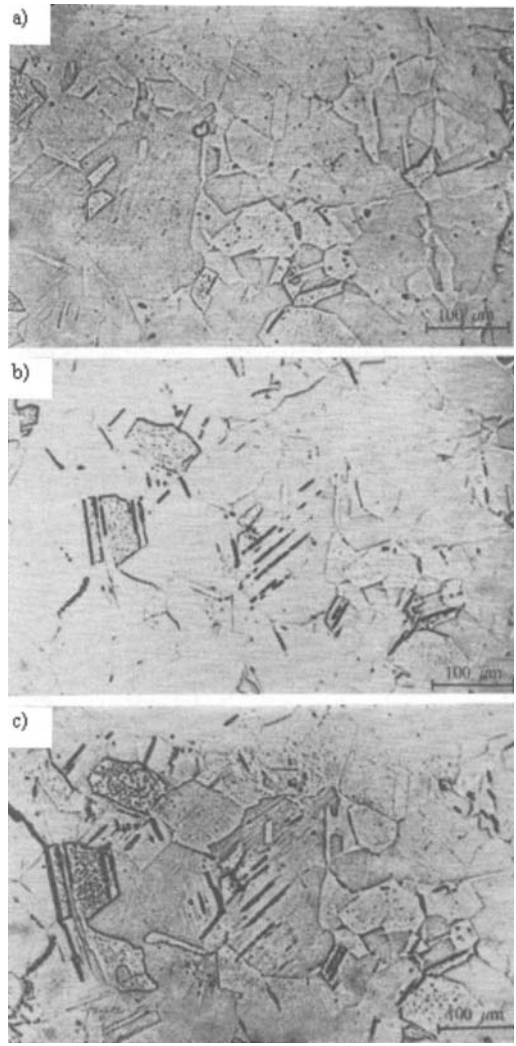

Figure 3.3. *Slip bands observed in copper [THO 56]; a) after 7.5% of the lifetime; b) after 42% of the lifetime; and c) after 77% of the lifetime [THO 56]*

These bands have been observed in many single phase metals and alloys, such as:

– aluminum [FOR 72];

– iron [KLE 65];

– copper [THO 56];

– zinc [BRO 63];

– nickel [LAI 63];

– brass [JAC 60];

– carbon steels [KLE 65];

– austenitic steels; and

– aluminum alloys.

In a large number of metals the slip bands lead to the formation of microcracks due to the intrusion-extrusion mechanism (see Chapter 4). Indeed, the atmosphere reacts with the fresh surfaces of the slip bands over the surface (extrusion), and prevent their back and forth movements, leading to metal damage. Figure 3.4 shows some examples of the formation of intrusions and extrusions in copper.

Wood [WOO 58] suggested that the formation of the microcracks at the free surface was a simple geometric consequence of back and forth movements within large slip bands (see Figure 3.5).

Cottrell and Hull [COT 57] proposed a formation model of intrusions and extrusions at the free surface, based on elementary mechanical movement of the atoms. This model, shown in Figure 3.6, involves two slip bands that cross each other and give rise to the formation intrusions and extrusions during tension and compression cycles.

The formation of extrusions is favored by cross slip. Nevertheless, there is still no intrusion and extrusion formation; cracks are then initiated from surface irregularities caused by slip bands (see Figure 3.6). Microcracks are formed within these bands, which are then called "persistent".

Slip bands are not the only sites for crack initiation. Within some alloys strengthened by precipitation, narrow and internal slip bands occur at the same time as we observe a dissolution of the precipitates [BRO 63]. Moreover, even when there is formation of deformation bands, cracks can be initiated at grain boundaries.

Inclusions are usually the sites where crack initiation occurs, due to the stress concentrations they bring or due to the cleavages occurring within these particles (see Figures 3.7 and 3.8). In 2024 or 7075 aluminum alloys, these particles enriched in iron or silicon are cleaved, whereas within the 2618 alloy, the Al_9FeNi component is cleaved [BAT 74].

Crack initiation depends on the quantity, size, nature and inclusion distributions, as well as on their shape regarding load direction. In addition, cohesion of the matrix-inclusion interface plays a key role.

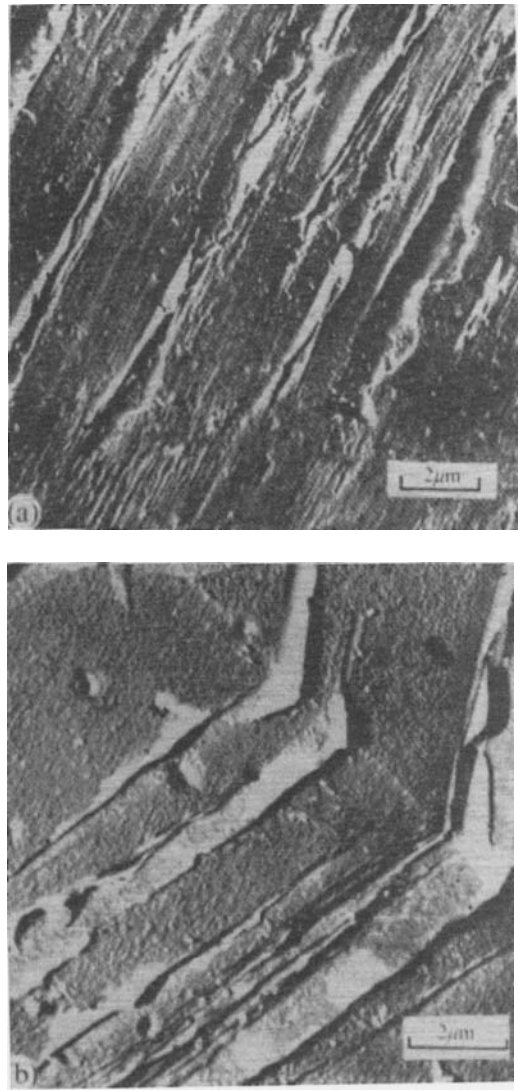

Figure 3.4. *Intrusions and extrusions associated with slip bands in copper subjected to fatigue cycles at 183°C [COT 57]*

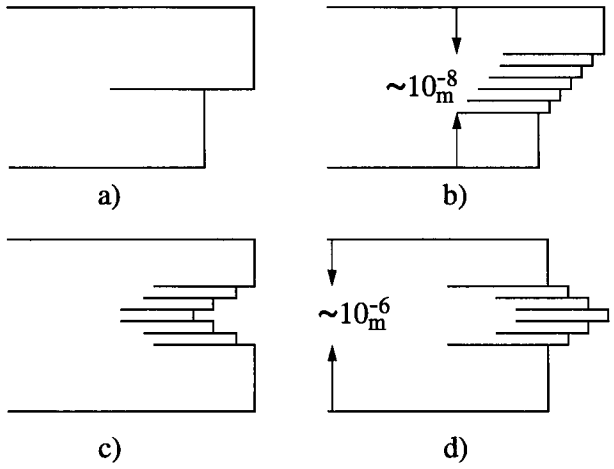

Figure 3.5. *Surface crack formation due to glide: stair formation due to "statistical" glide (a, b); intrusion (c); or extrusion (d) formation due to fatigue. Wood model [WOO 58]*

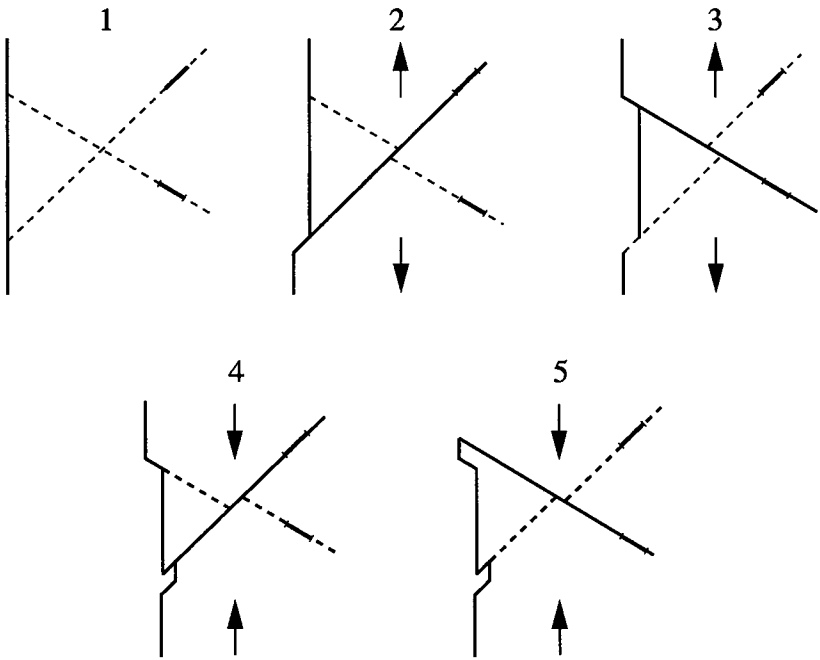

Figure 3.6. *Intrusion and extrusion formation; Cottrell and Hull model [COT 57]*

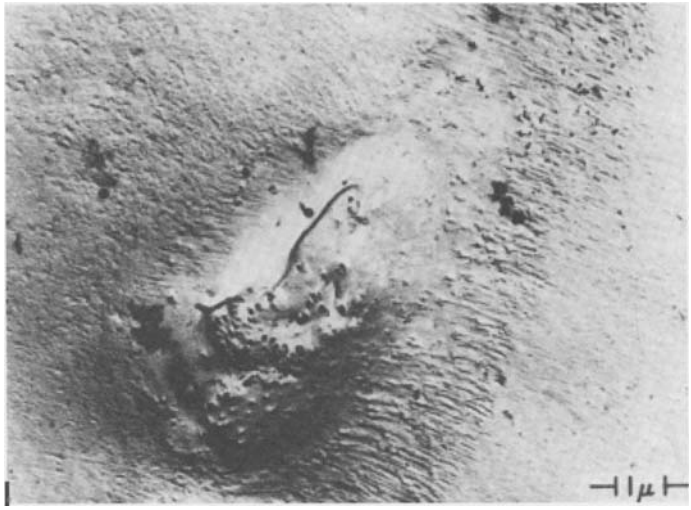

Figure 3.7. *Slip bands close to an inclusion in an aluminum alloy of 2024-T4 type*

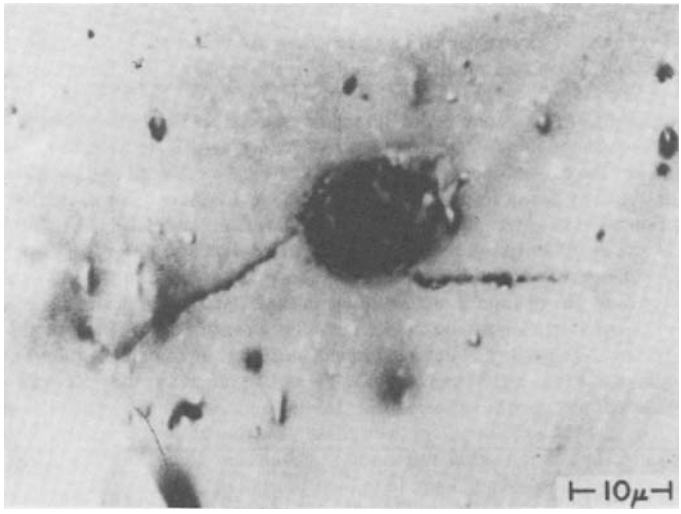

Figure 3.8. *Initiation of a surface fatigue crack in an aluminum alloy after 5% of its total lifetime*

Cracking of the interface, which is sometimes observed in aluminum alloys [BOW 73], is also the preferential initiation site in high strength steels of 40 NCD 8

type (AISI 4340) [LAN 73]. In this steel, inclusions of MnO, SiO_2 and Al_2O_3 are not cleaved during the fatigue phenomenon and it seems that the increase in shear stress close to the inclusions leads to matrix cracking (see Figure 3.9).

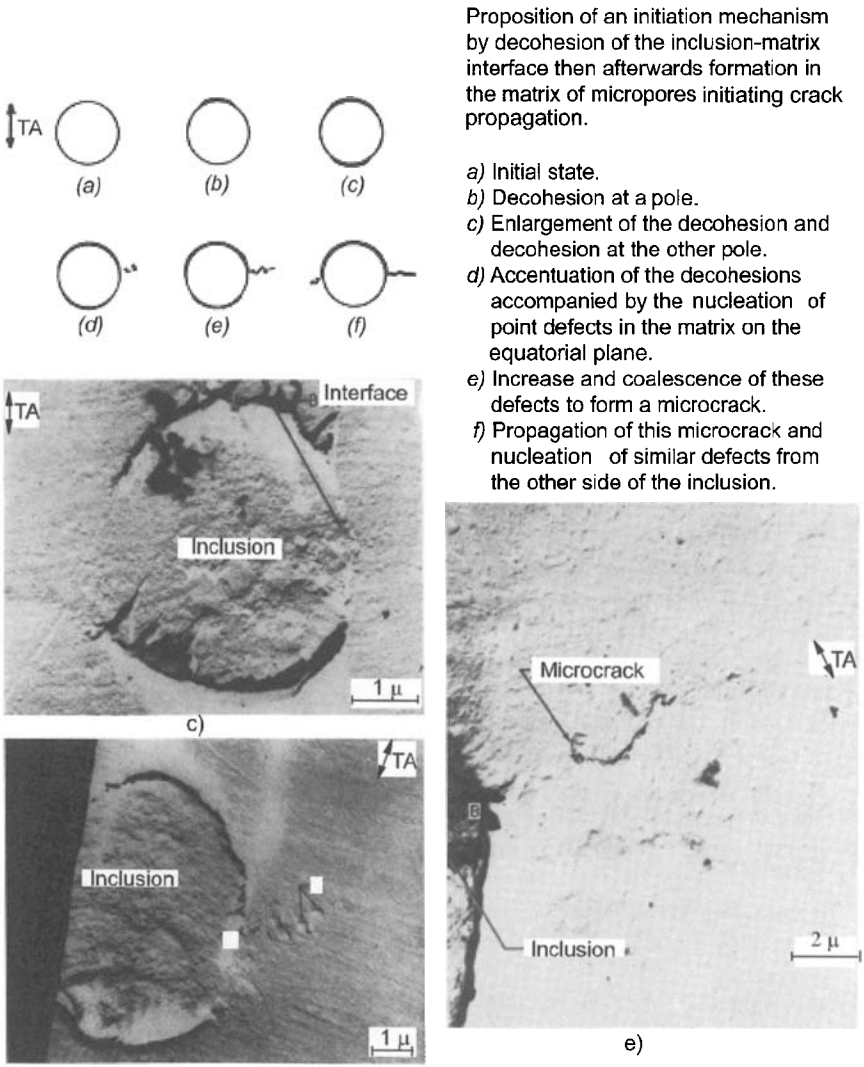

Figure 3.9. *Mechanism of fatigue crack initiation from surface inclusions proposed by Lankford and Kusenberger [LAN 73]. TA arrows show the direction of the tensile axis*

3.2.2.3. *High stress region*

The initiation of fatigue cracks at high stresses involves a number of mechanisms that can be compared to those described in the previous section. Nevertheless, in this case the formation of microcracks occurs more rapidly and a greater number of initiation sites can be found.

3.2.2.4. *Stage I crack propagation*

The initiation of a microcrack is caused by one of the mechanisms previously described and is usually followed by a transgranular propagation along a defined crystallographic direction, even if initiation is intergranular. This stage has been described by Forsyth as being the first stage (stage I) of crack propagation (see Figure 3.10).

Stage I cracks are characterized by their fractographic aspect, which is brittle without any striations, and by the orientation of the crack, which is typical of a shearing process.

Stage I has been observed within aluminum, copper, iron, nickel and titanium alloys. It is sensitive to the grain size, especially within alloys where cross slip is difficult [THO 71]. According to some authors [BAT 74], a reduction of grain size leads to an increase in the duration of stage I in copper alloys (brass), austenitic stainless steels, zirconium, titanium (TA6V), refractory materials and also in low carbon steels.

Stage I is limited to the area close to the free surface. It is then followed by stage II crack growth, where cracking first propagates in a direction perpendicular to the main principal stress (see Figure 3.10).

Transition between stage I and stage II is due to the decrease in shear strain with crack growth and the concomitant increase in normal stress.

The crack length during stage I has a magnitude of about 20 μm in copper, 5 μm in titanium alloy/TA6V, and 80 μm in large-grain brass.

We can then see that the fracture surface in stage I is limited compared to the total fracture surface; however, this stage represents a significant portion of a specimen's lifetime, as the crack growth at each cycle is of the order of a few nanometers per cycle. We will focus on the importance of stage I in Chapter 4.

We should keep in mind that the stage of crack formation and stage I represent 40–99% of the lifetime of the specimens that are commonly used to determine the

Wöhler curve. We then note that the formation of slip bands is usually premature and that the nucleation of microcracks within these slip bands is particularly slow.

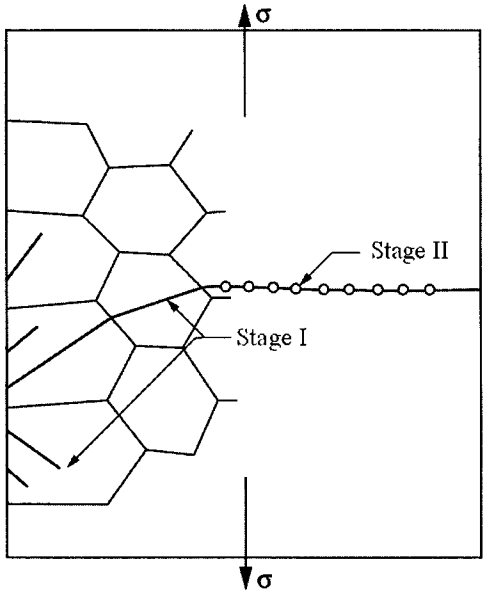

Figure 3.10. *Simplified representation of stages I and II of the propagation stages for fatigue cracks*

Stage I does not always occur. Indeed, a crack can be directly initiated according to stage II mechanism. This can happen, if significant cleaved inclusions are present [FOR 72], during rough machining/manufacturing leading to sharp slits, or within cast alloys when cracks are initiated from solidification microporosities.

3.3. Methods of evaluating crack initiation

3.3.1. *Smooth specimens*

As indicated in Chapter 1, classic analysis methods allow us to determine the curve giving the number of cycles to failure as a function of stress or applied nominal strain (for a given type of loading) where we can usually distinguish three regions:

– a low cycle fatigue (LCF) region;

– a fatigue or limited endurance region;

– a limited endurance region.

We have already indicated that the initiation and propagation times vary depending on the number of cycles.

In the case of fatigue with a high number of cycles (10^7 cycles), the endurance limit can be comparable to the lowest stress that leads to the initiation of a crack.

This estimation gives a value that is far too high, as in some cases we observe that an applied stress below the endurance limit can initiate cracks that do not propagate. Nevertheless, this property is sufficient to characterize crack initiation in materials tested at high cycle numbers.

As we previously stressed, at this stress level the number of cycles to crack propagation is very low compared to the number of initiation cycles. Thus, in this region the Wöhler curve provides a good approximation of the number of initiation cycles.

According to the endurance limit at 10^7 cycles in many materials, we can directly link the resistance to crack initiation to the mechanical strength of the material, and in particular to the conventional tensile strength R_m [EEL 75]. Although there are many factors that affect the endurance limit of a material (surface state, geometry, loading spectrum, etc.), many studies have shown that the resistance to crack initiation, within the region of high cycle numbers, is directly related to the mechanical resistance of the material

Although for high cycle numbers ($N > 10^6$) fatigue resistance essentially depends on the hardness level of the material, for intermediate and low cycle fatigue, ductility becomes an important factor. This fact is highlighted in Figures 3.11a and b, which give a comparison of a mild, semi-mild and hard steel. In the case of large stresses, hard steel demonstrates poor fatigue resistance due to its low ductility, whereas in the case of low stresses this material exhibits a very high resistance to fatigue. We can observe the opposite in mild steel, and an intermediate behavior in medium strength steel.

A large number of low cycle fatigue results have been obtained for different materials. Chapter 4 focuses on this type of damage and the associated behavior of various materials. If we consider – due to the small dimension of specimens used, and therefore short propagation time – that these results represent a qualitative measurement of the resistance to low cycle fatigue initiation, we can conclude that the resistance to low cycle fatigue initiation depends on both the ductility and the tensile strength of the material.

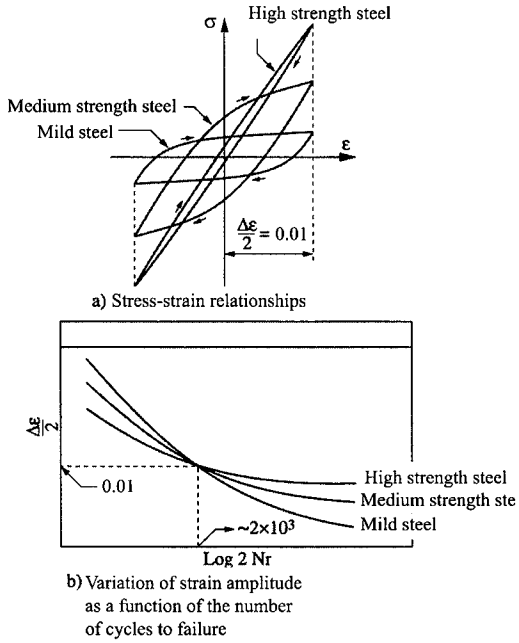

Figure 3.11. *Schematic representation of the low cycle fatigue behavior of different materials*

However, these data do not provide any quantitative measurement of crack initiation as they do not show the initiation and propagation phases.

3.3.2. *Notch effect*

The effect of a geometric discontinuity in a loaded structural element is to intensify the value of the nominal stress near the discontinuity.

Localized stresses can lead to local plastic strains. As the nominal stresses are elastic, the region of plastically deformed metal remains confined within a field that is globally elastic. In this region, the deformations that act on the structure are controlled by the deformations of neighboring regions that remain elastic. In other words, when the structure is stressed with an imposed load, the regions of localized plastic deformation are submitted to imposed local strains.

As a consequence, in order to predict the effects of stress concentrations in the structures, the fatigue behavior of the localized plastic regions has been simulated

using smooth specimens under strain controlled conditions (see Figure 3.12a). A better simulation of the effects of stress concentrations is obtained using notched specimens that are of the same type as those used in fracture mechanics and loaded under imposed stress (see Figure 3.12b).

Three main methods of initiation evaluation are being investigated. The first is based on the Neuber coefficient, the second on the stress intensity factor and the last method on the local strain amplitude.

3.3.2.1. *Stress distribution around a notch*

A section change in a specimen due to the presence of a notch, threading, hole, etc., leads to the modification of the uniform strain distribution and to the formation of local stress concentration (see Figure 3.13). This local stress concentration is measured using a stress concentration coefficient defined by:

$$K_t = \frac{\sigma_{max}}{\sigma_{nom}} \text{ (tension or bending)} \qquad [3.1]$$

or:

$$K_{ts} = \frac{\tau_{max}}{\tau_{nom}} \text{ (torsion)} \qquad [3.2]$$

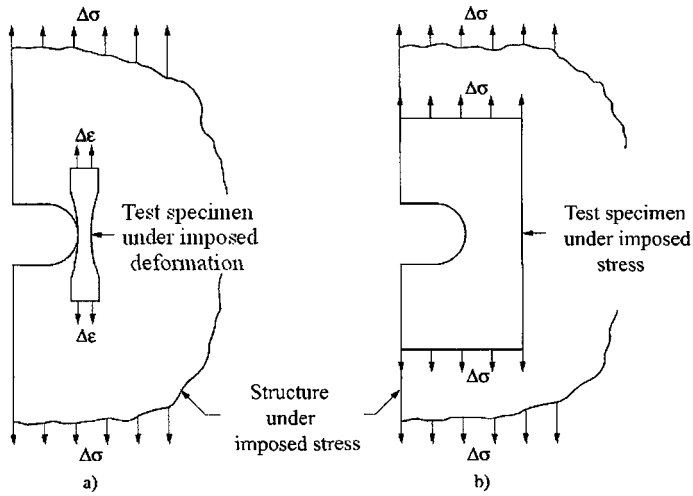

Figure 3.12. *Simulation specimens of strain concentration within a structure*

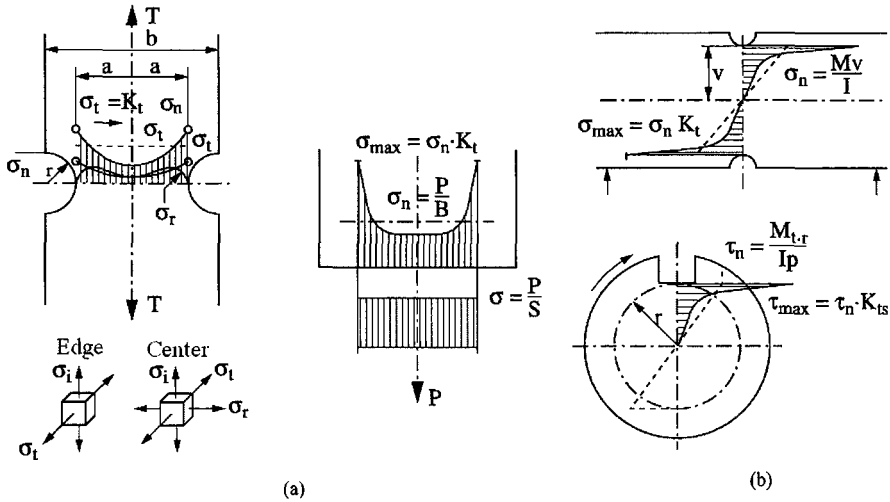

Figure 3.13. *Notch stress concentration in tension (a) and bending (b)*

Index t is used in order to show that these coefficients are theoretical and that their calculation relies on the hypotheses of elasticity theory. They are static coefficients that, for a given solicitation mode, result from the geometric shape of the specimens. They are mathematically determined using formulae established thanks to the work of Neuber (Petersen formula) [PET 53]. In the case of more common notches, we have:

$$K_t = 1 + \frac{1}{\sqrt{A\frac{2r}{D-d} + B\frac{2r(1+2r/d)^2}{d}}} \qquad [3.3]$$

where:

D = external diameter or external width of the specimen;

d = notch root diameter or notch root width;

r = radius of the notch root.

Coefficients A and B depend on the type of loading (tension, bending or torsion).

In practice, calculation has been performed for many simple situations that can occur in mechanical construction. Curves giving the values K_t or K_{ts} corresponding to the different shape parameters have been published [PET 63].

All of these results are valid if the highest calculated tensile stress does not exceed the elastic limit of the material. If the metal has a good capacity for permanent deformation (is a ductile metal) and the notch root stress exceeds its elasticity limit, a localized plastic flow occurs. This plastic flow, modifying the shape of the notch, leads to a decrease in stress concentration (relaxation). However, plastic deformation generates a local hardening due to cold working. Thus, a ductile metal adapts itself to the presence of a notch by decreasing the stress concentration and increasing the resistance of the notched section.

In brittle materials there is no stress reduction or work hardening. Fracture can then occur at a low nominal stress when a notch is present in these materials.

With fatigue, metals behave differently in the presence of a notch depending on whether they have a high capacity for permanent deformation. Experience has shown that, in all cases, the endurance limit is reduced when there is a notch, but its influence is stronger when the metal has a low adaptation capacity.

Stress concentration factors provide a parameter that is useful for describing stress conditions at the notch root, but do not give any information on the stress distribution around the notch.

The localized character of high stress around the notch is shown using the elastic strain field around a circular hole within a rectangular plate of infinite length (see Figure 3.14).

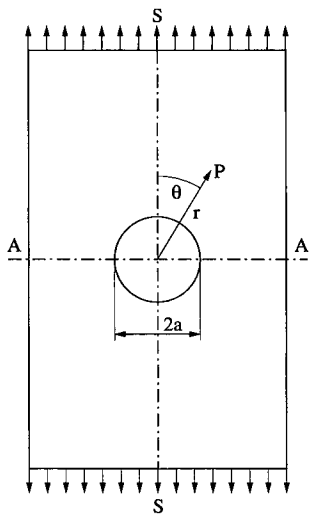

Figure 3.14. *Stresses around a hole within a plate*

In the case of a uniformly distributed tensile loading, the stresses at point P are given by [TIM 51]:

$$\sigma_r = \frac{S}{2}\left(1-\frac{a^2}{r^2}\right)+\frac{S}{2}\left(1+\frac{3a^4}{r^4}-\frac{4a^2}{r^2}\right)\cos 2\theta$$

$$\sigma_\theta = \frac{S}{2}\left(1-\frac{a^2}{r^2}\right)-\frac{S}{2}\left(1+\frac{3a^4}{r^4}\right)\cos 2\theta \qquad [3.4]$$

$$\tau_{r\theta} = \frac{S}{2}\left(1-\frac{3a^4}{r^4}+\frac{2a^2}{r^2}\right)\sin 2\theta$$

The longitudinal stress along the AA direction is obtained with $\theta = \pi/2$ in the second equation:

$$\sigma_{\theta AA} = \frac{S}{2}\left(2+\frac{a^2}{r^2}+\frac{3a^4}{r^4}\right) \qquad [3.5]$$

At the edge of the hole ($r = a$) in this section, $\sigma_{\theta AA}$ has a maximum value of 3 S; this value rapidly tends towards S when r increases.

In the case of a cylindrical notched specimen subjected to tension or bending, the stress field depends on the notch root radius ρ (see Figure 3.15).

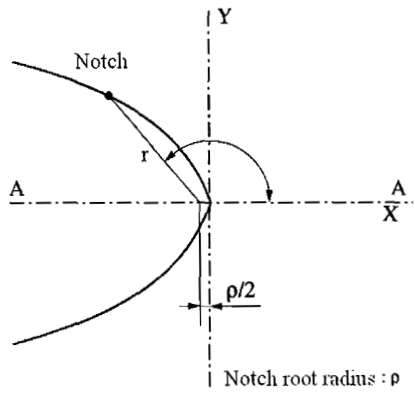

Figure 3.15. *Notch root geometry in the case of a notched cylindrical specimen*

If the depth of the notch is at least equal to ρ and the lowest diameter is at least equal to 10 ρ, σ_{AA} is given by [NIS 68]:

$$\sigma_{\theta AA} = \frac{\sigma_{\max}}{2\left(1+\frac{2r}{\rho}\right)^{1/2}}\left(1+\frac{1}{1+\frac{2r}{\rho}}\right) \qquad [3.6]$$

where σ_{max} is the notch root stress.

When $\rho \to 0$, the stress field is close to the field of a crack and can be described by using the stress intensity factor K_I. Using the coordinates of Figure 3.15, the stresses at a point close to the notch root are given by [CRE 67]:

$$\sigma_x = \frac{K_I}{(2\pi r)^{1/2}}\cos\frac{\theta}{2}\left(1-\sin\frac{\theta}{2}\sin\frac{3\theta}{2}\right) - \frac{K_I}{(2\pi r)^{1/2}}\frac{\rho}{2r}\cos\frac{3\theta}{2} \qquad [3.7]$$

$$\sigma_y = \frac{K_I}{(2\pi r)^{1/2}}\cos\frac{\theta}{2}\left(1+\sin\frac{\theta}{2}\sin\frac{3\theta}{2}\right) + \frac{K_I}{(2\pi r)^{1/2}}\frac{\rho}{2r}\cos\frac{3\theta}{2} \qquad [3.8]$$

$$\tau_{xy} = \frac{K_I}{(2\pi r)^{1/2}}\sin\frac{\theta}{2}\cos\frac{\theta}{2}\cos\frac{3\theta}{2} - \frac{K_I}{(2\pi r)^{1/2}}\frac{\rho}{2r}\sin\frac{3\theta}{2}$$

These equations contain some terms that disappear when $\rho \to 0$.

The stress intensity factor K_I is related to stress concentration factor K_t with the following equation [PAR 63]:

$$K_I = \lim_{\rho \to o}\frac{1}{2}K_t\,\sigma_{nom}(\pi\rho)^{1/2} \qquad [3.9]$$

where σ_{nom} is the nominal stress in the notched specimen.

3.3.2.2. *Reduction coefficient of fatigue resistance K_f (relationship $K_t - K_f$)*

The fatigue notch effect can be measured using the ratio:

$$K_f = \frac{\text{endurance limit on smooth specimens}}{\text{endurance limit on notched specimens}} \qquad [3.10]$$

(where we can see that K_f is a cyclic coefficient whereas K_t, is a static coefficient) and that sensitivity to the notch effect is expressed by factor q:

$$q = \frac{K_f - 1}{K_t - 1} \qquad [3.11]$$

We sometimes use factor K:

$$K = \frac{K_t - K_f}{K_t - 1} = 1 - q \qquad [3.12]$$

Factor q can vary from 0 to 1: when $q = 0$ ($K_f = 1$), the material is not sensitive to the notch effect; and when $q = 1$ ($K_f = K_t$), there is no adaptation and the effect obtained is equal to the theoretical effect.

A large number of test results on notched specimens tested with a mean stress equal to zero have been published. For stress concentration factors K_t, ranging from 1 to 4, we can observe that [FRO 74]:

– for low values of K_t, K_f can be equal to K_t, but is usually slightly lower;

– for specimens of different dimensions, but with similar geometries leading to the same K_t, depending on the situation we get some results that highlight a size effect and some that do not;

– different geometries giving the same K_t can give different values of K_f;

– for high values of K_t, K_f is usually lower than K_t;

– for a given material and different notch geometries, we have a particular value of K_t for which K_f reaches a maximum value;

– K_f seems to increase when grain size decreases.

3.3.2.3. *Method based on Neuber's coefficient*

To take the notch root radius and the material into account, Neuber [NEU 58] proposed an effective coefficient of stress concentration K_N under static conditions:

$$K_N = 1 + \frac{K_t - 1}{1 + \sqrt{\frac{\rho'}{\rho}}} \qquad [3.13]$$

where:

– ρ' is a constant of the material representing a distance beyond which there is no stress gradient;

– ρ is the notch root radius.

When ρ tends towards zero, K_N tends towards a constant value for a given material and a given notch root.

It has been shown that in fatigue [KUH 52], K_f can be expressed with a similar equation:

$$K_f = 1 + \frac{K_t - 1}{1 + \sqrt{\frac{\rho'}{\rho}}} \qquad [3.14]$$

The results obtained with this calculated value of K_f have been used to predict the lifetime of smooth and notched specimens and, in particular, to determine the notch effect on endurance limit [FRO 57, FRO 59].

Usually the stress concentration coefficient is only valid when there is no plastic notch root deformation.

Allery and Birbeck tried to apply the previous analysis to crack initiation and total lifetime on a carbon-manganese mild steel [ALL 72]. They used 300 x 25 x 6 mm specimens containing a lateral notch, and notch root radii ranging from 0.02 to 2.5 mm. Initiation has been optically detected on the free surface of the specimens, and defined as the formation of a crack of a 0.1 mm length.

These authors found a linear relationship between the number of initiation cycles N_i and the logarithm of K_N (see Figure 3.16):

$$\log K_N = 1.2969 - 0.1602\, N_i \qquad [3.15]$$

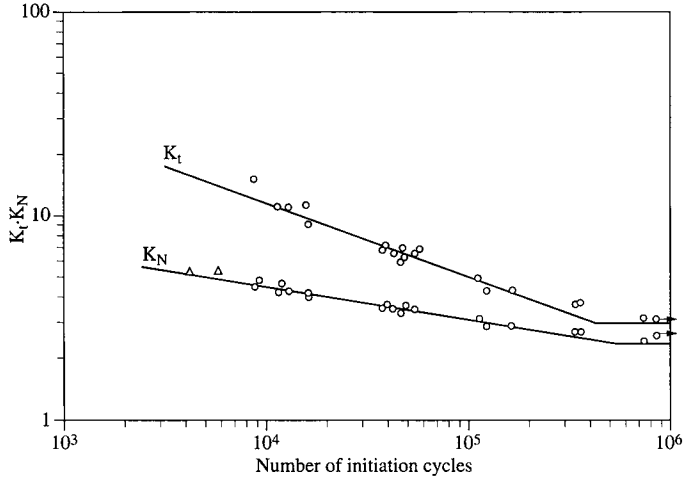

Figure 3.16. *Relationships between stress concentration factors and number of initiation cycles [ALL 72]*

Figure 3.17 shows the evolution of the notch root radius as a function of the number of initiation cycles N_i for a given stress amplitude. This figure shows that, for a radius lower than 0.1 mm, the variation of N_i is almost negligible and that, for a larger radius, the number of initiation cycles increases with notch radius.

Figure 3.18 shows that the notch root radius varies with the ratio of the number of initiation cycles to the number of cycles to failure.

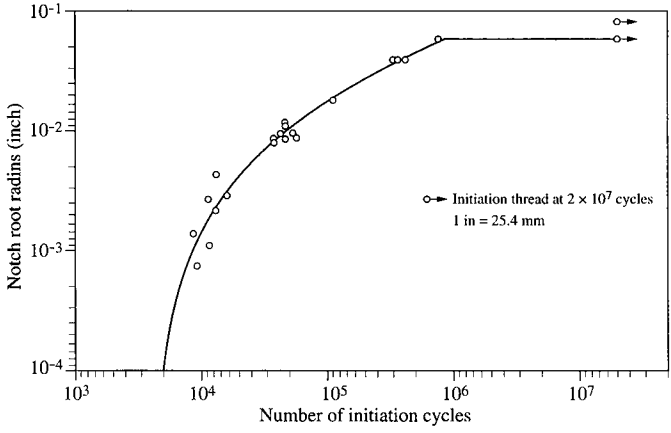

Figure 3.17. *Evolution of the notch root radius as a function of the number of initiation cycles for a given stress [ALL 72]*

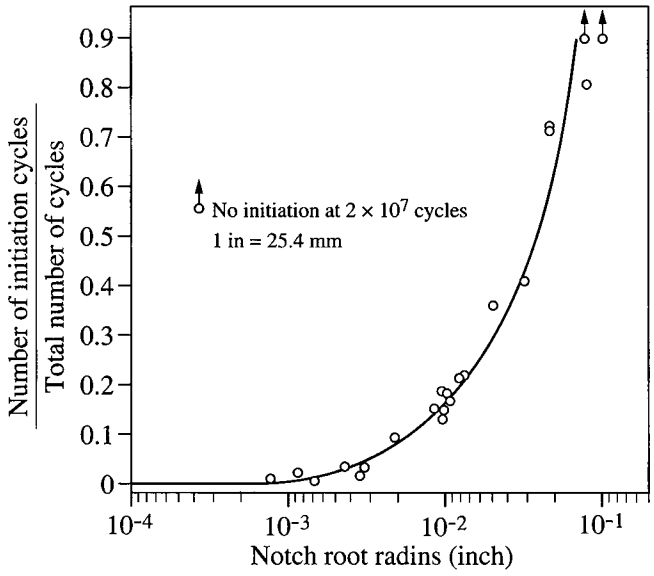

Figure 3.18. *Influence of notch root radius on the ratio of the number of initiation cycles to total number of cycles [ALL 72]*

3.3.2.4. *Method relying on the stress intensity factor*

Different authors have used the concepts of linear fracture mechanics to describe the results of initiation tests on notched specimens.

Jack and Price [JAC 70, JAC 72] showed that, in a mild steel, N_i depends on the thickness of the specimen for the highest stress levels (σ_{max} > 200 N/mm^2). Beyond a thickness of 5 mm, N_i is almost constant, all things considered. Initiation tends to be faster for low thicknesses and large stresses. The thickness threshold from which the number of initiation cycles is independent of this parameter can be related to the conditions of plane strain at the notch root.

According to Jack and Price [JAC 72], at equal stress the number of initiation cycles depends on the thickness of the specimen but, once again, there is a 20 mm threshold beyond which thickness loses its influence and N_i reaches a maximum and constant value.

The same authors confirmed the results of Allery and Birbeck, specifying that the number of initiation cycles is no longer dependent on the notch root radius when the radius is less than 0.25 mm (see Figure 3.19).

As a consequence, in the case of a sharp notch within a plate $\geq$ 20 mm wide and > 5 mm thick, the number of initiation cycles is as a simple function of the stress intensity factor. In the case of mild steel, Jack and Price found the following parametric equation:

$$N_i = \frac{2.9 \times 10^8}{(\Delta K)^4} \qquad [3.16]$$

In addition, these authors obtained a satisfying correlation of the results obtained with different notch root radii r using the parameter $\Delta K / \sqrt{\rho}$ where ρ is the notch radius (see Figure 3.20).

Figure 3.21 shows the results obtained by Clark [CLA 74] on a martensitic stainless steel of 403 type. The number of initiation cycles is represented as a function of the variation of maximum stress $\Delta\sigma_{max}$, obtained by analyzing the finite elements of the specimen.

We can see that the results covering a wide range of notch root radii (K_t ranging from 1.7 to 11) are located within a relatively narrow distribution band.

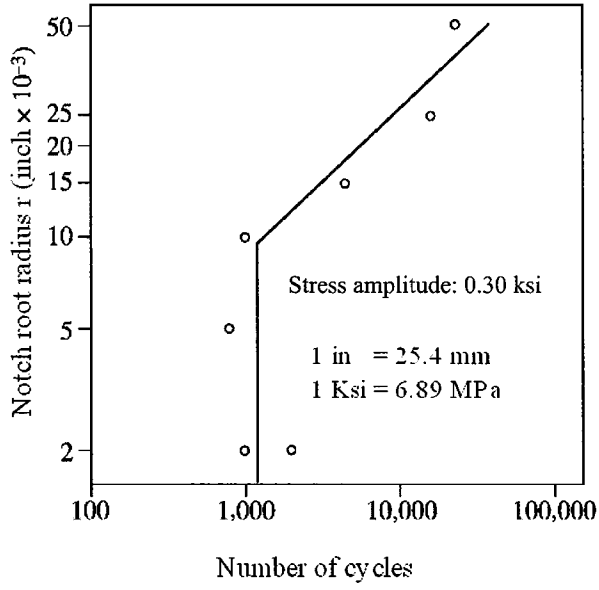

Figure 3.19. *Evolution of notch root radius r as a function of the number of cycles necessary to initiate a crack of 0.25 mm within a 25.4 mm thick specimen [JAC 72]*

Heckel, Wagner [HEC 75] and Clark [CLA 74] showed that there is no difference in the values of notch root stresses calculated using the finite element method and those calculated with the following formula:

$$\sigma_{max} = \frac{2K_I}{\sqrt{\pi r}} \qquad [3.17]$$

where K_I is the stress intensity factor calculated if the value of crack length is considered to be the length of the mechanical notch.

Similar results to those published by Clark have been obtained by Barsom and McNicol [BAR 74] for different notch geometries. Figures 3.22 and 3.23 show the results obtained by these authors on a steel of HY-130 type.

The results of Clark and Barsom and McNicol show that the parameter $\Delta\sigma_{max}$ or $\Delta K / \sqrt{\rho}$ correctly describes the initiation. In addition to these results is the existence of a value for $\Delta\sigma_{max}$ or $\Delta K / \sqrt{\rho}$ limit that agrees with the results of classic endurance if we consider the total variation of stress corresponding to the endurance limit and not its amplitude [SMI 70].

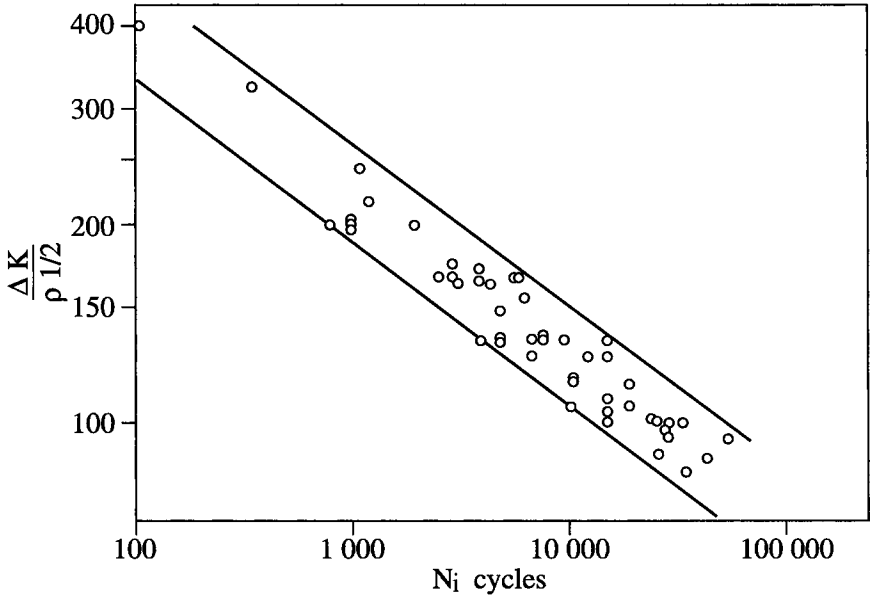

Figure 3.20. *Evolution of factor $\Delta K/\rho^{1/2}$ as a function of the number of initiation cycles N_i [JAC 72]*

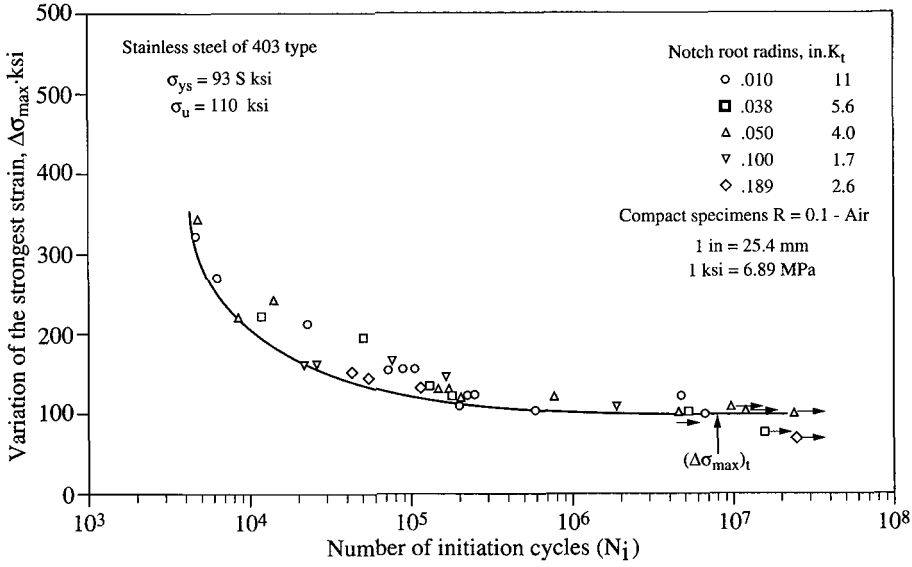

Figure 3.21. *Evolution of sress amplitude $\Delta\sigma_{max}$ as a function of the number of initiation cycles in a stainless steel of ASI-403 type [CLA 74]*

3.3.2.5. *Method based on local strain amplitude*

This method is based on the Neuber rule [NEU 61]:

$$K_t^2 = K_\sigma . K_\varepsilon \qquad [3.18]$$

where:

– K_t is the stress concentration factor for the elastic model of the material's behavior;

– K_σ is the stress concentration factor for the elastoplastic model;

– K_ε is the strain concentration factor for the elastoplastic model.

This formula has been modified by Morrow, Wetzel and Topper [MOR 70] by replacing K_t with the notch effect coefficient K. The modified Neuber rule then becomes:

$$K_f^2 = K_\sigma . K_\varepsilon \qquad [3.19]$$

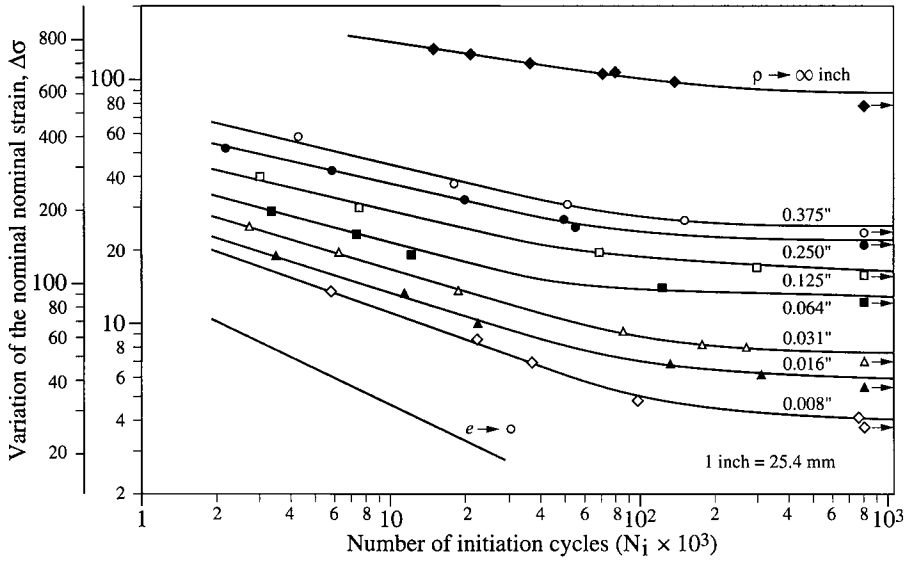

Figure 3.22. *Evolution of nominal stress amplitude as a function of the number of initiation cycles for different notch geometries in a HY-130 steel [BAR 74]*

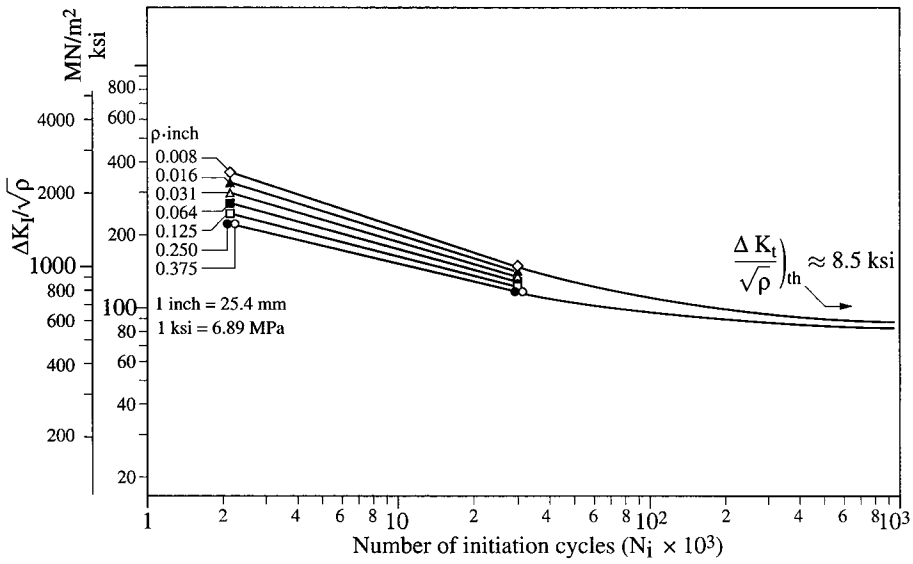

Figure 3.23. *Correlation of the number of initiation cycles with the parameter* $\Delta K/\sqrt{\rho}$ *for a HY-130 steel [BAR 74]*

Thanks to these expressions, these authors showed in an aluminum alloy that it is possible to accurately simulate tests on notched, specimens when the coefficient K_f is known. They have also shown that, in the case of a notched specimen tested under a nominal stress $\Delta\sigma_{nom}$ below the elasticity limit, the notch root is subjected to a stress-strain state such as:

$$\Delta\sigma \,.\, \Delta\varepsilon = \frac{K_f^2 \cdot \left(\Delta\sigma_{nom}\right)^2}{E} \qquad [3.20]$$

Smith and his co-workers [SMI 70] proposed the following expression that can be applied to both smooth specimens and notched specimens:

$$\log N_i = A + B \log (E\sigma_{max}\varepsilon_a)^{1/2} \qquad [3.21]$$

where:

– A and B are constants;

– σ_{max} is the maximum tensile stress;

– ε_a is the local strain amplitude along the loading direction;

– E is Young's modulus.

This equation has successfully been applied by Mowbray and McConnelee [MOW 73] to smooth and notched specimens:

– within a carbon steel and a 21/4Cr-1Mo steel that were tested at room temperature and at high temperature; and

– a stainless steel of 304 type tested at high temperature.

The values of σ_{max} and ε_a at notch root are determined using the finite element method. Figure 3.24 shows the results obtained by Mowbray and Mc Connelee.

3.4. Practical method of structure calculation

3.4.1. *Preliminary*

The prediction of crack initiation under spectral loading is a complex problem for many reasons.

First, the phenomenon is statistical. It is well known that, subjected to the same loading, "identical" specimens break at an inconsistent number of cycles. This cycle number obeys a statistical law and we rarely have enough specimens available to perform a rational analysis. We can check Chapter 2 for statistical aspects of this problem.

Second, the definition of an "initiated" crack is subjective. Industrially speaking, the crack length can be accurately determined using a measuring device; and it can be the crack strength for which "long crack" propagation law is applied.

At first, these two notions are definitely not the same; one is related to a device and we might think it does not change when we use another material, whereas the second notion is experimentally known to be dependent. We can refer to Chapter 4 regarding the definition of initiation.

Many other reasons could be put forward instead of trying to give the prediction method, however. Here we have chosen a more liberal approach, where the general concepts will be described. We will, when possible, explain the choices we made when we had to build a provisional method in order to give satisfying results.

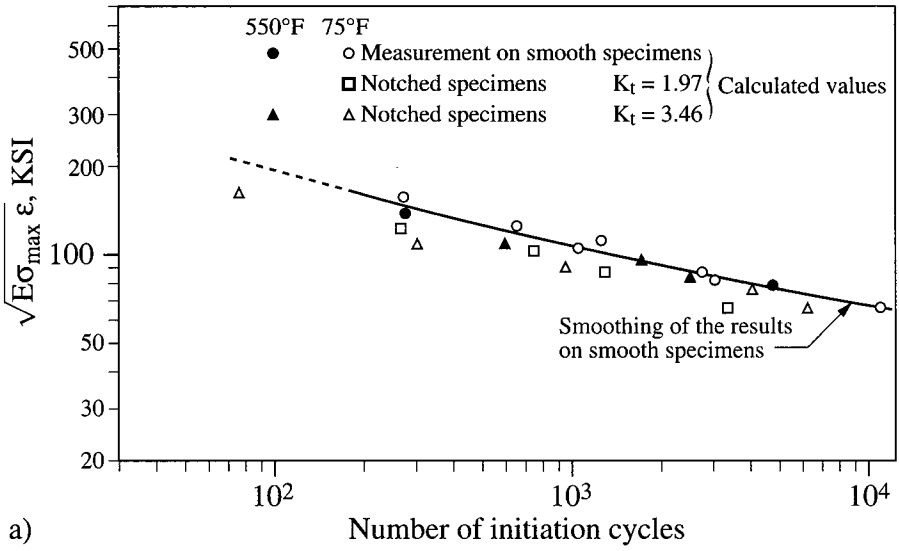

Figure 3.24. *Correlation of the initiation results on notched specimens for: a) a carbon steel*

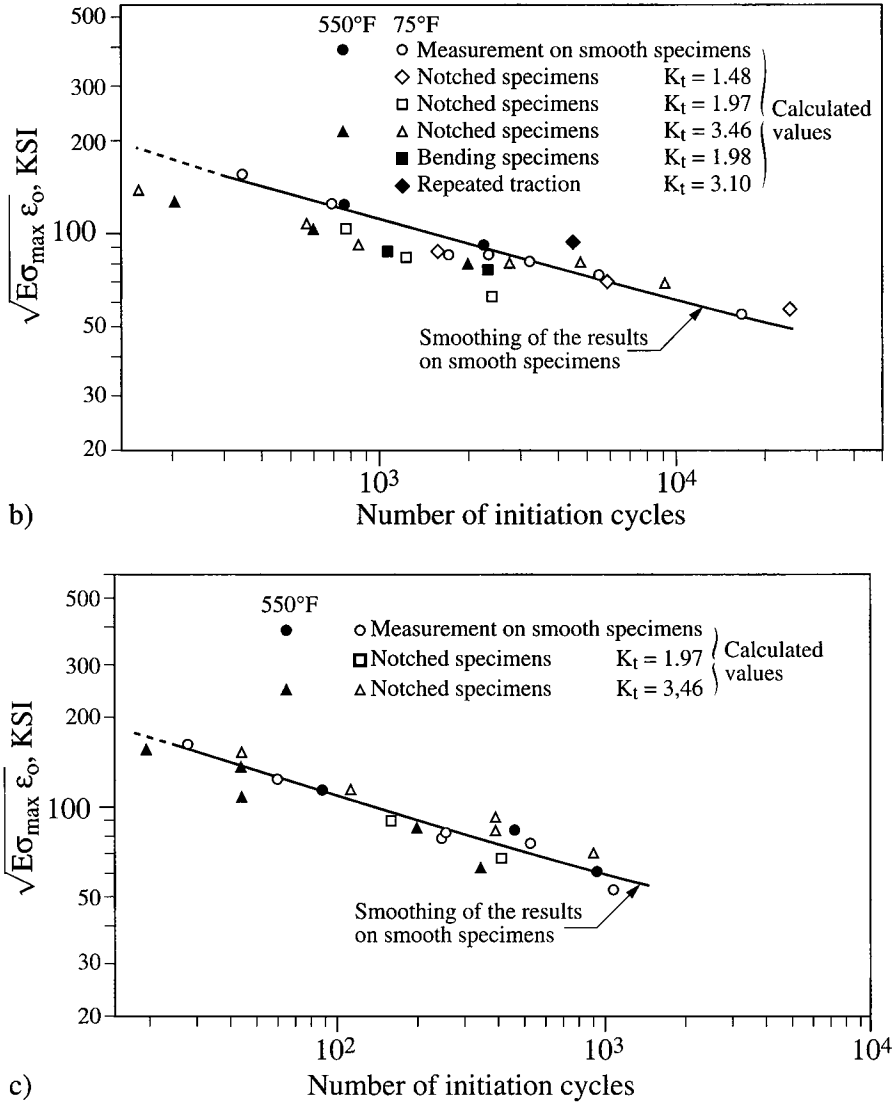

Figure 3.24. *Correlation of the initiation results on notched specimens for: b) a 21/4 Cr-1 Mo steel; and c) an austenitic stainless steel of 304 type*

3.4.2. *The problem to be solved*

Structures are not only submitted to static loading; they also undergo spectrum loading. Structural analysis at crack initiation then has to guarantee that during the

chosen lifetime of the structure no crack with a dimension larger than the detectable one will form within the structure. The influence of loading spectra is presented in Chapter 12.

We have to keep in mind, however, that we have imperfect knowledge of:

– applied loading;

– the distributed property of the static fractures of the materials;

– the inaccuracy in the knowledge of local strains; and

– inherent inaccuracy in the calculation of complex structures.

In addition to a lifetime guarantee, therefore, we have structures that have to statically hold when submitted to what is called extreme loading. This extreme loading is equal to the maximum loading that we can applied to a structure, at least once in its life, multiplied by a safety coefficient (equal to 1.5 in aeronautic engineering, for instance).

This limitation due to static, for instance, sets us free experimentally from fatigue with a low number of cycles. This limitation confines the plasticity induced by maximum loading to the over-strained region. This is an essential point, as it allows us to make sure that the local strains that are responsible for initiation continue to be controlled by the deformations of neighboring regions, which remain elastic.

The practical methods that we are trying to develop have to be judged by considering these simplifying limitations.

3.4.3. *Initiation parameters*

The condition, usually acknowledged as the cause of fatigue crack initiation, is that the material within an elementary volume located at the free surface of the specimen, undergoes a low-cycle fatigue evolution (open strain-deformation cycle, see Chapter 4).

Fatigue fractures that we can observe during the alternate loading of a specimen with $k_t = 1$ for stresses that are lower than the conventional elasticity limit are not, as a consequence, explained rationally if we do not admit that this low-cycle fatigue behavior occurs within the grains or subgrains of the material. These grains or subgrains are poorly oriented compared to the local loading direction. The low-cycle fatigue behavior of these few grains does not affect the macroscopically elastic behavior of the structure.

It is not then surprising that the first and main initiation parameter is the measurement of local shear amplitude. This shear amplitude can be measured using the second invariant of the stress amplitude (Mises-type formulation) or by using the maximum absolute value of the difference between two values of the main stress amplitude (Tresca-type formulation).

This first parameter is directly related to the parameter σ_a (the semi-amplitude of the applied stress), which is largely used to determine the ordinates of the Wölher curve in the case of some specimens with $k_t = 1$. We know that this parameter is not unique, since we have to account for the mean stress.

As a consequence, a second parameter is necessary. This is either "hydrostatic pressure" (equal to the trace of the average or maximum stress tensor) during the cycle when a Mises-type formulation is used as the first parameter, or the average or maximum normal stress to the facet of the maximum shear stress amplitude when we use a Tresca-type formulation.

These two parameters, used by Mohr, Coulomb, Tresca, von Mises and others, regarding brittle fracture are also used by Crossland, Sinès and Dang Van for unlimited endurance. The nature of these parameters is known but a choice has to be made between an "invariant"-type approach (Mises of the stress amplitude plus hydrostatic pressure) and a "facet"-type approach (Tresca of the stress amplitude and normal stress to the associated fact).

3.4.4. *The master Wöhler curve ($k_t = 1$)*

In the case of axisymmetric specimens with $k_t = 1$, whatever the adopted approach (Mises or Tresca), the two initiation parameters used are the same:

– σ_a being the semi-amplitude of the applied stress (first parameter); and

– σ_m or σ_{max} being the average stress or maximum stress of the applied cycle (second parameter).

An example of a result obtained on an aluminum alloy is shown in Figure 3.25.

As a rule a representation with the two parameters σ_a and σ_m is used.

If we plot the parts of the Wöhler curve (σ_a, $LogN_F$) for the various available values of σ_m on the same diagram, considering what was described in the second section it appears that the iso-curves σ_m can be deduced from each other with a simple translation (if we limit ourselves to the cycles leading to a fracture before 3.10^5 cycles).

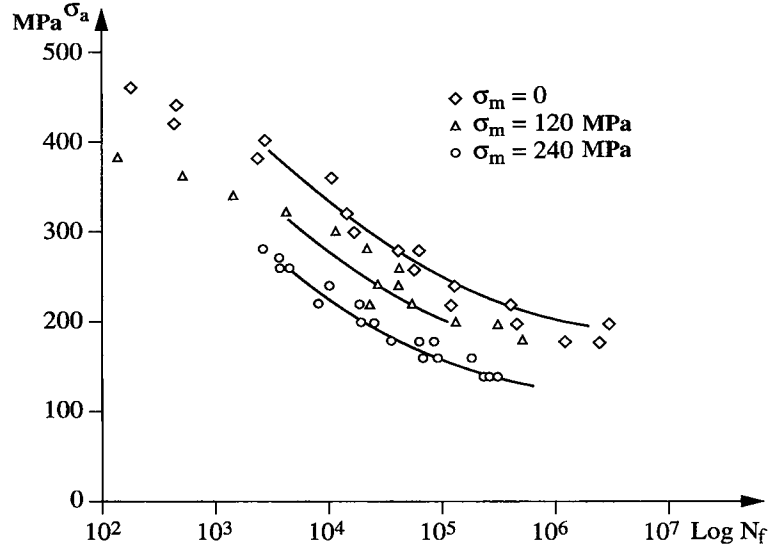

Figure 3.25. *Wöhler curves with a constant average stress (2024 T6 alloy)*

We can then rationalize the results by introducing a notion of equivalent stress, Σ:

$$\text{Log } N_F = f(\Sigma)$$

with:

$$\Sigma = \sigma_a + g(\sigma_m) \qquad [3.22]$$

If we have $g(0) = 0$, Σ is identical to alternate stress σ_a.

Identification of $g(\sigma_m)$ is an issue that is purely experimental and quite delicate as we have to work with averages. Nevertheless, it seems that there is a significant decrease in the number of tests and that we can set the following as a first and correct approximation:

$$\Sigma = \sigma_a + \alpha\, \sigma_m \qquad [3.23]$$

where α is a constant of the material to be identified as accurately as possible.

The values of α that we can identify in the case of aluminum alloys, titanium alloys or maraging steel are all located within a range of 0.3 to 0.5.

To summarize, it seems that it is possible to represent the experimental results with the following expression:

$$\text{Log } N_F = f(\sigma_a + \alpha\, \sigma_m) \qquad [3.24]$$

For couples of values (σ_a, σ_m) leading to a failure before 3 x 10^5 cycles and such as sup (σ_{MAX}, $|\sigma_{MIN}|$) is lower, at around 0.85 σ_R (where σ_R is the tensile static fracture).

3.4.5. *Cumulative damage ($k_t = 1$)*

Cumulative damage is an issue that has to be considered and resolved for smooth specimens with $k_t = 1$ as soon as we want to predict lifetimes under spectral loading.

The linear cumulative damage assumes that, if N_Σ cycles are necessary to fail a specimen submitted to an equivalent stress Σ the incremental damage per cycle, D is equal to $1/N_\Sigma$.

To verify or invalidate this hypothesis, the simplest thing to do is to apply sequential tests where N_1 cycles applied at Σ_1, are followed by N_2 cycles at Σ_2.

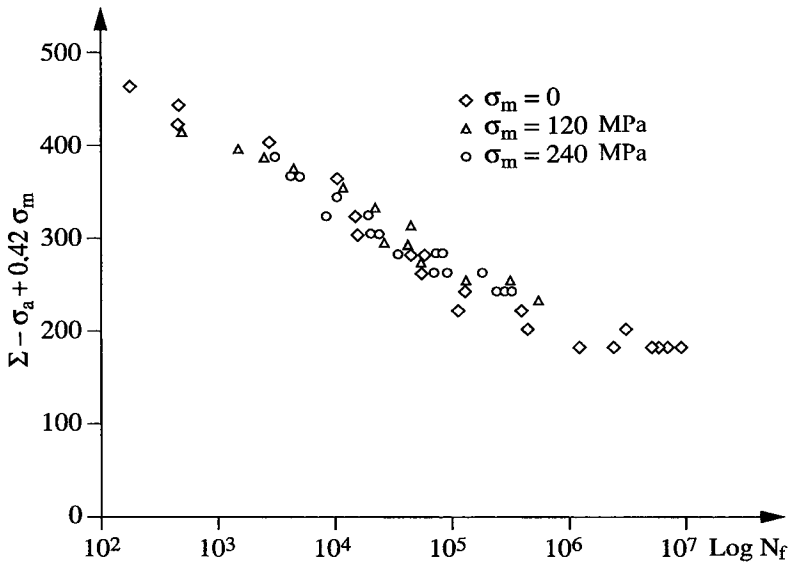

Figure 3.26. *Master Wöhler curve (2024 T6 alloy)*

If fatigue damage circulation is linear, the number N_B of sequences to need to be applied in order to reach failure is given by:

$$\frac{1}{N_B} = \frac{N_1}{N_{\Sigma_1}} + \frac{N_2}{N_{\Sigma_2}} \qquad [3.25]$$

(where N_{Σ_1} is the number of fracture cycles when Σ_1 is applied alone).

Usually, the experimental results obtained show that this equality is not satisfied, and therefore a non-linear cumulative damage rule must be introduced.

The non-linear cumulative damage sets itself up:

– *regarding linear accumulation*: mathematical formalization of the cumulative damage is as follows (for a constant amplitude loading):

$$D = \frac{N}{N_\Sigma} \qquad [3.26]$$

Damage, initially equal to zero, reaches 1 once N_Σ cycles have been applied. Here we must mention that D is, in this case, a mathematical variable that does not need to have any physical meaning;

– *regarding non-linear accumulation*: the damage D is usually expressed as:

$$D = \left(\frac{N}{N_\Sigma}\right)^{F(\Sigma)} \qquad [3.27]$$

where the non-linear property of the damage accumulation is given by an exponent which is a function of the applied stress Σ.

As an example, a simple expression for $F(\Sigma)$ is:

$$F(\Sigma) = 1 + \beta\left(\frac{\Sigma_R - \Sigma}{\Sigma}\right)^\gamma \qquad [3.28]$$

where β and γ are two constants to be determined. An example of the master Wöhler curve thus obtained is given in Figure 3.26.

3.4.6. *Specimens with $k_t > 1$: correspondence curve*

Specimens with $k_t = 1$ have a very particular property compared to specimens with k_t higher than 1: the elastic or elastoplastic stress is uniaxial and defined by the

operator. There is no issue in choosing the approach (von Mises or Tresca type) as the parameters coincide when the stress is uniaxial.

Analysis of notched axisymmetrical specimens with $k_t > 1$ creates more difficulties. At the free surface and at the notch root, the stress state is not uniaxial: when σ_{rr} is equal to zero, $\sigma_{\theta\theta}$ is not. The three stresses then evolve when we move away from the free surface towards the core of the specimen (presence of a gradient). Finally, everything becomes more complicated when local plasticity is reached. An example of experimental results is given in Figure 3.27.

In addition, an industrial approach to the problem demands that we follow the history of both initiation parameters (that is to say without relying on any elastoplastic calculations).

At this stage, a choice has to be made between a von Mises-type approach and Tresca-type approach.

We wanted to compare an alternating tension-compression curve with $k_t = 1$ and an alternating torsion Wöhler curve on a tubular specimen. For this reason we decided to use a Tresca-type approach to measure the local shear stress amplitude associated with the average normal stress of the facet where the highest shear occurs.

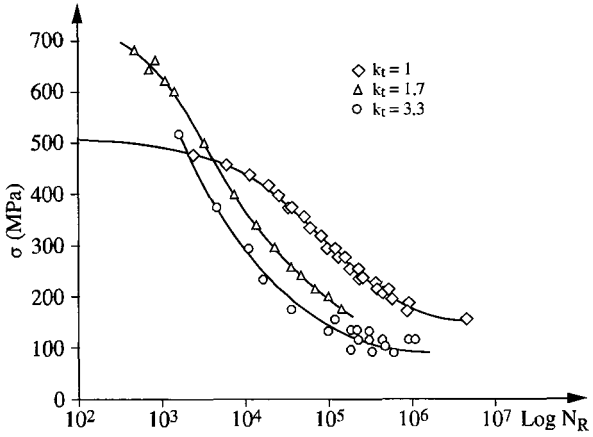

Figure 3.27. *Wöhler curve under an alternating stress for three different specimens*

We have to mention that this comparison, performed on two aluminum alloys (2024 T351 and 7010 T651), requires that the propagation between "initiated" cracks and failure is as low as possible in order to reduce interpretation errors.

As this choice has been made alternating tension compression tests with $k_t > 1$ are becoming more important. As a matter of fact, in this case we think that, even with plasticity, the stress states regarding the largest and smallest applied loads are equal and opposite. In this case, the second initiation parameter remains equal to zero (no mean stress effect).

Under alternating loading conditions, a specimen with $k_t = 1$ and one with $k_t > 1$ that both fail at an identical number of cycles have, where the loading is highest, the same Tresca value of stress amplitude. This value, which is difficult to calculate in the case where $k_t > 1$, is nevertheless easy to calculate when $k_t = 1$ as it is the alternating stress σ_a.

By simply processing the Wöhler curves of a specimen with $k_t = 1$ and of a specimen with $k_t > 1$, it is then possible to plot a corresponding curve between the applied reference stress for the specimen with $k_t > 1$ and the Tresca value of the amplitude of local stresses.

If the calculation point of the Tresca stress was at the free surface, where σ_{rr} is null and $\sigma_{\theta\theta}$ of the same sign as σ_{zz} (regarding elasticity, by definition of k_t, to k_t σ_{ref}), the Tresca stress is equal to k_t σ_{ref} as long as the material is elastic.

The slope of the correspondence curve within its first part would then be equal to $1/k_t$.

We can observe that this is not often the case, especially when the notch root radius is small (a standard specimen with $k_t = 3.3$ has a notch root radius equal to 0.35 mm). The value of the Tresca stress has to be calculated at a certain distance from the notch rather than at the free surface. This distance, which we will call critical distance, characterizes the material studied.

We notice that at this critical distance, σ_{rr}, remains low but is not equal to zero. This means that we will need two correspondence curves: the first relative to $\sigma_{zz} - \sigma_{rr}$ (given experimentally); and the other relative to $\sigma_{zz} + \sigma_{rr}$ (to deal with non-alternating loading). This curve is easy to plot if we admit that, as a first approximation, the three stresses evolve proportionally. This is strictly valid under elasticity, and more or less so under plasticity.

We should nevertheless highlight that this is not that serious because the second correspondence curve will be used to determine the average normal stress which, when calculating equivalent stress Σ, is multiplied by a coefficient ranging from 0.3 to 0.5, as we already mentioned. Therefore, if we make an error on the average normal stress it is not as bad as if we made one on the Tresca of the stress amplitude. This explains the fact that some approximations can be made.

3.4.7. *Use of correspondence curves*

Starting from the idea that correspondence curves are similar to cyclic work hardening curves, it is possible, if we adopt a rule of Masing type, to follow the elastoplastic evolution of two local parameters, $\sigma_{zz} - \sigma_{rr}$ and $\sigma_{zz} + \sigma_{rr}$, as a function of the evolution of σ_{ref}. As soon as a loop is closed, we calculate:

– the Tresca value of the stress amplitude;

– the average normal stress using the second correspondence curve.

3.4.8. *Plotting the correspondence curves*

The last problem that has to be solved is as follows: as we have a structural detail that we cannot closely analyze using elasticity, which correspondence curves must be used?

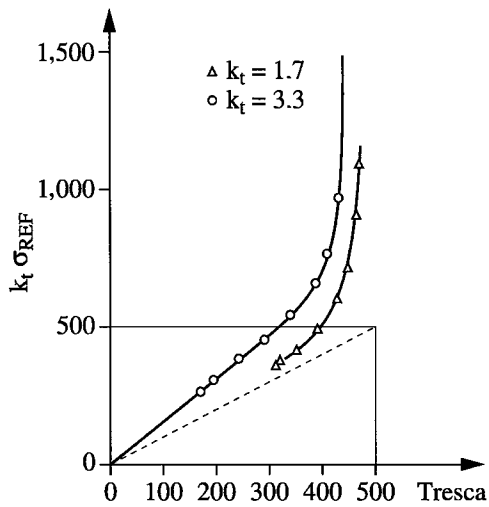

Figure 3.28. *Correspondence curves*

If we approximate the correspondence curve using a hyperbolic branch, there is no difficulty in plotting the branch going through the origin when the critical distance is known. As the center of the hyperbole is related to the elastic limit, if σ_1, σ_2 and σ_3 are known and a function of a reference stress, we can easily identify the position of this center. We then have to determine the slope of the hyperbole's plastic branch and the distance at the maximum. If we already have two or three correspondence curves, the identification rules can easily be deduced.

When the correspondence curves are plotted, we can transform the history of σ_{ref} into a local one of the two initiation parameters, and thus into the history of the equivalent stress Σ. As the history of Σ is known, linear and non-linear cumulative damage rules can be applied to determine the lifetime at crack initiation the detail of the structure being analyzed. An example of correspondence curves is given in Figure 3.28, whereas the use of the principle of correspondence curves is schematically shown in Figure 3.29.

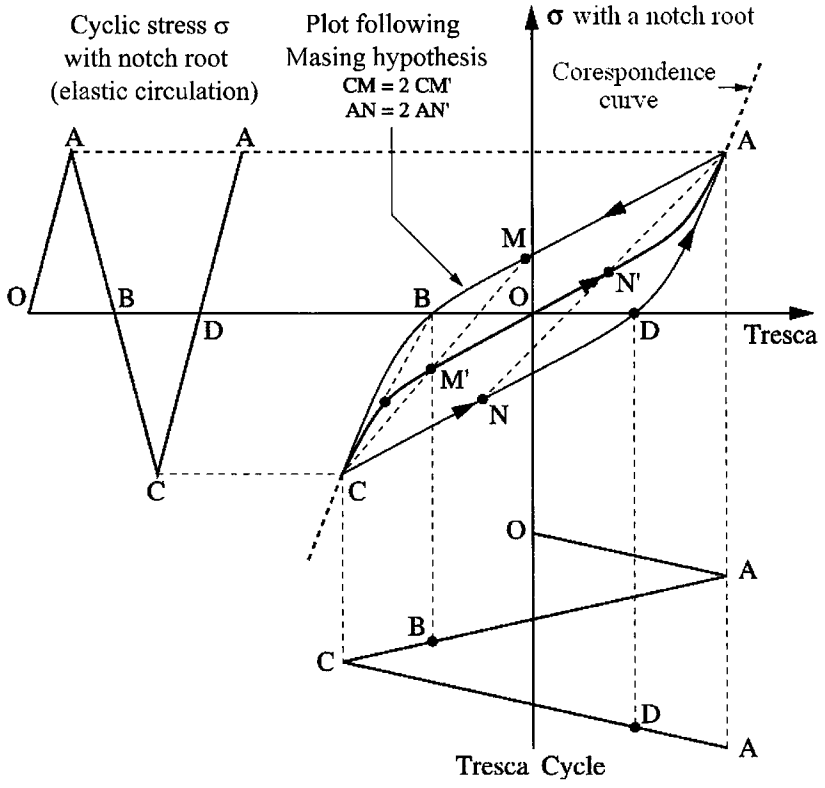

Figure 3.29. *Use of the corresponding curve (rule similar to the Masing rule)*

3.4.9. *Comments and conclusion*

We wanted to show that, if we already have a database that allows us to identify the various material parameters, we can develop a module of predictive calculation that is satisfactory from the point of view of precision.

We then appreciate that we do not completely trust the elastoplastic calculation and prefer to draw conclusions from experimental results. We think that this is the best way to ensure that we are relying on an appropriate data.

Each detail must be carefully examined through calculation tests and comparisons between tests and calculations before being implemented in the calculation module. The ideal case would be to rely on a database established from test results obtained on various specimens subjected to very different loading spectra.

3.5. Bibliography

[ALL 72] M.B.P. Allery, G. Birkbeck, "Effect of notch root radius on the initiation and propagation of fatigue cracks", *Eng. Fract. Mech.*, vol. 4, p. 325-331, 1972.

[BAR 74] J. M. Barson, R.C. Mc Nicol, "Effect of stress concentration on fatigue-crack initiation in HY-130 steel", *ASTM STP 559*, p. 183-204, 1974.

[BAT 74] C. Bathias, G. Sertour, *17e Colloque de Métallurgie de Saclay*, 647, Saclay, France, June 1974.

[BOW 73] C.Q. Bowles, J. Schive, "The role of inclusions in fatigue crack initiation in an aluminum alloy", *Int. J. Fract.*, vol. 9, p. 171-179, 1973.

[BRO 63] T. Broom, J. M. Summerton, "Fatigue of zinc single crystals", *Phil. Mag.*, vol. 8, p. 847-1862, 1963.

[CLA 74] W.G. Clark, "Evaluation of the fatigue crack initiation properties of type 403 stainless steel in air and steam environments", *ASTM STP, 559*, p. 205-224, 1974.

[COT 57] A.H. Cotrell, D. Hull, "Extrusion and intrusion by cyclic slip in copper", *Proc. Roy. Soc.*, A242, p. 211-213, 1957.

[CRE 67] M. Creager, P.C. Paris, "Elastic field equations for blunt cracks with reference to stress corrosion cracking", *Int. J. Fract. Mech.*, vol. 4, p. 247-252, 1967.

[EEL 68] E.G. Eeles, R.C.A. Thurston, "Fatigue properties of materials", *Ocean and Engineering*, vol. 1, pp. 159-187, 1968.

[FOR 72] P.J.E. Forsyth, "Fatigue behaviour and its dependence on microstructure", *15e Colloque de métallurgie de Saclay*, pp. 1-25, Saclay, France, June 1972.

[FRO 57] N.E. Frost, D.S. Dugdale, "Fatigue tests on notched mild steel plates with measurements of fatigue cracks", *J. Mech. Phys. Sol.*, vol. 5, p. 182-192, 1957.

[FRO 59] N.E. Frost, "A relation between the critical alternating propergation stress and crack length for mild steel", *NEL Rep.*, vol. 173, pp.811, 1959.

[FRO 74] N.E. Frost, K.J. Marsh , L. Pook, *Metal Fatigue*, Clarendon Press, Oxford, 1974.

[GRO 71] J.C. Grosskreutz, "Fatigue mechanisms in the sub-creep range", in S.S. Manson (ed.), *ASTM STP 495*, ASTM, p. 5-60, 1971.

[HEC 75] K. Heckel, R. Wagner., "Tensile fatigue behaviour of CT-specimens with small notch root radius", *Int. J. Fract.*, vol. 11, p. 135-140, 1975.

[JAC 60] P.A. Jacquet, "Technique de la réplique au vernis et du polissage électrolytique local pour les examens non destructifs sur les surfaces métalliques", *Revue du GAMI*, no. 3, p. 3-11, 1960.

[JAC 70] A.R. Jack, A.T. Price, "Initiation of fatigue cracks from notches in mild steel plates", *Int. J. Fract. Mech.*, vol. 6, p. 401-411, 1970.

[JAC 72] A.R. Jack, A.T. Price, "Effects of thickness on fatigue crack initiation and growth in notched mild steel specimens", *Acta Metal.*, vol. 20, p. 857-866, 1972.

[KLE 65] M. Klesnil, P. Lukas, "Dislocation arrangement in surface layer of alpha-iron grains during cyclic loading", *J. Iron Steel Inst*, vol. 203, p. 1043, 1965.

[KUH 52] P. Kuhn, H.F. Hardrath, "An engineering method for estimating notch-size effect in fatigue tests on steel", *Nat. Adv. Co. Art. Tech. Note 2805*, 1952.

[LAI 63] C. Laird, G.C. Smith, "Initial stages of damage in high stress fatigue in some pure metals", *Phil. Mag.*, vol. 8, p. 1945-1963, 1963.

[LAN 73] J. Lankford, F.N. Kusenberger, "Initiation of fatigue cracks in 4340 steel", *Met. Trans. B*, vol. 4, p. 553-559, 1973.

[LOU56] N. Louat, N. Thompson, N. Warsworth, "The origin of fatigue fracture in copper", *Phil. Mag.*, vol. 1, p. 113-126, 1956.

[MOR 70] J.D. Morrow, R.M. Wetzel, T.H. Topper, "Laboratory simulation of structural fatigue behavior", *ASTM STP 462*, p. 74-91, 1970.

[MOW 73] D.F. Mowbray, J.E. Mc Connelee, "Applications of finite element stress analysis and stress-strain properties in determining notch fatigue specimen deformation and life", *ASTM STP 519*, p. 151-169, 1973.

[NEU 58] H. Neuber, *Kerbspannungslehre*, Springer, Berlin, 1958.

[NEU 61] H. Neuber, "Theory of stress concentration for shear-strained prismatic bodies with arbitrary nonlinear stress-strain law", *J. Applied Mech.*, vol. 28, p. 544-550, 1961.

[NIS 68] H. Nisitani, "Effects of size on the fatigue limit and the branch point in rotary bending tests of carbon steel specimens", *Bull. J.S.M.E.*, vol. 11, p. 947-957, 1968.

[PAR 63] P. Paris, F. Erdogan, "A critical analysis of crack growth propagation laws", *J. Basic Eng*, vol. 85, p. 528-534, 1963.

[PET 53] C. Peterson, *Stress Concentration Design Factors*, John Wiley & Sons, New York, 1953.

[PET 63] R.E. Peterson, *Mat. Res. Stand.*, vol. 3, p. 122-139, 1963.

[PIN 76] A. Pineau, "Mécanismes d'accommodation et de fissuration en fatigue oligocyclique", *Mécanique-Matériaux-Électricité*, vol. 6, p 323-324, 1976.

[SMI 70] K.N. Smith, P. Watson, T.H. Topper, "Stress strain function for fatigue of metals", *Journal of Materials.*, vol. 5, p. 767-778, 1970.

[THO 56] N. Thomson, N.J. Wadjwer, N. Louat, "The origin of fatigue fracture in copper", *Phil. Mag.*, vol. 1, p. 113, 1956.

[THO 71] A.W. Thompson, W.A. Backofen, "Effect of grain size on fatigue", *Acta Met.*, vol. 19, p. 597-606, 1971.

[TIM 51] S. Timoshenko, J.N. Goodier, *Theory of Elasticity*, McGraw-Hill, New York, 1951.

[WOO 58] W. A. Wood, "Formation of fatigue cracks", *Phil. Mag.*, vol. 3, p. 692-699, 1958.

Chapter 4

Low-cycle Fatigue

4.1. Introduction

4.1.1. *Application domain of low cycle plastic fatigue*

4.1.1.1. *Background*

As we expect from its name, low cycle fatigue (LCF) has two fundamental aspects:

– a significant plastic deformation occurs in each cycle, i.e. plasticity;

– low cycle phenomenon, in that the materials have a finite endurance for this type of loading. Analysis of material behavior under this type of loading is quite common.

Indeed, if the first studies on the role of plastic deformation on fatigue endurance go back to the early 20th century: Bauschinger (1886) to Bairstow (1909), we have to wait until 1948 for the first strain-controlled tests to be carried out (Liu, Lynch and Ripling) and 1952–1953 for the formulae relating endurance to strain amplitude to be proposed (Manson and Coffin [COF 54, MAN 52]). Since then, studies on fatigue have been rapidly multiplied and their importance has been emphasized.

Chapter written by André PINEAU.

This chapter is largely inspired by the chapter written by André PINEAU and Pierre PETREQUIN for [BAT 97].

The interest in the studies related to low cycle fatigue lies mainly in two fields:

– application to the size and design of components in aeronautics, energy production, etc., which can be performed using advanced calculation methods;

– the use of LCF results allows us to analyze the behavior of the materials in greater detail and to better understand the complex mechanical and metallurgical phenomena (strain concentration, crack propagation, work-hardening, work-softening, etc.).

4.1.1.2. *Low-cycle fatigue in structural analysis*

Industrial devices are calculated in such a way that the materials in the main structures are not loaded within the plastic domain under normal operating conditions. "Primary" stresses are those that depend mainly on imposed forces and do not disappear under plastic deformation. "Secondary" stresses are those that are mainly due to imposed displacements and relax under a limited plastic deformation. If primary stresses are kept strictly below some fraction of the elastic limit of the materials, "secondary" stresses can be slightly higher than the elastic limit.

In addition, under exceptional working conditions we can accept a limited amount of plastic deformation.

Among the main causes of secondary stresses, we can include the temperature gradients and differential dilatations, deformation incompatibilities in geometrically complex structures, etc.

In practice, these types of loading occur mainly during transitory operating conditions:

– start-up and shut-down of a system;

– take off and landing of aircraft;

– etc.

Thus, we can associate LCF with plastic deformation and a limited number of cycles. Analysis of the durability of structures to LCF can usually be carried out by calculating the deformations the component is subjected to.

Calculation is often performed using elasticity theory, but at the present time elastoplastic calculation are only used for complex cases. This can be done thanks to the development of constitutive laws and numerical calculation methods. When a particular material is used, that is to say for a given number of cycles, the calculated deformation is compared to the acceptable deformation deduced from the LCF properties of the material.

This is why the basic data for these applications of LCF is the fatigue endurance curve, presented later in this chapter. The fatigue resistance curve for a given material provides the number of cycles the material can sustain under a given imposed deformation. In practice, as elasticity theory is largely used for the calculation of structures, the imposed plastic deformation is sometimes turned into ficticious elastic stress by multiplying it by Young's modulus. Nevertheless, as experimental results are obtained for particular test conditions, reduction coefficients are introduced to take different effects into account:

– bi-axiality;

– type of materials;

– role of a mean stress or mean strain;

– etc.

Thus, in the electro-nuclear industry the number of life reduction coefficients usually used for special codes is 20 and two as applied to stresses.

One of the first descriptions of the use of LCF data as a sizing criterion was suggested by Langer in 1962 [LAN 62].

Since then, construction codes, and especially the ones from the American Society of Mechanical Engineers (ASME), propose some analysis methods for LCF. From the aspect perspective of applications of LCF, we may suggest that the most productive lines are:

– determination of the basic data of materials and especially of the fatigue resistance curves;

– advanced analysis of the behavior of materials to better control the used reduction coefficients.

For instance, within this field we can use the example of:

– the combination rules of the cycles with different amplitudes;

– the role of deformation or average stresses;

– the connection with fatigue with high cycle fatigue;

– the effect of intermediate plastic deformations of different nature (creep for instance);

– etc.

4.1.1.3. *Low cycle plastic fatigue as the key to understanding mechanical or metallurgical phenomena*

Earlier, LCF was considered to be a global phenomenon whose consequences were simply controlled using reduction coefficients.

The modern calculation methods of the structures – calculation based on finite elements for instance – try to analyze the behavior of the materials as closely as possible in order to reduce the uncertainties and safety coefficients, which are usually excessively conservative and, as such, very limiting.

This then leads to the development of elaborate elastoplastic or even elastoviscoplastic calculation codes that, in order to work, need specific formulations of the behavior of the materials. The elastoplastic behavior laws and work hardening laws, etc., are complex and vary significantly from one material to another, often not being that well known. This remains a significant research topic where low cycle plastic fatigue is involved.

Finally LCF, which we have considered at the macroscopic and global scale, can also occur at the microscopic or localized scale in specific areas of a structure that is elastically loaded. Knowledge of these laws enables us to predict elastic macroscopic behavior by performing a local analysis. The use of LCF theories helps us a great deal in understanding the phenomena of deformation at strain concentrations.

It is exactly at this point that the use of LCF theories becomes widely applicable in the industry of rotary machinery. These theories are also commonly used for the analysis of crack propagation, etc.

4.1.2. *General description of the test methods: main issues*

4.1.2.1. *Background*

The general principle of LCF tests involves setting a load that triggers a cyclic plastic strain within the body of a specimen. We are then able to determine the number of cycles that the specimen can handle under a given strain, along with different parameters.

As LCF depends mainly on deformation, most tests are carried out with an imposed strain. This technique is discussed below.

Some tests with controlled load can also be performed, but then the analysis of the phenomena is more complex (including the possibility of the ratcheting effect or of adaptation) and the domain of study is more limited.

Nevertheless, the tests allow us to better evaluate the connection between LCF and classic fatigue. In addition, these tests are usually useful for identifying or testing the constitutive equations of the materials. Most of the time, tests are carried out with a total given reversed strain under strain controlled conditions:

$$\left(R_\varepsilon = \varepsilon_{min} / \varepsilon_{max} = -1\right)$$

However, in most cases, testing is done in total strain control. These tests are carried out using some analog systems and electronic controls that allow us to compensate for variations in elastic deformation due to hardening or softening of the material.

4.1.2.2. *Test machines*

In this section, we will focus on the test methods with imposed strain. We will not go into too much detail, but will simply identify the main issues and sources of inaccuracy.

Test methods are presented in detail in the literature [LIE 76]. ASTM International, originally known as the American Society for Testing Materials, has proposed a detailed standard for such tests (E606-77T) [AST 88].

In France, a working group of the Fatigue Committee of Metallurgy, French Society, has studied these issues. The French standard *A03-403 Pratique des Essais de Fatigue Oligocyclique*, which can be translated as *Methods of Low Cycle Fatigue Testing*, of December 1990, is the result of their work [AFN 90].

The first attempts to simplify the problem of reversal of the main strain involved performing alternate twisting tests. This method is still used but it is mainly for tension–compression that the most significant tests have been developed. In the case of compression, in order to avoid buckling we have to use specimens that are slightly thinner, with a short gauge section and significant connecting radii (see Figure 4.1). Tests are limited to about 10^5 cycles and are carried out with a low frequency or strain rate (a few cycles per minute), as the energy that is dispersed at each cycle is significant and could lead to a serious heating effect.

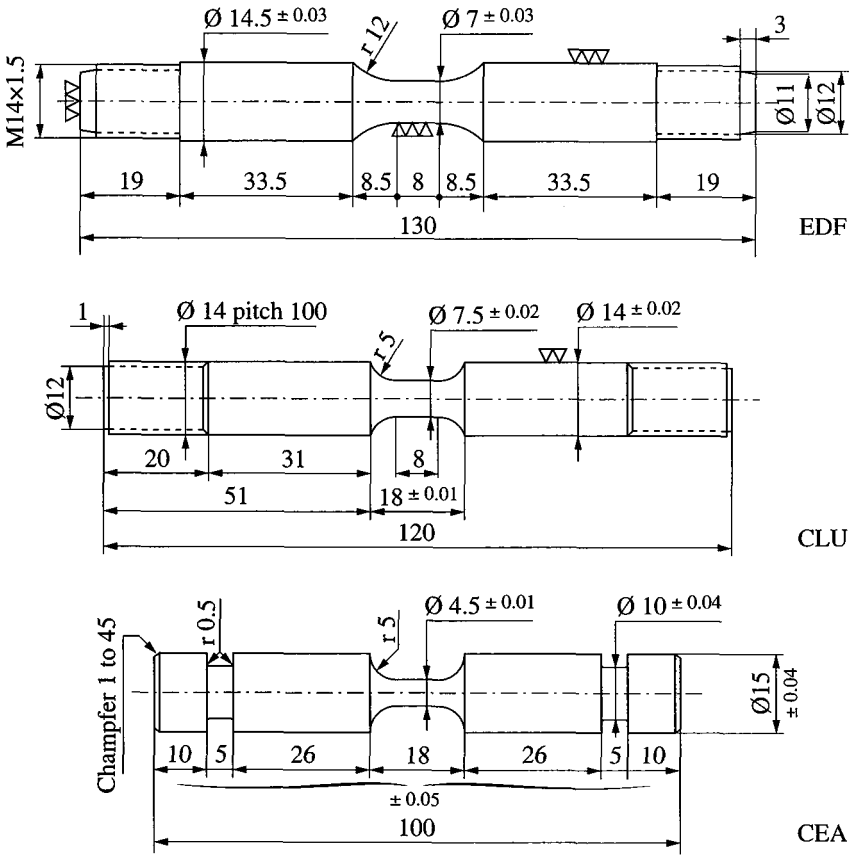

Figure 4.1. *Low-cycle fatigue specimens*

4.1.2.2.1. Mechanical machines

The first tension-compression machines devised were mechanical and had a system of eccentric bearing units that enabled tension/compression displacements to be imposed on the specimen. Recording the force and imposed displacement allowed people to control and analyze the test. After a time, this technique was discarded because of experimental uncertainties.

Indeed, as we mentioned earlier, the gauge section of the specimen is short. The reduced section compared to the loading system needs to be of large volume to avoid the problem of buckling. The sinusoidal displacement imposed to one end of the load train, therefore, is not entirely passed on to the calibrated part of the specimen. The elastic deformations of the loading line disturb the test.

This effect would be inconsequential if the forces passed on to the specimen and thus the elastic deformations were constant during the test. We will see later that this is often untrue, and thus the real strain imposed on the specimen can vary considerably during the test, which complicates the interpretation of the test results.

This is why we had to constantly control the strain imposed on the specimen using servo machines. This was first performed using electromechanical machines. The appearance at the beginning of the 1970s of servo-hydraulic machines allowed people to make significant progress regarding low-cycle fatigue tests.

4.1.2.2.2. Servo-hydraulic machines

These machines enable us to keep the strain or stress imposed on the specimen, as well as the strain rate, at a constant level. The strain does not have to be sinusoidal and we can carry out some tests with a constant strain rate.

If the variable we need to control is the strain, it is better to determine strain using an electrical system providing an analogical signal to control the machine.

Analysis of the results is then simplified as the parameters imposed are strictly controlled. The main problems come from the extensometry techniques, which will be presented in the next section. Finally, it is also worth mentioning that we can use servo-mechanical machines, but this type of machine is currently less popular than hydraulic techniques.

4.1.2.3. *Extensometry: set-up and grips*

Extensometry is usually performed using inductive sensors or strain gauges. Contact-free laser extensometry is being developed but is not widely used. The gauge length is small for reasons of compressive stability and this influences the way the extensometer is fixed on the specimen .

Depending on the test temperature, the extensometer is either attached directly to the specimen or is located on rods that transmit specimen deflection.

There are two main types of extensometry: axial and diametral. It is worth mentioning that, in some cases, it is better to rely on mechanical contact-free extensometers (optical or laser extensometers).

4.1.2.3.1. Axial extensometry

In axial extensometry, fixing an extensometer to the gauge section allows us to deduce the imposed deformation immediately. The basis for measurement can be defined by the extensometer or the specimen.

In the first case, the specimen is smooth and for accuracy of measurement, the extensometer is calibrated using known displacements. The extensometer may be fixed with various tightening devices.

In the second case, the specimen has a section increase that is a localized: flanked shoulder allowing the extensometer to be fixed.

The difficulty in both cases is to make sure that, for a given material and test condition, fixing the extensometer does not lead to a premature fracture of the specimen at the attachment point.

We have to mention that the sensitivity of materials to this phenomenon varies widely but the difficulties met are much greater in the case of tension–compression fatigue rather than for simple tension tests (tension or creep tests). These localized fracture phenomena are usually associated with large strain amplitudes.

It is likely that alignment problems of the machines and spurious bending moments, which can appear during the compression part of the cycle, play a significant role in test results. When there is a problem, the main solution consists of improving the alignment of the machines – for example with wood, metal pots and use of some wider specimens and grips. In the case of knife-edges, extensometer, tightening control has to be considered as well as the existence of any local deposits under the knives, such as varnish or electrolytic deposits.

With flange systems, we can attenuate the stress and strain concentrations by using larger connecting radii. We may then encounter a problem due to heterogenity of the deformation within the gauge section or the determination of the significant deformation. A correction factor has to be introduced, either by calculation or by prior calibration, or by using both techniques. The strain measurement is then no longer direct and involves a calculation. When we try to minimize all stresses and strains, we have to use an hour glass specimen. With such a specimen the gauge section is reduced to zero. The determination of the deformation from such a specimen is done through the use of diametral extensometers from which axial strains are calibrated.

4.1.2.3.2. Diametral extensometry

This type of extensometry was used extensively for the first LCF studies. Difficulties due to alignment problems and the rigidity of the loading systems can be limited. Nevertheless, diametral extensometry has been progressively replaced by longitudinal extensometry because of advances in equipment which minimizes alignment and measurement.

Within the reduced section of the specimen we can control variations in diameter. This can be done using rods of cylindrical extensometers. When the rods become blunt, the risk of indentation is limited. From measurement of the total diametral strain and from the measured force, we can determine and control the axial plastic strain. The axial strain may be obtained using a small calculating device. Unfortunately, this technique also presents some drawbacks. Calculation of the axial plastic strain requires knowledge of the elastic and plastic constants of the material. Anisotropy of plastic deformation can lead to significant problems.

Such problems are particularly noticeable in the case of Poisson's ratio in the plastic region. This is theoretically equal to 0.5 due to the conservation law of the volume during a plastic deformation. In reality, however, it can vary from 0.4 to 0.7 depending on the contact diameter chosen.

If the specimen was taken from a sheet of metal or a welding, it is often the case that a circular section becomes oval under plastic deformation due to the development texture. This is a serious issue that also occurs for single crystals.

Another problem connected to the volume of a deformed metal occurs for hour glass specimens. Plastic flow can be modified if the minimum radius is reduced due to a bulging phenomenon but the effect is particularly noticeable if the strained surface is reduced. As cracking leading to fracture usually occurs at the surface, a reduction in the initiation crack sites on an hour glass specimen can lead to longer life compared to that of cylindrical specimens, as shown by Soo and Chow [SOO 77].

These observations have led us to study the effect of surface condition on life. The sensitivity of the materials can vary a great deal. Finish machining is usually used and is often followed by manual or electrolytic polishing.

4.1.2.3.3. Summary of extensometry issues

It is really hard to find an extensometry system that is entirely satisfying if we want to avoid any premature fracture. The cases where deformation can be determined directly without any calculation are limited to materials that are not very sensitive to the effects of strain concentration, allowing the extensometer to be fixed directly to the gauge section. In other cases – such as axial extensometry with connecting radii or diametral extensometry – corrections and preliminary calibration are essential. Calibration and inclusion of corrections usually makes the test programs more complex because the results depend on every operating parameter: materials, temperature and specimen geometry. As the phenomenon of premature fracture for such conditions is limited and the deformations are correctly determined, the remaining problem is to determine whether these results, obtained under axial and diametral extensometry, are identical.

The sensitivity of materials to local effects can be different depending on whether LCF or high cycle fatigue (HCF) occurs. For instance, stainless steels, which exhibit significant plasticity are much more sensitive to the phenomena described above than the medium-strength ferritic steels.

4.2. Phenomenological description of low-cycle fatigue

4.2.1. *Background*

In order to describe the LCF behavior of materials, consider the simplified case of a test with fully-reversed deformation: $\left(R_\varepsilon = -1\right)$. We will describe the following phenomena: cyclic cold working, the stress-strain relationships, fracture resistance and, finally, analytic methods used to represent these different behaviors.

4.2.2. *Cyclic work hardening*

When a specimen is subjected to an imposed cyclic plastic deformation, we can see that the highest and lowest stresses do not remain constant throughout the test. Most of the time, after a transitory stage where the highest stresses vary slightly (increasing or decreasing), they become relatively steady for a long time. After this time, the tensile stress begins to decrease and this can be associated with the onset of cracking.

This decreasing strain, associated with crack initiation, is sometimes used to define a conventional number of cycles to fracture. N5, for instance, corresponds to the number of cycles that give a 5% drop in highest tensile stress. The compressive curve with an inflexion point is less frequently used to characterize crack formation.

In Figure 4.2, we can see the behavior of two different steels: 304 type stainless steel, which presents cyclic work-hardening (the stress increases at the start of the test); and high-strength 4340 steel, which shows a cyclic work-softening effect (the stress decreases slightly).

The presence of a stable stage allows us to associate the imposed strain with a resulting stress. The period of time taken to reach this equilibrium stage may be called "adaptation". Later in this chapter, we will introduce the notion of "adaptation limit", which corresponds to a more specific phenomenon. Some cases exist (for example, welding 9-12% Cr ferrito-martensitic steels [FOU 06a, FOU 06b]) where there is no adaptation and the properties evolve continually during the test. It is not possible to study these particular materials using non-servo-hydraulic machines because, as we have previously indicated, neither stress nor strain can be controlled.

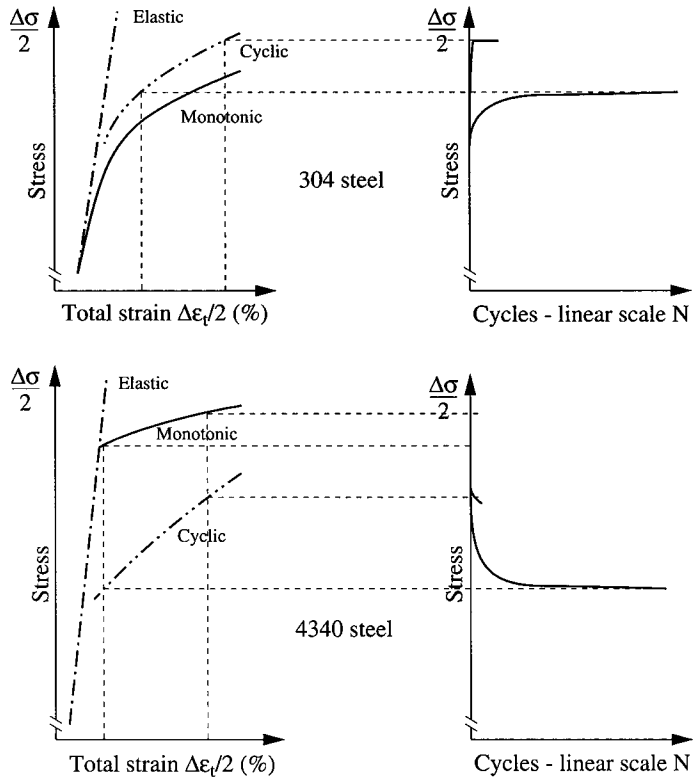

Figure 4.2. *Examples of cyclic work-hardening (a) and work-softening (b)*

We also have to pay attention to the way in which the results are presented. Most of the time, the evolution of stress as a function of the logarithm of number of cycles is plotted on a graph. Nevertheless, this useful representation has the drawback of exaggerating the significance of the first cycles when plotted on a semi-log basis.

Figure 4.3 shows how a very brief transitory phenomenon on a 316-L steel is amplified using a log scale. We can see that with a Cartesian diagram the steady domain is more seems to last far longer than on a log scale.

It is important to define what is meant by stable cycle. Observation of these diagrams usually shows that the stress obtained at half a lifetime is much more representative of what a material experienced during most of the test compared to the highest stress or a conventional stress corresponding to a given number of cycles (10, 20 or 50 cycles).

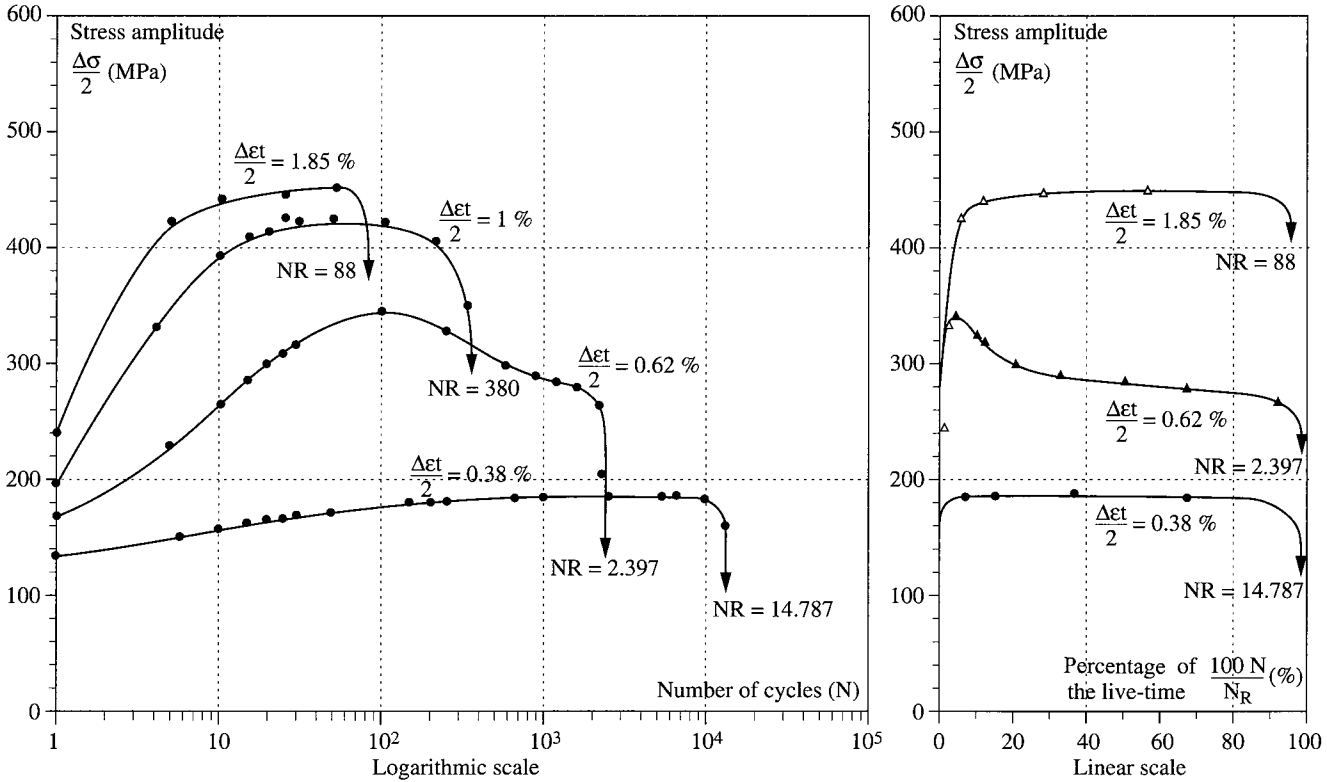

Figure 4.3. *Evolution of the stress amplitude as a function of the number of cycles Z2 CND 17 12 steel (AISI 316L steel) at 450°C*

Cyclic work-hardening is sometimes quite spectacular. The stresses reached are usually higher than the tensile strength of the material. What we said about tests where strain is controlled can also be applied to alternative tests carried out under controlled stress, with some precautions.

When a material is cycled under an imposed strain (work-hardening), the stress increases. Under a controlled force, strain decreases. The reverse of this effect occurs in work-softening.

Usually, a stabilized state does exist. The stress-strain relationship is relatively independent from the type of test if tests with imposed forces are carried out with caution. As a matter of fact, if the material cyclically work-hardens, we see that the stabilized stress can become higher than the tensile strength. In order to reach consolidation under a controlled stress, we have to progressively increase the strain applied to avoid a premature fracture.

We will now examine cyclic stress-strain relationships in more detail.

4.2.3. *Cyclic stress-strain relationships*

If stress is recorded as a function of strain, we obtain hysteresis loops that evolve and become stable provided that a stable regime exists. Figure 4.4 illustrates cyclic work-hardening observed in a 316-L type austenitic stainless steel.

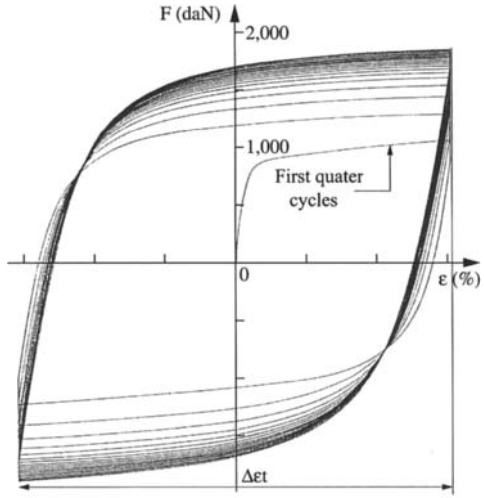

Figure 4.4. *Example of force-strain cycles exhibiting cyclic work-hardening: Z2 CND 17 12 steel (AISI 316L steel) at 20°C*

Figure 4.5 shows an idealized plot of a stable hysteresis loop as well as the definitions of different variables that are described in detail in AFNOR A 303-403 standard.

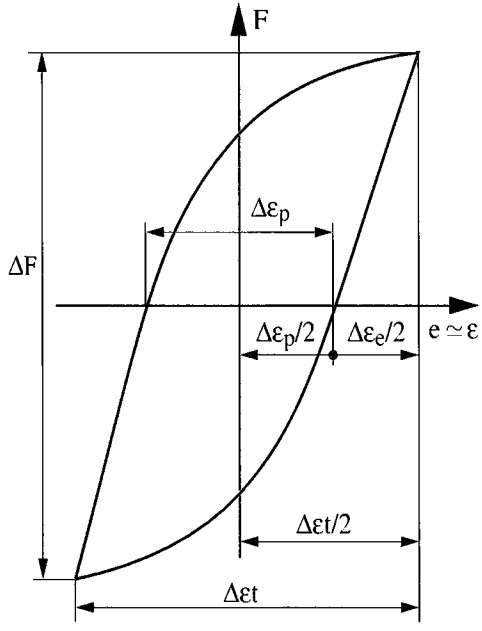

$\Delta\varepsilon_t$ = total strain range
$\Delta\varepsilon_e$ = elastic strain range
$\Delta\varepsilon_p$ = plastic strain range
ΔF = load range

$\Delta\sigma = \frac{\Delta F}{A}$ = stress range

$\sigma_a = \frac{\Delta\sigma}{2}$ = stress amplitude

$\varepsilon_a = \frac{\Delta\varepsilon}{2}$ = strain amplitude

} stabilized

$\Delta\varepsilon_{ei}, \Delta\varepsilon_{pi}, \Delta\varepsilon_{ti}, \Delta F_i, \Delta\sigma_i$ = values referring to the first cycle

N_F = number of cycles to fracture
m = exponent of COFFIN – MANSON's law
$\Delta\varepsilon_p = C_p \times N_R^{-m}$
p = exponent of $\Delta\varepsilon_e = C_e \times N_R^{-p}$ law
n' = cyclic strain hardening exponent

$\sigma_a = K'\left[\frac{\Delta\varepsilon_p}{2}\right]^{n'}$

n = monotonic strain hardening exponent
law (first 1 / 4 cycle) $\sigma_{ao} = K[\varepsilon p_{ao}]^n$

Figure 4.5. *Plot of the hysteresis loop*

We can see that the variation in global imposed variation $\Delta\varepsilon_t$ is made of a plastic part $\Delta\varepsilon_p$, and an elastic part, $\Delta\varepsilon_e$. The initial part of the loading curve is linear and is equal to Young's modulus E. The elastic strain range is:

$$\Delta\varepsilon_e = \Delta\sigma / E$$

Usually, the linearity of the stress-strain relationship is greatly reduced.

This shows that the elastic limit under compression after a tension cycle or *vice versa* is slightly reduced: it is a consequence of what is called the "Bauschinger effect", or kinematical work-hardening effect.

We usually have:

$$\Delta\varepsilon_t = \Delta\varepsilon_e + \Delta\varepsilon_p \qquad [4.1]$$

but sometimes:

$$\Delta\varepsilon_t = \Delta\varepsilon_e + \Delta\varepsilon_p + \Delta\varepsilon_i \text{ with } \Delta\varepsilon_e = \Delta\sigma / E \qquad [4.2]$$

where $\Delta\varepsilon_i$ is defined as an inelastic strain.

Decomposition of global deformation sometimes requires a sophisticated statistical analysis (see [FOU 07], for instance).

It is important to be precise when calculating the evolution of the elastic limit because it allows us to define the model of cyclic work-hardening, which can be introduced in the calculations.

Here we make a distinction between two main models: isotropic work-hardening (the elastic limit increases in both tension and compression) and kinematic work-hardening (the elastic limit under tension compression remains constant and equal to the limit of the virgin material). In reality, most materials display behavior in between these two extremes. When the stabilized state exists, we can plot the curve representing stabilized stress as a function of stabilized strain, as seen in Figure 4.6.

The curve thus obtained is called the "cyclic stress-strain curve". We have to distinguish the cyclic consolidation curve from the stress-strain relationship during a given cycle.

In order to obtain this cyclic stress-strain curve, we will now present several techniques:

– starting from several test specimens at different levels of constant strain;

– starting from a specimen with a strain amplitude that is low at first, waiting for stabilization to appear, and then choosing a higher deformation level, etc.;

– finally, cycling by block in which the strain amplitude is linearly increasing or decreasing.

In some cases there is a reasonable agreement between the three methods but this is not always so. This point is discussed in [LIE 76].

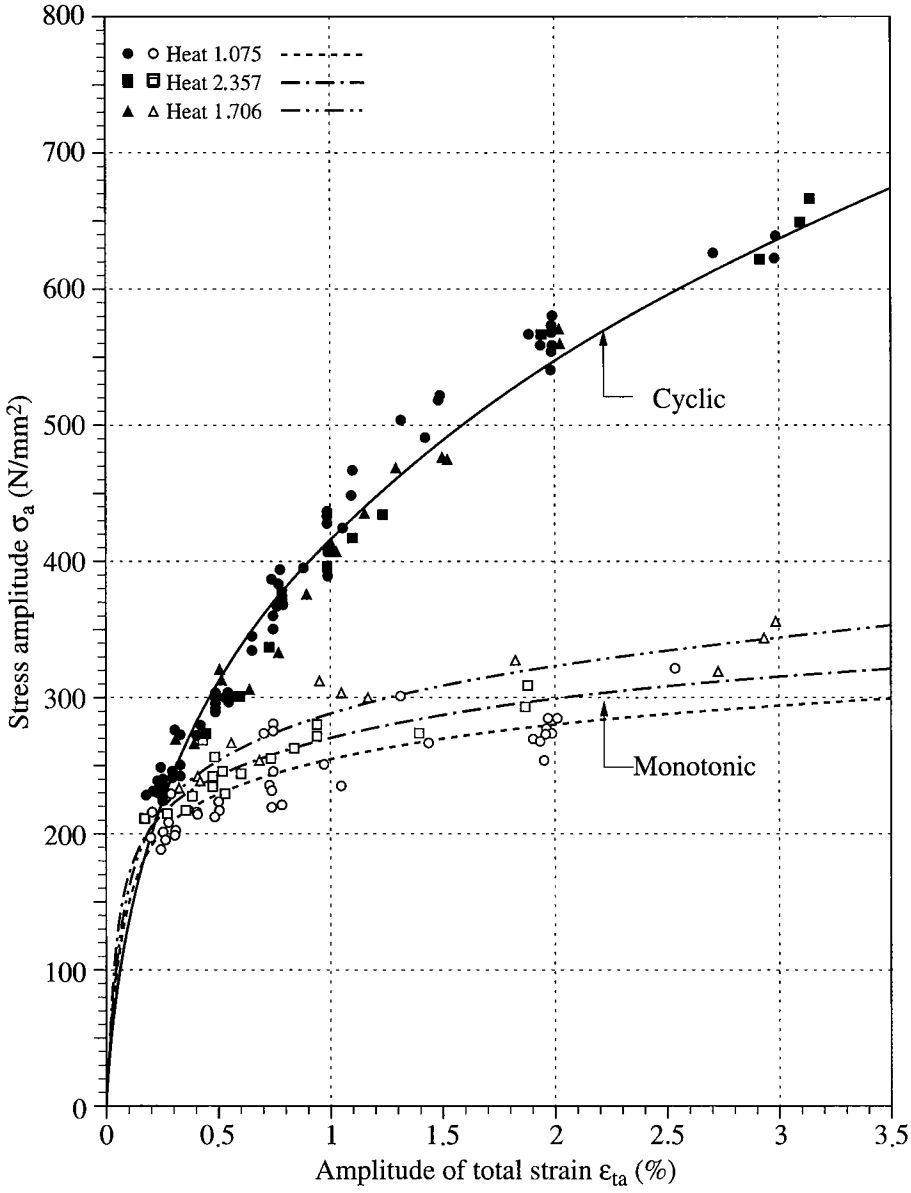

Figure 4.6. *Example of a cyclic work-hardening curve: three different Z2 CND 17 12 steel samples (AISI 316L steel) tested at 20°C*

Experience has shown the first method to be the best. The second method can be affected by strong deformations due to the start of a fracture.

With the third method, the cycle of highest amplitude has the greatest significance. This point is always in agreement with the other methods. For the rest of the curve, however, the method produces results that remain under the curve determined using several specimens if the material softens or remains over the curve if it hardens.

An example of a cyclic stress-strain curve compared to a tensile curve (or a curve at the end of the first cycle), represented in Figure 4.6. These curves refer to a 316 L type steel showing a strong work-hardening effect.

4.2.4. *Fatigue strength*

The cyclic stress-strain curve provides the essential data from which we can choose the most suitable model of cyclic behavior or analyze the microstructural behavior of a metal. When designing a device, fatigue strength is an obvious asset for anyone who wants to control fatigue by LCF.

A diagram of fatigue strength relates strain to the number of cycles leading to fracture. In this diagram, the total plastic and elastic deformations are separated. This type of diagram is illustrated in Figure 4.7. These curves are usually known as Coffin-Manson curves and were introduced in the early 1950s [COF 54, MAN 52]. If we multiply the elastic deformation by Young's modulus, the plot of the real stress thus obtained as a function of the number of cycles to failure gives a curve usually known as the Basquin curve. This curve often provides a good connection between the high numbers of cycles and classic endurance curves [SOO 76, SOO 77].

We notice here that in most of the HCF tests carried out under bending, within the region of low endurance (i.e. with a plastification side), the calculated elastic stress is usually overestimated and incorrect. This can sometimes explain the relative disagreement seen in the relationship between LCF and HCF.

Using the Coffin-Manson and Basquin equations within the $\Delta\varepsilon$ – log N diagrams, which we will see later on, we obtain lines for $\Delta\varepsilon_p$ and $\Delta\varepsilon_e$. Data obtained on a large range of materials (steels, titanium and aluminum alloys, nickel and cobalt super alloys) have been gathered by Baumel and Seeger [BAU 90].

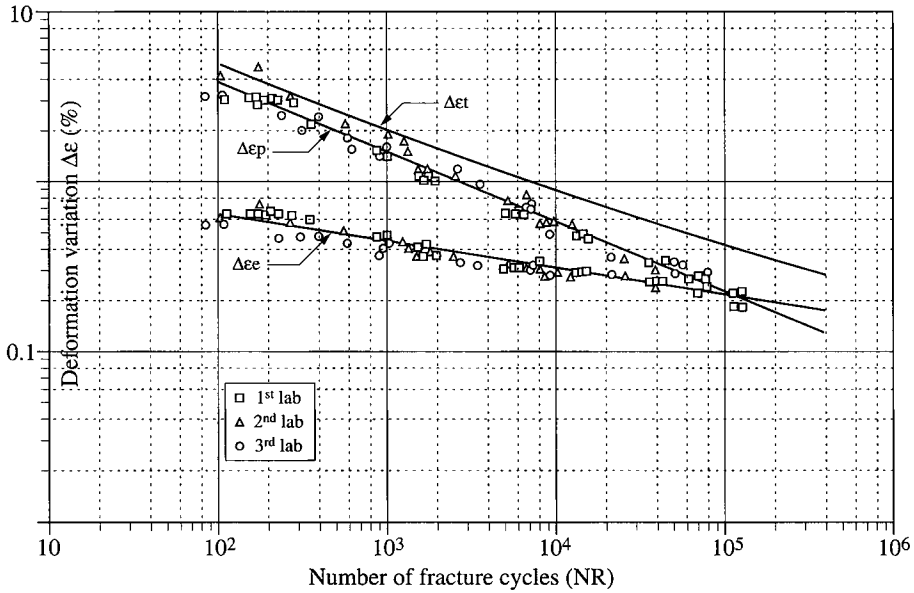

Figure 4.7. *Example of to low-cycle fatigue curves:Z2 CND 17 12 steel (AISI 316L steel) tested at 20°C in three different laboratories*

4.2.5. *Mathematical equations*

4.2.5.1. *Cyclic work-hardening*

The cyclic hardening curve can usually be well represented by the power law $\sigma = K'.(\Delta\varepsilon_p/2)^{n'}$, which we can compare to the tensile curve:

$$\sigma = K.(\varepsilon_p)^n$$

Most of the time this equation is used to represent the stress-strain curve of the material during the test [JAM 62, MAS 26].

A change of origin and of scale (by a factor of two) sometimes allows us to determine the monotonic stress-strain curve from the cyclic one [HAL 62] (details of this procedure are shown in Figure 4.8). This action is not always accurate and usually only works for moderate plastic strains of the order of elastic deformation [ABD 77, SCH 70]. The relationship between this procedure and the Bauschinger effect is discussed in [ABD 77].

It seems to be more suitable, therefore, to use the isotropic and kinematical work-hardening concepts, or even viscoplasticity, to describe the shape of the

mechanical hysterisis loops as well as the cyclic work-hardening curve [LEM 85]. The reader can find further information in the following references: [FOU 06a, FOU 06b].

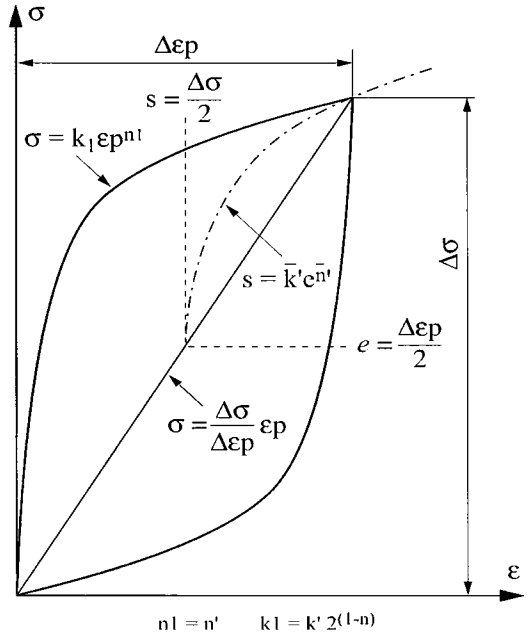

Figure 4.8. *Comparison between the cyclic work hardening curve ($\sigma - \varepsilon$) and the stress-strain relationship ($\sigma - \varepsilon$) with a change of origin*

4.2.5.2. *Fatigue strength*

A power equation has been shown by [COF 54, MAN 52] to relate plastic deformation ($\Delta\varepsilon_p$) and elastic deformation ($\Delta\varepsilon_e$) to the number of cycles to fracture, N_F.

This leads to the following equations:

$$\Delta\varepsilon_p = A.N_F^{-a} \qquad [4.3]$$

$$\Delta\varepsilon_e = B.N_F^{-b} \qquad [4.4]$$

$$\Delta\varepsilon_t = A.N_F^{-a} + B.N_F^{-b} \qquad [4.5]$$

The first experiments showed that a is close to 0.5, which gives the Coffin law: $\Delta\varepsilon_p N_F^{1/2} = C$.

Exponent b is usually close to 0.12. Parameters a and b do not vary much between materials and many attempts have been made to predict resistance to fatigue from tensile properties. These methods are known as the "universal slope law" and "four correlation points" method. They are described in detail in [MAN 65] and highlighted in Figure 4.9.

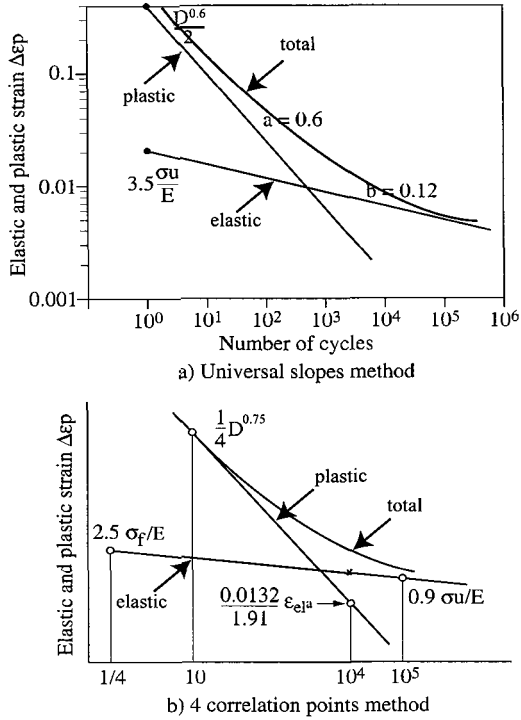

Figure 4.9. *Prediction of the resistance to low-cycle fatigue [MAN 65]*

The method of universal slopes assumes that a tensile test is a very short fatigue test under a plastic strain equal to the tensile ductility D and the elastic ductility proportional to σ_u/E:

$$D = \mathrm{Ln}\,100/(100 - \%\mathrm{RA}), \qquad [4.6]$$

RA being the reduction of area in percent and σ_u the ultimate tensile strength.

Many variants also appear depending on whether the number of cycles corresponding to the tensile test is equal to 1, 1/2 or 1/4.

According to Manson [MAN 65] the best description is obtained with $a = 0.6$ and $A = D^{0.6}/2$, thus:

$$\Delta\varepsilon_e = D^{0.6}.N^{-0.6} \quad [4.7]$$

and also:

$$\Delta\varepsilon_e = 3.5.(\sigma_u)/E.N^{-0.12} \quad [4.8]$$

These methods enable us to estimate the LCF life of a material. It clearly appears from all these diagrams that the life, in terms of total strain, is closely connected to the ductility of a material with a low number of cycles (predominant equation $\Delta\varepsilon_p - N$) while the elastic limit and tensile strength, dominate at a high number of cycles (predominant equation $\Delta\varepsilon_e - N$).

Since the Manson's proposal in 1965, other laws have been proposed. Here it is worth mentioning the modified law of universal slopes introduced by Muralidharan and Manson [MUR 88] and the "universal" law proposed by Baumel and Seeger [BAU 90]. These last authors suggested two slightly different approaches, one for steels, the other for aluminum and titanium alloys.

4.2.6. *General behavior: sequence effects and control mode*

In the models we have presented up to this point, we have considered the ideal case of constant amplitude cyclic loading. Now let us focus on how things are modified if we are no longer in this situation.

4.2.6.1. *Cumulative damage law*

This is a large field and we present the major approaches here. Usually, we use a Miner–type law in order to combine cycles of variable amplitudes.

For classic LCF at $\Delta\varepsilon_p$, the number of cycles to failure is N_F, we can see that a cycle of this type generates damage $1/N_F$, with fracture occurring when $\Sigma\, 1/N_i = 1$.

If we consider Coffin's law, we obtain the following as a fracture criterion:

$$\Sigma.(\Delta\varepsilon_{pi})^2 = C \quad [4.9]$$

This has led some authors to look for a fracture criterion incorporating the cyclic mechanical energy (which is proportional to $(\Delta\varepsilon_p)^2$ within a plastic elastic model). Readers can refer to [POL 91] for further information.

This useful rule nevertheless has to be viewed with caution. Indeed, the behavior of materials is rarely linear and is very rarely cumulative, as the material has a memory. In addition, there is also doubt about the meaning of an energetic criterion, which presents at least two draw-backs:

– by nature, energetic criterion is scalar and so cannot easily be applied to directional phenomena for initiation facets of fatigue cracks;

– as only a low part of the energy during plastic deformation is stored within the materials (several percent), most of the energy being dispersed as heat, an energy-based criterion seems to be inappropriate for representing fatigue damage.

4.2.6.2. *Influence of mean strain or mean stress*

It is commonly said that an average strain does not influence behavior under low cycle plastic fatigue. This is true if we perform a test between two values of ε_1 and ε_2 with an average value different to zero. The effect has been well observed during the first cycle, but the mean stress obtained during the first cycle rapidly relaxes and, besides the initial elongation, everything behaves as if the mean stress is equal to zero.

In a test with an imposed stress different from zero, we frequently observe the phenomenon of ratcheting. Depending on the amplitude of the applied stress, this progressive deformation can become stabilized. During repeated tests we can then define the adaptation limit which, if it is reached, pushes the material past its stability stage and leads to failure [LIE 72, PLE 68].

After this general description of the behavior of materials, the following sections will focus on the relationships between the phenomenological behavior and microstructural evolutions.

4.3. Adaptation mechanism and cracking during low-cycle fatigue

4.3.1. *Introduction*

During low-cycle or high-cycle fatigue, the lifetime can be split into different stages which are:

– microstructural evolution;

– crack initiation; and then

– propagation of the cracks which leads to the final fracture.

As we mentioned earlier, we can observe that when a test is carried out under an imposed total strain, the stress and, as a consequence, the plastic strain evolve more or less progressively towards stable values in most cases. This is because the stress amplitude and amplitude of the plastic part of the cycle become almost constant or evolve slowly with the number of cycles. In general this stage, which we call the "adaptation stage", represents 10 to 50% of the lifetime. During this time, the structure of the material evolves in order to bear the imposed cyclic strain. The adaptation stage is followed by or overlaps with the initiation stage of cracking, which leads to the formation of microcracks that are usually located at the free surface of the specimen.

As we will see later, the definition of the start of crack initiation is rather sensitive.

Nevertheless, we often notice that, after a certain number of cycles which will be given later on, one of these microcracks propagates more rapidly than the others ("propagation stage"), first steadily, and then leading to fracture of the sample.

A detailed study of these three stages is interesting for different reasons. First of all, the observation of adaptation time allows us to relate the mechanical behavior of the material to its microstructural evolution. Indeed, the observed cyclic behavior is, just as for the monotonic tensile curve, an indicator of the microscopic mechanisms that occur during cyclic deformation. In addition, as the global lifetime recorded on the Manson-Coffin curves incorporates initiation and propagation of phenomena, it is necessary to clearly distinguish the predominant mechanical and metallurgical factors for each of these stages.

4.3.2. *Adaptation of the material*

In order to present this stage, we will adopt the metallurgist's point of view by trying to show how, for a material whose microstructure is known, it is possible to predict its mechanical behavior. Consider the case of structural steels, for instance. As the hardening of these steels usually involves several mechanisms (cold working, phase change and precipitation hardening) we will first examine the simplest microstructures (annealed or pre-deformed solid solutions) and then try to explain the behavior of more complex structural materials, such as quenched and tempered steels. Beforehand, we will focus on single crystals.

4.3.2.1. *Single crystals*

In the past single crystalline metals of face-centered cubic (FCC) structure (such as copper, nickel and aluminum) have largely been studied. Readers can refer to

Polak [POL 91] and Suresh's [SUR 98] work to get a general idea of the results obtained from these metals.

The cyclic work-hardening curve of a copper single crystal oriented for single slip presents a particular shape, as shown in Figure 4.10, where τ_a is the shear stress resolved on the glide plane and γ_{ap} the applied shear strain. This figure exhibits three different domains.

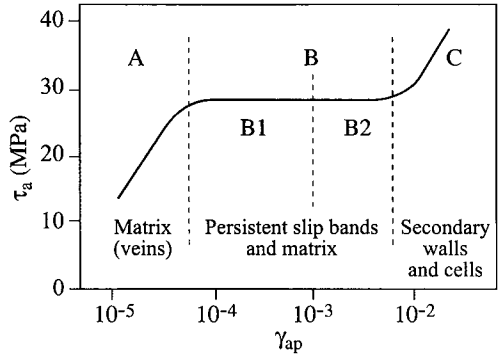

Figure 4.10. *Cyclic work-hardening curve of a copper single crystal oriented for single glide [POL 91]*

Within domain A, which precedes the saturation plateau, the single crystal is cyclically and uniformly deformed. However, the dislocation structure is heterogenous on a smaller scale. We can observe the formation of tangles of dipoles and dislocation loops located on the primary glide plane. This dislocation structure is usually represented by the term "veins" because of the geometric organization of dislocations. The veins line up along the $[1\,\bar{2}\,1]$ direction, which is perpendicular to the Burgers vector.

Within domain B of the cyclic cold-working curve, the saturation stress is almost constant and independent of the imposed shearing amplitude. Deformation along the gauge length of the specimen is heterogenously distributed. This deformation is localized and concentrated within slip bands called "persistent slip bands" (PSBs). These PSBs form dislocation layers that possess various microstructures parallel to the primary slip plane. These layers are trapped within the matrix made of the veins. The thickness of these layers is a few microns. They are made of very thin dislocation walls (about 0.1 μm), regularly spaced out and separated by some channels. The walls are perpendicular to the direction of the primary slip plane and contain a high density of dislocation dipoles.

When we analyze the crystal on a plane, approximately parallel to the primary slip plane (111), we can easily highlight these walls. When we examine the crystal within a $(1\,\bar{2}\,1)$ plane or a $(1\,\bar{1}\,1)$ plane, we can observe a structure made of really special bands in the shape of ladder rungs. The deformation is localized within these PSBs, which are shown in Figure 4.11. Crack initiation occurs within these PSBs when the shear amplitude is increased to reach the saturation plateau on the cyclic work-hardening curve (see Figure 4.10).

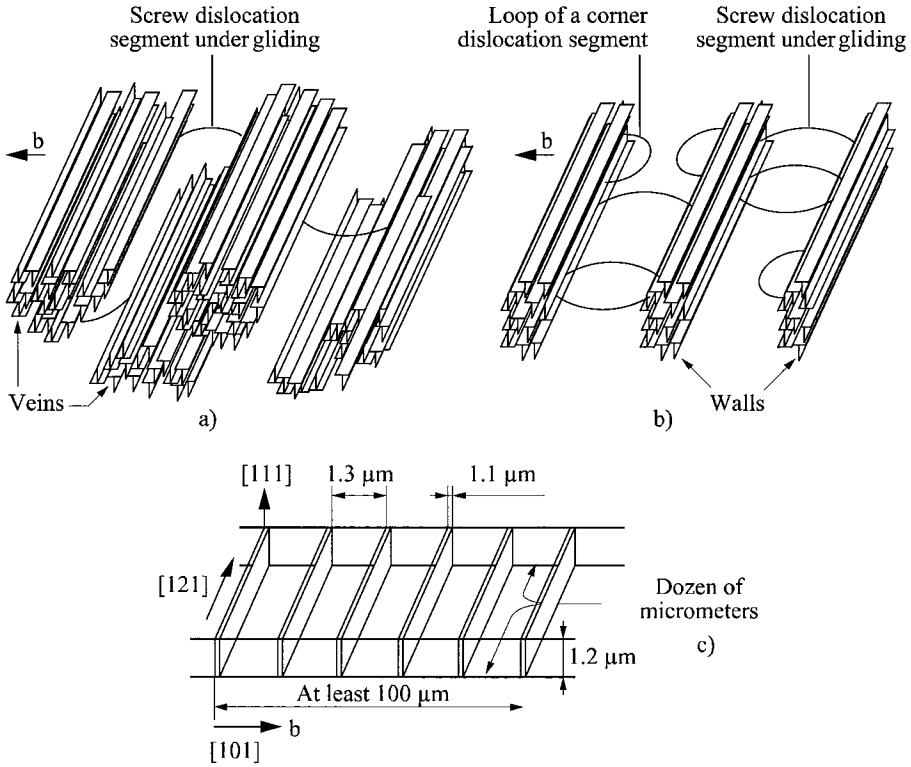

Figure 4.11. *Dislocation structures within face-centered cubic metals: a) veins within the matrix; b) dipole walls and dislocation fragment within persistent slip bands (PSBs); and c) 3D representation of a PSB within copper*

Within area C of the cyclic work-hardening curve, we can also observe an increase in the shear stress an addition to the increased amplitude of the imposed strain. Some secondary slip systems are activated which can explain the fact that the structure of the dislocations becomes more complex.

When the crystals are oriented for multiple slip, we observe the formation of PSBs on different slip systems that intersect at some point. The corresponding shearing stress is much higher than the plateau stress for a single slip. We can therefore often observe an initial hardening followed by softening.

4.3.2.2. *Poly-crystalline metallic alloys*

In order to characterize the cyclic behavior of a material, we can use various methods.

As previously presented, comparison of the monotonic tensile curve and cyclic work-hardening curve is an easy method to characterize a material's behavior. This does not present any difficulties when a material possesses a unique and well defined cyclic work-hardening curve. Nevertheless, as we have already said, plotting the cyclic stress-strain curve is difficult in some circumstances as some materials have a memory effect.

In addition, when our major interest is in the mechanisms involved during cyclic work-hardening, it is better to use curves that give the evolution of stress with the number of cycles, plotted for various amplitudes of imposed strain. We want a curve that for a given material shows whether the strain leads to strong or weak memory effects and how it does so.

The adaptation stage, which has been examined in this way, has been studied for various single-phase alloys, especially copper-based ones. An important factor here is the initial state of the solid solution, which can be in the annealed or pre-strained state.

A certain number of studies have also dealt with alloys hardened by the precipitation of a second phase. Here, it seems that we have to distinguish between alloys containing some particles that can be sheared by dislocations from the alloys containing precipitates that cannot be penetrated by the dislocations.

4.3.2.2.1. Solid solutions

Adaptation stage within annealed body-centered cubic (BCC) and FCC solid solutions

The behavior of solid solutions, initially in the annealed state, is highlighted in Figure 4.12.

The material progressively hardens and then reaches a stable regime, which we can assume to be a saturation stress σ_s. The evolution of stress σ_p, with number of cycles or cumulative $\Sigma\Delta\varepsilon_p$ is shown in Figure 4.12b. The stable regime is more

rapidly reached when the deformation amplitude $\Delta\varepsilon_p$, which is kept constant during the test, is large. It is then easy to match saturation and the cyclic work-hardening curve, which most of the time is expressed as follows:

$$\sigma_S = K'.(\Delta\varepsilon_p / 2)^{n'} \qquad [4.10]$$

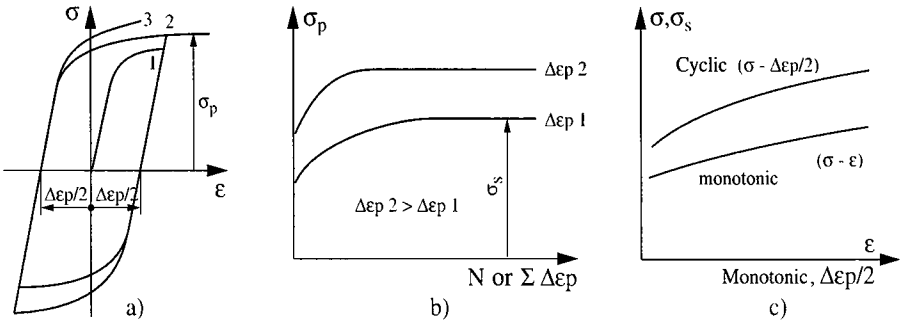

Figure 4.12. *Cyclic behavior of annealed materials: a) evolution of the hysteresis loop; b) stabilized regime observed; and c) comparison of the monotonic and cyclic work-hardening curves*

Comparison of this curve with the monotonic stress-strain curve shows that in the annealed state, cycle loading has a hardening effect on the material.

The substructures introduced during cyclic deformation have been observed by a number of authors. The most detailed observations were those relating to FCC metals, and especially with copper. For a detailed description of the results thus obtained, readers can refer to the review published by Grosskreutz [GRO 71].

During the hardening stage of copper, we can observe microstructural modifications that look like those observed during stage I and II of deformation under monotonous traction. Dislocations gather to form bands and we can see the presence of many dipoles. As the stress increases, the density of these gatherings increase and we observe the formation of a cellular arrangement of dislocations. This reorganization of dislocations into cells becomes more uniform as the deformation increases in importance. The typical cells resulting from high amplitude fatigue possess different properties to those formed during a monotonic strain as the fatigue walls are thinner. The size of the cells decreases when the amplitude of the imposed strain, and as a consequence the saturation stress, increases. Several authors have tried to correlate saturation stress σ_s to cell size d, as shown in Figure 4.13 for copper.

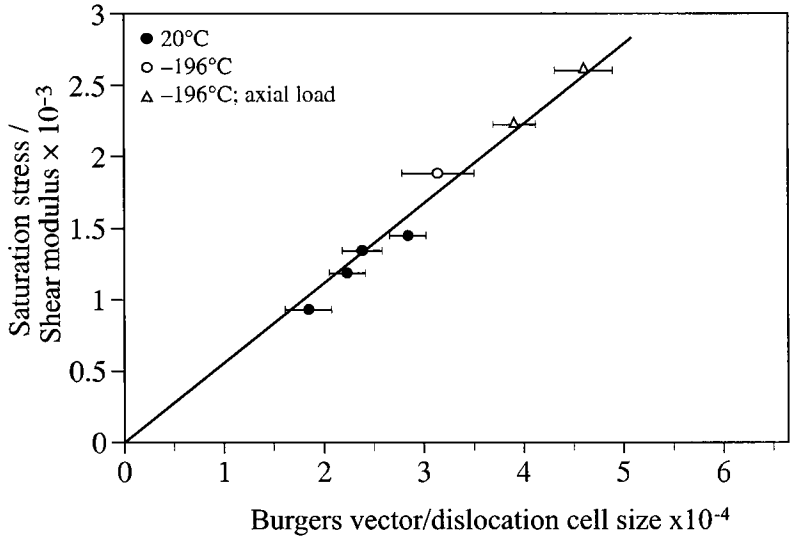

Figure 4.13. *Variation of the size of dislocation cells with increasing saturation stress [PRA 67]*

Another important phenomenon is the formation of intense slip bands, which are similar to the PSBs observed in single crystals. These develop at the saturation stage. The consequence of this is a heterogenous deformation that is localized within the intense slip bands, as has been shown by Finney and Laird [FIN 75]. The heterogenity of the deformation occurs with a modification of the sub-structures of dislocations. At low strains, dislocations are grouped in bands. As strains increase these bonds are replaced by cells and PSBs. This structure leads to localized fatigue damage.

When the adaptation stage is reached point defects are formed. Resistivity measurements seem to show that the resistivity changes recorded for copper are not only due to the increase of the dislocations density during cyclic deformation, but also to the formation of point defects [POL 59].

Recent observations have been reported on FCC metals possessing a relatively high stacking fault energy. These observations can also be applied to BCC metals, such as iron, where cross slip occurs easily. Nevertheless, within FCC alloys of copper-zinc and copper-aluminum type it is much harder for the dislocations to form. For these materials, the slip character remains planar and the dislocations retain their planar arrangements. All of these observations were made by Lukas and Klesnil [LUK 73] and are summarized in Figure 4.14.

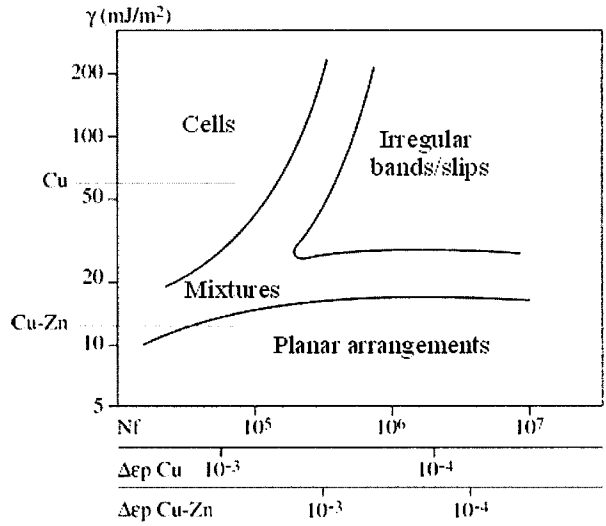

Figure 4.14. *Different arrangements of dislocations as a function of the stacking fault energy γ and of strain amplitude $\Delta\varepsilon_p$ for copper and copper-zinc [LUK 73]*

Saxena and Antolovich [SAX 75] compared the cyclic behavior of copper and copper-aluminum alloys (Cu-2.2 Al; Cu-4.2 Al; Cu-6.3 Al). The addition of aluminum to copper modifies the slip character such that dislocation movements occur in a more planar direction within alloys that than within pure copper. Saxena and Antolovich's results are shown in Figure 4.15. We can see here that, although the most highly alloyed material leads to the highest stress values, it is the one giving the longest lifetime. We can also observe that all of the alloys containing aluminum have a cyclic work-hardening curve that cannot be represented by a single value of the exponent n'.

These results suggest that an improvement in lifetime can be obtained if the stacking fault energy is lowered. Nevertheless, it has not yet been clearly established whether this improvement in lifetime is due to a late initiation or to the reduction in propagation rate within the high deformation fatigue domain.

It is important to consider this difference in behavior – which is related to the stacking fault energy and the slip character – when we focus on plotting the cyclic work-hardening curve. Indeed, the materials that easily lead to cellular arrangements have an almost unique cyclic work-hardening curve that does not really depend on the way hardening is established (increment, block methods or the method of using a single specimen for each level). Nevertheless materials that possess a lower stacking

fault energy, and that as a consequence give rise to planar arrangements of the dislocations, are more likely to demonstrate a memory effect. Metals that, like Cr-12 Ni type austenitic stainless steel that easily give rise to mechanical twinning due to monotonic or cyclic deformation, are those where most of the difficulties in defining the cyclic cold work-hardening effect are addressed.

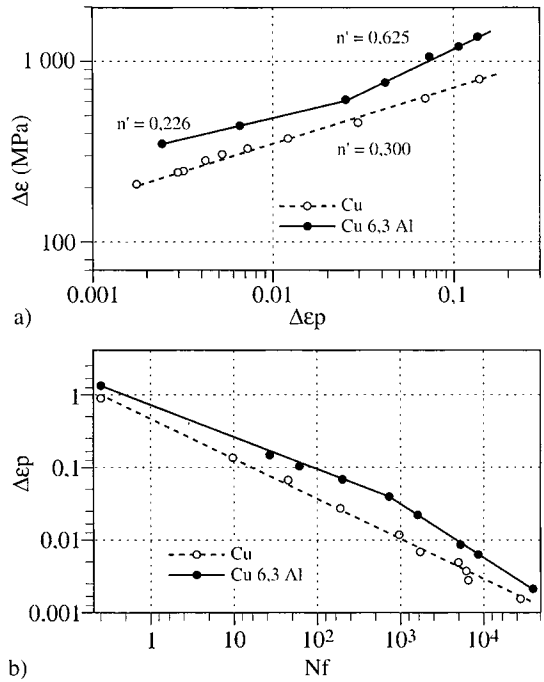

Figure 4.15. *Comparison of the behavior of Cu and Cu-6.3Al: a) cyclic work-hardening curves; and b) fatigue lives [SAX 75]*

Pre-strained initial state

On pre-strained materials, we can usually observe a softening stage as soon as the pre-strain level is higher than the amplitude of the imposed cyclic deformation. The corresponding behavior is presented in Figure 4.16, which shows that softening is chiefly significant at the beginning of cyclic deformations. In this case, we can also discern a stationary regime s_s, the cyclic cold-working curve being below the monotonic tensile curve.

Instability of work-hardening due to pre-straining has to be considered as it shows that the material has a lower flow stress when it is cyclically strained. It is also worth noting that this softening phenomenon occurs within some structures that are

naturally "cold worked" such as from a martensitic type phase change, as we will show further on.

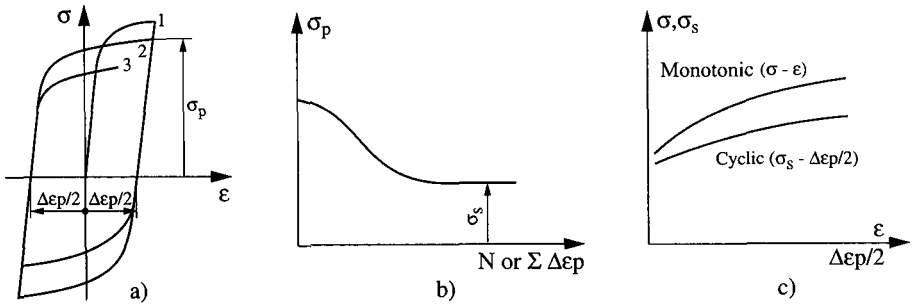

Figure 4.16. *Cyclic behavior of pre-strained materials: a) evolution of the hysteresis loop; b) softening and stable regime; and c) comparison of the monotonic and stress-strain curves*

In the annealed state, the materials cyclically harden, whereas in the pre-strained state they soften. For this reason we may ask whether in these conditions a given metal possesses a unique cyclic stress-strain curve independent of its initial state.

For metals such as copper and nickel, we can observe a behavior similar to that described in Figure 4.17a. However, Lukas and Klesnil [LUK 73] showed that in most cases this situation can be observed when the amplitude of cyclic deformation is high. They also showed that for lower strains there is a difference between the two types of work-hardening curves. Nevertheless, within these materials, the difference between the annealed state and pre-strained condition remains small.

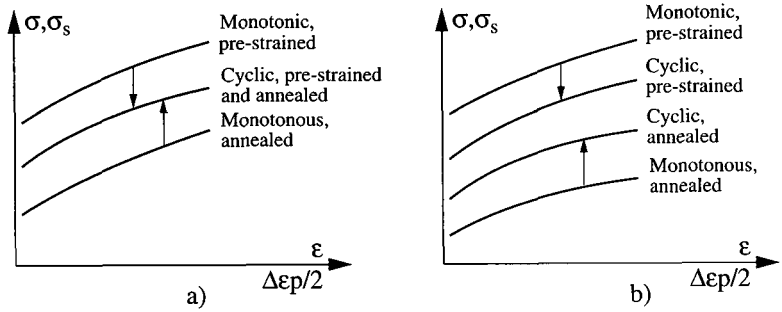

Figure 4.17. *Monotonic and cyclic curves: a) materials without any memory effect (for instance Cu, Al, etc.); and b) materials with memory effect (for instance Cu-Zn, Cu-Al, etc.)*

Alloys with a lower stacking fault energy, such as copper-zinc and copper-aluminum, show a more significant memory effect, as described in Figure 4.17b. If they are always different in their pre-strained state, softening is insufficient to provide us with a unique cyclic work-hardening curve.

Feltner and Laird showed that the kind of mechanical instability that we can observe in pre-strained states exists as instability at the microstructural level [FEL 67]. These same authors noticed that, for copper and nickel, dislocation cells induced by monotonic pre-strain become organized according to their size and degree of perfection during cyclic deformation. This happens particularly when:

– the amplitude of cyclic plastic deformation is large;

– the cells associated with the pre-strain conditions are progressively erased; and

– when saturation is reached.

Here, the size of the newly formed dislocation cells roughly corresponds to those formed directly from the annealed state under the same conditions. Changes in the microstructure can therefore be reversed and we think that, in these conditions, there is no memory effect on saturation stress. In the case of lower strains, especially strains leading to significant irreversibility in alloys (Cu-Zn, Cu-Al), the situation is more complex. Even here, however, part of the pre-deformation sub-structure is "erased" because of the later cyclic deformation.

Mechanisms controlling the adaptation stage

All the observations that have been made suggest that the rapid work-hardening stage is controlled by a phenomenon of defect multiplication. In this stage, the hardening mechanisms are similar to those that can be found during a monotonic deformation.

Fatigue hardening raises the question of the reversibility of deformation. In general terms the dislocations carrying the tensile deformation can only carry part of the compressive deformation [MOR 75].

Qualitatively, we expect the reversibility of the deformation to be large when the amplitude of the deformation is low. When the amplitudes are significant, tensile deformation, along with the compressive cycle, require the accumulation of new defects. The situation is then close to what is encountered during a continuous tensile test. This hypothesis has generally been confirmed by experiments performed on an unstable stainless steel using the martensitic transformation $\gamma \rightarrow \alpha'$ induced by deformation in order to estimate the level of reversibility of plastic deformation in the specimen [BAU 77].

Within the stabilized regime, the observations showing that the dislocation substructure is not modified during the cycle have also led several authors to suggest that the deformation that occurs is mainly reversible, in line with a back and forth movement of the dislocations within the cells. Grosskreutz argued with this interpretation [GRO 71]. One of the difficulties with the proposed models lies in the fact that we do not know how the steady hysteresis loop affects the movement of dislocations within the matrix [WIN 75] or within the intense slip bands. Kuhlmann Wildsdorf and Laird [KUH 77] proposed some relatively sophisticated models in order to analyze this state. How we can find a saturation stress still remains unclear, however. It is unlikely that saturation stress is directly related to the size of the dislocation cells, as suggested by the correlation established by Pratt [PRA 67].

The reversibility of deformation is still important, although indirectly, in the approaches developed to take the Manson-Coffin endurance law into account, in terms of the energy of plastic deformation. As we have already seen, many authors have tried to use cyclic mechanical energy as a low-cycle fatigue damage criterion. If ΔW stands for the mechanical energy per cycle, a very simple damage law consists of assuming that a fracture will occur when the total energy Wt, where $Wt = N_f \Delta W$, has reached a critical value independent of $\Delta\varepsilon_p$. In general, it is observed that most of the time the value of $Wt = N_f \Delta W$ becomes lower when the strain amplitude $\Delta\varepsilon_p$ is lowered. As a consequence of this, the lifetime becomes longer. Moreover, a better representation of the results can be obtained if we write the following empirical equation:

$$N_f (\Delta W)^{\alpha} = C \qquad [4.11]$$

where α is constant for a given material, and C is a constant, the value of α being higher than 1. The value of α being known, this equation enables us to determine the Manson-Coffin law. Indeed, we can use the equation proposed by Halford and Manson [HAL 67] to measure the area under the hysteresis loop:

$$\Delta W = \Delta\sigma . \Delta\varepsilon_{p.} (1 - n') / (1 + n') \qquad [4.12]$$

This equation, combined with the previous one and with the one giving the expression of the cyclic stress-strain curve (see Figure 4.5), leads to the following endurance equation C:

$$N_f \left(\Delta\varepsilon_p\right)^{(1+n')\alpha} = C \qquad [4.13]$$

Using an energy criterion as a fatigue damage criterion leads to some issues as its physical origin is not that certain. As a matter of fact, we have already observed that in most cases the energy accumulated as defects, which then contribute to

damage, represents just a small part of the mechanical energy ΔW applied, this proportion being just a small percentage of the energy, the rest being dissipated as heat. We therefore have to estimate damage using a measure that is usually 10 to 20 times larger than the one we wish to use. This problem is not that serious as this "amplification factor" is not constant and is independent of $\Delta\varepsilon_p$. Nevertheless, we are not sure that the ratio of the accumulated energy per cycle to imposed strain is independent; the increase in total energy $N_f.\Delta W$, along with the lifetime suggests something different. We actually think that the increase in $N_f.\Delta W$ is due mainly to the fact that the reversibility level of the deformation increases when the applied strain $\Delta\varepsilon_p$ decreases.

Despite these facts, in some cases, such as low-cycle fatigue with various deformation levels, the previous equations based on an "energy criterion" approach ([4.11] and [4.13]) allow us to evaluate, with a sufficient precision, the number of cycles to fracture.

4.3.2.2.2. Alloys strengthened by precipitates

In order to present the behavior of alloys reinforced by the precipitation of a second phase, we will use the results that we obtained on two important types of alloys: the light aluminum-copper type alloys on one hand and the nickel-based alloys of Waspaloy type, hardened by the precipitation of γ' phase (Ni_3 Ti Al) on the other. As a matter of fact, because of the behavior of these alloys we are able to distinguish two extreme cases:

– one corresponding to the shearing of some particles by dislocation; and

– another associated with the bypass of precipitates by dislocations.

These two modes of dislocation-particle interaction can correspond to the nature of the different precipitates (in the case of aluminum-copper alloys) or to the different sizes of particles of a phase (in case of the γ' phase within the forged alloys based on nickel).

Adaptation where the particles are sheared by dislocations

This shearing mechanism occurs for the aluminum-copper alloy when it contains some precipitates θ''. Within nickel-based forged alloys this sharing mechanism occurs with fine particles γ', or for Waspaloy when the diameter of the particles ϕ_γ, is lower than about 20 nm. The behavior of the aluminum-copper alloy has been studied by Calabrèse and Laird [CAL 74], whereas the Waspaloy treated alloy in these conditions was examined by Stoltz and Pineau [STO 79] (see Figure 4.18).

Although some differences do exist between the two cases considered, the important phenomenon to focus on is hardening followed by a progressive softening,

the curve giving the evolution of the highest stress (tension or compression) going through a maximum.

Thus, the behavior of similar alloys is very different from that of solid solutions and in such cases the precise definition of the cyclic work-hardening curve is more challenging as a steady regime does not necessarily appear.

To make it simple, we can interpret this behavior as follows. First of all, the hardening period has physical origins that are generally the same as those described for single-phase solid solutions; that is to say the dislocation density increases with the presence of precipitates that prevent easy gliding within the matrix.

The softening phenomenon is more characteristic and has been noticed in other cases. Various explanations have been proposed to take softening into account. Among them, the hypothesis of putting the precipitates within the slip bands back into solution has often been accepted [CLA 64].

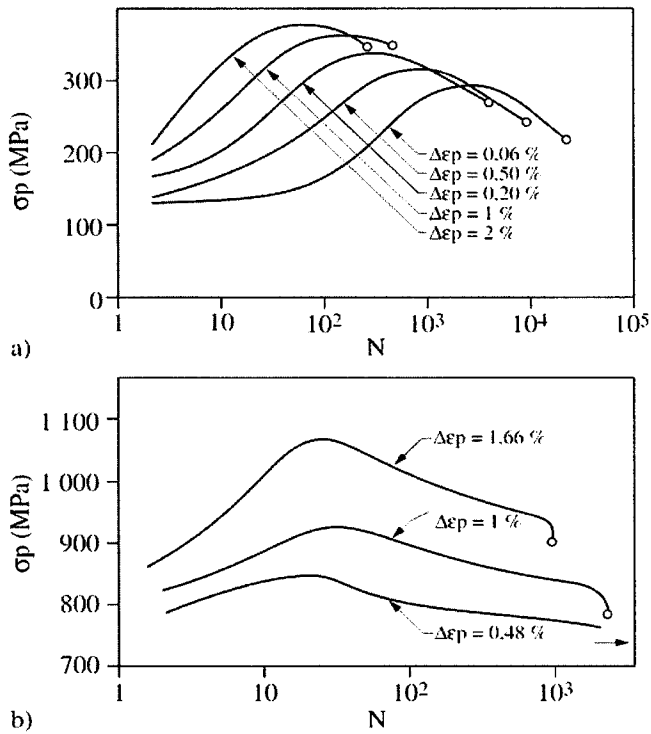

Figure 4.18. *Examples of alloys presenting some sheared precipitates due to dislocations: a) aluminum-copper [CAL 74]; and b) Waspaloy ϕ_γ: 80 Å [STO 79]*

Nevertheless, with the nickel-based alloy Inconel 718, Fournier and Pineau [FOU 77] have shown that the lack of precipitate contrast within these bands does not correspond to a dissolution of the particles, but to a change in their crystallographic structure due to the slip itself.

Thus, as Calabrèse and Laird [CAL 74] in their study on an aluminum-copper alloy suggested, it is more sensible to assume that the softening mechanism is triggered by a progressive diminution of the precipitation hardening, this diminution being basically due to a decrease of the "order" within the particles. Thus, in the case of Waspaloy for instance, the observations made using an electronic microscope show that the deformation remains localized within bands. Within these bands, the back and forth movement of the dislocations progressively decreases the average fraction of the surface taken up by the particles intersecting a glide plane and, as a consequence, leads to a diminution of the stress necessary to shear the particles.

Basically, the behavior observed is the sum of two competing phenomena (see Figure 4.19). The loss of hardening by precipitation can be more important than the hardening due to dislocations within the solid solution.

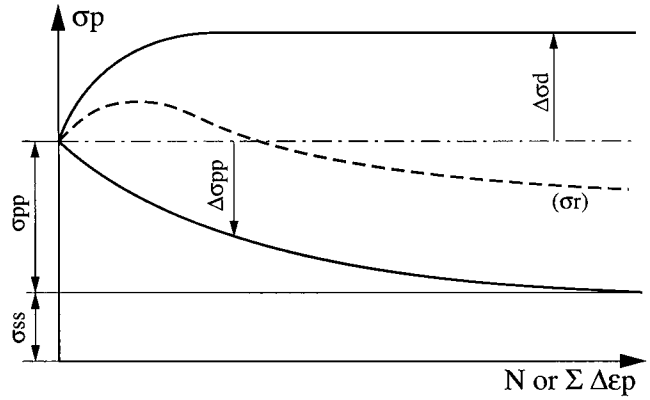

Figure 4.19. *Evolution of the various components of softening: σ_{ss}: solid solution hardening; σ_{pp}: hardening due to precipitation; $\Delta\sigma_d$: hardening due to an increase in dislocation density; σ_r: resulting stress*

Adaptation where particles are by-passed by the dislocations

This type of particle bypass occurs within aluminum-copper alloys treated to contain the phase θ' and within Waspaloy alloys treated to contain larger precipitates γ'. Some examples of curves giving the evolution of stress along with the number of cycles are given in Figure 4.20.

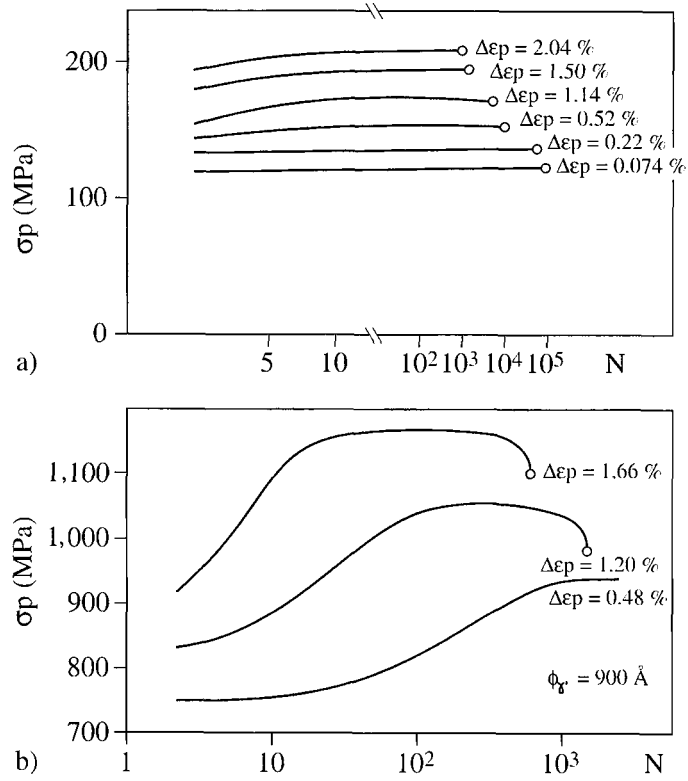

Figure 4.20. *Examples of alloys showing particle bypass by dislocations: a) aluminum-copper (from Calabrese and Laird [CAL 74]); b) Waspaloy $\phi_{\gamma'}$: 800 Å (from Stoltz and Pineau [STO 79])*

In both cases, after a stage of rapid consolidation we can observe a saturation regime. This behavior seems to be characteristic of alloys that contain some non-sheared particles.

In this case, contrary to shearing, the distribution of deformation bands is much more homogenous at the grain scale. This is because there are no weak spots in the crystal that concentrate dislocation activity.

Although it is not necessarily fundamental for the study of LCF, especially regarding endurance, it is interesting to point out that the large internal stresses due to the formation of dislocation loops, which we can observe around the precipitates, can significantly modify the shape of the $\sigma - \varepsilon$ hysteresis loops, especially during the first cycles. This was noticed for the first time by Stoltz and Pelloux [STO 76]

and was then confirmed and studied by other authors. For example, in Figure 4.21 we have reproduced the shape of the hysteresis loops recorded on a Fe-20 Cr-4 Ni-2 Al alloy, hardened by the precipitation of the Ni Al phase [TAI, TAI 82]. We can compare the shape of these loops when the particles are small and are sheared and also when they have a size that allows them to be bypassed by the dislocations. Contrary to the first case, we can observe that, when the by-passing mechanism occurs, the first hysteresis loops present a reverse curve and an inflection point, this phenomenon disappearing when the number of cycles is increased. This effect, associated with a strong Bauschinger effect, was studied by Stoltz and Pelloux [STO 76] and Atkinson and Brown [ATK 74].

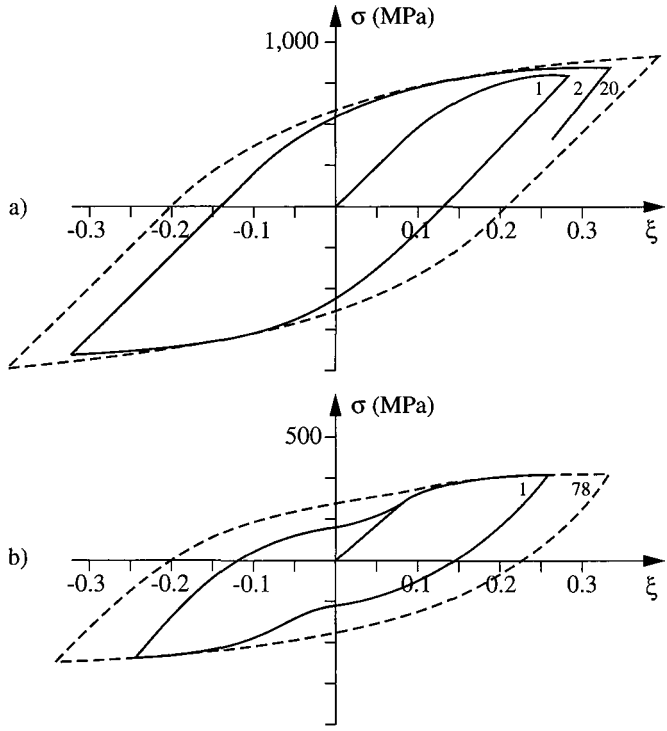

Figure 4.21. *Shape of the hysteresis loops recorded within the same alloy (Fe-20Cr-4Ni-2Al). The figures next to the curves indicate the numbers of cycles: a) under-aged state – precipitates sheared by the dislocations; and b) over-aged state – precipitates by-passed by the dislocations*

The interpretation of the hardening effect that was observed when the by-passing mechanism occurs is the same with monotonic tension; the presence of particles, that cannot be sheared by the dislocations, accelerates the multiplication of

Chapter 5

Gigacycle Fatigue

5.1. Introducing the real-life fatigue life of machines

When Wöhler introduced the SN curve, the applications at that time were actually steam engines used by locomotives or ships. These slow machines were running at a few dozen cycles per minute, which led to fatigue life ranging from a million to tens of millions of cycles. It was therefore totally acceptable, on a practical basis, to consider a high cycle fatigue limit as these fatigue machines could not exceed more than a dozen Hertz.

Nowadays, as the rotation rate of engines are several thousand cycles per minute, the fatigue life of an internal combustion engine reaches more than a 10^4 cycles per minute and that of turbines can reach around a billion cycles, for example. Nevertheless, we have to say that the fatigue tests of more than 10^7 cycles are rare due to the cost related to the operating mode of the conventional machines used.

To summarize the present situation, it is accepted that the concept of fatigue limit is related to the hypothesis of a horizontal asymptote on the SN curve above 10^6 or 10^7 cycles. We thus consider that every non-broken specimen after 10^7 cycles has an infinite lifespan/time, which is a convenient and economical assumption albeit not a rigorous one (see Figure 5.1).

Chapter written by Claude BATHIAS.

Actually, we have to understand that if the staircase method is widely used today in order to determine fatigue limit, we need to shorten the duration of the tests. A fatigue limit determined using this method with 10^7 cycles requires about 30 hours of tests in order to break a specimen of 10^7 cycles with a machine working at 100 Hz. In order to reach 10^8 cycles, 300 hours of tests are necessary, which is then a costly process.

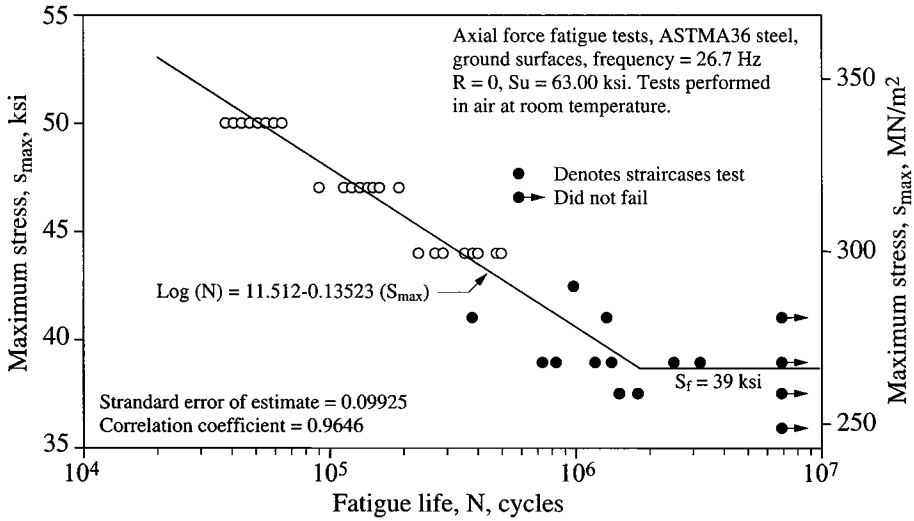

Figure 5.1. *SN curve according to international standards*

Figure 5.1 reminds us that this endurance concept, which can be approximately applied to carbon steels, is not a global characteristic. Experience shows us that fatigue fracture occurs between 10^7 and 10^{10} cycles. Another useful way of assessing the risk of fatigue fracture is given by the SN curve between 10^6 and 10^{10} cycles. Since Wöhler, the SN curve is usually shown with a hyperbole that is more or less modified as indicated below:

– hyperbole $\text{Ln } Nf = \text{Ln } a - \text{Ln } \sigma_a$;

– Wöhler $\text{Ln } Nf = a - b\,\sigma_a$;

– Basquin $\text{Ln } Nf = a - b\text{Ln } \sigma_a$;

– Stromeyer $\text{Ln } Nf = a - b\text{Ln } (\sigma_a - c)$.

Obviously, an accurate model can only be found if we analyze the fatigue life domain between 10^6 and 10^{10} cycles. For all these reasons, it is worth studying the

very-long life spans from accelerated fatigue tests carried out at 20 kHz using machines equipped with a piezoelectric converter [BAT 05].

5.2. Testing process

5.2.1. *Piezoelectric machines*

In the literature [HOP 11], the first publications on vibratory fatigue with a frequency of 33 Hz go back to 1911. They were written by Hopkinson, then Jenkins and Lehmann, but the first machine that could reach 20 kHz was invented by Mason in 1950 [MAS 50]. This frequency is a threshold below which the wave becomes inaudible. In 1959 and 1965, Girard and Vidal respectively carried out tests to increase the frequency to 92 and 199 kHz, but these were difficult to perform and were of little interest. At that time, controlling the tests using computer techniques was not possible and the results obtained were wrong. Numerical control of piezoelectric machines has only relatively recently been achieved by Bathias and his team [WU 95]. This technique, with an unofficial standard of about 20 kHz, is used to study the very long life span of these materials and fracture mechanics.

Since 1970, experimental means in the field of vibratory fatigue have been improved and other systems and test devices have been developed. In 1998, the first international congress entitled Fatigue Life in the Gigacycle Regime [BAT 98] was held in France by Euromech. Following this, three others followed in Vienna (2001), Kyoto (2004) and Ann Arbor (2007), proving that attention is now being paid to fatigue at a very high number of cycles. A book dealing with this topic was written by Bathias and Paris [BAT 05]. The highly technical vibratory fatigue testing system, which has been developed by Bathias in the last 10 years, is presented in the next section.

5.2.2. *Principle of vibratory fatigue*

The general principle of vibratory fatigue has already been the main topic of several publications [STA 86, STA 98]. We will therefore focus on the essential theory developed in [BAT 05, KON 91].

The basic principle of the vibratory fatigue machine is to produce a stable vibratory resonance within the specimen. To do so, we first need a converter that is capable of converting the sinusoidal signal produced by the electric generator into a mechanical vibration. The commercially available converters and generators usually have a set frequency of 20 kHz.

In most cases the vibration of the converter is too low to damage the specimen. In these cases, therefore a sonotrode is necessary to increase the amplitude of the vibratory movement. If the vibratory system (converter, sonotrode and specimen) has the same intrinsic frequency (20 kHz), we can then obtain a strong vibration amplitude with low energy and a stable wave within the system.

The different hypothesis regarding vibratory fatigue is as follows:

– the metal being studied is homogenous and isotropic;

– the metal is purely elastic (the plastic domain being considered is negligible compared to the elastic one in the case of fatigue with a really long lifespan);

– as vibration moves longitudinally, the theoretical analysis can be reduced to one dimension from the differential element which is presented in Figure 5.2.

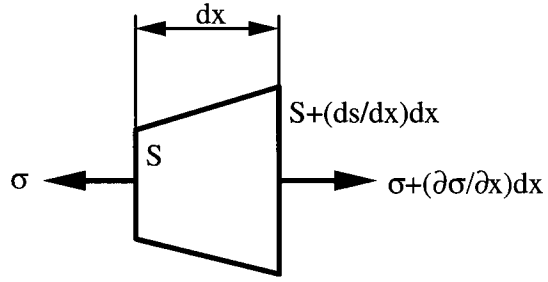

Figure 5.2. *Differential element*

The equilibrium equation based on Newton's second law, $\vec{F} = m\vec{a}$, can be written as:

$$\left(\sigma+\frac{\partial\sigma}{\partial x}dx\right)\left(S+\frac{ds}{dx}dx\right)-\sigma S = ma \qquad [5.1]$$

$$\left(\sigma+\frac{\partial\sigma}{\partial x}dx\right)\left(S+\frac{ds}{dx}dx\right)-\sigma S = \rho S dx\frac{\partial^2 U}{\partial_t^2} \qquad [5.2]$$

If we ignore the second-order terms, we then have:

$$\sigma\frac{dS}{dx}+S\frac{\partial\sigma}{\partial x}-\rho S\frac{\partial^2 U}{\partial_t^2}=0 \qquad [5.3]$$

Here, σ is the axial vibratory strain, S the section area, U the displacement, and ρ volume mass.

For linear elasticity, if we suppose that the behavior laws that are valid for static situations are also valid for dynamic ones with inertia effects, we can then write:

$$\sigma(x,t) = E_d \frac{\partial U(x,t)}{\partial x} \qquad [5.4]$$

where E_d is the dynamic Young's modulus.

The mechanical equation of the longitudinal and planar wave in a single dimension rod with a variable section is:

$$\frac{\partial^2 U(x,t)}{\partial x^2} + \frac{S'(x)}{S(x)} \frac{\partial U(x,t)}{\partial x} - \frac{\rho}{E_d} \frac{\partial^2 U(x,t)}{\partial t^2} = 0 \qquad [5.5]$$

where U is displacement, S section area, ρ volume mass and E_d dynamic Young's modulus.

If we consider a harmonic vibration regime:

$$U(x, t) = U(x) \exp.(i\omega t) \qquad [5.6]$$

after derivation, equation [5.5] becomes:

$$\frac{d^2 U(x)}{dx^2} + \frac{S'(x)}{S(x)} \frac{dU(x)}{dx} - K^2 U(x) = 0 \qquad [5.7]$$

where:

$$K^2 = \frac{\omega^2}{C^2}, \ \omega = 2\pi f, \text{ and } C = \sqrt{\frac{E_d}{\rho}}$$

In which f is intrinsic frequency and C propagation rate of the wave within the material.

Equation [4.7] enables us to determine the natural modes of longitudinal vibration and the resonance frequency for a beam with a given section.

5.2.3. *Calculation of resonance lengths*

In order to operate a machine under vibratory fatigue, the profiles of the specimen and sonotrode have to be designed based on the following considerations:

– the geometry has to lead to a longitudinally vibratory system with the same frequency as the one provided by the piezoelectric converter;

– the geometry has to be easily manufactured and the profile of the section has to allow a suitable amplification of the strain within the specimen in order to damage it;

– the global mass of the specimen and sonotrode has to be acceptable relative to the power of the excitation generator.

5.2.4. *Calculation of the specimens*

The geometry of the specimens under vibratory fatigue is usually designed with either an hour-glass axisymmetric profile (see Figure 5.3a) for endurance tests, or a flat profile (see Figure 5.3b) of crack growth tests.

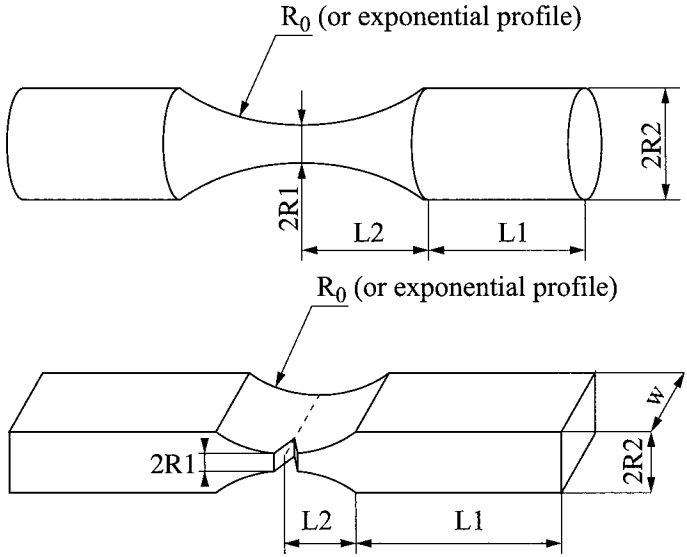

Figure 5.3. *Profile example of a specimen working at 20 kHz*

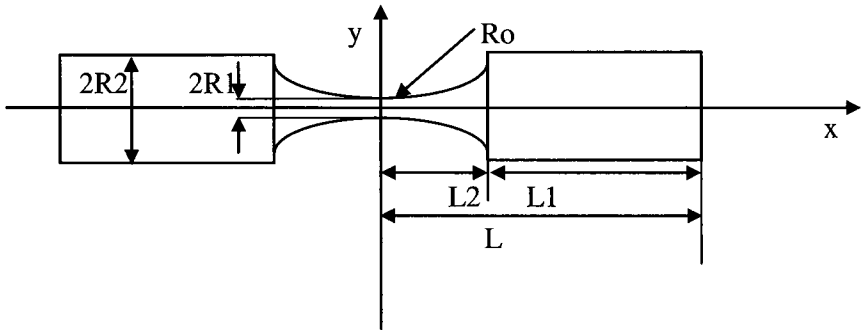

Figure 5.4. *Geometry of an axisymmetric endurance specimen*

The geometry of the axisymmetric specimen is based on the following equations:

$$y(x) = \begin{cases} R_2 & x\{[L_2, L],\ x\{[-L, -L_2] \\ R_1\ \mathrm{ch}(\alpha x),\ x\{[-L_2, L_2] \end{cases} \quad [5.8]$$

$$S(x) = \pi y^2 = \begin{cases} \pi R_2^2 & x\{[L_2, L],\ x\{[-L, -L_2] \\ \pi R_1^2\ \mathrm{ch}^2(\alpha x),\ x\{[-L_2, L_2] \end{cases} \quad [5.9]$$

with:

$$\alpha = \frac{1}{L_2}\ \mathrm{arc\ ch}\left(\frac{R_2}{R_1}\right) \quad [5.10]$$

The length L_1 has to be determined in order to obtain a fundamental resonance frequency of the vibratory system at 20 kHz.

If we develop equation [5.8] with the boundary conditions, we then obtain the analytical resolution of the resonance length given by the following equation:

$$L_1 = \frac{1}{K}\mathrm{arctg}\ \frac{1}{K}\left[\frac{\beta}{\mathrm{th}(\beta L_2)} - \alpha\,\mathrm{th}(\alpha L_2)\right] \quad [5.11]$$

$$\text{or } \beta = \sqrt{\alpha^2 - K^2}$$

and the displacement, deformation and strain distributions at half the length of the specimen ($0 \leq x \leq L$) within the elastic domain is developed below:

– catenary part:

-($0 \leq x \leq L_2$)

$$u_{ch}(x) = U_0\, \phi(L_1,L_2)\, sh\,(ßx)/ch\,(\alpha x)$$

$$\varepsilon_{ch}(x) = U_0\, \phi(L_1,L_2)\, [ß\, ch\,(ßx)\, ch\,(\alpha x) - \alpha\, sh\,(ßx)\, sh\,(\alpha x)]/ch^2\,(\alpha x)$$

$$\sigma_{ch}(x) = E_d\, U_0\, \phi(L_1,L_2)\, [ß\, ch\,(ßx)\, ch\,(\alpha x) - \alpha\, sh\,(ßx)\, sh\,(\alpha x)]/ch^2(\alpha x)$$

where:

$$\phi(L_1,L_2) = \cos(KL_1)\, ch\,(\alpha L_2)/sh\,(\beta L_2) \qquad [5.12]$$

– cylindrical part:

-($L_2 \leq x \leq L$)

$$u_{cy}(x) = U_0 \cos K(L - x)$$

$$\varepsilon_{cy}(x) = K\, U_0 \sin K(L - x)$$

$$\sigma_{cy}(x) = E_d\, K\, U_0 \sin K(L - x) \qquad [5.13]$$

At the center of the specimen ($x = 0$), the strongest deformation and strongest strain can be written as:

$$\varepsilon_{max}(x) = U_0\, \phi(L_1,L_2)\, ß$$

$$\sigma_{max}(x) = E_d\, U_0\, \phi(L_1,L_2)\, ß$$

We can observe that the calculated strain is proportional to Young's modulus, which is one of the properties of the metal that we have to carefully determine under a dynamic regime.

5.2.5. *Calculation of the sonotrodes*

The geometry of the chosen sonotrode is a rod with a constant section connected to a variable cross-section whose dimensions can dramatically affect the

amplification coefficient. Depending on the type of test (endurance, cracking, R = -1 and R variable, room or cryogenic temperature, traction or compression, etc.) and on the level of strain amplitude, we can choose the sonotrode with the most suitable geometry.

Two types of sonotrode (see Figure 5.5) enable us to cover a large range of applications. The so-called SC sonotrode is a standard device with an amplification factor of 2.4. The TGD sonotrode is a high amplification sonotrode with an amplification factor from 8 to10. This allows us to obtain the highest stress within the specimen at about 550 MPa in the case of steel for the SC sonotrode. For the other sonotrode, the maximum stress that develops is about 2,200 Mpa.

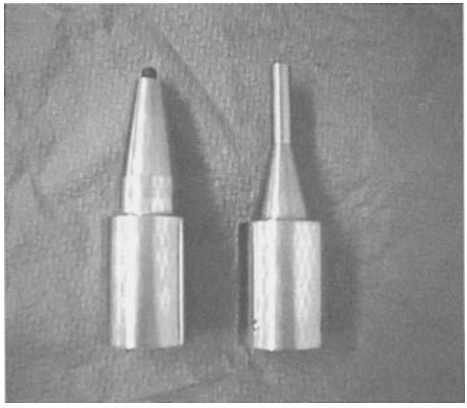

Figure 5.5. *SC and TGD sonotrodes*

In the case of a cone-shaped sonotrode, there is no calculation that will enable us to determine the resonance length in Eigen mode. The problem has to be resolved using the finite element method.

A finite element equation is done using the following vibration equation:

$$[K]\ \{u\} = \omega^2\ [M]\ \{u\} \qquad [5.14]$$

where ω is pulsation equal to $2\pi f$, [K] rigidity matrix as a function of the temperature, {u} displacement vector or the intrinsic mode, and [M] mass matrix.

The sonotrodes are meshed, as shown in Figure 5.6. The boundary conditions are u = 0 along the axis of the sonotrode and displacement towards this is free. As a

consequence, the inertia force automatically moves in the direction of y to keep the balance.

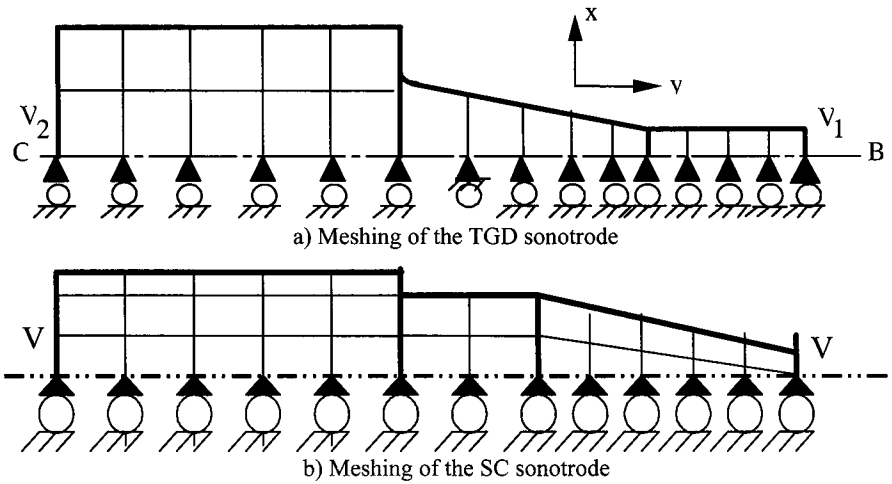

Figure 5.6. *Meshing and boundary conditions of: a) TGD and b) SC sonotrodes*

5.3. Systems of piezoelectric fatigue machines

The vibratory fatigue system illustrated in Figure 5.7 is made of several elements:

– a Branson vibration generator that can reach a power of 2 KW and whose frequency is calculated at 20 kHz. It gives a sinusoidal signal to the converter, which triggers vibration;

– a converter to turn electric vibrations into mechanical ones;

– a sonotrode (amplifier) made of a cylindrical part followed by a cone-shaped profile section. As the displacement amplitude of the converter is limited, the cone allows us to increase the vibratory amplitude of the specimen in order to reach the necessary strain. The specimen is fixed to the end of the sonotrode using a screw;

– a digital system made from a computer, a 16-channel and 12-bit A/D converter (analog to digital) whose conversion rate is theoretically of 20 υs, and a 5-channel and 12-bit D/A converter (digital to analog) in order to control the machine.

The computer controls the generator and converter in order to put a constant strain amplitude on the specimen using an automation program that was specially designed for vibratory fatigue tests. At the same time, the vibration frequency and

vibratory amplitude of the head of the sonotrode (and therefore of the specimen) are locked. The number of vibration cycles is memorized.

An optical fiber gauge or a capacitive gauge is used to directly measure the vibratory amplitude at the head of the specimen. Its frequency ranges from 10 Hz to 70 kHz and it can measure displacements of 1 μm to 199 μm with a resolution of 0.1 μm. We can also perform some vibratory fatigue tests with an average load equal to zero (R = -1).

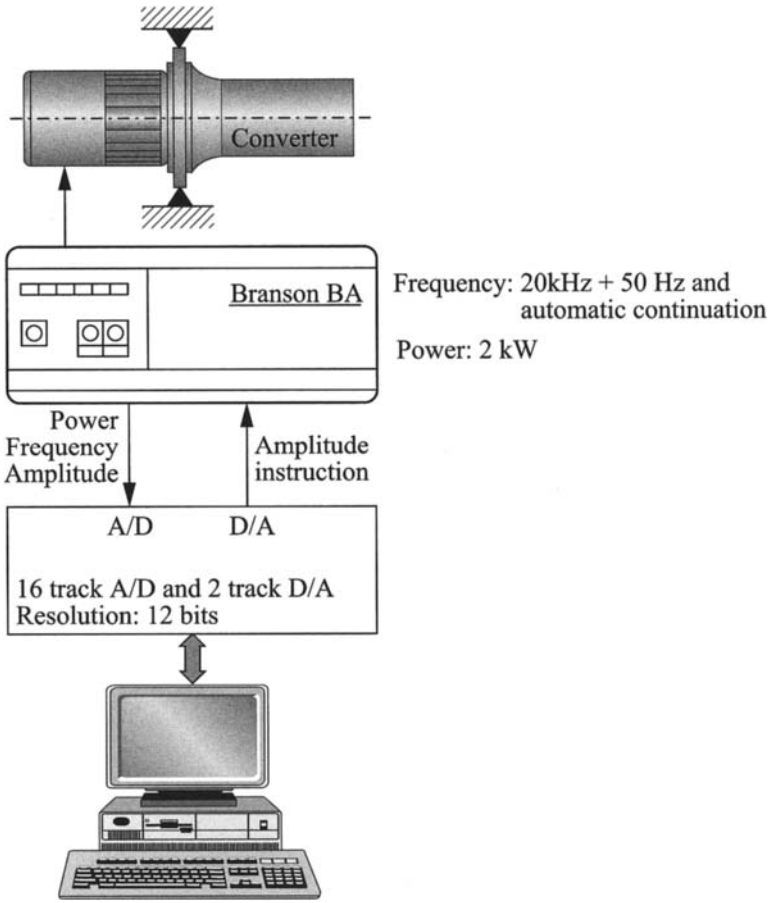

Figure 5.7. *General view of a piezoelectric and vibratory fatigue device*

Using a traction machine, which allows us to exert a constant traction on the specimen without preventing the resonator from working and producing vibrations,

we can carry out vibratory fatigue tests with an average loading different to zero (R being variable).

5.4. SN curves above 10^7 cycles

5.4.1. *General aspects of SN curves*

Currently the results of fatigue tests 10^7 are pretty rare because of the cost of operating conventional machines. It is worth noting that the fatigue tests are accelerated by resonance machines, but these were not popular. One of the drawbacks of resonance machines is that control of the test parameters along with the resonance machines are now being replaced with computer control and high speed sensors.

Nowadays there are some very reliable fatigue machines that can produce 10^{10} cycles in less than a week, whereas the conventional systems led to tests taking over three years for a single specimen.

For this reason, we may wonder whether we need to apply the rules in order to determine a reliable fatigue limit at 10^7 cycles from a statistical approach or not, or if we need to determine a SN curve up to 10^{10} cycles and more.

We have selected four examples to convince the reader that a crack may occur due to fatigue after 10^7 cycles and that the SN curve does not present any asymptote.

The first example, given in Figure 5.8, presents an SN curve that has been determined up to 10^9 cycles, at 20 kHz, 300 K and R = -1 for various forging types of a 6,246 titanium alloy and, as a consequence, for the different microstructures.

Within these titanium alloys, where there are neither inclusions nor porosity, it is particularly striking that cracks can occur up to 10^9 cycles and that there is no horizontal asymptote as predicted by the models inspired by Wöhler. The initiation strain at 10^9 cycles is much lower than the conventional fatigue limit at 10^6 cycles (100 to 200 MPa).

Finally, we note that the microstructure of titanium has a significant impact on very long lifespans (325 to 490 MPa at 10^9cycles).

The second example (see Figure 5.9) confirms that there is no asymptote and that fractures occur at 10^8 cycles within titanium alloys subjected to cyclic strains at 20 K, into liquid hydrogen or helium, either with R = -1 or with R = 0.1.

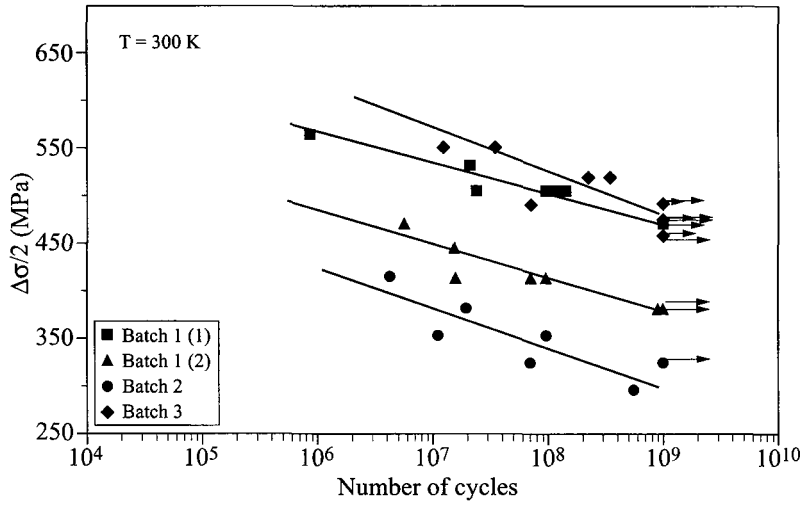

Figure 5.8. *Influence of the forging range on the fatigue of a titanium alloy at a very high number of cycles (6,246); T = 300 K; -R = -1; - f = 20 kHz*

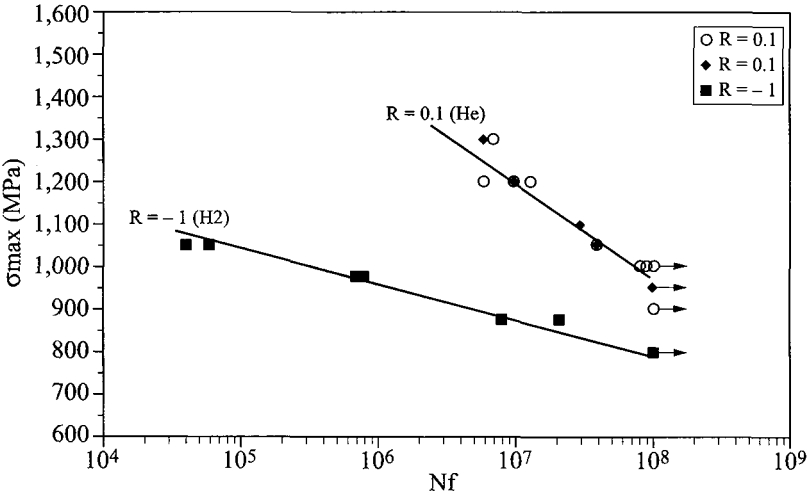

Figure 5.9. *Test results at R = 0.1 and R = -1/TA6V PQ at 20 K*

Finally, Figures 5.10 and 5.11 present the results of very long lifespan fatigue in the case of nickel alloys at room temperature and at 450°C. No asymptote is detected at any temperature. The alternate strain at the fracture seems to be two times lower at 10^{10} cycles than at 10^{6} cycles in Udimet 500.

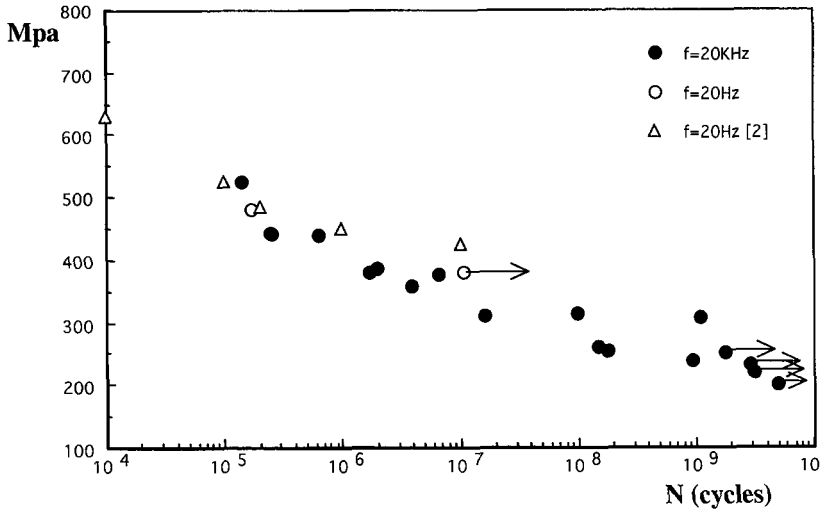

Figure 5.10. *SN curve of Udimet 500 at room temperature, 20 kHz and R = -1*

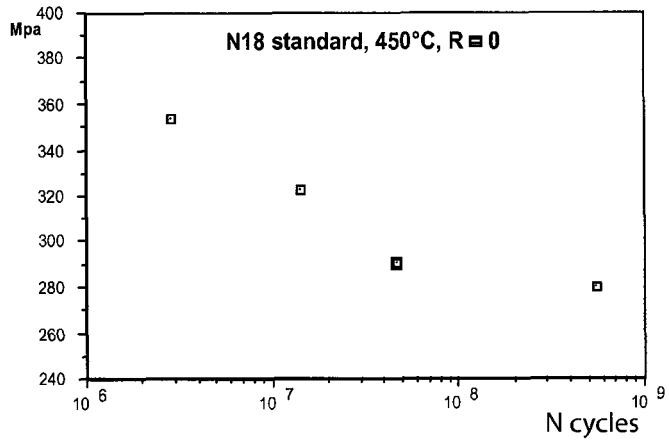

Figure 5.11. *SN curve of the N18 alloy at 450°C, 20 kHZ, R=0*

In order to generalize gigacycle fatigue, several types of alloys have been chosen whose behavior is known to be different under gigacycle fatigue. All of these alloys, details of which are listed in Tables 5.1 and 5.2, are of obvious interest in industry. Micrograph images of these alloys (steels, cast irons and foundry aluminum alloys) are shown in Figures 5.12 to 5.21.

5.4.2. *Case of ferrous metals*

5.4.2.1. *Steels and cast irons*

Nuance	C	Mn	P	S	Si	Al	Fe	Mg	Ni	Cr	Cu	Mo
SAE 8620	0.183	0.62	0.017	0.027	0.324				1.768	0.481		0.243
D38MSV5S	0.384	1.23	0.012	0.064	5.67	0.025			0.063		0.063	0.018
XC 70	0.669	0.568	0.011	0.062	0.158	0.002			0.071	0.136	0.127	0.21
40Si7	0.392	0.62	0.008	0.004	1.608	0.014			0.092	0.125	0.115	0.036
100 C6	1.03	0.339	0.012	0.008	0.242				0.147	1.461		0.032
SUJ 2	1.01	0.36	0.012	0.007	0.23				0.04	1.45	0.06	0.02
35 MV7	0.344	1.813	0.011	0.074	0.247	0.22			0.189	0.213	0.256	0.044
42CD4	0.428	0.827	0.012	0.024	0.254	0.023			0.173	1.026	0.21	0.224
SAF 2507	0.03	2			1				5	22		32
SAF 2205	0.03	1.2			0.8				7	22		48
Fonte GS 51	3.65	0.5			2.49			0.04			0.7	
AS5U3G		0.32			5.1		0.55	0.36			3.15	

Table 5.1. *Chemical composition of the alloys studied (% weight)*

	E_s (GPa)	$E_{d,}$ 20 KHz (GPa)	R_e (MPa)	$R_{0.2}$ (MPa)	R_m (MPa)	A (%)	d	HV_{30}	Microstructure
SAE 8620		204.8			720	26	7.85		25% ferrite + perlite
D38MSV5S		211.5	439	608	878	20	7.85	246	45% ferrite + perlite
XC 70	210	217.9	463	513	927.2	8.12	7.85	304	10% ferrite + perlite
40 Si7	213		838	1,141	1,677	0.9	7.85	432	10% ferrite + martensite
100 C6	210			1,158	2,300		7.86	780	martensite
SUI 2	210				2,316		7.86	778	martensite
35MV7	208		447	632	894	5.51	7.85	294	bainite
100 G6	210		1,179		2,358		7.86	704	bainite
42CD4	210		754	1482	1,508	2.71	7.85	469	martensite
42CD4	210		517	963	1,035	6.39	7.85	335	martensite
SAF 2507	200				956	37.2	7.80	470	55% austenite + ferrite
SAF 2205	200				723	48.2	7.80	297	45% austenite + ferrite
Fonte GS51		169	397	460	795	9	7.10	265	5% ferrite + perlite
		71	111	182	222	1	2.70	98.6	

Table 5.2. *Mechanical properties of the studied alloys*

We have chosen a wide range to cover several steel families that are known to give an asymptotic SN curve. The properties, chemical composition and microstructure are mentioned here in order to facilitate the interpretation of the results (Tables 5.1 and 5.2). It seems that this review is necessary as the microstructure and microdefects are of primary significance in understanding crack initiation under gigacycle fatigue.

The micrographs of Figures 5.12 to 5.20, taken after polishing with 1μm alumina and etched with Nital, show ferrito-perlite, austenite-ferrite, martensite, bainite or cementite microstructures in order to demonstrate to the reader that there is no steel capable of escaping gigacycle fatigue.

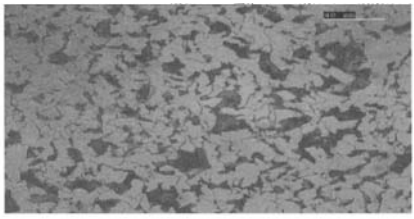

Figure 5.12. *SAE 8620 ferrite-perlite steel*

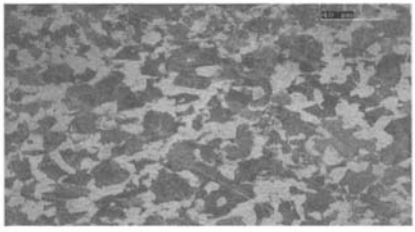

Figure 5.13. *D38MSV5S ferrite-perlite steel*

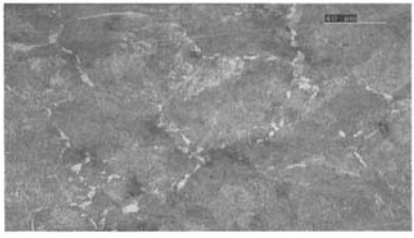

Figure 5.14. *XC70 ferrite-perlite steel*

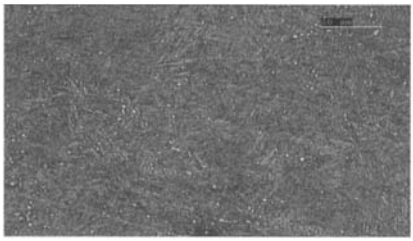

Figure 5.15. *100C6 steel*

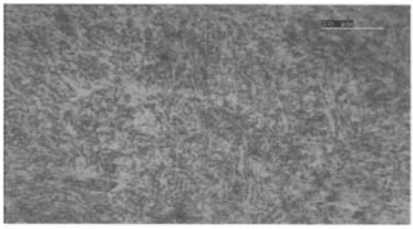

Figure 5.16. *Bainitic 35MV7 steel*

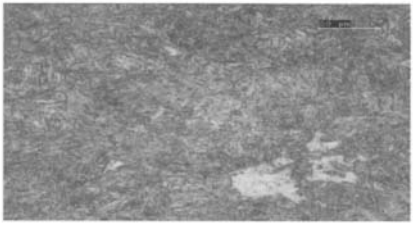

Figure 5.17. *Ferrite-martensitic spring 40Si7 steel*

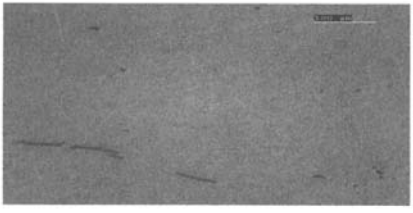

Figure 5.18. *42CD4 steel*

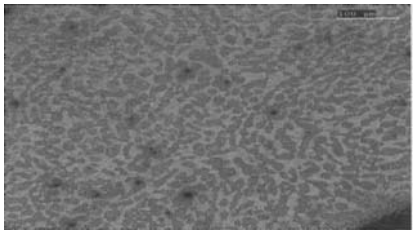

Figure 5.19. *SAE 2507 steel*

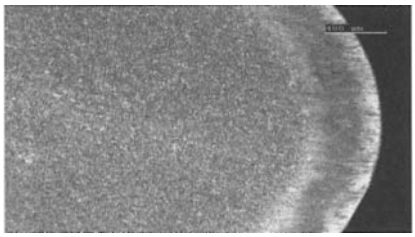

Figure 5.20. *Cemented SAE 8620 (430 μm) steel*

5.4.2.2. *Experimental results and comparison of results obtained under ultrasonic fatigue with those of classical methods*

Within the 8620 ferrite-perlite steel, failure through gigacycle fatigue will always occur between 10^6 and 10^{10} cycles. Initiation occurs at the surface before reaching 10^7 cycles and, in the core, this part of the lifespan SN curve is really flat, but the fatigue strength may drop and reach 35 MPa between 10^6 and 10^{10} cycles, see Figure 5.21.

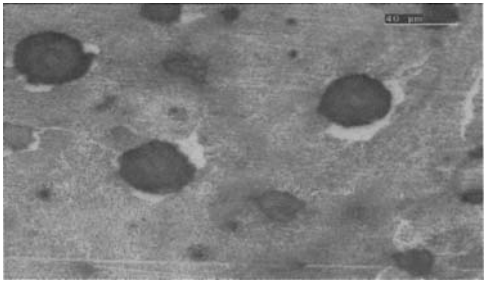

Figure 5.21. *GS 51 cast iron*

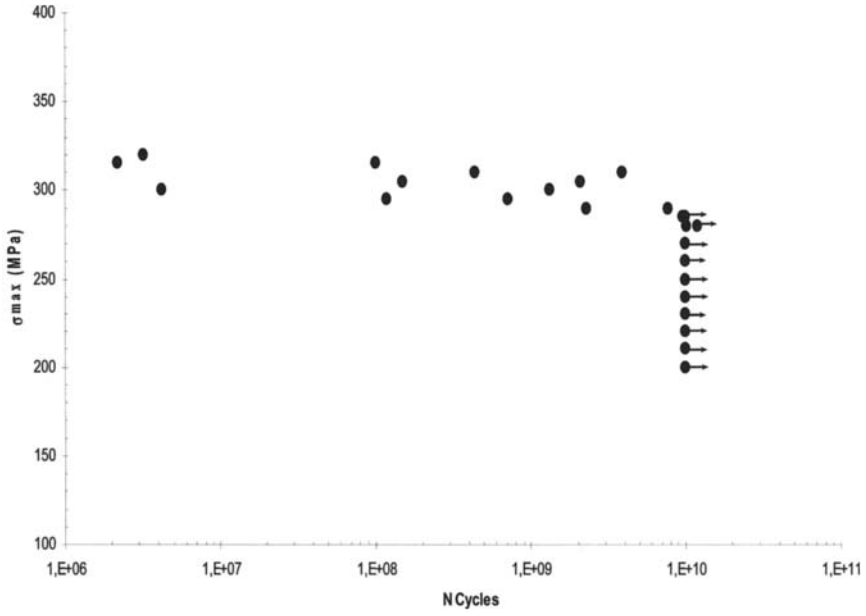

Figure 5.22. *SN curve in the case of SAE 8620 at R = -1 and 20 kHz*

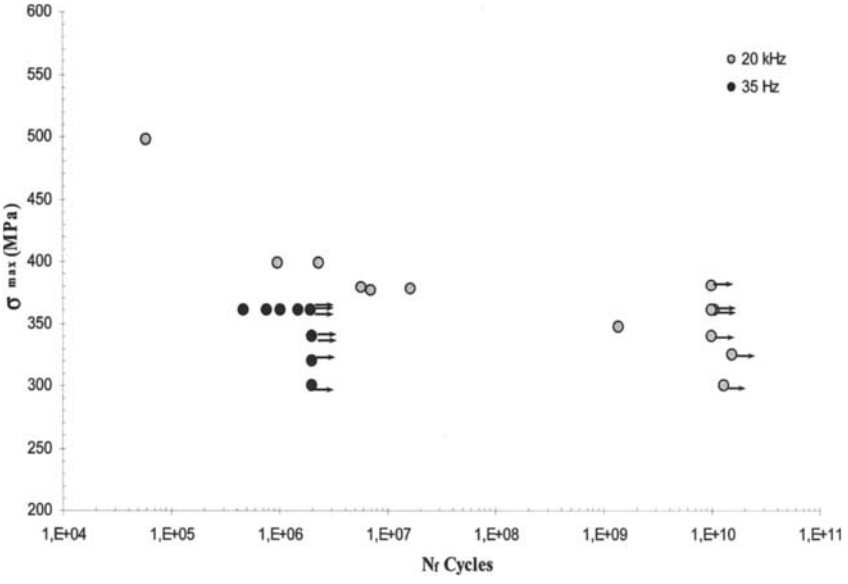

Figure 5.23. *SN curve in the case of XC 70, R = -1 at 20 kHz and 35 Hz*

XC70 ferrite-perlite steel can crack under fatigue between 10^6 and 10^9 cycles, with a drop in resistance of about 75 MPa. We note that there is a slight difference between the results obtained at a high (20 kHz) and a low (35 Hz) frequency, see Figure 5.23.

Within D38 ferrite-perlite steel, fatigue failure occurs up to 2.10^8 cycles but not beyond. In this case, five tests were carried out at up to 10^{10} cycles in order to make sure that an asymptote would appear. Nevertheless, we can observe a 100 MPa drop between 10^7 and 2.10^8. We do not observe any frequency effect between the tests carried out at 35 Hz and 20 kHz.

Under tension-tension, we find that the D38 ferrite-perlite steel fatigue resistance drops down to 275 Mpa, with a very large distribution. The results of tension-tension fatigue at 35 Hz and at 20 kHz drop into a distribution band of about 100 MPa, which remains a significant but usual distribution under conventional fatigue. Whereas with R = -1 we can observe a fatigue limit after 2.10^8 cycles, with R = 0.1, a fatigue limit is reached as soon as 6.10^6 cycles (see Figures 5.24 and 5.25).

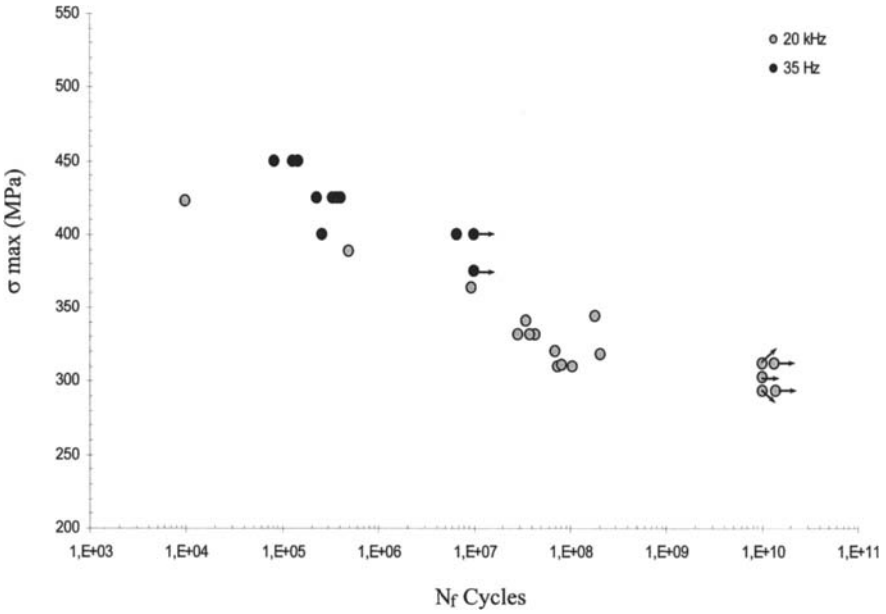

Figure 5.24. *SN curve of D38 steel, R = -1, at 20 kHz and 35 Hz*

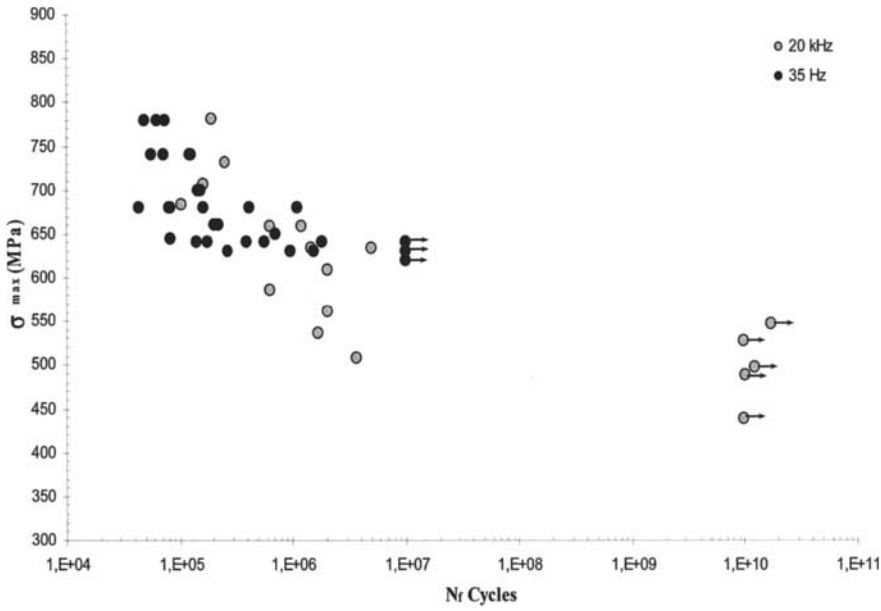

Figure 5.25. *SN curve of D38 steel, R = 0.1, at 20 kHz and 35 Hz*

The family of bearing steels, regardless of their origin, displays a particular aspect of gigacycle fatigue for industrial as well as scientific reasons. Martensitic or bainitic steels, whether notched (k_t =2.2) or not, of 100C6 type, can crack under fatigue beyond 10^{10} cycles! The notion of fatigue limit obviously loses any practical meaning in such cases (Figures 5.26 and 5.27).

It is therefore interesting to compare the SN fatigue curves obtained under rotating-bending and traction-compression strain.

In the Japanese literature, a large number of results were obtained under rotating-bending strain, giving a SN curve with a plateau, which is considered to be the transition of gigacycle fatigue.

As long as it remains difficult to detect this plateau under axial loads, we can assume that the plateau is related to the calculation of nominal strain under rotating bending when initiation is internal.

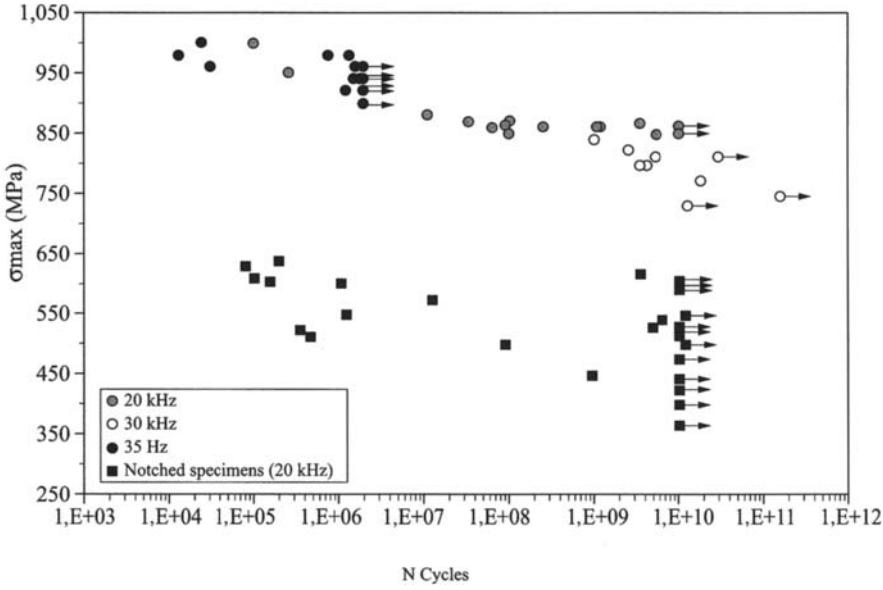

Figure 5.26. *SN curves of the 100Cr6 martensitic steel, at 20 kHz,30 kHz and 35 Hz*

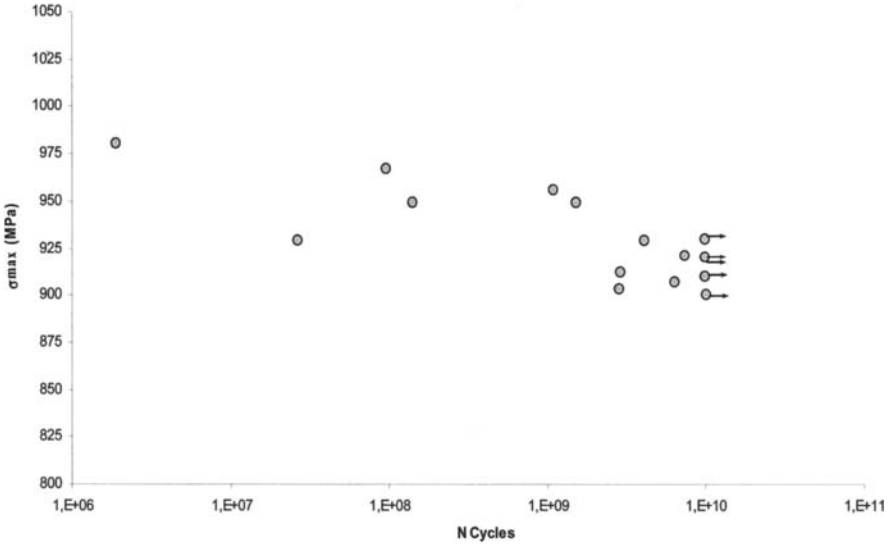

Figure 5.27. *SN curve of the bainitic 100Cr6 steel, with R = -1, at 20 kHz*

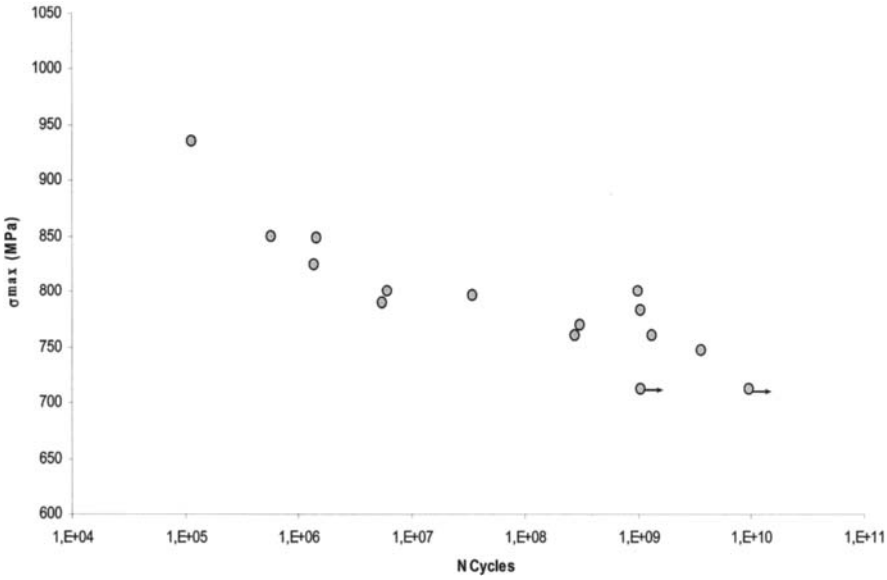

Figure 5.28. *SN curve of the SUJ2 steel at R = -1, under tension-compression, at 20 kHz*

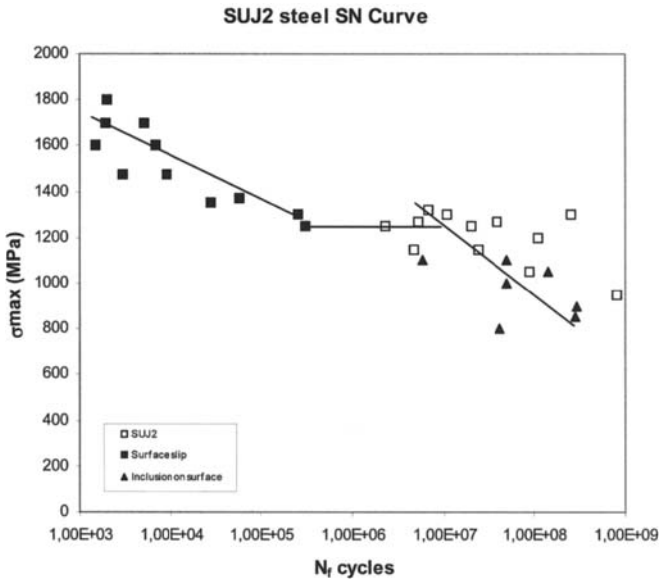

Figure 5.29. *SN curve of the SUJ2 steel under rotating bending*

The curve of the bainitic 35MV7 steels presents a low slope within the gigacycle domain, with a shape that is almost asymptotic, the initiation always occurring within the sub-layers at up to 10^8 cycles. As the distribution/dispersion is quite significant, no influence of frequency is observed (see Figure 5.30).

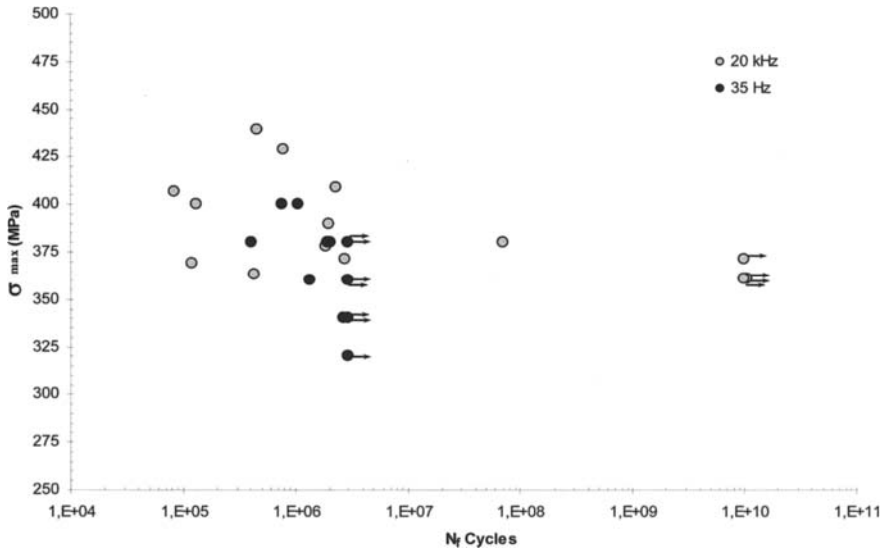

Figure 5.30. *Fatigue results of 35MnV7 steel R = -1at 20 kHz and 35 Hz*

The ferrite-martensitic spring 40Si7 steels can crack due to fatigue beyond 10^9 cycles (Figure 5.31). The dispersion/distribution is rather important, as the SN curve is really flat. The results obtained under gigacycle fatigue do agree with the ones obtained under megacycle fatigue. As a consequence, a frequency effect is discarded.

The case of 42CD4 steels (Rm =1,510 MPa) is especially interesting because of the difference between the results depending on the direction of sampling. Lengthwise, the fatigue resistance at 10^9 cycles is 0.45 R; it drops down to 0.33 R crosswise, where the dispersion of the results is very high and related to the distribution of thick inclusions (see Figures 5.32 and 5.33).

The austenite-ferrite SAF2507 and 2205 steels also show that cracking due to fatigue can occur above and beyond 10^9 cycles. We do not observe any influence of frequency between 140 Hz and 20 kHz (see Figures 5.34 and 5.35).

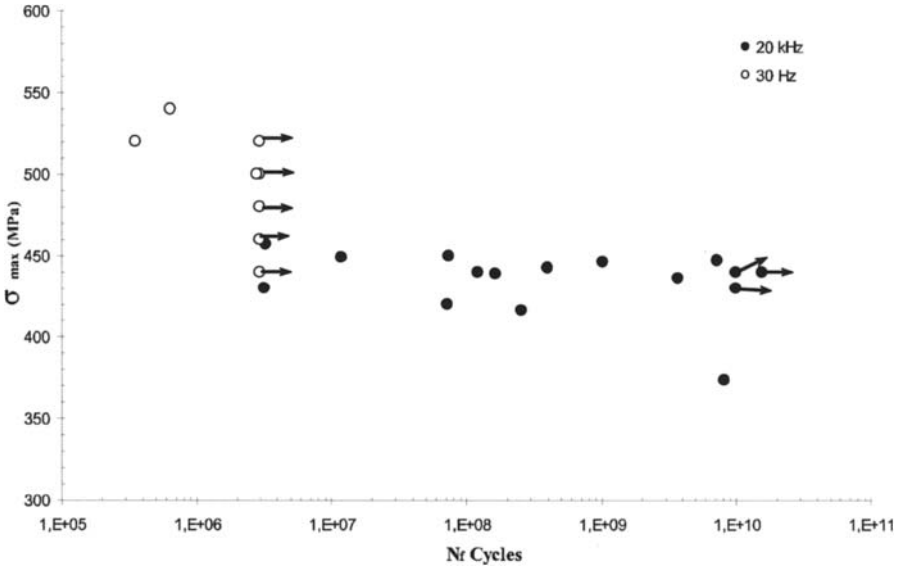

Figure 5.31. *SN curve of 40Si7steel, R = -1, at 20 kHz and 30 Hz*

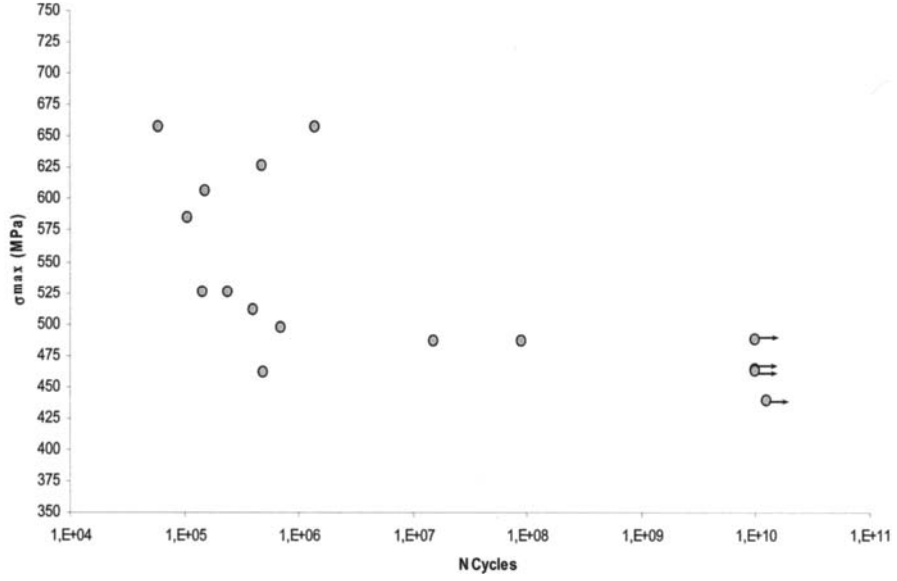

Figure 5.32. *Fatigue of the 42CD4 steel, Rm = 1510 MPa, crosswise, R = -1, at 20 kHz*

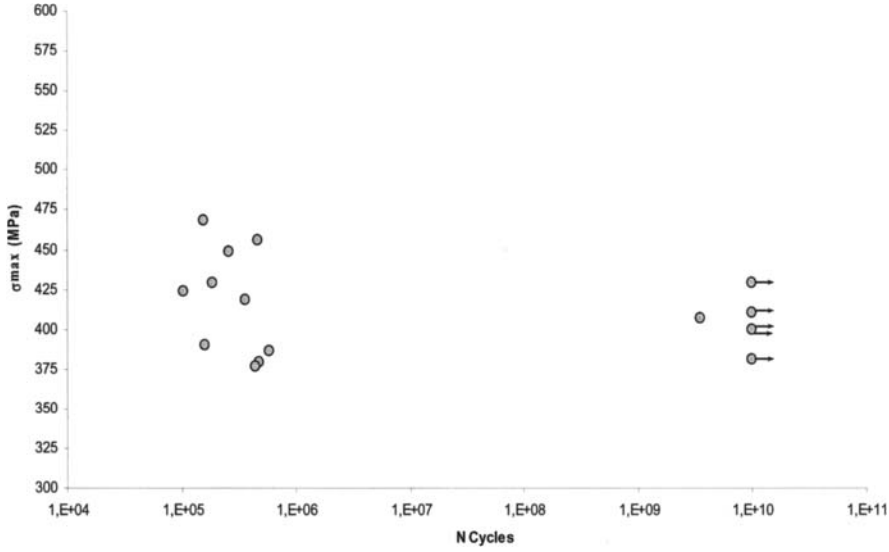

Figure 5.33. *SN curve of 42CD4, Rm = 1035 MPa, crosswise, R = -1, at 20 kHz*

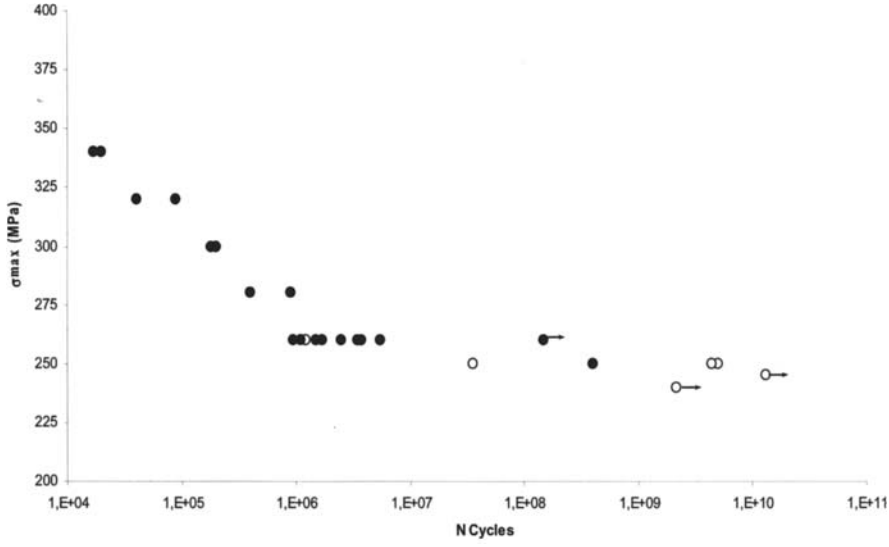

Figure 5.34. *SN curve of the SAF 2205 steel, R = 0, at 20 kHz and 140 Hz*

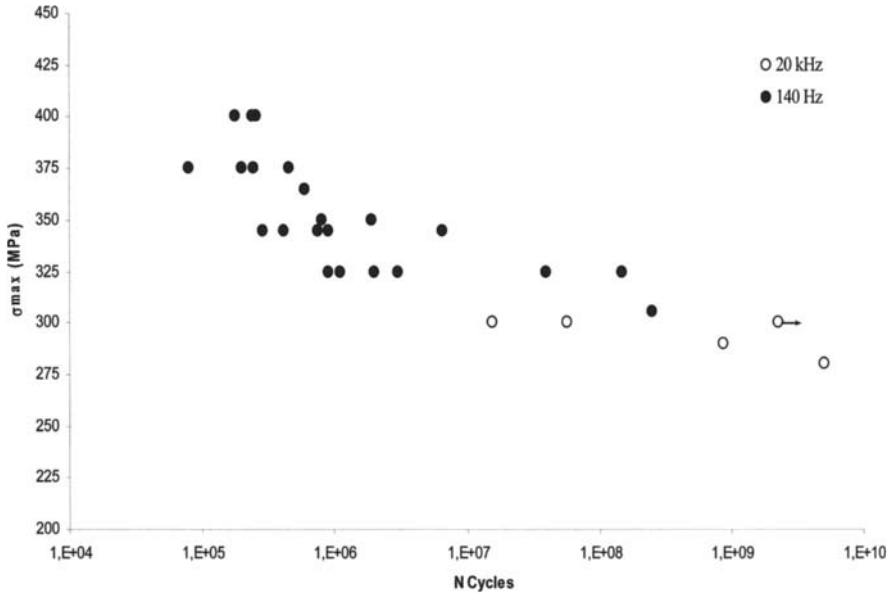

Figure 5.35. *SN curve of the SAF 2507curve, R = 0, at 20 kHz and 140 Hz*

The SAE 8620 steel cemented between 0.4 and 0.8 mm thickness cracks under gigacycle fatigue beyond 10^9 cycles following a very steep and dispersed SN curve.

We can see that the infulence of cement thickness on fatigue strength is slightly less obvious under gigacycle fatigue than under rotary/rotative bending, as no difference is detected before 10^9 cycles (see Figures 5.36 and 5.37).

We might then think that cementation has no effect on fatigue strength after a billion cycles.

Nodular cast iron also cracks under gigacycle fatigue up to 10^{10} cycles under alternate and undulating tractions. The SN curve is almost flat but failure can occur at up to 10^{11} cycles, which means that there is no infinite lifespan for car industry pieces made of nodular cast iron.

We do not observe any frequency effect between 20 kHz, 30 kHz and 30 Hz (see Figures 5.37 and 5.38).

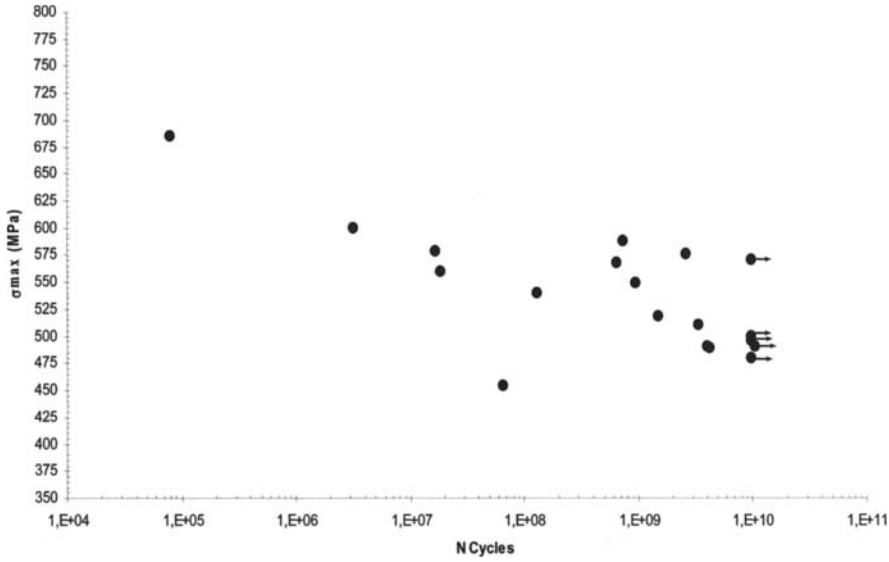

Figure 5.36. *SAE 8620 steel, cemented layer, 0.43mm thick, R = -1 at 20 kHz*

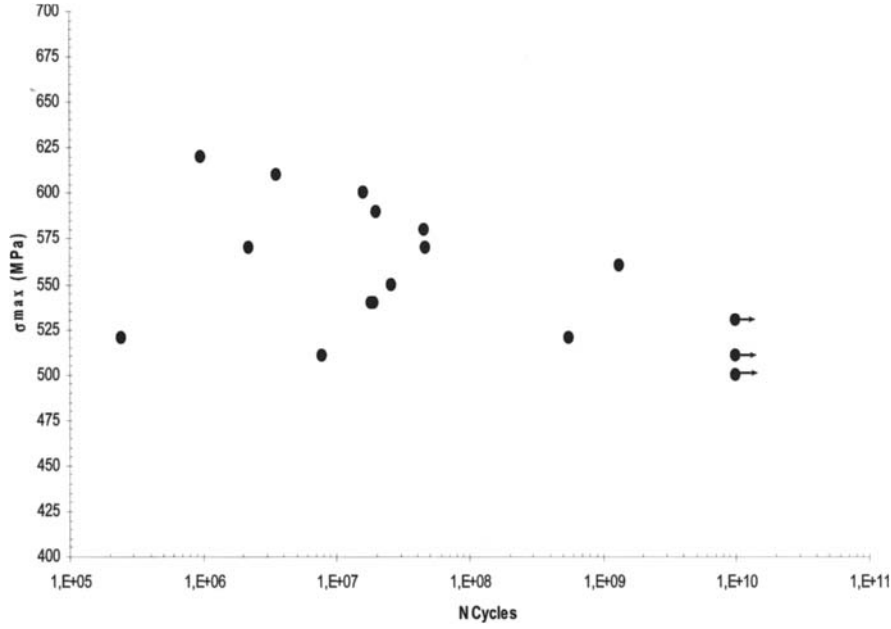

Figure 5.37. *SAE 8620 steel, cemented layer, 0.81 mm thick, R = -1 at 20 kHz*

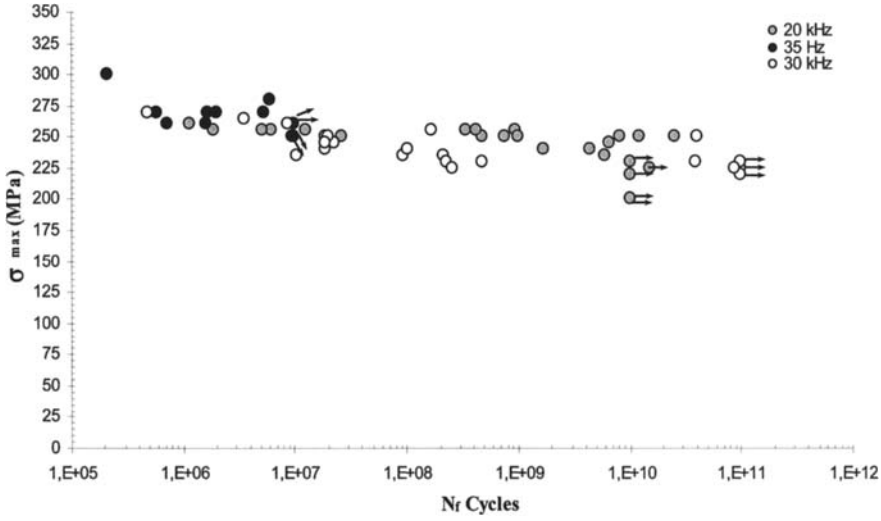

Figure 5.38. *SN curve of nodular cast iron GS51, R = 0.1, at 20 kHz and 35 Hz*

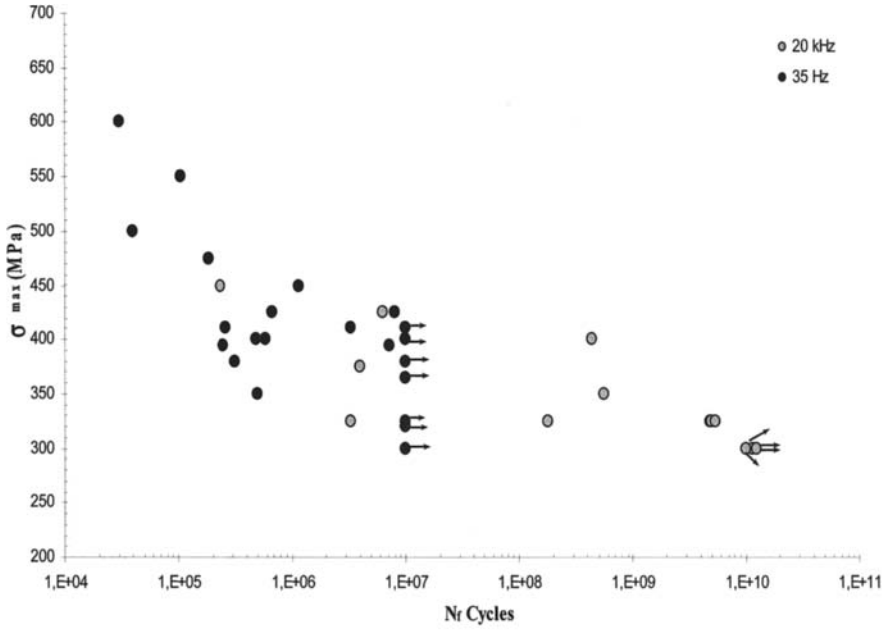

Figure 5.39. *GS 51 SN curve, R = -1, at 20 kHz, 30 kHz and 35 Hz*

5.4.3. *Case of aluminum alloys*

The AS5U3G-Y35 aluminum alloy, like steels and cast iron, is a material that is widely used in the construction of car industry pieces. This aluminum cast iron is mainly used to manufacture engine cylinder heads.

Tables 5.1 and 5.2 show the chemical composition and the mechanical properties of the aluminum alloy. Figure 5.40 shows the aspects of the microstructure (chemical etching with 5% fluorhydric acid for 30 seconds and polishing with 1 μm alumina).

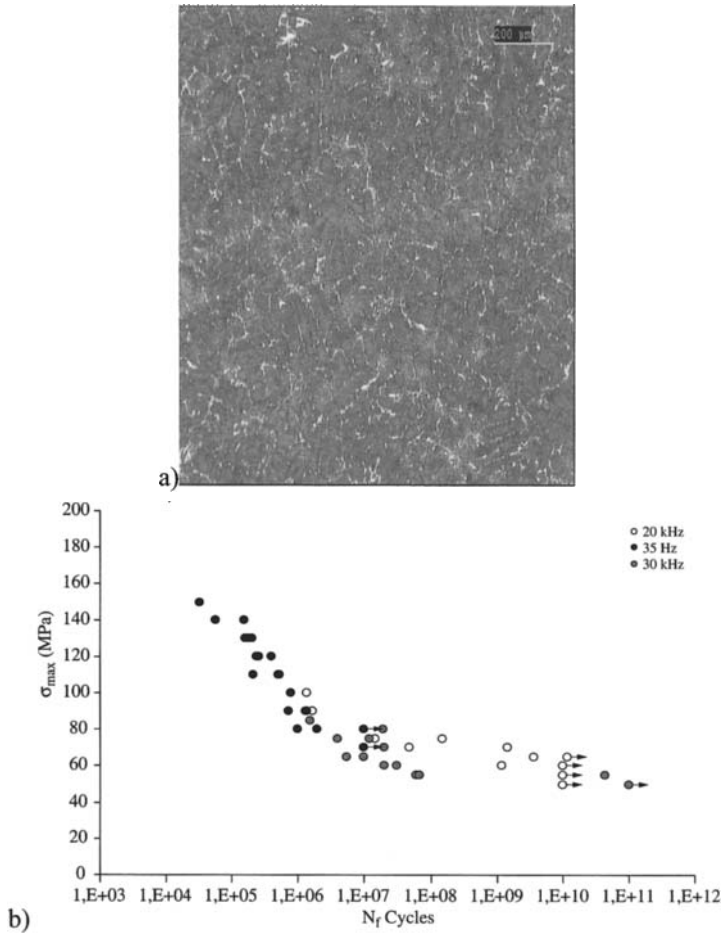

Figure 5.40. *a) Microstructure of the AS5U3G-Y35 alloy; b) SN curve up to 10^{10} cycles. Tests at various frequencies and R = -1*

We can see that, as is expected for aluminum alloys, there is a significant drop in fatigue resistance between 10^6 and 10^9 cycles.

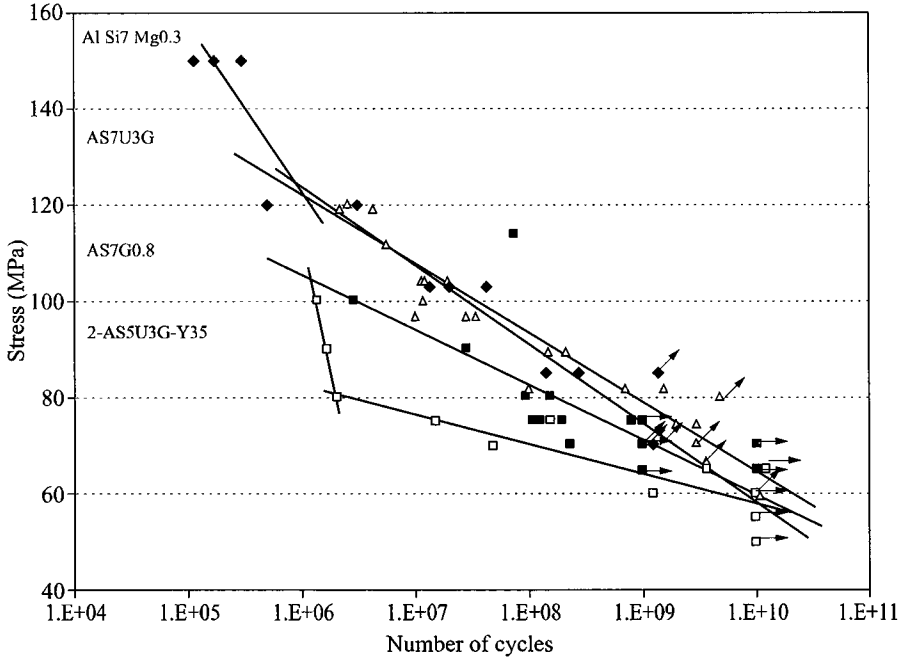

Figure 5.41. *SN curves of aluminum foundry alloys within the gigacycle domain, compared to the SN curve of AS5U3G, at 20 kHz*

5.5. Initiation mechanism under gigacycle fatigue

Observations show that initiation at the surface becomes less frequent after and/or beyond cycles, whereas typical localization of the initiation site within the metal is a characteristic of long lifespans. If the initiation of fatigue cracks occurs at the surface, however, it is due to the planar strain effect and to the von Mises plasticity criterion. Nevertheless, from a load that is low enough, the surface plasticity tends to be evanescent and only the localized strain concentration around the defects can lead to nucleation of a crack.

Mughrabi [MUG 07] suggested that the nucleation mechanism at the microscopic scale is almost the same whatever the fatigue regime, but what changes is the localization of the permanent slip bands. As the likelihood of getting a defect within a volume is higher than the chance of a defect at the surface-envelope, internal initiation under gigacycle fatigue can easily be understood. Nevertheless,

the defects of a metal are various, an inclusion having a different behavior depending on the porosity or defect of a microstructure [BAT 05, WAN 98].

A discussion dealing with a few specific cases is presented in the following section.

5.5.1. *Non-metallic inclusions*

Non-metallic inclusions lead to an internal initiation within high-strength steels and nickel alloys with really long lifespans. This is also the case for some foundry alloys, such as cast iron, and some alloys resulting from powders that are used in metallurgy (see Figures 5.42 to 5.49).

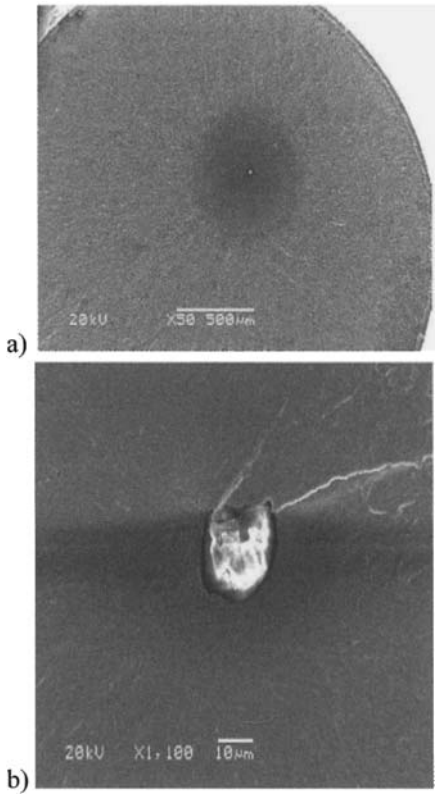

Figure 5.42. *Marensitic 100C6 steel, $\Delta\sigma$ = 960 MPa, N_f = 1.0816 X 10^8 cycles at 20 kHz, R = -1: a) internal initiation of failure; b) inclusion (2.8% MgO + 2.2% Al_2O_3 + 47% CaO + 48% SiO_2), a_0 = 20 µm, a = 608 µm and h = 371 µm*

Within the three chosen steels, 100C6, 4240 and SAE 8620, initiation occurs at an inclusion. Even in the case of cemented steel, cracking is initiated in the core and bears the shape of a fish eye.

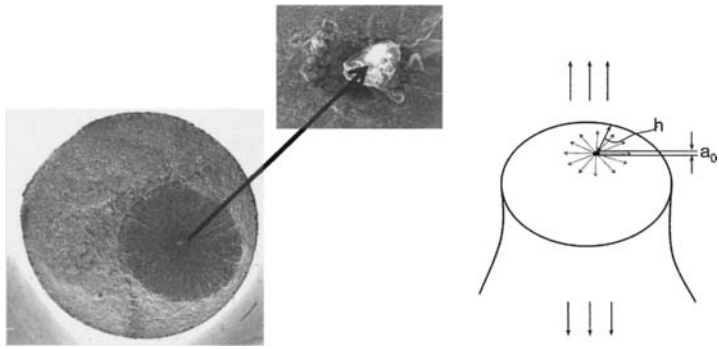

Figure 5.43. *Martensitic 42CD4 steel with lengthwise inclusions, Rm = 1,530 MPa, $\Delta\sigma$ = 760 MPa, $N_f = 5.75.10^8$ cycles, 20 kHz, R = -1, internal initiation on an inclusion, a_0 = 20 μm*

Later on, we will see that a_0 is the radius of the circumscribed circle around the inclusion corresponding to the corner of the Paris curve at the cracking threshold. Letter h gives the distance of the inclusion at the edge and a is the radius of the fish eye when the regime is unstable.

5.5.2. *Metallurgic defects within the matrix*

Within some alloys like titanium or some other ferrite-perlite steels, microstructure defects such as the grain size prevail over the inclusions as initiation sites of gigacycle fatigue cracks. This is the consequence of the presence of two phases that possess different tensile strengths. Within steels, the initiation site is related to the size of the ferrite grains, and within titanium alloys the large platelets are involved. There is then a microplasticity localized within the less resistant grains.

5.5.3. *Microporosities*

Beyond 10^7 cycles, porosity is the most frequent cause of crack initiation within cast alloys. Microporosities can occasionally trigger initiation within powder metallurgy alloys and rarely within wrought alloys presenting a dual phase matrix. Sometimes porosities can be associated with inclusions.

Figures 5.46 and 5.48 illustrate this type of initiation, which occurs either at the surface when there are many porosities, or within the core, which is within the sub-layer most of the time.

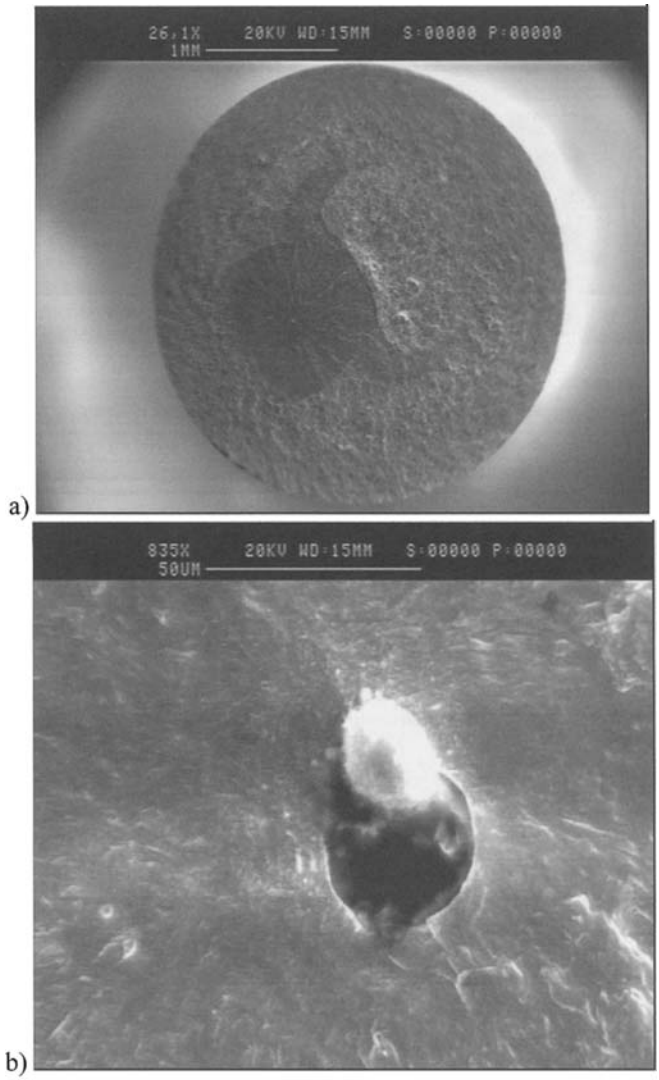

Figure 5.44. *SAE 8620 (20NiCrMo2) cemented steel, 0.81 mm of the cemented layer, $\Delta\sigma$ = 570 MPa, N_f = 4.6603 X 10^7 cycles, 20 kHz, R = -1, internal initiation of the failure, inclusion (SiO_2 + Al_2O_3), a_0 = 34.5 µm, a = 1024 µm and h = 1,010 µm: a) the defect in the steel; and b) a close-up of the defect*

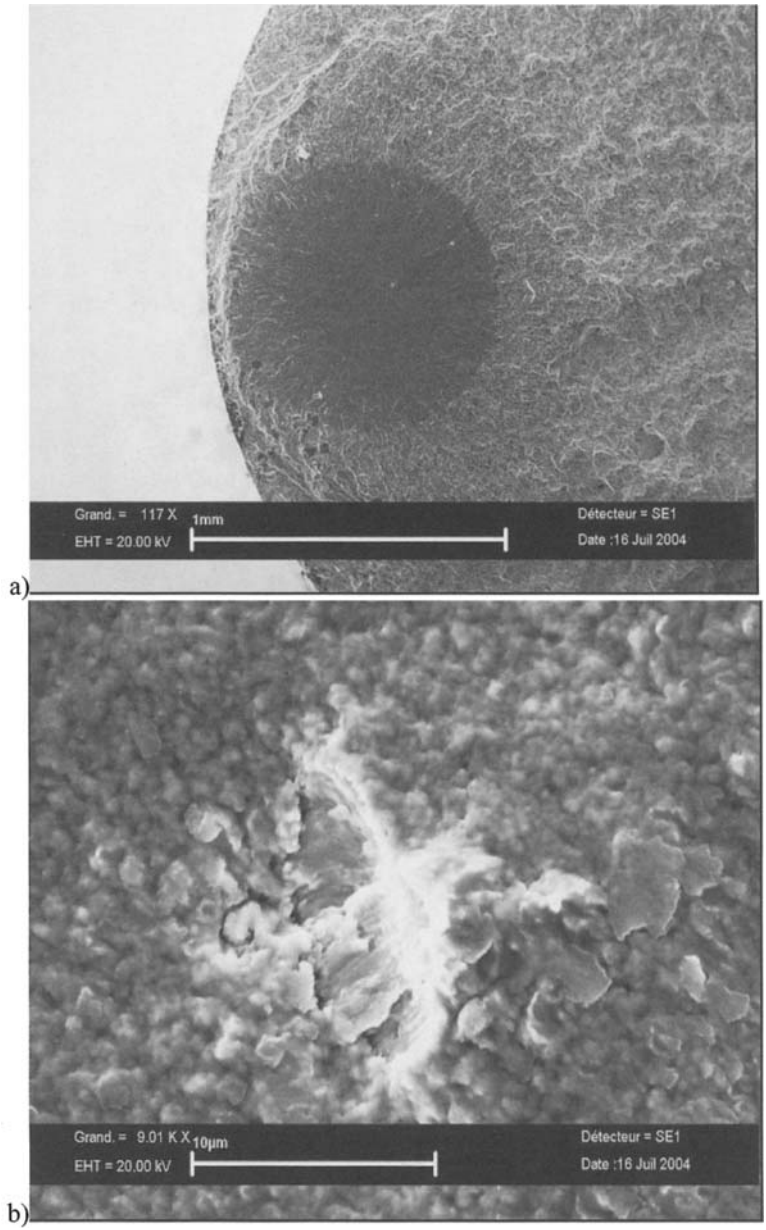

Figure 5.45. *SAE 8620 (20NiCrMo2) ferrite-perlite steel, $\Delta\sigma$ = 290 MPa, N_f= 2.3072 X 10^9 cycles, 20 kHz, R = -1, internal initiation, microstructure (ferrite grain), a_0 = 10.9 µm, a = 846.8 µm and h = 576 µm: a) the defect in the steel; and b) a close-up of the defect*

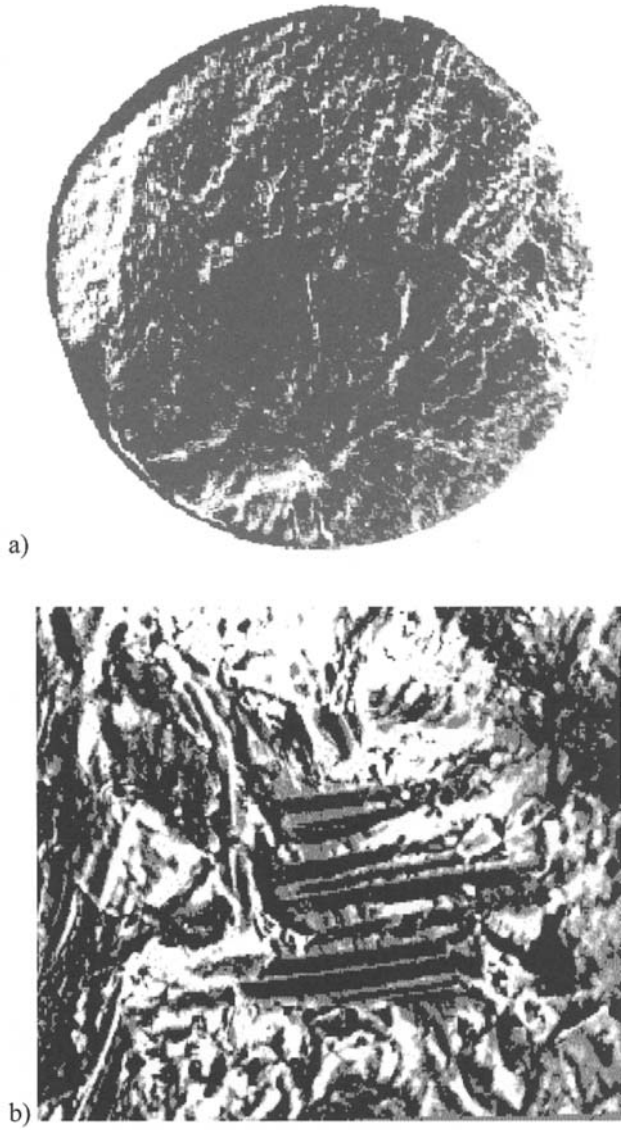

Figure 5.46. *Titanium alloy 6246. Internal initiation on large platelets α related to the forging range; a) the defect in the titanium alloy; and b) a close-up of the defect*

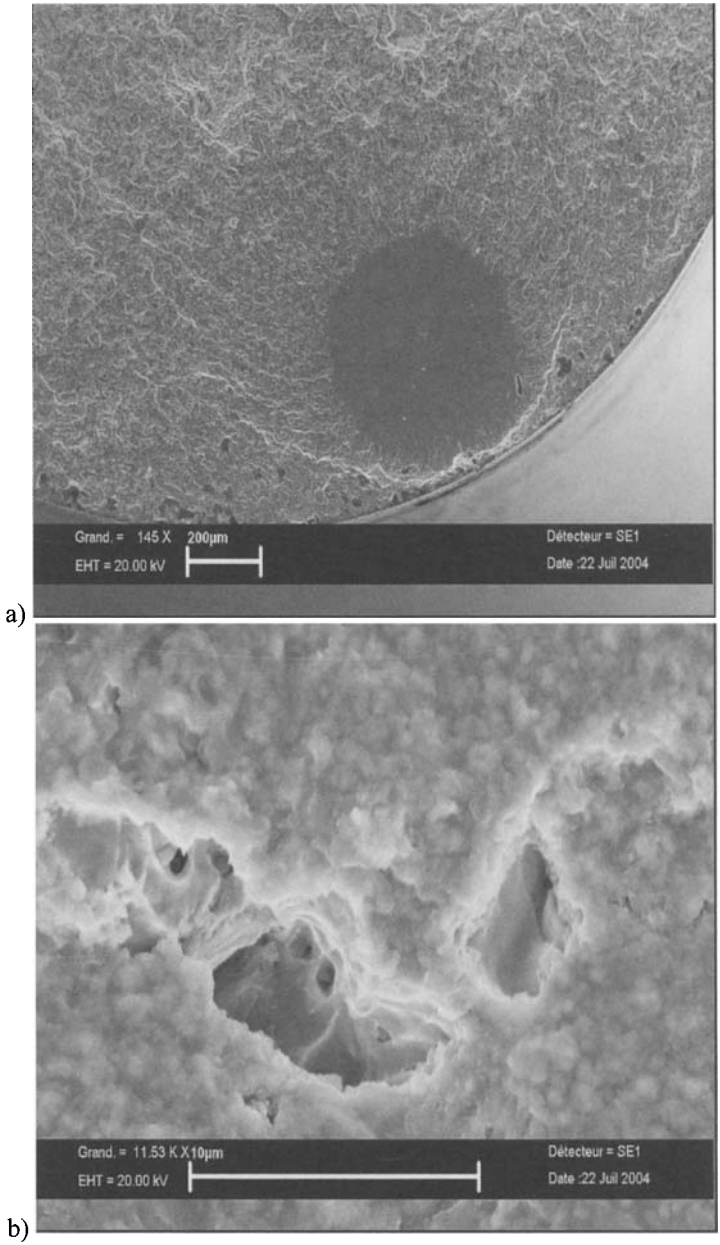

Figure 5.47. *SAE 8620 (20NiCrMo2) ferrite-perlite steel, $\Delta\sigma$ = 305 MPa, N_f = 2.0854 X 10^9 cycles, 20 kHz, R = -1, internal initiation of the failure, microporosity, a_0 = 19.8 µm, a = 531 µm and h = 317 µm: a) the defect in the steel; and b) a close-up of the defect*

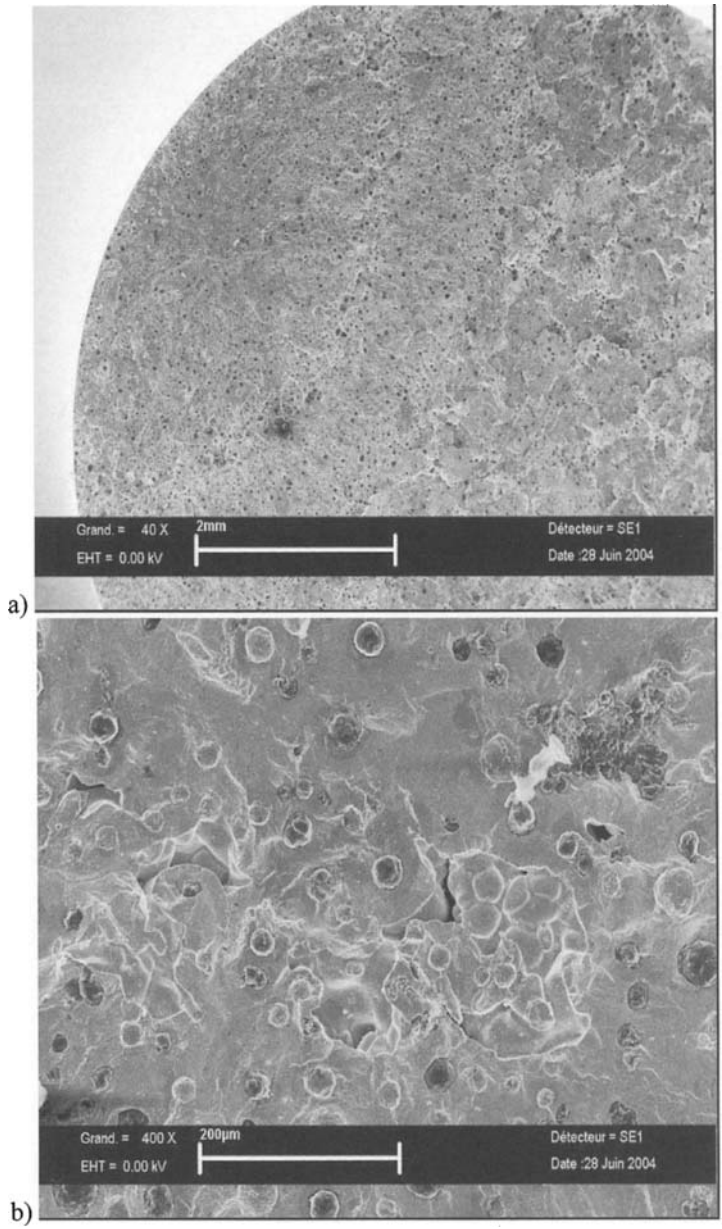

Figure 5.48. *GS51 ferrite-perlite cast iron, $\Delta\sigma$ = 250 MPa, N_f = 1.0131 X 10^9 cycles, 20 kHz, R = -1, internal initiation of the failure, microporosity, a_0 = 431 µm and h = 1,000 µm:a) the defect in the steel; and b) a close-up of the defect*

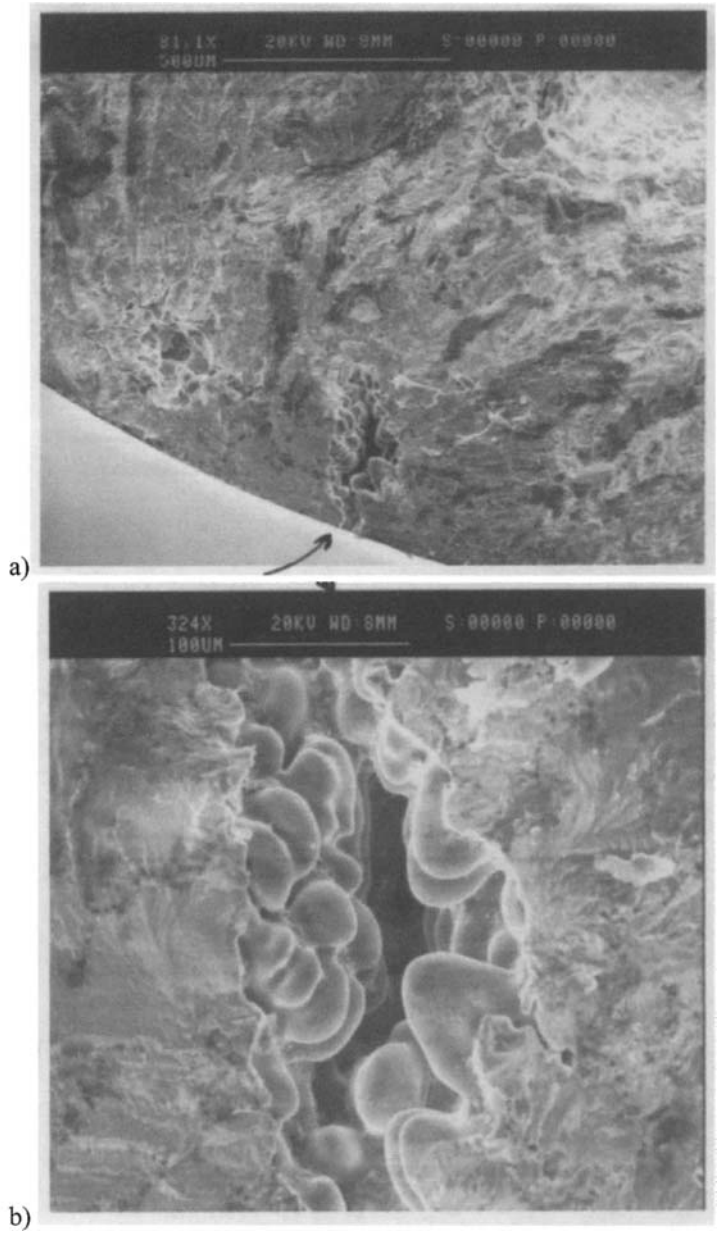

Figure 5.49. *Aluminum AS5U3G-Y35, $\Delta\sigma$ = 60 MPa, N_f = 1.929 × 10^9 cycles, 20 kHz, R = -1, internal initiation, microporosity; a) the defect in the aluminum; and b) a close-up of the defect*

For a large range of alloys, we can conclude that the initiation for very-high cycle fatigue (between 10^6 and 10^{10} cycles) is mainly governed by the following internal initiation mechanisms:

– From non-metallic *inclusions* with a size of a_0 (μm) within homogenous matrix alloys, cast ones (GS51 cast iron) and occasionally within dual phase matrix alloys, where in summary we have:

- D38MSV5S ferrite-perlite steel: $13.5 \leq a_0$ (μm) ≤ 46,

- 100C6 martensitic steel 2: $10 \leq a_0$ (μm) ≤ 26,

- 100C6 martensitic steel SUJ2: $6.7 \leq a_0$ (μm) ≤ 20.3,

- 100C6 bainitic steel: $5 \leq a_0$ (μm) ≤ 22,

- 42CD4 martensitic steel, inclusions in transverse direction, Rm = 1,508 MPa: 25.5 X 36.8 $\leq a_0$ (μm) $\leq$ 223.8 X 21.8,

- SAE 8620 steels with 0.41 and 0.83 mm of carburized layer: $21.8 \leq a_0$ (μm) ≤ 66.8,

- GS51 cast iron (graphite): $73 \leq a_0$ (μm) ≤ 138;

– From *big grains* within the matrix with a size of a_0 (μm) (mainly ferrite grains) within the dual-phase alloys and occasionally within the homogenous matrix of the alloys, we have:

- SAE 8620 ferrite-perlite steel: $6.3 \leq a_0$ (μm) ≤ 34.6,

- D38MSV5S ferrite-perlite steel: $27 \leq a_0$ (μm) ≤ 119,

- XC70 ferrite-perlite steel: $21.4 \leq a_0$ (μm) ≤ 29,

- 100C6 martensitic steel 2: $17 \leq a_0$ (μm) ≤ 20,

- 100C6 bainitic 2 steel: $17 \leq a_0$ (μm) ≤ 21,

- 40Si7 martensitic steel with ferrite traces: $8 \leq a_0$ (μm) ≤ 44,

- SAE 8620 steels with 0.41 and 0.83 mm of cemented layer: $21 \leq a_0$ (μm) ≤ 41.9;

– From *microporosities* within cast alloys, such as the GS51 cast iron and AS5U3G-Y35 aluminum. Nevertheless, in some cases, we can find that initiation occurs from the porosities within a dual-phase matrix as well as from a homogenous matrix.

Within ductile cast iron and some alloys coming from powder metallurgy, complex initiations simultaneously involving porosity and inclusion frequently occur.

5.6. Assessing fatigue strength

5.6.1. *Comparison between the staircase, Bastenaire, Wöhler, Basquin and Stromeyer/linear methods*

The results from gigacycle fatigue were treated using an agreed standard statistical method. This is not in order to predict a hypothetic fatigue limit with an infinite life span, but to validate the dispersion results. In order to compare the different statistical methods used in fatigue, we propose to calculate the fatigue strength and find the most efficient method.

Several equations can be obtained using the ESOPE software that describes the possible different behaviors:

– Stromeyer/linear model: $N = A/(S - E)$;

– Bastenaire model: $N = A \text{ Exp } [-((S - E)/B)^c]/[S - E]$;

– Wöhler model: $\text{Log } N = A\ S + B$;

– Basquin model: $\text{Log } N = A \text{ Log } S + B$.

The staircase method can also be described using the ESOPE software.

Calculations have been developed on different levels, with lifespans ranging from 10^6 to 10^{10} cycles. The methods indicated above are applied in order to determine the fatigue strength σ_D with a probability of failure of 50% and standard deviation s.

Theoretically, σ_D at 10^6 cycles, minus $3s$, should be equal to or lower than σ_D at 10^9 cycles, which is not the case for some alloys. We found that the Bastenaire model best suits the experimental results. The Wöhler and Basquin models are also correct, as long as the SN curve presents a constant decreasing slope. If this is not the case, a curve presenting two different segments is necessary (see Figure 5.49). This type of model is associated with the staircase method and will allow us to obtain the fatigue strength σ_D (50%) at the expected lifespan, as recommended by international standards.

The results show that in general the Wöhler curves determined under megacycle (regular) fatigue on one hand, and under gigacycle fatigue on the other, are in agreement with the cross-check domain (~ 10^7 cycles), thus validating the use of high frequency vibratory fatigue.

Nevertheless, this is not the case with endurance limits determined by these two methods: the endurance limits determined under gigacycle fatigue are usually lower or at best equal to the ones measured under megacycle fatigue. The difference between the two fatigue limits is not constant and strongly depends on the material.

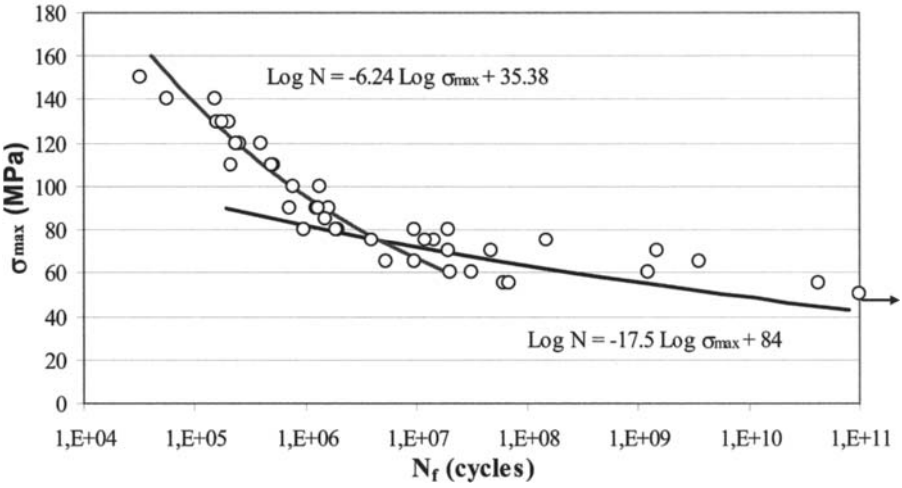

Figure 5.50. *Fatigue SN curve with two different segments for aluminum AS5U3G-Y35, R = -1, 30 Hz, 20 kHz and 30 kHz*

Figure 5.51 presents the fatigue strength drop at 10^7 and 10^{10} cycles for some materials, that is to say regarding the fatigue limit measured at 10^7 cycles:

$$\frac{\left(\sigma_d{}^{10^7} - \sigma_d{}^{10^{10}}\right)}{\sigma_d{}^{10^7}}$$

which is represented by:

$$\frac{\Delta\sigma_d}{\sigma_d}$$

Observing the results in Figure 5.52, we can see that the drop in fatigue strength depends on the traction as well as the microstructure, that is to say on the chemical composition, thermal treatment, processing, etc., at the same time.

5.6.2. *Kitawaga diagram under gigacycle fatigue*

Kitawaga proposed an approach that enables us to appreciate the relative role of the matrix and defects on the fatigue strength of materials.

The Kitawaga diagram is a simple and efficient tool that can be used by engineers. It is useful in the analysis of the evolution of fatigue strength σ_D (50%) at 10^{10} cycles as a function of the size of the defect localized within the initiation zone.

The Kitawaga diagram brings to light two different domains, as shown in Figure 5.51:

– the domain where fatigue strength is ruled by the matrix; and

– the domain where fatigue strength is ruled by the defects.

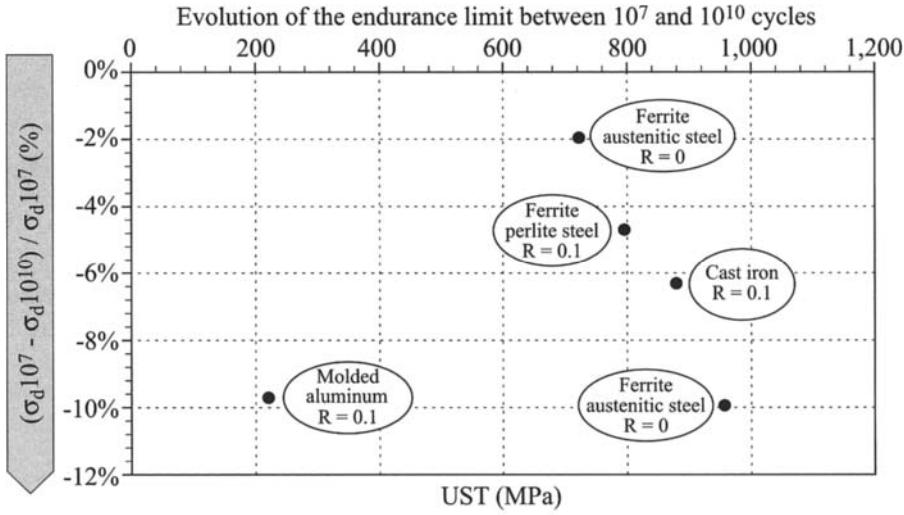

Figure 5.51. *Evolution of fatigue strength between 10^7 and 10^{10} cycles for different materials at the tensile strength level (results obtained when R = 0.1 and R = 0). The staircase method of statistical calculation was used*

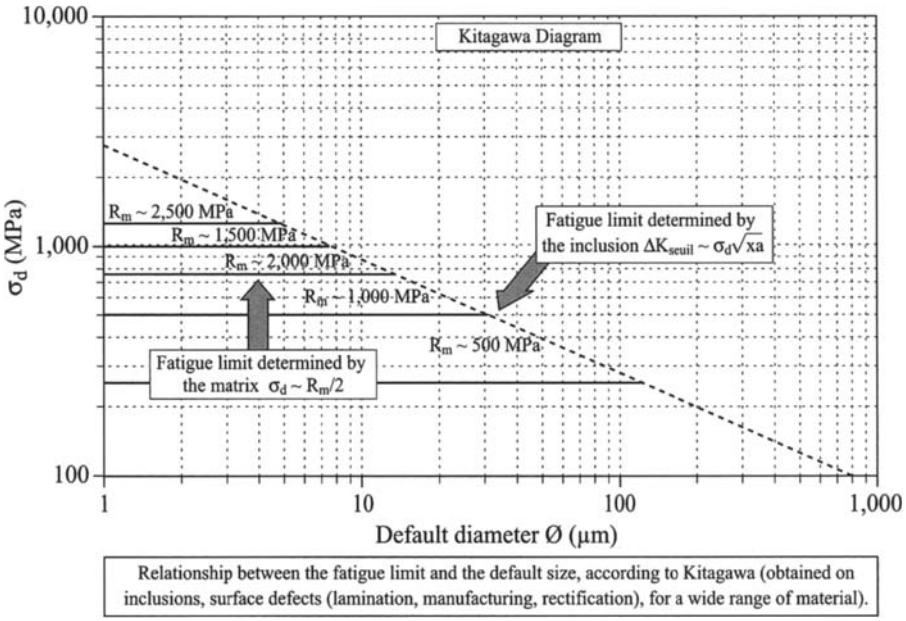

Figure 5.52. *Relationship between fatigue strength and the size of the defect, according to Kitawaga*

5.6.3. *Assessment of initiation fatigue life using the ITMA model and Paris-Hertzberg law*

The observations made on the initiation mechanisms with really long lifespans show that the almost circular fish eye, centered on the defect, typically characterizes the domain of gigacycle fatigue. The formation of a fish eye corresponds to a number of cycles much higher than 10^6 to 10^7 cycles. As cracking will occur within a domain of short cracks and depending upon the cracking threshold, it is worth integrating the Paris-Hertzberg equation [5.15] which seems to suit these conditions.

Paris, Tada, and Bathias have shown, from the model represented in Figures 5.43 and 5.53, that for most of the materials studied under gigacycle fatigue the crack growth within the fish eye is low, compared to the very long fatigue life reached until the final failure occurs [BAT 05].

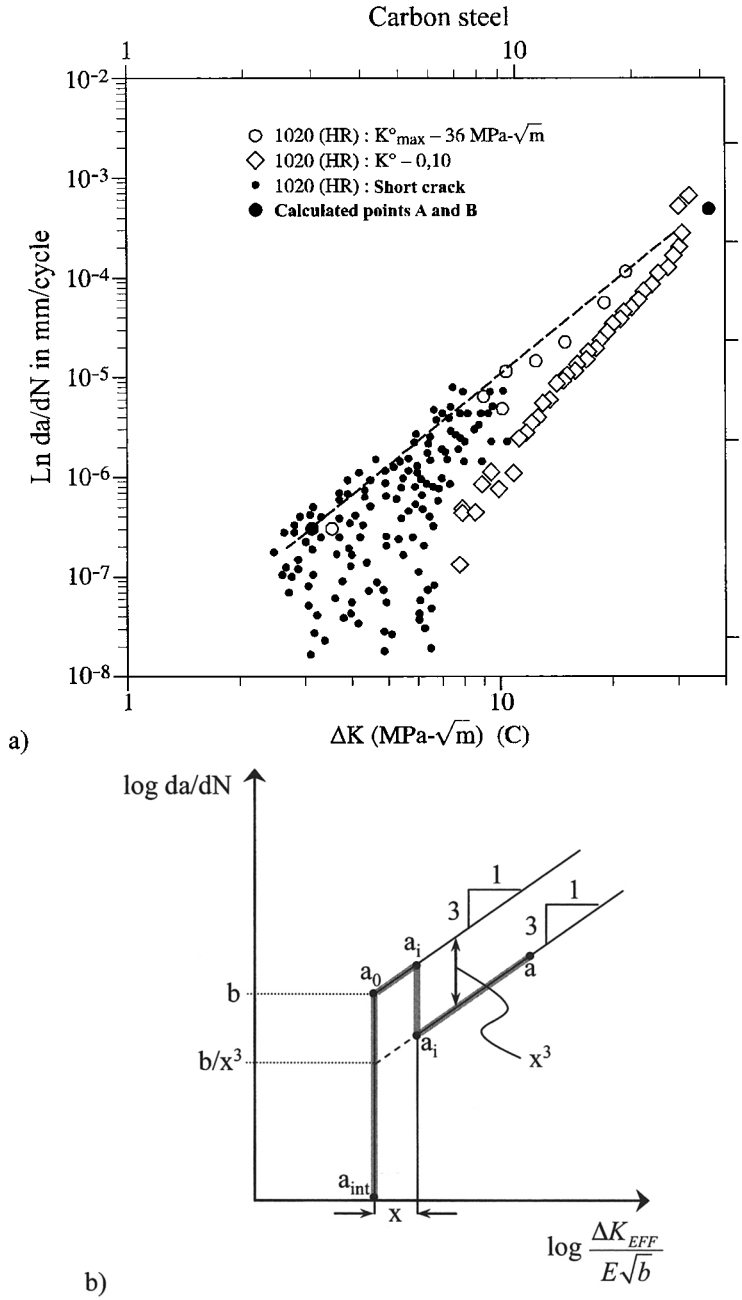

Figure 5.53. *a) Model of the Paris-Hertzberg curve; b) model of the fish eye*

The Paris-Hertzberg law is written as:

$$\frac{da}{dN} = b\left(\frac{\Delta K_{eff}}{E\sqrt{b}}\right)^3 \qquad [5.15]$$

The equation of the strain intensity factor for a circular line is given by:

$$\Delta K = \frac{2}{\pi}\Delta\sigma\sqrt{\pi a} \qquad [5.16]$$

Integration of equation [5.15], from the threshold crack propagation corner ΔK_0, corresponds to an initial circular crack with a radius a_0 (see Figure 5.42). By replacing the subsequent equations and integrating from a_0 to a_{final}. Using the ITMA results, Paris obtained an equation that is capable of predicting the number of cycles necessary for crack growth inside the fish eye. This equation is:

$$N_f = \frac{\pi E^2}{2(\Delta\sigma)^2} \qquad [5.17]$$

The part of the number of cycles relating to growth of an internal crack within the fish eye N_f is usually much lower than 1% of the total fatigue life within the gigacycle regime. This was the case for the results obtained at the ITMA, with few exceptions, as shown in [PAR 04]. Some more complex calculations considering the short-to-long crack transition do not bring any significant modifications to the magnitudes obtained by the above equation, which has the advantage of remaining very simple.

It is quite obvious that as soon as the fish eye appears at the surface the crack becomes unstable, as failure occurs rapidly. If the formation of the fish eye is very short, it implies that initiation of the crack around the defect is the main phase of the gigacycle regime. In order to experimentally check this model, confirmation was given by a thermo-graphical study in some fatigue tests. An example illustrating these results is given in Figure 5.54. From this we can see the thermal dissipation occurring at the beginning of crack propagation within the fish eye, right at the end of the test.

Thermal dissipation can easily be measured within an aluminum alloy where the fish eye is visible before crack propagation. The phenomenon is the same in the case of steels but is harder to observe. As a consequence, it appears that fatigue strength within the gigacycle regime is ruled by initiation of the microcracks around any defects, as the influence of other factors like hydrogen is not necessary. This is why

it appears that the area called ODA attributed to the influence of hydrogen could also be related to the transition from a short to long crack.

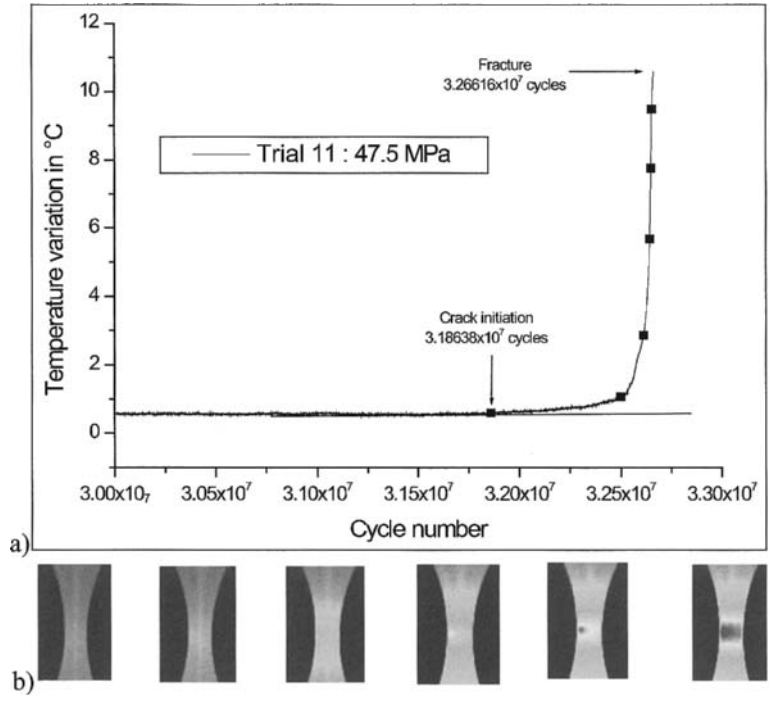

Figure 5.54. *Thermo-graphical test highlighting thermal dissipation in AS5U3G: a) beyond 10^7 cycles; and b) at the formation of the fish eye*

5.6.4. *Prediction of fatigue strength using the Murakami model*

Murakami [MUR 90, MUR 94, MUR 96, MUR 98] proposed an equation to predict the fatigue strength of steels. This equation is determined from the cracking threshold and the size of the defect (equation [4.18]). To use this equation, we have to know the Vickers hardness of the material and square root of the area of the initial size of the defect at the center of the fish eye:

$$\sigma_w = \frac{1.56(HV+120)}{(\sqrt{area})^{1/6}}\left[\frac{1-R}{2}\right]^{\alpha} \qquad [5.18]$$

where:

– C: 1.56 for internal defects;

– σ_w: fatigue strength (MPa);

– R: loading ratio, $\alpha = 0.226 + Hv.10^{-4}$.

Within the gigacycle regime, coefficient β can be adapted to incorporate the number of cycles:

$$\sigma_w = \frac{\beta(HV+120)}{(\sqrt{area})^{1/6}}\left[\frac{1-R}{2}\right]^{\alpha} \qquad [5.19]$$

where:

– $\beta = 3.09 - 0.12 \log N_f$ for the internal inclusions or defects;

– $\beta = 2.79 - 0.108 \log N_f$ for the inclusions or the defects at the surface.

The prediction of fatigue strength provided by using Murakami's parametrical model is an interesting and practical approximation for the engineer. Nevertheless, we can see in the results published in [MUR 90, MUR 94, MUR 96, MUR 98] that the error between experience and prediction can sometimes reach 26% and is often of about 10%.

5.7. Conclusion

The discovery of gigacycle fatigue at the end of the 1980s cast doubts on international standards and calculation codes. For instance, we can no longer design mechanical components based on the concept of an infinite fatigue life of over a million cycles. Even if the fatigue strength gap is low (between 1 million and 1 billion cycles), the approach to fatigue is still modified due to gigacycle fatigue.

Finally, we can consider the elasticity limit at 0.2% to be a design criterion because a high number of elastic cycles, regarding the von Mises criterion, leads to very localized microplasticity and failure within the metal. For this reason, a local approach seems mandatory.

5.8. Bibliography

[AMB 93] M.H. Ambroise, T. Bretheau, A. Zaoui, "Crack initiation from the interface of superficial inclusion", *Proceeding Fatigue '93 International Conference*, vol. 1, p. 169-176, 1993.

[BAT 04] C. Bathias, "Piezoelectric fatigue testing machines", *VHCF Proceedings 3*, p. 472, 2004.

[BAT 05] C. Bathias, P.C. Paris, *Gigacycle Fatigue in Mechanical Practice*, Marcel Dekker, New York, 2005.

[BAT 07] C. Bathias, P. Paris, "Initiation in gigacycle fatigue regime", *VHCF Proceedings 4*, p. 83, 2007.

[BAT 98] C. Bathias, S.E. Stanzl, Euromech 382, *Fatigue Life in the Gigacycle Regime*, Paris, p. 75 June 29 to July 1, 1998.

[BUC 84] L. Buchinger, S. Stanzl, C. Laird, "Dislocation structure in copper single crystals fatigue at low amplitudes", *Philosophical Magazine*, vol. 50, no.2, p. 275-298, 1984.

[FRA 93] D. Francois, A. Pineau, A. Zaoui, *Comportement Mécanique des Matériaux*, Hermes, Paris, 1993.

[IBR 80] M.F.F. Ibrahim, K.J. Miller, "Determination of fatigue crack initiation life", *Fatigue of Engineering Materials and Structures,* vol. 2, p. 351-360, 1980.

[KAN 97] K. Kanazawa, S. Nishijima, "Fatigue fracture of low alloy steel at ultra-high-cycle region under elevated temperature condition", *J. Soc. Mater. Sci., Jpn.*, vol. 46, no. 12, p. 1396-1401, 1997.

[KON 91] X. Kong, K. Saanouni, C. Bathias, "On the fatigue at very high frequency - Part 2: Application to some materials", *Journal of Engineering Materials and Technology*, vol. 113, p. 210-214, 1991.

[KON 91] X. Kong, K. Saanouni, C. Bathias, "On the fatigue at very high frequency - Part 1: Theoretical and variational formulation", *Journal of Engineering Materials and Technology*, vol. 113, p. 205-209, 1991.

[KUZ 84] V.A. Kuzmenko, "Fatigue of structural materials at high frequency cyclic loading", S.R Valluri, D.M. Taplin *et al.*, *Advanced in Fracture Research*, vol. 3, p. 1791-1798, 1984.

[LAI 82] C. Laird, P. Chrisley, "Strain rate sensitivity effects in cyclic deformation and fatigue fracture, Ultrasonic Fatigue", in J.M. Wells *et al* (eds), *Proceedings of the first international conference on fatigue and corrosion fatigue up to ultrasonic frequencies*, AIME, p. 187-206, 1982.

[LANK 77] J. Lankford, "Initiation and early growth of cracks in high strength steel" *Eng Fract Mech*, vol 9, p. 617-624, 1977.

[MAS 50] W.P. Mason, *Piezoelectric Crystals and Their Application in Ultrasonics*, Van Nostrand, New York, p. 161, 1950.

[MAS 68] W.P. Mason, "Low and high amplitude internal friction measurements in solids and their relationship to imperfection notion", *Advances in Materials Research*, vol. 2, p. 287-364, 1968.

[MUG 07] H. Mughrabi, S. Stanzl, *VHCF Proceedings 4*, Ann Arbor, p. 75, 2007.

[MUR 90] Y. Murakami, "Effects of small defects, small cracks and nonmetallic inclusions on fatigue strength of high strength steels", *Fatigue 90*, p. 377-382, 1990.

[MUR 94] Y. Murakami, M. Endo, "Effects of defects, inclusions and inhomogeneities on fatigue strength", *Fatigue*, p. 163-182, 1994.

[MUR 96] Y. Murakami, "Effects of small defects and inhomogeneities on fatigue strength: Experiments, model and applications to industry", *European Conference of Fracture 11th, Conference*, Poitiers, France, p. 30-42, 1996.

[MUR 98] Y. Murakami, M. Takada, T. Toriyama, "Super-long life tension compression fatigue properties of quenched and tempered 0.46 % carbon steel", *Int. J. Fatigue*, vol. 16, no. 9, p. 661-667, 1998.

[NAI 84] T. Naito, H. Ueda, M. Kikuchi, "Fatigue behavior of carburized steel with internal oxides and nonmartensitic microstructure near the surface", *Metallurgical Transactions A*, vol. 15A, p. 1431-1436, 1984.

[NAV 88] A. Navarro, E.R. De Los Rios, "Short and long fatigue crack growth: a unified mode", *Philosophical Magazine A*, vol. 57, no. 1, p. 15-36, 1988.

[NI 94] J. Ni, C. Bathias, "Development of an ultrasonic fatigue device and its application in fatigue behavior studies", *Recent Advances in Experimental Mechanics*, Balkema, p. 1121-1126, 1994.

[PAR 04] P.C. Paris, I. Marines, R.W. Herzberg, J.K. Donald, *VHCF Proceedings 3*, Ritsumekan, 3, p. 1, 2004.

[PIN 90] A. Pineau, "Superalloys discs durability and damage tolerance in relation to inclusions", in Kluwer, in E. Bachelet *et al.* (eds), *High Temperature Material Power Engineering*, Kluwer Academic Publishers, Dordrecht-Boston-London, p. 913, 1990.

[PUS 77] A. Puskar, "The thermal activation of cumulative fatigue damage at ultrasonic frequencies", *ULTRASONICS*, p. 124-128, May 1977.

[SIR 82] C.R. Sirian, A.F. Conn, R.M. Mignogna, R.E. Green, *Ultrasonic Fatigue*, p. 461-472, The Met Soc. AIME, PA, USA, 1982.

[SRI 97] T.S. Srivatsan, W.O. Soboyejo, *Proceedings on High Cycle Fatigue of Structural Materials*, A collection of papers from Materials Week'97 held in Indianapolis, Indiana, USA, 1997.

[STA 77] S. Stanzl, Mitshe, *Proceedings of the 4th International Conference on Fracture*, vol. 2, Waterloo, Canada, p. 749, June 1977.

[STA 86] S. Stanzl, "Fatigue testing at ultrasonic frequencies", *J. Soc. Environ. Eng.*, vol. 25, no. 1, p. 11-16, 1986.

[STA 98] S. Stanzl, Tschegg, "Ultrasonic fatigue", *FATIGUE '96*, vol. III, p. 1887-1898, 1996.

[SUN 98] Z. Sun, Q.Y. Wang, C. Bathias, *et al.*, "Réalisation d'essai de fretting-fatigue vibratoire à 20 KHz", presented at *17es Journées de Printemps*, Fatigue de Contact, Senlis, France, May 27-28, 1998.

[TIEN] J.K. Tien, "The state of ultrasonic fatigue", *Ultrasonic Fatigue*, AIME, p. 1-14, 1982.

[WAN 98] Q.Y. Wang, A. Dubarre, G. Baudry, C. Bathias, "High cycle fatigue and life prediction of high strength steels", presented at *Euromech 382, Fatigue Life in the Gigacycle Regime*, Paris, June 29 to July 1, 1998.

[WIL 81] L.E. Willertz, T.M. Rust, V.P. Swaminathan, "Ultrasonic fatigue", *First Conference Proceedings*, AIME Society, p. 321-331, p. 333-347, 1981.

[WIT 82] G.A. Whitlow, J.K. Tien, "Effects of frequency on the corrosion fatigue of Udimet 720 in a molten sulfate salt", *Ultrasonic*, p. 321-331, 1982.

[WU 94] T. Wu, C. Bathias, "Application of fracture mechanics concepts in ultrasonic fatigue," *Engineering Fracture Mechanics*, vol. 47, no. 5, p. 683-690, 1994.

[WU 95] T. Wu, Ni Jingang, C. Bathias, *ASTM, STP 1231*, 1995.

Chapter 6

Fatigue Crack Growth Laws

6.1. Introduction

In order to predict the fracture of mechanical components stressed under fatigue, many laboratories have tried, for practical reasons, to establish empirical crack laws that are useful for design. Some laws result in theoretical models and some models are just descriptive. Some hypotheses are approximate, and some models try to isolate and understand the behavior of cracks under fatigue. We can place the parameters involved in cracking into two categories:

– intrinsic parameters that depend on the material: Young's modulus, elasticity limit, cyclic properties and the metallurgic state of the material;

– extrinsic parameters that depend on the test conditions for any material being tested: temperature, frequency, environment, dimensions of the specimen, load ratio R, etc.

Nevertheless, we should note that the influence of these last parameters depends on the material being studied and its state.

Chapter written by Jacques MASOUNAVE, Jean-Paul BAÏLON and John-Ivan DICKSON.

6.2. Models describing crack propagation

Models that try to describe the propagation of a crack should consider all of the parameters relating to propagation within a given material. Initially engineers wrote down the empirical equations that, as accurately as possible, described the effect of various parameters on propagation rate: these are the phenomenological models, whose number increased significantly between 1969 and 1980. We will now distinguish some important types of model and briefly explain them by way of examples.

6.2.1. *Phenomenological models*

Using an empirical approach, these models try to describe the variations that were experimentally observed in the simplest manner. Usually, the principle is to isolate and transcribe the effect of these parameters on growth rate itno equations.

In 1963, Paris and Erdogan [PAR 63] proposed a law that is probably be the most useful in practice. The authors used some modifications of the notions of stress intensity factor, K, developed by Irwin [IRW 57]. Calculation of K is applicable only to brittle and semi-brittle materials. Thus, plastic materials are not usually included. As long as plasticity remains low, calculation of K remains acceptable. Paris and Erdogan proposed:

$$\frac{da}{dN} = C\,\Delta K^{m} \qquad [6.1]$$

In the case of their material (2024-T3), the value of exponent m is 4. Usually, most results obtained in the laboratory are expressed using equation [6.1]. If this equation allows us to present the results in a simple manner, it does not precisely reflect the influence of intrinsic or extrinsic parameters on propagation phenomenon. It does not describe the behavior of the crack close to ultimate failure or at the threshold of non-propagation ΔK_{th} either (see Figure 6.1). Nevertheless, it allows us to perform a simple calculation in order to predict the propagation time. When K_{max} becomes higher than $0.7\,K_{c'}$, Paris' equation under-predicts the crack growth rate [LIN 78].

The opposite applies when ΔK tends towards ΔK_{th}: Paris' equation over-estimates the propagation rate.

Several authors have since tried to modify equation [6.1] in order to take these boundary conditions into consideration and integrate parameters such as the load ratio R or K_{max}.

Broek and Schijve [BRO 63] proposed an empirical equation:

$$\frac{da}{dN} = C_1 \left(\frac{\Delta K}{1 - R} \right)^3 exp\left(- C_2 \; R\right) \qquad [6.2]$$

where C_1 and C_2 are parameters that are characteristic to the material and have to be determined.

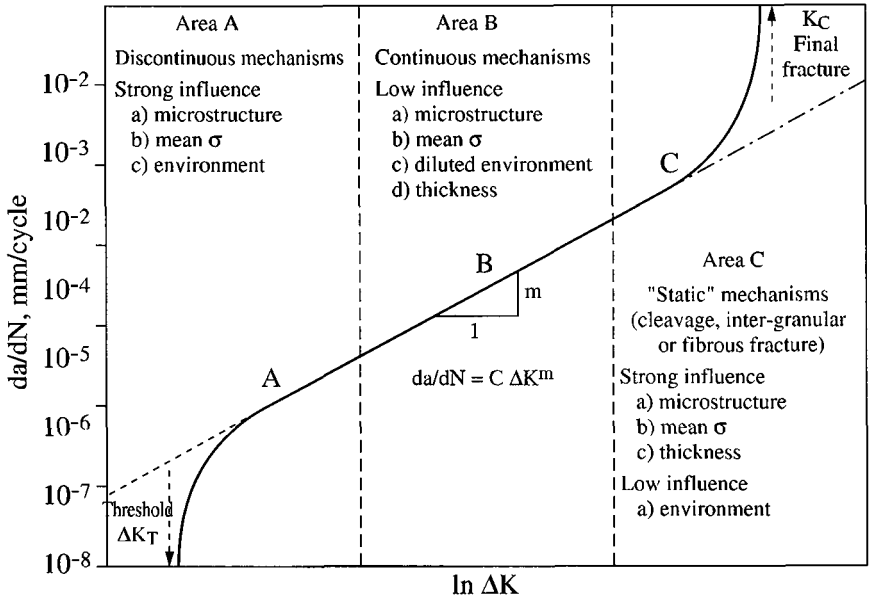

Figure 6.1. *Representation of the propagation rate of a crack da/dN as a function of the strain intensity factor ΔK. Region A = low cracking rate (threshold), region B = intermediate regime (Paris equation) and region C = high cracking rate (Kc)*

When $R = 0$, this equation leads to:

$$\frac{da}{dN} = C_1 \; \Delta K^3 \qquad [6.3]$$

Experimentally, we can observe that the exponent m of Paris' equation can vary from 2 to 6 for most materials. In addition, equation [6.2] only involves the effect of R on the parameter C of Paris' equation. This was experimentally observed by Broek and Schijve for several aluminum alloys (2024-T3 and 7075-T6).

Similar observations can be made for the equation proposed by Frost and Dugdale [FRO 68]. These authors studied several materials (mild steels, stainless steels and aluminum alloys). From dimensional analysis considerations and the analysis of their experimental results, they proposed the following equation:

$$\frac{da}{dN} = \left(P + Q\overline{\sigma}\right).\Delta\sigma^3.a \qquad [6.4]$$

with P and Q as adjustable parameters. They also noticed that steels are often not that sensitive to the influence of the mean/average stress (Q ranging from 0.8 to 4.4). This variation in the behavior of steels and aluminum alloys towards the mean strain $\overline{\sigma}$ was confirmed experimentally.

Forman *et al.* [FRO 67] observed that equation [6.4] is not valid for fracture when $K = K_c$ and thus, they proposed an empirical equation:

$$\frac{da}{dN} = \frac{C\,\Delta K^m}{(1-R)\,K_c - \Delta K} \qquad [6.5]$$

This equation has been confirmed many times in the case of aluminum alloys [BAT 76, CRO 68, HUD 69], but does not appear to correctly describe the behavior of steels [YAH 74] where the influence of the ratio R observed is less than the Forman equation expects.

Pearson [PEA 72] noticed that the Forman equation works best for thin aluminum alloy specimens that are thin and that the rate calculated using equation [6.5] depends mainly on the value chosen for K_c.

Erdogan and Ratwani [ERD 70], on observing that the Forman equation does not describe crack growth behavior for low crack growth rates when ΔK tends towards ΔK_{th}, proposed the following equation:

$$\frac{da}{dN} = \frac{C\,(1+\beta)^{\alpha}\,(\Delta K - \Delta K_{th})^m}{K_c - (1+\beta)\,\Delta K} \qquad [6.6]$$

with:

$$\beta = \frac{1+\mathrm{R}}{1-\mathrm{R}}$$

where C, m and α represent experimental parameters.

Sperr [SPE 77], starting from the same observations, proposed the equation:

$$\frac{da}{dN} = C \frac{(\Delta K - \Delta K_{th})^m}{(1-R)\, K_c - \Delta K} \qquad [6.7]$$

This equation is valid on three high-strength alloys, except for a small change in rate.

Nicholson [NIC 73] applied the same analysis the previous authors had: he wished to describe the whole cracking curve. He thus proposed the following empirical equation:

$$\frac{da}{dN} = A \left[\frac{(\Delta K - \Delta K_{th})}{(K_c - K_M)} \right]^m \qquad [6.8]$$

Richards and Lindley [RIC 72] proposed an equation close to the one Nicholson introduced:

$$\frac{da}{dN} = A \frac{(\Delta K - \Delta K_{th})^m}{\sigma^2 \left(K_c - K_M \right)} \qquad [6.9]$$

where σ is the "fracture" stress of the material.

The above equation is obtained from the modifications of Bilby *et al.*'s theory [BIL 63]. This equation has the advantage of correctly describing the high and low propagation rates, but parameter σ (the strength of the material) is not well defined (σ_u, σ_f, σ_c, etc.).

We should note that the influence of K_{max} on equation [6.9] is only important when the values of K_{max} are high, which is usually accepted [LIN 78, RIC 72]. This influence can usually be explained by the appearance of "static" fracture modes, such as microcleavage or intergranular fracture.

Fitzgerald [FIT 77] studied the influence of R using a different approach. He followed the work of Elber [ELB 70, ELB 71] and looked at a wide variety of materials fatigued at two different ratios, R_1 and R_2, both of which have propagation rates proportional to a certain "efficient" strain intensity factor:

$$\frac{\left(\frac{da}{dN}\right)_{R_1}}{\left(\frac{da}{dN}\right)_{R_2}} = \frac{\left(\Delta K_{eff}\right)_{R_1}}{\left(\Delta K_{eff}\right)_{R_2}} \qquad [6.10]$$

where:

$$\Delta K_{eff} = \Delta K - \Delta K_0 \qquad [6.11]$$

ΔK_0 is the apparent threshold, which is essentially a fitting parameter to be determined between the measured and the calculated values. When all of the equations obtained with different values of R were incorporated into the equation obtained when $R = 0$, Fitzgerald obtained:

$$\left(\frac{da}{dN}\right)_R = C K_{max}^{m-2} \left(\Delta K\text{-}\Delta K_0\right) \qquad [6.12]$$

He verified that this equation was applicable to steels (A514, A316), aluminums (7075-T6, 2024-T3) and titanium alloy (Ti-6AI-4V) was valid. He also integrated the effect of the environment, considering:

$$\left(\frac{da}{dN}\right)_R = C K_{max}^{m-2} \left(K_{max}\text{-}K_e\right) \left(1 - R\right)^2 \qquad [6.13]$$

where parameter K_e is the effect of the environment.

Sullivan and Crooker [SUL 76a, SUL 76b] also used the notion of ΔK_{eff} developed by Elber [ELB 70, ELB 71]. They do not give any physical sense to the effective intensity stress intensity factor, however. As in most models using the notion of ΔK_{eff}, they define:

$$\Delta K_{eff} = U.\Delta K \qquad [6.14]$$

In order to calculate U, they define:

$$\Delta K_{eff} = \left(1 - bR\right) K_{max} \qquad [6.15]$$

where b is a constant. Knowing that, by definition, $\Delta K = (1 - R)\, K_{max}$ they obtain:

$$\frac{da}{dN} = A\left(\frac{1-bR}{1-R}\right)^m \Delta K^m \qquad [6.16]$$

This equation works fairly well for sinusoidally cycled aluminum alloys, and for some cycled high-strength steels under a loading spectrum [CLE 78, MAS 76, OGU 77, PIT 74, RIC 74, SHI 77]. Constant b, however, does not have a physical meaning and remains a fitting parameter.

6.2.2. *Models based on dislocation theory*

During the 1960s and 1970s, several theoretical models appeared that attempted to calculate the propagation based on crack tip dislocation movement [BIL 63, DUG 60].

The best known of these models is probably the one developed by Bilby *et al.* [BIL 63], which considers a crack under plane strain and calculates the displacements at the tip of the crack.

The effect of stress concentration creates some forces that can take dislocations out of the plasticized zone. A friction force that Bilby *et al.* associated with the elasticity limit of the material acts against this movement. The authors calculated the equilibrium that occurred and then deduced the displacement, which was calculated for each cycle. When this sum of displacements reached a critical value, the crack propagated by release of the accumulated energy through a propagation, they thus found that:

$$\frac{da}{dN} \propto \frac{\Delta K^4}{\Psi\ \mu\sigma_y^2} \qquad [6.17]$$

where ψ corresponds to the work associated with the plastic deformation.

Weertman [WEE 69] generalized his theory to the case of a crack that propagates as a planar deformation and for any values of mean stress. He then experimentally found the following equation:

$$\frac{da}{dN} = \frac{\pi}{96\ \sigma_y^2} \cdot \frac{\Delta K^4}{K_{IC}^2 - K_{max}^2} \qquad [6.18]$$

Within the same group of models, the one proposed by Tomkins [TOM 68] was based on a plastic deformation concentrated along two slip bands inclined at 45°

from the propagation plane. He made use of the Bilby-Swinden theory [BIL 65], which has been verified [HAH 65]. Formulation of the Tomkins model is discussed in Chapters 4 and 8 of this book.

It should also be noted that the Bilby-Swinden equation can only be applied to elastic-plastic and not to plastic-plastic cases, as Tomkins did in the past [PEL 70]. Nevertheless, several experimental results seem to agree with Tomkins model, especially under high stress fatigue [FRO 58, LIU 63].

Finally, we can introduce the Yokobori model [YOK 77]. This author presented a kinetic theory using the elementary forces being applied to the dislocations.

In his work, Yokobori considers a dislocation at the crack-tip, at a distance ρ and forming an angle ϕ with the propagation plane. After an analysis of the various forces being applied on this dislocation, Yokobori concluded that the strongest forces are the applied force f_t and image force f_i because the force due to surface energy is assumed to be negligible.

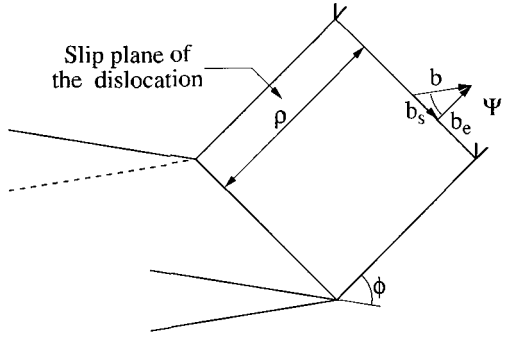

Figure 6.2. *Relative representation of a dislocation and of the crack according to Yokobori's model [YOK 77]*

Yokobori proposed the following equations:

$$f_\tau = \tau_{p,\phi} \cdot b_e = \frac{K_1 b}{\sqrt{8\,\pi\rho}} \sin\phi \cos\frac{\phi}{2} \cos\psi$$

$$f_i = -\frac{\mu b^2}{4\,\pi\rho}\left(\frac{1}{1-\upsilon}\right)$$

He choses $\psi = 0$ and $\phi = 90°$ (see Figure 6.2). He calculates the activation energy U_{act} for a moving dislocation. He then deduces that, for the values of K_I usually used

with fatigue, that $dU_{act}/da < 0$. He concludes that in the case of body-centered cubic and face-centered cubic materials, there is always a spontaneous emission of dislocations at the crack-tip during part of the tension cycle. Thus the crack tip radius (see Figure 6.3) in the opening of the crack root model is equal to 2 *nb*, where *n* is the number of dislocations and *b* their Burgers vector, and the propagation rate is equal to ½δ.

We then obtain:

$$da / dN \cong nb$$

Yokobori calculates the propagation rate of the crack and he reminds us that:

$$v = v_0 \left(\frac{\tau}{\tau_0} \right)^p$$

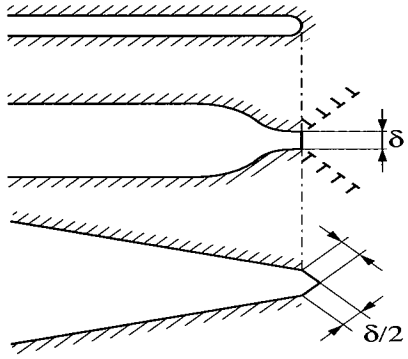

Figure 6.3. *Crack blunting due to the emission of dislocations. The variable δ stands for the opening of the crack root [YOK 77]*

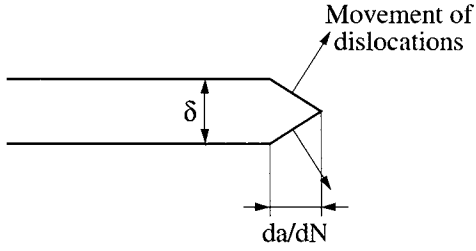

Figure 6.4. *McClintock model [CLI 65]*

where v is the displacement rate of a dislocation subjected to a shear τ, and he thus obtains:

$$\frac{da}{dN} = A(4\ f)^{-\left(\frac{p+1}{p+2}\right)} \left(\frac{\Delta K}{\mu\sqrt{x}}\right)^{\frac{(p+1)^2}{p+2}} exp - \left(\frac{U_0 - a\ InK}{KT}\right) \qquad [6.19]$$

where f is the frequency, μ the shearing module, x the average distance where the strain is applied (arbitrarily chosen) and U_0 the activation energy.

This equation shows the influence of some parameters. The influence of frequency remains low with the usual values of coefficient p (between 1 and 4). It is only at high frequencies that there is a significant effect on the FCP rate. A temperature rise usually tends to increase the propagation rate [AND 74, KAW 75]. According to Yokobori's model, the exponent of Paris' equation is equal to:

$$m = \frac{(p+1)^2}{p+2}$$

when $1 < p < 4$. We thus obtain $1.32 < m < 4.2$, which is in agreement with the usual values of the exponent of Paris' equation.

Yokobori considered the case where there was strain hardening:

$$\frac{da}{dN} \propto \left[\frac{\Delta K}{\sqrt{2 \times \sigma_{YC}}}\right]^{\frac{2n'}{1+n''}\frac{(p+1)^2}{p+2}} \qquad [6.20]$$

As a consequence:

$$m = \frac{2n'}{1+n'}\frac{(p+1)^2}{p+2} \qquad [6.21]$$

With $0.08 < n' < 0.3$ and $4 < p < 10$, we can find suitable values of m.

We should also note that Yokobori's model predicts a relationship between parameters m and C of Paris' equation. With constant frequency and temperature, the Yokobori equation becomes:

$$\frac{da}{dN} = B\left[\frac{\Delta K}{\mu\sqrt{x}}\right]^{\frac{(p+1)^2}{p+2}} \qquad [6.22]$$

and with:

$$\frac{da}{dN} = C\,\Delta K^m$$

we obtain:

$$C = \frac{B}{\left(\mu\sqrt{x}\right)^m}$$

This equation is of the type: $m = a \ln C + b$ with:

$$a = \frac{-1}{ln\left(\mu\sqrt{x}\right)}$$

and:

$$b = \frac{ln\ B}{ln\left(\mu\sqrt{x}\right)}$$

This relation between m and C was experimentally proven by Yokobori *et al.* [YOK 73, YOK 77]. We will focus on it in section 6.3.2.

6.2.3. *Models based on the behavior of a material at the crack-tip*

Models based on crack tip opening displacement [CLI 63, CLI 65, LAR 68, PEA 66] have been discussed previously. We will therefore sort out the number of models that rely on a fracture criterion at the crack-tip in this section. The crack will expand and/or go forward:

– if the strain at the crack-tip reaches a critical value σ_F; or

– if the deformation reaches a critical value ε_F.

According to the first hypothesis, the models predict that for every material, we can find a given value of the stress, usually arbitrarily chosen in such a way that cracking does not propagate below it.

Pook and Frost [POO 73], from the calculation performed by Frost and Dixon [FRO 67], determined the distribution of strains at the crack-tip in the case of a central crack with a length of 2 a, within an infinite plate subjected to cyclic stress varying from 0 to σ. Due to this loading, the crack opens up and takes the shape of an ellipse. The authors then obtained:

$$\frac{da}{dN} = \frac{9}{\pi}\frac{K_I^2}{E} \text{ under plane stress} \qquad [6.23]$$

and:

$$\frac{da}{dN} = \frac{9}{\pi}\frac{\left[K_I\left(1-\nu^2\right)\right]^2}{E} \text{ under plane strains} \qquad [6.24]$$

Pook and Frost included the effect of mean stress with the substitution of K_I by ΔK in the previous two equations. Pook and Frost verified their equation under plane stress in the case of mild steel and some aluminum, copper and titanium alloys. The gap observed with the experimental results can be explained due to the micro-structure effect. We should also note that the crack, in this model, propagates during the closing of the cycle, which is at the opposite of what is observed experimentally.

Lal and Weiss [LAL 78] calculated the strain distribution at the crack tip using an elastic calculation. Plasticity at the crack-tip is introduced using the length of a Neuber microsupport ρ. On this length ρ, we can calculate the average strain. Under fatigue, by analogy with the static model, Lal and Weiss introduced a fictitious length $2\ \rho_F$. If we assume that the crack spreads when the stress at the crack-tip becomes higher than a given value σ_F, we obtain:

$$\frac{da}{dN} = a\left[\frac{\sigma_a}{\sigma_F}\right]^{\frac{n'+1}{n'}} f\left(a/W\right) - \frac{\rho_F}{2} \qquad [6.25]$$

where σ_a is the applied stress, and $f(a/W)$ is a function that considers the geometry of the sample. The crack propagates when the stress at the crack-tip σ_{YY} becomes higher than a critical stress σ_F.

In this model σ_F depends on the material and the applied strain. The higher the applied stress, the smaller the critical stress σ_F; and the volume V_c where the stress is applied thus becomes very high (see Figure 6.5).

By studying variations of the stress σ_F and coefficient of the cyclic strain hardening exponent, the authors were able to develop an expression for the three regimes of crack propagation. In stage 1, for instance, $\sigma_F = \sigma_c$, where σ_c is the fracture stress of a non-notched sample, and $n' = 1$. We usually accept that $\sigma_c \cong 0.1\ E$. We then obtain:

$$\frac{da}{dN} = a\left(\frac{\sigma_a}{0{,}1\,E}\right)^2 - \rho_F\,/2 \qquad [6.26]$$

We have already observed from some results [FRO 71, PEA 66] that the *da/dN* curves where normalized on the basis of delta ΔK (see Figure 6.1). Note that the model is applicable even when the mechanism is not a striation formation.

In the second group of models in this section, we have added models based on deformation rather than those based on stress, which is presently the case. The authors suggest therefore that the crack spreads when the deformation at the crack-tip reaches a certain value ε_F. We must then calculate the distribution of deformations at the crack-tip.

Purushothaman and Tien [PUR 75] adopted the distribution calculated by Rice [RIC 65] in the ideal elastic-plastic case. This distribution is modified to introduce the curvature radius of the crack into the calculation process. These authors obtained two expressions, which illustrate two extreme cases. First, the radius curvature is equal to a_0, the lattice parameter. In this case, we obtain:

$$\frac{da}{dN} = \frac{1}{\pi\,\sigma_{YC}\,\varepsilon_F}\frac{\Delta K^2}{E} - a_0\,Ln\left[\frac{2}{2-(1-R)^2}\right] \qquad [6.27]$$

In the second case, they assumed that the radius of curvature was equal to $\delta/2$, a hypothesis that McClintock had previously adopted. We thus find:

$$\frac{da}{dN} = \frac{2-\varepsilon_F}{\pi\sigma_Y\,\varepsilon_F}\cdot\frac{\Delta K^2}{E} \qquad [6.28]$$

The truth probably lies in between these two extremes.

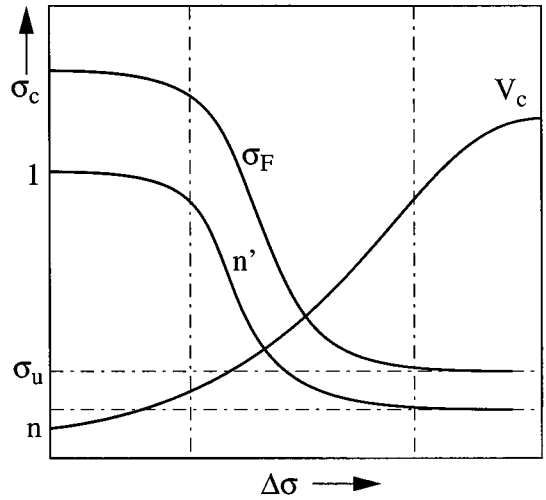

Figure 6.5. *Variation of the cyclic volume Vc where critical stress occurs at the crack-tip. Variation of the fracture critical stress σ_F and of the cyclic consolidation coefficient is shown as a function of variation of the applied hardening exponent [LAL 78]*

This model, which describes a crack spreading continuously during each cycle, cannot be applied to the propagation with striation formation. While the McClintock [CLI 75] and Liu [LIU 63] models (see section 6.2.4.1) do not predict any variation in the rate of propagation with the ratio R, the current model predicts a low variation as a function of R. The experimental results do not therefore reflect what is really happening.

6.2.4. *Models based on the cyclic properties of the material*

In this section, we will discuss the models that rely on the macroscopic and cyclic properties of a material, such as the cyclic or static consolidation coefficient, the Miner or Manson-Coffin laws, the measurement of the strain hardening exponent, etc.

We divided these models into two different groups. In the first one, we do not try to precisely elucidate the mechanism of propagation. Miner assumes that the material at the crack-tip is fatigued due to significant strain amplitude and behaves like the bulk material subjected to the same deformations, i.e. it is governed by the low-cycle fatigue laws. In the second group, we find the models built from the energy balance study. Most of the time, Mason and Coffin use measurement of the hysteresis loops in order to evaluate the propagation rate.

6.2.4.1. *Models based on low-cycle fatigue laws*

Duggan [DUG 77] focused on the deformation of a volume element located at the crack-tip. This volume element is only subjected to elastic deformations and so the effect of softening or of hardening is disregarded.

Propagation will occur when the Manson-Coffin and Miner laws are obayed. Thus, when:

$$N_f = \left[\frac{\varepsilon_f' - \bar{\varepsilon}}{\Delta\varepsilon - \Delta\varepsilon_a} \right]^{1/\alpha} \quad \text{(modified Manson-Coffin law)} \qquad [6.29]$$

where:

– ε_f' is a characteristic constant of the fatigue ductility;

– $\bar{\varepsilon}$ the mean value of the strain;

– $\Delta\varepsilon_a$ the endurance limit;

– $\Delta\varepsilon$ the total strain range;

– β a characteristic constant of the material usually equal to 1/2;

– N_f the number of cycles to failure of the microscopic crack tip element; and then:

$$\sum_{i=1}^{L} \left[\frac{\Delta\varepsilon_i - \Delta\varepsilon_a}{\varepsilon'_f - \bar{\varepsilon}_i} \right]^{1/\beta} = 1 \text{ (Miner's law)} \qquad [6.30]$$

where L is the total number of cycles required for a crack to spread by the amount Δr.

Duggan, once he considered the boundary conditions ($\Delta K \to \Delta K_{th}$ or $K_{max} \to K_c$), found that:

$$\frac{da}{dN} = \left(\frac{\pi}{32} \right)^{1/\alpha} \frac{1}{\alpha} \left\{ \frac{2}{\varepsilon'_f E (K_c - K_{max})} \left(1 - \frac{\Delta K}{K_c} \right) \right\}^{1/\alpha} \Delta K^{2/\alpha} \qquad [6.31]$$

With $\alpha = 1/2$, the above equation then gets simplified:

$$\frac{da}{dN}=\frac{\pi}{4}\left(\frac{1}{\varepsilon'_f EK_c}\right)^2 \Delta K^4 \qquad [6.32]$$

The simplified law is not rigorously exact as exponent m is constant.

Chanani *et al.* [CHA 72] assumed that damage accumulation ahead of the crack tip controls the crack propagation rate. The criterion they used was:

$$\Delta N^{1/2} \cdot \overline{\Delta\varepsilon}_{pc} = \frac{1}{2}\varepsilon_f \qquad [6.33]$$

with $\Delta\varepsilon_{pc}$ being the average value of the amplitude of cyclic deformation within the whole region where fracture criterion is applied. This deformation is calculated using the elastic-plastic model designed by Hult and McClintock [HUL 57]. The size of the plastic zone is calculated according to Dugdale's [DUG 60] model. We then obtain:

$$\frac{da}{dN}=\frac{J}{l}\left(\frac{\varepsilon_Y}{\varepsilon_f}\right)^2 a^2 \sec\left(\frac{\pi\Delta\sigma}{4\sigma_Y}-1\right)^2 \cdot \frac{Y^4}{\pi^2} \qquad [6.34]$$

where Y is a correction function of the finite dimensions of the specimen, l the distance on which the fracture criterion is applied and J a constant.

The above equation can be simplified when $\Delta\sigma/\sigma_Y < 0.2$ and a/W ranges from 0.3 to 0.7, which is often the case. We then have:

$$\frac{da}{dN}=\frac{8}{l}\left(\frac{\varepsilon_Y}{\varepsilon_f}\right)^2 \left(\frac{\Delta K}{\sigma_Y}\right)^4 \qquad [6.35]$$

The equation of the propagation rate then becomes:

$$\frac{da}{dN}= A\,\Delta K^4 \qquad [6.36]$$

This equation is experimentally verified for high strength steels. It is obvious that it could not be applied to every metal, where the exponent of the Paris equation varies from 2 to 10.

Antolovich *et al.* [ANT 75] assumed that fracture occurs within a process zone of length l. The crack moves by a length l in ΔN cycles. They then applied the Coffin-Manson law in order to obtain equation [8.18] (see Chapter 8).

Experimentally, these authors [ANT 75, CHA 72] found that l has a magnitude similar to that of the dislocation cells and then becomes a constant of the material.

6.2.4.2. *Models based on plastic energy dissipation at the crack-tip*

In this section, we have gathered together the models whose authors have computed the plastic energy dissipated at the crack tip. They basically calculated the monotonic and cyclic plasticized zones created by cycling of the force and we usually assume that the propagation rate is proportional to the energy lost within these plasticized zones. Once again, we have to rely on a macroscopic behavior characterized by hysteresis loops in order to explain microscopic behavior at the crack-tip.

Lal and Garg [LAL 77] developed a model that integrates some notions, such as the effective strain intensity factor defined by Elber. These authors calculate the monotonous and cyclic plasticized zones:

$$\omega_r = \left(\frac{0.5\,\Delta K}{\sigma_Y} \right)^{1+n'} a^{(1-n')/2} \qquad [6.37]$$

This equation is obtained from the calculation performed under a simple tension if the monotonous cold-working coefficient is replaced by the cyclic cold-working coefficient and K is replaced by ΔK. If we apply Elber's hypothesis, Lal and Garg presume that a single part of a cycle is necessary to close the crack, and thus to create the plasticized zone, the other part of the cycle inducing the grounding of the crack lips. They then use the definition of the monotonous plastic zone that was calculated previously, by replacing ΔK by ΔK_{eff}, and thus obtain the dimensions of the cyclic plasticized zone:

$$\omega_c = \omega_r \cdot U^{1+n'} \qquad [6.38]$$

Using the hypothesis suggested by Tomkins [TOM 68], Lal and Garg define:

$$\frac{da}{dN} = \Delta\varepsilon_p \cdot \omega_c \qquad [6.39]$$

In order to calculate $\Delta\varepsilon_p$, they use the equation $\Delta\sigma_N = k_z\ \Delta\varepsilon_p^{n'}$, which describes the hysteresis loops, where $\Delta\sigma_N$ is the variation of strain within the ligament. The propagation rate is then equal to:

$$\frac{da}{dN}=(0.5\,U)^{1+n'}\frac{1}{\left(k_z\sqrt{\pi}\right)^{1/n'}\sigma_y^{1+n'}}\left(\frac{\left(\sqrt{a/W}\right)^{n'(1-n')}}{\sqrt{a/W}\cdot(1-a/W)}\right)\left(\sqrt{W}\right)^{1-n'-1/n'}\Delta K^{1+n'+1/n'} \quad [6.40]$$

This long equation has been verified for many materials (aluminum, mild steel, stainless steel and copper) and the calculated and measured values of parameters C and m of Paris' equation agree with it.

Two of the parameters of equation [6.40], a and ω are geometric and easily measurable. The other three, U, σ_Y and k_Z depend on the material. The rate decreases when the elasticity limit increases, and it increases if R increases, which matches the experimental results well. Parameters σ_Y and k_Z might be easy to calculate, but U (except for some aluminum alloys) is less well known. There is not enough experimental evidence, however, to determine variation of the rate as a function of crack length, however.

Schwalbe [SCH 77] studied a model of the same type as the previous one, but simpler. His hypotheses and final equation are also simple. By giving several hypotheses on monotonous crack propagation and on the plasticized zone, he obtains:

$$\frac{da}{dN}=\frac{(1-2\nu)^2}{4(1+n)\pi\sigma_Y^2}\left(\frac{2\sigma_Y}{E\varepsilon_f}\right)^{1+n}\cdot(\Delta K-\Delta K_{th})^2\cdot\frac{K_c}{K_c-K_{max}} \quad [6.41]$$

Predicted variations of the rate as a function of σ_Y, of Young's modulus, and of the fracture deformation agree with experimental measurements. Only the first term of equation [6.41] comes from the theoretical model. The formula da/dN that this author has found is very sensitive to the values of ΔK_{th} and K_c chosen.

Liu [LIU 63] proposed a simpler model than the two previous ones. He calculates the strains and the deformations occurring at the head of the crack. He then deduces, by considering some simple geometrical hypotheses on the shape of the hysteresis loop, the energy absorbed for every cycle. When the energy absorbed reaches a critical value, propagation occurs. He thus finds that the propagation rate is proportional to ΔK^2. As in McClintock's model (see section 6.5.5), Liu's model can be well applied to the formation of streaks. He does not predict any influence of R on microscopic propagation rate. Under vacuum, displacement of the dislocations would be reversible and there would not be any streak formation.

After summarizing several models, Irving and Cartney [IRV 77] developed a new model based on an energy criterion and the notion of a fracture process zone. They thus obtain:

$$\frac{da}{dN} = \frac{A}{\sigma_Y^2} \frac{\Delta K^2 \left(\Delta K^2 - \Delta K_T^2\right)}{K_{IC}^2 - K_{max}^2} \qquad [6.42]$$

6.3. Critical evaluation of the models

Evaluation of the validity of a model is difficult in most instances. In addition, the number of adjustable parameters is high, so the ability of the model to predict the experimental results becomes a calculation of parameters.

Theoretical models often use parameters that are not available in practice as they are rarely measured (for example σ_{YC}, n', α, k_z) or are dificult to measure (for example, α_F, ε_F, etc.). To varify the models, we therefore have to make approximations in order to obtain the values of the desired coefficients.

6.3.1. *Influence of the parameters of cyclic behavior*

We propose to evaluate the influence of the:

– cyclic consolidation coefficient n';

– coefficient α of the Manson-Coffin law;

– cyclic resistance coefficient k_z ; and

– cyclic ductility coefficient ε'_f.

In most of the models, the cyclic consolidation coefficient n' is involved. An empirical equation was obtained by Bauss *et al.* [BAU 77] for a wide range of steels:

$$m = 20\, n' \qquad [6.43]$$

This equation totally contradicts the theoretical results of three models and of a number of experimental results.

Indeed, Tomkins' model predicts that:

$$m = 2 + 1/n'$$

Weiss' model, that:

$$m = 1 + n' + 1/n' \qquad [6.44]$$

and Lal and Garg's model:

$$m = 1 + 1/n'$$

These three equations indicate that m increases if n' decreases. Experimentally, Kickerson and Hertzberg [HIC 72] find a variation that is inversely proportional between m and n' for a wide range of steels. This is:

$$m = 1/En' \qquad [6.45]$$

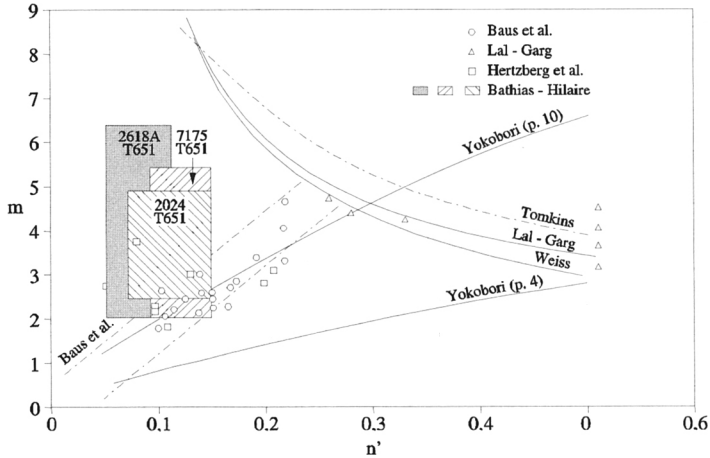

Figure 6.6. *Variation of the exponent of Paris' equation m as a function of cyclic consolidation coefficient n'*

Nevertheless, the equation found by Bauss *et al.* [BAU 77] indicates the same variation direction between m and n' as the theoretical prediction of Yokobori (see section 6.2.2):

$$m \propto 2\, n'/(1 + n') \qquad [6.46]$$

if we admit that exponent p of the displacement rate of a dislocation is independent from n'.

The problem is then unresolved. We need to know whether the crack spreads faster [BAU 77, YOK 77] or more slowly [HIC 72, LAL 77, LAL 78, TOM 68] when the material consolidates.

Morrow [MOR 65] found a semi-empirical equation between exponent α of the Coffin-Manson law and cyclic consolidation coefficient n':

$$\alpha = \frac{1}{1+5n'} \qquad [6.47]$$

This empirical equation allows us to rapidly calculate one of the two coefficients. Knowing n', we can calculate the cyclic resistance coefficient k_Z from Ramberg and Osgood's rule [RAM 43]:

$$\Delta\varepsilon = \frac{\Delta\sigma}{E} + 0.002\left(\frac{\Delta\sigma}{\sigma_Y}\right)^{1/n'}$$

thus:

$$k_z = \frac{\sigma_y}{(0.002)^{n'}}. \qquad [6.48]$$

The cyclic consolidation curve for the ductility coefficient under fatigue ε'_f, must also be known. Even if this curve cannot be measured, several authors have proposed that ε'_f be replaced by ε_u or ε_f, which were measured from the monotonous traction curves. The same goes for when no precise measurements are performed – the exponent of Coffin-Manson's law can be chosen to equal 1/2.

Once these coefficients are determined, we still have to compare the theoretical predictions with experimental results. The simplest technique consists of graphically comparing both results. This is how we find [BAT 78] that Forman's law can usually be correctly applied in the case of aluminum alloys and rarely in the case of steels, where the influence of R is less noticeable. Schwalbe [SCH 74] compared the predictions of eight models with experimental results obtained within different metals. He concludes that the equations designed by Paris, Frost and Dixon, Schwalbe, and Liu, more or less correctly describe the results for these metals.

McCarney and Cooper [CAR 77] propose a mathematical method, more rigorous than visual appreciation, in order to control the validity of the equations obtained. For the first time, these authors can minimize the error on the derivative. This method has the advantage of enabling us to easily calculate the primary and secondary derivatives of a function without increasing the errors, as is often the case with classic differentiation methods. One of the important observations of the analysis performed by both authors is that the measurement of length, a, of the crack has to be really precise in order to minimize the errors in the propagation rate.

McCartney and Cooper [CAR 77] then proposed to analyze the precision of calculation methods for the proposed models. For every equation, they calculated the square root of the sum of least squares of the residues and the sum of these residues. Thus, they tested five equations (Paris, Forman, Pearson, Nicholson and McCartney) with four different steels and found that, for the steels studied, the most acceptable was the Paris equation with the exponent $m = 4$.

6.3.2. *Equations between m and C*

Yokobori [YOK 73] was the first to notice (see section 6.2.2) that an equation connected m to C:

$$m = a \ln C + b \qquad [6.49]$$

Several authors verified this equation for different materials [MAS 76, NIC 76. LIE 73]. Figure 6.7 illustrates the results of these studies. Two main facts can be obtained from Figure 6.7:

– the curve $m = a \ln C + b$ remains parallel, regardless of the material considered;

– the coefficient b seems to vary along with Young's modulus.

We then tried to write Paris' equation as follows:

$$\frac{da}{dN} = \frac{C^*}{E^2} \Delta K^m \qquad [6.50]$$

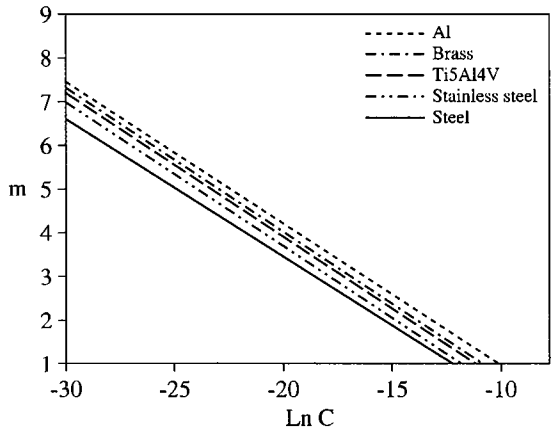

Figure 6.7. *Variation of exponent m of Paris' equation as a function of logarithm of parameter C of this equation for different materials*

Figure 6.7 illustrates the relationship between the C^* and m values obtained. We can then write $m = a \ln C^* + b^*$, therefore:

$$\frac{da}{dN} = \frac{1}{E^2} \exp\left(\frac{m - b^*}{a}\right) \Delta K^m \qquad [6.51]$$

with a and b^* being independent parameters of the material as a first approximation.

This comes to be written:

$$\frac{da}{dN} = \frac{\exp(-b^*/a)}{E^2} \left(\frac{\Delta K}{\Delta K_0}\right)^m \qquad [6.52]$$

with $\Delta K_0 = \exp(1/a) \approx 21.7$ and $\exp(-b^*/a) = 2.155.10^{-7}$ if the units are mm/cycles and $\text{MPa}\sqrt{\text{m}}$ for the rate and ΔK respectively.

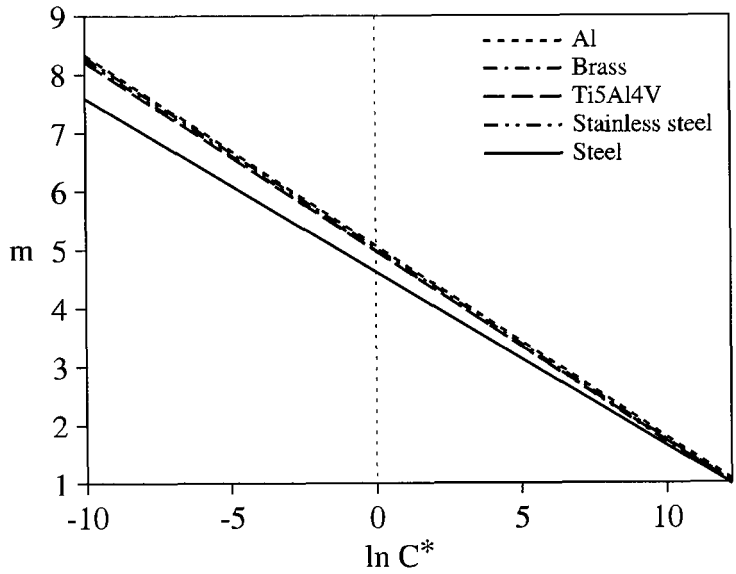

Figure 6.8. *Variation of exponent m in Paris' equation as a function of parameter C* [AUB]*

6.3.3. *Influences of the intrinsic parameters on cracking*

Although the different models lack precision, we can still observe a certain number of tendencies relative to some intrinsic parameters that have an effect on cracking.

6.3.3.1. *Influence of Young's modulus*

As any parameter can be constant, the propagation rate is low when Young's modulus E is high. Some authors propose a variation with $1/E$. Others plot the Paris laws with AK/E. If this last approach rationalizes cracking somehow, it nevertheless involves E as a variable power function ($1/E^m$). It is likely that this rationalization is not valid in the particular case where $m = 2$. Figure 6.9 shows the same observation: for a given ΔK, the higher Young's modulus is, the more slowly the crack propagates. Most of the models agree with this fact.

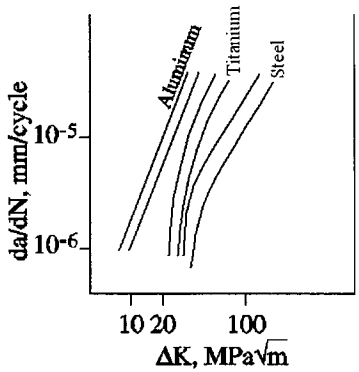

Figure 6.9. *Comparison of the propagation rates of several metals [BAT 69]*

6.3.3.2. *Influence of grain size*

During initiation of the crack, the stage close to the propagation threshold, and the final stage when fracture occurs, the size of the grain has a major role.

During the initiation stage, the number of fracture cycles, measured with non-notched specimens, was proven to vary depending on an equation of the following type:

$$N_f = N_0 + kd^{1/2} \qquad [6.53]$$

We also know that:

– the endurance limit varies in the same way, as a function of the size of the grain:

$$\sigma_D = \sigma_0 + k_E\, d^{-1/2} \qquad [6.54]$$

– the propagation threshold varies in the opposite way [MAS 76]:

$$\Delta K_{th} = K_0 + K_f\, d^{1/2} \qquad [6.55]$$

During stage II of propagation, the size of the grain does not seem to have any influence [HAH 70, TOM 75], unless the thickness is much greater than the size of the grain [TOM 73].

6.3.3.3. *Influence of the elasticity limit*

In comparison to the previous result, it is normal that the elasticity limit σ_y has no effect on cracking. Nevertheless, in the literature there are many contradictory results. For steels and brass, it has been proven that the propagation rate is independent of the elasticity limit [HOE 67, TOM 73, TRO 70]. Strong variations of the elasticity limit do not cause a significant variation in the propagation rate.

It is likely that the dislocation cells that were formed at the end of the crack are significant obstacles to propagation and thus mask the effect of grain size. This therefore, indirectly makes propagation independent from the initial elasticity limit. The cyclic elasticity limit at the end of the crack would then be independent of the elasticity limit.

6.3.3.4. *Effect of tenacity K_{IC}*

We will now consider the tenacity, measured by K_{IC} or the fracture deformation, in order to introduce a ductility factor within the equations [BUR 70]. With all of the models where K_{IC} is involved, it appears that the denominator is:

$$\frac{da}{dN} \alpha \frac{1}{K_{IC}^{n}} \qquad [6.56]$$

with n a variable coefficient.

This proposition is physically acceptable: an increase in ductility has to lead to a decrease in propagation rate, with all of the other parameters remaining constant.

Lindley *et al.* [LIN 76] also showed that exponent m is related to K_{IC}. It is usually accepted that m decreases when K_{IC} increases (see Figure 6.10).

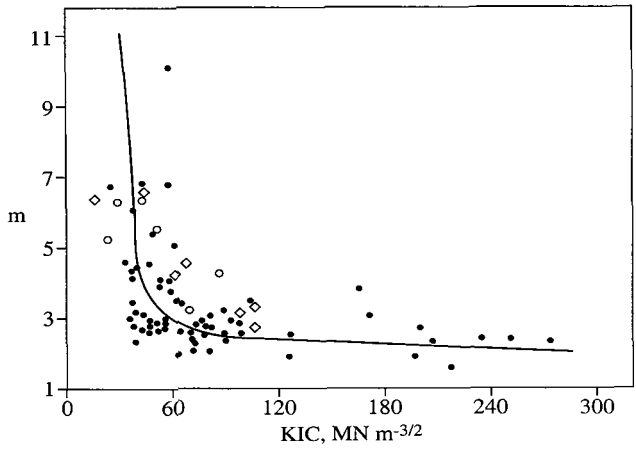

Figure 6.10. *Relationship between the exponent m of Paris' equation and the toughness K_{IC}. Most of the points plotted in this graph come from [LIN 76], ○ come from [HAY 77] and ◊ from [MIL 68]*

6.3.4. *Influence of the parameters extrinsic to cracking*

In this section, we gathered together all of the parameters that were not intrinsic to the material. These are the parameters that depend on the person performing the test:

– frequency of loading;

– thickness of the specimen;

– corrosion;

– type of signal;

– temperature; etc.

There are only a few theoretical or empirical laws that consider the effect of these parameters. We usually observe that the variation of some of these parameters hardly had any consequence on the cracking rate.

It is the case, for instance, that the parameters that mattered were the frequency, the type of signal, the thickness of the specimen, etc.

6.3.4.1. *Influence of the thickness of the specimen*

The description of cracking using Paris' equation $da/dN = C\Delta K^m$ assumes that we are capable of calculating the stress intensity factor for a given geometry. These

factors were calculated in the case of planar deformations for many specimen geometries [BRO 66]. This calculation of K is only variable if the cracking occurs under a plane strain. In practice, as soon as the thickness reaches a certain value, the influence of the thickness of the specimen becomes low [HAH 73, RIT 77].

6.3.4.2. *Influence of frequency*

The influence of frequency is related to the influence of the environment. Within a corrosive medium, the loading frequency plays a major role [VOS 88]. We can summarize the interaction of these parameters in Figure 6.11. Beyond a certain critical frequency, the frequency only slightly influences propagation rate. For a given material, this critical frequency depends on the environment [BRA 69]. At room temperature and in the laboratory atmosphere, it seems that the regular frequencies used (ranging from 0.1 Hz to 100 Hz) do not have any important influence within steels [MAS 76, TOM 75] or brasses [TOM 73].

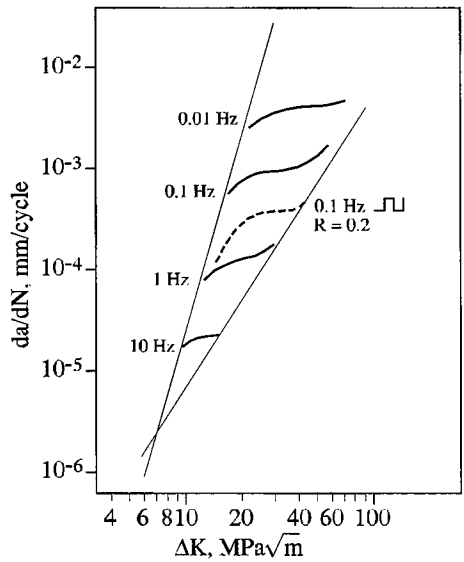

Figure 6.11. *Effect of frequency in a corrosive medium on the propagation rate within a pipeline steel X65 [VOS 76]*

6.3.4.3. *Effect of corrosion*

The influence of corrosion will be presented in Chapters 10 and 11. Here we will only give the phenomenological description of the action of corrosion on the propagation rate of a crack. Depending on the response of the material to corrosion

under tension, the action of this phenomenon only acts on coefficient C or acts on coefficients m and C simultaneously:

$$\frac{da}{dN} = C(t)\,\Delta K^m \qquad [6.57]$$

and:

$$\frac{da}{dN} = C(t)\,\Delta K^{m(t)} \qquad [6.58]$$

We usually admit that when K_{max} remains lower than K_{iscc}, the second of these above reactions remains valid. We have to remember that the frequency has to be low enough for corrosion to have an influence that can be observed (see Figure 6.11).

6.3.4.4. *Effect of temperature*

The effect of temperature on cracking is complex. An increase in temperature acts at different levels. It usually leads to an increase in oxidation and, as a consequence, cracking becomes sensitive to the frequency of the test. On the other hand, a temperature rise changes the cold-working modes of the material. This effect is mainly sensitive in metals that are slightly ductile at room temperature.

Unfortunately, this effect is not known precisely and the information obtained has to be qualitative. A temperature rise usually leads to an increase in propagation rate [AND 74, JAM 77, KAW 75]. Yokobori [YOK 73, YOK 75] has presented this effect and he developed a model that considers the influence of temperature.

6.4. Future plans

In section 6.3.4 we have already stressed, the weaknesses of Paris' equation. The dimensions of parameter C are variable and are a function of the value of parameter m. We have also seen that by using the equation proposed by Yokobori, $m = a\ ln\ C + b$, we can get a simpler equation than Paris' one from the dimensional point of view.

We can also find another hypothesis dealing with this topic. The notion of ΔK, variation of the strain intensity factor, is only valid if there is no plastic deformation at the end of the crack, that is to say that it is only valid for a material where the crack propagates easily. However, under fatigue there is always a plastic deformation at the end of the crack. This plastic deformation is negligible close to the propagation threshold, but very significant when K gets close to K_C. In this last case, the notion of K would not be applied.

Rice [RIC 68] defined a criterion, the integral J, which defines certain plasticity at the end of the crack. This definition is more general than that of K in the case where plasticity at the end of the crack is higher, but still low overall. In the case where plasticity is negligible, we can have simple equations between J and K ($J = K^2/E$ under plane strain).

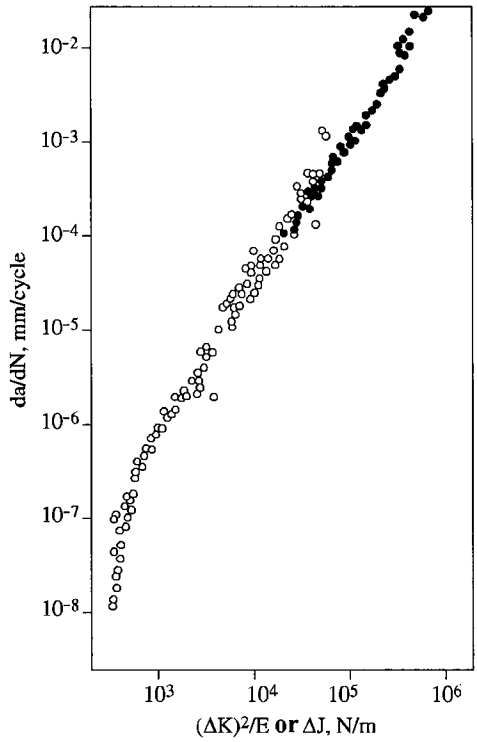

Figure 6.12. *Comparison of the propagation rate measured as a function of $(\Delta K)^2/E$ (linear mechanics) or ΔJ (plasticity). The • results are obtained from measurements of the value of integral J and 0 from the linear mechanics (measurement of K) [DOW 76]*

In Figure 6.12 we present the results that Dowling [DOW 76] obtained using linear fracture mechanics (if we define $\Delta J = \Delta K^2/E$) and the results obtained by the measurement of ΔJ. With high rates, we can observe that application of the definition of ΔJ continues the application range of Paris' equation, which can then be written as:

$$\frac{da}{dN} = C\,\Delta J^m \qquad [6.59]$$

Thus, the propagation rate becomes proportional to the energy necessary to initiate crack propagation, that is to say the energy necessary to spread the crack with an elementary length, represented by ε.

Within this newly modified Paris equation we should then introduce the action of all the parameters that we presented earlier.

6.5. Conclusion

We can see that building a model is not easy. Some of the phenomena are not clearly known and the action of the different parameters is sometimes controversial. Many models, theoretical or empirical, correctly describe a given situation but then become invalid as soon as a parameter in the experiment varies. We can, however conclude that a certain number of criteria define a model that has to consider various parameters.

6.5.1. *Metallurgic parameters*

The propagation rate has to be of the type $da/dN \propto 1/E^n$. The exponent of E remains uncertain.

The influence of grain size is only involved in two extreme cracking cases: when $\Delta K \rightarrow \Delta K_{th}$ and $K_{max} \rightarrow K_C$. The size of the grain does not have a pronounced effect within the central area of the cracking curves.

The effect of the cyclic consolidation coefficient is still controversial. The study of the influence of the consolidation coefficient is a way to control propagation rates. For high-strength steels, this consolidation coefficient varies slightly (0.15 ± 0.05) and risks diminishing the practical interest in the control of propagation through n'; the tenacity, measured with coefficient K_{IC} (or K_C), is interconnected with the cracking rate.

We usually accept that an increase in K_{IC} (or K_C) leads to a decrease in propagation rate.

We often propose equations that are inversely proportional between the propagation rate and K_{IC}.

The exponent of K_{IC} still has to be defined.

6.5.2. *Extrinsic parameters*

The exact influence of temperature is not yet perfectly established experimentally and theoretically; the boundary conditions have to be respected:

$$\frac{da}{dN} \to 0 \text{ when } \Delta K \to \Delta K_{th} \quad \text{and} \quad \frac{da}{dN} \to \infty \text{ when } K_{max} \to K_C$$

Usually, the models based on the notion of crack-tip opening do not fulfil the last boundary condition. A correction has to be arbitrarily introduced. The influence of the strain ratio, R, has to be correctly described:

– the propagation rate increases when R increases;

– the influence of the ratio R decreases when Young's modulus increases.

There is no model yet that correctly describes this influence.

Without any corrosion, the influence of frequency remains low. There is a cut-off frequency f_{CN} beyond which the effect of corrosion is low. There is no model yet that correctly describes this phenomenon.

Finally, we have to mention the importance of equations regarding the dimensions of theoretical or empirical formulae given by the models: we believe that it is essential that the dimension of every parameter being used is independent from the values given to the other parameters. It will then be easier to determine the physical meaning of the parameters.

It is likely that the notion of ΔJ, or that of ΔC^* [LAN 76], will become increasingly significant. The opposite of the concept of K, these two last notions consider, to some extent, the plasticity occurring at the crack tip.

6.6. Bibliography

[AND 74] D.H. Andreasen, H. Vitovec, "Effects of temperature on fatigue crack propagation in line pipe steel", *Met. Trans.*, vol. 5, p. 1779-1783, 1974.

[ANT 75] S.D. Antolovich, A. Saxena, G.D. Chanani, "A model for fatigue crack propagation," *Eng. Fract. Mech.*, vol. 7, p. 649-652, 1975.

[AUB] M. Aubert, personal communication.

[BAI 77] J.P. Bailon, J. Masounave, C. Bathias, "On the relationship between the parameters of Paris' law for fatigue crack growth in aluminium alloys", *Scripta Met.*, vol. 11, p.1101-1106, 1977.

[BAT 69] R.C. Bates, W.G. Clark, "Fractography and fracture mechanics", *Trans. ASM*, vol. 62, p. 380-389, 1969.

[BAT 76] C. Bathias, M. Gateau, J. Philippe, "Influence of relationship between minimal and maximal strength on speed of fatigue cracking in light alloys", *Rev. Met.*, p. 559-569, July-August, 1976.

[BAT 78] C. Bathias, "Application of fracture mechanics to aluminum alloys selection", *Eng. Fract. Mech.*, vol. 10, p. 267-282, 1978.

[BAU 77] A. Bauss, H.P. Lieurade, B. Michat, M. Truchon, *IRSID Report*, vol. 267, July 1977.

[BIL 63] B.A. Bilby, A.H. Cottrell, K.H. Swinden, "Spread of plastic yield from a notch", *Proc. Roy. Soc.*, vol. A272, p. 304-314, 1963.

[BIL 65] B.A. Bilby, K.H. Swinden, "Representation of plasticity at notches by linear dislocation arrays", *Proc. Roy. Soc.*, vol. A285, p. 22-33, 1965.

[BRA 69] F.J. Bradshaw, C. Wheeler, "The effect of gaseous environment and fatigue frequency on the growth of fatigue cracks in some aluminum alloys", *Int. J. Fract. Mech.*, vol. 5, p. 255-268, 1969.

[BRO 63] Broek, Schijve, *NLR-TR-101-361 Report*, National Aeronautical and Astronautical Research Institute, Amsterdam, 1963.

[BRO 66] W.F. Brown, J.E. Strawley, "Plane strain crack toughness testing of high strength metallic materials", *ASTM STP 410*, 1966.

[BUR 70] J.J. Burke, J. Weiss, *Ultrafine Grain Metals*, Syracuse University Press, Syracuse, 1970.

[CAR 77] L.N. McCartney, P.M. Cooper, "A numerical method of processing fatigue crack propagation data", *Eng. Fract. Mech.*, vol. 9, p. 265-272, 1977.

[CAR 77b] L.N. McCartney, P.M. Cooper, "A new method of analyzing fatigue crack propagation data", *Eng. Fract. Mech.*, vol. 9, p. 273-290, 1977.

[CHA 72] G.R. Chanani, S.D. Antolovich, W.W. Gerberich, "Fatigue crack propagation in trip steels", *Met. Trans.*, vol. 3, p. 2661-2672, 1972.

[CLE 78] A. Clerivet, PhD Thesis, University of technology of Compiègne, France, 1978.

[CLI 63] F.A. Mc Clintock, "On the plasticity of the growth of fatigue cracks", in *Fracture of solids*, John Wiley, New York, 1963.

[CLI 67] F.A. Mc Clintock, "Fatigue crack propagation", *ASTM STP 415*, written discussion, vol. 170, 1967.

[CRO 68] T.W. Crocker, L.A. Cooley, E.A. Lange, C.N. Freed, *Trans. ASME*, vol. 61, p. 568-574, 1968.

[DOW 76] N.E. Dowling, J.A. Begley, "Fatigue crack growth during gross plasticity and the J-integral", *ASTM STP 590*, p. 82-103, 1976.

[DUG 60] D.S. Dugdale, "Yielding of steel sheets containing slits", *J. Mech. Phys. solids*, vol. 8, p.100-104, 1960.

[DUG 77] T.V. Duggan, "A theory for fatigue crack propagation", *Eng. Fract. Mech.*, vol. 9, p. 735-747, 1977.

[ELB 70] W. Elber, "Fatigue crack closure under cyclic tension", *Eng. fract. mech.*, 2, 37-44, 1970.

[ELB 71] W. Elber, "The significance of fatigue crack closure", *ASTM STP 486*, p. 230-242, 1971.

[ERD 70] F. Erdogan, M. Ratwani, "Fatigue and fracture of cylindrical shells containing a circumferential crack", *Int. J. Fract. Mech.*, vol. 6, p. 379-392, 1970.

[FIT 77] J.H. Fitzgerald, "Empirical formulations for analysis and prediction of trends for steady-state fatigue crack growth rates", *J. Test. Eval.*, vol. 5, p. 343-353, September 1977.

[FOR 67] A.G. Forman *et al.*, *J. Basic Eng.*, vol. 89, p. 459-464, 1967.

[FRO 58] N.E. Frost, D.S. Dudgale, "The propagation of fatigue cracks in sheet specimens", *J. Mech. Phys. Solids*, vol. 6, p. 92-110, 1958.

[FRO 61] N.E. Frost, J. Holsen, C.E. Phillips, Crack Propagation Symposium (Cranfield), 1961.

[FRO 67] N.E. Frost, J.R. Dixon, "A theory of fatigue crack growth", *Int. J. Fract.*, vol. 3, p. 311-316, 1967.

[FRO 68] N.E. Frost, D.S. Dugdale, "The propagation of fatigue cracks in sheet specimens", *J. Mech. Phys. Solids*, vol. 16, p. 92-110, 1968.

[FRO 71] N.E. Frost, L.P. Pook, K. Denton, "A fracture mechanics analysis of fatigue crack growth data for various materials", *Eng. Fract. Mech.*, vol. 3, p. 109-126, 1971.

[HAH 65] G.T. Hahn, A.R. Rosenfield, "Local yielding and extension of a crack under plane stress", *Acta Met.*, vol. 13, p. 293-306, 1965.

[HAH 70] G.T. Hahn, M. Sarrate, A.R. Rosenfield, *Proceedings of the Air Force Conference on Fatigue and Fracture of Aircraft Structure AFFDLTR*, vol. 425p. 70-144, 1970.

[HAH 73] C.T. Hahn, C.J. Simon, "A review of fatigue crack growth in high strength aluminum alloys and the relevant metallurgical factors", *Eng. Fract. Mech.*, vol. 5, p. 523-536, 1973.

[HAY 77] R. Hay, J. Masounave, N. Bassim, *CDT internal report*, Ecole Polytechnique, Montréal, 1977.

[HIC 72] J.P. Hickerson, R.W. Hertzberg, "Role of mechanical properties in low stress fatigue crack propagation", *Met. Trans.*, vol. 3, p. 179-189, 1972.

[HOE 67] D.W. Hoeppner, "The effect of grain size on fatigue crack propagation in copper", *Fatigue crack propagation, ASTM STP 415*, p. 486-504, 1967.

[HUD 69] C.M. Hudson, J.T. Scardina, "Effect of stress ratio on fatigue-crack growth in 7075-T6 aluminum-alloy sheet", *Eng. Fract. Mech.*, vol. 1, p. 429-446, 1969.

[HUL 57] J.A.H. Hult, F.A. Mc Clintock, *Proceedings of the 9th International Congress of Applied Mechanics*, University of Brussels, vol. 8, p. 51, 1957.

[IRV 77] P.E. Irving, L.N. Mc Cartney, "Prediction of fatigue crack growth rates: theory, mechanisms and experimental results", *Met. Science*, vol. 11, p. 351-361, 1977.

[IRW 57] G.R. Irwin, "Analysis of stress and strain near the end of a crack transversing a plate", *J. Applied Mech.*, p. 361-364, 1957.

[JAM 77] L.A. James, "The effect of temperature upon fatigue-crack growth behavior in nimonic PE16", *J. Nuclear Mat.*, vol. 67, p. 283-288, 1977.

[KAW 75] T. Kawasaki, S. Nakanishi *et al.*, "Fracture toughness and fatigue crack propagation in high strength steel from room temperature to −180 °C", *Eng. Fract. Mech.*, vol. 7, p. 465-472, 1975.

[KLE 72] M. Klesnil, P. Lukas, "Influence of strength and stress history on growth and stabilisation of fatigue cracks", *Eng. Fract. Mech.*, vol. 4, p. 77-92, 1972.

[LAL 77] K.M. Lal, S.B.L. Garg, "A fatigue crack propagation model for strain hardening materials", *Eng. Fract. Mech.*, vol. 9, p. 939-949, 1977.

[LAL 78] D.N. Lal, V. Weiss, "Notch analysis of fracture approach to fatigue crack-propagation", *Met. Trans A*, vol. 9A, p. 413-426, 1978.

[LAN 76] J.D. Landes, J.A. Begley, "A fracture mechanics approach to creep crack growth", *ASTM STP 590*, p. 128-148, 1976.

[LAR 68] R.W. Lardner, "A dislocation model for fatigue crack growth in metals", *Phil. Mag.*, vol. 17, p. 71-82, 1968.

[LIE 75] H.P. Lieurade, "Study, using fracture mechanics, of toughness, fatigue cracking and stress corrosion cracking of ultrahigh strength steels", *Mem. Sci. Rev. Met.*, p. 891-935, 1975.

[LIN 76] T.C. Lindley, C.E. Richards, R.O. Ritchie, "Mechanics and mechanisms of fatigue crack growth in metals-review", *Metallurgia and Metal Forming*, vol. 43, p. 268-281, 1976.

[LIN 78] T.C. Lindley, I.G. Palmer, C.E. Richards, "Acoustic emission monitoring of fatigue crack growth", *Mater., Sci., Eng.*, vol. 32, p. 1-15, 1978.

[LIU 63] H.W. Liu, "Fatigue crack propagation and applied stress range", *J. Basic Eng.*, vol. 85, p. 116-122, 1963.

[MAS 76] J. Masounave, J.P. Bailon, "Effect of grain size on threshold stress intensity factor in fatigue of a ferritic steel", *Scripta Met.*, vol. 10, p. 165-170, 1976.

[MAS 76] J. Masounave, PhD thesis, Ecole Polytechnique, Montréal, 1976.

[MIL 68] G.A. Miller, "The dependence of fatigue-crack growth rate on the stress intensity factor and the mechanical properties of some high-strength steels", *Trans. ASM*, vol. 61, p. 442-448, 1968.

[MOR 65] J. Morrow, "Cyclic plastic strain energy and fatigue of metals, internal friction, damping and cyclic plasticity", *ASTM STP 378*, p. 45-87, 1965.

[NIC 73] C.E. Nicholson, Proceedings BSC, *Proceedings of the Conference on Mechanics and Mechanisms of Crack Growth*, Churchill College, Cambridge, April 1973.

[NIC 76] E.H. Niccolls, "A correlation for fatigue crack growth rate", *Scripta Met.*, vol. 10, p. 295-298, 1976.

[OGU 77] K. Ogura, K. Ohji, K. Honda, "3 dimensional aspect of fatigue crack closure in plate specimens", *Int. J. Fract.*, vol. 13, p. 524-527, 1977.

[PAR 63] P. Paris, F. Erdogan, "A critical analysis of crack propagation laws", *J. Basic Eng.*, p. 528-534, 1963.

[PEA 66] S. Pearson, "Fatigue crack propagation in metals", *Nature*, vol. 211, p. 1077-1078, 1966.

[PEA 72] S. Pearson, "The effect of mean stress on fatigue crack propagation in half-inch (12.7 mm) thick specimens of aluminum alloys of high and low fracture toughness", *Eng. Fract. Mech.*, vol. 4, p. 9-24, 1972.

[PEL 70] R.M. Pelloux, *Proceedings of the Air Force Conference on Fatigue and Fracture of Aircraft structures and materials, AFFDL TR.* p. 70-144, 1970.

[PIT 74] F.J. Pitoniak, A.F. Grandt, L.T. Montulli, *et al.*, "Fatigue crack retardation and closure in polymethylmethacrylate", *Eng. Fract. Mech.*, vol. 6, p. 663-670, 1974.

[POO 73] L.P. Pook, N.E. Frost, "Fatigue crack growth theory", *Int. J. Fract.*, vol. 9, p. 53-61, 1973.

[PUR 75] S. Purushothaman, J.K. Tien, "A fatigue crack growth mechanism for ductile materials", *Scripta Met.*, vol. 9, p. 923-926, 1975.

[RAM 43] W. Ramberg, W.R. Osgood, *Description of strain-stress curves by three parameters,* NACA report TN902, July 1943.

[RIC 67] J.R. Rice, "Mechanics of crack tip deformation and extension by fatigue", *Fatigue crack propagation, ASTM STP 415*, p. 247-311, 1967.

[RIC 68] J.R. Rice, "A path independent integral and the approximate analysis of strain concentration by notches and cracks", *J. Appl. Mech.*, vol. 6, p. 379-386, 1968.

[RIC 72] C.E. Richards, T.C. Lindley, "The influence of stress intensity and microstructure on fatigue crack propagation in ferritic materials", *Eng. Fract. Mech.*, vol. 4, p. 951-978, 1972.

[RIC 74] C.E. Richards, T.C. Lindley, "The relevance of crack closure to fatigue crack propagation", *Mat. Sci. Eng.*, vol. 14, p. 281-293, 1974.

[RIT 77] R.O. Ritchie, *Proc. of Fracture 77*, vol. 2, p. 1325, Waterloo, Canada, 1977.

[SCH 74] K.H. Schwalbe, "Comparison of several fatigue crack propagation laws with experimental results", *Eng. Fract. Mech.*, vol. 6, p. 325-341, 1974.

[SCH 77] K.H. Schwalbe, "Some aspects of crack propagation under monotonic and cyclic load", *Eng. Fract. Mech.*, vol. 9, p. 547-556, 1977.

[SHI 77] M. Shiratori *et al.*, *Proc. of Fracture 77*, vol. 2, p. 19-24, Waterloo, Canada, 1977.

[SPE 77] W.R. Sperr, *Proc. of Fracture 77*, 2, p. 1049-1056, Waterloo, Canada, 1977.

[SUL 76] A.M. Sullivan, T.W. Crooker, "Analysis of fatigue crack growth in a high strength steel. 1. stress level and stress ratio effects at constant amplitude", *J. Pressure Vessel Technol.*, vol. 98, p. 179-184, 1976.

[SUL 76a] A.M. Sullivan, T.W. Crooker, "Analysis of fatigue crack growth in a high strength steel. 2. variable amplitude block loading effects", *J. Pressure Vessel Technol.*, vol. 98, *p.* 208-212, 1976.

[TOM 68] B. Tomkins, "Fatigue crack propagation, an analysis", *Phil. Mag.*, vol. 18, p. 1041-1066, 1968.

[TOM 73] A.W. Thompson, R.J. Bucci, "Dependence of fatigue crack growth rate on grain size", *Met. trans.*, vol. 4, p. 1173-1175, 1973.

[TOM 75] A.W. Thompson, "Fatigue crack propagation in austenitic stainless steels", *Eng. fract. mech.*, 7, 61-66, 1975.

[TRO 70] J.F. Troop, G.A. Miller, *ASTM STP 467*, p. 154-168, 1970.

[VOS 76] O. Vosikovsky, "Closed Loop", *MTS Corporation*, vo.l 6, p. 1-13, April 1976.

[VOS 78] O. Vosikovsky, "Frequency, stress ratio, and potential effects on fatigue crack growth of HY130 steel in salt water", *J. Testing Eval.*, vol. 6, p. 175-182, 1978.

[WEE 66] J. Weertman, "Rate of growth of fatigue cracks calculated from the theory of infinitesimal dislocations distributed on a plane", *Int. J. Fract. Mech.*, vol. 2, p. 460-467, 1966.

[WEE 69] J. Weertman, "Theory of rate of growth of fatigue cracks under combined static and cyclic stresses", *Int. J. Fract. Mech.*, vol. 5, p. 13, 1969.

[YAH 74] B. Yahiaoui, P. Petrequin, "Propagation of fatigue cracks in low-C austenitic stainless steels types 304L and 316L", *Rev. Phys. Appl.* 9, p. 683-690, 1974.

[YOK 73] T. Yokobori, T. Aizawa, "The influence of temperature and stress intensity factor upon the striation spacing and fatigue crack propagation rate of aluminum alloy", *Int. J. Fract.*, vol. 9, p. 489-491, 1973.

[YOK 73] T. Yokobori, I. Kawada, H. Hata, *Proceedings of the International Conference on Strength and Fracture of Materials*, vol. 9, p. 35, Tohuku University, Sendai, Japan, 1973.

[YOK 75] T. Yokobori, "Fracture toughness and fatigue crack propagation in high strength steel from room temperature to -180 °C", *Eng. Fract. Mech.*, vol. 7, p. 465-472, 1975.

[YOK 77] T. Yokobori, S. Konosu, A.T. Yokobori Jr, *Proc. Fracture 77*, vol. 1, p. 665-682, Waterloo, Canada, 1977.

Chapter 7

Short Crack Propagation

7.1. Introduction

Numerous experimental results highlight the fact that the theory of linear elastic fracture mechanics (LEFM), which is applied to long cracks under confined plasticity, cannot describe the behavior of short cracks that are growing at the smooth surface of a material or from the root of a notch. Depending on the material, the geometry and the type of loading, cracks whose size can vary from grain to millimeter scale do not match the univocal equation (with R constant) between the propagation rate da/dN and variation in stress intensity factor ΔK. The three following differences are observed with respect to long cracks:

– for a given ΔK, short cracks grow faster than long cracks (by at least one order of magnitude);

– short cracks grow with ΔK values lower than the propagation threshold ΔK_{th};

– their initial growth can present some decelerations: we can observe a minimum rate, or sometimes, at low loading levels, the crack stops; it becomes a so-called non-propagating crack.

In practice, these differences have consequences. Most of the life of parts in service is spent within the short-crack regime, especially in the domain of high-cycle fatigue. The fatigue lives predicted by the calculation methods based on LEFM therefore over estimate the real lives of a material if initial defects of small size are taken into account. In addition, the stress amplitude at the propagation threshold is

---

Chapter written by Yves VERREMAN.

lower than the fatigue strength but also lower than the value calculated with the threshold of the long cracks, ΔK_{th}.

It seems that there is no global explanation whatever the material, geometry, and type of loading. Depending on the individual case, the differences in behavior are attributed to one or more of the following conditions that question the similitude principle of LEFM:

– the crack has a size comparable to that of a grain or to another characteristic dimension of the microstructure. Its propagation is very sensitive to the heterogenity of the microstructure; continuum mechanics cannot be applied at this scale;

– the condition of confined plasticity at the crack tip is no longer verified. The short crack can be surrounded by a plastic zone of comparable or larger size because of a high stress level close to full yielding or to a notch that leads to a stress concentration;

– even under an elastic regime, the stress and strain fields at the tip of a crack whose depth tends towards zero are no longer described by the singular term that defines factor K;

– the short crack has a limited wake and the crack closure mechanisms cannot yet be developed, for example the closure induced by the residual plastic deformation left along the crack lips.

Authors in this field use a varied terminology in order to distinguish different types of short cracks. In this book, we will use the term "microstructurally short" crack when the first condition prevails and "mechanically short" crack for the other three macroscopic conditions. We should also note some other terms used in the literature, for instance [CLU 92, EVI 98]:

– "physically short" crack in order to introduce the fourth condition;

– "small crack" instead of "short crack" in order to describe that the crack is small in both dimensions (depth and width);

– "chemically short" crack when the effects of the environment are amplified at low crack depth.

In order to better enlighten the reader who might not be familiar with this topic, we will first present some theoretical considerations that demonstrate the limits of LEFM to describe the behavior of short cracks, from a smooth edge or a notch root. We will then provide a review of the experimental observations and interpretations reported in the literature (influence of the microstructure, influence of a notch and development of the closure). Finally, we will present the main models that are

proposed in order to describe either the behavior of microstructurally short cracks or that of mechanically short cracks.

7.2. Theoretical considerations showing the limits of LEFM

7.2.1. *Propagation of cracks from a smooth edge: Kitagawa diagram*

The diagram presented in Figure 7.1a, called the "Kitawaga diagram" [KIT 76], simply illustrates a limit of the LEFM theory when the length of the crack is too short. It represents, on logarithmic scales, the stress amplitude at the propagation threshold as a function of the depth of a crack.

According to LEFM, if the propagation threshold ΔK_{th} is a material constant, we then obtain a line with a slope of -1/2. Nevertheless, this prediction cannot be applied to cracks that are too short as the stress amplitude is limited by the "fatigue limit" ΔS_o of the material without defect (fatigue strength at 5.10^8 cycles, for instance). The intersection of the two lines allows us to calculate a first critical length a_o:

$$a_0 = \frac{1}{\pi}\left(\frac{\Delta K_{th}}{Y\Delta S_o}\right)^2 \qquad [7.1]$$

where Y is a correction factor function of the geometry. It has no dimension ($Y = 1.12$ for a straight-fronted crack; and $Y = 0.728$ for a semi-circular crack). This critical length, as a function of ΔK_{th} and ΔS_o, can vary a lot depending on the material. For instance, it is lower than 10 μm in the case of high-strength alloyed steel, whereas it can reach a millimeter in the case of mild steel.

The Kitagawa diagram can be turned into a second diagram (see Figure 7.1b), which represents the decrease in the ΔK_{th} threshold under the regime of short cracks. In other terms, short cracks grow with values of ΔK that are lower than the propagation threshold of long cracks.

The critical length, where LEFM gives non-conservative predictions, is actually higher than a_o. The experimental results obtained by Kitagawa and many other authors [TAN 87] are given as a transition curve between the two previous lines and give a deviation from LEFM, which occurs at a depth a_2 higher than a_o (see Figure 7.1; dotted lines).

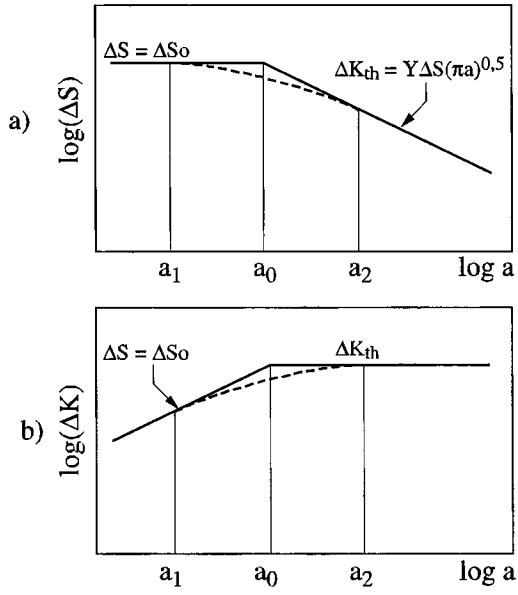

Figure 7.1. *Kitagawa-Takahashi diagram: a) in the plane ΔS – a; and b) in the plane ΔK – a*

Considering the first two interpretations of the abnormal behavior of the short cracks previously introduced, Taylor [TAY 89] proposed and verified for different materials that the value of a_2 corresponds to the highest of the following two values:

$$a_2 = 10d \qquad [7.2a]$$

$$a_2 = 10r_p \qquad [7.2b]$$

where d is the average grain size (or another characteristic dimension of the microstructure) and r_p is the cyclic plastic zone size at the propagation threshold:

$$r_p = \frac{1}{3\pi}\left(\frac{\Delta K_{th}}{2\sigma_{yc}}\right)^2 \qquad [7.3]$$

with σ_{yc} the cyclic yield strength of the material.

Equation [7.2b] is a small scale yielding condition at the crack tip: the crack length has to be an order of magnitude higher than r_p for the plasticity to remain confined within the elastic singularity. This condition is equivalent to limit the

nominal stress ΔS with respect to yield strength. As a matter of fact, equation [7.3] can be written as:

$$\frac{r_p}{a} = \frac{Y^2}{3}\left(\frac{\Delta S}{2\sigma_{yc}}\right)^2 \qquad [7.4]$$

Brown [BRO 86] proposed, for instance, that $\Delta S \leq 2\ \sigma_{yc}/3$ with $R = -1$.

Murakami [MUR 02] carried out a systematic study on the influence of the depth and geometry of small defects on the resistance of different steels and some other metals at 10^7 cycles. The resistance of carbon steels, 1013 and 1046, is not affected by any defects that have a depth lower than 70 μm and 45 μm respectively. The cracks that are initiated do not grow anymore. Within the transition zone between a_1 and a_2 (see Figure 7.1a), he could gather almost all of the experimental data using the following empirical equation:

$$\Delta S_0 / 2(\text{MPa}) = 1.43\ (HV + 120)(\sqrt{\text{area}})^{-1/6} \qquad [7.5]$$

where HV is the Vickers hardness of the material and $\sqrt{area}$ (μm) is the square root of the area of the defect projected on a plane perpendicular to the applied stress. The corresponding increase in the propagation threshold is given by:

$$\Delta K_{th} / 2\left(\text{MPa}\sqrt{\text{m}}\right) = 3.3\ (HV + 120)(\sqrt{\text{area}})^{1/3} \qquad [7.6]$$

In logarithmic scales, the equation between ΔK_{th} and $\sqrt{area}$ is approximately linear up to 1,000 μm with a slope of 1/3.

7.2.2. *Propagation of cracks from a macroscopic notch root: Frost diagram*

Some experimental results, that we will focus on later, show that short cracks from notches that are severe enough initially have decreasing growth rates, before accelerating and joining the trend of the long cracks, where da/dN is an increasing function of ΔK. Nevertheless, the cracks can stop growing if the level of nominal stress is low enough.

It seems that Frost [FRO 59] was the first to observe this behavior, which is not predicted by LEFM as ΔK always increases with crack length if the nominal stress amplitude ΔS remains constant. Using specimens made of mild steel that are notched with a V shape and subjected to rotating bending ($R = -1$), he showed that these

cracks could be initiated but that they stop if the radius of curvature ρ is small enough (see Figure 7.2; $k_t > 2.5$ corresponds to $\rho < 600$ μm).

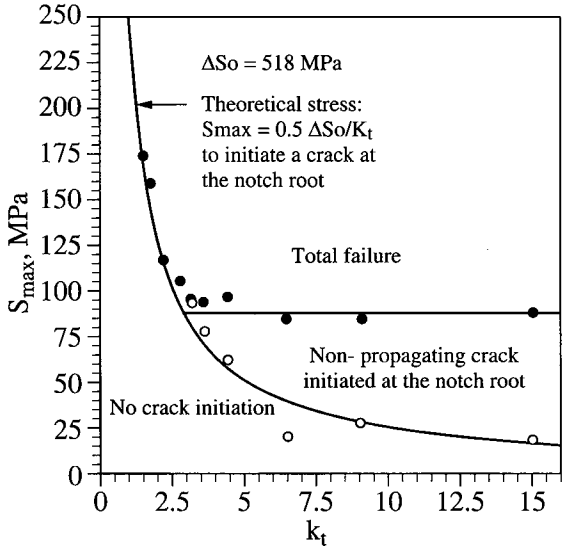

Figure 7.2. *Resistance of V-notched specimens made of mild steel as a function of stress concentration factor k_t [FRO 59]. The open symbols represent the stress that is necessary to initiate a crack and the full symbols to get a propagation leading to a complete fracture*

Smith and Miller [SMI 78] proposed a simple theoretical interpretation of this experimental result. Let us consider the case of a notch with a constant depth D. The concentration factor k_t remains variable according to the chosen radius of curvature at the notch root. The condition at the initiation of a crack can be written as:

$$\Delta S \geq \frac{\Delta S_0}{k_t} \qquad [7.7]$$

and is represented by the hyperbola in Figure 7.2. On the other hand, the stress intensity factor of a crack that passes over the notch field will rapidly tend towards that of a crack with a depth of $D + a$. In order to get a complete fracture, this crack will also have to fulfill the propagation condition:

$$Y \Delta S \sqrt{\pi(D+a)} \geq \Delta K \geq \Delta K_{th}$$

which can also be written as:

$$\Delta S \geq \frac{\Delta K_{th}}{Y\sqrt{\pi D}} \qquad [7.8]$$

if a is neglected compared to D. This second condition, independent from k_t, is represented by the horizontal line in Figure 7.2.

A domain of non-propagating cracks is then observed if the notch is severe enough, i.e. when the stress concentration factor exceeds a certain value:

$$k_t^* = \left(\frac{Y\Delta S_0}{\Delta K_{th}}\right)\sqrt{\pi D} \qquad [7.9]$$

Within this domain, the nominal stress is enough for the crack to be initiated [7.7], but not enough to create a propagation leading to a complete fracture [7.8].

We can also observe that, if D varies whereas k_t remains constant, the propagation stress is higher than the initiation stress when the notch does not reach a given depth:

$$D^* = k_t^2 a_0 \qquad [7.10]$$

7.3. Experimental observations

7.3.1. *Propagation rates of short cracks*

Some divergences between the propagation rates of short cracks and those of long cracks were observed for the first time by Pearson [PEA 75] within an aluminum alloy. He found that the surface cracks with a size similar to the average size of a grain were growing more rapidly than the long cracks when the correlation parameter was ΔK. Later on, this phenomenon was reported for different materials and geometries, and even beyond the microstructural scale. Sometimes, nevertheless, we cannot observe any significant gap between the rates of long cracks and short ones, which is the case with a nickel-based super-alloy and with tempered and quenched steels [LAN 85].

For the same material, the evolutions of small cracks at the surface present a great deal of scatter. Curves A to E in Figure 7.3 are a summary of various tests that were carried out by Lankford [LAN 85] on crack propagation at the microstructure scale within an aluminum alloy. Here:

– the propagation rate was up to two orders of magnitude higher than those predicted by the extrapolation of data from the long cracks;

– short cracks are propagated with ΔK values lower than ΔK_{th};

– slowing down was relatively significant when the size of the crack was about the depth of a superficial grain (curves B to D) and could lead to a complete stop in development of the crack (curve A).

The average rates of short cracks are sensitive to the level of applied stress as the slope of the S-N curves can be very low within the domain of high-cycle fatigue. The rate well is less deep when ΔS increases and tends to disappear at a high stress level [PIN 86].

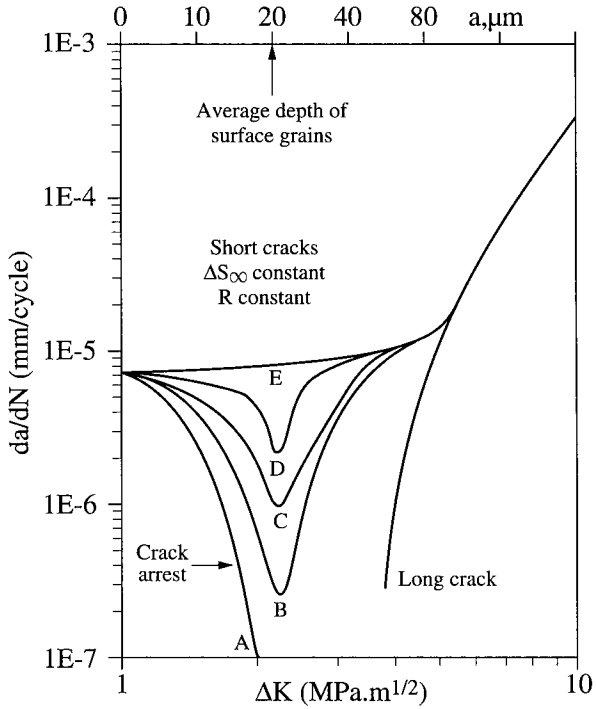

Figure 7.3. *Propagation rates of microstructurally short cracks within the aluminum alloy 7075-T651, compared to the ones of long cracks, as a function of ΔK*

The cracks growing from a notch root present similar divergences on a *da/dN* – ΔK diagram (see Figure 7.4) but the mechanisms responsible are different. The influence of a notch will be presented in section 7.3.4.

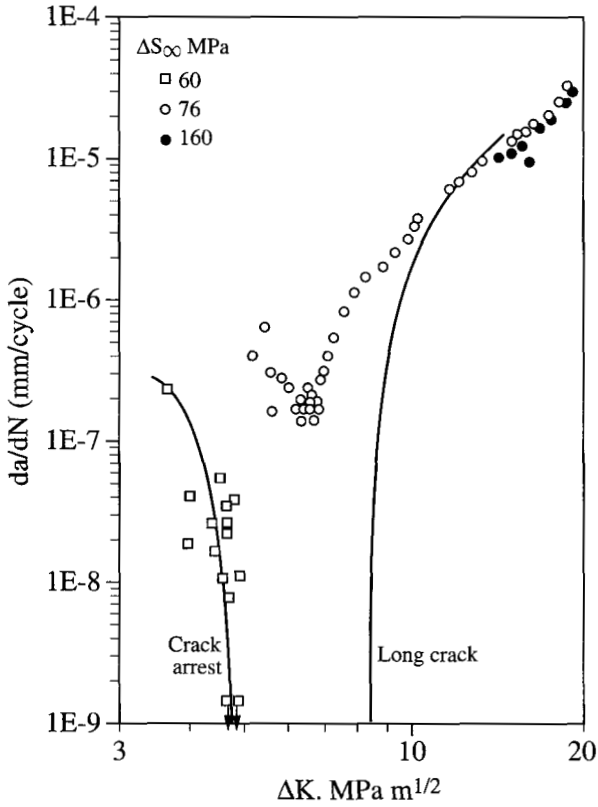

Figure 7.4. *Propagation rates of some cracks from a notch root as a function of ΔK, compared to propagation rates of long cracks within a standard specimen according to Tanaka and Nakai [TAN 83] (steel SM41B, R = 0)*

7.3.2. *Microstructurally short cracks*

7.3.2.1. *Microstructural barriers*

Short cracks initiated at the surface of smooth samples rapidly and irregularly grow with significant variations in rate. In addition, we can observe one or two reductions in growth rate that are often related to the interaction of the crack with the grain boundaries or other "microstructural barriers" [PED 88], at deviations of the crack [GRA 92] and when the mechanism of the propagation changes [PED 88].

In most cases, stage I cracks that grow along slip bands slow down when they get close to a grain boundary. This is because of the crystallographic disorientation of the adjacent grain [LAN 85, PED 88]. Many of the cracks stop but one of them

will continue at a significant rate until it reaches the next grain boundary. The process can be repeated several times before the transition to stage II occurs [EVI 98, ZHA 02]. The propagation rate then increases but at this point the crack does not necessarily behave as a long crack (see sections 7.3.3 and 7.4.2).

Crack decelerations and stops have been observed on the surface within the grain. They were attributed to:

– the interaction between the crack and a discontinuity of the microstructure underneath the surface [LUD 03];

– the variation of the shape of the crack front [PIN 86, TOK 87]; and

– the deviation of the crack within the grain due to the change in orientation of the slip bands [GRA 92, PED 88].

On the other hand, some cracks can cross a grain boundary without experiencing any deceleration (see Figure 7.3, curve E). The blocking mechanism at the grain boundaries is a function of the inclination and rotation angles of the sliding planes of the adjacent grains with the plane of the crack [ZHA 05]. The crack goes from one grain to another if the rotation angle remains very low [LUD 03].

Miller [MIL 93] showed how the fatigue strength of smooth and slightly notched specimens is controlled by microstructural barriers of the material. The resistance ΔS_o (see Figure 7.1a) corresponds to the stress level that is necessary for a crack to reach the strongest barrier. Below this level, the pre-existing cracks do not grow further and the specimen cannot be damaged [MUR 02]. Nevertheless, the length of a_1 in Figure 7.1a can be greater than the size of the grain as the grain boundaries may not be the only ones or the strongest barriers; the distribution of a second hard phase can reduce or take over the effect of grain size. Within ferritic-pearlitic steels, for instance, cracks can easily progress through the grain boundaries α until they have to interact with a pearlite band [DAV 06, MUR 02].

7.3.2.2. *Influence of the grain size*

Long cracks within the propagation threshold region grow more slowly if the grain size increases due to the corresponding increase in propagation threshold [BAI 80]. Usually the opposite seems to occur for microstructurally short cracks.

Tokaji *et al.* [TOK 94] observed an increase in propagation rates in the case of pure titanium when the grain size increases. The difference seems to be due to a lower number of perturbations of the propagation by microstructural barriers. This trend was reported for other materials too (Ti-8.6 Al, low carbon steel) and was predicted by several models of the behavior of short cracks that consider hindrance to propagation due to grain boundaries (see section 7.5.1).

Nevertheless, other experimental observations have been made. No grain size effect was observed within the titanium alloy Ti- 6Al-4V α/β. A slight diminution of the propagation rate was observed when the grain size increased from 12 to 130 μm in the aluminum alloy 7075-T6 and a more significant decrease was observed in A533B steel [JAM 89].

7.3.2.3. *Irregularity of the evolution of the crack tip*

At the microstructure scale, the crack is still far from adopting a planar surface with a regular semi-circular or semi-elliptic front. As a matter of fact, it can remain still in most places and only grow in the "easy" zones where the crystallographic orientation is favorable. The crack front does not grow homogenously; for instance, it alternatively goes from a grain in depth to a grain in width [RAV 97a]. Nevertheless, when the crack grows towards a certain number of grains, its front will progressively adopt a stable semi-circular shape [NAD 97, RAV 97a].

Ravichandran [RAV 97b] worked on the propagation of cracks within a Ti-8Al alloy with large grains (200 μm) using surface photomicroscopy as well as laser interferometry by measuring the compliance between two Vickers prints located on both sides of the crack. The material is an alloy α that is only deformed on a single slip band per grain, which leads to a strong interaction between the crack and grain boundary and to a very crystallographic fracture. However, the compliance of the crack presents an almost continuous growth, which shows that the crack continuously grows in different locations. In addition, the author shows that the extensive variability of the data $da/dN - \Delta K$ comes partly from the error made when calculating ΔK with a constant ratio of $a/2c$. By taking the irregularity of the crack front into account, polynominal regressions allowed him to reduce the data scatter of short cracks to that of long cracks.

7.3.2.4. *Stage I to stage II transition*

The progression of microstructurally short cracks at high rates has been associated with crystallographic propagation in stage I [GRA 92, PED 88]. Some results, reported by Pedersen [PED 88], prove this clearly in the case of an aluminum alloy Al-Mg-Si hardened by tempering and cycled at $R = -1$. The most significant propagation rates (up to 10^{-7} m/cycle) were measured in the case of cracks growing crystallographically along a persistent slip band within grains oriented towards a single slip. Close to the grain boundaries, when several slip systems were activated, the crack propagation turned into a non-crystallographic mode (stage II) and was observed to be lower, the rate decreasing from one to two orders of magnitude.

Brown and Hicks [BRO 83] reported similar results in the case of titanium alloy IMI 685. The crystallographic short cracks grow faster than the long ones when the

correlation parameter is ΔK; nevertheless, when the short cracks were compelled to grow non-crystallographically, they do so at rates just slightly higher than those of the long cracks.

The stage I to stage II transition usually occurs at the first grain boundaries [EVI 98], but crystallographic cracks presenting marked interactions with the microstructure (slowing down at the grain boundaries, and an irregular front) were observed in certain conditions up to 10 times the grain size [RAV 97, ZHA 02]. An inert environment encourages a long propagation in stage I, whereas an average tensile stress can result in a more rapid stage I to stage II transition and even to the disappearance of stage I [EVI 98, PAT 99]. As is the case for long cracks, the transition would occur at the crack length where the size of the plastic zone exceeds the grain size [HAL 99, LAN 85]. In this case, the crack no longer behaves like a monocrystal. Several slip systems have to be activated within adjacent grains in order for their deformations to match.

In the context of multi-axial fatigue, we should mention that the term "stage I" is only valid for a crack within the first grains. Propagation within further grains, even if crystallographic, occurs in mode I – that is to say perpendicularly to the highest normal stress. After the first grains, a stage I-like crack becomes established that this time has a slower mechanism than stage II [PET 00] and should therefore give way to stage II.

The stage I to stage II transition corresponds perhaps to the strongest microstructural barrier to crack propagation. Miller [MIL 93] noticed that this transition phase, when a crack becomes deeper and wider through several grains with different sizes and crystallographic orientations it represents the main part of the fatigue life at a low stress level. It is also the main component of the fatigue strength of a material.

7.3.3. *Mechanically short cracks*

7.3.3.1. *Non-confined plasticity*

After a few grains, the crack growth from a smooth edge increases at a continuous rate with depth. In some studies, growth rates seem to be at the same level as the $da/dN - \Delta K$ curve of long cracks [NEW 00]. Other studies, however, show that they can also be higher than the rates of long cracks at a given ΔK [ESP 95, LUO 04]. Thanks to an indirect technique using the response of miniature deformation gauges, Espinosa studied the behavior of semi-elliptical cracks ($0.7 < a/c < 1.1$) growing between a depth of 100 and 500 μm at the surface of an offshore construction steel [ESP 95, VER 97]. On a $da/dN - K_{max}$ graph, the rates of these

cracks at $R = 0$ and $R = -1$ appear between 10 and 100 times higher than the rates of long cracks growing at a low stress level (see Figure 7.5).

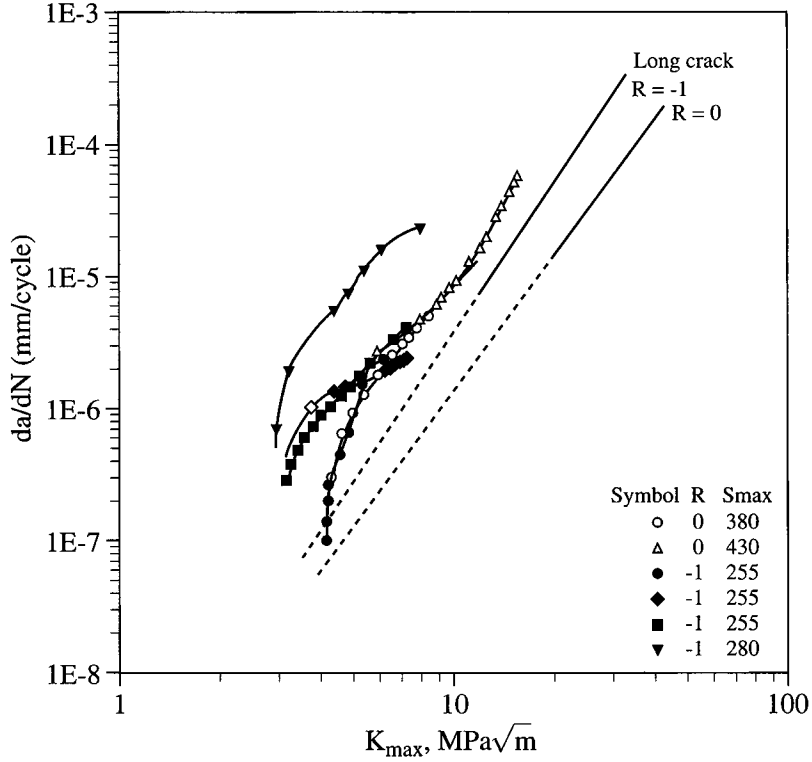

Figure 7.5. *Propagation rates as a function of K_{max} for semi-elliptical cracks at the surface of smooth specimens made of structural steel (σ_{yc} = 265 MPa) [ESP 95]. The depth of the cracks, which varies from 100 μm to 500 μm, exceeds the grain size, which is about 30 μm*

In addition to the closure effects that will be presented in section 7.4.2, this type of divergence is understandable since, to apply the LEFM theory, the plasticity has to be confined at the notch root ($r_p/a << 1$) and be completely constrained by an elastic region. As we said in section 7.2.1, however, this condition is no longer fulfilled for the high values of nominal stress that are necessary to get the short crack to grow. The crack is then termed "mechanically short".

Lankford *et al.* [LAN 84] and Davidson and Lankford [DAV 86], using techniques of retro-diffused electron diffraction and of stereoimaging, found a value of r_p/a of about unity ($S_{max}/\sigma_y = 0.8$) for short cracks, whereas for long cracks, r_p/a

was far lower than unity ($S_{max}/\sigma_y = 0.2$). At $R = 0.1$, the sizes of the monotonous and cyclic plastic zones were almost the same for short cracks, whereas for long cracks the LEFM predicts a ratio of 1/4.

In a recent article, Davidson summarized the main differences observed between short and long cracks [DAV 04]. He highlights that, close to the threshold, the long ones at the same ΔK value, due to the absence of stress triaxiality. Although long cracks often propagate under plane strain, short cracks undergo an almost plane stress state as long as they make a small perturbation within a uniaxial field.

Finite element calculations also show that the plastic zones are more easily developed when the crack is short, and that they reach the free surface under high nominal stress [CHI 82, ESP 95, RIT 87]. At the same value of ΔK, the plastic zone of a short crack is eight times larger than the one of a long crack [RIT 87], and more importantly plastic deformations compared to short cracks have been reported [CHI 82, ESP 95].

The increase in plastic deformation of short cracks, related to negative opening levels (see section 7.4.2), can explain more important damage and therefore higher propagation rates. Espinosa [ESP 95] highlights the fact that plastic deformation, which occurs ahead of short cracks spreads, farther from the crack tip than it does from long cracks. The damage could then start when the material elements are farther from the crack tip. A cracking model based on cumulative damage would be an interesting research topic.

7.3.3.2. *T stress*

Some authors have suggested other ideas that could explain the different behavior of mechanically short cracks. Even under pure elasticity, the singular term that corresponds to K is no longer enough to describe the stress and strain fields at the crack tip. We also have to consider a second parameter, the T stress, which corresponds to a higher-order term in the Williams series [LIN 95]:

$$\sigma_{ij}(r,\theta) = \frac{K}{\sqrt{2\pi r}} f_{ij}(\theta) + T\,\delta_{1i}\,\delta_{1j} \qquad [7.11]$$

This second term, which consists of a constant tensile or compressive normal stress in the cracking direction, affects the distribution of plastic strain around the crack. It is evident when comparing the effect of a uniaxial loading ($T < 0$) with the one of a bi-axial loading ($T = 0$) within a large cracked plate [RIE 02].

In addition, numerical analyses [BLO 90] and photoelasticity results [SMI 88] of surface and straight-fronted cracks show that the dominance of the inverse square

root singularity of the stress and strain fields is lost at the intersection of the crack with the free surface. Blom and Anderson [BLO 90] show, under isotropic elasticity, that this situation is still occurring under the surface at a depth up to about 2.5% of the material's thickness. This zone can contain a significant fraction of the short crack regime.

7.3.3.3. *Influence of a notch (stress concentration)*

When a short fatigue crack grows from a notch, its growth can be strongly influenced by the plastic deformation due to this notch. It is actually a mechanically short crack, whose size goes beyond the microstructure scale, but which is initially surrounded by the plastic zone of the notch.

On a $da/dN - \Delta K$ diagram, we can observe the three differences that were presented in the introduction (see Figure 7.4). If the notch is severe enough, the propagation rate can initially decrease before increasing again and reaching the rates of long cracks under confined plasticity. Nevertheless, when the nominal loading has a too low an amplitude, the propagation rate continues to decrease until the crack stops growing (see Figure 7.4, $\Delta S = 60$ MPa).

Here we observe the case of non-propagating cracks that Frost first described (see section 7.2.2). It seems that this notch effect is observed when the ratio R is low. Verreman *et al.* [VER 87], who studied stress-relieved welded joints made of mild steel (V-shaped notches with a low radius of curvature), did not observe any effect when $R = 0$, but found differences with respect to long cracks that are pronounced when R is negative ($R = -1$ and $R = -2$). We also know that a crack can grow at a given distance from a notch root under fully compressive loading ($R = -\infty$) [SUR 91].

Many geometric configurations have been studied in the past. Here we present two different ones:

– Shin and Smith [SHI 88] studied the behavior of thin plates (of 2 to 3 mm thickness) of different materials (stainless steel 316, low carbon steel and semi-hard aluminum alloy) mainly when $R = 0.05$. Semi-elliptic notches, with a 35 mm depth but variable curvature radius, were machined in these plates. Using an optical microscope, they observed straight-fronted cracks presenting abnormal behaviors up to a depth of 8 mm. Nevertheless, they were unable to record any initial decrease in crack growth rate of the bluntest notches, or when the ratio R was increased;

– Espinosa and Verreman [ESP 95, VER 97] tested mild steel specimens of significant thickness at $R = 0$ and $R = -1$. These specimens that are close to a plane strain state, have a cruciform profile where the notch is L-shaped with two possible curvature radii: 0.1 and 3 mm. The notch field has a low depth, of about 1 mm, but

the main part of the fatigue life is spent in this field. In specimens with a low curvature radius, they observed straight-fronted cracks or elongated semi-elliptical cracks that grew faster than long cracks and presented some decelerations at $R = -1$ up to a depth of 0.3 mm. However, the specimens with a curvature radius of 3 mm presented a behavior similar to the one observed in smooth specimens: a single crack with high *a/c* ratio, high but continuously increasing propagation rates (see Figure 7.5).

To describe the propagation of a mechanically short crack from the notch root, Smith and Miller [SMI 78] proposed that, when the crack is still within the plastic zone of the notch, its driving force is the sum of two contributions:

– the first from the plasticity of the notch;

– the second from the plasticity of the crack (see Figure 7.6).

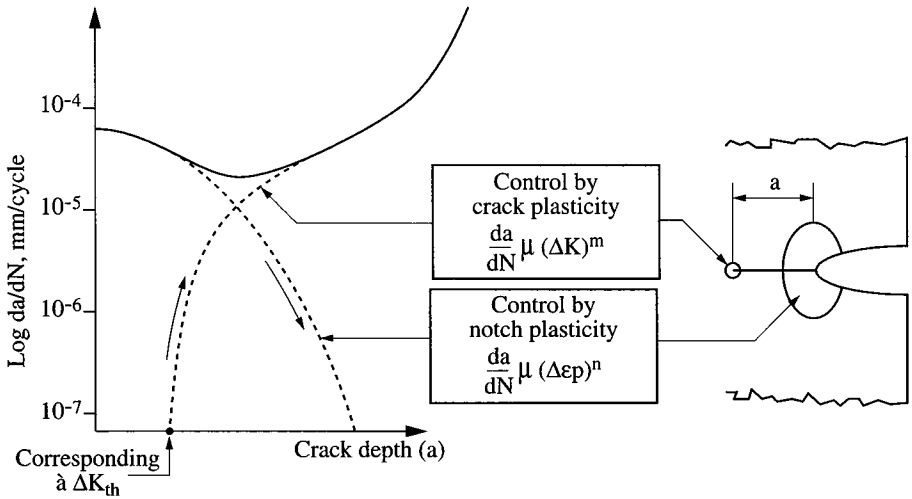

Figure 7.6. *Propagation rate of a crack from the notch root, according to Smith and Miller [SMI 78]. The driving force is the sum of the contributions of notch plasticity and crack plasticity*

LEFM under-estimates the propagation rate as it only considers the plasticity of the crack. The relative significance of every contribution depends on the loading level as well as the crack length. The contribution of the notch decreases when the crack grows, whereas the contribution of the crack increases as a power function of ΔK. If the contribution of the notch decreases more rapidly than the contribution of the crack increases, propagation will slow down and the crack will no longer grow

if, out of the plastic zone of the notch, the plasticity of the crack is not high enough ($\Delta K < \Delta K_{th}$).

The proposition suggested by Smith and Miller seems to be in agreement with experimental results. Leis roughly found a one-to-one correspondence between the extent of the plastic zone and the transition length where cracks reach the LEFM behavior, for different notch geometries and loading levels, the crack lengths concerned varying from 50 μm to 12 mm [LEI 82]. Verreman also showed that the transition length of cracks growing at the toe of stress-relieved welded joints increases with loading level and is comparable to the size of the notch's plastic zone [VER 86].

Nevertheless, some other authors reported that the short crack effect can still occur beyond this zone [SHI 88]. With 3D finite elements Espinosa and Verreman [ESP 95, VER 97] precisely calculated the plastic flow around their L-shaped notch: the plastic zone depth did not go beyond 0.1 mm for the highest stress levels, whereas they observed some decelerations in propagation up to 0.3 mm.

We may wonder whether the diagram in Figure 7.6 is correct from a theoretical point of view. If we do not consider the cyclic nature of the mechanical stress, the plastic deformation at the crack tip should always increase when the crack grows from a notch root (under a constant nominal stress). If we consider the extreme case of a notch whose shape is close to a crack, for instance a saw cut, the plastic deformation always increases with the extension of this crack, whereas in this case we still observe an initial deceleration in propagation [SHI 88].

We then have to consider another mechanism: the progressive development of the closure of a crack that leads to a decrease in amplitude of cyclic deformation at the crack tip. The notch plasticity is certainly significant, as the closure level will become steady after the crack extends beyond the initial plastic zone. What really makes propagation slow down, however, is the decrease in amplitude of plastic deformation at the crack tip, which is produced by the development of crack closure. The authors, who measured the evolution of closure level in parallel to crack propagation, agree that the lowest propagation rate occurs when crack closure reaches its highest level.

7.4. Role of closure in the behavior of short cracks

7.4.1. *Closure of fatigue cracks*

The concept of the closure of plasticity-induced cracks was introduced by Elber [ELB 70], who observed the premature contact of the crack lips during unloading

when the nominal stress was still positive. During the propagation of the crack, a zone of residual plastic elongations is left in its wake, thus decreasing the driving force of the crack propagation. Considering that a crack can only grow when it is entirely open, Elber then concluded that in the Paris equation, $da/dN = C(\Delta K)^m$, the total variation of stress intensity factor has to be replaced by its effective variation:

$$\Delta K_{eff} = K_{\max} - K_{op} \qquad [7.12]$$

where K_{max} is the maximum stress intensity factor, and K_{op} the stress intensity factor corresponding to the nominal stress necessary to entirely open the crack. Elber found that the effective fraction of the amplitude of the stress intensity factor:

$$U = \frac{\Delta K_{eff}}{\Delta K} \qquad [7.13]$$

is a linear function of the R ratio:

$$U = 0.5 + 0.4\,R \qquad [7.14]$$

for the conditions he studied (thin plates made of an aluminum alloy, $-0.1 < R < 0.7$). The propagation rates obtained for different R ratios are consolidated close to the same line in a log da/dN – log ΔK_{eff} graph.

Newman [NEW 81] developed a semi-analytical method in order to calculate plasticity-induced crack closure as a function of R, the nominal stress level and the stress triaxiality. This method is based on a Dugdale model that was modified to leave residual plastic elongations within the wake of the crack. The closure is more important for plane stress than for plane strain but it disappears in every case when R is high enough (see Figure 7.7). In addition, the closure level decreases when the nominal stress increases, especially in the case of a plane stress state. It comes close to zero and even becomes negative when plasticity is extensive. These results are in good agreement with more recent studies [PAN 01].

Nowadays, the finite element method is a tool that is being increasingly used to model plasticity-induced crack closure [SOL 04]. More complex problems have been analyzed (for instance, the influence of geometry and influence of consolidation), but improvements have still to be made (propagation of a semi-elliptical crack, variable amplitude loading, etc.).

The concept of closure and the use of ΔK_{eff} has allowed many authors to interpret, or even rationalize, several aspects of the propagation of fatigue cracks: the effects of the R ratio and of the thickness; and the effects of residual stresses and variable amplitude loadings.

The literature tends also to highlight the significant role of closure in the behavior of mechanically short cracks. When a short crack presents a limited wake we can expect the closure effects to be less pronounced compared to a long crack. A higher effective driving force will lead then to a faster propagation and to a lower apparent threshold.

7.4.2. *Development of the closure of short cracks*

Espinosa and Verreman [ESP 95, VER 97] tested smooth and notched specimens made of mild steel at $R = 0$ and $R = -1$ (see section 7.3.3). They used miniature strain gauges in order to study the evolution of closure as a function of crack depth.

The notched specimens present a transient variation from $U = 1$ at $a = 0$ to a stabilized value typical of a long crack under confined plasticity ($U \cong 0.6$ when $R = 0$ and $U \cong 0.3$ when $R = -1$). The depth of stabilization is about 0.1 to 0.3 mm. The significant variation of U when $R = -1$ explains the deceleration of the crack that was observed in this case.

Within smooth specimens where the nominal stress is the highest, U always remains equal to 1 when $R = 0$ and it is always above 0.5 when $R = -1$ for any crack length. This behavior is predicted by calculations (see Figure 7.7). It explains that the propagation rate is one order of magnitude higher than that for long cracks under confined plasticity (see Figure 7.5).

The available studies usually show that short cracks initially open at a level close to the minimum load (negative values when R is negative, and close to zero when $R = 0$). During crack propagation, there is a progressive increase in opening level to reach a stabilized level that is equal to or lower than that of long cracks under confined plasticity. This transient variation, where the opening level increases and stabilizes, was observed in the case of short cracks growing from a smooth surface [JAM 89, JON 96, LEE 86] and from the root of a notch [SAV 94, TAN 83, VER 86]. Figure 7.8 shows the evolution of the opening level of elongated cracks that grow from the toe of stress-relieved fillet-welded joints made of mild steel (V-shaped severe notch) when $R = -1$ [VER 86]. This study shows a correlation between the depth of the crack where U becomes stabilized and the extent of the notch plastic zone.

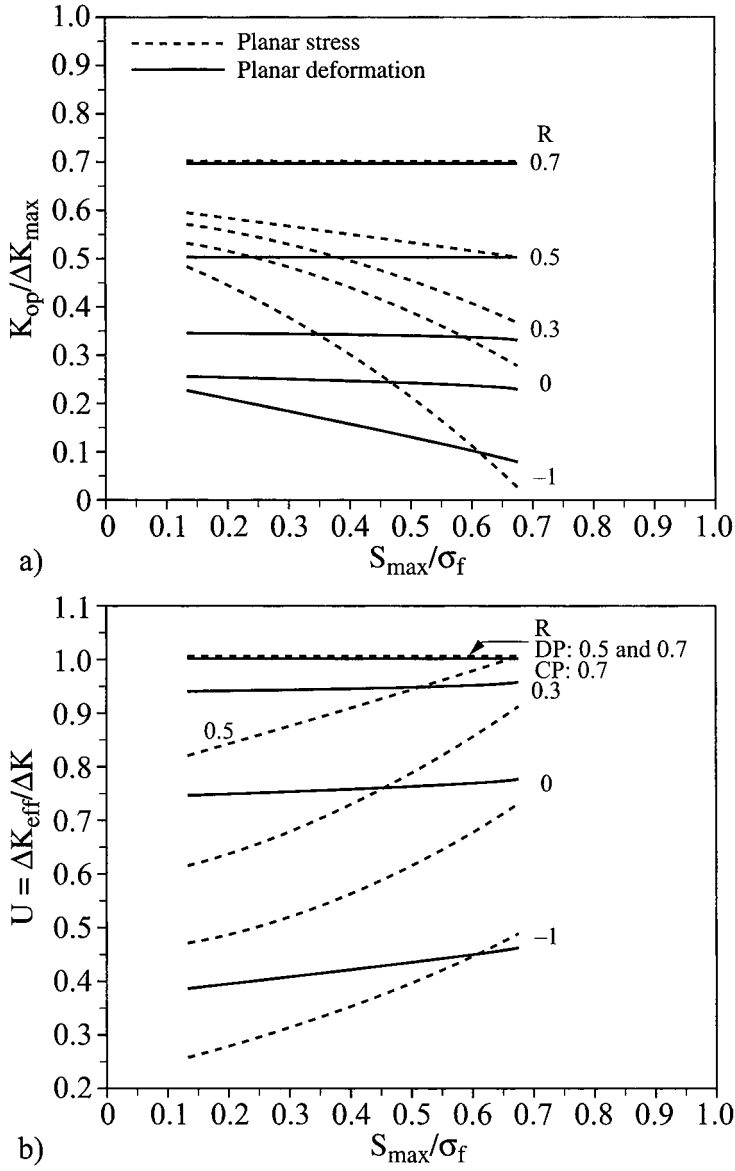

Figure 7.7. *Effects of stress level and of R ratio on plasticity-induced crack closure under plane stress and plane strain [NEW 81]: a) relative opening level; and b) effective fraction of the cycle as a function of* S_{max}/σ_f; $\sigma_f = (\sigma_y + \sigma_{UTS})/2$

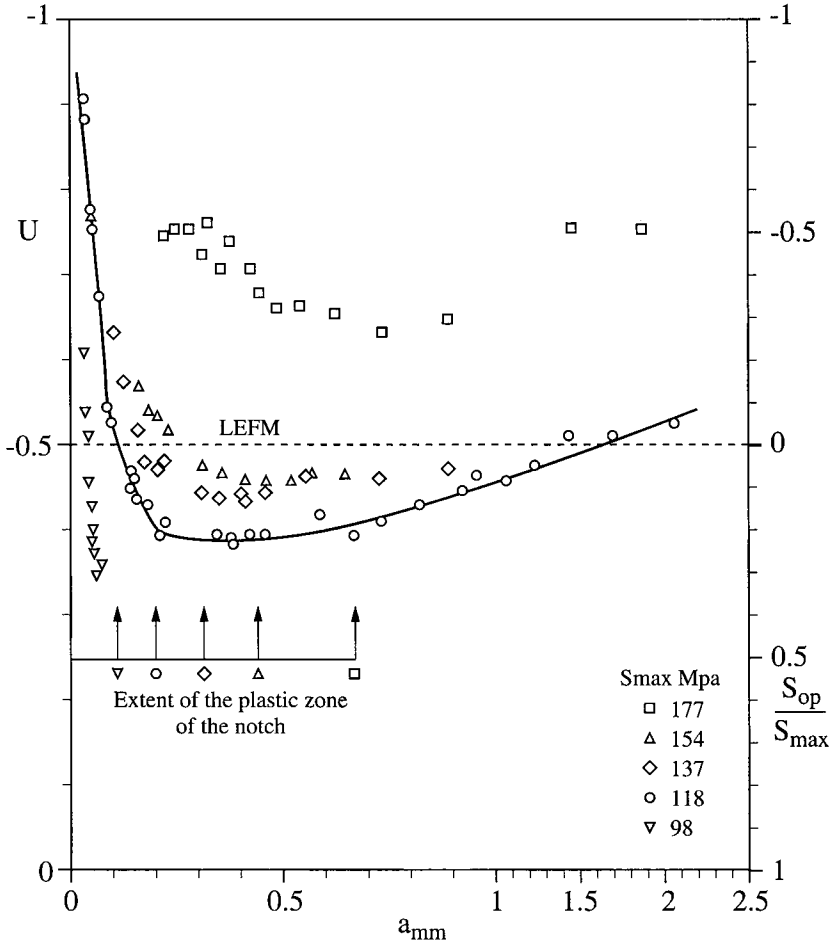

Figure 7.8. *Evolution of the opening level with the depth of crack that is growing from a V-shaped severe notch; mild steel, R = -1, σ_{yc} = 167 MPa [VER 86]*

7.4.3. *Correlation between propagation rates and ΔK_{eff}*

The use of ΔK_{eff} in order to determine the effect of closure on the propagation of fatigue cracks usually manages to eliminate differences between the propagation rates of short and long cracks, with short cracks growing from a smooth surface [NAD 97, RAV 97b, VER 97] or growing at a notch root [SHI 88, TAN 83, VER 86].

The variations of U or of S_{op}/S_{max} presented in Figure 7.8 in the case of a severe notch with $R = -1$ enables us to understand that:

– the initial propagation rates were more than one order of magnitude higher than those of long cracks at the same ΔK;

– the decrease in propagation rate: even if ΔK increases with crack length, the decrease in U is significant enough to lead to the decrease in ΔK_{eff};

– the existence of a non-propagating crack at the lowest level of nominal stress ($S_{max} = 98$ MPa).

In addition, the short crack effect was less pronounced when $R = 0$, where lower variations in U were recorded, and the opposite occurred when $R = -2$ [VER 87].

Within severe notches, factor ΔK_{eff} is at its lowest when the opening level reaches its highest value or when it gets close to this value. Several authors have associated this moment to the one where the propagation rate is at its lowest value [SHI 88, TAN 83, VER 86, VER 97]. This agreement shows the role of closure in the behavior of short cracks. Nevertheless, the use of factor ΔK_{eff} as a correlation parameter is questionable. In the cases of cracks that are becoming increasingly short, its value has to decrease in order to tend towards zero when $a = 0$; and the notion of stress intensity factor theoretically has no more meaning when the plasticity is not confined within the crack tip. Experimentally, some differences have been observed by different authors. For instance, Jono and Sugeta [JON 96] correlated the propagation rates of short and long cracks with ΔK_{eff} within a HT80 steel, but they observed some differences for a titanium alloy.

7.4.4. *Roughness-induced crack closure*

Other closure mechanisms can be observed, especially the roughness–induced crack closure surfaces [SUR 91, WAL 79]. This closure occurs in the case of crystallographic propagation at the propagation threshold. Local mode II displacements prevent the two fracture surfaces fitting perfectly during unloading which leads to a very high closure level when the crack opening displacement is low. This closure mechanism was identified as the one resulting in the effect of grain size on propagation threshold [BAI 80].

For long cracks within an aluminum alloy 7075-T651 tested at $R = 0$, Lankford and Davidson reported that U decreases towards zero ($K_{op} \rightarrow K_{max}$) when ΔK decreases towards the threshold. For short cracks within the same alloy, U remains more or less constant at around 0.4, even with the smallest crack lengths [DAV 04]. Some measurements, that were made *in situ* under a scanning electron microscope,

suggest that closures induced by the plasticity and roughness should be combined in order to better understand the behavior of short cracks [ZHA 97].

7.5. Modeling of the behavior of short cracks

7.5.1. *Modeling of microstructurally short cracks*

Several models were proposed to describe the propagation of small cracks, remaining at the microstructure scale (see section 7.3.2). They consider in particular that grain boundaries and other microstructural barriers hinder crack propagation.

7.5.1.1. *Hobson's model*

According to Hobson *et al.* [HOB 86], the propagation rate at any crack length can be calculated as the sum of two terms:

– the first one, which characterizes short cracks, predicts the slowing down of the crack as it gets close to the microstructural barrier (grain boundary or other metallurgical obstacle);

– whereas the second one, which characterizes long cracks, predicts the acceleration of the crack.

These two terms respectively are:

$$\frac{da}{dN} = B_1 \left(\Delta S\right)^m (d - a) \qquad [7.15]$$

$$\frac{da}{dN} = B_2 \left(\Delta \varepsilon\right)^n a - B_3 \qquad [7.16]$$

where B_1, B_2, B_3, m, n and d are material constants, and ΔS and $\Delta \varepsilon$ are the nominal stress and strain ranges ($\Delta \varepsilon$ being equal to $\Delta S/E$ when there is no macroscopic plastic deformation). The constant d, which represents the distance at the microstructural barrier, is empirically determined by representing the experimental data on a $da/dN - a$ graph, and then by extrapolating at zero a linear regression carried out on the first points where the propagation rate is decreasing.

Figure 7.9 presents the predictions of the model for three levels of applied stress. The stress level has to be high enough otherwise the crack will stop when $a = d$. When the stress level increases, the crack growth rate becomes higher and there are less significant decelerations. This is observed during the experiments. Brown [BRO 86] used the Hobson model to reproduce the Kitagawa diagram with an iso-rate

curve of 10^{-7} mm/cycle = 0.1 nm/cycle (see Figure 7.10). On the $\Delta S - a$ plane, Brown also represents other higher iso-rates and he distinguishes on it different behavior regimes. The diagram shows that, under constant loading amplitude, a crack can be initiated below ΔS_0, but it does not continue to propagate when it approaches the microstructural barrier.

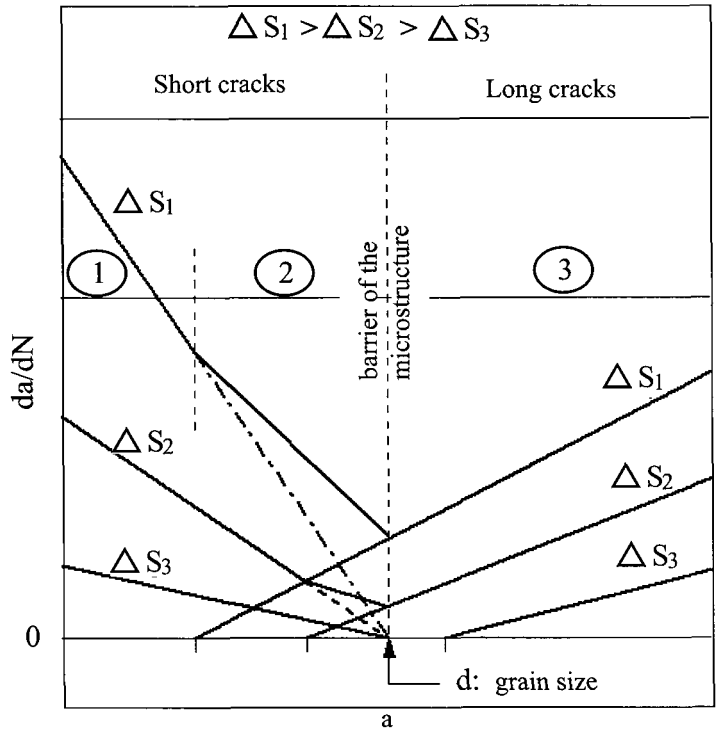

Figure 7.9. *Hobson et al.'s model of the behavior of microstructurally short cracks [HOB 86]. Propagation rate is shown as a function of crack length for three levels of applied stress. At the intermediate level two equations, [7.15] and [7.16], are added*

Hobson's model only considers one microstructural barrier, and this barrier is the most disturbing one. Some other models try to consider several barriers met by the crack.

Yates and Grabowski [YAT 90] used the Hobson model in order to describe the propagation of a crack beyond the first grain. Cracking in stage I is characterized by equation [7.15], expressed in terms of strain, but this time d represents the distance

between the initiation site and the next barrier. The propagation of long cracks (stage II) is described by Paris' equation. The transition from stage I to stage II occurs when the propagation rate of long cracks exceeds that of short cracks in stage I.

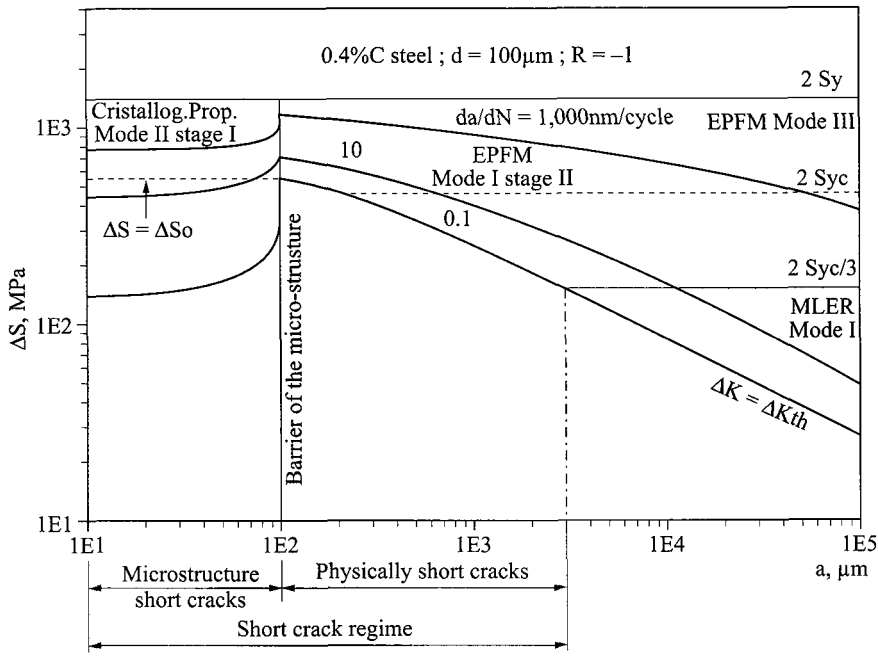

Figure 7.10. *Generalization of the Kitagawa diagram [BRO 86] according to the predictions of Hobson's model [HOB 86]*

Grabowski and King [GRA 92] developed a model that can be applied to a nickel-based super-alloy – the Waspaloy – which presents a faceted fracture. According to this model, propagation occurs at a high rate, as in a crystal, but is slowed down by two types of microstructural barriers:

– the grain boundaries (strong barriers) that strongly hinder propagation by decreasing the rate until it reaches a minimum level; and

– defects within the grain (weak barriers), like annealing twins, which lead to deviation of the crack and to its propagation slowing down at an intermediate level.

McDowell proposed a generalization of the Hobson model to multi-axial fatigue using the concept of critical plane [DOW 97]. He considers just one microstructural barrier, but he distinguishes three different regimes corresponding to the three zones of Kitagawa diagram ($a < a_1$, $a_1 < a < a_2$ and $a > a_2$; see Figure 7.1).

7.5.1.2. *Navarro and de los Rios model*

The Navarro and de los Rios [NAV 88] model is based on the idealization of a crack that grows along a persistent slip band whose end is blocked at a grain boundary. The propagation rate is proportional to the plastic displacement in mode II at the crack tip, $\Delta CTSD$:

$$\frac{da}{dN} = f.\Delta CTSD \qquad with \qquad \Delta CTSD = \frac{2k}{G}\frac{\sqrt{1-n^2}}{n}\Delta S\, a \qquad [7.17]$$

where G is the shearing modulus, ΔS is the applied stress, and $k = 1$ or $k = 1 - \nu$ if we consider screw or edge dislocations. Parameter n is the ratio between the crack length a and the sum of length a and the extent of the plastic zone (persistent slip band blocked at a grain boundary).

According to the model, the crack slows down by growing towards the grain boundary until n reaches a critical value for which stress concentration within the adjacent grain triggers a new persistent slip band. Parameter n then suddenly decreases and the crack grows rapidly before it slows down again as it gets close to the grain boundary.

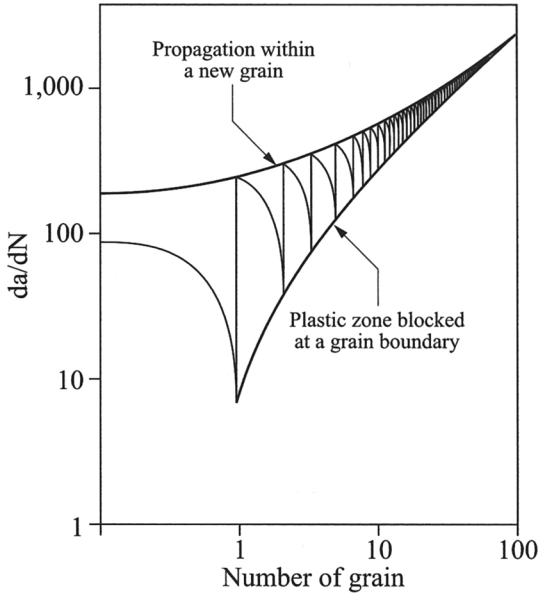

Figure 7.11. *Oscillations of plastic displacement at the crack tip and of the propagation rate according to the Navarro-Rios model [NAV 88]*

Figure 7.11 schematically illustrates the predictions of the Navarro-Rios model. The propagation rate oscillates between two envelopes whose gap rapidly narrows after crossing a few grains.

Turnbull and de los Rios compared the $da/dN - a$ data from a commercially pure aluminum alloy with the predictions of Navarro-Rios and Hobson's models [TUR 95]. They obtained better life predictions with the Navarro-Rios model, even if this model only has two adjustable constants instead of four (as is the case with Hobson's model).

Hussain also made some comparisons between different experimental data and the predictions of Navarro-Rios; and Hobson's models [HUS 97]. He suggested a variant of Navarro-Rios' model where the decelerations/accelerations of the crack do not occur after three to four grains, as is observed experimentally.

Based on Navarro-Rios' model, Rodopoulos [ROD 02] proposes two equations that would predict the behavior of both short and long cracks:

– one of them gives the stress amplitude at the propagation threshold as a function of crack length; it includes a crystallographic orientation factor in order to incorporate the increasing number of grains that are crossed by the crack front during propagation;

– the other one gives the stress amplitude at the transition between stage I to stage II as a function of crack length; this amplitude makes the size of the cyclic plastic zone twice as large as the average grain size.

These two equations correspond to two decreasing curves in the Kitagawa diagram (the second one being above the first one). The propagation regime in stage I (the surface between the two curves) gets smaller when the ratio of yield stress on the material strength decreases and when the ratio R increases [ROD 04]. Stage I entirely disappears when $R = 0.5$. The predictions are confirmed by data obtained with an aluminum alloy 2024-T351.

7.5.1.3. *Current tendencies*

Navarro-Rios' model is based on a physical description of the microstructurally short cracks. The reality, however, is simplified: progression of the crack in one dimension, sliding on a single plane per grain, assumptions where we want to calculate the displacement at the crack tip. The model does not consider several tri-dimensional aspects, such as the predominant influence of rotation angle of the crack with respect to inclination angle (see section 7.3.2.1) and the irregularity of the crack front (see section 7.3.2.3). This evolution does not come down to the variation of a single crack "length".

Several authors are currently developing numerical models that try to deal with the physical complexity of cracking at microstructure scale. The combined use of the finite element method and crystal plasticity theory is one of the models being used. The growth of a planar crack within an aluminum grain possessing different crystallographic orientations was studied using a bi-dimensional model (two sliding planes) [POT 04], and then a tri-dimensional model (12 sliding systems) [JOH 06]. These studies showed how the shape and extent of the plastic zone, the displacements at the crack tip and the crack opening levels vary as a function of grain orientation.

Lillbacka [LIL 06] built a "numerical crystal" made of two grains with a face-centered cubic structure within a set of grains with a body-centered cubic structure (austenitic-ferritic steel). A crack is initiated and propagates on a sliding plane of the first austenitic grain, and then turns towards another plane within the second grain. The result of the calculation (in two dimensions) shows that the evolution of the displacement in mode II at the crack tip ($\Delta CTSD$) as a function of crack length, thus the evolution of the crack propagation rate, is strongly influenced by the crystallographic disorientation between both austenitic grains.

7.5.2. *Modeling of mechanically short cracks*

Many microstructurally short cracks are also mechanically short, but here we will focus on short cracks whose size goes beyond the microstructure scale. Within this regime, continuum mechanics can be applied, even if the condition of confined plasticity is not respected or the closure significantly influences propagation due to fatigue. Different approaches have been proposed in order to predict the behavior of mechanically short cracks.

7.5.2.1. *Empirical approaches*

Some authors suggested describing the propagation rates of short cracks using an equation of the type:

$$da / dN = D\,\Delta S^n\, a \qquad [7.18]$$

where D and n are material constants that are determined by adjustment with the experimental data. This approach, which is not based on the principles of fracture mechanics, was proposed, for instance, by Nisitani for different steels [NIS 86]. Although it should be equal to two for a long crack under confined plasticity, exponent n varies from 3 to 8.5 depending on the material. Note that these values are approximately in inverse proportion to exponent b in Basquin's law for S-N curves.

By saying that plastic deformation of surface grains is more important because of there is no stress triaxiality, El Haddad *et al.* [HAD 79] proposed to increase the real crack length of the fictive length $a_o = (1/\pi)(\Delta K_{th}/\Delta S_o)^2$. In addition, according to an initial idea proposed by Haigh and Skelton, they replaced ΔS with $E\Delta\varepsilon$ within the expression of ΔK so they obtained a "strain intensity factor":

$$\Delta K_\varepsilon = E\,\Delta\varepsilon\sqrt{\pi(a+a_0)} \qquad [7.19]$$

where $\Delta\varepsilon$ is the amplitude of the local deformation when there is no crack. This parameter allowed the data of short cracks to be consolidated with the ones of long cracks for smooth and notched specimens made of steel.

Such a consolidation, however, was not observed by other authors. Lankford *et al.* [LAN 84] used ΔK_ε to correlate the data obtained with smooth specimens made of an aluminum alloy. This parameter allowed the correlation of the data obtained in laboratory air, but the opposite occurred when data were obtained under a vacuum. They thus concluded that the success obtained in the first case was just chance.

The approach of El Haddad has no real physical meaning. The advantage of adding the fictitious length a_o to the real length is to enable us to model the curves of Figures 7.1a and 7.1b (Kitagawa diagram) using the two following equations:

$$\Delta S = \Delta K_{th} / \sqrt{\pi(a+a_0)} \qquad [7.20]$$

$$\Delta K = \Delta K_{th} \sqrt{a/(a+a_0)} \qquad [7.21]$$

The approach of El Haddad also allows us to consider higher rates in the case of short cracks, but its use is questionable when describing their deceleration at a notch tip (see section 7.3.3.3). Note that geometry correction factor Y in the expression of a_o (see equation [7.1]) is omitted for simplicity; it is not necessarily equal to one.

Other authors proposed approaches similar to that of El Haddad, where the driving force is not equal to zero when $a \to 0$ but tends to ΔK when $a \to \infty$. For instance, Kfouri suggests the use of parameter $\Delta\sigma(\pi a_o)^{1/2}$ where $\Delta\sigma$ is the stress amplitude at a distance $a_o/2$ from the crack tip [KFO 97]. This approach was inspired by the concept of critical distance [TAY 00].

7.5.2.2. *Effective variation of the stress intensity factor*

As the influence of plasticity-induced crack closure has been observed by numerous experiments, it is natural for us to try to model the behavior of short cracks using a Paris-Elber equation:

$$da/dN = C\,(\Delta K_{eff})^m = C\,(U\Delta K)^m \qquad [7.22]$$

where U is the effective fraction of the cycle.

We can also predict the threshold of short cracks by introducing an effective threshold:

$$\Delta K_{th} = \Delta K_{eff,th}/U \qquad [7.23]$$

Some models, such as the Newman one, can be used to appreciate the increase of U in the regime of short cracks. Nevertheless, this type of calculation is made in two dimensions and it is sensitive to the plastic constraint factor resulting from stress triaxiality. In addition, it can lead to non-conservative predictions if, instead of a plastic wake of constant thickness, we consider a linear variation of the wake with the crack length [ROS 01]. On the other hand, in practice it seems acceptable to predict the rate of short cracks by simply using the data from long cracks where closure is negligible ($U \cong 1$ when R is high).

A few authors used the finite element method in two dimensions to calculate the evolution of the opening level of a crack growing from a notch root (see Figure 7.8). Different geometric configurations were studied [CLU 92, SAN 02, SUN 90]. For instance, we can refer to Sun and Sehitoglu who developed a model under plane stress regarding the propagation of a crack from severe lateral notches ($3 \leq k_t \leq 7$; $0.4 \leq S_{max}/\sigma_y \leq 0.8$). This model predicts the conditions which favor the rapid decrease of factor U, thus the slowing down of the propagation and the possibility of getting non-propagating cracks (high k_t, low S_{max}/σ_y, negative R ratio). In the opposite conditions, the crack propagates at a growing rate until the final fracture. The predictions match the experimental results.

7.5.2.3. *Elastic plastic fracture mechanics (EPFM)*

Even if it takes into account the closure phenomenon, the ΔK_{eff} parameter is not theoretically valid, as the notion of stress intensity factor no longer makes sense if plasticity is not confined at the crack tip. When the nominal stress is of about 0.5-0.7 σ_y, it can still be correct to use K, providing a first-order plastic correction is made, such as the Irwin correction [ISH 02]. Nevertheless, when the nominal stress gets close to σ_y, the plasticity becomes generalized. Factor K should then be replaced by an EPFM parameter, such as the J-integral.

Dowling was the first to use a ΔJ parameter to correlate the behavior of short cracks under extensive plasticity [DOW 77]. He reported an excellent match between the behavior of small surface cracks and that of long cracks within a steel A533B, except for cracks with a length below 0.18 mm where continuum mechanics

can no longer be applied. Nevertheless, such a match was not verified in later studies, such as [LEI 82]. Recently, Laue and Bomas [LAU 06] reused an approximate formulation of J that was previously proposed by Dowling. They tried to correlate the rates of short and long cracks within 1017 steel with a parameter that takes crack closure within the elastic and plastic parts of J into account:

$$\Delta J_{eff} = \left[1.24 \frac{\Delta S_{eff}^{\ 2}}{E} + \frac{1.02}{\sqrt{n'}} \Delta S_{eff} \Delta \varepsilon_{p,eff} \right] . a \qquad [7.24]$$

where n' is the cyclic consolidation exponent of the material. Nevertheless, they underwent some problems, including an overestimation of short crack growth rates within the domain of high-cycle fatigue.

The application of J to a cyclic loading has always been questioned in the literature. Although some authors now use ΔJ in the case of multi-axial fatigue [HOF 06], others still question its theoretical basis [RIE 02]. A second parameter that proposed to rationalize the behavior of mechanically short cracks is the cyclic plastic displacement at the crack tip [PAN 01]. It is defined by:

$$\Delta CTOD = \delta_{\max} - \delta_R \qquad [7.25]$$

where δ_{max} is stretching at the crack tip at maximum load and δ_R is the residual plastic stretching at minimum load.

Analytical solutions were obtained in the case of Dugdale's model [ROS 01]. The cyclic displacement $\Delta CTOD$ is proportional to $\Delta S^n.a$ (high n), which was brought close to the experimental equation of Nisitani [7.18]. In addition, the ratio δ_R/δ_{max} is as high as 0.8 when $S_{max}/\sigma_y = 0.2$ but it rapidly decreases (at $R < 0$) when the nominal stress increases.

7.5.2.4. *A new approach to predicting the life of notched components*

Even though some methodologies were developed in particular cases [NEW 00], applying fracture mechanics to the prediction of fatigue life consumed in the regime of short cracks is not that easy. The integration of equation [7.22] presents several unknown variables or uncertainties:

- initial dimensions of the crack;
- evolution of the aspect ratio a/2c;
- solutions of K or J as a function of a;
- evolution of U as a function of a; etc.

To predict the macroscopic "initiation" life at the notch root, the engineer usually relies on traditional methods based on local stress or strain amplitude. Within the domain of high-cycle fatigue, some empirical equations (Peterson, Neuber, etc.) are available to calculate the fatigue notch factor k_f, i.e. the reduction in strength with respect to the unnotched material. Factor k_f, which can be significantly lower than k_t, depends on geometry and loading but also on the material and number of cycles. Most of the time, the formulae are inaccurate [BRA 80].

Several authors used the old concept of critical distance or volume to interpret and predict sensitivity to the notch effect in different conditions [KAD 02, TAY 00]. The material is not sensitive to maximum stress at the notch root but it is, for instance, sensitive to the local stress at a certain distance from the notch root. This "critical distance" r_c depends on the material. It can be determined by considering the extreme case of a notch turning into a crack [TAY 00]:

$$r_c = \frac{1}{2\pi}\left(\frac{\Delta K_{th}}{\Delta S_0}\right)^2 \qquad [7.26]$$

nevertheless, although the concept of critical distance or volume has been experimentally approved, it does not directly consider the initiation and propagation mechanisms of short cracks at the notch root. In addition, the critical distance r_c depends on the number of cycles considered.

Analysis of the propagation of short cracks leads to a more rational explanation of the notch effect. Figure 7.12 compares two typical evolutions of crack depth with the number of cycles recorded for mild steels at R = -1 within the domain of high-cycle fatigue [LAU 06, VER 97]. For the smooth specimen as well as for the severe notch, the macroscopic initiation life N_I (defined here by the crack depth $a_I = 0.5$ mm) represents most of the total life. Nevertheless, the parts relative to microscopic initiation life N_0 (microstructurally short cracks) and propagation life N_p (mechanically short cracks, up to a= 0.5 mm) are very different. Within the smooth specimen, most of the life N_I is spent during the initiation and propagation of microcracks ($N_I \cong N_0$; $N_p \cong 0$) whereas the opposite occurs at the root of a severe notch ($N_I \cong N_p$; $N_0 \cong 0$).

In the general case of a notch of arbitrary severity, the fatigue life can be split into two non-negligible parts:

$$N_I = N_0 + N_p \qquad [7.27]$$

dividing the S-N curve of a smooth sample by k_t will then lead to an over-estimation of the notch effect. The fatigue life taken for crack initiation is the same as the value

of local stress is $k_t.S$, but the fatigue life for crack propagation will be longer than in the case of smooth specimen. As a consequence, the total fatigue life is longer and the S-N curve higher than the one obtained by dividing with k_t; thus factor k_f is lower than k_t.

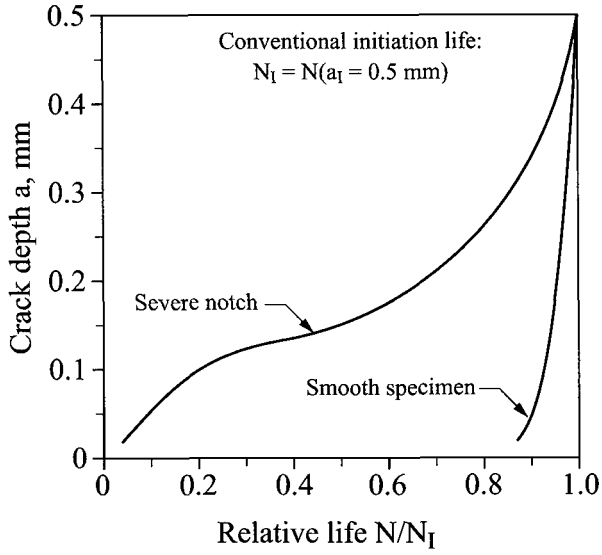

Figure 7.12. *Evolution of crack depth as a function of relative life within the domain of high-cycle fatigue*

A recent study enabled us to quantify the relative weight of N_0 and N_p within the life of V-notched components. The notch has a constant angle (for instance 90°) but has a variable size and curvature radius [VER 06, VER 08]. The initiation life is correlated with maximum stress at the notch root, whereas propagation life is correlated with the stress intensity factor of the notch's singular field. The study showed that fatigue is controlled by crack initiation ($k_f \cong k_t$) or by crack propagation ($k_f < k_t$), depending on:

– the severity of the notch (radius and size);

– the material resistance to crack initiation; and

– short crack propagation at the considered life.

Both resistances are determined by a SN curve, one measured with a smooth specimen the other measured with a specimen with a very severe notch ($\rho \rightarrow 0$). This new approach is interesting for two reasons:

– it enables us to understand the notch effect as a function of the physical mechanisms involved, i.e. crack initiation and short crack propagation;

– it enables us to perform a global prediction of the proportion of a material's macroscopic initiation life spent at the notch root without making any elastic plastic description of the propagation of short cracks. The notion of notch stress intensity factor is correct as long as the plastic zone is confined within the elastic singularity of the notch.

7.6. Conclusion

The propagation of short cracks is an important topic in the field of fatigue, as in most cases it represents the main part of the life of the parts in service, especially within the domain of high-cycle fatigue. In addition, fatigue strength can be controlled by a condition of propagation of a short crack. Reliable predictions of fatigue performance then require us to have a good understanding of the behavior of short cracks and of appropriate models.

The behavior of short cracks has been studied for the past 30 years and is still a really active research field. Many experimental results have been gathered for a wide variety of conditions and new concepts have been adopted by the scientific community, such as the interaction of cracks with microstructural barriers, and the development of crack closure at the notch root.

Nevertheless, from a quantitative point of view, most of the models are still limited to one or two dimensions and do not consider the tri-dimensional reality of crack propagation. Several aspects need to be better understood, such as the irregular evolution of the crack front, the stage I to stage II transition and, at the continuous mechanics scale, the cyclic plastic deformation around the front of a semi-elliptical crack.

If we have to consider the tri-dimensional complexity of the propagation of a crack to better understand its behavior, we also have to prepare simple and safe calculation tools to be used by the engineer. For instance, the approach based on the notch stress intensity factor allows us to make a global prediction of the macroscopic initiation life spent at the notch root.

Finally, the study of short cracks has to be extended to multi-axial fatigue and to variable amplitude loadings. It is not sufficient to "extrapolate" uniaxial behavior under constant amplitude loading. Several challenges still have to be addressed. The effect of the environment is important and needs to be taken into consideration. Also to date, very few studies on chemically short cracks have been carried out.

7.7. Acknowledgements

Thanks to the National Science and Engineering Research Council (NSERC) of Canada for the financial support of this work.

7.8. Bibliography

[BAI 80] J.P. Bailon, J. Masounave, J.I. Dickson, "Le seuil de propagation", in C. Bathias, J.P. Baïlon (eds.), *La fatigue des Matériaux et des Structures*, Maloine, Paris, p. 237-269, 1980.

[BLO 90] A.F. Blom, B. Anderson, "On the semi-elliptical surface crack problem: detailed numerical solutions for complete elastic stress fields, Surface-crack growth: models, experiments and structures", *ASTM STP 1060*, p. 77-98, 1990.

[BRA 80] A. Brand, R. Sutterlin, *Calcul des Pièces à la Fatigue, Méthode du Gradient*, CETIM, Senlis, France, 1980.

[BRO 83] C.W. Brown, M.A. Hicks, "A study of short fatigue crack growth behaviour in titanium alloy IMI 685", *Fatigue of Engineering Materials and Structures*, vol. 6, no. 1, p. 67-76, 1983.

[BRO 86] M.W. Brown, "Interfaces between short, long, and non-propagating cracks", *The Behaviour of Short Fatigue Cracks,* in K.J. Miller, E.R. de los Rios (eds.), EGF Pub. 1, Mechanical Eng. Pub., London, p. 423-439, 1986.

[CHA 88] K.S. Chan, J. Lankford, "The role of microstructural dissimilitude in fatigue and fracture of small cracks", *Acta metallurgica*, vol. 36, no. 1, p. 193-206, 1988.

[CHI 82] W.T. Chiang, K.J. Miller, "Elastic-plastic finite element analyses of short cracks", *Fatigue of Engineering Materials and Structures*, vol. 5, no. 3, p. 249-263, 1982.

[CLU 92] R.G. Mc Clung, H. Sehitoglu, "Closure and growth of fatigue cracks at notches", *Journal of Engineering Materials and Technology*, vol. 114, no. 1, p. 1-7, 1992.

[DAV 06] A. Davidkov, R. Pippan, "Studies on short fatigue crack propagation through a ferrite-pearlite microstructure", *Fatigue 2006, 9th International Fatigue Congress*, Elsevier Ltd, p. 10, 2006 (available on CD-ROM).

[DAV 04] D.L. Davidson, "Characterizing small fatigue cracks in metallic alloys", *Metallurgical and Materials Transactions A*, vol. 35 A, no. 1, p. 7-14, 2004.

[DAV 86] D.L. Davidson, J. Lankford, "High resolution techniques for the study of small cracks", in R.O. Ritchie, J. Lankford (eds.), *Small Fatigue Cracks,* Metallurgical Society of Aime, Warrendale, p. 455-470, 1986.

[DOW 97] D.L. Mc Dowell, "Multi-axial small fatigue crack growth in metals", *International Journal of Fatigue*, vol. 19, additional issue 1, p. S127-S135, 1997.

[DOW 77] N.E. Dowling, "Crack growth during low-cycle fatigue of smooth axial specimens, Cyclic stress-stress and plastic deformation aspect of fatigue crack growth", *ASTM STP 637*, p. 97-121, 1977.

[ELB 70] W. Elber, "Fatigue crack closure under cyclic tension", *Engineering Fracture Mechanics*, vol. 2, p. 37-45, 1970.

[ESP 95] G. Espinosa, La propagation de fissures courtes à partir d'entailles, PhD thesis, École Polytechnique de Montréal, 1995.

[EVI 98] A.J. Mc Evily, "The growth of short fatigue cracks: a review", *Materials Science Research International*, vol. 4, no. 1, p. 3-11, 1998.

[FRO 59] N.E. Frost, "A relation between the critical alternating propagation stress and crack length for mild steel", *Proceedings of the Institution of Mechanical Engineers*, vol. 173, no. 35, p. 811-827, 1959.

[GRA 92] L. Grabowski, J.E. King, "Modelling short crack behaviour in nickel-base superalloys", *Fatigue and Fracture of Engineering Materials and Structures*, vol. 15, no. 6, p. 595-606, 1992.

[HAD 79] M.H. El Haddad, K.N. Smith, T.H. Topper, "A stress based intensity factor solution for short fatigue cracks initiating from notches, Fracture Mechanics", *ASTM STP 677*, p. 274-289, 1979.

[HOB 86] P.D. Hobson *et al.*, "Two phases of short crack growth in a medium carbon steel", in K.J. Miller, E.R. De Los Rios (eds.), *The Behaviour of short fatigue cracks*, Mep, London, p. 441-459, 1986.

[HOF 06] J. Hoffmeyer Doring, T. Seeger, M. Vormwald, "Deformation behaviour, short crack growth and fatigue lives under multi-axial non-proportional loading", *International Journal of Fatigue*, vol. 28, no. 5-6, vol. 508-520, 2006.

[HUS 97] K. Hussain, "Short fatigue crack behaviour and analytical models: a review", *Engineering Fracture Mechanics*, vol. 58, no. 4, p. 327-354, 1997.

[ISH 02] S. Ishihara, A.J. Mc Evily, "Analysis of short fatigue crack growth in cast aluminum alloys", *International Journal of Fatigue*, vol. 24, no. 11, p. 1169-1174, 2002.

[JAM 89] M.N. James, W.N. Jr. Sharpe, "Closure development and crack opening displacement in the short crack regime for fine and coarse grained A533b steel", *Fatigue and Fracture of Engineering Materials and Structures*, vol. 12, no. 4, p. 347-361, 1989.

[JOH 06] S.R. Johnston, G.P. Potirniche, S.R. Daniewicz, M.F. Horstemeyer, "Three-dimensional finite element simulations of micro-structurally small fatigue crack growth in 7075 aluminum alloy", *Fatigue and Fracture of Engineering Materials and Structures*, vol. 29, no. 8, p. 597-605, 2006.

[JON 96] M. Jono, A. Sugeta, "Crack closure and effect of load variation on small fatigue crack growth behaviour", *Fatigue and Fracture of Engineering Materials and Structures*, vol. 19, no. 2-3, p. 165-174, 1996.

[KAD 02] N. Kadi, G. Pluvinage, "Analysis of fatigue failures for shafts with key-seats : application of a volumetric approach", in Wu X.R., Wang Z.G. (eds.), *Fatigue 2002*, vol. 3, Mep-Emas, p. 1865-1872, 2002.

[KFO 97] A.P. Kfouri, "Limitations on the use of the stress intensity factor K, as a fracture parameter in the fatigue propagation of short cracks", *Fatigue and Fracture of Engineering Materials and Structures*, vol. 20, no. 12, p. 1687-1698, 1997.

[KIT 76] H. Kitagawa, S. Takahashi, "Applicability of fracture mechanics to very small cracks or the cracks in the early stage", *Proc. 2nd Int. Conf. Mech. Behaviour of Materials*, Boston, p. 627-631, 1976.

[LAM 96] R.C. Mc Clung, K.S. Chan, S.J. Hudsak, D.L. Davidson, "Behavior of small fatigue cracks", in *ASM Handbook. Volume 19, Fatigue and Fracture*, ASM International, Materials Park, Ohio, p. 153-158, 1996.

[LAN 84] J. Lankford, D.L. Davidson, K.S. Chan, "Influence of crack tip plasticity in the growth of small fatigue cracks", *Metallurgical Transactions A*, vol. 15a, no. 8, p. 1579-1588, 1984.

[LAN 85] J. Lankford, "Influence of microstructure on the growth of small fatigue cracks", *Fatigue and Fracture of Engineering Materials and Structures*, vol. 8, no. 2, p. 161-175, 1985.

[LAU 06] S. Laue, H. Bomas, "Spectrum fatigue life assessment of notched specimens based on the initiation and propagation of short cracks", *International Journal of Fatigue*, vol. 28-29, p. 1011-1021, 2006.

[LEE 86] J.J. Lee, W.N. Jr. Sharpe, "Short cracks in notched aluminum specimens", in R.O., Ritchie, J. Lankford (eds.), *Small Fatigue Cracks,* Metallurgical Society of Aime, Warrendale, p. 323-339, 1986.

[LEI 82] B.N. Leis, "Fatigue crack propagation through inelastic gradient fields", *International Journal of Pressure Vessels and Piping*, vol. 10, p. 141-158, 1982.

[LI 01] W.F. Li, X.P. Zhang, "Investigation of initiation and growth behavior of short fatigue cracks emanating from a single edge notch specimen using in-situ sem", *Materials Science and Engineering A*, vol. 318, no. 1-2, p. 129-136, 2001.

[LIL 06] R. Lillbacka, E. Johnson, M. Ekh, "A model for short crack propagation in polycrystalline materials", *Engineering Fracture Mechanics*, vol. 73, no. 2, p. 223-232, 2006.

[LIN 95] T. Lindley, A. Pineau, "Short crack effects in fracture and fatigue", *Revue de Métallurgie*, vol. 92, no. 2, p.187-201, 1995.

[LUD 03] W. Ludwig, J.Y. Buffiere, S. Savelli, P. Cloetens, "Study of the interaction of a short fatigue crack with grain boundaries in a cast Al alloy using X-ray microtomography", *Acta Materialia*, vol. 51, no. 3, p. 585-598, 2003.

[LUO 04] J. Luo, P. Bowen, "Small and long fatigue crack growth behaviour of a Pm Ni-based duperalloy, Udimet 720", *International Journal of Fatigue*, vol. 26, no. 2, p. 113-124, 2004.

[MIL 93] K.J. Miller, "The two thresholds of fatigue behaviour", *Fatigue and Fracture of Engineering Materials and Structures*, vol. 16, no. 9, p. 931-939, 1993.

[MUR 02] Y. Murakami, *Metal Fatigue: Effects of Small Defects and Nonmetallic Inclusions*, 1st edn, Elsevier, Amsterdam, 2002.

[NAD 97] Y. Nadot, N. Ranganathan, J. Mendez, A.S. Beranger, "A study of natural cracks initiated on casting defects by crack front marking", *Scripta Materialia*, vol. 37 no. 5, p. 549-553, 1997.

[NAV 88] A. Navarro, E.R. De Los rios, "A micro-structurally-short fatigue crack growth equation", *Fatigue and Fracture of Engineering Materials and Structures*, vol. 11, p. 383-396, 1988.

[NEW 81] J.C. Jr. Newman, "A crack-closure model for predicting fatigue crack growth under aircraft spectrum loading, Methods and models for predicting fatigue crack growth under random loading", *ASTM STP 748*, p. 53-84, 1981.

[NEW 00] J.C. Newman, X.R. Wu, M.H. Swain, W. Zhao, E.P. Phillips, C.F. Ding, "Small-crack growth and fatigue life predictions for high-strength aluminum alloys. Ii. crack closure and fatigue analyses", *Fatigue and Fracture of Engineering Materials and Structures*, vol. 23, no. 1, p. 59-72, 2000.

[NIS 86] H. Nisitani, M. Goto, "A small-crack growth law and its application to the evaluation of fatigue life", in K.J. Miller, E.R. De Los Rios (eds.), *The Behaviour of Short Fatigue Cracks*, Mechanical Eng. Pub., London, p. 387-404, 1986.

[PAN 01] V.V. Panasyuk, O.Y. Andreykiv, R.O. Ritchie, O.I. Darchuk, "Estimation of the effects of plasticity and resulting crack closure during small fatigue crack growth", *International Journal of Fracture*, vol. 107, no. 2, p. 99-115, 2001.

[PAT 99] A.M. Patel, R.W. Neu, J.A. Pape, "Growth of small fatigue cracks in Ph 13-8 Mo stainless steel", *Metallurgical and Materials Transactions A*, vol. 30, no. 5, p. 1289-1300, 1999.

[PEA 75] S. Pearson, "Initiation of fatigue cracks in commercial aluminum alloy and the subsequent propagation of very short cracks", *Engineering Fracture Mechanics*, vol. 7, p. 235-247, 1975.

[PED 88] K. Pedersen, "Fatigue crack growth of short cracks in an Almgsi alloy", in C. Moura Branco, L. Guerra Rosa (eds.), *Advances in Fatigue Science and Technology*, Martinus Nijhoff Publishing, p. 773-783, 1988.

[PET 00] J. Petit, G. Henaff, C. Sarrazin-Baudoux, "Mechanisms and modeling of near-threshold fatigue crack propagation, Fatigue crack growth thresholds, endurance limits and design", *ASTM STP 1372*, p. 3-30, 2000.

[PIN 86] A. Pineau, "Short fatigue crack behavior in relation to three-dimensional aspects and crack closure effect", in R.O. Ritchie, J. Lankford (eds.), *Small Fatigue Cracks*, Metallurgical Society of Aime, Warrendale Pa, p. 191-211, 1986.

[POT 04] G.P. Potirniche, S.R. Daniewicz, J.C. Jr. Newman, "Simulating small crack growth behaviour using crystal plasticity theory and finite element analysis", *Fatigue and Fracture of Engineering Materials and Structures*, vol. 27, p. 59-71, 2004.

[RAV 97a] K.S. Ravichandran, "Effects of crack aspect ratio on the behavior of small surface cracks in fatigue: Part I. simulation", *Metallurgical and Materials Transactions*, vol. 28a, no. 1, p. 149-156, 1997.

[RAV 97b] K.S. Ravichandran, J.M. Larsen, "Effects of crack aspect ratio on the behavior of small surface cracks in fatigue: Part II. Experiments on a titanium (Ti-8al) alloy", *Metallurgical and Materials Transactions A*, vol. 28a, no. 1, p. 157-169, 1997.

[RIE 02] F.O. Riemelmoser, R. Pippan, "Consideration of the mechanical behaviour of small fatigue cracks", *International Journal of Fracture*, vol. 118, p. 251-270, 2002.

[RIT 87] R.O. Ritchie, W. Yu, A.F. Blom, D.K. Holm, "An analysis of crack tip shielding in aluminum alloy 2124: a comparison of large, small, through-thickness and surface fatigue cracks", *Fatigue and Fracture of Engineering Materials and Structures*, vol. 10, p. 343-362, 1987 Discussion/Responses, vol. 12, p. 71-75, 1989.

[ROD 02] C.A. Rodopoulos, E.R. De Los Rios, 'Theoretical analysis on the behaviour of short fatigue cracks", *International Journal of Fatigue*, vol. 24, no. 7, p. 719-724, 2002.

[ROD 04a] C.A. Rodopoulos, J.H. Choi, E.R. De Los Rios, J.R. Yates, "Stress ratio and the fatigue damage map - Part I: modeling", *International Journal of Fatigue*, vol. 26, no. 7, p. 739-746, 2004.

[ROD 04b] C.A. Rodopoulos, J.H. Choi, E.R. De Los Rios, J.R. Yates "Stress ratio and the fatigue damage map - Part II: The 2024-T351 aluminum alloy", *International Journal of Fatigue*, vol. 26, no. 7, p. 747-752, 2004.

[ROS 01] L.R.F. Rose, C.H. Wang, "Self-similar analysis of plasticity-induced closure of small fatigue cracks", *Journal of the Mechanics and Physics of Solids*, vol. 49, no. 2, p. 401-429, 2001.

[ROY 04] S. Roychowdhury, R. H. Jr. Dodds, "Effect of T-stress on fatigue crack closure in 3-D small-scale yielding", *International Journal of Solids and Structures*, vol. 41, no. 9-10, p. 2581-2606, 2004.

[SAN 02] F. Sansoz, B. Brethes, A. Pineau, "Propagation of short fatigue cracks from notches in a Ni base super-alloy: experiments and modeling", *Fatigue and Fracture of Engineering Materials and Structures*, vol. 25, no. 1, p. 41-53, 2002.

[SAV 94] G. Savaidiz, T. Seeger, "An experimental study on the opening and closure behaviour of fatigue surface, corner and through-thickness cracks at notches", *Fatigue and Fracture of Engineering Materials and Structures*, vol. 17, no. 11, p. 1343-1356, 1994.

[SHI 88] C.S. Shin, R.A. Smith, "Fatigue crack growth at stress concentrations-the role of notch plasticity and crack closure", *Engineering Fracture Mechanics*, vol. 29, p. 301-315, 1988.

[SMI 78] R.A. Smith, K.J. Miller, "Prediction of fatigue regimes in notched components", *International Journal of Mechanical Sciences,* vol. 20, p. 201-206, 1978.

[SMI 88] C.W. Smith, "Measurement of three-dimensional effects in fracture mechanics, Fracture Mechanics", *ASTM STP 969*, p. 5-18, 1988.

[SOL 04] K. Solanki, Jr. Newman, S.R. Daniewicz, "Finite element analysis of plasticity-induced fatigue crack closure: an overview", *Engineering Fracture Mechanics*, vol. 71 no. 2, p. 149-171, 2004.

[SUN 90] W. Sun, H. Sehitoglu, "An unified model for crack growth from notches", quoted in Ting J.C., Lawrence F.V.Jr (1993), *Fatigue and Fracture of Engineering Materials and Structures*, vol. 9, p. 205-217, 1990.

[SUR 91] S. Suresh, *Fatigue of Materials*, Cambridge University Press, 1991.

[TAN 83] K. Tanaka, Y. Nakai, "Propagation and non-propagation of short fatigue cracks at a sharp notch", *Fatigue and Fracture of Engineering Materials and Structures*, vol. 6, p. 315-327, 1983.

[TAN 87] K. Tanaka, "Short-crack fracture mechanics in fatigue conditions", *Current Research on Fatigue Cracks,* in T. Tanaka (ed.), Elsevier, p. 93-117, 1987.

[TAY 89] D. Taylor, *Fatigue Thresholds*, Butterworths, 1989.

[TAY 00] D. Taylor, G. Wang, "Component design: the interface between threshold and endurance limit, Fatigue crack growth thresholds, endurance limits and design", *ASTM STP 1372*, p. 361-373, 2000.

[TOK 94] K. Tokaji, T. Ogawa, K. Ohya, "The effect of grain size on small fatigue crack growth in pure titanium", *International Journal of Fatigue*, vol. 16, p. 571-578, 1994.

[TUR 95] A. Turnbull, E.R. De Los Rios, "Predicting fatigue life in commercially pure aluminum using a short crack growth model", *Fatigue and Fracture of Engineering Materials and Structures*, vol. 18, no. 12, p. 1469-1481, 1995.

[VER 86] Y. Verreman, J.P. Bailon, J. Masounave, "Fatigue short crack propagation and plasticity - induced crack closure at the toe of a fillet welded joint", in K.J. Miller, E.R. De Los Rios (eds.), *The Behaviour of Short Fatigue Crack*, Mechanical Eng. Pub., London, p. 387-404, 1986.

[VER 87] Y. Verreman, J.P. Bailon, J. Masounave, "Closure and propagation behavior of short fatigue cracks at different R-ratios", in R.O. Ritchie, E.A. Starke Jr. (eds.), *Fatigue 87,* Emas, vol. I, p. 371-380, 1987.

[VER 97] Y. Verreman, G. Espinosa, "Mechanically short crack growth from notches in a mild steel", *Fatigue and Fracture of Engineering Materials and Structures*, vol. 20, no. 2, p. 129-142, 1997.

[VER 06] Y. Verreman, N. Limodin, "Fatigue life prediction of V-notched components", *Fatigue 2006, 9th International Fatigue Congress*, Elsevier, 2006 (8 pages on CD-ROM).

[VER 08] Y. Verreman, N. Limodin, "Fatigue notch factor and short crack propagation", *Engineering Fracture Mechanics*, vol. 75, p. 1320-1335, 2008.

[WAL 79] N. Walker, C.J. Beevers, "A fatigue crack closure mechanism in titanium", *Fatigue of Engineering Materials and Structures*, vol. 1, p. 135-148, 1979.

[YAT 90] J.R. Yates, L. Grabowski, "Fatigue life assessment using a short crack growth model", in K. Kitagawa, T. Tanaka (eds.), *Fatigue 90*, vol. 4,Mep, Birmingham, p. 2369-2376, 1990.

[ZHA 05] T. Zhai, X.P. Jiang, J.X. Li, M.D. Garratt, G.H. Bray, "The grain boundary geometry for optimum resistance to growth of short fatigue cracks in high strength Al-alloys", *International Journal of Fatigue*, vol. 27, p. 1202-1209, 2005.

[ZHA 97] J.Z. Zhang, M.D. Halliday, P. Poole, P. Bowen, "Crack closure in small fatigue cracks - a comparison of finite element predictions with in-situ scanning electron microscope measurements", *Fatigue and Fracture of Engineering Materials and Structures*, vol. 20, no. 9, p. 1279-1293, 1997.

[ZHA 02] X.P. Zhang, C.H. Wang, L. Ye, Y.M. Mai, "In situ investigation of small fatigue crack growth in poly-crystal and single-crystal aluminum alloys", *Fatigue and Fracture of Engineering Materials and Structures*, vol. 25, no. 2, p.141-150, 2002.

Chapter 8

Plastic Deformation Mechanisms at the Crack Tip

8.1. Introduction

In the 1960s, around 100 years after the first studies carried out by Wöhler, advances in optical and electronic microscopy combined with electro-polishing enabled the presence of a plastic zone at the fatigue crack tip to be revealed. From that moment, cracking mechanisms could be understood and theoretical models could be proposed to complete the parametric approaches, with the most popular being invented by Paris. A new and important step was taken thanks to digital calculation in the 1980s.

It is also noted that cracking mechanisms due to fatigue depend on plastic deformation and the effects of the environment. Knowing the plastic zone at the fatigue crack tip enables us to answer at least three questions on the propagation mechanisms of a crack, dealing with:

– the morphology of cracks and microscopic fracture processes;

– the establishment of behavior laws from a low-cycle fatigue at the crack tip;

– the influence of the closure of a crack on plasticity, which is itself related to cumulative damage effects experienced in the history and fatigue of the material being studied.

Chapter written by Claude BATHIAS.

This chapter is strongly related to Chapters 6, 7 and especially Chapter 9, which was written by Sylvie Pommier, and deals with the same topic but with a more mechanical than physical approach. In this chapter, we successively develop the main aspects of cracking mechanisms due to fatigue, and insist on the role of plastic deformation, take a micro-structural point of view of the dislocation arrangement and, from a mechanical point of view consider the opening of the crack tip during crack propagation.

8.2. Fatigue plastic deformation at the crack tip

As we saw in Chapter 6, the growth of a fatigue crack is usually expressed as a function of stress intensity factor K with a parametric equation initially proposed by Paris:

$$\frac{da}{dN} = C.\Delta K^m \qquad [8.1]$$

The drawback of such an equation is that the influence of the usual mechanical parameters, such as Young's modulus and the stress-stress coefficient of the elasticity limit, cannot easily be determined.

Using more theoretical theories, for a long time we tried to express the cracking rate due to fatigue by isolating the influence of various mechanical parameters. Up until now, the most successful trials have relied on the theory of opening at the crack tip [CLI 67, PEL 70] and on cyclic stress-stress behavior at the crack tip [CLI 63].

In both cases, knowing the plastic zone at the crack tip is useful but, obviously, it is when we consider that progression of the crack depends on a localized plastic fatigue that determination of the plastic zone and profiles of the deformation more directly leads to a better understanding of the problem.

8.2.1. *Theoretical aspect*

8.2.1.1. *Reminder: fracture mechanics*

In order to focus on the plastic zone under fatigue, we will briefly talk about the research led by Irwin on the formation of the plastic zone at a crack tip, contained within a plate, and subjected to a constant tensile stress that is perpendicular to the crack plane.

Within this stress mode (mode I), the stress state close to the crack is given by the Westergaard equations, written as:

$$\sigma_1 = \frac{K_I}{(2\pi r)^{1/2}} Cos\frac{\theta}{2}\left(1+\sin\frac{\theta}{2}\sin\frac{3\theta}{2}\right) \quad [8.2]$$

where:

– K = stress intensity factor;

– θ,r = polar coordinates of a point at the front of the crack.

Under a planar stress, σ_3 is equal to zero and because σ_2 is not involved the only active component is σ_1. When r = O, we have:

$$\sigma_1 = \frac{K_I}{(2\pi r)^{1/2}} \quad [8.3]$$

During traction, the stress σ_1 will locally reach the elasticity limit and at that moment plasticization at the crack tip within this zone will occur, leading to:

$$\sigma_1 = \sigma_y = \frac{K_I}{(2\pi r)^{1/2}} \quad [8.4]$$

thus:

$$r = \frac{K_I^2}{2\pi\sigma_y^2} \quad [8.5a]$$

Irwin then defined the radius (r) of a plastic zone at the crack tip, within mode I, and under a planar stress.

This simple model predicts that the section of the plastic zone is a circle. Actually, the shape and the size of this zone depend on several parameters.

8.2.1.2. *Shape and size of the plastic zone*

The size of the plastic zone mainly depends on the stress state. Under a planar deformation, Irwin suggests multiplying the value σ_y by a factor of 1.68. It then leads to the following new equation:

$$r = \frac{K_I^2}{6\pi\sigma_y^2} \qquad [8.5b]$$

which shows that the plastic zone is smaller under planar deformation than under planar stress. This is then verified at the core and surface of a specimen.

The shape of the plastic zone is not as simple as the shape predicted by this elementary approach. In reality, within mode I the plastic zone is made of two wings that are determined by calculation using the finite element method [LEV 71], as shown in Figure 8.1.

In mode II, the plastic zone is elongated towards the direction crack propagation, mode II being the only one where we find a circular shape.

We can then see that Irwin's model, which allows us to introduce the plasticity notion at the crack tip, is not really reliable for performing a precise study of the phenomenon.

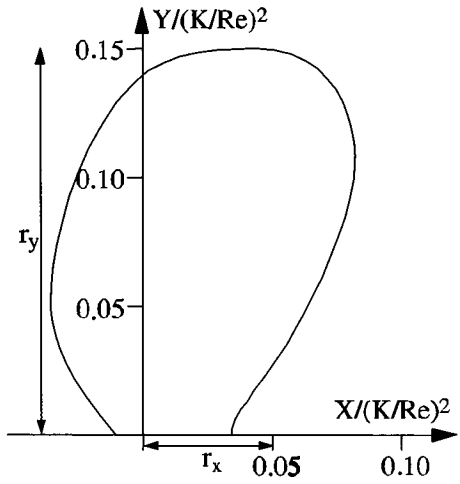

Figure 8.1. *Outline of the plastic zone at the crack tip calculated by Rice for an elastic-plastic solid without any consolidation*

In mode I, it seems that currently the most convenient model is that the one proposed by Rice [LEV 71]. The two wings of the plastic zone can be determined by the coordinates r_x and r_y, with r_x in the direction of cracking and r_y in the perpendicular direction.

Under a planar deformation, Rice finds that:

$$r_y = 0.15\frac{K_I^2}{\sigma_y^2} \qquad [8.6]$$

$$r_x = 0.036\frac{K_I^2}{\sigma_y^2}.$$

The dimensions of the plastic zone calculated by Rice are close enough to the dimensions experimentally measured, as we will see later on. Nevertheless, the cold-working coefficient, that is to say the ability of the metal to consolidate, influences the shape of the plastic zone. When this coefficient increases, both wings tend to straighten up. The average direction of the wing with regards to the cracking direction is 60° with Rice's model. Some experiments show that it varies from 44 to 30° when the cold-working coefficient goes from 0.25 to 0.07 [MAI 73]. Some other factors, such as the chosen plasticity criterion or configuration of the crack, can also affect the shape of the plastic zone [LAL 77, LAR 73].

We should also mention that calculation (see Figure 8.1) shows that plasticization occurs mainly on both sides and at the front of the crack. To some extent it also occurs at its back.

We will now see how we can apply this information in the case of cyclic loading, starting with the model proposed by Rice.

8.2.1.3. *Mechanism of plasticity at the fatigue crack tip*

The plastic zone at the fatigue crack tip will be modified for the most part by closure of the crack at each cycle. Even when the nominal stress remains within the traction domain, a local compression still occurs during closure [RIC 67].

Figure 8.2 roughly shows how the plastic zone gets formed at the fatigue crack tip. For repeated tensile loading with a triangular shape, we can suppose that, during the opening of the crack, plasticity occurs when the elasticity limit is reached locally. We can also assume that during the closure a stress amplitude that is twice as high as the elasticity limit will lead to a new plastic deformation within the plastic zone during the opening of the crack. Under fatigue, we then find a double plastic zone. The radius of the external plastic zone can be written as $(K_{max}/\sigma_y)^2$ whereas the radius of the reverse zone is written as $(\Delta K/2\ \sigma_y)^2$.

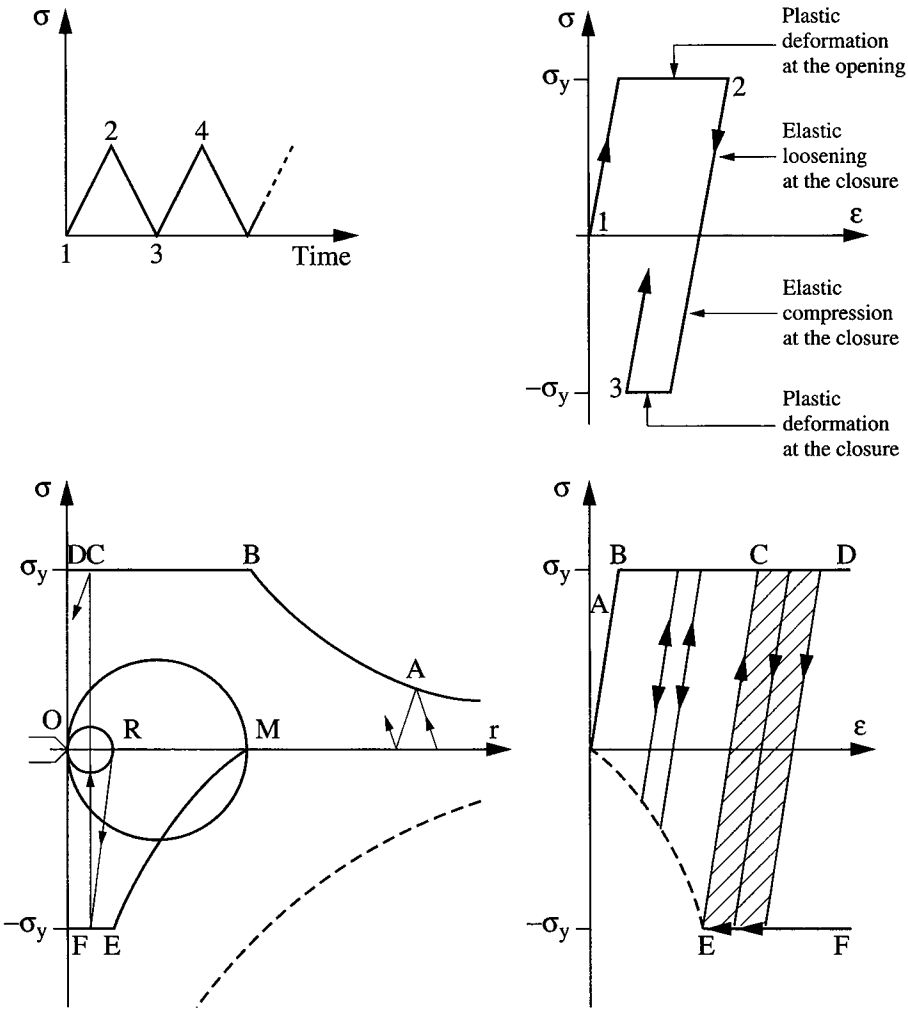

Figure 8.2. *Mechanism of plastic deformation at the fatigue crack tip [BAT 72, BAT 73]*

As a consequence, the central plastic zone *OR* is four times smaller than the external plastic zone *OM* (see Figure 8.2). The variations in stress amplitude $\Delta\sigma$ and deformation amplitude $\delta\varepsilon$ are presented in Figure 8.3, where the respective positions of the crack tip and of plastic zone are considered to be fixed.

Outside the external zone, deformation is elastic. Within this external zone, cyclic deformation remains elastic so the stress-deformation cycles are closed (see

Figure 8.2). Nevertheless, the monotonic plastic deformation due to the opening of the crack regularly increases from M to R, according to a function of $1/r$. Within the central plastic zone, the amplitude of the stress reaches 2 σ_y and cyclic plastic deformation occurs.

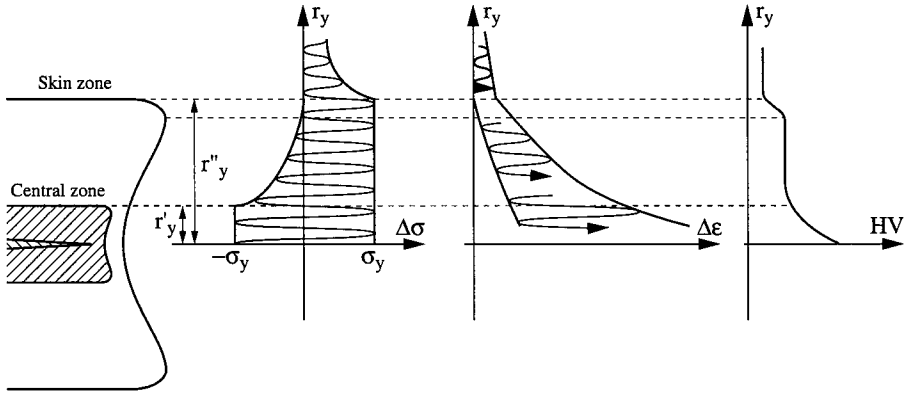

Figure 8.3. *Stresses at the fatigue crack tip. Evolution of the microhardness [BAT 72, BAT 73]*

The cyclic stress hardening that occurs within the central plastic zone comes strictly with a variation in the elasticity limit σ_y depending on the hardening or softening of the alloy. We should therefore not expect the radius of the central plastic zone to be exactly four times smaller than that of the external zone. Plastic deformation at the limit of the external zone and the central zone ε_{pR} can be determined if we consider the deformation ratio to be inversely proportional to distance at the crack tip. We then find that $\varepsilon_{pR} = 3\ \varepsilon_e$, ε_e being deformation at the elasticity limit.

The monotonic deformation at point R is therefore relatively low; from what we know of ε_e, using calculations we determine that the plastic deformation of the plastic external zone will not exceed 1%. In addition, we can assume that the limits of both plastic zones are well defined because both stress hardening states of the metal are different.

At every cycle, the crack moves forward with a length of da and thus leads to progression of the plastic zone, which occurs mainly through the extension of the outline of the external zone, and then with an increase in plastic deformation within this zone. The central plastic zone grows as the crack closes.

Because of the shape of the plastic skin zone, within a plane perpendicular to that of the crack, the metal is subjected to an increasing number of cycles towards increasing r_y. At the same time, however, the amplitude of the deformation decreases. The deformation obtained within the plastic external zone then has to be relatively uniform in a direction perpendicular to the plane of the crack. Obviously, the same does not occur regarding the direction of crack propagation.

To summarize, at the front of a fatigue crack, we can find three different zones:

– a first zone, the furthest away from the crack tip, where deformations are mainly elastic;

– a second zone, which displays plasticification during the opening of the crack, and where deformations are low and uniform;

– a third zone where the amplitude of the stress is of about 2 σ_y. Plastification occurs due to the closure of the crack and deformations are significant, especially those close to the crack tip.

8.2.2. *Experimental trials*

Experience usually agrees with theory in our case. Different methods – metallographic etching, microhardness measurement, X-ray diffraction, moiré and electron microscopy, and Moiré techniques – were used to show how plastification at the crack tip occurs. Several authors have been able to confirm the existence of both plastic zones [BAT 73, HAH 72] (see Figure 8.4).

Among the oldest experimental trials is the work carried out by Hahn and Rosenfield on 4% silica steel [HAH 72]. Thanks to an appropriate metallographic etching, they were able to determine not just the shape and dimensions of the plastic zone surrounding the fatigue crack, but also the deformation ratio. The measured dimensions of the external zone were close to the dimensions calculated by Rice. In addition, the number of cycles that were necessary to describe the plastic zone agrees with that predicted by Coffin's law within the deformation domain considered. This observation proves that the propagation of a crack can be considered to be due to a localized low-cycle fatigue.

The drawback of Hahn's method is that it is specific to silica steels and cannot be applied to any other alloys. With the metallographic etching, the microhardness technique offers two main advantages:

– using microhardness techniques, we can detect local plastic deformations as low as a hundredth within any kind of material. This technique can then therefore usually be used in any situation;

– as a consequence, we can then identify the nature of the cold working: hardening or softening. Calibration/standardization of the values of hardness enables us to link the evolution of hardness within the plastic zone to the distribution of plastic deformations at the crack tip.

Using this method, we could study several alloys [BAT 73, KUD 70] and determine the shape and dimensions of the plastic zones. This theory could be verified on different levels:

– existence of a twin plastic zone;

– uniformity of the plastic deformation zone within the external zone; and

– the shape and the dimensions of this zone.

The evolution of microhardness could enable us to determine either the hardening (carbon steels, austenite steels) or the softening of the metal (maraging steels).

In every case, the external zone is characterized by a hardness plateau. Some examples are given in Figures 8.4, 8.5 and 8.6.

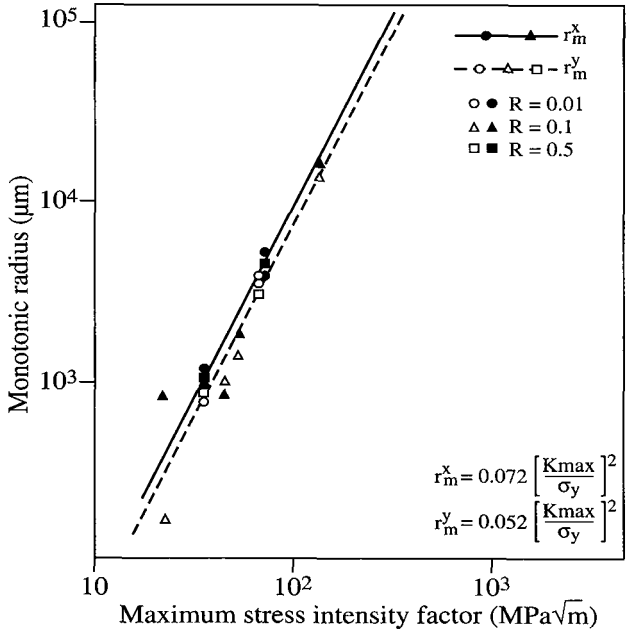

Figure 8.4. *Experimental determination of dimensions of the plastic zone within steel 316. The plastic skin zone depends on K_{maxi} alone [BAT 72, BAT 73]*

The main limitation of the microhardness technique lies in the size of the prints (of about 10 μm), which limits measurements of the radius of the plastic zone to about 50 microns. The fluctuations in hardness due to the orientation and anisotropy of the stress-hardened grains are almost discarded, using parallel filiations and by going through different grains.

Different techniques using X-rays have been used in an attempt to measure the size of plastic zones and to determine the deformations. The most classical one consisted of studying the evolution of Debye and Scherrer's diagrams. The continuity of rings observed on the diagrams depends on the deformation of grains and we can observe the limit of the plastic zone as discontinuous stains appear. To perform this process, we have to use numerous diagrams, but it could still be successfully carried out on some steels [FEL 56].

Another technique is based on the evolution of Lauë diagrams. By the time the grain reaches a diameter of about 0.1 mm, we can gain an idea of the size of the plastic zone using a single diagram [LAT 73]. For some alloys bearing small grains, we have to take several pictures and we have to use an alloy that was quenched beforehand in order to rearrange the structure of the plastic zone and to discriminate the Lauë stains.

A Moiré process was used by Liu within a light alloy and a steel to measure the plastic zone [LIV 69]. Other measurements have been preformed using the same technique by Ohta *et al.* within a microalloyed steel where the deformations close to the crack tip were of about 4% [OHT 77]. Finally, Davidson and Lankford used the crystallographic contrast of the scanning microscope to measure the plastic zone [DAV 76].

8.2.3. *Crystallographic aspects*

From a crystallographic point of view, some studies were carried out using both transmission and optical electron microscopy.

Plastic deformations are very different within the external and central zones. In the external zone, we can observe an increase in density of dislocations that agree with the low level of deformation that was theoretically predicted. Within the central zone, the dislocation cells are replaced by some configurations typical of strong deformations and that differ depending on the stacking fault energy.

Dislocation cells appear within copper [WK 69], aluminum [BRO 72], carbon steels [BAT 72] and even within maraging steels [BAT 72], and apparently within the other high-fault energy alloys. Within stainless austenite steels [BAT 72] with

lower fault energy, the central zone is mainly occupied by mechanical twins or martensite strips (see Figure 8.7 and 8.8).

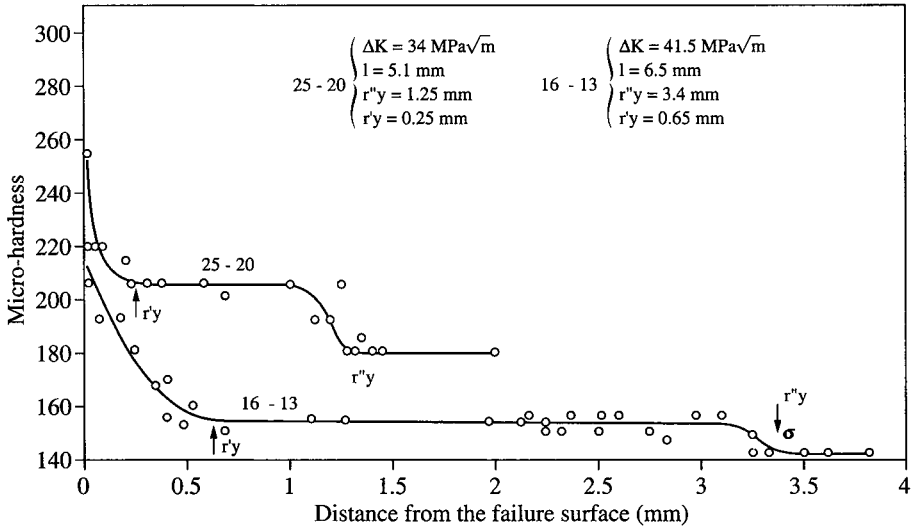

Figure 8.5. *Evolution of the micro-hardness of two chromium-nickel austenite steels [BAT 72, BAT 73]*

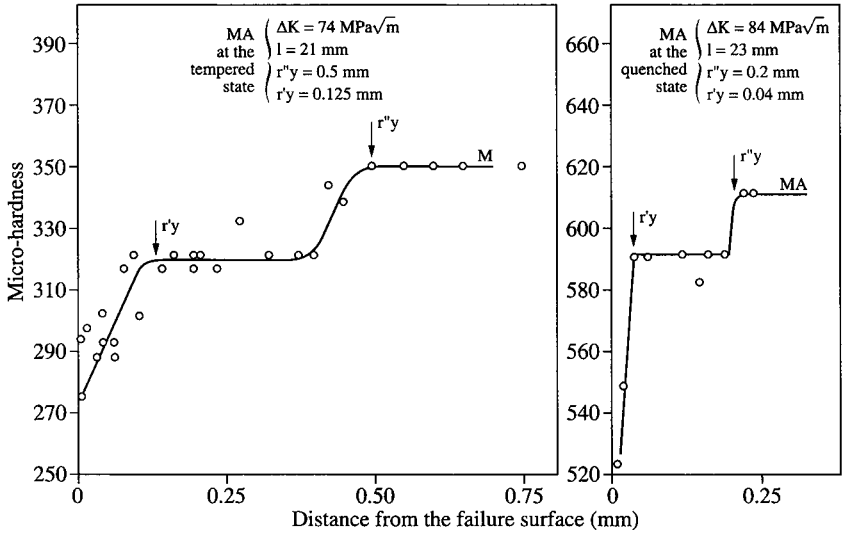

Figure 8.6. *Evolution of microhardness after the cracking of a maraging steel [BAT 72, BAT 73]*

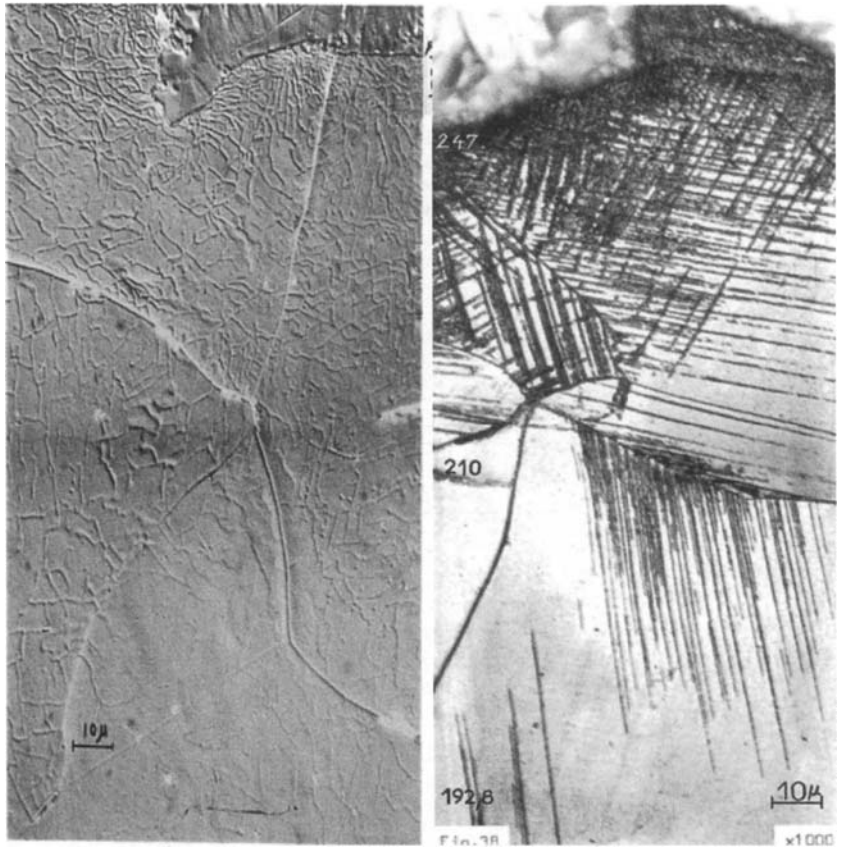

Figure 8.7. *Plastic zones after cracking within low-carbon steel (cells) and within a 25-20 stainless steel (twins)*

When formation of dislocation cells occurs, the diameter of the cells increases with distance from the crack, and immediately below it the cells are packed parallel to the striations. The disorientation of the cells inversely varies with their size [DAV 76, LUK 69]. For instance, within a 0.5% carbon steel, the diameter of the cells is 2 to 6 µm [DAV 76]. It can reach up to 20 µm within low-carbon steel [BAT 72].

Baïlon *et al.* [BAI 96] measured some dislocation cells at the crack tip within a copper whose diameter varied from 1 to 10 µm. They showed that, for the same loading, the cells that were formed during cracking under a vacuum are smaller than if they had been formed under standard air pressure. Finally, from the size of the cells, the plastic deformation can be determined at less than 1% of the crack with uncertainty due to the deformation gradient close to the crack.

Figure 8.8. *Plastic zones under fatigue cracks X 1,000 within a maraging steel. The platelet structure almost disappears next to the crack*

8.3. Microfractographic aspects of the fatigue crack

8.3.1. *Fractographic observations*

Fatigue cracks are usually initiated at the surface of the material, from one or several points, where it first grows under a planar stress, corresponding to stage I of cracking, and then under a planar deformation, corresponding to stage II where the crack reaches a macroscopic dimension.

The surface of the crack presents some lines in the direction of propagation that are split due to the initiation of the crack. The lines, usually related to other concentric marks centered on the initiation, enables us to determine without doubt what caused the cracking to be initiated.

On the macroscopic scale, a fatigue crack usually presents a regular and smooth relief. Its aspect is matte. Most of the time, there are many secondary cracks.

The fatigue crack is mainly transgranular at the microscopic scale. It then grows along with the formation of striations, which is the most typical cracking mechanism due to fatigue but is not the only one. We usually wrongly assume that the surface of the crack due to fatigue is covered with striations *s*. As a matter of fact, striations cannot always be observed, for various different reasons. We should first note that within some alloys, high-strength steels for example, striations are not well defined and, as a consequence, cannot be observed. We should also bear in mind that when the cracking rates are high, static mechanisms such as cleavages and dimples occur when striations are formed.

In reality, when striations are significant cracking rates can range from 10^{-5} mm/c to 10^{-3} mm/c, depending on whether we are observing a steel or an aluminum alloy.

Even within this domain, the formation of striations is not always global and some other mechanisms that have been developed to a greater or lesser extent can be observed. We can use the cracking of copper alloys to illustrate the different phenomena that can occur [BAI 96]. Neumann observed within copper monocrystals that in order to obtain a striation fracture surface its plane has to be oriented towards a crystallographic plane of type (100). Some similar observations have been made in the case of an α polycrystalline brass. When the orientation of cracking does not correspond with a later one, the fracture facies presents some steps and occasionally inter-granular facets. In addition, the facies distribution strongly depends on the value of the stress intensity factor, as the ratio of non-striation fracture surface increases with decreasing loading. At the non-propagating fatigue threshold, fatigue striations do not usually occur.

8.3.2. *Mechanisms of striation formation*

It seems that Zapffe was the first person to discover the existence of striations in 1945 using an optical microscope, before other researchers described the striation mechanisms that were observed using an electron microscope. It was only 20 years later that Pelloux proved that a striation is formed during a single cycle.

In 1961, Forsyth discovered two different types of striation: ductile striations and fragile striations [FOR 61] (see Figures 8.9 and 8.10).

At this time, we noticed that a corrosive medium encourages the formation of fragile striations; nevertheless, within failed light alloys in humid air we can find two types of striations simultaneously. The mechanism by which striations are formed will be presented later on, but first let us deal with the morphology of the surfaces of fatigue cracks.

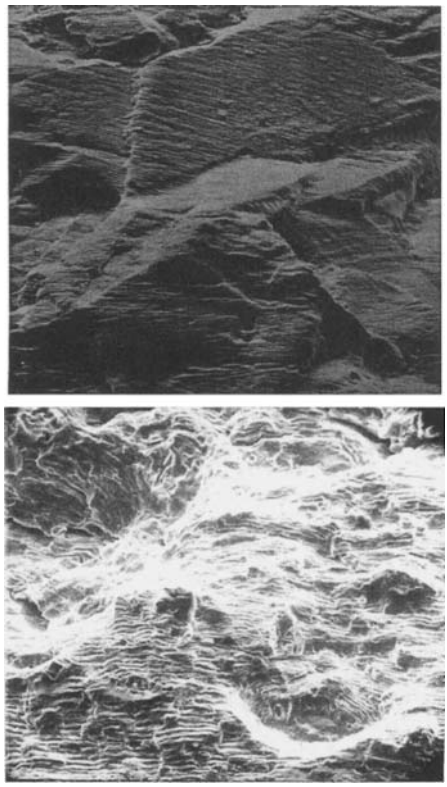

Figure 8.9. *Fatigue fracture surface of a stainless steel 25-20 (top) and of a ferritic steel (X 5000) (bottom) [BAT 73]*

In short, this morphology is characterized by the fact that striations are arranged roughly perpendicularly to the cracking direction, at least within carbon steels and high-fault stacking energy alloys. Some exceptions to this rule are observed within low-fault stacking energy alloys and some austenite stainless steels, for instance, where twinning occurs. It is also worth mentioning the case of nodular cast irons, where the arrangement of the striations depends on graphite nodules [MAI 72]. The truth is that the rule presented above can only be applied if we consider the local propagation of the crack.

The direction of striations is connected to the crystallographic orientation of the grains. Within a 2024 alloy or in copper alloys, the fracture plane is close to a (100) plane and the striations are parallel to a (110) direction [PEL 69]. The striations of austenite stainless steel also present a well-defined crystallographic property [BAT 72].

Nevertheless, it seems that this property is weakened within carbon steels. Indeed, within mild steels the orientation of striations does not change when crossing a grain boundary [POM 70].

We should finally note that the profile of the ductile striations is usually more or less flat and serrated: the root of the striations is often characterized by a microcrack. It appears that within face-centered cubic alloys, the sides of the serrated striations are oriented towards (111) planes.

Plastic deformation at the crack tip plays a significant role in the cracking process: the formation of striations and, as a consequence, the cracking rate, both depend on the nature of the plastic deformations.

Usually, fatigue cracks seem to be transgranular and the plastic deformation that results is mainly located within a thin band. The study of the plastic zone shows us that the surface of the crack is connected with the plastic deformation of the sub-layers. Within aluminum alloys, the striations are associated with dislocation walls that are oriented towards (110) directions [BRO 72].

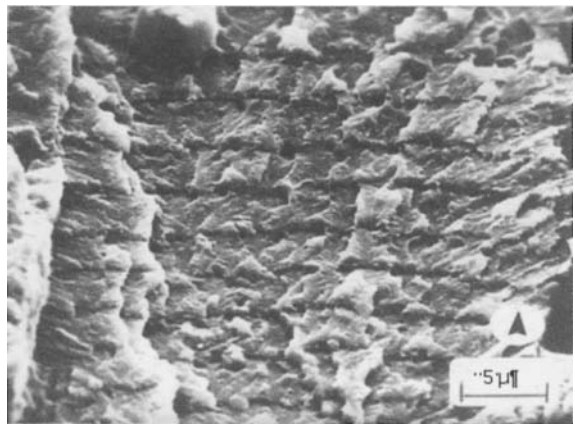

Figure 8.10. *Fragile striations within a cracked 7,075 alloy within a solution containing 3.5% sodium chloride, with ΔK = 22 MPa m. The dark line highlighting every striation represents the step during the decreasing part of the stress cycle [PEL 70]*

Within carbon steels, we can also find a correlation between striations and dislocation walls [BAT 72], whereas within austenite stainless steels, martensite strips or twins are the ones to be connected to striations [BAT 72] (see Figure 8.11).

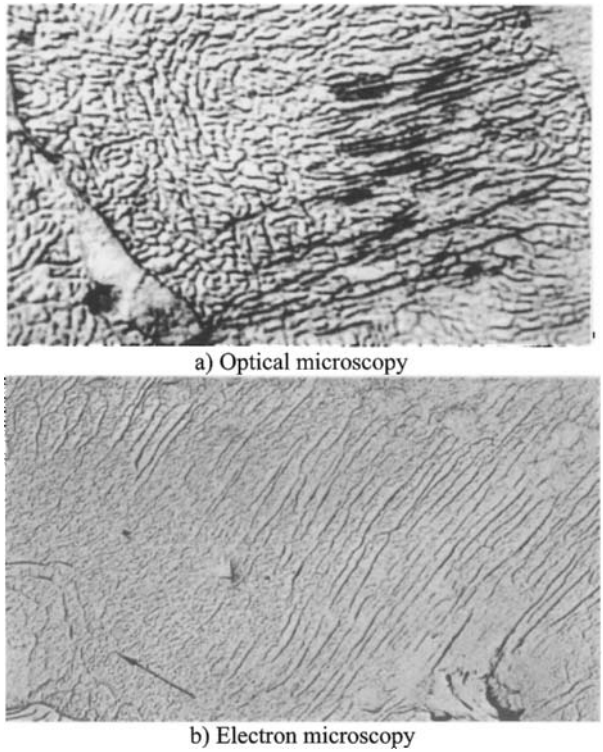

a) Optical microscopy

b) Electron microscopy

Figure 8.11. *Fatigue fracture surface within a mild steel after polishing and electrolytic etching. The network of dislocation walls perpendicular to the direction of propagation is indicated by the arrow. Magnification is X 1,600 in a) and 2,500 in b)*

Within α brass, the striations are correlated with some deformation bands created by dislocation stacking depending on the bisector plane of easy (111) sliding planes [NEU 74].

We can therefore conclude that when cracking occurs at every cycle we can observe an ultimate rearrangement of dislocations to prepare for sliding of the crack tip, as this rearrangement will only be final when closure occurs. Depending on the sliding property, we can observe the formation of a martensite strip, sub-boundary or twin at the same time as the formation of a striation.

In addition, the gap between striations depends on the sliding property. The same goes for the arrangement of striations, regarding orientation and growth of striation planes, to plastic deformation and to the stacking fault energy (see Figure 8.12).

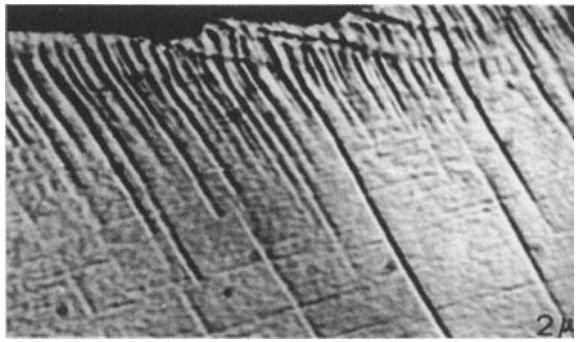

Figure 8.12. *Mechanical twins appearing at the surface of a fatigue crack within an austenite stainless steel 25-20 (magnification X 1,600)*

8.4. Model based on displacement on crack tip opening

One of the two main theoretical models for understanding crack growth is based on the opening at the crack tip [CLI 63, CLI 67]. In this model, we assume that the fatigue crack spreads due to the sliding of the crack tip in directions oriented at 45° to the propagation direction [PEL 69]. The model of striation formation that was proposed by Pelloux agrees with this hypothesis.

In these conditions, if we have d representing the crack tip opening displacement and da/dN as the gap between the striations, then da/dN and δ_c are proportional due for various geometrical reasons. If we do not consider the external plastic zone but just the most cold-worked central plastic one, the cyclic crack tip opening displacement δ_c, under a plane stress can be written as:

$$\delta_c = \frac{\Delta K^2}{4E\sigma_y} \qquad [8.7]$$

thus:

$$\frac{da}{dN} = \frac{1}{8}\frac{\Delta K^2}{E\sigma_y} \qquad [8.8]$$

This equation can be written differently to get the dimension of the plastic zone. We then highlight the fact that the growth of the crack has to be proportional to the size of the plastic zone:

$$\frac{da}{dN} = \frac{1}{8}\frac{\Delta K^2}{\sigma_y^2} x \frac{\sigma_y}{E} \qquad [8.9]$$

Unlike Paris' equation, this theory considers *da/dN* as a function of ΔK^2 instead of ΔK^4.

In practice, we find that the propagation rate of the crack is a function of the:

– length of the crack;

– amplitude;

– applied stress;

– highest stress;

– frequency;

– temperature;

– environment;

– geometry; and

– history of the crack.

In addition, for a given ΔK, the macroscopic rate is different from the microscopic one by an amount that varies depending on the domain considered. For low ΔK, the microscopic rate is higher than the macroscopic rate (see Figure 8.13). We can explain this difference as the striations are locally disoriented from the general propagation direction at the subdivision of the striation planes and especially at the temporary halt of the crack front [BAT 72].

It is worth mentioning that the tenet that rules the microscopic rate is a function of (ΔK^2), as predicted by equation [8.8], the value of the exponent of ΔK not being that different from its theoretical value. Nevertheless, we cannot apply the same rules to the macroscopic rate, which is a function of $(\Delta K)^m$ where the value of m ranges from 2 to 10 in the case of steels [CLA 70] and from 3 to 5 in the case of light alloys.

Some attempts to correlate m to the toughness, expressed with factor K_{IC} were not entirely satisfying [BRO 72]. Usually, we can observe that a high value of m corresponds to a low value of K_{IC}, but some exceptions like austenite steels show that the propagation under a constant regime does not allow us to predict propagation under a cyclic regime.

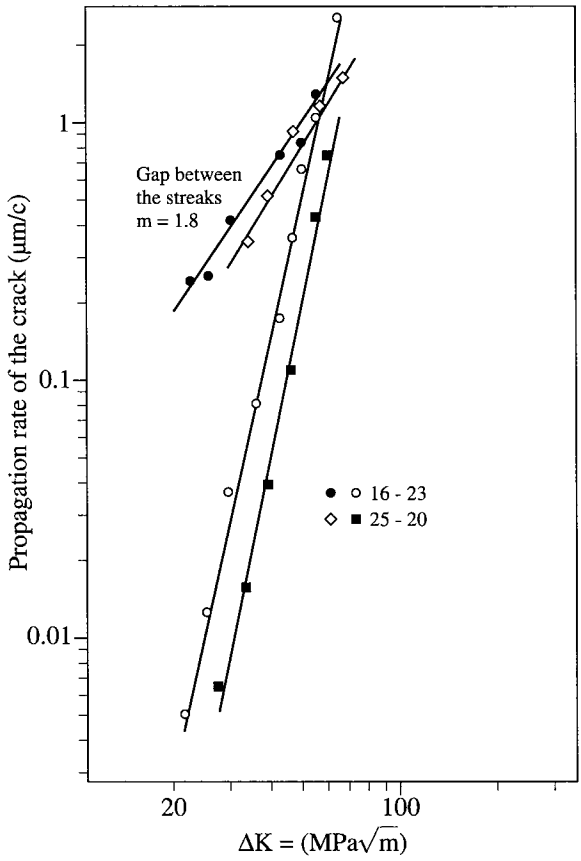

Figure 8.13. *Gap of the streaks within austenite steels and macroscopic cracking rate [BAT 72, BAT 73]*

In summary, we should mention first that if the spacing between striations is really a function of ΔK^2 – as the gap theory of crack opening displacement (COD) says – it cannot be applied to the macroscopic rate. In addition to the COD theory at the crack tip, we know that the spacing between striations can vary instantaneously when a loading variation is set [MIL 66]; the average spacing between striations is a linear function of the radius of the plastic zone [BAT 72].

In opposition to this theory, experience shows us that, if *da/dN* really depends on the elasticity modules, the conventional elasticity limit has almost no consequence for a given type of alloy [BAI 96, DAV 76, NEV 74]. This apparent contradiction shows us how unsuitable the model based on COD is.

8.5. Cyclic stress hardening at the crack tip

Another way to write the growth of fatigue cracks is to consider that the zone at the front of the crack tip is where a localized low-cycle fatigue occurs.

In 1963 McClintock [CLI 63] proposed a model of crack propagation due to fatigue based on cumulative damage at the front of the crack due to the plastic deformation of increasing amplitude.

He assumed that the amplitude of the plastic deformation ε_p at a distance r from the crack tip, within the plastic zone of dimension R is given by:

$$\varepsilon_p = \varepsilon_e \left(\frac{R}{r} - 1 \right). \qquad [8.10]$$

The damage leading to an increase in elementary cracks is supposed to match the Manson-Coffin equation, such as:

$$\int_0^N 4 \left(\frac{\varepsilon_p}{\varepsilon_f} \right)^{1\rho} dN = 1 \qquad [8.11]$$

Considering the fact that dimension P of the equivalent damaged zone is a fraction of the plastic zone, McClintock finds that:

$$\frac{da}{dN} = \frac{7.5}{16} \frac{\Delta K^4}{\varepsilon_f E^2 \sigma_y^2 \rho} \qquad [8.12]$$

Antolovich [ANT 75] completed the McClintock model by using several approximations. The first one consists of determining the plastic deformation with the following equation:

$$\varepsilon_p = \varepsilon_e \frac{R}{r + c} \qquad [8.13]$$

where $c = R \dfrac{\varepsilon_e}{\varepsilon_f}$. If we admit that at the limit, when $r = 0$, we have:

$$\varepsilon_p = \varepsilon_f \qquad [8.14]$$

the average plastic deformation within the damaged equivalent zone ρ comes to:

$$\varepsilon_p = \frac{\varepsilon_e}{\rho} R \ \log\left(\frac{\rho}{c}+1\right) = 0.7\varepsilon_e \frac{R}{\rho} \qquad [8.15]$$

if we assume ρ/c is close to 1.

Antolovich then defines the radius R of the plastic zone, as follows:

$$R = \alpha\left(\frac{\Delta K}{\sigma_y}\right)^{2+S} \qquad [8.16]$$

and finally finds, if he assumes that the crack grows when:

$$4 \ \Delta N\left(\frac{\overline{\varepsilon_p}}{\varepsilon_f}\right)^{1/\beta} = 1 \qquad [8.17]$$

that:

$$\frac{\rho}{\Delta N} = \frac{da}{dN} = 4\left(\frac{0.7\alpha}{E\sigma_y{}^{(i+s)}\varepsilon_f}\right)^{1/\beta} \frac{1}{\rho^{1/3}-1} \Delta K^{(2+S)/\beta} \qquad [8.18]$$

The model proposed by Tomkins [TOM 73] is different from the two first because of the calculation hypotheses. He considers that damage occurs within two bands of length R at both ends of the crack at an angle of 45° to the direction of propagation. He supposes that the opening of the crack for every cycle is the sum of a plastic term and of an elastic one, thus:

$$\delta = \int_0^{\Delta\varepsilon_p} R d\varepsilon_p + \int_0^{\Delta\varepsilon_e} C d\varepsilon_e \qquad [8.19]$$

with:

$$C = \frac{\varepsilon_e}{\varepsilon_f}$$

The cracking rate is then given by the following equation:

$$\frac{da}{dN} = \frac{\delta}{\sqrt{2}} \qquad [8.20]$$

If we consider that the cold-working law of the material is:

$$\Delta\sigma = k\Delta\varepsilon_p^n \qquad [8.21]$$

and that the Manson-Coffin equation can be written as:

$$\Delta\varepsilon_p N_f^{1/(2n+1)} = Cte \qquad [8.22]$$

Tomkins gives the global equation:

$$\frac{da}{dN} = \frac{\pi^2}{8\sqrt{2}}\left(\frac{5}{2\sigma_y}\right)^2 \Delta\sigma^2 \quad a \left[\frac{\Delta\varepsilon_p}{(2n+1)} + \left(\frac{\varepsilon_e}{\varepsilon_f}\right)\frac{\Delta\varepsilon_e}{6}\right] \qquad [8.23]$$

which is presented in Chapter 4.

Under plastic fatigue, this global equation comes to:

$$\frac{da}{dN} = \frac{\pi^2}{8\sqrt{2}}\left(\frac{k}{2\sigma_y}\right)^2 \frac{\Delta\varepsilon_p^{(2n+1)}}{(2n+1)} a \qquad [8.24]$$

Under fatigue, at a low stress level the global equation can be simplified to give:

$$\frac{da}{dN} = \frac{\pi^2}{48\sqrt{2}}\left(\frac{1}{2\sigma_y}\right)^2 \frac{\varepsilon_e}{\varepsilon_f}\frac{\Delta\sigma^3 a}{E} \qquad [8.25]$$

The theories of damage due to cyclic cold-working have the advantage when explaining the influence of the metallurgical parameters. In equations [8.13] and [8.25], the cracking rate is a function of σ_y, E and ε_f. As long as σ_y varies inversely with ε_f, we can then find a suitable explanation for the apparent absence of influence of the elasticity limit on the cracking phenomenon.

8.6. Model based on the effective stress intensity factor

8.6.1. *Elber's model*

Elber [ELB 71] showed that a fatigue crack within an aluminum plate can be closed when the entire set of specimens is still subject to traction. Some compressive stress is then created around the crack when the loading tends towards zero [RIC 67]. He concluded that a fatigue crack is different from an ideal mechanical one as it creates a zone of residual deformation during its propagation. The theoretical crack tip opening displacement is then decreased.

By assuming that a fatigue crack does not spread when it is closed, he concluded that considering the total amplitude of the cycle to establish Paris' equation – $da/dN = f(\Delta K)$ – is wrong, and proposed replacing the stress intensity factor ΔK of this equation with an effective stress intensity factor: $\Delta K_{eff} = K_M - K_{op}$, where K_M is the maximum stress intensity factor and K_{op} the stress intensity factor necessary to entirely open the crack.

In order to determine ΔK_{eff} Elber [ELB 71] recorded the displacement d at the tip of the crack as a function of stress, using an extensometer sensor on thin plates made of 2024-T3 aluminum alloy. The example, shown in Figure 8.14, allows us to distinguish three different stages that were defined by Elber and which are presented bellow.

Between C and D, the equation is also linear and the measurement is equal to that of a similar plate containing a mechanical notch of the same lengths as the fatigue crack.

Between B and C, the curve d^2P/dd^2 is negative. As the plastic behavior of a material leads to a positive curve during the unloading, the only explanation of the negative curve that we can find is a change in configuration that increases the rigidity of the specimen under decreasing loads. This change in configuration can be explained by the closure phenomenon. The crack is entirely open between D and C, during the unloading, gets closed gradually between C and B and is then closed between B and A.

Depending on the position of the sensor, and the nature of the material, the last part CD can be split into two sections: a linear section that is more or less significant and a curve section, being also negative, corresponding to CD and DE respectively. As a tensile plastic deformation can only occur when the crack is completely open, Elber concluded that the BC curve is entirely due to progressive opening of the crack, whereas the DE curve is due to a plastic deformation at the crack tip. The determination of point C allows P_{op} and finally K_{op} to be identified.

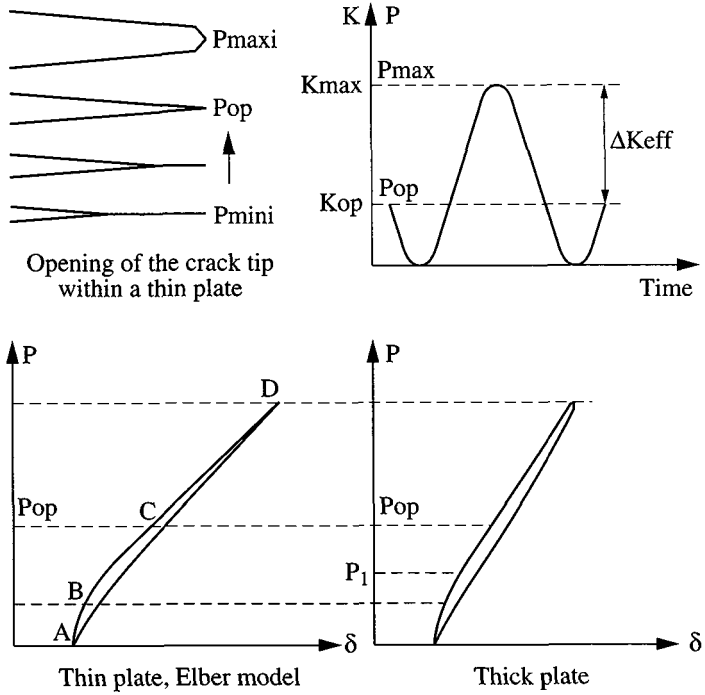

Figure 8.14. *Opening and closure at the fatigue crack tip. Notion of $\Delta K_{effective}$*

Elber carried out tests where he allowed some parameters to vary, such as:

– the length of the crack,

– the stress intensity factor, and

– the ratio R;

in order to observe their influence on the efficiency of loading, defined by the ratio U:

$$U = \frac{K_{\max} - K_{op}}{\Delta K} \qquad [8.26]$$

Only ratio R seems to have a significant influence on ratio U. Elber found a linear equation between these two parameters that can be written with the following function $U = 0.5 + 0.4\,R$. It had $-0.1 < R < 0.7$, in the case of the aluminum alloy 2024-T3, thus explaining the influence of ratio R on the propagation rate of fatigue

cracks within this alloy. We should finally mention that these results were obtained mainly under plane stress conditions. Some experimental verifications show that U can vary from 0.4 to 0.75 when $R = 0$, depending on the geometry and the alloy.

The notion of ΔK_{eff} leads us to admit that there is no stress singularity at the front of the crack as long as its root is not entirely open.

8.6.2. *Application of Elber's model*

When a crack spreads towards a configuration of plane stress, the problem is slightly more complicated because the plastic zone at the crack tip is about three times bigger at the surface than within the core. As a consequence, the residual stresses associated with this plastic deformation are more important at the surface than within the core.

The opening of the crack tip is therefore more premature within the core than at the surface. When the force applied to the specimen increases, we can initially observe the phases described by Elber under a plane stress, until opening of the center of the specimen occurs. Between this moment and the opening at the surface, however, in the case of the cracking under plane stress there is a transitory phase during which the opening of the crack goes from the inside to the outside at the same time as the crack gets a new configuration (see Figure 8.15). The definition of ΔK_{eff} can appear to be ambiguous as it usually varies at the front of the crack. Apparently, we have to calculate ΔK_{eff} from the opening at the surface. In these conditions we can observe that ΔK_{eff} increases with the thickness of the specimen [SCH 77].

A number of authors, including Lindley, McEvily, Pineau, Schijve, [LIN 74, EVI 77, SCH 77], have experimentally shown that the crack tip is less open at the surface than within the core. They performed some metallographic cuts and surface dissolutions.

The experimental detection of the closure or opening of the cracks is not easy to interpret correctly using the recordings from various methods. If we use an extensometer and mechanical method, an electric one or a method with ultrasound transmission, the interpretation of results leads to different conclusions. It seems that mechanical opening does not always correspond to "electric" opening or to "acoustic" opening because of the formation of an isolating oxide film, for instance. It is thus more suitable if we consider the extensometric measurement to be the reference measurement. We should then bear in mind that the measurement of the opening at the surface will give some precise but localized information; and that the measurement of the opening of the notch will give some rough but global

information on the evolution of opening along the crack tip under a plane stress [BAT 78, BRO 72, GAR 77, SHI 77].

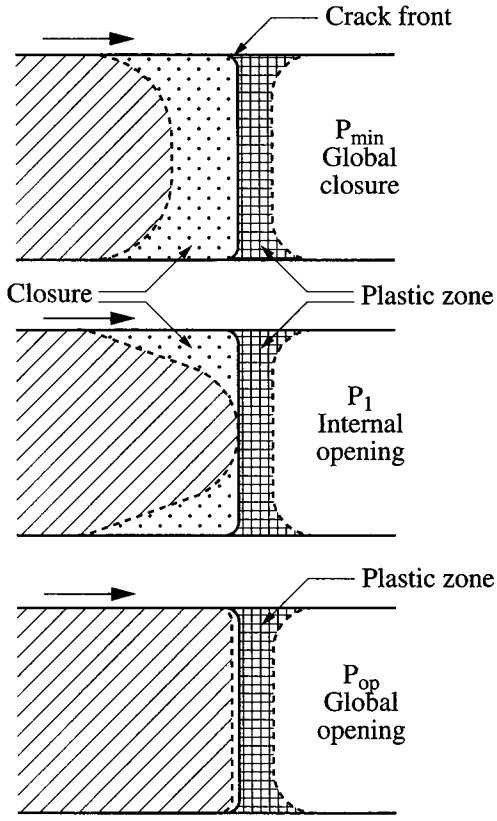

Figure 8.15. *Evolution of the opening of the crack tip for an increasing loading within a thick plate [BAT 72, BAT 73]*

8.6.3. *Interpretation of the fundamental mechanisms*

8.6.3.1. *Influence of ratio R*

Experience shows us that when the ratio $R = \sigma_{min}/\sigma_{max}$ increases, the cracking rate increases and becomes more significant when the alloy is less ductile. This increase cannot be described by the amplitude of the opening of the crack tip, but can be considered with the concept of ΔK_{eff} [PET 96]. An example of a cracking curve given as a function of ΔK is presented in Figure 8.16. These results, obtained

on aluminum alloys with ratios R ranging from 0 to 0.75, show that the growth of the crack depends on the effective intensity factor.

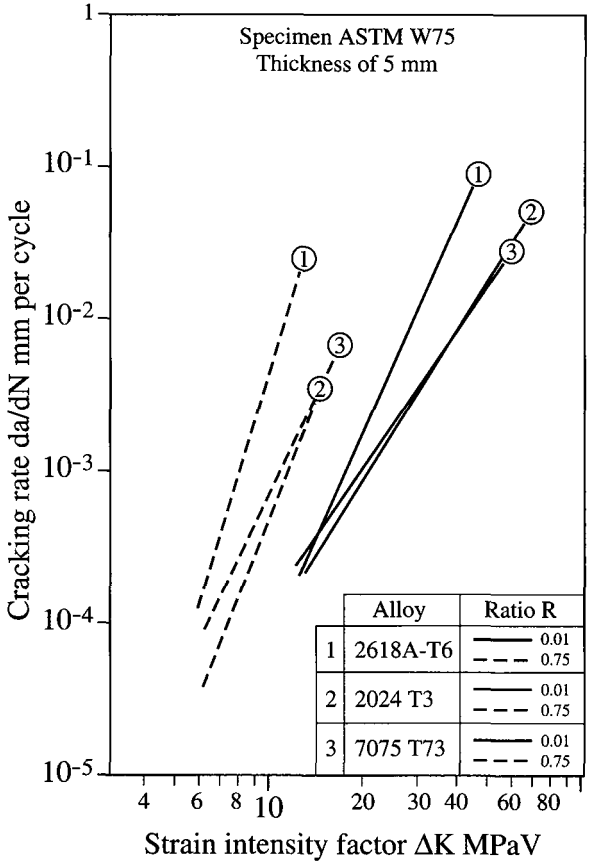

Figure 8.16. *Influence of ratio R on the cracking rate of aluminum alloys*

8.6.3.2. *Influence of the environment*

It is well-known that some aggressive or salted mediums increase the speed of fatigue cracking. We have been wondering for a long time whether the influence of the surroundings was a key in the opening of the crack tip or the effective stress intensity factor. Some contradictory results have been published [BAT 78, BUC 74, IRV 75]. As a matter of fact, the influence of the environment on fatigue cracking depends on the interaction of absorption at the crack tip with the microstructure, and on the formation of oxide layers that can modify the efficiency of the cycle.

We can finally say that for an identical ΔK_{eff}, cracking does depend on the surroundings [PET 96]. The reader will find more information on this topic in Chapter 11.

8.6.3.3. *Influence of overloading*

During a fatigue test, when we temporarily increase the stress intensity factor from a given initial value, we can first observe that growth of the crack during overloading is not ruled by Paris' equation. We can also observe that after going back to the conditions of the initial loading, the propagation of the crack is significantly slowed down if the temporary overloading is due to traction. It goes slightly faster if the overloading is due to compression. These disturbances in cracking rate due to the application of overloading are really interesting for the engineer, as they represent the conditions usually met in practice.

The typical phenomenon in the slowing down of a crack after overloading has been described as presenting several phases (see Figure 5.17), with one of them where the cracking rate reaches a constant and minimum value $(da/dN)_{delay}$. This maximum slowing down phase is framed by two transitory phases, both limited by the rate of the established regime $(da/dN)_0$. The lowest rate is not immediately reached after overloading except when a sequence of several consecutive peaks is observed.

The process of slowing down is correctly described using two parameters:

– the number of cycles N_D, which is affected by the rate of crack development slowing down; and

– the crack length a_D, where the rate is disturbed as soon as the loading is applied (see Figure 8.17).

Many studies have shown that, for a given material, the deceleration of crack development increases with the surface K_{peak}, the ratio K_{peak}/K_0, and the number of overloading peaks. On the other hand, it decreases when ratio R increases. Due to the high number of parameters, this phenomenon is complex and its modeling is not satisfying for various different reasons [SCH 77].

The low-intensity overloading, whose ratio does not exceed 10%, leads to a temporary disorientation of the crack and to the low rate of deceleration. The more intense overloading leads to a static failure within the core of the specimen when the specimen is several millimeters thick. The crack then remains blocked at the surface due to the significant plastic deformation occurring under a planar stress (see Figure 8.18). The crack, which is then disturbed, is initiated again at the surface within the ligaments limiting the failure (see Figure 8.19). In these conditions, the

deceleration/retardation phenomenon after overloading will depend upon the thickness of the specimen.

Wheeler and Willenborg [WHE 70, WIL 71] considered that the length of a crack affected by overloading is equal to the journey necessary for the plastic zone at the crack tip to become tangential to the one produced by the overloading. This hypothesis corresponds to a rough approximation in the case of thin plates under a planar stress but is not accurate enough, however, under a plane stress.

Some measurements of the plastic zones confirmed that their size in relation to the propagation direction is three to five times smaller than the maximum size. This can lead us to believe that the retardation is apparently unrelated to structural overloading at the front of the crack [BAT 78].

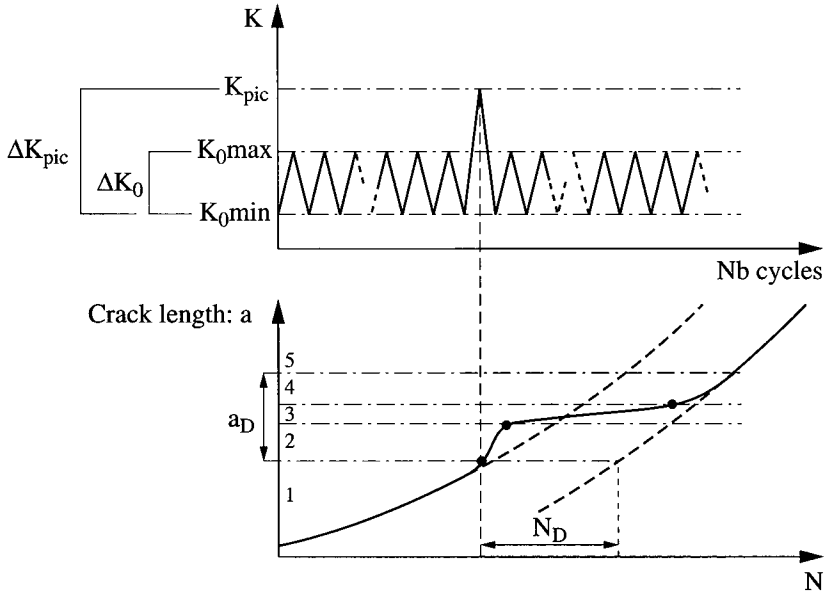

Figure 8.17. *Retardation phenomenon after over-loading [BAT 78]*

We should mention that experience shows that there is no simple and unique relationship between the length of the affected crack and the real diameter of the plastic zone with overloading. For every ratio, every value of K_{peak}, every frequency, we can find a different equation between these two dimensions. It then leads us to find that for a diameter of a given plastic zone, the length that is affected by the retardation is not always the same.

It appears that the retardation phenomenon does not exclusively depend on modifications of the microstructure by overloading or the geometry of the subsequent plastic zone, but rather on residual stresses connected to plastic deformations [CHA 77]. As a consequence, the effective stress intensity factor is strongly affected by the residual stresses, which are compressive after tensile overloading [SCH 77]. The reduction in effective stress intensity factor better explains this retardation phenomenon.

The experimental verifications and calculations [SCH 77] have shown that determination of the effective stress intensity factor allows us to predict the growth of cracks after an overloading for a crack growing under a plane stress regime within thin plates.

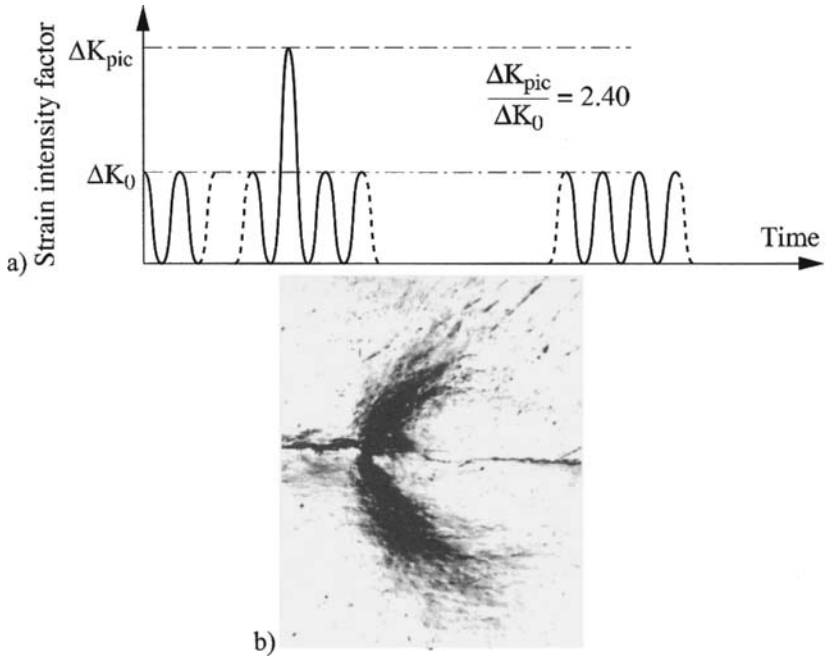

Figure 8.18. *a) Cracking mechanism after overloading within a 2024 T 351 alloy; and b) plastic zone at the surface*

Within the thick plates, the problem is more difficult. Depending on the thickness of the specimen, the strong overloading intensities lead to a crescent-like failure and, as a consequence, modify the almost straight profile of the crack front. It is therefore likely that the relative variations $K_{efficient}$ within the core and at the surface of the specimen will be different. Indeed, after overloading, at the surface

the crack spreads within the ligaments located between the failure and the surface, whereas they remain totally blocked within the core.

Right after intense overloading, $K_{efficient}$ is lower within the core than at the surface. After an acceptable number of cycles, the crack front tends to change back to its initial shape, leading to a higher $K_{efficient}$ within the core than at the surface. This inversion can be explained by the combined action of dullness of the crack within the specimen's core by the formation of cupules and by the existence of residual compressive stress due to plasticity at the crack tip.

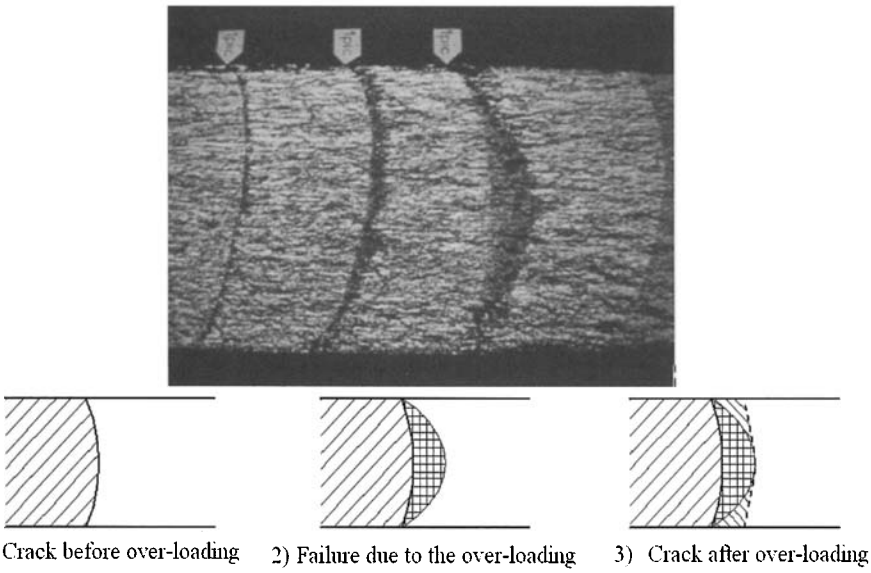

Figure 8.19. *Cracking model before and after overloading under planar deformation conditions [BAT 78]*

8.7. Conclusion

In this chapter, the relationships between the mechanisms of plastic deformation and those related to cracking propagation are presented. In summary, we should bear in mind that:

– fracture surfaces due to fatigue depend on plastic deformation at the crack tip, on the dislocation arrangements of the twinning, etc.;

– the spacing between fatigue striations and opening of the crack tip depend on the size of the cyclic plastic zone;

– the efficiency of the fatigue cycle mostly depends on the plastic zone, but it also depends on the roughness of the crack, which is additionally related to the plastic deformation and to the size of the grain.

Nevertheless, cracking due to fatigue more often than not depends on the surroundings and it seems that we cannot entirely understand the cracking mechanisms if we do not consider interactions with the environment and plastic deformation.

8.8. Bibliography

[ANT 75] S.D. Antolovich, A. Saxena, G.R. Chanani, "A model for fatigue crack propagation", *Eng Fract Mech*, vol. 7, p. 649-652, 1975.

[BAI 96] J.B. Bailon, Tong Zhao-Xing, *Fatigue 96*, vol. 1, Pergamon, p. 387-392, 1996.

[BAT 72] C. Bathias, R.M. Pelloux, *15^e Colloque de Métallurgie de Saclay*, 1972.

[BAT 72] C. Bathias, J. De Fouquet, De Leiris, *C.R.A.S.*, vol. 274, p. 867-870, 1972.

[BAT 72] C. Bathias, PhD Thesis, University of Poitiers, June 1972.

[BAT 73] C. Bathias, R.M. Pelloux, "Fatigue crack-propagation in martensitic and austenitic steels", *Metallurgical Trans*, vol. 4, no. 5, p. 1265-1274, 1973.

[BAT 78] C. Bathias, A. Clerivet, *E.F.Q.F. Symposium*, 1978.

[BAT 78] C. Bathias, M. Vancon, "Mechanisms of overload effect on fatigue crack propagation in aluminum alloys", *Eng Fracture Mech*, vol. 10, p. 409-424, 1978.

[BRO 72] D. Broek, C.Q. Bowles, "On the formation of fatigue striations", *Int J Fract Mech*, vol. 8, no. 1, p. 75-85, 1972.

[BUC 75] O. Buck, J.D. Frandsen, H.L. Marcus, "Crack tip closure and environmental crack propagation", *Eng Fract Mech*, vol. 7, p. 167-168, 1975.

[CHA 77] G.R. Chanani, B.J. Mays, "Observation of crack-closure behavior after single overload cycles in 7075-T6 single-edge-notched specimens", *Eng Fract Mech*, vol. 9, p. 65-73, 1977.

[CLA 70] W.G. Clark, E.T. Wessel, "Application of fracture mechanics technology to medium strength steels", *ASTM STP 463*, p. 160-190, 1970.

[CLI 63] F.A. Mc Clintock, *Fracture of Solids*, John Wiley, New York, 1963.

[CLI 67] F.A. Mc Clintock, *ASTM STP 415*, p. 169, 1967.

[DAV 76] D.L. Davidson, J. Lankford, "Plastic stress distribution at tips of propagating fatigue cracks", *J Eng Mat Tech*, p. 24-29, 1976.

[DAV 76] D.L. Davidson, J. Lankford, T. Yokobori, K. Sato, "Fatigue crack tip plastic zones in low-carbon steel", *Int J Fract*, vol. 12, no. 4, p. 579-585, 1976.

[ELB 71] W. Elber, "The significance of fatigue crack closure", *ASTM STP 486*, p. 230-242, 1971.

[EVI 77] Mc Evily, *Fatigue*, University of Cambridge Press, 1977.

[FEL 56] W. Felix, T,H. Geiger, *Revue Technique Sulzer*, vol. 38, no. 1, p. 14, 1956.

[FON 78] A. Font Filax, C. Bathias, *E.F.Q.F. Symposium*, 1978.

[FOR 61] P.J. Forsyth, D.A. Ryder, *Metallurgia*, vol. 63, p. 117-124, 1961.

[GAR 77] G.G. Garrett, J.F. Knott, "Effect of crack closure on rate of fatigue crack propagation", *Int J Fract*, vol. 13, p. 101-104, 1977.

[HAH 72] G.T. Hahn, R.G. Hoagland, A.R. Rosenfield, "Local yielding attending fatigue crack growth", *Metallurgical Trans.*, vol. 3, p. 1189-1202, 1972.

[IKE 77] S. Ikeda, Y. Izumi, M.E. Fine, "Plastic work during fatigue crack propagation in a high strength low alloy steel and in 7050 Al-Alloy", *Eng Fract Mech*, vol. 9, p. 123-136, 1977.

[IRV 75] P.E. Irving, J.L. Robinson, C.J. Beevers, "A study of the effects of mechanical and environmental variables on fatigue crack closure", *Eng Fract Mech*, vol. 7, p. 619- 630, 1975.

[KUD 70] V. Kudryavtsev, A.I. Besman, *Zavods Kaya Laboratoriya*, vol. 36, no 4, p. 469-473, 1970.

[LAL 77] K.M. Lal, S.B.L. Garg, "On the evaluation of monotonic and cyclic plastic zones", *Eng Fract Mech*, vol. 9, p. 433-442, 1977.

[LAR 73] S.G. Larsson, A.J. Carlsson, "Influence of non-singular stress terms and specimen geometry on small-scale yielding at crack tips in elastic-plastic materials", *J Mech Phys Solids*, vol. 21, p. 263-277, 1973.

[LAT 69] H.J. Latiere, H. Caumon, *Comptes Rendus Ac. des Sci.*, Paris, 1973.

[LEV 71] N. Levy, P.V. Marcal, W.J. Ostergren, J.R. Rice, "Small scale yielding near a crack in plane stress: a finite element analysis", *Int J Fract Mech*, vol. 7, p. 143-156, 1971.

[LIN 74] T.C. Lindley, C.E. Richards, "The relevance of crack closure to fatigue crack propagation", *Mat Sci Eng*, vol. 14, p. 281-285, 1974.

[LUK 69] P. Lukas, M. Klesnil, R. Fiedler, "Plastic zone around propagating fatigue crack", *Philosophical Magazine*, vol. 20, p. 799, 1969.

[MAI 72] A. Maillard, L. Meny, J. King, Y. Deleon, *J.M.A.*, 1972.

[MAI 73] R.I. Mair, E.E. Banks, "Spread of yield with mild steel", *Exp Mechanics*, p. 77-82 1973.

[MIL 66] Mc Millan, R.M. Pelloux, "Fatigue crack propagation under program and random loads", *ASTM STP 415*, p. 505-535, 1966.

[NEU 74] P. Neumann, "New experiments concerning the slip processes at propagating fatigue cracks-I", *Acta Metallurgica*, vol. 22, p. 1155-1165, 1974.

[OHT 77] A. Ohta, M. Kosuge, E. Sasaki, "Measurement of stress distribution by moiré fringe multiplication method at a tip of propagating fatigue crack", *Int. J. Fracture*, vol. 13, p. 289-300, 1977.

[PEL 69] R.M. Pelloux, "Mechanisms of formation of ductile fatigue striations", *Trans ASM*, vol. 62, p. 281-285, 1969.

[PEL 70] R.M. Pelloux, "Crack extension by alternating shear", *Eng Fract Mech*, vol. 1, p. 697-700, 1970.

[PET 96] J. Petit, J. Mendez, "Some aspects of the influence of microstructure on fatigue", *Fatigue 96*, vol. 1, p. 15-26, 1996.

[PLU 77] G. Pluvinage, C. Robin, S, Dominiak, "Variation of crack opening-load diagram with fatigue crack growth rate", *Mat Sci Eng*, vol. 29, p. 145-150, 1977.

[POM 70] G. Pomey, *Rev. de Métallurgie*, pp. 327-341, 1970.

[RIC 67] J.R. Rice, "Mechanics of crack tip deformation and extension by fatigue", *ASTM STP 415*, p. 247-311, 1967.

[SCH 77] J. Schjve, "Observations on the prediction of fatigue crack growth propagation under variable amplitude loading", *ASTM STP 595*, p. 3-23, 1977.

[SCH 77] J. Schjve, *Report LR 254*, Delft University, October 1977.

[SHI 77] T.T. Shih, R.P. Wei, *Int J Fract*, vol. 13, 1977.

[TOM 73] B. Tomkins, *Fatigue 1973*, University of Cambridge, March 1973.

[WHE 70] O. Wheeler, *General Dynamics Report*, FZM 5602, 1970.

[WIL 71] Willembourg, Engle, Wood, *AFFD Report*, TM, FRB, January 1971.

Chapter 9

Local Approach to Fatigue Crack Growth

9.1. Introduction

Within ductile materials, constrained crack tip plasticity can lead to some quite spectacular effects. Among them, the overload retardation effect may be the most well-known effect. When overloading is applied to a cracked structure, the crack growth rate strongly decreases immediately afterwards. This phenomenon can be qualitatively explained as follows: during the application of the overload, the material is plastically deformed within a region confined to the end of the crack, whereas the bulk of the structure remains elastic.

Thus, at unloading, the main part of the structure comes back to its original, undeformed shape and imposes its deformation on the plastic region at the crack tip. The plastic zone is then in compression. The level of compressive residual stresses and the extent of the residual stress field strongly depend on the cyclic elastic-plastic behavior of the material. In any case, these compressive stresses decrease the efficiency of the subsequently applied fatigue cycles. The fatigue crack growth rate strongly decreases after the application of an overload, and this remains true until the crack propagates enough for its end to come out of the overload plastic zone.

Chapter written by Sylvie POMMIER.

Some other effects, which will be presented in this chapter, also come from the ability of the material to be plastically deformed, such as the short crack effect and the so-called "constraint" effect related to the shape of the specimen.

In this chapter, we will see how to estimate the dimension of the plastic zones and level of residual stresses.

Then, we will show how these residual stresses occur experimentally and, finally, how to consider, more or less simply, the effects of plasticity on the crack growth rate.

9.2. Plasticity at the crack tip

9.2.1. *Irwin's plastic zones*

The first evaluation of the dimension of the zone disturbed by plasticity is due to Irwin [IRW 60]. In mode I, the asymptotic solutions of the linear elastic fracture mechanics (LEFM) (equations [9.1] to [9.5]), enable us to calculate the von Mises equivalent shear stress [9.4] in the case of a planar crack within a plane that is orthogonal to the y axis and whose front is locally parallel to the z axis.

The strains T, T_{xz} and T_z are the first non-singular terms of the asymptotic development of stresses at crack tip . In mode I, in local plane strain conditions, T_z is equal to zero. If the uncracked equivalent structure does not undergo any shearing, T_{xz} is also equal to zero:

$$\sigma_{xx} = \frac{K_I}{\sqrt{2\pi r}} \cos\frac{\theta}{2}\left(1 - \sin\frac{\theta}{2}\sin\frac{3\theta}{2}\right) + T \qquad [9.1]$$

$$\sigma_{yy} = \frac{K_I}{\sqrt{2\pi r}} \cos\frac{\theta}{2}\left(1 + \sin\frac{\theta}{2}\sin\frac{3\theta}{2}\right) \qquad [9.2]$$

$$\sigma_{xy} = \frac{K_I}{\sqrt{2\pi r}} \cos\frac{\theta}{2}\sin\frac{\theta}{2}\cos\frac{3\theta}{2} \qquad [9.3]$$

$$\sigma_{zz} = \nu\left(\sigma_{xx} + \sigma_{yy}\right) + T_z, \quad \sigma_{xz} = T_{xz} \qquad [9.4]$$

$$\sigma_{eq}^2 = \frac{3}{2}\underline{\underline{s}} : \underline{\underline{s}}$$

with:

$$\underline{\underline{s}} = \underline{\underline{\sigma}} - \frac{Tr\underline{\underline{\sigma}}}{3}\underline{\underline{1}} \qquad [9.5]$$

To estimate the dimension of the plastic zone, we calculate the distance r_Y beyond which the von Mises equivalent shear stress determined using the LEFM stress fields (equations [9.1] to [9.5]) is lower than the yield stress σ_Y of the material. In this calculation, only singular terms are considered. When θ=0, which is to say on the plane of the crack, for r_Y with ν=0 under plane strain conditions, we obtain:

$$r_Y = \frac{(1-2\nu)^2}{2\pi}\left(\frac{K_I}{\sigma_Y}\right)^2 \qquad [9.6]$$

If we assume that the behavior of the material is elastic-ideally plastic, the von Mises equivalent shear stress is equal to σ_Y within the whole plastic zone. To calculate the value of each term of the stress tensor, we presume that the ratio between these terms within the plastic zone is unchanged when the material reaches the yield point, which is to say that when θ= 0:

$$\sigma_{xx} = \sigma_{yy} \qquad \sigma_{zz} = 2\nu\sigma_{yy} \qquad \sigma_{eq} = (1-2\nu)\sigma_{yy} \qquad [9.7]$$

Then, to calculate the dimension r_p of the plastic zone, Irwin [IRW 60], came up with an additional hypothesis. Between r = 0 and $r = r_Y$, the tensile stress σ_{yy} is limited and equal to $\sigma_Y/(1\text{-}2\nu)$. As a consequence, the forces are distributed beyond $r = r_Y$. Between $r = r_Y$ and $r = r_p$, this distribution allows the material to reach its yield stress. Beyond r_p the material remains elastic. The elastic fields are assumed to be similar to those of a crack that is longer than the real crack with a difference of r_Y. The distribution of forces, illustrated in Figure 9.1, allows us to calculate the dimension of the plastic zone:

$$\int_{r=0}^{r=\infty} \frac{K_I}{\sqrt{2\pi r}}dr = r_p\sigma_f + \int_{r=r_p}^{r=\infty} \frac{K_I}{\sqrt{2\pi(r-r_Y)}}dr \qquad [9.8]$$

We can then deduce the equation of the dimension of the monotonic plastic zone, which evolves as the square root of the ratio between K_I and σ_Y:

$$r_p = 2r_Y = \frac{(1-2\nu)^2}{\pi}\left(\frac{K_I}{\sigma_Y}\right)^2 \qquad [9.9]$$

If a load release with amplitude ΔK_I is then applied from this point, the local stress amplitude that needs to be applied to create plasticity at unloading is equal to $2\sigma_Y$. If we simply apply equation [9.9], we find that the dimension of the zone that is plastically deformed at unloading, also called the cyclic plastic zone, is equal to a quarter of the dimension of the monotonic plastic zone when the stress intensity factor amplitude ΔK_I is equal to the maximum value of the stress intensity factor K_I:

$$r_{pc} = \frac{(1-2\nu)^2}{\pi}\left(\frac{\Delta K_I}{2\sigma_Y}\right)^2 = \frac{1}{4}r_p \qquad [9.10]$$

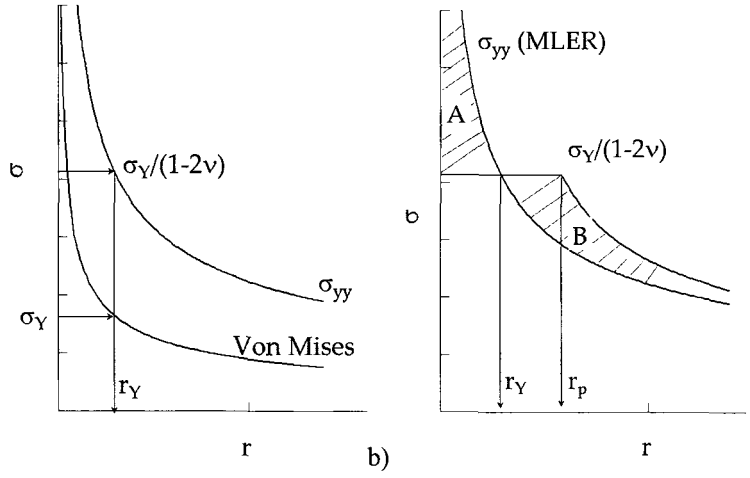

Figure 9.1. *a) Determination of r_Y using von Mises' equivalent stress from the linear elastic fracture mechanics fields; and b) determination of the dimension r_p of the plastic zone from the distributions of the tensile stress ahead of the crack tip. Stresses are plotted as a function of distance from the tip of the crack r*

If we compare this simplified method with finite elements calculations under elastic ideally plastic conditions, it correctly estimates the stress level σ_{yy} reached within the plastic zone, either under plane stress or plane strain conditions , as well as the area of the plastic zone in plane stress conditions. In plane strain conditions, the area of the plastic zone reaches its maximum on an axis with an angle 70° from the crack plane and not with $\theta = 0$.

9.2.2. *T-Stress effect*

In the particular case of a through thickness crack in an infinite plane subjected to a bi-axial loading state at infinity (S_x, S_y) (Griffith cracks), the stress intensity factor is equal to $K_I = S_y(\pi a)^{1/2}$, whereas the T-stress is equal to $T = S_x - S_y$.

Usually, in mode I, the non-singular terms T, T_z and T_{xz} depend:

– on the stress normal to the crack plane σ_{yy};

– on stresses σ_{xx}, σ_{xz} and σ_{zz} applied to the uncracked structure;

– on the distance between the crack tip and the free surfaces;

– on the crack length.

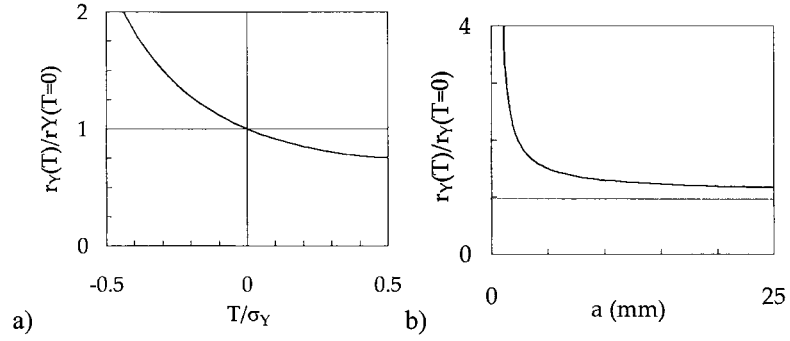

Figure 9.2. *Dimension of Irwin's plastic zone with T-stress non-dimensioned by the one calculated when T = 0: a) as a function of the ratio between the T-stress and the yield stress of the material σ_Y; b) As a function of crack length a, when σ_Y = 400 MPa, K_I =15MPa.m$^{1/2}$ and for a Griffith crack with a length of 2a under a uni-axial loading*

Using the same simplified hypotheses that were presented above, we can study the effect of T-stress on the plastic zone dimension at the crack tip. Simple calculation [9.11] under plane stress conditions shows that the dimension of the plastic zone strongly depends on the ratio between stress T and the elasticity limit of the material σ_Y:

$$\frac{r_Y(T)}{r_Y(T=0)} = \frac{2}{2-\left(\frac{T}{\sigma_Y}\right)^2 + \left(\frac{T}{\sigma_Y}\right)\sqrt{4-3\left(\frac{T}{\sigma_Y}\right)^2}} \qquad [9.11]$$

In the particular case of a Griffith crack, and for an infinite uni-axial loading ($S_x = 0$), we can calculate the T-stress as a function of the stress intensity factor and of the length of the crack: $T = -K_I (\pi a)^{-1/2}$. Thus, equation [9.11] enables us to show that, for an identical stress intensity factor, the dimension of the plastic zone strongly decreases when the crack length increases (Figure 9.2b).

Terms T_z and T_{xz} have the same role regarding plasticity at the crack tip. Negligible in the case of a short crack, these terms are significant when the dimension of the crack decreases.

9.2.3. *Role of strain hardening of the material*

The previous calculations allow us to estimate the dimension of the plastic zone for an elastic ideally plastic material. Nevertheless, the materials usually present some strain hardening, which can significantly modify the dimension and shape of the plastic zone at the crack tip.

In order to study the role of strain hardening, the strain fields at the crack tip were independently calculated by Hutchinson [HUT 68], Rice and Rosengren [RIC 68] for a non-linear elastic behavior (HRR fields).

Let us consider an elastic-plastic material following the Ramberg-Osgood behavior law, with hardening exponent n under uni-axial traction conditions. This law can be used in multi-axial conditions [9.12] through a hypo-elastic formulation:

$$\dot{\underline{\underline{\varepsilon}}} \approx \dot{\underline{\underline{\varepsilon}}}_p = \frac{3}{2}\frac{1}{E}\alpha\left(\frac{\sigma_{eq}}{\sigma_o}\right)^{n-1}\dot{\underline{\underline{s}}} \qquad [9.12]$$

To obtain the stress fields at the crack tip, Rice *et al.* [RIC 68] calculated the order of the singularity using energetic considerations based on integral J, and then determined the angular functions. Coefficient I_n, along with the angular functions $\tilde{\underline{\underline{\sigma}}}_n(\theta)$ is a function of the hardening exponent. Solutions of differential equations are quite complex. Some tabulated solutions can be found in [SHI 83].

The asymptotic stress field at the crack tip can be written with the following [9.13]:

$$\underline{\underline{\sigma}} = \sigma_o\left(\frac{1}{\alpha\sigma_o\varepsilon_o I_n}\right)^{\frac{1}{n+1}}\tilde{\underline{\underline{\sigma}}}_n(\theta)\left(\frac{J}{r}\right)^{\frac{1}{n+1}} \qquad [9.13]$$

These calculations enabled us to show that the strain hardening of a material strongly influences the distribution of stresses around the crack tip. Indeed, the stress field presents a singularity with order $1/(1 + n)$ where n is the strain hardening exponent.

In addition, Rice *et al.* [RIC 68] present a figure where the shape of the approximate boundary between the plastic and elastic zones at the crack tip is plotted (see Figure 9.3). We can clearly see in this figure that the shape of the plastic zone strongly depends on the hardening exponent. Located around the y axis in plane strain conditions and for an ideally elastic plastic behavior, this plastic zone bows backwards when the strain hardening of the material is increased (see Figure 9.3). Finite element calculations have enabled us to confirm these results.

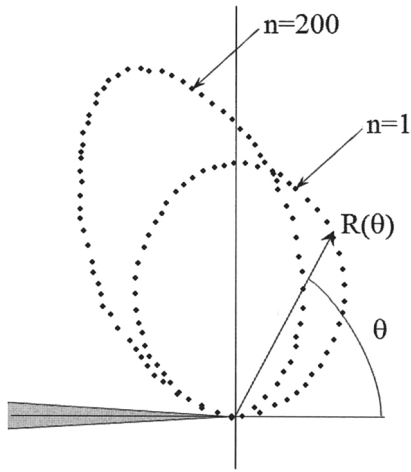

Figure 9.3. *Shape of the approximate boundary between the elastic and plastic domains following the exponent of the Ramberg-Osgood law [RIC 1968]*

Nevertheless, the singularity of the stress at (J/r) with a power of $1/(1 + n)$ means that the stresses are infinite when r tends towards zero. This is not often the case as the bluntness at the crack tip leads to a free surface in $r = 0$ where, depending on the Tresca criterion, the maximum principal stress does not exceed the yield stress of the material.

Ma and Kuang [MA 95] published an analytical calculation of the stress fields for a hypo-elastic behavior and for a blunted crack. Using this approach, the stress is not singular anymore at the crack tip and reaches its maximum ahead of the crack tip, within the plastic zone.

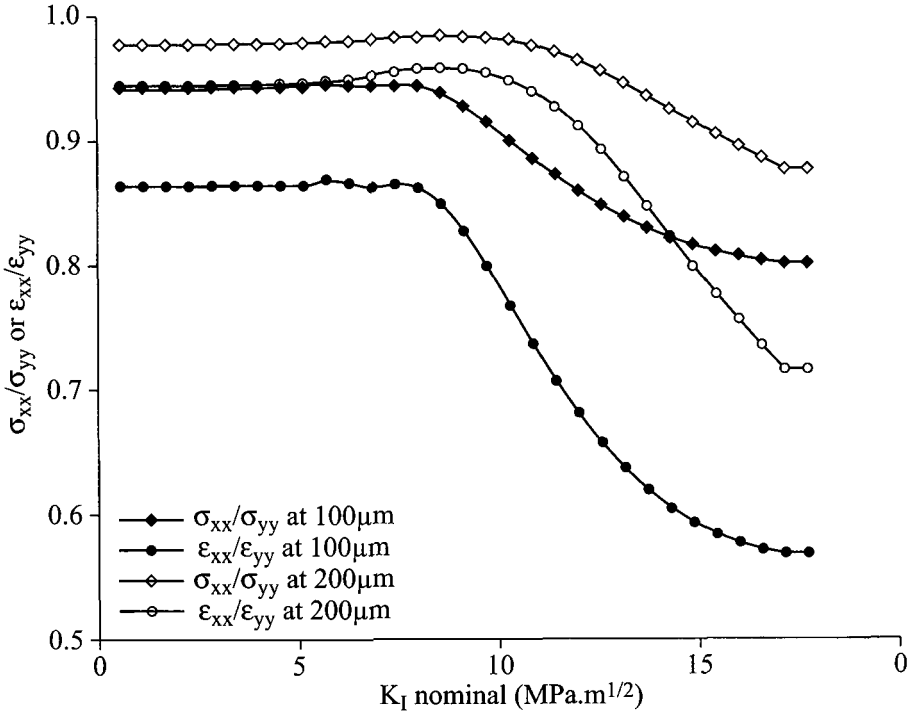

Figure 9.4. *Ratios between ε_{xx} and ε_{yy} or between σ_{xx} and σ_{yy} on the crack plane at 100 μm and 200 μm from its end; the dimension of Irwin's plastic zone being about 130 μm. Calculations were performed using the finite element method, with an elastic-plastic law presenting some isotropic hardening (R_e=350 MPa, R_m=700 MPa) and size of the elements being 10 μm*

The HRR fields were established to deal with non-linear fracture mechanics problems for which plastic deformation is not constrained at crack tip, and for which it is possible to neglect elastic deformation compared with plastic deformation. This is not the case, however, in fatigue.

In Figure 9.4, for instance, the stresses and strains that were calculated using the finite element method within the plastic zone are plotted as a function of the nominal stress intensity factor applied. During the loading of the specimen, the ratio between two stress or strain terms is not constant.

Thus, the distribution of stresses and strains, and not only their intensity, depends on the loading applied. For instance, as deformation ε_{yy} increases, ε_{xx} also increases at the start, as predicted by the linear elastic fracture mechanics fields. Then, since

plastic strain occurs without any changes in volume, the plastic deformation in the y-direction comes with a contraction towards direction x.

Thus, the sign of the ratio between ε_{yy} and ε_{xx} is changed when the plastic deformation increases. The same thing can be observed for stresses. These path changes, due to competition between the relative importance of elastic deformation (with volume change) and plastic deformation (without volume change), cannot be ignored under fatigue conditions as the elastic deformation cannot be neglected when compared with plastic deformation in most of the plastic zone at the crack tip.

9.3. Cyclic plasticity at the crack tip

One of the characteristics of the fatigue crack growth phenomenon is the cyclic nature of the loading scheme. It has two main consequences.

First of all, the material that is located within the plastic zone undergoes cyclic plastic deformation. As a consequence, the characteristics of the cyclic material behavior have to be considered instead of that of the monotonic tensile behavior.

Then, the plastic zone formed during loading remains constrained and residual stresses appear during unloading. Since these residual stresses lead to some spectacular memory effects, the unloading phase (the minimum stress of the cycle) is just as important as the loading phase (the maximum stress of the cycle).

9.3.1. *Cyclic elastic-plastic behavior of the material*

Cyclic push-pull tests enable us to distinguish the kinematics hardening component from the isotropic one. Indeed, if we plot the stress as a function of plastic strain (see Figure 9.5), we can observe that there are some loading phases during which the plastic deformation does not evolve at all. The material behaves elastically. Its elastic domain can then be characterized by two variables: the position of its center (X) and its dimension ($2R$).

During the first cycle, the initial yield stress R_e lies around 170 MPa. The direction of the deformation is reversed for a plastic strain of $\varepsilon_p = 0.9\%$. During unloading, the material remains within its elastic domain until plastic deformation occurs, at a stress of -113 MPa. The elastic domain of the material is then strongly shifted towards the positive stresses, its center X being around +100 MPa when $\varepsilon_p = 0.9\%$. After a compression step at $\varepsilon_p = -0.9\%$, X is then located around -100 MPa. This effect, which is called the "Bauschinger effect" or "kinematic hardening", is commonly observed within metallic materials.

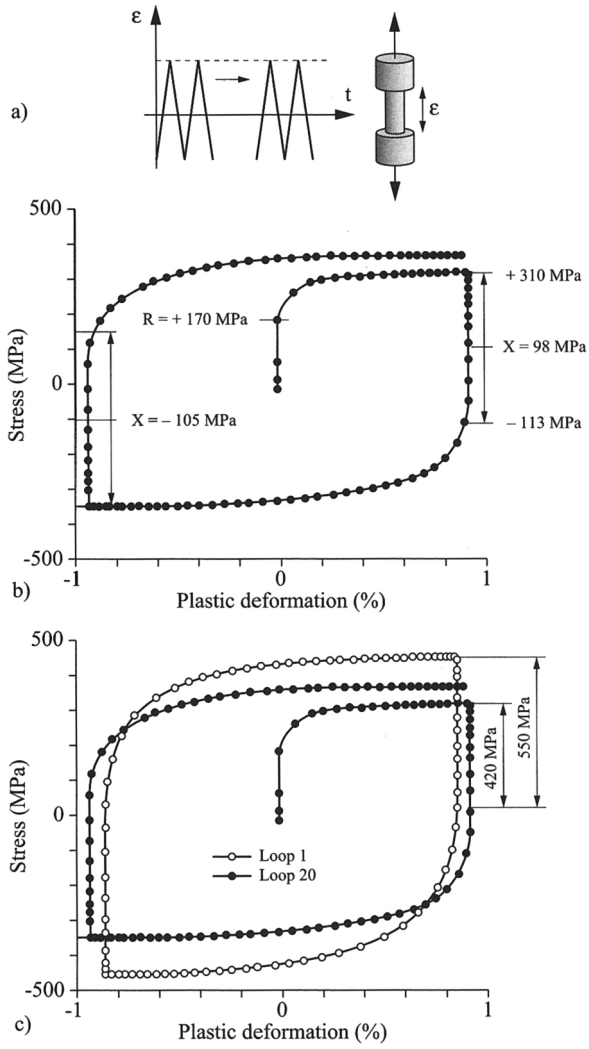

Figure 9.5. *a) Illustration of a push-pull test under strain controlled conditions; b) hysteresis loops N°1; c) loops N°1 (whole circles) and N°20 (empty circles). Test run at room temperature on stainless steel 316L with an imposed strain rate of* $0.001s^{-1}$

In addition, these tests also enable us to follow evolution of the dimension of the elastic domain. For a deformation of ε_p= 0.9%, the dimension *2R* of the elastic domain has a value of 420 MPa after the first cycle and of 550 MPa after 20 cycles. This phenomenon is called the isotropic hardening of the material. The reverse effect or softening can also be observed.

As tension-compression cycles are applied within the cyclic crack tip plastic zone, it is important to correctly consider the characteristics of the cyclic elastic plastic behavior of the material, including kinematic and isotropic hardening components [LEM 85] to predict the cyclic plastic deformation at the crack tip.

9.3.2. *Plasticity induced history effect in fatigue crack growth*

9.3.2.1. *Residual stresses*

During the initial opening of a crack, the material is plastically deformed within a region confined to the end of the crack, whereas the bulk of the structure remains elastic. Thus, at unloading, the main part of the structure comes back to its original, un-deformed shape and imposes its deformation on the plastic region at crack tip. The plastic zone is then in compression. Compressive residual stresses superimpose with subsequent applied stresses and reduce the residual stresses' efficiency. This effect leads to plasticity induced history effect in fatigue crack growth.

As discussed above, the level of these residual stresses strongly depends on the behavior of the material. In Figure 9.6, two push-pull test simulations are plotted in for two behavior laws [CHA 77]. Both laws rigorously simulate the same result in monotonic tension, but are significantly different under cyclic conditions. Indeed, the first law involves a kinematic type of strain hardening whereas the second one presents an isotropic strain hardening.

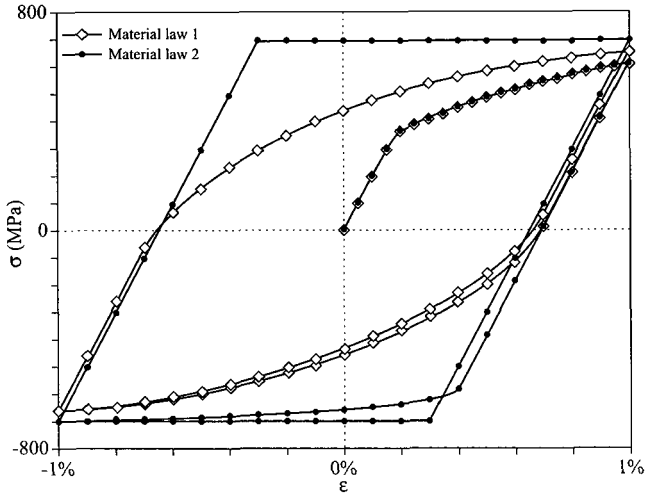

Figure 9.6. *Push-pull test simulation with two material laws: the first material law presenting a kinematic hardening; and the second isotropic hardening. Both laws have the same behavior under uni-axial monotonic tension conditions. Chaboche model [CHA 77]*

These two laws were used in finite element analysis to determine plastic deformation at the crack tip. Calculations were performed under plane strain conditions. For these calculations, the maximum nominal stress intensity factor was 42 MPa.m$^{1/2}$. During the unloading phase, a zone of about 400 μm is subjected to compressive residual stresses. In Figure 9.7, the evolution of the stress component σ_{yy} is plotted as a function of strain component ε_{yy} at 62 μm from the crack tip. This figure leads us to two observations. First of all, even at a short distance from the crack tip, elastic strains are not negligible compared to plastic strains. Second, the residual stress level reached after unloading strongly depends on the behavior of the material.

The residual stress profiles after unloading are plotted in Figure 9.8. We can observe that, if the material presents a kinematic-type hardening law(law 1), the plastic zone is wider but the residual stresses within this zone are lower than for an isotropic-type hardening law (law 2). Finally, the residual stresses are more multi-axial. Within the entire plastic zone, for instance, the ratio between σ_{xx} and σ_{yy} is close to 1 (law 1).

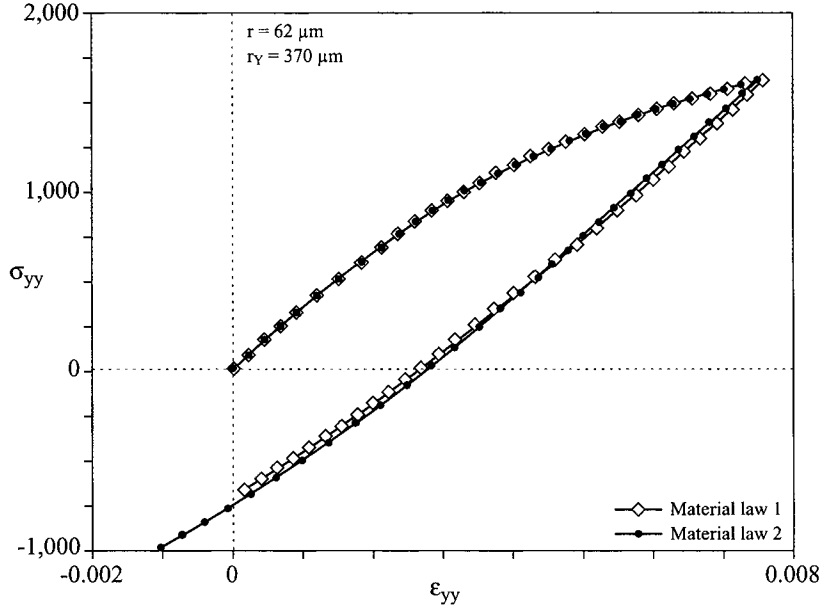

Figure 9.7. *Finite elements simulations, under plane strain conditions, of a uni-axial tension phase with K_{max} = 42 MPa.m$^{1/2}$ followed by complete unloading with the two material laws presented in Figure 9.6. Plot of the evolution of the stress component σ_{yy} (normal to the plane of the crack) as a function of ε_{yy} on the plane of the crack at 62 μm from its end, i.e. at about one seventh of the dimension of the plastic zone*

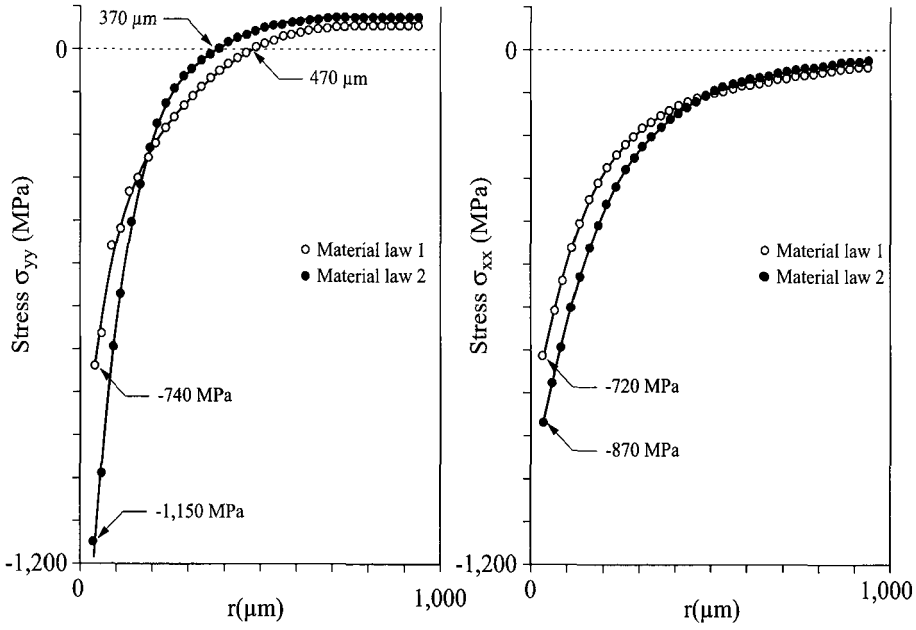

Figure 9.8. *Finite elements simulations, under plane strain conditions, of a uni-axial tension phase with K_{max} = 42 MPa.m$^{1/2}$ followed by complete unloading with the two material laws presented in Figure 9.6. Plot of the profiles of residual stress components σ_{yy} and σ_{xx} for each law as a function of distance from its end.*

9.3.2.2. *Effects of residual stresses on the crack propagation*

Residual stresses have different effects on the propagation of fatigue cracks. It is worth noting, for instance, the overload retardation effect or the stress ratio effect [ELB 71, FOR 67, SCH 73, WHE 72, WIL 71].

In Figure 9.9, for example, we can observe the evolution of the length of fatigue cracks that were measured during tests on a ferritic-pearlitic steel in constant amplitude fatigue, either without any application of overload or after a unique overload with a factor of 1.5 or 1.8 was applied [HAM 07]. After the application of an overload, the crack growth rate significantly decreases as long as its end is inside the overload plastic zone (in this case, about 0.5 mm for an overload factor of 1.8). The crack growth rate then progressively increases until it returns to the level it should be without any overloading. In the present case, the crack has to propagate more than 4 mm after an overload with a factor of 1.8 to "forget" that overload.

This overload retardation effect was associated with crack tip plasticity in the early 1970s. Wheeler [WHE 72] and Willenborg [WIL 71] models directly connect the crack growth rate due to fatigue to the plastic zone created by overloading.

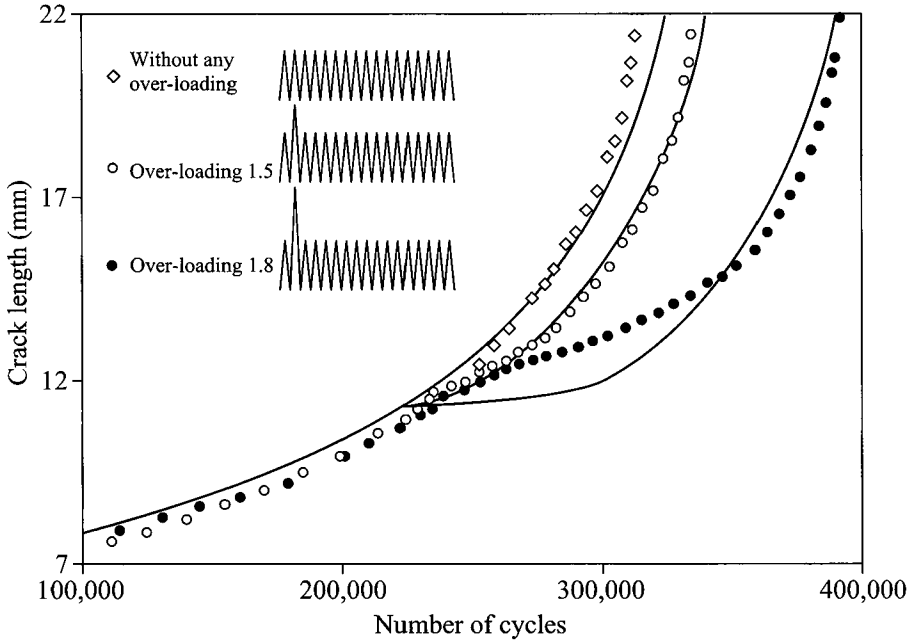

Figure 9.9. *Results of fatigue crack growth tests on a ferritic-pearlitic steel with 0.48%C. CCT specimen. Amplitude of the applied stress $\Delta\sigma$=100 MPa, stress ratio R = 0.05. Overload of 150 MPa or 180 MPa. Symbols: experiments. Lines, simulations using the LMT model [HAM 07]*

For instance, the Wheeler's model consists of multiplying the crack propagation rate, by a delay function ϕ. The value of this delay function is below one as long as the plastic zone of the propagating crack remains within the overload plastic zone:

$$\left(\frac{da}{dN}\right)_{delay} = \varphi\left(\frac{da}{dN}\right)_{no\ delay} \qquad [9.14]$$

The delay function ϕ is defined as follows: it is a function of the current dimensions of the crack a_i and its the plastic zone ZP_i, the dimensions of the crack $a_{overload}$ and the size of the plastic zone $ZP_{overload}$ when the overload is applied:

$$\varphi = \left(\frac{ZP_i}{\left(a_{overload} + ZP_{overload}\right) - a_i} \right)^{m_w} \qquad [9.15]$$

The Willenborg model [WIL 71] is also related to the dimension of the plastic zone, determined by applying Irwin's method except the delay effect is applied on the stress intensity factor. These empirical models directly associate plasticity and history effect in fatigue crack growth but do not, however, explain why the crack growth rate remains lower after an overload than that observed in the absence of an overload even once the crack tip has moved out of the overload plastic zone.

Around the same time, Elber [ELB 71] introduced the concept of plasticity induced crack closure. This closure effect is explained as follows. After the application of an overload, compressive residual stresses appear within the overload plastic zone. When the crack propagates through this plastic zone, the residual stresses may keep the crack closed during a significant part of the fatigue cycle. The loading is therefore only efficient above a threshold stress intensity factor K_{op} at which the crack opens. The propagation rate of the cracks can then be calculated with:

$$\frac{da}{dN} = C\left(\Delta K_{eff}\right)^m \qquad \text{where} \qquad \Delta K_{eff} = K_{\max} - K_{op} \qquad [9.16]$$

9.3.2.3. *Crack closure effect*

With this approach, in order to predict the fatigue crack growth rate we still have to determine the crack opening threshold K_{op}. This threshold is a consequence of the development of a crack tip plastic zone. However, we can measure this opening threshold using conventional tests, whereas the measurement of the dimension of the plastic zone still remains delicate.

We can fix an opening sensor at the crack mouth and plot the force-displacement curve, for example, and then calculate the rigidity of the specimen when the crack is completely open or fully closed. The gap between measured displacement and the displacement calculated using this rigidity allows us to define the opening threshold and its evolution, for instance after an overload. It is worth noting that different methods are proposed to analyze experimental results, leading to different values of the opening or closure level. Some test results, reported in Figure 9.10b, show that the opening threshold is located at 30% of K_{max}, right before the overloading, and then significantly increases to be around 80% of K_{max} 5,000 cycles after the overload has been applied, before decreasing to be around 50% of K_{max} 10,000 cycles after the overload has been applied.

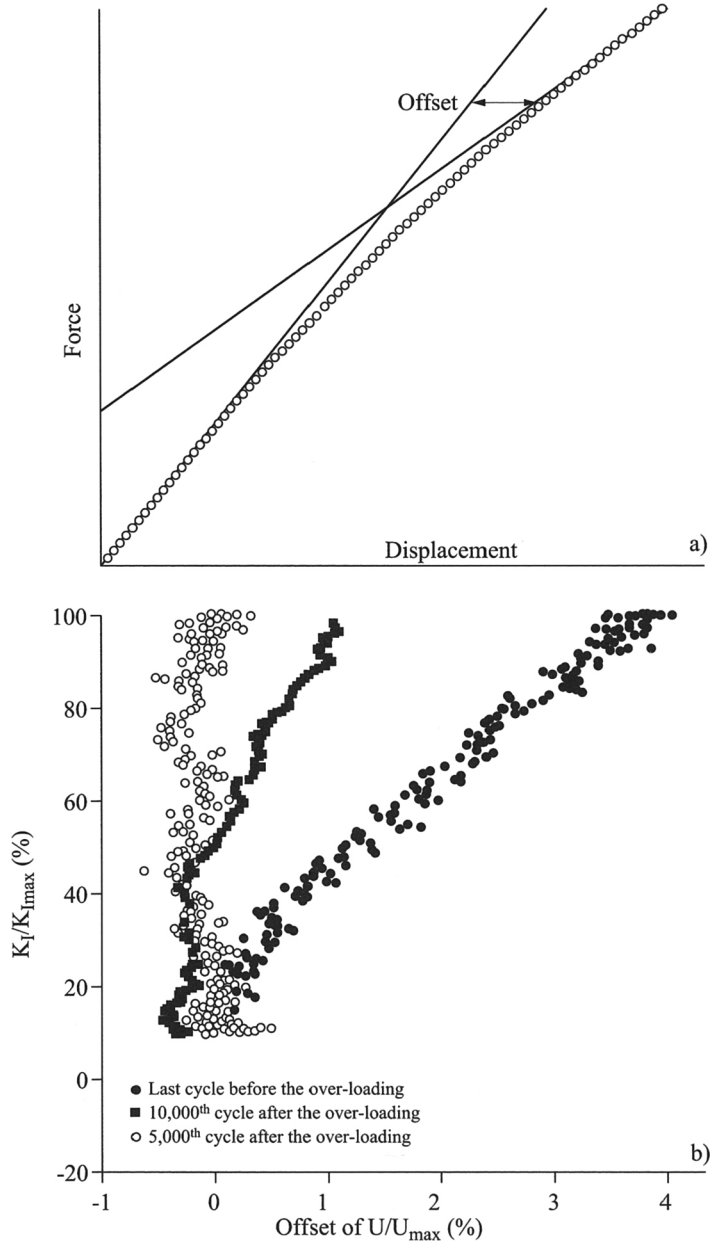

Figure 9.10. *a) Schematic of the analysis of a load displacement curve to determine the opening level and to calculate the offset; b) test results using 0.3% C ferritic-pearlitic steel (CT specimen, before and after the application of an overload)*

9.3.2.4. *Calculation of the opening threshold K_{op}*

Numerous models have been developed to determine the crack opening threshold. Three main strategies can be distinguished.

The first strategy consists in identifying the models semi-empirically (*preffas*, *corpus*, *onera*) [FLE 88, NEW 88, NEW 92]. In these models, one or two evolution laws are defined for K_{op} as a function of its current value and of the applied stress intensity factor. The parameters of these evolution laws are experimentally adjusted using fatigue crack growth tests in constant or variable amplitude fatigue.

The advantage of this approach is that it can be well adapted to any material as we can adjust the coefficients in relation to experimental results. The drawback is the experimental cost and difficulty in extrapolating the results to some cases that were not explored in the experimental database.

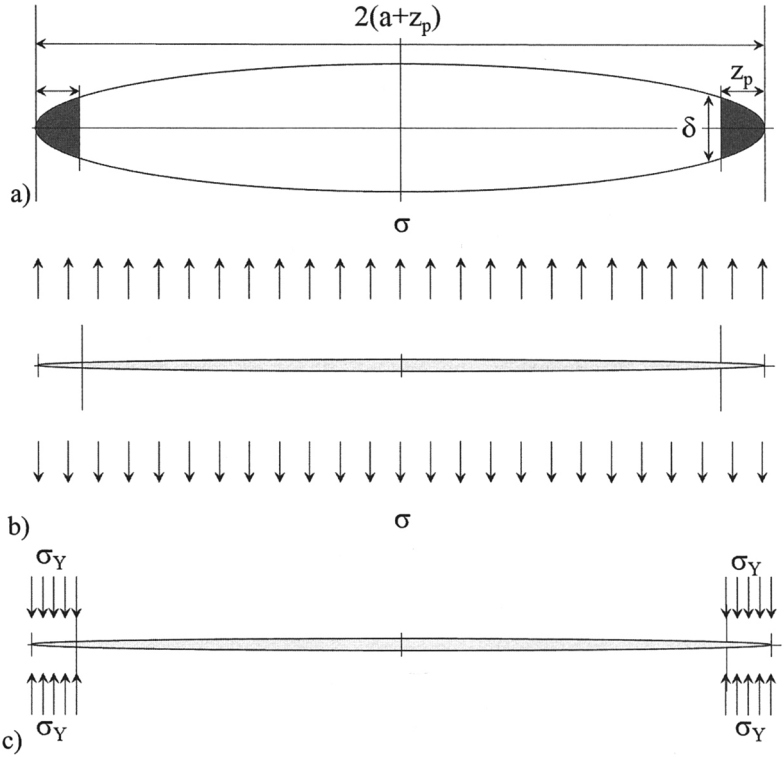

Figure 9.11. *a) Definition of the terms; b) calculation of $K_I(\sigma)$; c) calculation of $K_I(\sigma_Y)$*

The second main strategy is to set up a semi-numerical method to determine K_{op} [DEK 81, NEW 92], based on Dugdale's model [DUG 60]. Dugdale's model [DUG 60] enables us to calculate the plastic zone size for a crack within an elastic-ideally plastic material in plane stress conditions. To some extent, this model can also be applied to plane strain conditions. This model considers a crack with a fictitious length of $a + z_p$ where a is the physical length of the crack and z_p the size of its plastic zone. For a through thickness crack within an infinite plate subjected to stress σ at infinity, the applied stress intensity factor can be calculated as follows:

$$K_I(\sigma) = \sigma\sqrt{\pi(a+z_p)} \qquad [9.17]$$

Within the plastic zone, cohesive stresses are assumed to maintain the crack closed. These cohesive stresses are equal to the yield stress of the material, σ_Y. The corresponding stress intensity factor can be calculated as follows:

$$K_I(\sigma_Y) = -\sigma_Y\left(1-\frac{2}{\pi}arcsin\left(\frac{a}{a+z_p}\right)\right)\sqrt{\pi(a+z_p)} \qquad [9.18]$$

$$K_I^* = K_I(\sigma_Y) + K_I(\sigma) = 0 \Rightarrow z_p \approx \frac{\pi}{8}\left(\frac{K_I(\sigma)}{\sigma_Y}\right)^2 \qquad [9.19]$$

The resulting intensity factor K_I^* is calculated by superposition (see Figure 9.11). As the singularity disappears at the end of the crack, due to plasticity, we can determine the value of z_p, which allows K_I^* to be canceled (see equation [9.19]). For a through thickness crack within an infinite plate, calculations can be easily carried out and the dimension of the plastic zone obtained is close to Irwin's. We then calculate displacement at a distance z_p from the end of the fictitious crack, which is the end of the real crack, using the displacement field corresponding to the applied stress intensity factor:

$$\delta = \frac{1}{E}\frac{K_I^2}{\sigma_Y} \qquad [9.20]$$

Now, to calculate the crack closure level, we can discretize the plastic zone into strip yields that are elongated during crack opening [BUD 78, DEK 81, NEW 92] depending on equation [9.21]. Each strip is considered as a uni-axial tension specimen, it is elastic at unloading and allows the determination of the residual

stress level in each strip. This method enables us to calculate the residual stresses along the crack faces when the crack is growing, and then to deduce K_{op} by superposition (Figure 9.12):

$$u_y = \delta \frac{\sqrt{r}}{\sqrt{z_p}} \qquad [9.21]$$

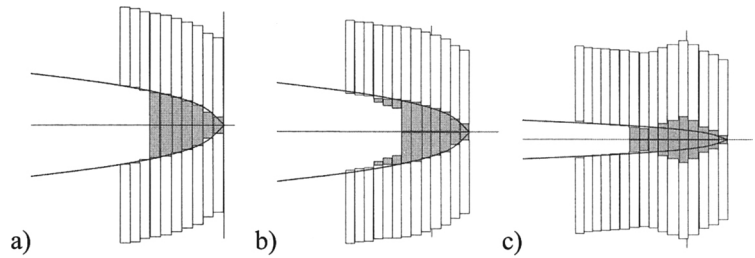

Figure 9.12. *Strip Yield method; a) plasticized zone in front of the crack tip; b) plastic wake being formed during propagation of the crack; and c) idem, but once the crack is closed*

This semi-numerical method allows us to calculate load history effects for quite complex variable amplitude loading scheme. It gives good results under plane stress conditions for a various materials (thin aluminum sheet, for instance). Nevertheless, under plane strain conditions the method cannot be applied as successfully because of the strong stress triaxiality within the plastic zone.

Newman *et al.* [NEW 88] suggested considering the triaxiality effect through a constraint factor α applied to the yield stress of the strip yields in tension. The method does not, however, allow us to correctly consider the effects related to material hardening, shape and size of the plastic zone.

Finally, the most precise strategy to calculate opening stress intensity factor is the finite element method [MCC 96, POM 00, POM 01]. Some rules have to be respected for the results to be valid [MCC 96]. The size of the elements has to be at least a tenth of the cyclic plastic zone's dimension, which corresponds to a fortieth of the monotonic plastic zone. To establish a stable plastic wake along the crack faces, we have to propagate the crack, element by element, to at least two or three times the dimension of the monotonic plastic zone. Whenever an element is set free, a sufficient number of cycles have to be applied to stabilize the elastic-plastic response of the material at crack tip. Thus, numerically simulating the effect of an overload on the opening threshold usually requires the simulation of a few hundred non-linear cycles. Thus, even if the finite element method is very efficient and has experimentally been shown to be valid, it is still difficult to carry out.

9.4. Local approach to fatigue crack growth

The simulation of fatigue crack growth including history effects therefore requires reliable modeling of cyclic plasticity within the crack tip region. The finite element method allows us to consider complex material laws and to test various configurations. Nevertheless, calculations using finite elements are still hard to carry out, which is why a scale-up has been suggested.

9.4.1. *Approach*

The reasoning used to model the propagation of fatigue cracks in mode I with their history effects is now explained. The local approach (very fine calculations using finite elements) is used to precisely calculate the evolution of stresses and strains within the crack tip region while considering the cyclic elastic-plastic behavior of the material.

A scale-up method is then applied to identify a model of the cyclic elastic-plastic behavior of the crack tip region at a global scale. Once the model has been identified, there is no further need to perform any finite element calculations; the model can be used directly for different types of loading.

The principle of scale-up is simple. It is based on an approximation of the kinematics in the crack tip region. In mode I, the displacement field at the crack tip is assumed to be partitioned into an elastic and a plastic part. Both parts are assumed to come from an intensity factor (as a function of the boundary conditions and of geometry of the crack) and from a reference field (only as a function of the space coordinates). This second approximation allows us to perform a scale-up from the local scale – where finite element calculations are carried out – to the global scale, where the evolutions of both intensity factors are useful.

If the plastic zone is well confined, the intensity factor of the elastic part of the displacement field remains close to the nominal stress intensity factor of the linear elastic fracture mechanics. At the global scale, cyclic plasticity within the crack tip region can be followed through the variations of a unique scalar variable – the intensity factor of the plastic part of the displacement field ρ_I.

The evolutions of ρ_I, calculated using finite elements, enable us to identify a global cyclic elastic-plastic behavior model for the crack tip region. It is basically a model allowing us to calculate $d\rho_I/dt$ as a function of the loading applied (dK_I/dt).

In addition, we introduce a crack growth law that connects the rate of a creation of cracked area per unit length of crack front (da/dt) to the variation rate ($d\rho_I/dt$) of the intensity factor of the plastic part of the displacement field.

To identify this model, we have to carry out at least two tests: one to determine the cyclic behavior of the material (local elastic-plastic model) and another one identify the unique coefficient in the crack growth law. This second test should be a crack propagation experiment in constant amplitude fatigue.

The main advantages of this approach is that it combines the advantages of local approaches, that allow a fine description of effects due to the behavior of the material, and that of semi-empirical approaches, that ensure reduced calculation time during the simulations [HAM 07, POM 07].

9.4.2. *Scale-up method*

The scale-up approach is based on the following hypothesis. First of all, we write an incremental model that gives the instantaneous crack growth rate (da/dt). We can then assume that elastic and plastic deformations within the crack tip region and the extension of the crack are infinitesimal. Then, we suppose that plastic deformation at the crack tip remains well confined. We can then fit our calculations into the linear fracture theory, and also improve the crack tip fields in order to consider cyclic plastic deformations. To do so, we suppose that the displacement field within a coordinate system attached to the crack tip can be calculated as follows:

$$\underline{u}(\underline{x},t) \approx k_I(t)\underline{u}^e(\underline{x}) + \rho_I(t)\underline{u}^c(\underline{x}) \qquad [9.22]$$

where:

– $u(x,t)$ is the displacement field calculated using the finite element method during a time increment;

– k_I is the intensity factor of the elastic part of the displacement fields;

– u^e is the solution to the elastic problem for a nominal stress intensity factor equal to 1;

– ρ_I is the intensity factor of the plastic part; and

– u^c is a complementary field. This field can be built directly from the numerical results by using, for instance, the Karhunen-Loève transformation. Alternatively, however, we can use the displacement field of an edge dislocation (equations [9.23]-[9.24]). In any case, we can approximate the displacement field $u(x,t)$ with less than a 10% error when the material is isotropic.

$$u_x^c(r,\theta) = \frac{1}{\pi(\kappa+1)}\left[(\kappa-1)\log r - 2\cos^2\theta\right] \quad [9.23]$$

$$u_y^c(r,\theta) = \frac{1}{\pi(\kappa+1)}\left[(\kappa+1)\theta - 2\cos\theta\sin\theta\right] \quad [9.24]$$

Once the elastic field u^e and the plastic complementary field u^c are known, approximation [9.22] is carried out using the least squares method for each time increment of a non-linear finite element calculation. We find that k_I is very close to the nominal stress intensity factor if the plastic zone at the crack tip is well confined.

Evolution of intensity factor ρ_I of the plastic part is presented in Figure 9.13. After each change of the loading direction , we can find a domain (called C) within which ρ_I does not vary. As ρ_I is a measurement of plasticity at the global scale, this domain can be considered to be an elasticity domain for the crack tip region. We can then introduce two internal variables to characterize this elasticity domain. By analogy with the plasticity of continuous mediums, we can define a variable X^c to define the position of the center of this domain and a variable R^c to define its size.

In addition, if we reload the crack tip region beyond the maximum previously reached (called D in Figure 9.13) the curve presents a change of slope. Indeed, beyond point D, the monotonic plastic zone of the crack increases. We will then have to introduce two elasticity domains: one for the cyclic plastic zone and another for the monotonic plastic zone. The elasticity domain of the monotonic plastic zone is also characterized by its position X^m (closure point) and by its size R^m.

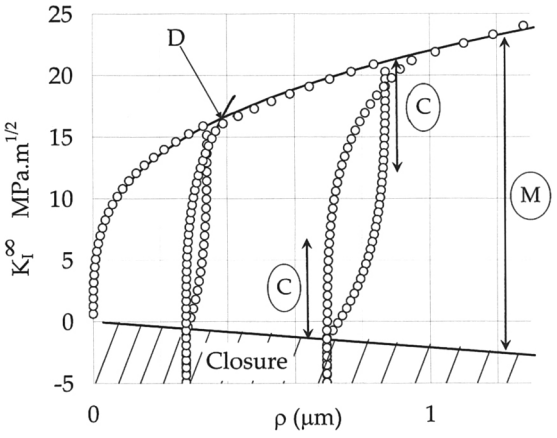

Figure 9.13. *Evolution of intensity factor ρ_I of the plastic part of the displacement field during simulation of loading-unloading cycles using the finite element method*

Various calculations are carried out using the finite element method, including simulations with node release to simulate a crack extent. These calculations, enable us to identify the empirical evolution laws for the internal variables, [POM 07] and their coefficient for each material:

$$\frac{\partial X^c}{\partial \rho_I}, \frac{\partial X^c}{\partial a}, \frac{\partial R^c}{\partial \rho_I}, \frac{\partial R^c}{\partial a}, \frac{\partial X^m}{\partial \rho_I}, \frac{\partial X^m}{\partial a}, \frac{\partial R^m}{\partial \rho_I}, \frac{\partial R^m}{\partial a} \qquad [9.25]$$

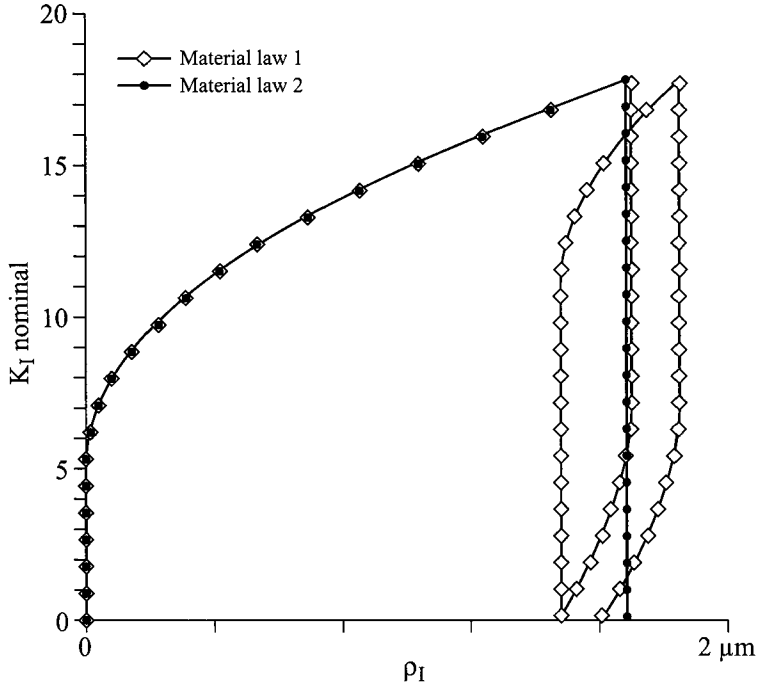

Figure 9.14. *Evolution of intensity factor ρ_I of the plastic part of the displacement field during simulation of loading-unloading cycles for two material laws: one (law 1) presents kinematic strain hardening and the other (law 2) isotropic strain hardening (see Figure 9.6)*

In Figure 9.14, for example, we can find the evolution of ρ_I calculated for the two behavior laws of Figure 9.6 for two loading-unloading cycles. We can clearly see the effect of the material's behavior on the evolution of ρ_I. When the material presents kinematic-type hardening (law 1) some cyclic plasticity occurs at each cycle, whereas when the hardening law is isotropic, the cycle remains essentially elastic (law 2).

Once the scale-up process, described above, has been carried out, we can rely on a cyclic elastic-plastic behavior model within the crack tip region at the global scale. To deduce a fatigue crack growth model, we then suppose that the crack rate da/dt is a function of $d\rho/dt$. At first, we can simply assume that:

$$\frac{da}{dt} = \alpha \left\langle \frac{d\rho_I}{dt} \right\rangle \qquad [9.26]$$

where α is a constant to be identified. This last hypothesis agrees with all the previous observations [CLI 67, LAI 67] that showed that, under Paris' regime, the macroscopic crack growth rate is proportional to the striation spacing, this striation spacing also being proportional to the level of plastic deformation at the crack tip. This equation can be modified; for example, to consider the effects of corrosion, which also depend on time [RUI 06].

9.4.3. *Application*

A model was identified [HAM 07] for a steel containing 0.48% carbon used to manufacture train wheels. The behavior of the wheels' material was identified with cyclic traction-compression tests on cylindrical specimens. Its behavior was modeled through the use of three non-linear kinematic hardening terms and one non-linear isotropic one.

The scale-up process, described above, allowed us to identify the coefficient of the model of the cyclic elastic-plastic behavior of the crack tip region, using finite element simulations.

Finally, equation [9.26] allows us to calculate the fatigue crack growth rate.

This model was then used to simulate a constant amplitude fatigue test at $R = 0$ (see Figure 9.15). The results were plotted in a Paris diagram.

We can observe that the simulated crack growth rate is a straight line in the Paris diagram, which agrees with the experimental results. The exponent of Paris' law, close to 3, does not depend on the chosen value of α, but on the cyclic plasticity model identified for the crack tip region.

Finally, we adjust coefficient α to obtain the best possible match between the simulation and a fatigue crack growth test result when $R = 0$ (see Figure 9.15).

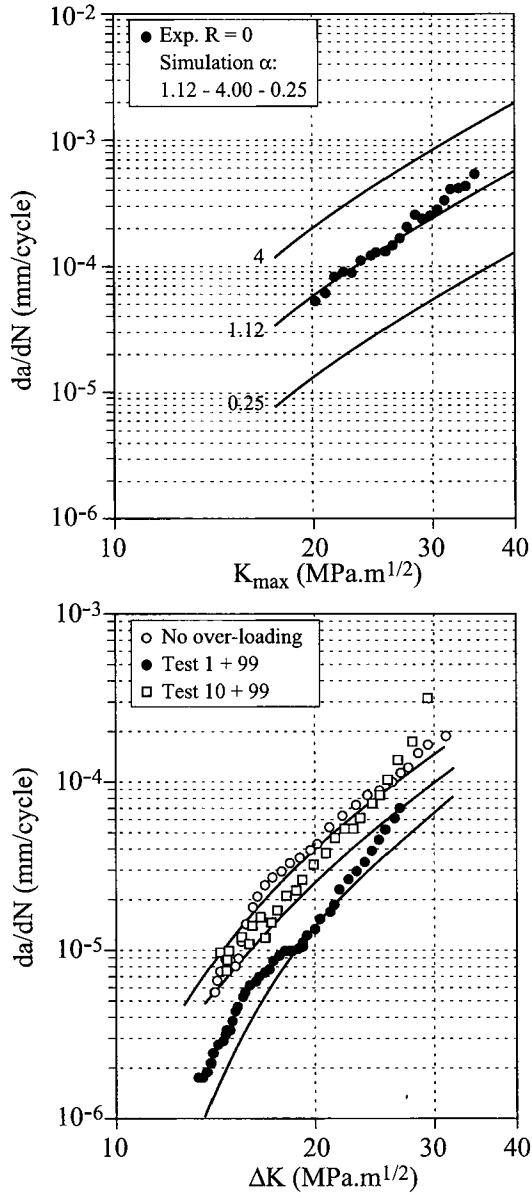

Figure 9.15. *a) Fatigue crack growth experiment with a constant amplitude and R = 0 and simulation for various values of α (see equation [9.26]); b) tests/simulation comparison for block tests of 100 cycles containing 1% or 10% overloading with a factor of 1.5. Simulations are represented by continuous lines*

Once the model has been identified from traction-compression tests on cylindrical specimens and from a constant amplitude fatigue crack growth test, we can then simulate any variable amplitude fatigue crack growth experiment. For example, some block tests were simulated and compared to the experimental tests in Figure 9.15b. In these tests, 1% or 10% overloading was applied, where the level is 1.5 times higher than the basic cycles. The simulations and experiments agreed with each other. Some other validations were also performed (see Figure 9.9).

9.4.4. *Extensions*

This method has the main advantage of enabling us to study various configurations easily, either at the level of the material's behavior or at the level of the loading scheme.

For instance, we tried to study the effect of the T-stress with this method and were then able to show that the elastic-plastic behavior of the crack tip region significantly depends on this T-stress [HAM 05, THI 07]. It is then possible to include the effect of the T-stress within the model and simulate the crack propagation rate using either *CT* or *CTT* specimens. A slight difference in crack growth rate (a factor of 1.25) was observed during the tests and reproduced by the model.

In addition, with this approach we can also study the effect of temperature on fatigue crack growth. If we can determine the cyclic behavior of a material at various temperatures, it is then possible to identify the model for each of these temperatures and to interpolate it to simulate non-isothermal loading. Finally, the crack growth law can be modified to consider the effect of fatigue corrosion [RUI 06].

This method is particularly interesting for simulating fatigue crack growth in mixed modes conditions. Indeed, cracking tests under mixed modes are still rare, especially the ones dealing with history effects (cracking in mode I and overloading in mode II) or sequence effects (a sequence in mode I, followed by a sequence of mode III). The method proposed here can be easily applied to mixed modes, at least when modeling plasticity at the crack tip [POM 06].

9.5. Conclusion

Within ductile materials, a plastic zone evolves at the crack tip. If the material is cyclically loaded, we can distinguish the monotonic plastic zone from the cyclic

plastic one where plasticity occurs during the loading and unloading steps. The dimension and shape of the plastic zone depend on:

– applied stress intensity factor;

– yield stress of the material;

– strain-hardening ability;

– T-stress.

Once the unloading step has been carried out, some residual stresses are left within the plastic zone; these stresses are multi-axial and depend on the behavior of the material. The residual stresses strongly influence the propagation of fatigue cracks and lead to the history effects of the loading step. It is therefore important to model cyclic plasticity at the crack tip.

9.6. Bibliography

[BUD 78] B. Budiansky, J.W. Hutchinson, "Analysis of closure in fatigue crack growth", *J. Applied Mech.*, vol. 45, pp. 267-276, 1978.

[CHA 77] J.L. Chaboche,"Viscoplastic constitutive equations for the description of cyclic and anisotropic behaviour of metals", *Bulletin de l'Académie Polonaise des Sciences*, vol. 25, no. 1, pp. 33-41, 1977.

[CLI 67] F.A. Mc Clintock, Discussion on C. Laird's paper "The influence of metallurgical microstructure on the mechanisms of fatigue crack propagation", *Fatigue Crack Propagation, ASTM STP 415*, pp. 170-174, 1967.

[DEK 81] A.U. De Koning, "A simple crack closure model for prediction of fatigue crack growth rates under variable amplitude loading", *Fracture Mechanics, 13th Conference, ASTM STP 743*, pp. 63-85, 1981.

[DUG 60] D.S. Dugdale, "Yielding of steel sheets containing slits", *J. Mech. Phys. Sol.*, vol. 8, pp. 100-108, 1960.

[ELB 71] W. Elber, "The significance of fatigue crack closure", *ASTM STP 486*, pp. 230-242, 1971.

[FLE 88] N.A. Fleck, J.C. Newman, "Analysis of crack closure under plane strain conditions", *Mechanics of Fatigue Crack Closure, ASTM STP 982*, pp. 319-341, 1988.

[FOR 67] R.G. Forman, V.E. Kearney, R.M. Engle, "Numerical analysis of crack propagation in cyclic loaded structures", *J. Basic Eng.*, vol. 89, pp. 459-64, 1967.

[HAM 05] R. Hamam, S. Pommier, F. Bumieler, "Mode I fatigue crack growth under biaxial loading", *Int. J. Fatigue*, vol. 27, no. 10, pp. 1342-1346, 2005.

[HAM 07] R. Hamam, S. Pommier, F. Bumieler, "Variable amplitude fatigue crack growth, experimental results and modelling", *Int. J. Fatigue*, vol. 29, pp. 1634-1646, 2007.

[HUT 68] J.W. Hutchinson, "Singular behaviour at the end of a tensile crack in a hardening material", *J. Mech. Phys. Solids*, vol. 16, pp. 13-31, 1968.

[IRW 60] G.R. Irwin, "Plastic zone near a crack and fracture toughness", *Proceedings of the 7th Sagamore Ordnance Materials Conference*, vol. 4, pp. 63-78, Syracuse University, New York, 1960.

[LAI 67] C. Laird, "The influence of metallurgical structure on the mechanisms of fatigue crack propagation", *ASTM STP 415*, pp. 131-168, 1967.

[LEM 83] J. Lemaitre, J.L. Chaboche, *Mécanique des Matériaux Solides*, Dunod, Paris, pp. 213-234, 1983.

[MA 95] F.S. Ma, Z.B. Kuang, "Stress and energy density fields near a blunted crack front in power hardening material", *Theoretical and Applied Fracture Mechanics*, vol. 23, pp. 165-176, 1995.

[MCC 96] R.C. Mc Clung, "Finite elements perspectives on the mechanics of fatigue crack closure", *Proceedings of Fatigue 96, 6th International Fatigue Congress*, Berlin FRG, 6-10 May 1996.

[NEW 88] J.C. Newman, W. Elber, "Mechanics of fatigue crack closure", *ASTM STP 982*, 1988.

[NEW 92] J.C. Newman, *COSMIC, Fastran II - A Fatigue Crack Growth Structural Analysis Program. NASA TM 104159*, Langley Research Center, Hampton, Virginia, 1992.

[POM 00] S. Pommier, P. Bompard, "Bauschinger effect of alloys and plasticity-induced crack closure: a finite element analysis", *Fatigue Fract. Eng. Mat. Struct.*, vol. 23, pp. 129-139, 2000.

[POM 01] S. Pommier, "A study on the relationships between variable amplitude fatigue crack growth and the cyclic constitutive behaviour of an alloy", *Int J. Fatigue*, vol. 23, pp. 111-118, 2001.

[POM 06] S. Pommier, "Cyclic plasticity of a cracked structure submitted to mixed mode loading", *Plasticity'06 - 12th International Symposium on Plasticity and its Current Applications*, 2006.

[POM 07] S. Pommier, R.Hamam, "Incremental model for fatigue crack growth based on a displacement partitioning hypothesis of mode I elastic–plastic displacement fields", *Fatigue Fract. Eng. Mat. Struct.*, vol. 30, pp. 582-598, 2007.

[RIC 68] J.R. Rice, G.F. Rosengren, "Plane strain deformation near a crack tip in a power-law hardening material", *J. Mech. Phys. Solids*, vol. 16, pp. 1-12, 1968.

[RUI 06] J.A. Ruiz-Sabariego, S. Pommier, "Modeling environment-assisted fatigue crack propagation", *ECF 16 - 16th European Conference of Fracture*, 2006.

[SCH 73] J. Schijve, "Effect of load sequences on crack propagationunder random and program loading", *Eng. Fract. Mech.*, vol. 5, pp. 269-280, 1973.

[SHI 83] C.F. Shih, *Tables of Hutchinson-Rice-Rosengren Singular Field Quantities, Brown University Report, MRL E-147*, Brown University, 1983.

[THI 07] E. Thieulot-Laure, S. Pommier, S. Frechinet, "A multiaxial fatigue failure criterion considering the effects of the defects", *Int J. Fatigue*, vol. 29, pp. 1996-2004, 2007.

[WHE 72] O.E. Wheeler, "Spectrum loading and crack growth", *J. Basic Eng.*, vol. 4, pp. 181, 1972.

[WIL 71] J. Willenborg, R.M. Engle, H.A. Wood, "Crack retardation model using an effective stress concept", *AFFDL-TM 71-1*, February 1971.

Chapter 10

Corrosion Fatigue

10.1. Introduction

Even though McAdam used the term corrosion fatigue [MAC 26] in 1926, it was only in 1971 that an international symposium at Storrs, Connecticut [DEV 72] was held that dealt with this complex problem. Some 20 years later, the Kohler symposium [GAN 90], held in Wisconsin, reviewed recent progress in the field of corrosion fatigue and proposed new avenues for research. A number of publications have described current theories, and examined their strengths and weaknesses in terms of the specific material being considered. Experimentally-oriented papers in this symposium dealt with the two main mechanisms of corrosion fatigue: hydrogen embrittlement and the dissolution/repassivation theory.

This chapter is based on publications presented at this symposium and on advances made in the following decade or so. We will review and discuss the current state of knowledge on the mechanisms of crack initiation and propagation in corrosion fatigue. Various theories will be thoroughly presented with particular attention being given to examples that illustrate the complexity of the synergism between corrosion and fatigue.

Current practice is to avoid arbitrary distinctions between crack initiation and propagation, since it has become obvious that the same phenomena occur for both processes. Nevertheless, due to the limits of detectability that introduce a de facto

---

Chapter written by Régis PELLOUX and Jean-Marc GENKIN.

crack length into the problem, it is convenient to maintain the old terminology by introducing the concept of "short cracks" between the initiation and propagation stages.

10.2. Crack initiation

10.2.1. *Aqueous medium*

The study of corrosion fatigue is motivated by the necessity of predicting the reduction in life associated with this process. As we will see in the next section, the propagation phase is deterministic and is well described by the so-called Paris' law [PAR 61]. Although the initiation phase is not as well modeled, many experimental observations are available and the causes of corrosion fatigue initiation have now been identified. The initiation of fatigue within an aqueous corrosive medium can be divided into three distinct regimes:

– active dissolution;

– electrochemical passivity; and finally

– the regime of local passivity failure [DUQ 90, FOR 90].

Fatigue initiation for conditions of electrochemical passivity has been explained in terms of repetitive rupture and formation an oxide film. The oxide film is locally fractured due to the application of tensile strains or by the emergence of slip bands. Each fracture of the film leads to local dissolution of the metal and therefore to the formation of a micronotch. When this notch becomes sufficiently large, corrosion fatigue cracks are initiated.

This periodic embrittlement is governed by mechanical parameters, such as the frequency and amplitude of the cyclic deformation, while the film formation depends upon the electrochemical repassivation rate. During each loading cycle a transitory increase in corrosion current [DUQ 90, FOR 90] is observed that corresponds directly with the exposure of new surfaces, which are subsequently covered by a protective oxide film.

The corrosion current is determined by the electrochemical reactions shown in Figure 10.1. If the current corresponds to an average metal layer removal rate whose thickness is less than the interatomic spacing, then initiation occurs in the same way as it does in an ambient atmosphere. Thus a current density limit is defined in the following, in which the environment plays no role.

Uhlig [DUQ 69] was able to show that the fatigue limit of 1015 steel in a de-aireated 3% NaCl solution is the same as in air but is considerably reduced when the

same solution is aireated. In the first case, the corrosion rate is 100 times slower than in the second case. The explanation for this behavior has to be related to the dissolution/repassivation theory for the propagation of corrosion fatigue cracks. It should also be noted that this model does not *a priori* make any distinction between initiation and propagation.

We should also mention that the initiation of corrosion fatigue for a cathodically polarized material is close to that of passivation where an oxide film is formed. The lives of materials increase as long as hydrogen embrittlement does not intervene. Figure 10.1 shows the effect of cathodic polarization on total lifetime. The problem of hydrogen embrittlement will be covered in detail during the discussion of crack propagation.

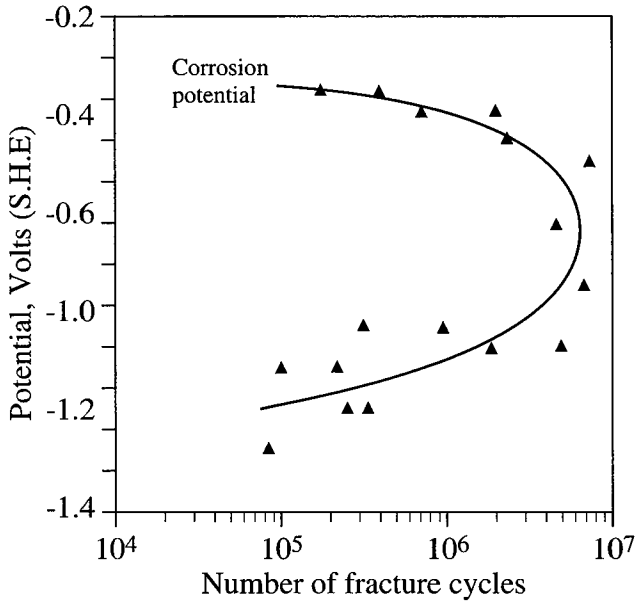

Figure 10.1. *Influence of cathodic potential on the life of a 4140 steel (R_C 52) in a 3% NaCl solution in contact with air (141 ksi, 25°C). R =-1, [LEE 72]*

Under active dissolution conditions, persistent slip bands (PSBs) react with the corrosive medium and we can then observe an increase in slip irreversibility [DUQ 90]. The distribution of the slip bands is modified by the surroundings. The electrochemical reactions are enhanced due to the presence of mobile dislocations that are generated by interactions between slip mechanisms and the surface of the

material. Consequently, the PSBs are anodic compared to the undeformed material and are preferentially dissolved, which enhances local plastic deformation, i.e. slip.

The transition between passivation and active dissolution leads to various corrosion morphologies. These are corrosion pitting (see Figure 10.2, [GEN 96]), stress corrosion cracking (SCC) or inter-granular corrosion. Corrosion fatigue cracks are then initiated on these defects. The reduction in lifespan due to corrosion defects has often been attributed to a notch effect introduced by these surface defects. Unfortunately, this explanation does not entirely explain initiation kinetics [COO 70]. The complexity of the synergy between fatigue and corrosion is clearly manifested by various initiation modes that can occur in the same material.

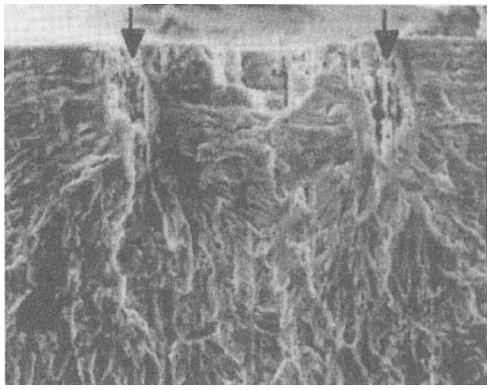

Figure 10.2. *Fracture surface of the 2091-T351 aluminum alloy, maintained at a potential of -660 mV (Calomel) in a molar NaCl solution at 25°C. Loading parameters: 100 MPa, f=10Hz, R=0.05. Crack propagation from top to bottom.. Two corrosion pits initiated semi-elliptical cracks which interacted [GEN 96].*

The initiation of corrosion fatigue cracks is not only affected by the mechanical and chemical properties of the material, but also by the fatigue test parameters. Thus, it is observed that for an Al-Zn-Mg alloy [MAG 87] (3.5% NaCl), an increase in the imposed deformation rate changes initiation from inter-granular to trans-granular. At a low deformation rate, intergranular stress corrosion cracks are formed, whereas at a high deformation rate transgranular initiation occurs within the slip bands.

Similarly, Magnin [REB 90] showed that we can distinguish up to three initiation modes of corrosion fatigue (3.5% NaCl) in an Al-Li-Cu (8090) alloy. As the strain rate decreases, the initiation mode changes from preferential dissolution of slip bands to pitting and then to stress corrosion. Initiation by pitting itself can be split into two regimes:

– a moderate degree of pitting strongly degrades the strength of the material under fatigue conditions; whereas

– a more severe pitting is beneficial, since it decreases the crack tip notch acuity thereby reducing the stress concentration.

These two examples caution us against hastily drawn conclusions about the initiation mode.

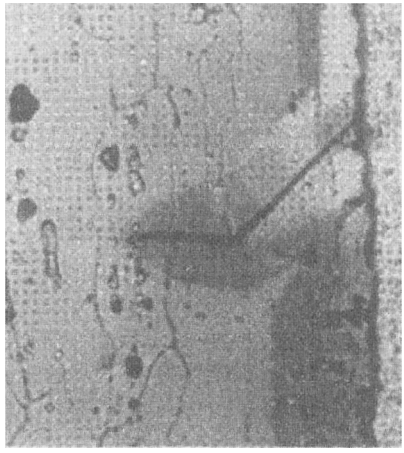

Figure 10.3. *Cross-section of a specimen made from 7075-T6 Al alloy showing stage I cracking as a result of increased slip activity at the surface due to a corrosive environment (X 500) [COO 70]*

By way of example, the fatigue strength of alloy 7075-T6 [LEE 72] is significantly reduced in a saline solution. A meticulous fractographic analysis shows a large increase in the density of stage I cracks. We can also distinguish some corrosion pitting, which is unconnected to these microcracks. A metallographic cross-section is presented in Figure 10.3. We then conclude that the reduction in life of the 7075-T6 alloy, for these specific experimental conditions, is mainly due to preferential attack of the slip bands and not to pitting. To determine the initiation kinetics, we have to clearly identify its mechanism.

Corrosion pitting has been extensively studied because of its industrial importance. The first modeling approaches considered corrosion pits to be equivalent to through cracks of the same depth as the original pits. A stress intensity factor is then associated with pitting, which accounts for the notching effect. The transition from pitting to cracking occurs when the stress intensity factor is equal to the non-propagation threshold for long cracks under fatigue conditions. The

drawback of this model is the assumption that pitting introduces a singularity within the stress field, whereas in reality it is actually a notch.

To this day, this approach has not been modified. Refinements have been primarily related to the geometry of the equivalent crack; the through crack was replaced by a semi-elliptical crack [NEW 86]. The fatigue threshold for short cracks is now used as the critical stress intensity factor. Nevertheless, the fundamental idea of the model has not changed: it still deals with a transition between fatigue and corrosion that occurs at constant ΔK.

Significant improvements were made by Kondo [KON 89] when he proposed considering pitting corrosion and corrosion fatigue in steels as competitive processes. The fastest process governs the fracture mode: if corrosion is faster, pitting is observed. If fatigue is faster, initiation occurs.

The pitting law can be written as follows:

$$c = C_p \, t^{1/3} \qquad [10.1]$$

where c is the pitting depth and t the time. Modeling the pit as a semi-elliptical crack, he then calculates the equivalent stress intensity factor. The pitting law [10.1] is then written in terms of ΔK:

$$\frac{dc}{dN} = \frac{1}{3} C_p^{\,3} f^{-1} \left(\frac{\pi}{Q} \right)^2 \left(\frac{1.12 \Delta \sigma}{\Delta K_{eq}} \right)^4 \qquad [10.2]$$

where:

– $\Delta\sigma$ is the stress;

– f the test frequency;

– Q a geometrical factor; and

– ΔK the stress intensity factor.

In Figure 10.4, equation [10.2] is shown as a set of straight lines of slope -4 for different stress levels. The intersection of such a line with the propagation curve for short cracks defines the initiation point for a corrosion fatigue crack. A complete analysis of the initiation of a corrosion fatigue crack from a pit requires the introduction of statistical variables that take into account the stochastic nature of the corrosion process [HAR 94].

The key to understanding initiation phenomena lies in detailed studies of the different degradation modes and their time dependence. We have to compare these damage modes on the same scale, which is why the Kondo approach has led to improved understanding of initiation phenomena.

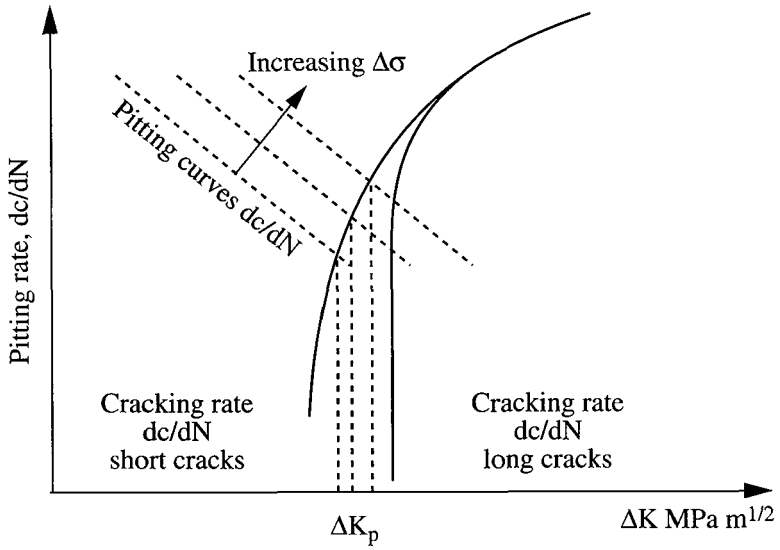

Figure 10.4. *Competition between corrosion fatigue and pitting corrosion*

10.2.2. *Gaseous environment*

It is well known that the presence of a gaseous environment significantly reduces fatigue life compared to the life in vacuum or in an inter atmosphere. According to some researches [THO 56], the principal effect of a gaseous environment is to reinforce the irreversibility of slip through adsorption of oxygen atoms on freshly-exposed metallic surfaces. This mechanism could also prevent the surfaces of the incipient cracks from closing up.

Another theory [SHE 66] suggests that the formation of an oxide film prevents the escape of dislocations at the free surface. Under cyclic loading conditions, vacancies and voids form and give rise to crack formation.

Water vapor is a main contributor to crack initiation in aluminum alloys. The mechanism is either through reinforcing slip irreversibility or by hydrogen embrittlement.

To summarize, the initiation mechanism within a gaseous medium is far from being perfectly understood.

10.3. Short cracks

After a crack nucleus is formed, the propagation phase starts. At this stage, we have to distinguish between short and long cracks. Indeed, the notion of a short crack is necessary since similitude, implicit in the use of the stress intensity factor ΔK, is not applicable to cracks shorter than a critical length. Short cracks propagate for values of the stress intensity factor that are lower than the fatigue threshold of long cracks on one hand; on the other hand, their propagation rates are faster than for long cracks with the same nominal ΔK. While it is difficult to precisely determine this critical length, the notion of a short crack can be used as soon as one or more of the following criteria are true:

– the crack length has the same dimension as the characteristic dimension of the microstructure. Here the hypothesis of an isotropic medium is inapplicable; for example, the cracks interact with the grain boundaries. This phenomenon is observed when the plastic zone is of the same magnitude as grain size;

– a crack is physically short when the plastic wake associated with propagation of the crack is not sufficiently developed for plasticity-induced closure to occur. This phenomenon can be observed for a crack that is typically shorter than a millimeter;

– a crack is mechanically short when the size of the plastic zone is significant compared to the size of the crack.

This notion of short crack is applicable to fatigue in air as well as to corrosion fatigue. In this latter case, the effects of the surroundings and transport phenomena make a description of the system much more complex. Indeed, in the general case, the crack tip environment is determined by diffusion, convection, migration of chemical species and by the electrochemical reactions at the metal/solution interface. For short cracks, the environment is not that different between the crack mouth at the surface and at the crack tip, where the corrosion fatigue phenomenon occurs.

Therefore, the limiting process is not the same for long cracks (limited bytransport phenomena, for instance) as it is for short cracks (limited bymechanical phenomena or electrochemical reactions).

This effect was first noticed in 4130 steel by Gangloff [GAN 85]. In ambient air, short (0.1 to 0.8 mm) and long (50 mm) propagation was well-correlated with the stress intensity factor. However, when the same measurements were carried out in synthetic sea water, short cracks propagated 100 to 1,000 times faster than long

cracks. This effect was less pronounced for steels with Rockwell hardnesses lower than 30 R_c.

In practice, the propagation of short cracks is not as easily predicted as is the propagation of long cracks. In the case of aluminum 2024, Piasick and Willard [PIA 94] showed that there is no short crack effect in terms of crack propagation rates. In particular, for synthetic sea water, similitude was conserved for short cracks over 100 μm in length. The major difference was that the fatigue threshold disappeared. It was suggested that closure was the parameter controlling the propagation of short cracks whose length was greater than 100 μm. For lengths shorter than 100 μm cracks propagated intergranularly, whereas above 100 μm cracks propagated transgranularly. It is therefore not surprising that the similitude principle cannot be applied, since there is a sudden change in the propagation mechanism.

10.4. Long crack propagation

10.4.1. *Experimental observations*

As briefly discussed in the section on initiation phenomenon, a corrosive environment always leads to a reduction in lifespan compared to that observed in an inert environment, in a vacuum or in a noble gas. Crack growth rates may increase by as much as several orders of magnitude.

10.4.1.1. *Stress intensity factor*

The propagation of fatigue cracks in the regime of ΔK close to the threshold is poorly understood. It is assumed that the environment simultaneously lowers the fatigue thresholds observed in ambient air and increases the crack growth rates. Indeed, this phenomenon is observed for X65 C-Mn steels [BAR 85, BOO 84]. The behavior of steel close to the fatigue threshold is the same in humid air as it is in a saline solution. Experimental data for aluminum alloys are rare within the domain of the fatigue threshold.

The crack growth rates increase markedly for ΔK levels slightly above the threshold. The corresponding Paris' law exponent is high, indicating control of the cracking process by mechanical failure.

The third regime deals with moderate ΔK levels. The Paris exponent is much lower. In this regime, it is assumed that the cracking process is limited by a chemical process that is not significantly influenced by a higher cyclic loading level. Finally, the cracking rates within a corrosive environment become similar to those measured in ambient air for ΔK close to K_C, the stress intensity factor for final failure of the sample.

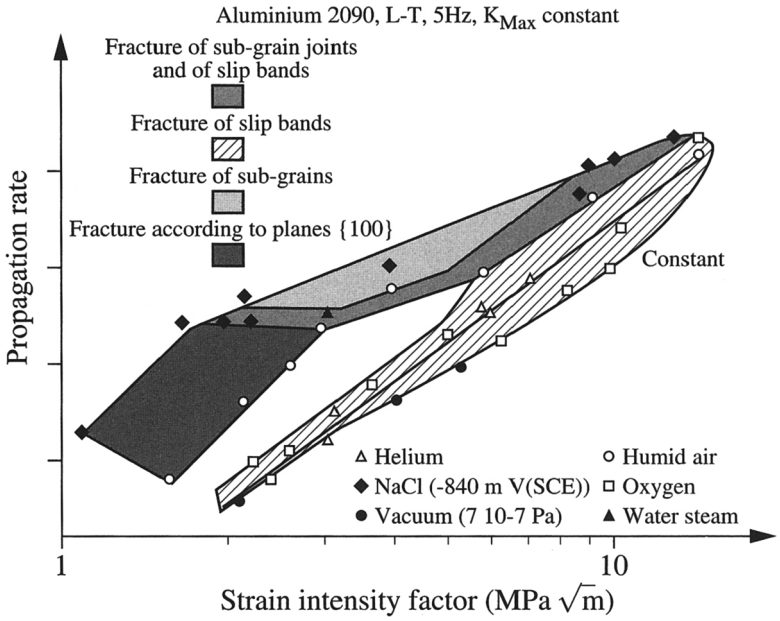

Figure 10.5. *Cracking curves with multiple slopes showing their relationship to the observed fracture mechanisms. From Piasick and Gangloff [PIA 90]*

In general, the $da/dN - \Delta K$ curves do not follow a single Paris' law over the entire domain of ΔK. However, for local regions, a Paris' law can be used to describe cracking behavior. For aluminum alloys, Piasick and Gangloff [GAN 23] showed that these slope changes correspond to well-defined changes in the failure mode (see Figure 10.5).

10.4.1.2. *Mean stress effects*

Mean stress effects are taken into account by the ratio K_{min}/K_{max}, which is also denoted by R, just as in classical fatigue studies. At low crack growth rates, an increase in R usually leads to an increase in the crack growth rate for both inert and corrosive environments. For corrosion fatigue in an aqueous medium, this phenomenon has been explained by crack closure [VOS 80].

To date, it has not been possible to separate the R-ratio effect from the actual mean stress effect. Some hydrogen embrittlement models [WEI 69] ascribe an important effect to the mean stress for ΔK above K_{ISCC}. So far, it has not been possible to differentiate a reduction in closure phenomenon from enhanced hydrogen embrittlement.

10.4.1.3. *Effect of frequency*

In general, the effect of frequency depends on the stress intensity factor applied. Near the fatigue threshold, two types of behavior may be seen: the crack growth rate either increases with frequency [DAW 26] or remains constant [PIA 28, SPE 27].

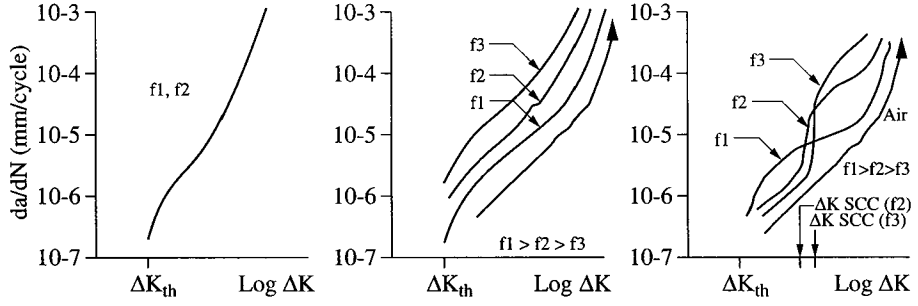

Typ 1: independent from the frequency

Typ 2: da/dN increases when we decrease the solicitation frequency

Typ 3: the effect of the frequency can be reversed with when stress corrosion occurs

Figure 10.6. *Effect of frequency on the crack growth rate of long cracks*

For moderate ΔK levels, different types of behavior are observed as illustrated in Figure 10.6:

– Type 1 behavior is rarely seen.

– Type 2 is valid for most steels, titanium and aluminum alloys. By way of example, Figure 10.7 illustrates the behavior of a stainless steel [PEL 71].

– Type 3 behavior is typical of materials that have a well-defined SCC threshold. Above this threshold, stress corrosion occurs. Since this phenomenon is time-dependent, a decrease in frequency causes an immediate increase in the cyclic crack growth rate. This behavior is illustrated in Figure 10.8.

A decrease in frequency can also lead to a decrease in crack growth rate below the SCC threshold. This phenomenon can be explained by passivation of the crack tip. Decreasing the frequency leads to a decrease in the crack tip deformation rate. Less damage, therefore, occurs to the protective oxide film. For moderate stress intensity factors close to the SCC threshold, an increase in crack growth rate is observed when the frequency is decreased. However this effect becomes saturated at a low frequencies.

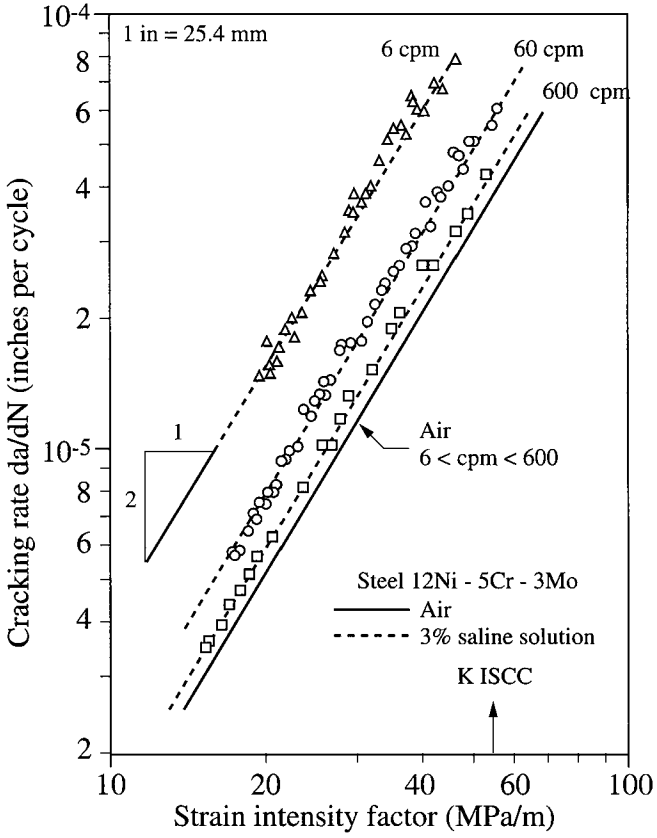

Figure 10.7. *Cracking rates under corrosion fatigue conditions of a 12Ni-5Cr-3Mo steel for various load frequencies [PEL 71]*

10.4.1.4. *Effect of the environment*

The variables that define the activity of chemical species are:

– for gaseous environments, pressure and purity; and

– for electrolytes, the pH, the composition, the potential of the electrode and the flow rate of the solution.

Temperature is also a significant parameter for both environments, as many chemical mechanisms are thermally activated.

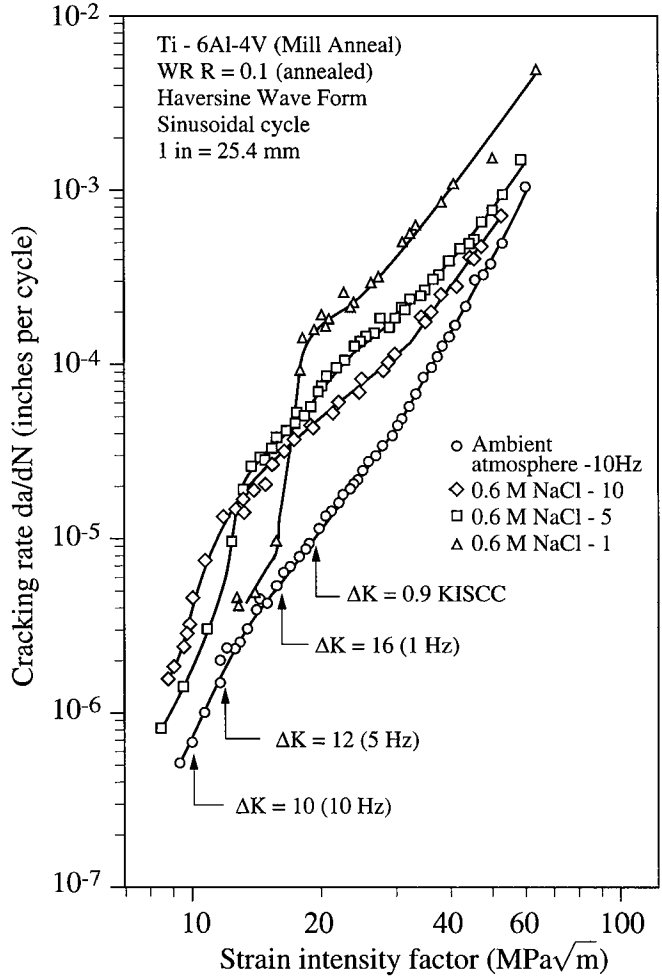

Figure 10.8. *Effect of test frequency on the crack growth rates in corrosion fatigue [DAW 26]*

For a gaseous environment, it has been shown [JOH, NEL 89] that 4340 steel was sensitive to corrosion fatigue in hydrogen-donor gases (hydrogen and water vapor). The addition of unsaturated hydrocarbons to these gasses decreases the sensitivity to corrosion fatigue since their molecules can tie up hydrogen atoms by bonding [GAN 90]. These unsaturated hydrocarbon additives have no other effect on the process. The presence of impurities, such as CO or O_2, also decreases the sensitivity to corrosion fatigue [JOH, NEL 89]. It has been suggested that these

atoms could be preferentially adsorbed on the newly formed surfaces and thus displace the hydrogen-donor species (i.e. provide a kind of protective barrier).

For aluminum alloys, Wei [WEI 80] has shown that crack growth rates depended upon a parameter describing exposure of the crack tip to the environment (Figure 10.9). For water vapor, this parameter is the product of the partial pressure and test frequency. Bradshaw and Wheeler [BRA 69] showed that the effects of frequency and partial pressure of water vapor were quite interchangeable by testing an Al-Cu-Mg alloy at two different frequencies, 1 and 100 Hz.

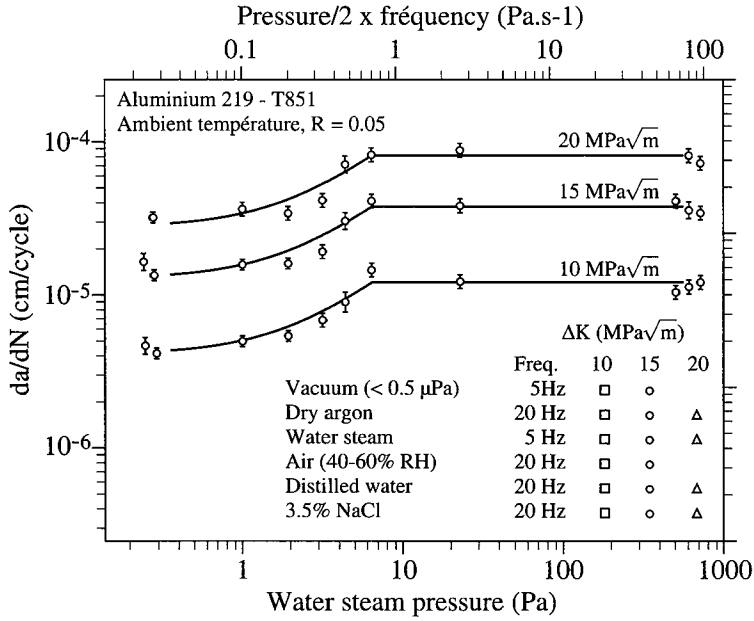

Figure 10.9. *Effect of exposure to a corrosive environment on crack growth rates of an aluminum alloy in corrosion fatigue. The main correlating parameter is the product of pressure and test frequency [WEI 80]*

For steels in an aqueous environment, applying a cathodic potential leads to different effects. If the cathodic polarization is not very strong, the cracking rates are similar to those in air. If the polarization is much larger, the lifespan is reduced [LEE 72]. A cathodic potential causes a reduction in H_3O^+ ions on the metal surface, thus producing adsorbed hydrogen atoms that then diffuse into the material and damage it. For an anodic potential, crack initiation does not occur if the current densities are less than a critical value [DUQ 69]. This phenomenon has been explained using the oxide film fracture/repassivation model.

Aluminum alloys behave similarly. Anodic potentials reduce an alloy's resistance to corrosion fatigue. Cathodic polarization results in crack growth rates similar to those observed in ambient atmosphere. Piasick [PIA 90] observed that the application of a cathodic potential caused crack arrest in an aluminum-lithium alloy (Figure 10.10). Even after applying an anodic potential, it took 76 hours before the crack started to propagate again. He suggested that the cathodic polarization created a protective film made up of hydroxides that had to be ruptured to expose fresh metal surface.

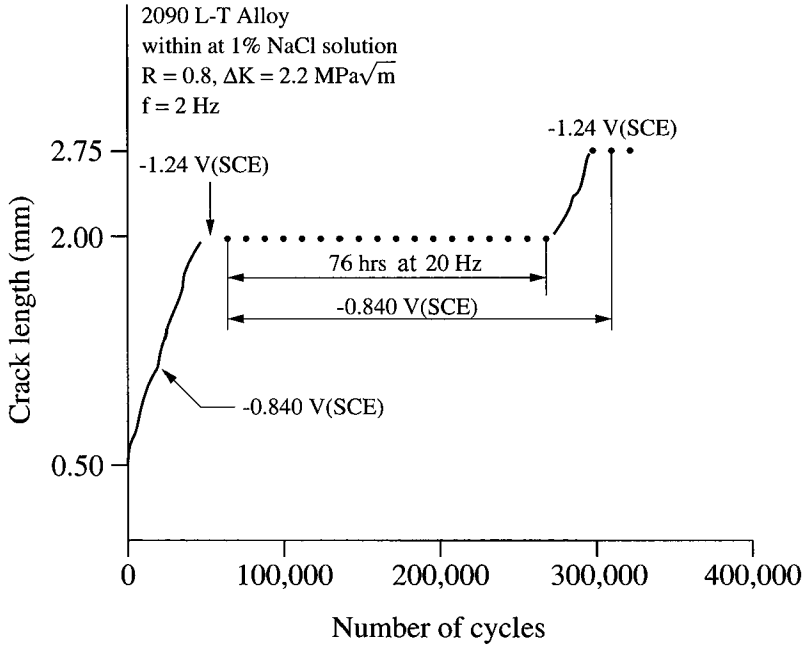

Figure 10.10. *Effect of cathodic polarization on an aluminum-lithium alloy. Crack arrest occurred when a cathodic potential was applied. It took 150,000 cycles under anodic polarization before reinitiation of crack growth by corrosion fatigue [GAN 88]*

The pH of the solution also strongly influences crack propagation rates in corrosion fatigue. For example, Figure 10.11 illustrates the effect of an acidic environment on a titanium alloy. Once again, the effect of the test frequency is seen. The effect of the pH is more significant for stress intensity factors above the SCC threshold [DAW 74].

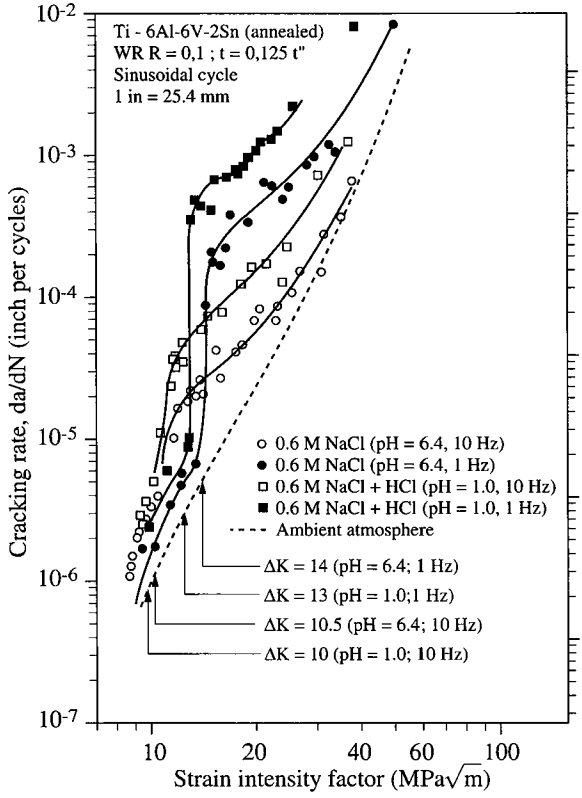

Figure 10.11. *Effect of pH of a NaCl solution (0.6 M) on the crack propagation rates in corrosion fatigue at frequencies of 1 and 10 Hz. Hot rolled Ti-6Al-6V-2Sn*

10.4.1.5. *Conclusions based on experimental observations*

The stress intensity factor alone cannot describe the mechanisms governing mechanical and chemical processes at the crack tip. Analysis and experimental data show that the *da/dN versus ΔK* relationship strongly depends on mechanisms such as:

– premature contact of the crack surfaces;

– the cracking mode (deviations in the crack path or multiple crack formation); and, finally

–on the chemical composition of the environment at the crack tip, which itself depends on time and geometry.

The crack growth curves are generally reproducible for any given set of experimental conditions.

10.4.2. *Corrosion fatigue models*

Development of chemical-mechanical models for mechanisms acting at the crack tip and in the damage zone constitutes a new approach to corrosion fatigue. The goal is to predict and extrapolate the effects of previously-introduced variables by modifying the traditional fracture mechanics approach, which is based on similitude for ΔK and which has been shown to be inadequate to describe corrosion fatigue.

These models [GAN 90] successfully predict the effect of the test frequency, of electro-chemical potential, of composition of the environment and chemical activity of the gas. Nevertheless, there are always some uncertainties due to the damage mechanisms at the crack tip and the basic mechanism of hydrogen embrittlement. A model describing the damage zone in front of the crack tip does not yet exist for corrosion fatigue conditions. The effects of yield strength, stress intensity factor and microstructure can thus not be predicted.

10.4.2.1. *Dissolution/repassivation model*

Ford and Hoar [FOR 78] suggested that the increased crack growth rate in corrosion fatigue was entirely due to the amount of metal dissolved at the crack tip. This model supposes that the metal is within the passivation domain, i.e. its surface is covered by a protective film. Within the passive domain the metal is thermodynamically unstable, its apparent stability being only due to the oxide film. The deformation at the crack tip breaks the oxide film. The exposed surface rapidly corrodes during the time that the film is being regenerated.

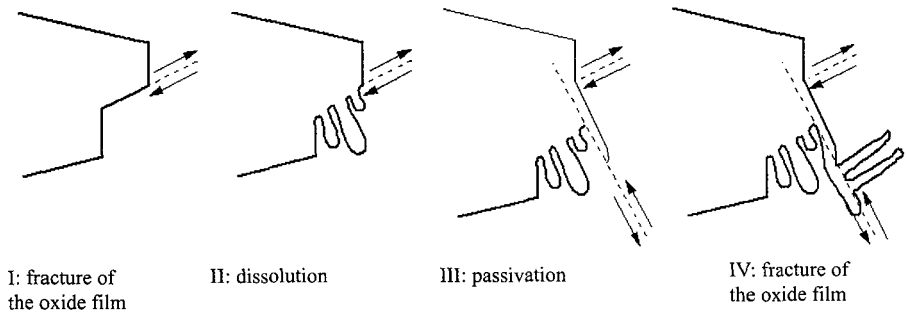

Figure 10.12. *Dissolution/repassivation model of the oxide film*

An increment of crack growth then occurs during each cycle. The whole scenario is presented in Figure 10.12. The important parameters are the amount of deformation and the cyclic frequency.

10.4.2.2. *Hydrogen embrittlement model*

Hydrogen embrittlement has long been considered to be one of the phenomena involved in corrosion fatigue. In a gaseous environment, the chemical species that decompose by releasing hydrogen embrittle the material. For example, water vapor degrades the corrosion fatigue resistance of aluminum alloys under conditions where no electrolyte can form, thus excluding the film rupture/repassivation theory. On the other hand, when a material has been exposed to an environment containing hydrogen and is then tested within in inert environment, an acceleration of the crack growth rate is seen. This phenomenon disappears when a thermal treatment is applied to remove gas from the bulk material. In addition, the behavior of steels under a cathodic potential (hydrogen reduction) can only be explained by hydrogen embrittlement.

The hydrogen embrittlement sequence is shown in Figure 10.13.

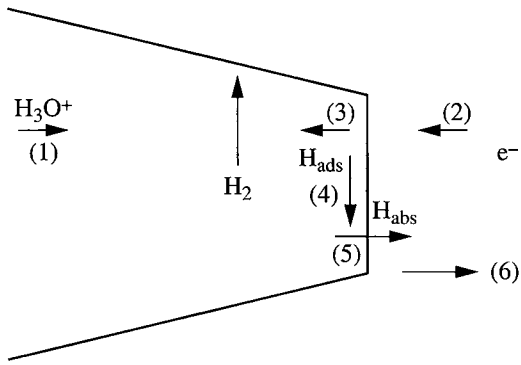

Hydrogen embrittlement model:
(1) : diffusion within the liquid phase
(2) : reduction of the H^+ ion: $H_3O^+ + e^-$' $H_2O + H$
(3) : recombination of the adsorbed hydrogen
(4) : diffusion of the adsorbed atoms
(5) : absorption of the hydrogen atom
(6) : diffusion of the hydrogen atom

Figure 10.13. *Hydrogen embrittlement model*

Hydrogen is absorbed and diffuses within the metal. Two schools of thought exist as to the details of this mechanism. One is based on the idea that the production

of hydrogen is the rate-limiting step. The other assumes that hydrogen diffusion is the rate-limiting step. In the latter case, hydrogen is assumed to diffuse within grains, along grain boundaries, and along dislocations that are generated at the crack tip. Unfortunately, these models have no damage criterion linking the stress intensity factor to the production or diffusion of hydrogen. For this reason it is not possible to use them to predict crack growth rates.

10.4.2.3. *Linking previous models to transport equations*

The previous section described the most probable fracture mechanisms. We now focus on the transport phenomena that occur along the crack and that are likely to be the rate-limiting step in fracture.

For instance, consider Knudsen-type diffusion [DUS 62] within gaseous environments. At low pressure, transport of the gas molecules is controlled by interactions between the molecules and the crack surfaces, rather than by inter-molecular interactions. The partial pressures in the crack-tip region are thus attenuated.

Of course, the equations presented here are only applicable to aqueous solutions. For more information, we recommend the book by Newman entitled *Electrochemical Systems* [NEW 91]. A corrosion fatigue crack is shown schematically in Figure 10.14. Various electrochemical reactions can occur, e.g. dissolution of the metal. Hydroxides are also formed. Ions will migrate under the combined influence of a concentration gradient ∇C_j and a potential gradient φ. In addition, the periodic opening and closing of the crack introduces convection phenomena that obviously affect the transport of the chemical species.

The transport equation is given by:

$$J_j = -D_j \nabla C_j - \frac{z_j F}{RT} D_j C_j \nabla \varphi + C_j V \qquad [10.3]$$

The first term represents the diffusion due to a concentration gradient, the second one represents electro-migration (z_j is the charge of ion j) and the last one accounts for convection.

The conservation equation is:

$$\frac{\partial C_j}{\partial t} = div\, J + S_j \qquad [10.4]$$

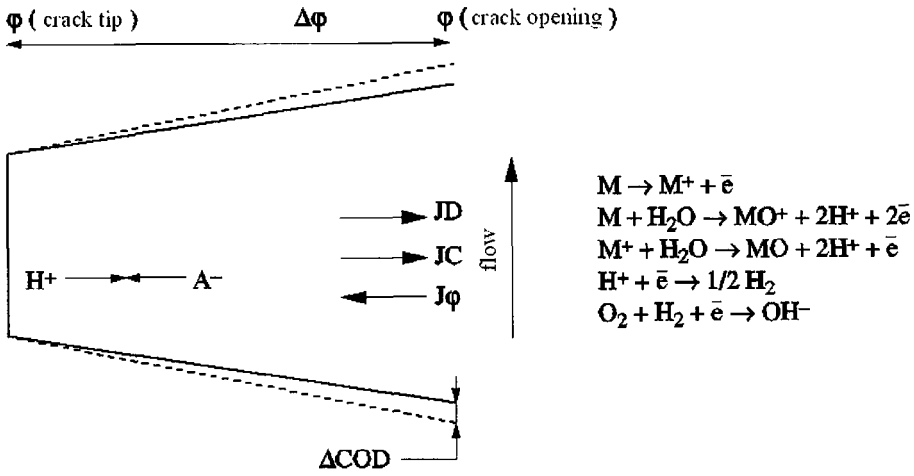

Figure 10.14. *Crack in a corrosive solution. The electrochemical reactions occur along the crack faces and especially at the crack tip. Ions move due to diffusion, electro-migration (potential) and convection. Convection is due to periodic opening and the closing of the crack which decreases the volume of liquid contained in the crack.*

Finally, electroneutrality is imposed at any point:

$$\sum_i z_i C_i = 0 \qquad [10.5]$$

Moreover, the ionic flow and electrochemical current are related through the following equation:

$$i_d = \sum_i z_i J_i \qquad [10.6]$$

These equations strictly apply only to dilute solutions, since activity coefficients have not been taken into account. Coupling equations with a cracking mechanism in a sensible way should allow the prediction of crack growth rates. For steels that follow the dissolution/repassivation mechanism, this approach is quite satisfying and is already being implemented in industry. However, for aluminum alloys that are more susceptible to hydrogen embrittlement, the crack growth rate cannot be predicted from these first principles.

10.5. Conclusions

In this chapter, a review of the state-of-the-art in corrosion fatigue has been presented. Concrete examples have been used to illustrate the extreme complexity of this phenomenon. Since there is no global model to explain corrosion fatigue starting from first principles, the materials engineer must rely upon test programs to find practical solutions.

Nevertheless, the framework for research is now well established. Much experimental data exist. The key variables have been correctly identified. It is now primarily a matter of carrying out tests under well-controlled and reproducible experimental conditions. The analytical approach, developed over several years, now makes it possible to explain experimental results in terms of rate-limiting steps, such as transport phenomena, dissolution at the crack tip, or hydrogen embrittlement. A damage criterion allowing the electro-chemical equations, stress intensity parameter and microstructure to be put in a unified, comprehensive model is a major remaining challenge.

10.6. Bibliography

[BAR 85] E. Bardal, in A.A. Naess (ed.), "Effects of marine environment and cathodic protection on fatigue of structural steels", *Fatigue Handbook: Offshore Steel Structures*, Tapir, p. 291-312, 1985.

[BOO 84] G.S. Booth, J.G. Wylde, T. Iwasaki, "Corrosion fatigue crack propagation and threshold determinations in structural steel", *Fatigue 84*, p. 1471-1484, 1984.

[BRA 69] F.J. Bradshaw, C. Wheeler, "Influence of gaseous environment and fatigue frequency on the growth of fatigue cracks in some aluminum alloys", *Int. J. Fract. Mech.*, vol. 5, p. 255-268, 1969.

[COO 70] C. Cooper, Corrosion fatigue of high strength aluminum alloy, PhD Thesis, MIT, 1970.

[DAW 74] D.B. Dawson, R. Pellouse, "Corrosion fatigue crack growth of Ti alloys in aqueous environments", *Met. Trans. A*, vol. 5, p. 723-731, 1974.

[DEV 72] O.F. Devereux, "Corrosion fatigue of steels", in A.J. Mc Evily (ed.), *Corrosion Fatigue* Nace, p. 519-520, 1972.

[DUQ 69] D.J. Duquette, H.H. Uhlig, "Critical reaction rate for corrosion fatigue of 0.18% carbon steel and the effect of pH", *Trans ASM*, vol. 62, p. 839-845, 1969.

[DUQ 90] D.J. Duquette, Corrosion *Fatigue Crack Initiation Processes:* A state of the art review, Report, Rensselaer Polytechnic Institute, 1990.

[DUS 62] S. Dushman, *Scientific Foundations of Vacuum Techniques*, chapters 1-2, John Wiley, New York, 1962.

[FOR 78] F.P. Ford, T.P. Hoar, "Metal science", *Proceedings of the Conference on Mechanisms of Environment-sensitive Cracking of Materials*, University of Surrey, p. 326, 1978.

[FOR 90] F.P. Ford, "The Crack tip system and its relevance to the prediction of cracking in aqueous environments", *Environment-induced Cracking of Metals*, NANCE, Houston, p. 139-165, 1990.

[GAN 85] R.P. Gangloff, "Crack size effects of the chemical driving force for aqueous corrosion fatigue", *Met. Trans. A*, vol. 16A, p. 953-969, 1985.

[GAN 88] R.P. Gangloff, "Ethylene inhibition of gaseous hydrogen embrittlement in high strength steel", *Basic Questions in Fatigue, ASTM STP 924-2*, p. 230-251, 1988.

[GAN 90] R.P. Gangloff, "Environment-induced cracking of metals", in R.P. Gangloff, M.B. Ives, *Proceedings of the First International Conference on Environment-induced Cracking of Metals*, Nace, 1990.

[GEN 96] J.M. Genkin, Corrosion fatigue crack initiation in aluminum 2091, PhD Thesis MIT, June 1996.

[HAR 94] D.G. Harlow, R.P. Wei, "Probability approach for prediction of corrosion and corrosion fatigue life", *AIAA journal*, vol. 32, no. 10, p. 2073-2979, 1994.

[JOH 77] H.H. Johnson, "Hydrogen brittleness in hydrogen and hydrogen oxygen gas mixtures", in R.W. Staehle (ed.), *Stress Corrosion Cracking and Hydrogen Embrittlement of Iron Base Alloys*, p. 382-389, 1977.

[KON 89] Y. Kondo, "Prediction of fatigue crack initiation life based on pit growth", *Corrosion*, vol. 45, no. 1, p. 7-11, 1989.

[LEE 72] H.H. Lee, H.H. Uhlig, "Corrosion fatigue of type 4140 high strength steel", *Met. Trans.*, vol. 3, p. 2949-2957, 1972.

[MAC 26] D.J. Mc Adam, *Proc. Am. Soc. Testing Mat.*, vol. 26, p. 224, 1926.

[MAG 87] T. Magnin, P. Rieux, "The relation between corrosion fatigue and stress corrosion cracking in Al-Zn-MG alloys", *Scr. Metal.*, vol. 21, p. 907-911, 1987.

[MUL 82] M. Muller, "Theoretical considerations on corrosion fatigue crack initiation", *Met. Trans. A*, vol. 13A, p. 649-655, 1982.

[NEL 89] H.G. Nelson, *Effect of Hydrogen on the Behavior of Materials*, Tms, p. 602-611, 1989.

[NEW 86] J.C. Newman, I.S. Raju, "Stress-intensity factor equations for cracks in three dimensional finite bodies subjected to tension and bending loads", in S. N. Atluri (ed.), *Computational Methods in the Mechanics of Fracture*, p. 312-334, 1986.

[NEW 91] J.S. Newman, *Electrochemical Systems*, Prentice Hall, 1991.

[PAR 61] P.C. Paris, M.P. Gomez, W.E. Anderson, "A Rational theory of fatigue, the trend in engineering", *University of Washington Journal*, vol. 13, no. 1, January 1961.

[PEL 80] R.M. Pelloux, "Fatigue-corrosion", in C. Bathias, J.P. Baïlon (eds.), *La Fatigue des Matériaux et des Structures*, Les Presses de l'Université de Montréal, p. 271-289, 1980.

[PIA 90] R.S. Piasick, R.P. Gangloff, "Aqueous environment effects on intrinsic corrosion fatigue crack propagation in an Al-Li-Cu alloy", in R.P. Gangloff, M.B. Ives (eds.), *Proceedings of the First International Conference on Environment-induced Cracking of Metals* Nace, p. 233-239, 1990.

[PIA 93] R.S. Piasick, R.P. Gangloff, "Environmental fatigue of an Al-Li-Cu alloy", *Met. Trans. A*, vol. 24A, p. 2751-2770, 1993.

[PIA 94] R.S. Piasick, "The growth of small corrosion fatigue cracks in alloy 2024", *Fatigue Fract. Eng. Mat. Struct.*, vol. 17, p. 1247-1260, 1994.

[REB 90] M. Rebiere, T. Magnin, "Corrosion fatigue mechanisms of an 8090 Al-Li-Cu alloy", *Mat. Sci. Eng. A.*, vol. 128, p. 99-106, 1990.

[SHE 66] H. Shen, S.E. Podlaseck, I.R. Kramer, "Effect of vacuum on the fatigue life of aluminum", *Acta Met.*, vol. 14, p. 341-346, 1966.

[SPE 77] M.O. Speidel, "Corrosion fatigue in Fe-Ni-Cr alloys", *Stress Corrosion Cracking and Embrittlement of Iron Base Alloys*, Nace, p. 1071-1094, 1977.

[THO 56] A.W. Thompson, N. Wadsworth, N. Louat, "The origin of fatigue fracture in copper", *Phil. Mag.*, vol. 1, p. 113-126, 1956.

[VOS 80] O. Vosikovsky, "Effects of stress ratio on fatigue crack growth rates in X70 pipeline steel in air and saltwater", *J. Test. Eval.*, vol. 8, p. 68-73, 1980.

[WEI 69] R.P. Wei, J.P. Landes, "Correlation between sustained-load and fatigue crack growth in high-strength steels", *Mater. Res. Std*, vol. 9, p. 25-28, 1969.

[WEI 80] R.P. Wei, P.S. Pao, R.G. Hart, T.W. Weir, G.W. Simmons, "Fracture mechanics and surface chemistry studies of fatigue crack growth in a aluminum alloy", *Met. Trans. A*, vol. 11, p. 151-158, 1980.

Chapter 11

Effect of Environment

11.1. Introduction

Fatigue strength of structural metallic materials can be affected by liquid or gaseous surroundings. The term "corrosion fatigue" is usually used to characterize the combined action of cyclic mechanical strain and an active environment; this term is mainly approved in the case of fatigue within an aqueous liquid environment. Nevertheless, this chapter focuses on corrosion fatigue in a gaseous atmosphere, which especially concerns ambient air. Indeed, we have to mention that ambient air is a very active medium that usually tends to reduce the fatigue strength of metals, metallic alloys and inter-metallic materials.

This negative effect is presented in Figure 11.1, where lifetimes under fatigue conditions of an Al-4% Cu alloy under alternate cyclic strain in ambient air and under vacuum ($<10^{-4}$ Pa) are compared, the latter environment being considered as a reference without any effect on the surroundings. In ambient air, the number of fracture cycles is much lower than under vacuum [BOU 76]. The bi-logarithmic diagram in Figure 11.2 shows the propagation rate of a crack under fatigue condition da/dN (a being the length of the crack and N the number of cycles), as a function of the cyclic amplitude of the stress intensity factor, ΔK, during the cracking under alternate stress of a 304 stainless steel.

Chapter written by Jean PETIT and Christine SARRAZIN-BAUDOUX.

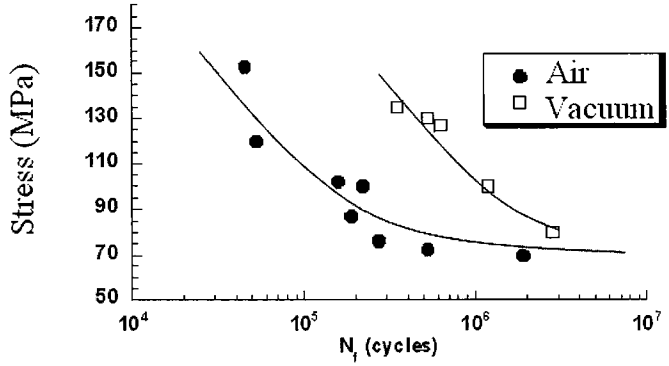

Figure 11.1. *Wöhler curve in air and under vacuum for an Al-4% Cu alloy [FOU 71]*

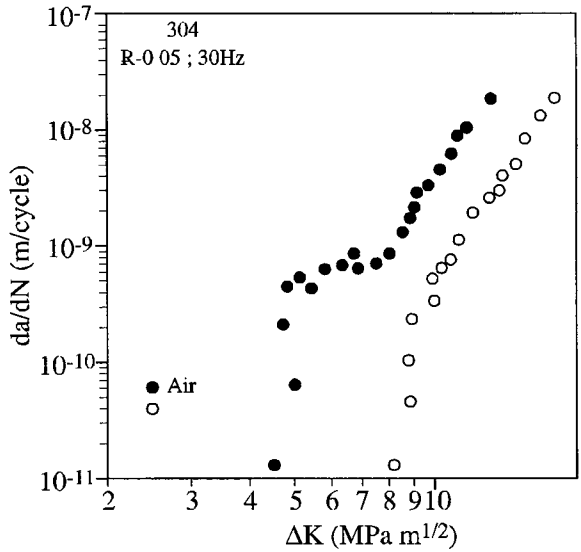

Figure 11.2. *Propagation rate of a fatigue crack within a 304 stainless steel in air and under vacuum [McE 92]*

Cracking in air occurs much more rapidly than under a vacuum, and the propagation threshold is much lower than under vacuum. These two examples typically illustrate the effect of the atmospheric environment on most metallic materials seen in experimental conditions.

The main goal of this chapter is to present in detail the effects of the gaseous environment on the behavior of metals and metallic alloys under fatigue conditions, focusing on the complex interactions that can be observed within the different intrinsic and extrinsic factors.

11.2. Effect of environment on lifetime under high-cycle fatigue conditions

11.2.1. *Initial work*

The first studies on various materials and alloys (copper, magnesium, lead and brass) showing a better behavior under fatigue conditions in air than under rough vacuum (1.3×10^{-1} Pa) were carried out by Gough and Sopwith in 1932 [GOU 32] (see Figure 11.3). Much later on, Wadsworth and Hutchings [WAD 58] and Broom and Nicholson [BRO 60] carried out some tests in different dry and humid atmospheres compared to tests under a vacuum. They attributed the reduction of in lifetime of aluminum in air to the presence of water vapor as they observed that there is no dry-oxygen effect. However, this same effect seems to occur because of the presence of oxygen in the case of copper.

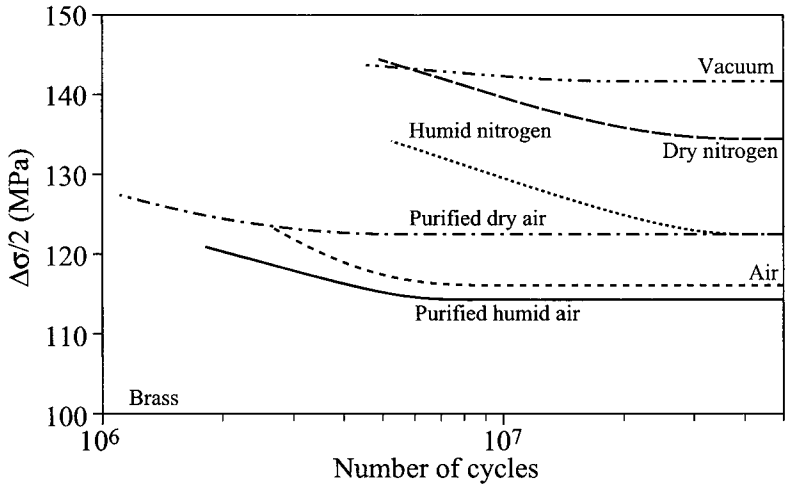

Figure 11.3. *Wöhler diagram for brass under various gaseous atmospheres [GOU 32]*

Following this initial work, numerous studies have focused on the negative role of some reputed non-corrosive atmospheres, such as atmospheric air, for most of the usual metals and alloys. The following references cover what has been published regarding these studies:

– iron and steels: [GRI 73, SCH 68, WAD 61];

– aluminum and alloys: [BEN 64, BOU 75, BRA 66, BRO 60, ENG 68, HOR 66, HOR 68, JAC 67, SCH 68, SHE 66, WAD 58];

– nickel-based alloys: [DUQ 71, DUQ 72, LAI 63, WAN 84];

– silver: [SMI 71];

– magnesium and alloys: [SCH 68, SUM 68];

– titanium alloys: [MEN 96, MEN 99, SCH 68];

– gold: [GRO 66, WAD 58].

The lifetime under fatigue conditions can be divided into the time necessary for the initiation step to occur and the time of the propagation step. It has been known for a long time and demonstrated that usually the initiation time (whose definition is not always the same, depending on the authors) is much longer under vacuum than in air [BRO 60, GRI 73, WAD 58].

11.2.2. *Mechanisms*

To understand the effect of atmospheric air on the behavior of some metals and alloys under fatigue conditions, Thompson *et al.* [THO 56] looked at chemical adsorption mechanisms. They were the first to mention that these mechanisms can occur on a freshly-obtained surface, leading to damage of the metal because of the oxygen (see Figure 11.4a).

Some other authors, suspecting the role of water vapor, mentioned a hydrogen embrittlement due to the dissociation of the adsorbed water [BEN 64, BRO 60]. Shen *et al.*, [SHE 66] (see Figure 11.4b) suggested that the presence of an oxide film is more likely to lead to the irreversibility of dislocations slip and the accumulation of dislocations close to the surface, thus boosting the formation of microcracks.

According to a first hypothesis, which suggests that lifetimes are longer under vacuum because of a rewelding mechanism [THO 56, WAD 58], many authors compared fatigue in materials under a vacuum and in air (which means that the behavior in air acts as a reference and not under vacuum) The inexistence of this mechanism, however, has been clearly acknowledged for a long time [LAI 63, MAR 68].

Some fine studies were then performed on monocrystals [GRO 66] and on copper, [HUN 88, WAN 84], showing a development close to persistent slip bands in air and under vacuum (see Figure 11.5).

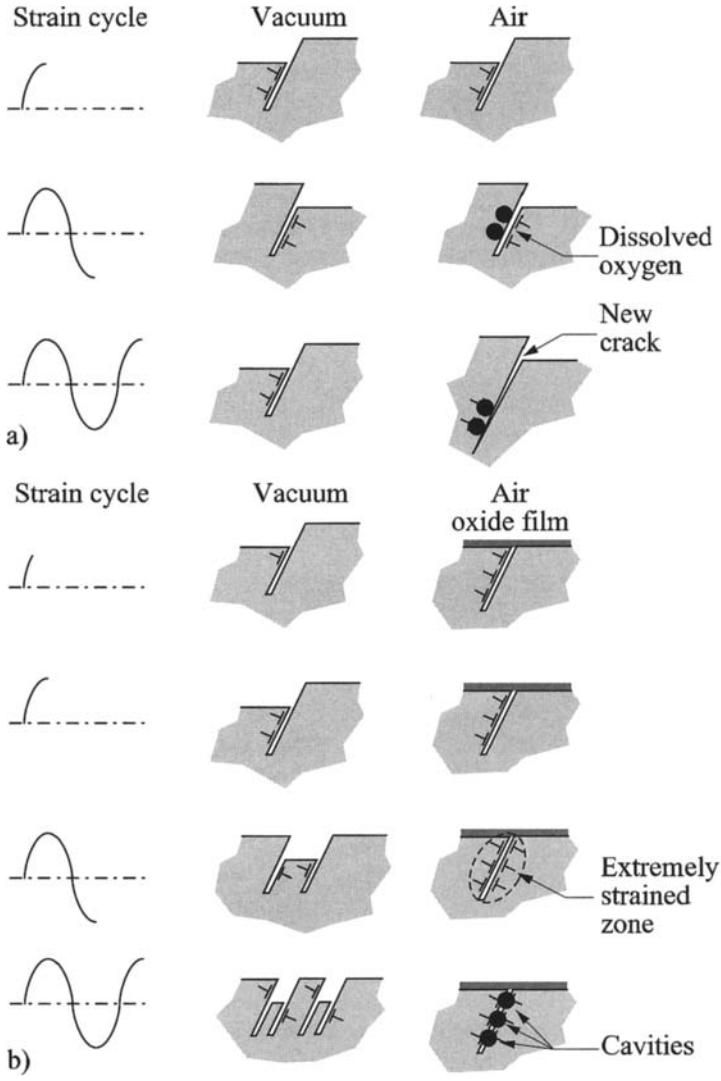

Figure 11.4. *Initiation models; a) interaction between oxygen and slip bands [LAI 71, THO 56]; and b) formation of cavities under the oxide layer [LAI 71, SHE 66]*

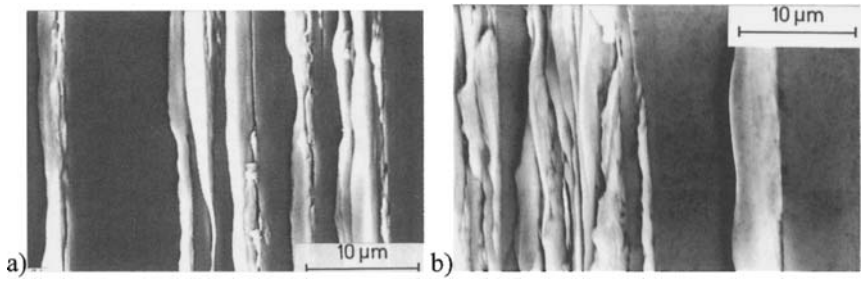

Figure 11.5. *Persistent slip bands within a single copper crystal stressed under fatigue conditions: a) in air; and b) under vacuum [WAN 84]*

The effect of the environment leads to an earlier formation of cracks in air. Under vacuum, the development process of persistent slip bands can go on for a much longer time and lead to a significant secondary hardening, as shown for a stainless steel [MEN 88]. This behavior enables us to understand the predominance of an initiation step within the grain joints under vacuum [MEN 88].

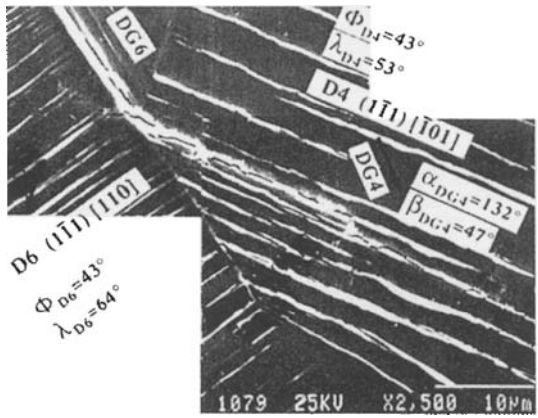

Figure 11.6. *Electron back scattering diffraction identification of the orientation of the grains close to the persistent slip bands in a stainless steel. Definition of the angles: λ = normal slip plane/normal surface; α = sliding direction/loading axis; β = sliding direction/normal surface [VIL 06]*

The electron back scattering diffraction technique allows a better understanding of the difference in the damage mechanisms between air and vacuum. It provides precise information on the orientation of the grains and of the slip bands at the surface. The example of a 316 stainless steel is given in Figure 11.6. Damage due to fatigue in air seems to be connected to a localized deformation within the slip bands,

whereas under vacuum a more homogenous deformation leads to an inter-granular initiation.

11.2.3. *Influence of atmospheric pressure and frequency*

Snowden [SNO 64] was the first to show an S-shaped evolution of lifetime curves as a function of the air pressure according to the loading amplitude on copper (see Figure 11.7). He defined a threshold of critical air pressure P_{cr} at the level of the inflexion point of the curves that correspond to the highest sensitivity in pressure variations. Some similar evolutions where then observed on various materials [HUD 76], specifying that the observed effect of the frequency in air [ACH 68, HOR 66, SHE 66] does not occur under vacuum [COF 72, DUQ 78] and that the divergence of the curves giving the number of cycles as a function of strain level between air and vacuum is less pronounced for the strong stresses and low lifetimes.

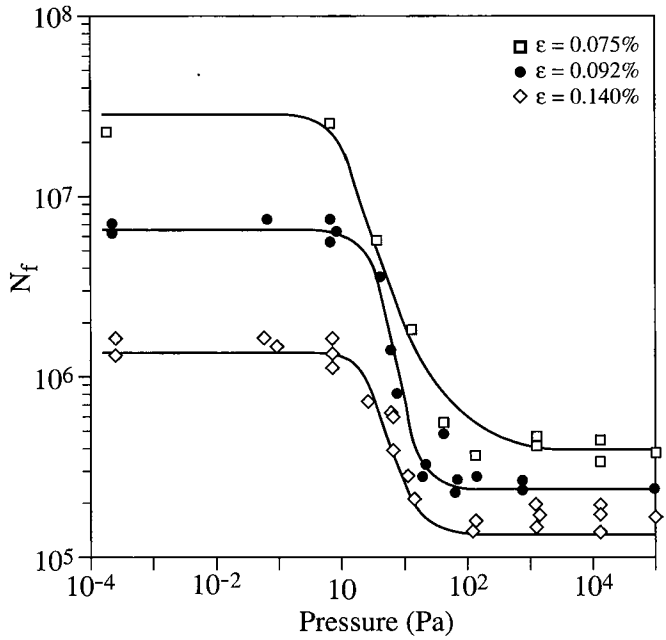

Figure 11.7. *Lifetime of copper as a function of air pressure [SNO 64]*

From all these results, we can say that for a given frequency, when the pressure of the surrounding gas $P >> P_{cr}$, the effect of the environment is at its maximum and is independent from the pressure variations. When $P << P_{er}$, however, the

environment has no effect at all, as if under a vacuum. Nevertheless, the pressure variations are very sensitive in a pressure range close to P_{cr}. When the pressure remains constant, we can determine a critical frequency in the same way, as the environment has no effect at a very high frequency and as it saturates at a very low frequency.

The influences of pressure and frequency are then connected. To draw this conclusion, we have to rely on both the exposure time $t = 1/2f$ (f = frequency) of the material to the surrounding gas and on the pressure P of this same gas, which leads to the equation of the exposure parameter $X = P/2f$.

The critical pressure thresholds can be then be written, using kinetics terms, by comparing the number of molecules that have to be used to homogenously cover the newly created surfaces during half a cycle to the number of gaseous molecules that hit the material per surface and time unit. The number of molecules that have to be used comes to $n_s \times f$, where n_s is the number of available sites per surface unit and f the frequency. The number of molecules hitting a unit surface per second is:

$$n_i = \frac{N.P}{\sqrt{2\pi MRT}} \qquad [11.1]$$

(N is the Avogadro number, M is the molecular weight, R is the constant of ideal gases and T the temperature). The highest sensitivity domain of the material variations in exposure is thus defined around a critical exposure, X_{cr}, which is a typical property to each material for a given temperature.

11.2.4. *Combined effects of microstructure and environment*

The effects of the environment and the microstructures can be combined. Thus, for instance, the Wöhler curves obtained in air and under a vacuum on an AU4 aluminum-copper alloy stressed under bending, respectively at the underaged state (Guinier-Preston zones) and at the highest hardness state (precipitates θ″) [BOU 75] can be combined. They show that in the underaged state, materials under vacuum have the longest lifetime and the highest hardness state θ″ in air relates to the shortest lifetime, as the air reduces the lifetime within both microstructures (see Figure 11.8).

However, it is quite hard to provide general rules for these phenomena as they are complex. These effects therefore have to be studied case by case.

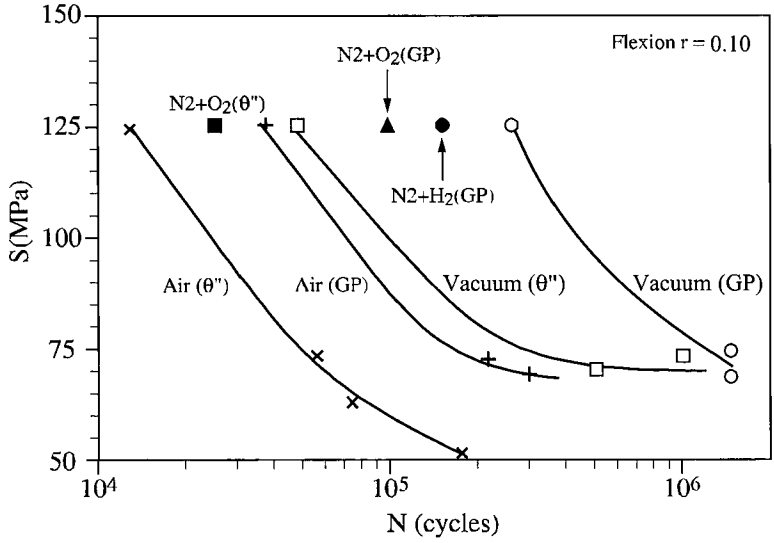

Figure 11.8. *Influence of gaseous atmosphere on the fatigue resistance of an Al-4%Cu alloy in two different aged conditions: underaged (GP zones) and overaged (s θ' precipitates) conditions [BOU 76]*

11.2.5. *Effects of combining temperature and environment*

The combined effects of temperature and environment can lead to some surprising behaviors at a first sight. For instance, a stressed 316L steel under a cyclic and plastic deformation $\Delta\varepsilon_p$ of about 10^{-3} [MEN 96] under vacuum presents a similar lifetime at room temperature and at 600°C (see Figure 11.9). Nevertheless, we observe a maximum lifetime that is three times longer at 300°C. This peculiar behavior is likely to occur because of a secondary hardening, related to some corduroy-shaped dislocations made of very thin bands of small loops [GER 86]. In air, the lifetime, which is always lower than the that under vacuum, continuously decreases with temperature without any specific effect at 300°C, as the secondary hardening only occurs for long lifetimes, which are only reached under vacuum.

This example illustrates the complex interactions that can be found between the microstructure, atmospheric environment and temperature. It is therefore necessary to always know the different mechanisms and effects that occur before any realistic modeling is carried out. This is because realistic modeling will have to consider the effects of the environment, especially the effects due to atmospheric air. We can therefore say that a model that does not consider environmental effects can only be approved by some tests run in an inert medium, such as a vacuum.

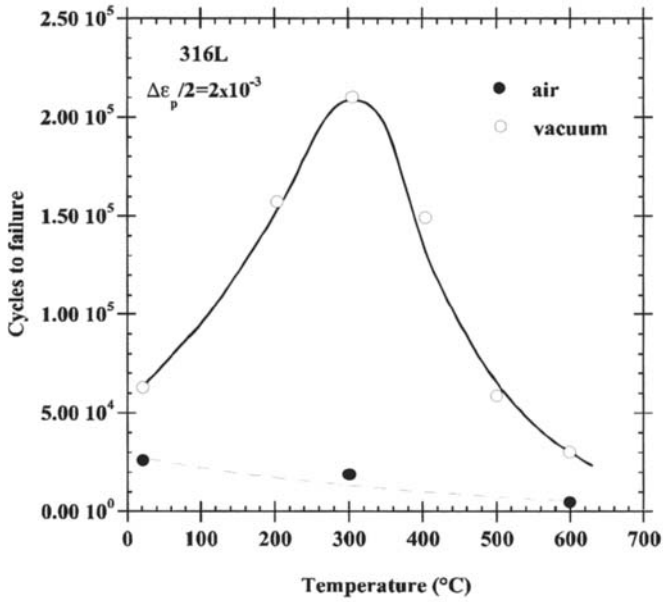

Figure 11.9. *Influence of temperature on lifetime under cyclic fatigue conditions of a 316L stainless steel tested at 1 Hz in air and under vacuum between room temperature and 600°C [ALA 97]*

11.2.6. *Effect of the environment under ultra high-cycle fatigue conditions*

The domain of fatigue with a high number of cycles has been increasingly studied as researchers are trying to get a more precise prediction of the initial and residual lifetimes in order to extend the lifetime of industrial structures. It is especially the case with turning parts (engines, turbines, wheels, etc.) and parts subjected to sound vibrations (for example, the taking-off of a rocket). It has been shown that the fatigue limit that was usually determined within the domain of one million cycles was no longer valid within the gigacyclic domain (10^9 cycles and more).

In the case of many metals and alloys, Wöhler curves (stress as a function of lifetime) can present a decrease in fatigue limit when the lifetimes go beyond 10^7 cycles. Nakajima *et al.* [NAK 01] proposed a split Wöhler curve that is connected by a plateau, whereas Murakami [MUR 01] and Bathias [BAT 01] proposed two curved lines separated by a plateau without any explicit fatigue limit (see Figure 11.10). In the case of high-strength steels (ball bearing steel) the ultra-long lifetimes are usually related to an internal initiation and the development of a fish-eye crack

[MUR 01]. The reasons for this behavior in the case of ultra-long lifetimes still have to be determined.

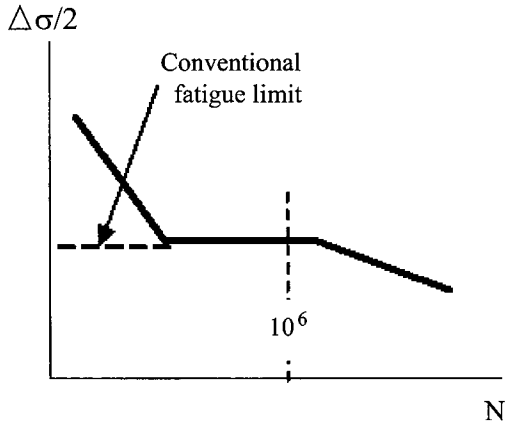

Figure 11.10. *Schematic curve according to Murakami [MUR 01] and Bathias [BAT 01]*

The atmospheric environment is also important in lifetime under ultra high-cycle fatigue conditions. Thus, Nakajima *et al.* [NAK 01] showed that ambient humidity strongly influences the endurance of high strength chromium steel (see Figure 11.11). The lifetimes in a dry air (5% residual humidity, RH) are much longer than in a humid air (85% RH). The strain level of the transition plateau from a superficial initiation to an internal initiation strongly decreases with the increase of the humidity.

A similar result was obtained on a titanium alloy at 300°C that was tested in air and under a vacuum. Within an inert atmosphere, there is no transition plateau, but the initiation mode still changes. As a consequence, the effect of the environment on cracks initiated at the surface of the specimen being tested might explain the presence of the plateau. The transition of the surface/core initiation, however, would remain mainly connected to the strain level and microstructure.

11.3. Influence of the environment on fatigue crack propagation

11.3.1. *Initial work*

The specific action of the environment on the propagation rates of fatigue cracks was observed for the first time by Dahlberg [DAH 65] on high-strength 4340 steel.

His results showed a 10-fold increase of the propagation rate in humid air compared to under a vacuum.

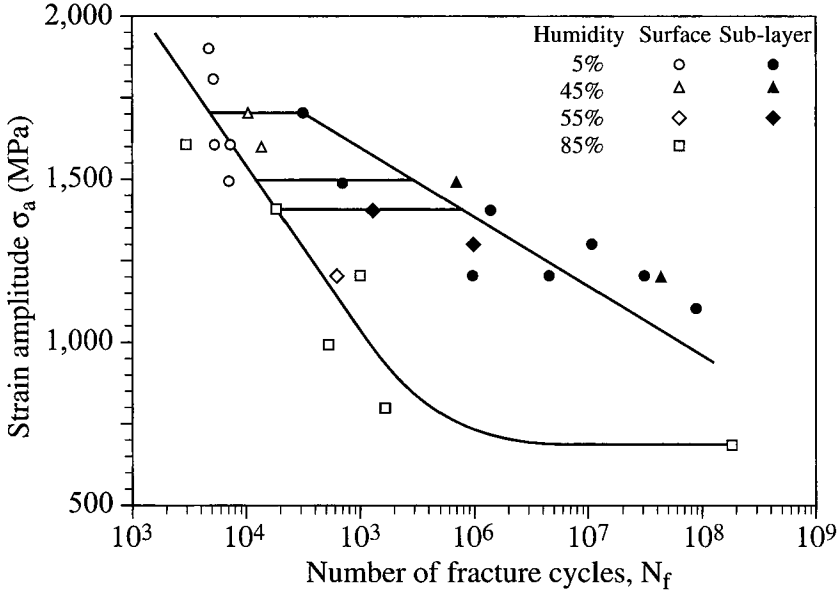

Figure 11.11. *Influence of relative humidity (5, 45, 55 and 85%) on the endurance of a very high-strength chromium steel: open symbols for an initiation at the surface and closed ones for an internal initiation [N0K 01]*

The first tests that allowed us to observe the influence of air pressure and of its different components were carried out on aluminum alloys [BRA 66, HAR 65, ISH 69].

The results obtained by Bradshaw and Wheeler [BRA 66], dealing with a 5070 alloy (see Figure 11.12), were the first to show the existence of narrow range of water vapor partial pressure where the propagation rate of a fatigue crack, for a given stress intensity factor amplitude ΔK, significantly depends on the variations of this same partial pressure. Like the lifetimes under fatigue, the cracking rate does not depend on the variations of pressure when this pressure is much higher or lower than the values corresponding to this gap. The crack lengths in Figure 11.12 actually correspond to increasing stress intensity factor ranges, as the tests are run under a cyclic loading with constant amplitude.

The first comparative study on the propagation of fatigue cracks in air and under a vacuum that allowed us to establish some laws giving the growth rate per cycle

da/dN as a function of amplitude of the strain intensity factor ΔK, was performed by Meyn [MEY 68]. This historical curve is presented in Figure 11.13.

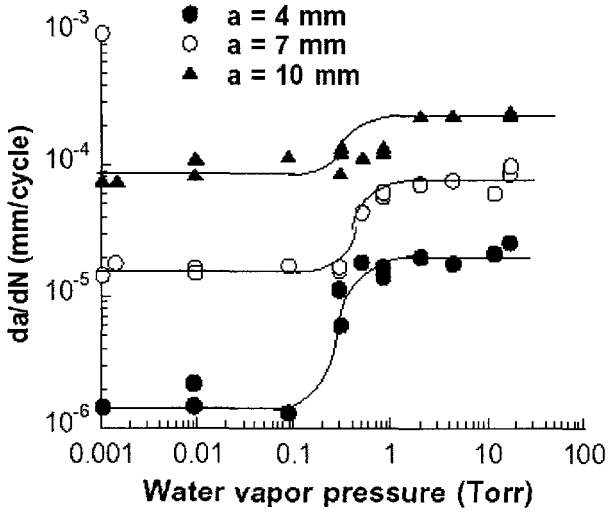

Figure 11.12. *Influence of partial water vapor pressure on the propagation rate of a fatigue crack in a light DTD 5070 alloy [BRA 67]*

After this, the effect of the air and of humid atmospheres on the propagation of fatigue cracks was studied a great deal. We can list the following references for the various alloy families:

– aluminum and alloys: [BAI 84, BOU 75, BOW 83, BRO 71, GUD 91, HEN 92, KIR 79, LAN 83, LIN 79, MEY 68, PET 00, PET 84, PET 90, PET 92a, PET 92b, PET 93, PIA 91a, PIA 91b, RAN 90, RAN 95, RAN 96, RUI 97a, RUI 97b, STA 84, SUR 83, WAN 75, WEI 67, WEI 68, WEI 72, WEI 81, ZEG 85];

– copper and alloys: [BAI 84, LIA 89];

– iron and steels: [BEE 77, BIG 90, BIG 94, BRA 83a, COO 75, EVA 71, FRA 75, FRA 77, HAB 93, HEN 92, IRV 78, JAM 99, KEN 88, LIA 82, LIA 83, LIN 81, MCE 65, MCE 88, PIP 91, RIT 75, RIT 79, RIT 80, SMI 87, STE 72, STE 80, SUY 90, WEI 72, ZHU 86];

– titanium and alloys: [COT 92, DAV 84b, FOE 93, GHO 91, IRV 74, LIN 79, MEY 76, PET 93, SAR 97, SAR 99; WEI 72];

– nickel and alloys: [FRA 75, KIN 82, RIC 78a, SWA 78, YUE 85].

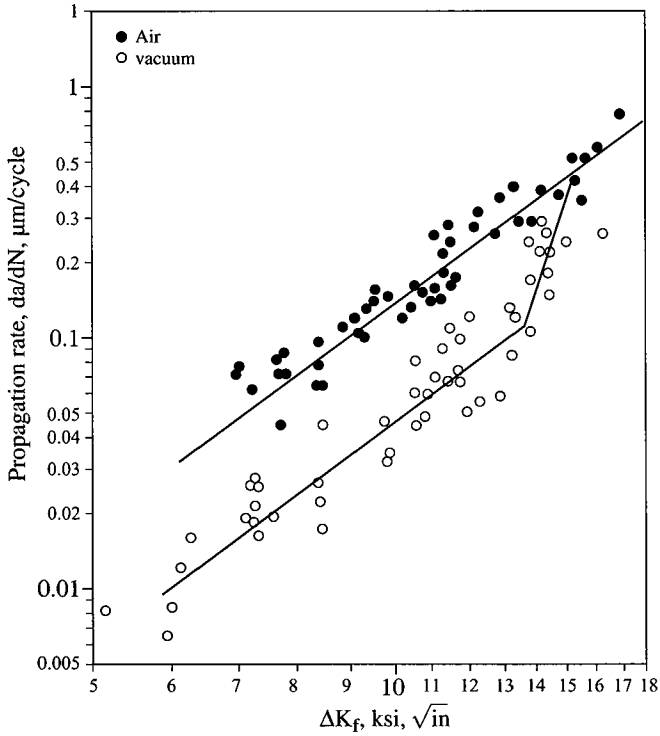

Figure 11.13. *First log-log diagram of da/dN versus ΔK for tests carried out in air and under vacuum on an Al-4Cu-Mg alloy [MEY 68]*

The main conclusions from all of these studies can be listed as follows:

– water vapor can be observed to have a detrimental effect on most metals and alloys, especially at room temperature;

– this effect depends on the loading conditions: stress level, loading ratio, amplitude variation, etc.;

– there is a strong interaction between microstructure and the environment;

– the gaseous environment typically influences the morphology of the fracture surfaces and the dislocations of slip mechanisms;

– there are some interactions between the environment and the crack closure, especially close to the propagation threshold;

– the effect of the environment depends on the geometry of the cracks, especially on their depth.

To analyze the effect of the environment on the propagation of fatigue cracks, three different steps have to be followed:

– isolating/decoupling of the external effects using appropriate tests:

- using an atmospheric chamber allowing us to operate under vacuum and under well-controlled gaseous environments with a mass spectrometer and accurate hygrometer,

- temperature control (high and low temperatures),

- strict control of the residual humidity: gas with certified purity, dew point imposed by cooling, etc.;

– identifying the intrinsic mechanisms:

- reference behavior under vacuum with a closure correction,

- specific influence of the microstructure,

- influence of the stress levels and the loading conditions, etc;

– identifying and modeling the effects of the environment:

- mechanisms of environment assistance for fatigue crack propagation,

- coupled effects between closure, microstructure, temperature,

- phenomenological and mechanical modeling.

11.3.2. *Propagation of fatigue cracks under a vacuum (inert reference environment)*

In order to understand the different factors, which can be both intrinsic (chemical composition, purity, microstructure, etc.) or extrinsic (environment, temperature, geometry of the cracks and induced effects, such as closure, loading conditions and loading ratio), reference tests have to be carried out under a vacuum which allows us to isolate the different effects. The results obtained on different materials can be compared once the closure effects – mainly due to the ductility of the material, the roughness and the loading ratio R – are removed or corrected. We then observe that the intrinsic behavior, given as a function of ΔK_{eff} can be described depending on three fundamental intrinsic regimes [PET 00a, PET 03, PET 92]:

– intrinsic stage I;

– intrinsic stage II; and

– intrinsic stage I-like.

11.3.2.1. *Intrinsic stage I*

This is a rapid cracking regime that can occur in materials, leading to a microstructural localization (shearable precipitates) or mechanical localization (initial propagation plane of short cracks oriented along the highest shearing plane). Propagation then usually occurs in mixed mode I plus II (see Figure 11.14).

11.3.2.2. *Intrinsic stage II*

This intermediate regime, in terms of cracking rate, is the most frequently observed in all metals and alloys (see Figure 11.15). In particular, it predominates within the conventional Paris' domain (average rates). At least two slip systems are alternatively active at the crack tip [PEL 69].

The propagation regime in stage II follows a law giving da/dN as a function of ΔK_{eff}, given by Petit *et al.* [PET 91, PET 94], from the initial models of Weertman [WEE 73], Rice, [RIC 65] and of McClintock, [MCC 63]. It can be written as:

$$da/dN = A/D_0^* [\Delta K_{eff}/E]^4 \qquad [11.2]$$

where:

– A is a digital coefficient;

– E is Young's modulus;

– D_0^* is the critical displacement accumulated at the crack tip leading to a cracking increment that is supposed to be proportional to U, the specific surface formation energy.

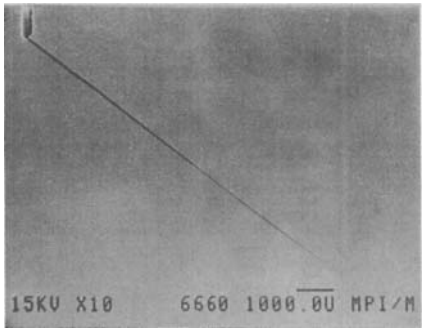

Figure 11.14. *Intrinsic stage I under vacuum in an Al-Zn-Mg alloy crystal in underaged condition (GP shearable zones) oriented for easy slip (plane (111) p at 45° against the horizontal loading axis within this figure)*

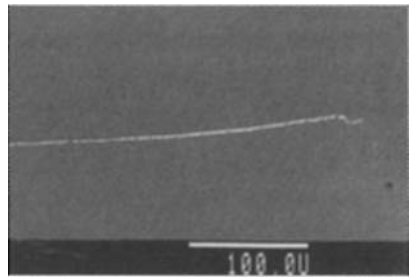

Figure 11.15. *Intrinsic stage II under vacuum within an Al-Zn-Mg alloy monocrystal, annealed up to the hardness peak (mixed precipitate) and oriented for easy sliding (vertical loading axis in this figure)*

Figure 11.16 shows that this law deals with the intrinsic behavior of numerous aluminum alloys, steels and titanium-based alloys [PET 91]. The low distribution in all the alloys comes from the values of D_0*, which poorly depends on the nature of the material and the structural state.

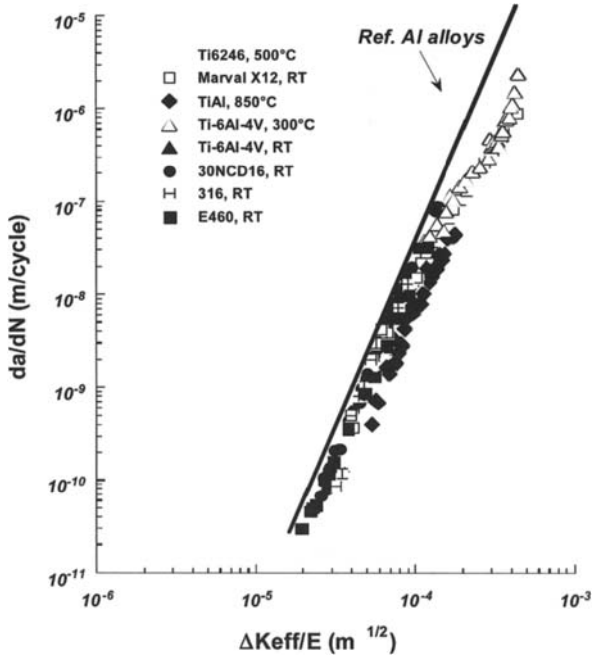

Figure 11.16. *Intrinsic stage II within metallic alloys (aluminum alloy reference: see Figure 11.19)*

Figure 11.17 shows how the propagation path goes from an intrinsic stage II to an intrinsic stage I within an Al-Zn-Mg single crystal oriented for easy slip when the amplitude of the stress intensity factor ΔK gets close to the threshold value. This kind of transition can also occur at the scale of each grain within a polycrystal. This phenomenon is reversible when ΔK increases again, once the threshold has been reached. The critical amplitude of ΔK for this transition therefore depends on the microstructural state. Usually, stage I tends to become predominant when close to the threshold.

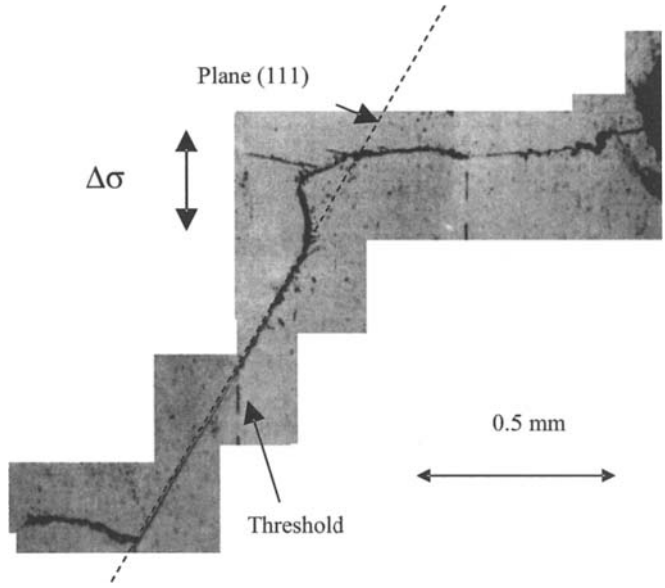

Figure 11.17. *Change of intrinsic propagation regime within an Al-Zn-Mg single crystal, annealed at the roughness peak and oriented for easy slip: stage II when cracking first occurs close to the notch; stage I when ΔK is slow and close to the threshold; back to stage II once the threshold has been reached when ΔK increases above a critical value*

11.3.2.3. *Intrinsic stage I-like*

This third intrinsic cracking regime has a slow or delayed crystallographic propagation and presents a wiggly nature (see Figure 11.18). It is identified as being intrinsic stage I-like.

This regime is mainly observed at the slow cracking rates in polycrystals, when the microstructural state leads to localization of the deformation, especially when the threshold gets closer or during the initial propagation of short cracks.

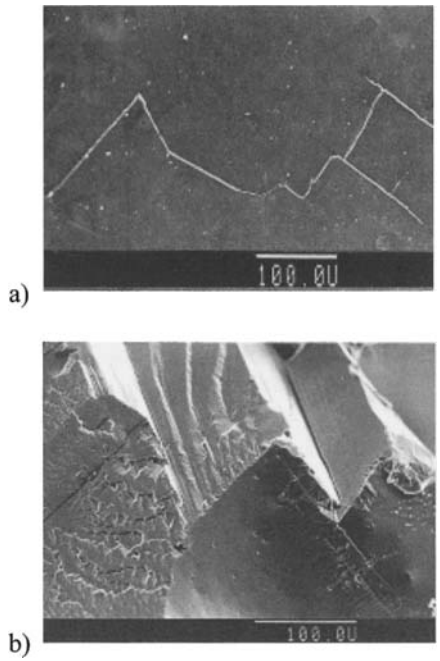

Figure 11.18. *Intrinsic stage I-like propagation under vacuum in an underaged Al-Zn-Mg polycrystal (shearable GP zones) at low ΔK; a) crack profile; and b) fracture surface*

This regime is more or less a restrained stage I within each grain, which then occurs when the size of the plastic zone is lower than that of the grains. The identification of this regime was mainly done using different light alloys (see Figure 11.19) in order to compare intrinsic stage I-like with intrinsic stage II. Propagation is delayed due to some stops at the grain boundary level that correspond to the number of cycles necessary to reactivate a new slip system within the following grains.

Figure 11.20 illustrates a grain in a high-purity Al-Zn-Mg alloy bicrystal. The crack spreads under a vacuum along a plane (111) of the face-centered cubic structure of the first grain and then reaches the grain boundary (see Figure 11.20a). A system of (111) slip planes with very different orientations gets formed within the second crystal before the growth of a new tilted crack (see Figure 11.20b), as suggested by the final fracture surface (see Figure 11.20c). The delay strongly depends on the disorientation, the microstructure and the number of possible slip systems available, which is, for example, more restricted in titanium alloys than in aluminum alloys [SAR 99].

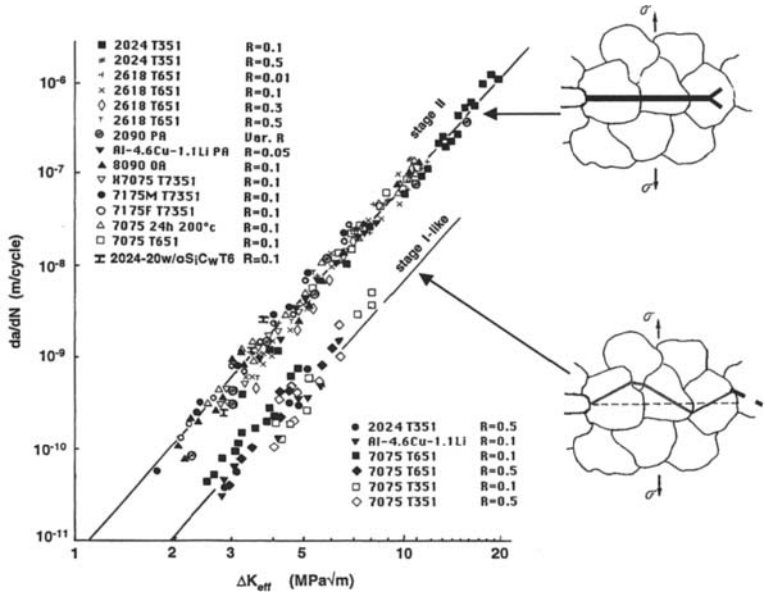

Figure 11.19. *Stage II and stage I-like intrinsic propagation regimes under a vacuum in various aluminum alloys [PET 92, PET 94, PIA 91]*

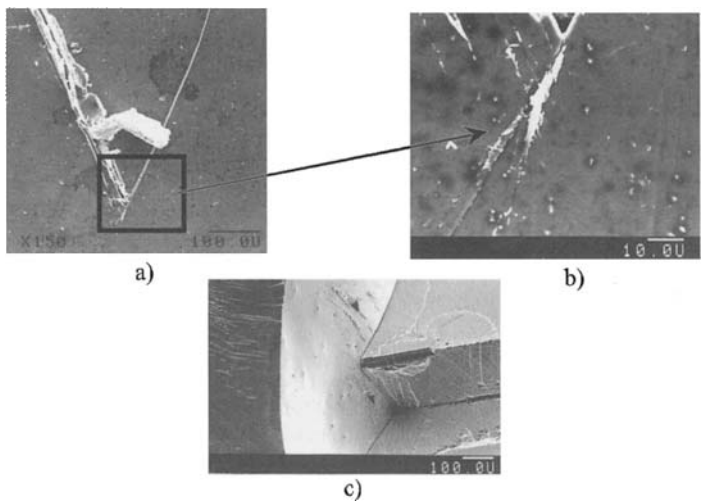

Figure 11.20. *Barrier effect of a grain boundary in an underaged Al-Zn-Mg bi-crystal cracked under vacuum [PET 06]: a) blocking of the crack on the grain boundary; b) magnification of a); and c) final fracture surface*

Usually, the delay is much more noticeable under vacuum, as the environment makes it is easier to cross the grain boundaries as it activates some other slip systems. Crack deviation and branching slow down the crack propagation rate as the stress intensity factor gets lower. Until now, there has not been a model to describe these complex and typically tri-dimensional processes. Nevertheless, Suresh [SUR 85] proposed a simple micromechanical model accounting for this delay by introducing a parameter χ, ranging from zero to one, which gives the reduction in the stress intensity factor induced by the geometrical effects of the crack path. Then the variation of the amplitude of the stress intensity factor ΔK has to be changed to $\chi \Delta K$ within the propagation laws.

11.3.3. *Environmentally-assisted propagation*

Figure 11.21 presents some effective propagation curves in air for a selection of steels and light alloys. Contrary to what can be observed under vacuum, there is clearly no rationalization, especially in the case of light alloys.

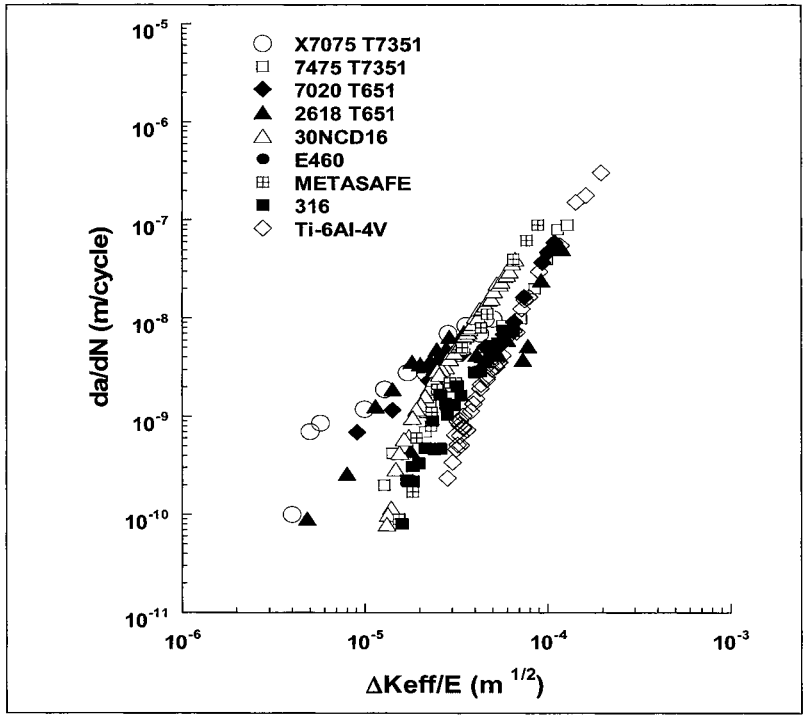

Figure 11.21. *Effective propagation curves in air for different metallic alloys*

In comparison to under a vacuum, propagation in air is always faster. This acceleration, due to the environment, is more pronounced when close to the threshold. The sensitivity to the atmospheric environment seems to depend a great deal on the nature of the metal, the components of the alloy and the microstructure. Nevertheless, they have something in common. In most of the cases, for tests run at conventional frequencies (about 10 to 100 Hz), a change of behavior occurs when the rates are lower than 10^{-8} m/cycle. This rate level is connected to the values of ΔK corresponding with cyclic plastic zones of small dimensions that become localized within a single grain or sub-grain. It is also a rate level under which it is generally admitted that propagation occurs step-by-step and no longer cycle-by-cycle [DAV 83].

According to some experimental results obtained on three alloy families made of aluminum, iron and titanium, under vacuum, in ambient air and under an inert gas containing some well-controlled water steam traces, a descriptive model was established by Petit *et al.* [PET 00a]. This model considers two additional environmentally-assisted propagation mechanisms in stage II, which are described and compared to the intrinsic regime in stage II (see Figure 11.22).

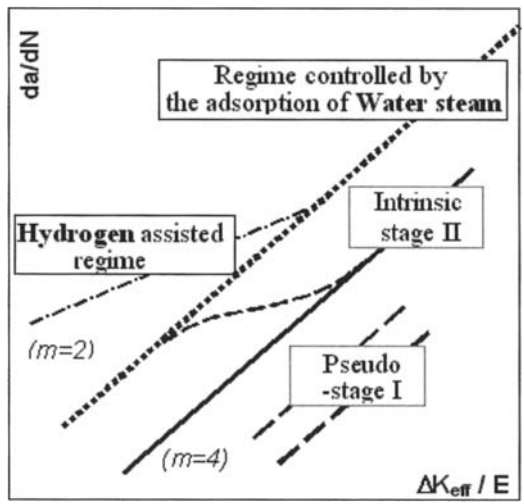

Figure 11.22. *Schematic illustration of the intrinsic and environmentally-assisted propagation regimes for polycrystalline metals and alloys [PET 00a]; reference intrinsic stage II without any environmental effects, adsorption stage II, assisted by the adsorption of water steam, and hydrogen assisted stage II [PET 00a]*

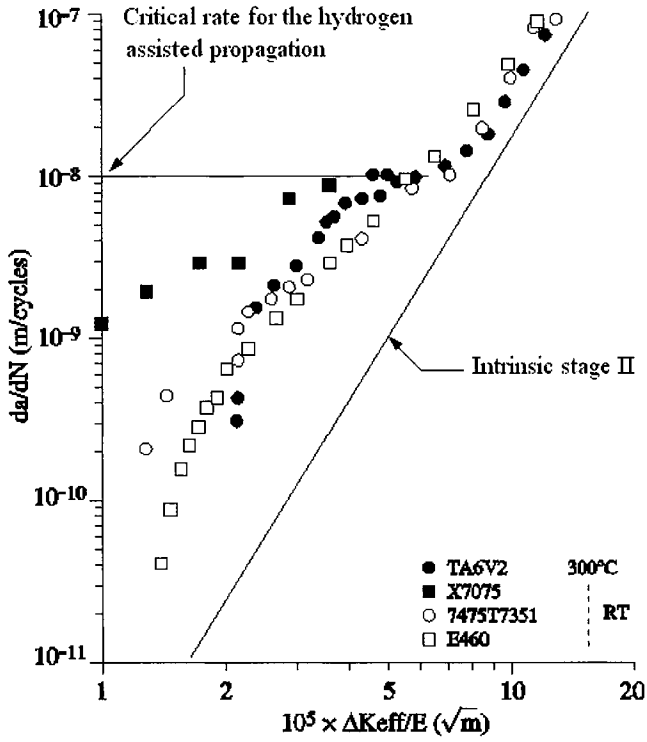

Figure 11.23. *Critical propagation rate $(da/dN)_r$ of hydrogen assistance [PET 00a]*

11.3.3.1. *Stage II assisted by the adsorption of water vapor*

For cracking rates higher than a critical level $(da/dN)_{cr}$, cracking under fatigue conditions is assisted by the adsorption of water vapor molecules on fresh surfaces at the crack tip. The damaging mechanism continues to be controlled by the local plasticity as if it were under vacuum.

Figure 11.23 sets this critical rate according to the curves of environmentally-assisted cracking. To describe the propagation assisted by adsorption of the water steam, a model was proposed [PET 00a] that is similar to the one of intrinsic propagation in stage II. It is given by an equation quite close to the former one:

$$da/dN = A/D^*[\Delta K_{eff}/E]^4 \qquad [11.3]$$

where the cumulated critical displacement D^* is connected to the coverage coefficient θ (ratio of the number of sites occupied by adsorbed water molecules to the number of initially available sites), with the following equation:

$$D^* = D_0^* D_1^* / (D_1^* + \theta(D_0^* - D_1^*)) \quad [11.4]$$

where D_0^* corresponds to an inert environment as under vacuum ($\theta = 0$) and D_1^* corresponds to an environment leading to a saturating adsorption with a complete first monolayer on the fresh surface ($\theta = 1$). The dependence of θ on the water vapor partial pressure was first described by Wei *et al.* [WEI 83]. When θ is controlled by the transport conditions of the gaseous phase up to the crack tip, these authors proposed the following equation:

$$\theta = (F/SN_0RT)P_0 t \quad [11.5]$$

where:

- S is the fresh surface exposed to the environment;
- N_0 the number of adsorption sites by surface unit;
- R the gas constant;
- T the temperature;
- P_0 the surrounding pressure;
- t the time; and
- F the Knudsen flow parameter.

Equation [11.5] corresponds to the case of a cycle-by cycle-propagation (Paris' domain). Close to the threshold, however, the crack grows step-by-step every Ns cycles. Hénaff *et al.* [HEN 90] proposed another equation giving the evolution of θ for a quasi-stable crack:

$$\alpha S_0 \theta / 4F - (1/N_s V_a) \text{ Log } (1 - \theta) = (P_0/4N_0RT)\, t \quad [11.6]$$

where:

- α is a roughness parameter (ratio of the physical surface to the geometrical one);
- V_a the average migration rate of the water molecules; and
- Ns the number of stable cycles.

As we cannot analytically calculate the cracking rate from this equation, the first simulations were carried out numerically [HEN 95]. Recently, an analytical equation was established to describe the variation of θ as a function of the exposure $P_{H2O}/2f$, where $P_{H2O}/2f$ is the partial pressure of water vapor and f the test frequency for the effective stress intensity factor range ΔK_{eff} [GAS 06, SAR 00]:

$$\theta = \{X^2/(X^2+9)\}^2 \qquad [11.7]$$

with the following expression of X, α being a material parameter:

$$X = \alpha (P_{H2O}/2f)\, \Delta K_{eff}^2 \qquad [11.8]$$

An example is given in Figure 11.24.

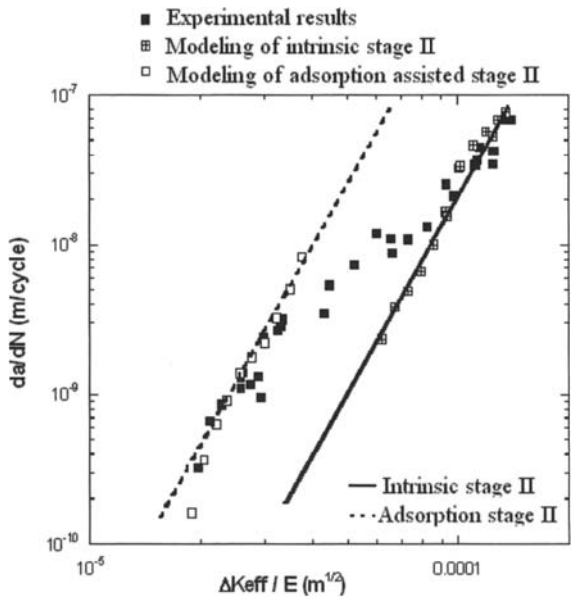

Figure 11.24. *Transition from intrinsic stage II in the mid-rate domain to effective stage II-assisted water vapor adsorption in the threshold domain in a 2022T351 alloy. The influence of adsorption is considered using equation [11.7] [GAS 06]*

11.3.3.2. *Hydrogen-assisted propagation in stage II*

For cracking rates lower than the critical value $(da/dN)_{cr}$ (see Figure 11.23), a hydrogen-assistance mechanism (see Figure 11.21) can occur, following the model

initially proposed by Wei *et al.* [WEI 83]. These authors described the process according to the following steps (see Figure 11.25):

– transport of the active molecules to the crack tip;

– reaction of the water molecules with the freshly created surface: physical adsorption;

– chemical adsorption with dissociation and penetration of the hydrogen due the dissociation phenomenon;

– interaction of the hydrogen with the dislocations: draining diffusion;

– trapping of the hydrogen on different microstructural sites, which can lead to some local embrittlement of the material within the process zone at the crack tip.

The assistance of hydrogen in fatigue cracking, at room and moderate temperature, comes mainly from the fourth point. It is also obvious that the assistance process by the adsorption has to be saturating to get hydrogen production going. Damage occurs for high hydrogen concentrations, which are not reached at room temperature according to the process described by the action of water vapor.

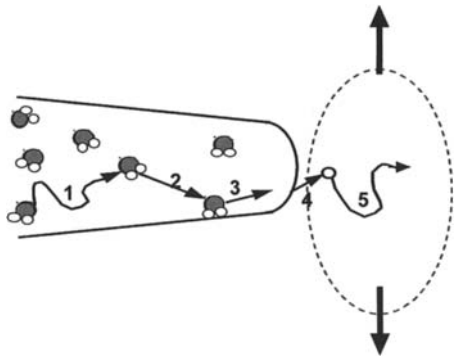

Figure 11.25. *1) Transport of the water molecules towards the crack; 2) physical adsorption; 3) chemical adsorption and dissociation; 4) penetration of the hydrogen; and 5) diffusion by draining within the plasticized zone*

The critical concentration of this element, coming from dissociation of the adsorbed water molecules, can only be reached for growth rates lower than a critical $(da/dN)_{cr}$, depending on various factors including:

– the water vapor partial pressure of the surrounding atmosphere;

– the loading ratio R;

- the test frequency;
- the chemical composition; and
- the microstructure of the alloy.

A law describing the propagation rate of a crack in effective stage II assisted by hydrogen is proposed by [PET 00a]:

$$da/dN = (B/\sigma_{yH}.E)[\Delta K_{eff}^2 - \Delta K_{eff,th}^2] \quad [11.9]$$

where B is a coefficient without any dimension and σ_{yH} the elasticity limit of the material loaded in hydrogen.

The atmospheric oxygen at room temperature has no role in the effective crack propagation behavior, as shown by Piasick and Gangloff [PIA 91] in the case of a light alloy at room temperature and by Sarrazin-Baudoux *et al.*, on titanium alloys at 300°C [SAR 97].

To conclude, the propagation rate of a stage II crack that is assisted by atmospheric water vapor can be described with the combination of two mechanisms, which means that by adding both adsorption and hydrogen contributions [PET 00a]:

$$da/dN = (A/D_1^*)[\Delta K_{eff}/E]^4 + (B/\sigma_{yH}.E)[\Delta K_{eff}^2 - \Delta K_{eff,th}^2] \quad [11.10]$$

where $\Delta K_{eff,th}$ is the effective value of the propagation threshold (without any closure).

11.3.4. *Cracking path*

Some different characteristics appear in the morphology of the surfaces of a crack when it breaks within an inert environment, such as under a vacuum or within an active environment, such as atmospheric air. For the stage II of the propagation step, which is the most commonly observed one for long cracks, the difference comes mainly from the striations. Indeed, for cracking rates between about 10^{-2} μm and a few μm per cycle, the fracture surfaces in mode I in air are characterized by the presence of ductile striations.

Different models were proposed to explain the formation of ductile streaks [HER 67, LAI 67, PEL 69], as these models do not require any environment effect. Meyn [MEY 68] was the first to observe the absence of striations under a vacuum, showing that the crack grows cycle-by-cycle (see Figure 11.26). The influence of the environment on the relation that connects the striation spacing at crack tip opening

displacement and the microscopic cracking rate *da/dN*, was studied in detail by Lankford and Davidson DAV 81, DAV 83a, DAV 83b, LAN 81, LAN 83] on a 7075-T651 alloy and a MA-87 alloy manufactured from powder metallurgy.

For propagation rates of about 10^{-7} to 10^{-6} m/cycle, the striation spacing in air corresponds to the crack advance every cycle. Under a vacuum, the striations are much less well defined and their spacing is more closely connected to the size of the dislocation cells than to the cycling. Thus it is not in accordance with a cycle-by-cycle progression. The blunting of the crack tip in air is much less important than under a vacuum.

At growth rates lower than 10^{-7} m/cycle, these authors were able to observe step-by step-crack propagation in air as well as under a vacuum. This was associated with a progressive bluntness in relation to accumulated plastic deformation at the crack tip preceding each propagation increment. For a cracking rate of 10^{-9} m/cycle, the number of cycles per striation in air is a few units, whereas under vacuum it becomes higher than 1,000 cycles. A more recent study, performed on austenitic steels by Mc Evily *et al.* [MCE 92], confirmed this effect of the ambient air on bluntness.

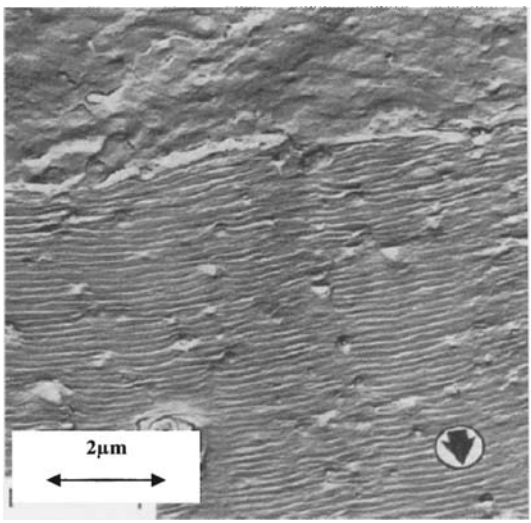

Figure 11.26. *Fracture surface of a 2024T3 alloy tested under a vacuum (top of the figure) and in atmospheric air (bottom). The arrow shows the propagation direction [MEY 68]*

These observations agree with the reduction, within an active environment, of the number of cumulated plastic cyclic deformations required to cause a crack increment. The reduced blunting in air corresponds to a reduced plastic zone size

(see Figure 11.27). This was observed with the following materials: Fe [OHT 72], Al–4%Cu [BOU 76], Fe–3.7Si [GRI 78] and ARMCO iron [GRI 82]. Such a cyclic deformation process in air has been shown to lead to a more premature initiation in Al [BOU 74], Cu [VIO 79], Fe, [ALE 79], Cu–7.5%Al, [SAX 75] and Mg [GRI 78]. Thus the same behavior can explain a premature cracking of the material at the crack tip in air.

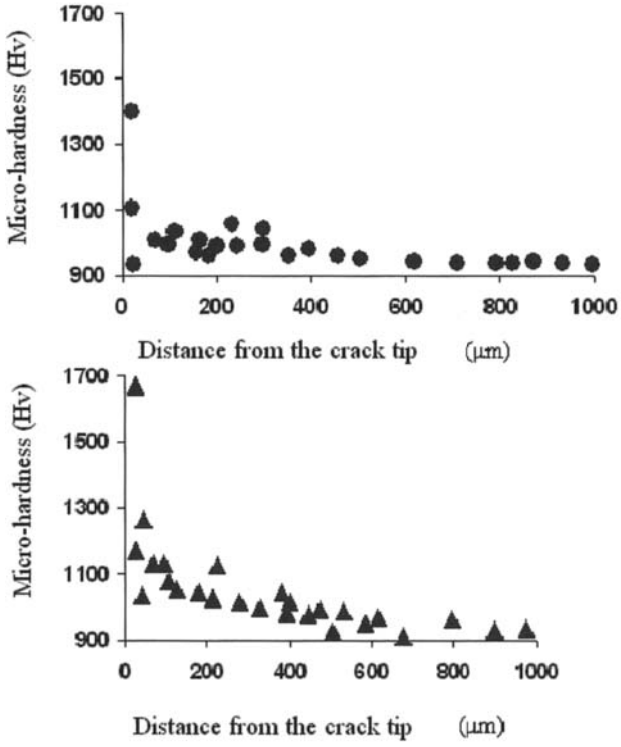

Figure 11.27. *Variation of microhardness within the plastic zone at the crack tip for the same crack length and subjected to the same stress amplitude in air (whole circles) and under a vacuum (triangles) in a light Al-4%Cu alloy [BOU 76]*

Nevertheless, the transcrystalline propagation in air, like under a vacuum, can also occur in stage I or in stage I-like regimes, the propagation mechanism at the grain scale being similar for both stages, as was described earlier. The propagation then occurs according to a crystallographic plane that is well-oriented towards the slip planes of the dislocations.

Figure 11.28a gives the example of the fracture surface of a stage I crack grown under a vacuum in an Al-Zn-Mg single crystal that is actually extremely planar. For some higher strain levels, the traces of dislocation cells appear (Figure 11.28b), showing the local activation of a second slip system and announcing a mechanism change in stage II (see Figure 11.29). The rough striations under vacuum have a spacing that typically corresponds to the size of the dislocation cells. The transition from stage I to stage II occurs as illustrated in Figure 11.17.

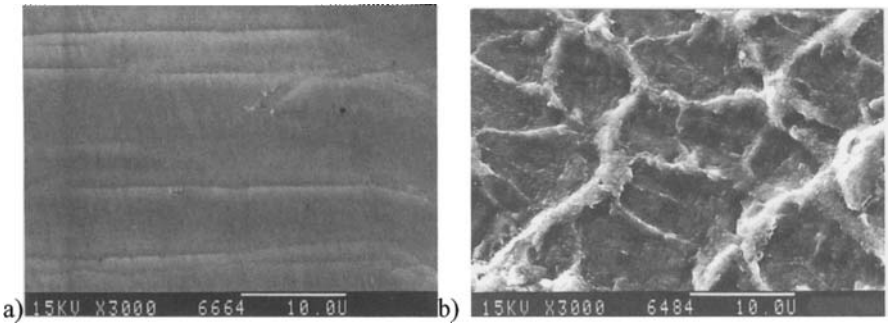

Figure 11.28. *Microfractographies of the surface of a crack grown under a vacuum close to the threshold in a peakaged Al-Zn-Mg single crystal (see crack profile in Figure 11.17): a) stage I (da/dN~ 1.5x10^{-11} m/cycle, ΔK_{eff}~ 0.9 MPa$\sqrt{m}$; b) stage I close to the stage I/ stage II transition after the threshold (da/dN ~ 10^{-8} m/cycle, ΔK_{eff}~ 4.2 MPa$\sqrt{m}$)*

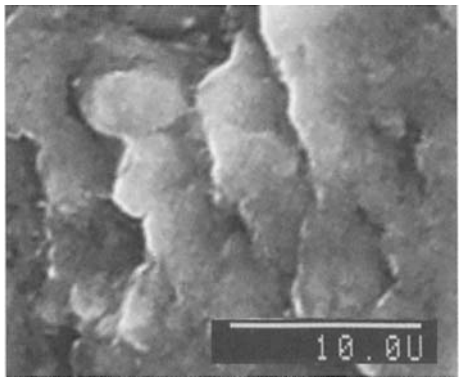

Figure 11.29. *Microfractography of the surface of a stage II crack under vacuum (da/dN ~ 3.10^{-8} m/cycle, ΔK_{eff}~ 6 MPa$\sqrt{m}$) in a peakaged Al-Zn-Mg single crystal (see Figure 11.17)*

Depending on the alloys and their microstructures, vacuum at every temperature or in a dry and cold atmosphere lead strongly to the occurrence of these two crystallographic propagation regimes, especially close to the threshold. The fracture

surfaces of light alloys and titanium alloys strongly depend on the environment. Generally such differences are more difficult to differentiate on the steels.

11.3.5. *Influence of different factors*

11.3.5.1. *Microstructure*

The influence of the microstructure on sensitivity to the environment was initially observed by Wei *et al.* on maraging steels [WEI 67] and Bradshaw and Wheeler [BRA 69] on aluminum alloys. The sensitivity of the crystallographic orientation to the effect of the environment was observed on the cracking of copper single crystals [VIO 79]. The environment (air or vacuum) can lead to a reverse effect on the microstructure, as indicated by Figure 11.30. Alloy 7075, tested in an underaged state (T351) containing shearable GP zones and in an overaged state containing some barely shearable precipitates, shows a better strength in air in the overaged stat. Tthis behavior can be explained by the alloy having a much higher sensitivity to the environment in the underaged state. This agrees with what can be observed for corrosion fatigue. Nevertheless, under a vacuum, the underaged state is much more resistant to cracking than the overaged state; indeed, in this case, localization of the deformation leads to significantly delayed crystallographic propagation compared to the intrinsic regime of stage II of the overaged alloy.

In conclusion, any interpretation of the effect of microstructure on the crack propagation process has to consider the eventual effect of the environment.

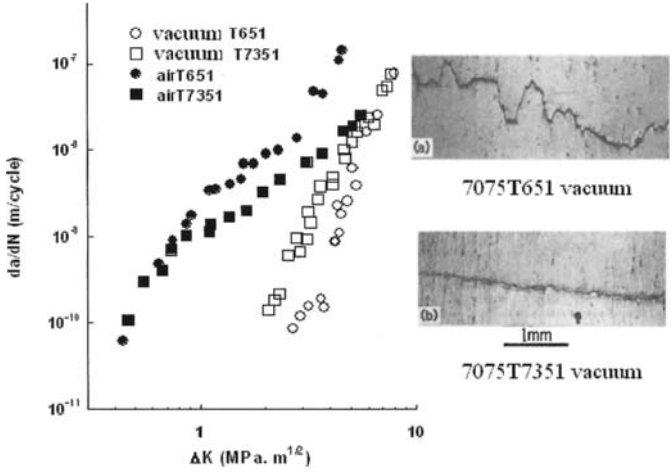

Figure 11.30. *Coupled effects of the environment and microstructure in a 7075 alloy*

11.3.5.2. *Temperature*

The influence of temperature on the action of oxygen, water vapor or hydrogen as a function of the pressure of frequency outside the domains where the corrosion and hot oxidation processes occur, has not been widely studied [SMI 71, STE 72].

However, some quite recent comparative studies on temperature have been carried out on titanium alloys at 300°C and on light alloys at low temperature (-50°C). In both cases, we were able to observe the influence of partial pressure of the water vapor, as the sensitivity to this active species strongly depends on both temperature and microstructure [GAS 06].

The Ti-6Al-4V titanium alloy [SAR 97], which is not that sensitive to the effect of air at room temperature, presents a significant effect at 300°C (see Figure 11.31) within the domain of slow propagation rates. The low effect of the environment on rates higher than 10^{-8} m/cycle comes from a low acceleration induced by the adsorption of water vapor in air compared to the intrinsic stage II under vacuum.

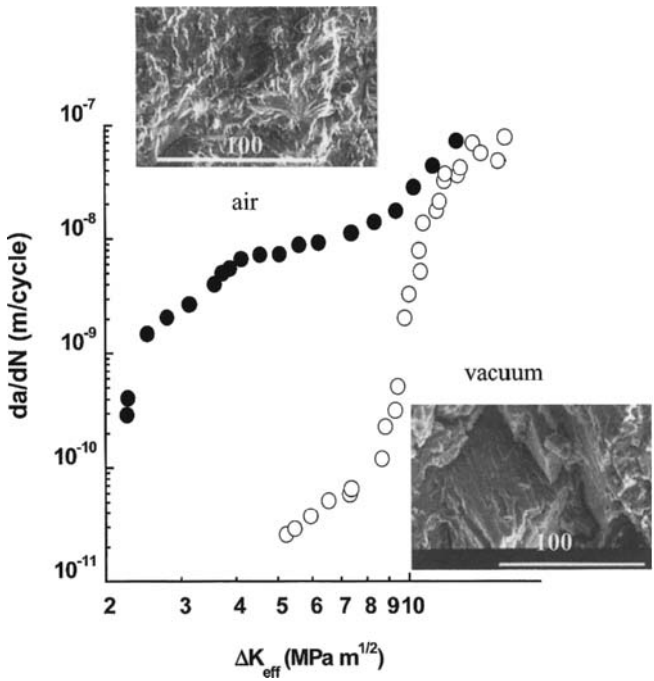

Figure 11.31. *Fatigue crack propagation rate in a Ti-6Al-4V titanium alloy at 300°C: in air, environmentally-assisted stage II; under vacuum, intrinsic stage II at mid-rates and delayed crystallographic stage I-like close to the threshold. Scale is in microns*

For lower rates, the effect of the environment is strongly increased by the combination of environmental and microstructure effects. In air, at 300°C, localization of the deformation within each individual grain leads to a hydrogen-assisted stage II, which accelerates the propagation and decreases the threshold. Under a vacuum, this same localization of deformation reverses the decelerating effect of the propagation as it induces a delayed stage I-like propagation. Thus, for the same stress amplitude, the cracking rate in air can be 500 times faster than under a vacuum. In terms of relative temperature T/T_f (T_f being the melting temperature), a temperature of 300°C for some titanium alloys would correspond to the room temperature for light alloys, which explains the similar behaviors observed (see Figure 11.30 (underaged alloys) and Figure 11.31).

A light Al-Cu-Mg alloy of 2022 T351 type, tested at -50°C – temperature that can be found at high altitude – shows a sudden change of propagation regime between the ambient air and the dry and cold air (see Figure 11.32) for a large range of propagation rates between the threshold and 10^{-6} m/cycle. A crystallographic stage I-like propagation with strongly reduced *da/dN* (about 20-fold), similar to the one under vacuum, prevails in dry and cold air (very low water vapor partial pressure), in opposition to a planar propagation in stage II in ambient air. The transition between the two regimes corresponds to an exposure of 10^{-2} Pa.s^{-1}.

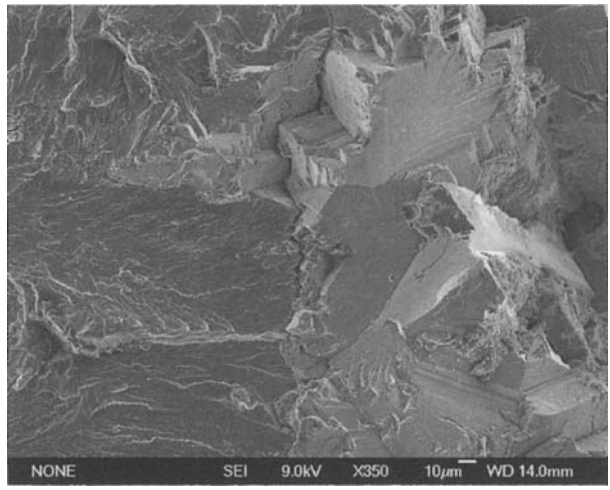

Figure 11.32. *Fracture surface due to fatigue of a 2022 T351 alloy. Left – in ambient air; right – in dry and cold air [GAS 06]*

To conclude, we will mention the low influence of microstructure and temperature on stage II, in contrast with the strong effect of these two factors on the

stress level required for the occurrence of the stage I-like regime and on associated retardation of the growth rate.

11.3.5.3. *Closure*

If plasticity usually controls the closure within Paris' domain, two main factors may control closure near the threshold and the threshold level in itself:

– the roughness of the crack surfaces, connected to the microstructure of the material, the environment, the temperature and also to the frequency to some extent;

– the possible presence of an oxide layer and of the fragment of oxide debris near the crack tip, which also depends on the material, the cracking mode and the environment.

The conjugated action of these two factors, and thus of the various parameters that define them, explains the multiplicity of the behaviors observed, depending on the materials, the stress mechanical conditions and the surrounding environment.

In particular, as seen earlier, an underaged aluminum alloy or a lamellar titanium under a vacuum lead to a pseudo-stage I crack path, with crystallographic surfaces presenting some sharp asperities; the latter can induce a premature closure that lowers the effective amplitude of the applied stress. Consequently, the closure effect is modified when the cracking mechanism induced by the environment changes.

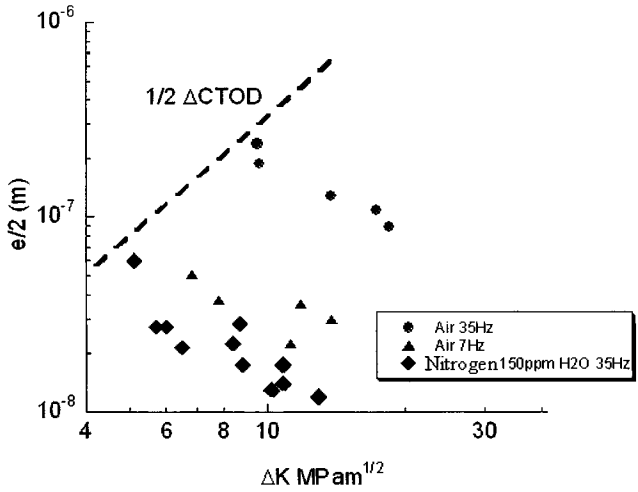

Figure 11.33. *Over-thickness of the oxide layer close to the threshold compared to the ΔCTOD according to the environment and to the frequency in E460 steel [BIG 84]*

In addition, when the lips of a crack come back together during closure can lead to the formation of an oxidized layer built up by tribo-contact. This effect is usually more pronounced when the surfaces are planar (stage II) than when the roughness is high (pseudo-stage I). The sub-layer penetration of the oxygen within an oxygen atmosphere of 10^4 Pa, induced by cracking, was observed on different alloys by Swanson and Marcus as early as 1978 [SWA 78]. The correspondence between this over-thickness and opening at the level of the propagation threshold was clearly shown, especially in the case of an off-shore construction E460 steel [BIG 84], as you can see in Figure 11.33.

The crack propagation curves of this same steel (see Figure 11.34) show a propagation threshold in air higher than the threshold under a vacuum, which is the opposite to what is usually expected. If the closure effect induced by oxidation is removed when operating at R = 0.7 (see Figure 11.35), the results show an acceleration of the propagation in air compared to the one under vacuum, and a lower effective threshold is, as expected, observed in air. The additional effect of closure due to oxidation at low R ratio is compensating for the detrimental effect of the environment. But such compensation vanishes at high R ratio.

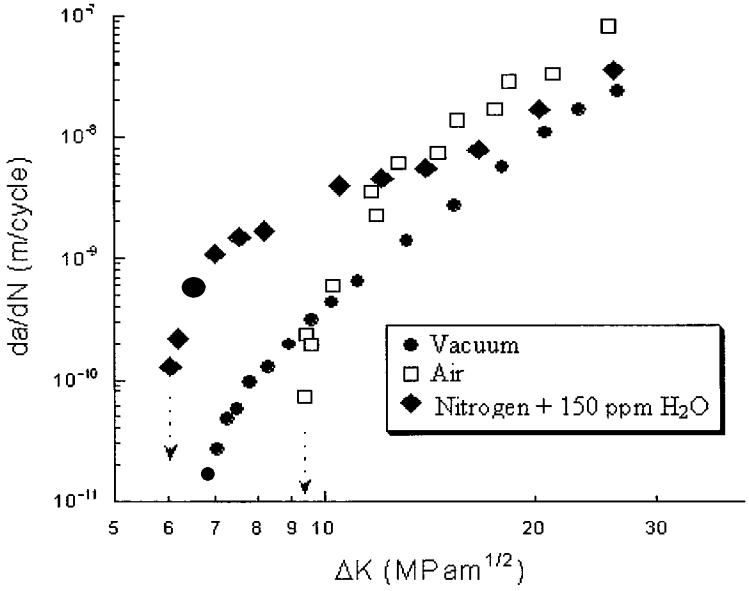

Figure 11.34. *Propagation curves da/dN – ΔK in the case of E460 steel within different environments when R=0.1 and 35 Hz*

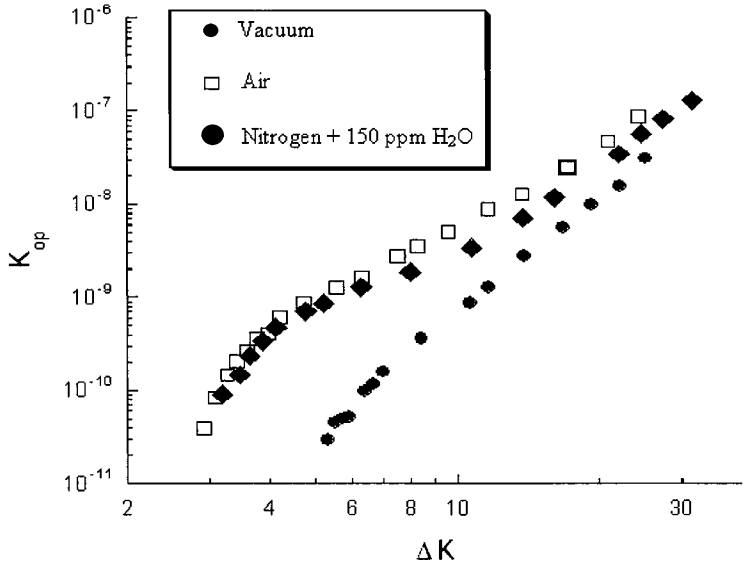

Figure 11.35. *Propagation curves da/dN – ΔK in the case of steel E460 within different environments when R = 0.7 and 35 Hz*

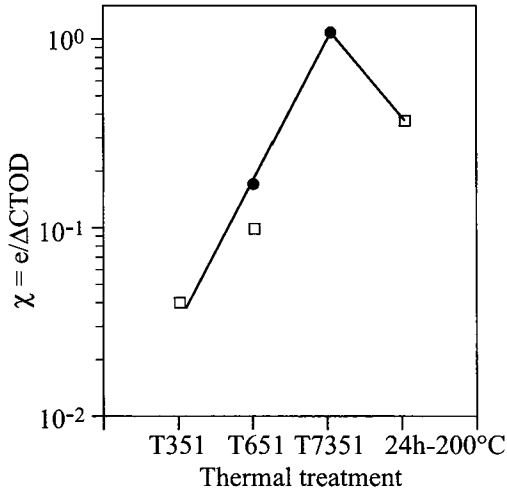

Figure 11.36. *Secondary ion mass spectrometry measurements of the over-thickness ratio $\chi = e/\Delta CTOD$ of the oxidized layer close to the threshold for four microstructural states of a 7075 alloy: underaged-T351, peakaged-T651, overaged-T7351 and highly overaged 24H at 200°C [PET 82, SUR 84]*

On a light 7075 alloy [PET 84], this closure mechanism induced by oxidation was proved to be very sensitive to the microstructural state (see Figure 11.36). The overaged condition, which leads to a planar stage II propagation, favors a substantial thickening. The underaged state, however, leads to a very rough fracture surface presenting an oxide thickening 20 times lower. This closure effect due to oxidation is also enhanced when the temperature is higher, especially on steels.

11.3.5.4. *Short cracks*

The faster propagation of short cracks that occurs for stress intensity factor ranges lower than the long crack threshold may be due to some microstructure influence but can also be related to the absence of closure or to a less important closure of physically short cracks. The few studies on the effect of the atmospheric environment [LAN 83, PET 90, ZEG 86] show that the environment effects both short and long cracks. Nevertheless, the short crack effect is usually less noticeable under a vacuum than in air (see Figure 11.37).

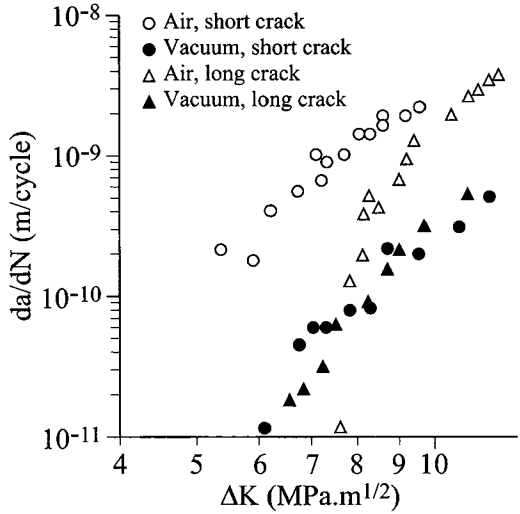

Figure 11.37. *Comparison of the crack propagation rate of short and long cracks in E460 steel in air and under a vacuum [PET 99]*

Figure 11.38 shows the example of the propagation of in-depth physically short cracks (2D cracks) within a steel with a high yield stress of E40 type. As there is almost no short crack effect under a vacuum, the contrast can be observed with the short crack effect in air. This example shows that, within an active environment, the hydrogen-assisted propagation within the domain of low rates comes with a significant decrease in closure to a depth of almost 1 mm, whereas under vacuum,

closure connected to plasticity occurs and rapidly becomes more stable (see Figure 11.38).

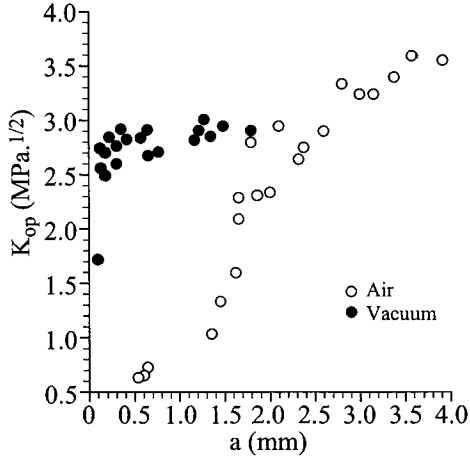

Figure 11.38. *Evolution of the level of the opening stress intensity factor as a function of the depth of a 2D crack in E460 steel [PET 99]*

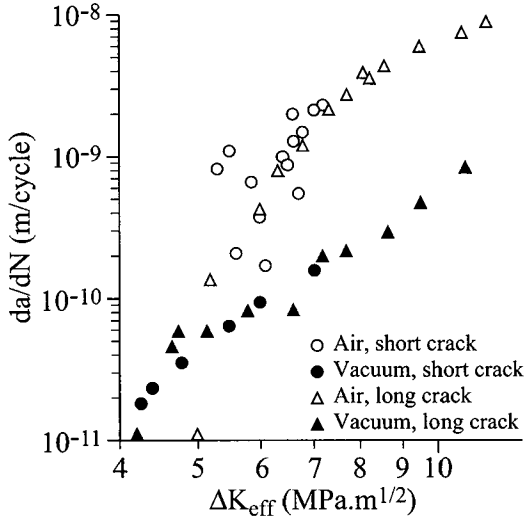

Figure 11.39. *da/dN curves as a function of ΔK_{eff} for 2D cracks in an E460 steel (corresponding to the nominal propagation curves of Figure 11.37 and to closure variations of Figure 11.38) [PET 99]*

After closure correction, the propagation rates of the short and long cracks are described in the same way as a function of ΔK_{eff} (see Figure 11.39).

11.3.5.5. *Fatigue under loading of a variable amplitude*

The fundamental studies were usually developed based on experiments performed with a constant amplitude of uniaxial loading.

Nevertheless, most of the structures that are used by engineers undergo complex changes of variable amplitudes. They can lead to large variations in lifetimes, either by increasing the cracking rate or by decreasing it (in the case of an overloading).

Many studies have been carried out to characterize the factors that influence behavior under fatigue conditions with a uniaxial loading of variable amplitude and loading spectra representing real conditions [GEA 92, SUR 83].

The effects of the atmospheric environment on these types of stress conditions, however, have not really been studied. Nevertheless, the influence of isolated or repeated peaks in stress amplitude was partially studied, showing that the response within an active environment can be very different to the response under vacuum. Buck *et al.* [BUC 76] were the first to observe a more delayed propagation in dry air in a light 7075-T651 alloy. Ranganathan *et al.* [RAN 79, RAN 90] then showed that the number of delay cycles due to a simple overload in a light 2024T3 alloy is 5 to 10 times shorter in air than under a vacuum. This effect is directly connected to a propagation accelerated by the atmospheric air.

The influence of the environment on low-high loadings (a constant amplitude depending on two successive blocks, one of a low height, the other being higher) is actually similar to an increase of the delay under vacuum compared to air on the two same light alloys.

In addition, Koterazawa and Nosho [KOT 92] showed that some intermittent loadings after a significant number of strain cycles of constant amplitude lead to an acceleration whose amplitude is strongly dependent on the environment. The lowest acceleration is observed under a vacuum and the highest one in dry air and under nitrogen containing some traces of humidity. However, in humid air an acceleration lower than that seen in dry air can be explained by the formation of an oxide curve that amplifies the closure effect.

A last example can be given with the study of the propagation of cracks within a high-strength steel under a high loading ratio $R = 0.7$ (see Figure 11.40), simulating the overloadings of the parts of a helicopter rotor in a curve during flight [HEN 92b]. The differences in the delay between air and vacuum as a function of amplitude of stress intensity factor and of number of cycles between loading times,

lead to some propagation curves that can be surprising. But these results can be analyzed in accordance with the effective propagation regimes defined for constant amplitude loading and a variable contribution of crack closure with respect to some residual stresses induced by overloading.

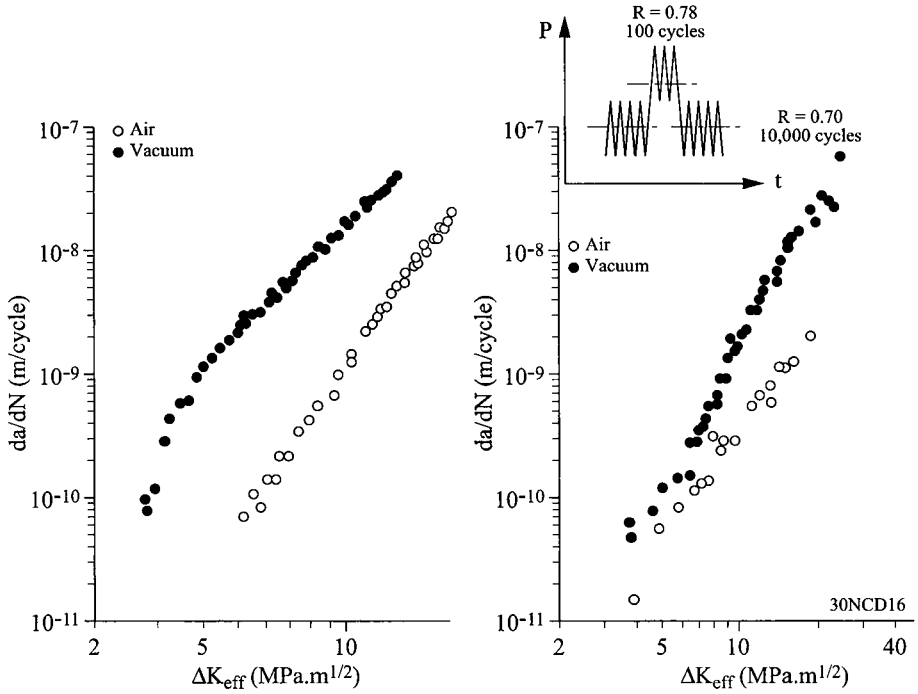

Figure 11.40. *Propagation rate of a fatigue crack in a 30NCD16 steel under constant and variable amplitude loading at R = 0.7 in air and under vacuum: a) constant amplitude loading tests with an environmental effect that is significant effect close to the threshold; and b) variable amplitude loading with a recurring overload every 10,000 cycles (R = 0.78) with an environmental effect that seems to be reduced close to the threshold [PET 03]*

11.3.5.6. *Super-slow propagation of fatigue cracks at 20 KHz*

Resistance to cracking due to the fatigue of some automotive components made of light alloys was recently studied [STA 84] in order to reduce the weight and thus save energy. These components being subjected to very high numbers of cycles (higher than 10^9 cycles), the estimation of their resistance to cracking involves the exploration of the ultra-slow rates domain, lower than 10^{-10} m/cycles, which can be performed with ultrasonic test facilities. In addition, as shown above, the ambient environment is known to modify the behavior of aluminum alloys under fatigue conditions.

Figure 11.41 shows the propagation curves *da/dN* as a function of ΔK obtained at 20 KHz on a 2024-T3 alloy, in air, in dry air, and under a vacuum [HOL 04]. The behavior at a high frequency agrees with that observed in conventional tests. In air, the water vapor pressure is always high enough to saturate the environment assisting the process of cracking, leading to propagation rates much higher than under a vacuum. In dry air, at a high frequency and for cracking rates higher than 10^{-10} m/cycle, the environment does not have an effect on the alloy. This is because the partial pressure of water is low enough and the area of fresh surfaces that is formed at every cycle is big enough for a monoatomic adsorbed layer not to appear.

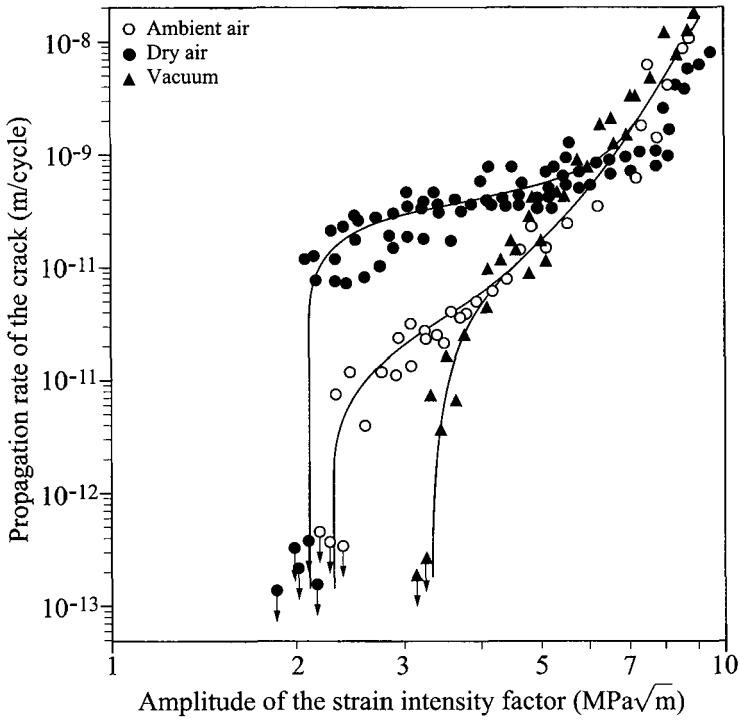

Figure 11.41. *da/dN – ΔK curves for 2024-T351 alloy at 20 KHz [HOL 04]*

Similar results were obtained at 35 Hz [PET 00a], as the transition is then between 10^{-8} and 10^{-7} m/cycle, which agrees with a frequency 570 times lower. For lower rates, the adsorption process of the water vapor becomes active. At the threshold level the conditions required for saturation similar to those occurring in ambient air, are reached. This explains why the thresholds in ambient air and in dry

air are identical. The behavior at a high frequency therefore totally agrees with the model presented above.

Recent studies on a Ti6Al4V titanium alloy [RIT 99] allowed us to compare behavior under cracking conditions in air and under a vacuum at conventional frequencies (35Hz to 50Hz) and at 1 KHz on a specific hydraulic machine. Figure 11.42 presents the results obtained at high frequencies with the R ratio of 0.6 to 0.8; such high R ratios limit the role of both closure and closure corrections for the conventional tests. The analysis of the domain of ultra-slow rates gives some vital information.

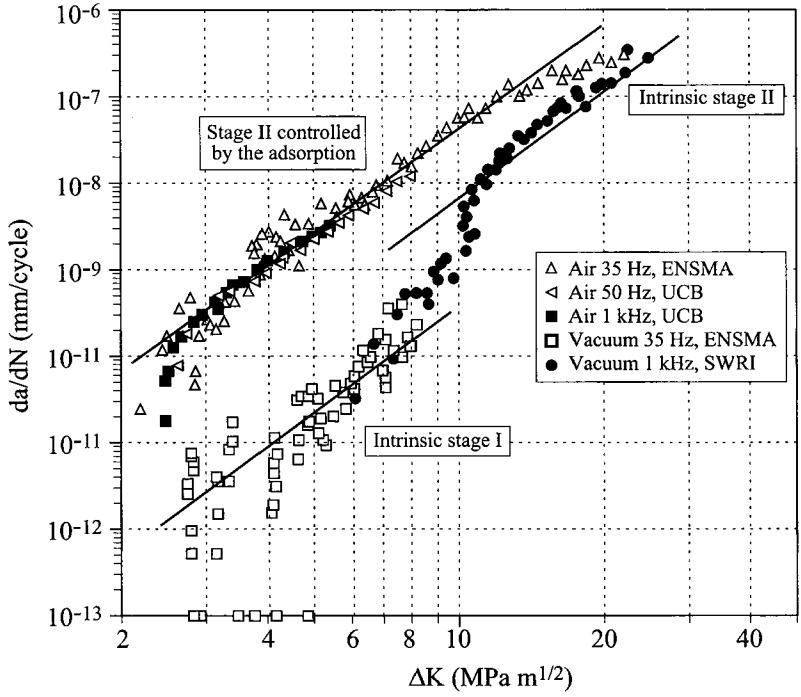

Figure 11.42. *Influence of the ambient air compared to vacuum on the propagation of fatigue cracks within Ti-6Al-4V alloy at conventional frequencies ranging from 35 to 50 Hz, and at a high frequency of about 1KHz. Comparison with the intrinsic regimes in stage II and stage I-like, and the regime of stage II assisted by the adsorption of water vapor [PET 06, RIT 99]*

First of all, for a stress amplitude corresponding to ΔK_{eff} lower than about 10 MPa$\sqrt{m}$ under a vacuum, we can observe a transition from the intrinsic stage II at mid ΔK towards the stage I-like, which prevails within the domain of ultra-slow rates. This transition, already described as being connected to the microstructure of

the alloy for a conventional frequency, actually does not depend on the frequency here. In addition, the effective threshold in air and the intrinsic threshold under vacuum are actually very close when we reach extremely low rates (ΔK_{th} = 2.6 MPa$\sqrt{m}$ in air and 2.7 MPa$\sqrt{m}$ under vacuum).

It can be also proposed that the environment no longer has any effect in air at a really low rate of ΔK, or that it even occurs under a high vacuum.

The question still remains, however. The absence of frequency effect in air shows that the partial pressure of water in ambient air is always high enough to create an adsorbed monolayer, as is the case for the light alloy we described above.

11.4. Conclusion

This chapter focused on the influence of the atmospheric environment on the resistance to fatigue of metals and metallic alloys. It led us to some conclusions and tried to provide a better understanding of mechanisms and of their modeling. The following provides an overview of the points made in this chapter:

– Ambient air is an aggressive environment that leads to substantial loss of fatigue strength, which depending on the materials used, leads to a reduction in lifetimes, an acceleration in the propagation of cracks, and to a decrease in propagation threshold. As a consequence, ambient air cannot be considered in corrosion fatigue as an inert reference medium, which is, however, usually the case.

– The knowledge of the mechanisms, both intrinsic and environmentally assisted, is much more advanced for crack propagation than crack initiation.

– The theoretical models developed since the initial studies of McClintock, Rice and Weertman to describe the progression of fatigue cracks do not usually consider the effects of the environment or the ones induced by closure. As a consequence, they can only be used to describe the intrinsic crack propagation due to fatigue conditions within an inert environment and once the closure has been corrected.

– The intrinsic propagation rate in stage II (mode I of the opening step) is proportional to a specific value of the amplitude of the effective stress intensity factor, being $\Delta K_{eff}/E$ where E is the Young's modulus. This propagation stage is described by a single law for any metal and metallic alloy, including the inter-metallic compounds.

– The concept of inert environment has to be carefully considered, especially within the domain of slow propagation rates and at a low frequency. Indeed, traces of water vapor of a few ppm can become very active close to the fatigue crack propagation threshold. As a consequence, the reference tests within an inert

environment should then be performed under a very high vacuum (lower than 10^{-7} torr), especially in the case of frequencies lower than 1 Hz.

– The detrimental effect of atmospheric water vapor has been widely studied at room temperature and at a moderate temperature within metals and metallic alloys in order to study both the initiation process and crack propagation. This effect does not exclude a possible role of oxygen. The main effect of this last element, which is more or less pronounced depending on the temperature and is often combined with water vapor, consists of the formation of an oxide layer on the fracture surfaces which leads to an additional closure effect, especially when close to the threshold. This mechanism means that cracking usually slows down and the effect of the water vapor tends to decrease. The role of oxygen in the initiation process is quite ambiguous at both room and moderate temperatures. To isolate both the effects of water vapor and oxygen, some adapted tests using ultra-dry gases should be carried out.

– To better understand and describe cracking mechanisms due to environmentally-assisted fatigue, we should improve the experimental databases under controlled environments as a function of temperature and perform some closure measurements regarding cracking.

– The interaction between the microstructure and gaseous environment has to be studied in its entirety in order to better understand and describe the propagation modes, especially the ones other than stage II, which is prevalent in air, but also in order to optimize the materials a function of their use.

– An exploration of the complex interactions occurring in the case of complex loadings (overloadings, spectra, mixed modes) is necessary to evolve towards a better understanding and description of damage due to fatigue of real structures within their environment.

– Modeling behavior under fatigue, whether assisted by the environment or not, demands a strong research effort in order to develop to practical digital models. Modeling needs the introduction of new tools, such as the cohesive zone models, that rely on the basic principles of fracture mechanics.

11.5. Bibliography

[ACH 68] M.F. Achter, "The adsorption model for environmental effects in fatigue crack propagation", *Scripta Met*, vol. 2, p. 525-527, 1968.

[ALA 97] R. Alain, P. Violan, J. Mendez, "Low cycle fatigue behavior in vacuum of a 316L type austenitic stainless steel between 20 and 600°C. Part I: Fatigue resistance and cyclic behavior", *Mat Sci Eng A*, vol. 229, no. 1-2, p. 87-94, 1997.

[BAI 84] J.P. Bailon, M. Elboujdaini, J.I. Dickson, "Environmental effects on delta K in 70-30 alpha brass and 2024 T351 Al alloy", in D.L. Davidson, S. Suresh (eds.), *Proceedings of Fatigue Crack Growth Threshold Concepts,* Philadelphia, Metallurgical Society of AIME, p. 63-82, 1984.

[BAT 01] C. Bathias, "Designing components against gigacycle fatigue", in S. Stanzl-Tschengg, H. Mayer (eds.), *Fatigue in the Very High Cycle Regime*, Universität für Bodenkultur Wien Pub., p. 97-110, 2001.

[BEE 70] C.J. Beevers, "Some aspects of fatigue crack growth in metals and alloys", in D.M.R. Taplin (ed.), *Fracture 1977*, Waterloo, Canada, University of Waterloo Press, vol. 1, p. 239-260, 1977.

[BEN 64] J.A. Bennet, "Changes in the influence of atmospheric humidity during fatigue of an aluminum alloy", *J. Res.NBS, C. Eng. Instrum.*, vol. 68C, p. 91-100, 1964.

[BIG 84] A. Bignonnet, D. Loison, N. Namdar Irani, B. Bouchet, J.H. Kwon, J. Petit, " Environmental and frequency effects on near-thresholds fatigue crack propagationin a structural steel", in D.L. Davidson, S. Suresh (eds.), *Proceedings of Fatigue Crack Growth Threshold Concepts,* Philadelphia, PA, p. 99-113, 1984.

[BIG 90] A. Bignonnet, S. Petit, A. Zeghloul, "The influence of environment on fatigue crack growth mechanisms", in P. Scott (ed.), *Environment-assisted \fatigue, EGF7*, Mechanical Engineering Pub., London, p. 205-222, 1990.

[BOU 75] B. Bouchet, J. De Fouquet, M. Aguillon, "Influence de l'environnement sur les faciès de rupture par fatigue d'éprouvettes monocristallines et polycristallines d'alliage Al-Cu 4%", *Acta Metal*, vol. 23, p.1325-1336, 1975.

[BOU 76] B. Bouchet, J. De Fouquet "Relation entre l'étendue de la zone plastique et la propagation des fissures de fatigue: influence de l'environnement", *Proceedings of the 4th International Conference on the Strength of Metals and Alloys*, Nancy, France, p. 485-489, 1976.

[BOW 83] C. Bowles, J. Schijve, "Crack tip geometry for fatigue crack grown in air and vacuum", in J. Lankford, D. Davidson, W. Morris, R. Wei (eds.), *Fatigue Mechanisms: Advances in Quantitative Measurements of Physical Damage, ASTM STP 811*, p. 400-426, 1983.

[BRA 66] F.J. Bradshaw, C. Wheeler, " The effect of environment on fatigue crack growth in aluminum and some aluminum alloys", *Applied Materials Research*, vol. 5, p. 112, 1966.

[BRA 67] F.J. Bradshaw, "The effect of gaseous environment on fatigue crack propagation", *Scripta Met*, vol. 1, p. 41-43, 1967.

[BRA 83] R. Brazill, G.W. Simmons, R.P. Wei, "Fatigue crack growth in 2-1/4Cr-1Mo steel exposed to hydrogen containing gases", *J Eng Mat Technol*, vol. 101, no. 3, p. 199-204, 1979.

[BRO 60] T. Broon, A. Nicholson, "Atmospheric corrosion-fatigue of age-hardened aluminum alloys", *J Inst Met*, vol. 89, p. 183-190, 1960.

[BRO 71] D. Broeck, A, Hartman, A, Nederveen, *Electron Fractography of Fatigue in Vaccum, NLR Report TR 71032 U,* NLR, p. 543-622, 1971.

[BUC 76] O. Buck, J.D. Frandsen, H.L. Marcus, "Spike overload and humidity effects on fatigue crack delay in A1 7075-T651", *Fatigue Crack Growth Under Spectrum Loading, ASTM STP 595*, p. 101-112, 1976.

[CLI 63] F. A. Mc Clintok, "On the plasticity of the growth of fatigue cracks", *Fracture of Solids*, vol. 20, Metall. Soc. Conf., Interscience Publishing, p. 65, 1963.

[COF 72] L.F.J Coffin, "The effect of high vacuum on the low cycle fatigue law", *Metall Trans*, vol. 3, p. 1777-1788, July 1972.

[DAH 65] E.P. Dahlberg, "Fatigue crack propagation in high strength 4340 steel in humid air", *Trans. ASM.*, vol. 58, p. 46-53, 1965.

[DAV 81] D.L. Davidson, J. Lankford, "The effect of water vapor on fatigue crack tip stress and strain range and the energy required for crack propagation in low-carbon steel", *Int J Fract*, vol. 17, no. 3, p. 257-275, 1981.

[DAV 83] D.L. Davidson, J. Lankford, "The effect of water vapor on fatigue crack tip mechanisms in 7075-T651 aluminum alloy", *Fatigue Eng Mater Struct*, vol. 6, p. 241-256, 1983.

[DAV 84a] D.L. Davidson, J. Lankford, "Fatigue crack growth mechanics for Ti-6Al-4V (RA) in vacuum and humid air", *Metal Trans*, vol. 15A, p. 1931-1940, 1984.

[DAV 84b] D.L. Davidson, J. Lankford, "Fatigue crack tip mechanics of a powder metallurgy aluminum alloy in vacuum and humid air", *Fatigue Eng Mater Struct*, vol. 7, no. 1, p. 29-39, 1984.

[DUQ 71] D.J. Duqette, M. Gell, "The effect of environment on the mechanism of stage I : fatigue fracture", *Metal. Trans.*, vol. 2, p. 1325-1331, 1971.

[DUQ 72] D.J. Duqette, M. Gell, "The effects of environment on the elevated temperature fatigue behavior of nickel-base superalloy single crystals", *Metal Trans*, vol. 3, p. 1899-1905, 1972.

[DUQ 78] D.J. Duqette, *Fatigue and Microstructure*, American Society for Metals, p. 335-363, 1978.

[ENG 68] W. Engelmaier, "Fatigue behavior and crack propagation in 2024-T3 aluminum alloy in ultra high vacuum and air", *Trans AIME*, vol. 242, p. 1713-1718, .

[EVA 71] P.R. Evans, N.B. Owen, B.E. Hopkins, "The effect of purity on fatigue crack growth in a high strength steel", *Eng Fract Mech*, vol. 3, p. 463-473, 1971.

[FOE 93] R. Foerch, A. Madsen, H. Ghonem, "Environmental interactions in high temperature fatigue crack growth of Ti-1100", *Metal Trans*, vol. 24A, p. 1321-1332, 1993.

[FOU 71] D. Fournier, Etude de la nature et de la repartition des faciés de rupture par fatigue dans un alliage léger type AU4, PhD Thesis, University of Poitiers, 1971.

[FRA 75] J.D. Frandsen, H.L. Marcus, "The correlation between grain size and plastic zone size for environmental assisted fatigue crack propagation", *Scripta Met*, vol. l, no. 9, p. 1089-1094, 1975.

[FRA 77] J.D. Frandsen, H.L. Marcus, "Environmentally assisted fatigue crack-propagation in steel", *Metal Trans*, vol. 8A, p. 265-272, 1977.

[GAS 06] C. Gasqueres, Fissuration par fatigue et ténacité d'alliages d'aluminum 2xxx à 223K, PhD Thesis, University of Poitiers, 2006.

[GEA 92] W. Geary, "A review of some aspects of fatigue crack growth under variable amplitude loading", *Int J Fatigue*, vol. 14, no. 6, p. 377-386, 1992.

[GER 86] M. Gerland, P. Violan, "Secondary cyclic hardening and dislocation structures in type 316 stainless steel at 600°C", *Mat Sci Eng*, vol. 84, p. 23-33, 1986.

[GHO 91] H. Ghonem, R. Foerch, "Frequency effects on fatigue crack growth behavior in a near-αtitanium alloy", *Mat Sci Eng*, vol. A138, p. 69-81, 1991.

[GOU 32] H.J. Gough, D.G. Sopwith, "Atmospheric action as a factor in fatigue of metals", *J Inst Metals*, vol. 49, p. 93-122, 1932.

[GOU 35] H.J. Gough, D.G. Sopwith, "Some further experiments on atmospheric action in fatigue", *J Inst Metals*, vol. 56, p. 55-89, 1935.

[GOU 46] H.J. Gough, D.G. Sopwith, "Inert atmospheres as fatigue environments", *J Inst Metals*, vol. 72, p. 415-421, 1946.

[GRI 73] N.M. Grinberg, A.I. Alekseyev, V.A. Taurikov, "Mechanisms by which vacuum affects the fatigue failure of copper and iron", *Trans. Fizico-Khimicheskaya Mekhanika Materialov*, vol. 9, p. 687-690, 1973.

[GRI 82] N.M. Grinberg, "The effect of vacuum on fatigue crack growth", *Int J Fatigue*, vol. 4, p. 83-95, 1982.

[GRO 66] J.C. Grosskreutz, C.Q. Bowles, "The effect of oxide films on dislocation surface interaction in aluminum", in A.R.C. Westwood, N.S. Stoloff (eds.), Gordon *Environment-sensitive Mechanical Behaviour*, Gordon & Breach, p. 67-105, 1966.

[HAB 93] K. Haberz, R. Pippan, H.P. Pippan, in J.P. Bailon, J.I. Dickson (eds *Proceedings of Fatigue'93*, Montreal, Canada.), EMAS, vol. I, p. 525-530, 1993.

[HAR 65] A. Hartman, "On the effect of oxygen and water vapor on the propagation of fatigue crack in 2024-T3 Alclad shee", *Int J Fract Mech*, vol. 1, p. 167-188, 1965.

[HEN 92a] G. Henaff, J. Pettit, B. Bouchet, "Environmental influence on the near-threshold fatigue crack propagation behaviour of a high-strength steel", *Int J Fatigue*, vol. 14, no. 4, p. 211-218, 1992.

[HEN 92b] G. Henaff, J. Pettit, B. Bouchet, "Fatigue crack propagation behaviour under variable amplitude loading in the near-threshold region of a high-strength low-alloy steel", *Fatigue Fract Eng Mater Struct*, vol. 15, no. 11, p. 1155-1170, 1992.

[HEN 95] G. Henaff, K. Marchal, J. Petit, "On fatigue crack propagation enhancement by a gazeous atmosphere: experimental and theoretical aspects", *Acta Met Mater*, vol. 43, p. 2931-2942, 1995.

[HER 67] R.W. Hertzberg, "Fatigue fracture surface appearance", *Fatigue Crack Propagation, ASTM-STP 415*, p. 205-225, 1967.

[HOL 04] B. Holper, H. Mayer, A.K. Vasudevan, S.E. Stanzl-Tschegg, "Near threshold fatigue crack growth at positive load ratio in aluminum alloys at low and ultrasonic frequency: influences of strain rate, slip behaviour and air humidity", *Int J Fatigue,* vol. 26, p. 27-38, 2004.

[HOR 66] M.J. Hordon, "Fatigue behavior of aluminum in vacuum", *Acta Metal*, vol. 14, p. 1173-1178, 1966.

[HUN 88] A. Hunsche, P. Neumann, "Crack nucleation in persistent slip bands", in R.P. Wei, R.P. Gangloff (eds.), *Basic Questions in Fatigue, ASTM STP 924*, Philadelphia, 26-38, 1988.

[IRV 74] P.E. Irving, C.J. Beebers, "The effect of air and vacuum environments on fatigue crack growth rates in Ti-6Al-4V", *Metal Trans*, vol. 5, p. 391-398, 1974.

[IRV 78] P.E. Irving, C.J. Beebers, "Measurements of intergranular failure produced during fatigue crack growth in quenched and tempered steels", *Metal Science*, vol. 12, p. 495-502, 1978.

[ISH 69] H. Ishii, J. Weertman, "The effect of air pressure on the rate of fatigue crack growth", *Scripta Met*, vol. 3, p. 229-232, 1969.

[JAC 67] JACISIN J.M., "Fatigue of an aluminum alloy in ultrahigh vacuum", *Trans AIME*, vol. 242, p. 821-823, 1967.

[JAM 99] M.N. James; L. Wenfong; "Fatigue crack growth in austempered ductile and grey cast irons-stress ratio effects in air and mine water", *Mater Sci Eng A*, vol. 265, no. 1-2, p. 129-139, 1999.

[KEN 88] J.M. Kendall, J.F. Knott, "Near threshold fatigue crack growth in air and vacuum", in R.P. Wei, R.P. Gangloff (eds.), *Basic Questions in Fatigue: Volume II, ASTM STP 924*, PA, p. 103-114, 1988.

[KIN 82a] J.E. King; "Surface damage and near-threshold fatigue crack growth in a Ni-base superalloy in vacuum", *Fat Eng Mater Struc*, vol. 5, no. 2, p. 177-188, 1982.

[KIR 79] B.R. Kirby, C.J. Beevers, "Slow fatigue crack growth and threshold behaviour in air and vacuum commercial aluminum alloys", *Fat Eng Mater Struct*, vol. 1, p. 203-215, 1979.

[KOT 92] R. Koterazawa, T. Nosho, "Acceleration of crack growth under intermittent overstressing in different environments", *Fat Fract Eng Mater Struct*, vol. 15, no. 1, p. 103-113, 1992.

[LAI 63] C. Laird, G.C. Smith, "Initial stages of damage in high stress fatigue of some pure metals", *Phil Mag*, vol. 8, p. 1945-1963, 1963.

[LAI 67] C. Laird, "The influence of metallurgical structure on the mechanisms fo fatigue crack propagation", *Fatigue Crack Propagation, ASTM STP 415*, p. 131-180, 1967.

[LAN 83] J. Lankford, D.L. Davidson, " Fatigue atigue crack micromechanisms in ingot and powder metallurgy 7xxx aluminum alloys in air and vacuum", *Acta Metall*, vol. 31, no. 8, p. 1273-1284, 1983.

[LAN 83] J. Lankford, "The effect of environment on the growth of small fatigue cracks", *Fat. Eng Mater Struct*, vol. 6, p. 15-31, 1983.

[LIA 82] P.K. Liaw, S.J. Hudak, J.K Donald, "Influence of gaseous environments on rates of near-threshold fatigue crack propagation in NiCrMoV steels", *Metall Trans*, vol. 13A, p. 1633-1645, 1982.

[LIA 83] P.K. Liaw, S.J. Hudak, J.K Donald, "Near-threshold fatigue crack growth investigation of Ni-Mo-V steel in hydrogen environment", in J.C. Lewis, G. Sines (eds.), *Proceedings of Fracture Mechanics: Fourteenth Symposium-Volume II: Testing and Applications, ASTM STP 791*, p. II.370-II.388, 1983.

[LIA 89] F.L. Liang, C. Laird, "The effect of environment on the mechanism of fatigue crack initiation and propagation in polycrystalline copper", *Maters Sci Eng A*, vol.117, p. 83-93, 1989.

[LIN 79] J. Lindigkett, G. Terlinde, A. Gysler, G. Lutjering, "The effects of grain size on the fatigue crack propagation behavior of age-hardened alloys in inert and corrosive environment", *Acta Met*, vol. 27, no. 11, p. 1717-1726, 1979.

[LIN 81] T.C. Lindley, "In subcritical crack growth due to fatigue, stress corrosion and creep", in L.H. Larsson (ed.), *Fatigue Threshold*, Elsevier, p. 167-213, 1981.

[MAR 68] D.E Martin, "Plastic strain fatigue in air and vacuum", *J Basic Eng*, vol. 87, p. 850-856, 1965.

[McC 63] F.A. Mc Clinctock, *Proceedings of Fracture of Solids*, Mapple Valley, p. 65-102, 1963.

[McE 88] A.J. Mc Evily, W. Zagrany, J. Gonzalez, S. Matsuoka, "Fatigue crack growth in type 304 stainless steels", in P. Lukas, J. Polak (eds.), *Basic Mechanisms of Fatigue of Metals*, Elsevier, p. 271-279, 1988.

[McE 92] A.J. Mc Evily, J. Gonzalez, J.L. Velazquez, "Fatigue crack tip deformation processes as influenced by the environment", *Metal Trans*, vol. 23A, p. 2211-2221, 1992.

[MEN 02] J. Mendez, S. Mailly, P. Villechaise, "Temperature and environmental effects on fatigue resistance of titanium alloys", in L. Rémy, J. Petit (eds.), *Temperature-fatigue Interactions*, ESIS pub 29, Elsevier, p. 95-102, 2002.

[MEN 88] J. Mendez, P. Violan, "Modifications in fatigue damage processes induced by atmospheric environment in polycristalline copper", *Basic Questions in Fatigue, ASTM STP 924*, vol. 2, p. 196-210, 1988.

[MEN 96] J. Mendez, X. Demulsant, "Influence of environment on low cycle fatigue damage in Ti-6Al-4V and Ti 6246 titanium alloys", *Mater Sci Eng A*, vol. 219, no. 1-2, p. 202-211, 1996.

[MEN 99] J. Mendez, "On the effects of temperature and environment on fatigue damage processes in Ti alloys and in stainless steel", *Mater Sci Eng A*, vol. 263, no. 2, p. 187-192, 1999.

[MEY 68] D.A. Meyn, "The nature of fatigue crack propagation in air and vaccum for 2024 aluminum", *Trans ASM*, vol. 61, no. 1, p. 52-61, 1968.

[MEY 76] D.A. Meyn, "Effects of very low pressure on fatigue fracture surface features in Ti-6AL-4V", *ASTM STP 600*, p. 75-87, 1976.

[MUR 01] Y. Murakami, "Mechanism of fatigue failure in ultralong life regime", in S. Stanzl-Tschengg, H. Mayer (eds.), *Fatigue in the Very High Cycle Regime*, Universität für Bodenkultur Wien Pub., p. 11-22, 2001.

[NAK 01] M. Nakajima, K. Tokaji, H. Itoga, H.N. Ko, "Effect of work-hardened layer and humidity on step-wise S-N curve in ahigh strengh steel", in S. Stanzl-Tschengg, H. Mayer (eds.), *Fatigue in the Very High Cycle Regime*, Universität für Bodenkultur Wien Pub., p. 181-188, 2001.

[OHT 72] A. Otha, E. Sasaki, "Plastic zone around fatigue cracks of pure iron in vacuum and dry air", *Acta Met*, vol. 20, p. 657-660, 1972.

[PEL 69] R.M.N. Pelloux, "Mechanism of formation of ductile fatigue striations", *Trans. Quaterly ASM*, 62, 281-285, 1969.

[PEL 70] R.M.N. Pelloux, "Crack extension by alternating shear", *Eng Fract Mech*, vol. 1, p. 697-700, 1970.

[PET 00a] J. Petit, G. Henaff, C. Sarrazin-Baudoux, "Mechanisms and modeling of near-threshold fatigue crack propagation", in J.C. Newman, R.S. Piascik (eds.), *Fatigue Crack Growth Threshold, Endurance Limits and Design, ASTM STP 1372*, p. 3-30, 2000.

[PET 00b] J. Petit, G. Henaff, C. Sarrazin-Baudoux, "Fatigue cracking and atmospheric environment", *Journal de Physique IV*, vol.10, P4, p. 203-212, 2000.

[PET 03] J. Petit, G. Henaff, C. Sarrazin-Baudoux, "Environmentally assisted fatigue in gaseous atmosphere", in J. Petit, P. Scott (eds.), *Comprehensive Structural Integrity*, vol. 6 Environmentally-Assisted Rupture, Elsevier, p. 211-280, 2003.

[PET 06] J. Petit, C. Sarrazin-Baudoux, "An overview on the influence of the atmosphere environment on ultra-high-cycle fatigue and ultra-slow fatigue crack propagation", *Int J Fatigue*, vol. 28, p. 1471-1478, 2006.

[PET 84a] J. Petit, "Some aspects of near-threshold crack growth : microstructural and environmental effects", in D.L. Davidson, S. Suresh (eds.), *Fatigue Crack Growth Threshold Concepts*, Philadelphia, PA, Metallurgical Society of AIME, p. 3-24, 1984.

[PET 89] J. Petit, A. Zeghloul, "Influence de l'environnement et de la microstructure sur la propagationdes fissures de fatigue", *Revue Phys Appl*, vol. 24, p. 905-913, 1989.

[PET 90] J. Petit, A. Zeghloul, "Environmental and microstructural influence on fatigue propagation of small surface cracks", *ASTM STP 1049*, p. 334-346, 1990.

[PET 91] J. Petit, G. Henaff, "Stage II intrinsic fracture crack propagation", *Scripta Metall Mater*, vol. 25, p. 2628-2687, 1991.

[PET 92] J. Petit, D. Bertheau, "Fatigue crack propagation in Al-SiC metallic matrix composites", in C. Bathias (ed.), *Proceedings of Mechanical properties and applications of MMC*, Elsevier, vol. 1, p. 93-101, 1992.

[PET 92] J. Petit, N. Ranganathan, "Fatigue crack propagation at low rate and near threshold in Al-Li alloys", in M. Peters, P.J. Winkler (eds.), *Aluminum-Lithium*, DGM pub., vol. 1, p. 521-532, 1992.

[PET 93] J. Petit, G. Henaff, "A survey of near threshold fatigue crack propagation : mechanisms and modelling", in J.P. Baïlon, J.I. Dickson (eds.), *Fatigue 93*, Montreal, CA, EMAS, p. 503-512, 1993.

[PET 99] J. Petit, "Influence of environment on small fatigue crack growth", in K.S. Ravichandran, R.O. Ritchie, Y. Murakami (eds.), *Small Fatigue Cracks*, Elsevier, p. 167-178, 1999.

[PIA 91a] R.S. Piascik, R.P. Gangloff, "Environmental fatigue of an Al-Li-Cu alloy: Part I - Intrinsic crack propagation kinetics in hydrogeneous environments", *Met Transact*, vol. 22A, p. 2415-2428, 1991.

[PIA 91b] R.S. Piascik, R.P. Gangloff, "Environmental fatigue on Al-Li alloy - Part II-Microscopic hydrogen cracking processes", *Metall Mater Trans* A, vol. 24A, p. 2751-2762, 1991.

[PIP 91] R. Pippan, "Threshold and effective threshold of fatigue crack propagation in ARMCO iron II: the influence of environment", *Mater Sci Eng A*, vol. 138, p. 15-22, 1991.

[RAN 79] N. Ranganathan, J. Petit, B. Bouchet, "A contribution to the study of fatigue crack retardation in vacuum", *Eng Fract Mech*, vol. 11, p. 775-789, 1979.

[RAN 90] N. Ranganathan, M. Quintard, J. Petit, J. De Fouquet, "Overload effect in aluminum alloys; influence of plasticity and environment", in W.B. Lisagor, T. W. Crooker, B. N. Lais (eds.), *Environmentally-assisted Cracking: Science and Engineering, ASTM STP 811*, p. 374-390, 1990.

[RAN 95] N. Ranganathan, F. Adiwijayanto, J. Petit, J.P. Bailon, "Fatigue crack propagation mechanisms in an aluminum lithium alloy", *Acta Metall Mater*, vol. 43, no. 3, p. 1029-1035, 1995.

[RAN 96] N. Ranganathan, S.Q. Li, J.P. Bailon, J. Petit, "On micromechanisms of fatigue crack growth in the 8090 T651 aluminum-lithium alloy", *Int J Fatigue*, vol. 18, no. 1, p. 62, 1996.

[RIC 65] J.P. Rice, "Plastic yielding at a crack tip", in: T. Yokobori (ed.), *Proceedings of the 1st International Conference on Fracture*, Sendai, Japan, 1965.

[RIC 78] R.J. Richards, S. Purushothaman, J.K. Tien, J.D. Frandsen, O. Buck, "Kinetics of environmental fatigue crack growth in a nickel-copper alloy: part II. In hydrogen", *Metall Trans*, vol. 9A, p. 1107-1111, 1978.

[RIT 75] R.O. Ritchie, Contribution on "Slow fatigue crack growth and threshold behaviour of a medium carbon steel in air and in vacuum", *Eng Fract Mech*, vol. 7, p. 187-189, 1975.

[RIT 79] R.O. Ritchie, "Near-threshold fatigue crack growth in steels", *Int Met Rev*, vol. 5-6, p. 205-230, 1979.

[RIT 80] R.O. Ritchie, S. Suresh, C.M. Moss, "Near-threshold fatigue crack growth in 21/4Cr-1Mo pressure vessel steel in air and hydrogen", *J Eng Mat Tech*, vol. 102, p. 293-299, 1980.

[RIT 99] R.O. Ritchie, D.L. Davidson, B.L. Boyce, J.P. Campbell, O. Roder, "High-cycle fatigue of Ti-6Al-4V", *Fatigue Fract Eng Mater Struct*, vol. 22, p. 621-631, 1999.

[RUI 97a] J. Ruiz, M. Elices, "Effect of water vapour pressure and frequency on fatigue behaviour in 7017-T651 aluminum alloy plate", *Acta Mater*, vol. 45, no. 1, p. 281-293, 1997.

[RUI 97b] J. Ruiz, M. Elices, "The role of environmental exposure in the fatigue behaviour of an aluminum alloy", *Corrosion Sci*, vol. 39, no. 12, p. 2117-2141, 1997.

[SAR 97] C. Sarrazin-Baudoux, S. Lesterlin, J. Petit, "Atmospheric influence on fatigue crack propagation in titanium alloys at elevated temperature", *ASTM STP 1297*, p. 117-139, 1997.

[SAR 97a] C. Sarrazin, S. Lesterlin, J. Petit, *Proceedings of Elevated temperature effects on fatigue and fracture, ASTM STP 1297*, p. 1249-1254, 1997.

[SAR 97b] C. Sarrazin, S. Lesterlin, J. Petit, "Environment dependence on fatigue crack growth at 500°C in a Ti6246 alloy", in T. Magnin (ed.), *Corrosion-deformation Interactions*, CDI 96, The institute of materials, London, p. 361-370, 1997.

[SAR 99] C. Sarrazin-Baudoux, Y. Chabanne, J. Petit, "Influence of environment and of mean stress on fatigue crack growth at near threshold stress intensities on a Ti6246 alloy at room temperature and 500 degrees C", *Scripta Mater*, vol. 40, no. 4, p. 451-457, 1999.

[SAX 75] A. Saxena, S.D. Antolovich, "Low cycle fatigue, fatigue crack propagation and substrructures in a series of polycristalline Cu-Al alloys", *Metall Trans*, vol. 6a, p. 1809-1828, 1975.

[SCH 68] T.R. Schives, J.A. Bennett, "The Effect of environment on the fatigue properties of selected engineering alloys", *J Materials*, vol. 3, p. 695-715, 1968.

[SHE 66] H. Shen, S.E. Podlaseck, I.R. Kramer, "Effect of vacuum on the fatigue life of aluminum", *Acta Met*, vol. 14, p. 341-346, 1966.

[SMI 71] H.H. Smith, P. Shahinian, "Environmental effects on fatigue crack growth rates in silver", *J Inst Met*, vol. 99, p. 243-247, 1971.

[SMI 87] P. Smith, "The effects of moisture on the fatigue crack growth behaviour of a low alloy steel near threshold", *Fatigue Fract Eng Mater Struct*, vol. 10, no. 4, p. 291-304, 1987.

[SNO 64] K.U. Snowden, "The effect of atmosphere on the fatigue of lead", *Acta Metall*, vol. 12, p. 295-303, 1964.

[SRI 92] T.S. Sriram, M.E. Fine, Y.W. Chung, "The application of surface science to fatigue: the role of surface chemistry and surface modification in fatigue crack initiation in silver single crystals", *Acta Metall Mater*, vol. 40, p. 2769-2780, 1992.

[STA 01] S. Stangl-Tschegg, H. Mayer, "Fatigue in the very high cycle regime", *Proc VHCF-2*, Vienne, Autriche, University of Agriculture Science Press, p. 300-303, 2001.

[STA 84] E.A. Starke, F.S. Fin, R.T. Chen, H.C. Heikkenen, "The use of the cyclic stress strain curve and a damage model for predicting fatigue crack growth thresholds", in D.L. Davidson, S. Suresh (eds.), *Fatigue Crack Growth Threshold Concepts*, Philadelphia, PA, Metallurgical Society of AIME, p. 43-62, 1984.

[STE 72] R.L. Stegman, P. Shahinian, "Environmental acceleration of fatigue - crack growth in a high-strength steel", *Metal Science J*, vol. 6, p. 123-127, 1972.

[STE 80] A.T. Stewart, "The influence of environment and stress ratio on fatigue crack growth at near threshold stress intensities in low-alloy steels", *Eng Fract Mech,* vol. 13, p. 463-478, 1980.

[SUM 68] H.T. Sumsion, "Vacuum effects on fatigue properties of magnesium and two magnesium alloys", *Journal of Spacecraft and Rockets*, vol. 5, no. 6, p. 700-704, 1968.

[SUR 83] S. Suresh, "Micromechanisms of fatigue crack growth retardation following overloads", *Eng Fract Mech*, vol. 18, no. 3, p. 577-593, 1983.

[SUR 83a] S. Suresh, R.O. Ritchie, "Near threshold fatigue crack propagation: a perspective on the role of crack closure", in D.L. Davidson, S. Suresh (eds.), *Fatigue crack growth threshold concepts*, Philadelphia, PA, Metallurgical Society of AIME, p. 227-261, 1983.

[SUR 83b] S. Suresh, R.O. Ritchie, "On the influence of environment on the load ratio dependence of fatigue thresholds in pressure vessel steel", *Eng Fract Mech*, vol. 18, no. 4, p. 785-800, 1983.

[SUR 85] S. Suresh, "Fatigue crack deflection and fracture surface contact: micromechanical models", *Metall Trans*, vol. 16A, p. 249-260, 1985.

[SUY 90] B.M. Suyitno, G. Chalant, J. Petit, "Environment and frequency effects on fatigue crack growth of microalloyed steel in the threshold region", in H. Kitagawa, K. Tanaka (eds.), *Fatigue 90*, Honolulu, Hawai, MCEP, p. 1381-1386, 1990.

[SWA 78] J.W. Swanson, H.L. Marcus, "Oxygen transport during fatigue crack growth", *Metall Trans*, vol. 9A, p. 291-294, 1978.

[THO 56] N. Thompson, N.J. Wadsworth, N. Louat, "The origin of fatigue fracture in copper", *Phil Mag*, vol. 1, p. 113-126, 1956.

[VIO 79] P. Violan, P. Couvrat, C. Gasc, "Influence of crystalline orientation on the environment affected fatigue crack propagation in copper", *Strength of Metals and Slloys*, vol. 5, p. 1189-1194, 1979.

[WAD 58] N.J. Wadsworth, J. Hutchings, "The effect of atmospheric corrosion on metal fatigue", *Phil. Mag.*, vol. 3, p. 397-401, 1958.

[WAD 59] N.J. Wadsworth, "The effect of environment on metal fatigue", in G.M. Rassweiler (ed.), *Internal Stresses and Fatigue of Metals*, Detroit, Warrendale, p. 382-396, 1959.

[WAD 61] WADSWORTH N.J., "The influence of atmospheric corrosion on the fatigue limit of iron-0.5 % carbon", *Phil Mag*, vol. 6, p. 397-401, 1961.

[WAN 75] R.J.H. Wanhill, "Fractography of fatigue crack propagation in 2024-T3 and 7075-T6 aluminum alloys in air and vacuum", *Metall Trans*, vol. 6A, p. 1587-1596, 1975.

[WAN 84] R. Wang, H. Mughrabi, S. Mc Govern, M. Rapp, "Fatigue of copper single crystals in vacuum and in air. I: Persistent slip bands and dislocation microstructures", *Mat Sci Eng*, vol. 65, p. 219-233, 1984.

[WEE 73] J. Weertman, "Theory of fatigue crack growth based on a B.C.S. crack theory with work hardening", *Int J Fract*, vol. 10, p. 125-131, 1973.

[WEI 67] R.P. Wei, P.M. Talda, C.Y. Li, "Fatigue-crack propagation in some ultrahigh strength steels", in *Fatigue crack propagation, ASTM STP 415, American Society for Testing and Materials*, p. 460-485, 1967.

[WEI 68] R.P. Wei, "Some aspects of environment-enhanced fatigue crack growth", *Eng Fract Mech*, vol. 1, p. 633-651, 1968.

[WEI 72] R.P. Wei, D.L. Ritter, "The influence of temperature on fatigue crack growth in a mill annealed Ti-6Al-4V alloy", *J Materials*, vol. 7, no. 2, p. 240-250, 1972.

[WEI 81] R.P. Wei, G.W. Simmons, "Recent progress in understanding environment-assisted fatigue crack growth", *Int J Fract*, vol. 17, no. 2, p. 235-247, 1981.

[WEI 83] R.P. Wei, M. Gao, "Reconsideration of the superposition model for environmentally-assisted fatigue crack growth", *Scripta Metall*, vol. 17, p. 959-962, 1983.

[WEI 83] R.P. Wei, G. Shim, "Fracture mechanics and corrosion fatigue", in T.W. Crooker, B.N. Leis (eds.), *Corrosion Fatigue, ASTM STP 801*, p. 5-25, 1983.

[WEI 83] R.P. Wei, G. Shim, K. Tanaka, "Corrosion fatigue and modeling", in *Embrittlement by the Localized Crack Environment,* The Metallurgical Society of AIME, p. 243-263, 1983.

[YUE 85] J.L. Yuen, C.G. Schmidt, P. Roy, "Effects of air and inert environments on the near-threshold fatigue crack growth behavior of alloy 718", *Fatigue Fract Eng Mater Struct*, vol. 8, no. 1, p. 65-76, 1985.

[ZEG 85] A. Zeghloul, J. Petit, "Environmental sensitivity of small crack growth in 7075 aluminum alloy", *Fatigue Fract Eng Mater Struct*, vol. 8, no. 4, p. 341-348, 1985.

[ZEG 89] A. Zeghloul, J. Petit, "Influence de l'environnement sur la propagation des fissures courtes et longues dans un alliage léger type 7075", *Revue Phys Appl*, vol. 24, p. 893, 1989.

[ZHU 86] W. Zhu, K. Minakaawa, A.J. Mc Evily, "On the influence of the ambient environment on the fatigue crack growth process in steels", *Eng Fract Mech*, vol. 25, no. 3, p. 361-375, 1986.

Chapter 12

Fatigue under Variable Amplitude Loadings

12.1. Introduction

Fatigue of materials and structures is a complex phenomenon where different factors simultaneously occur with couplings of various strengths.

The lifetime of a component is defined by:

– its design (especially its geometry);

– its manufacturing (process);

– its properties;

– the behavior of the material;

– the loading,

– the temperature and the surroundings (see Figure 12.1).

The effects of all of these factors on the lifetime of some structures are known – at least qualitatively – but it is still impossible to carefully predict the durability of structures without running any tests.

Chapter written by Thierry PALIN-LUC.

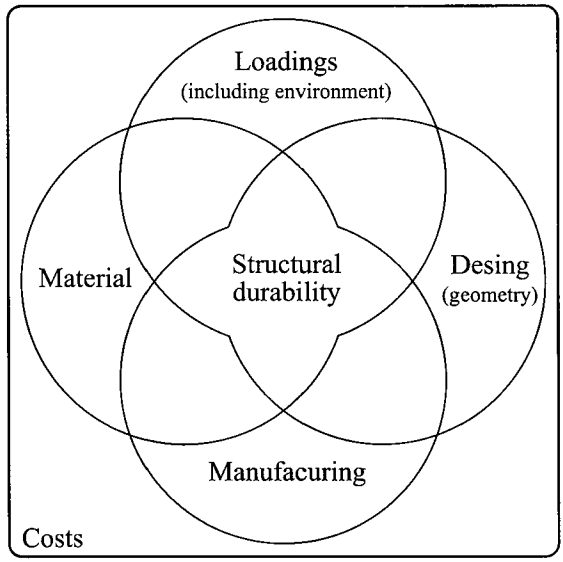

Figure 12.1. *Parameters influencing the lifetime of a structure (according to [BER 02])*

Since the first known fatigue issues (Wöhler, 1860), engineers have set up experimental procedures to test some specimens and structures under fatigue loadings in order to avoid the failures of structures due to fatigue. If we are dealing with the certification of the design of a structure before its release on the market or with the approval of the predictions of a methodology based on lifetime assessment, some fatigue tests today still have to be carried out in conditions closest to those the material and structure would undergo during its use. Assessing the lifetime of materials and structures in real conditions is a complex and multidisciplinary problem [SCH 03].

When the structures tested become more complex, the test results get closer to those seen in reality (see Figure 12.2). In aerospace, we talk about the "test pyramid" to describe the tests that are run on objects that are becoming increasingly complex (from the laboratory specimen to the entire structure, along with technological specimens). This is also the case in most industries (the automotive and railway industries, for instance). The number of tests is obviously higher on structures at the base of the pyramid (as the costs are low) than on the tests on real structures (top of the pyramid). In the same way, the loadings applied have to be close to real ones (see Figure 12.3) otherwise the mechanical parts might be over-sized [BER 02].

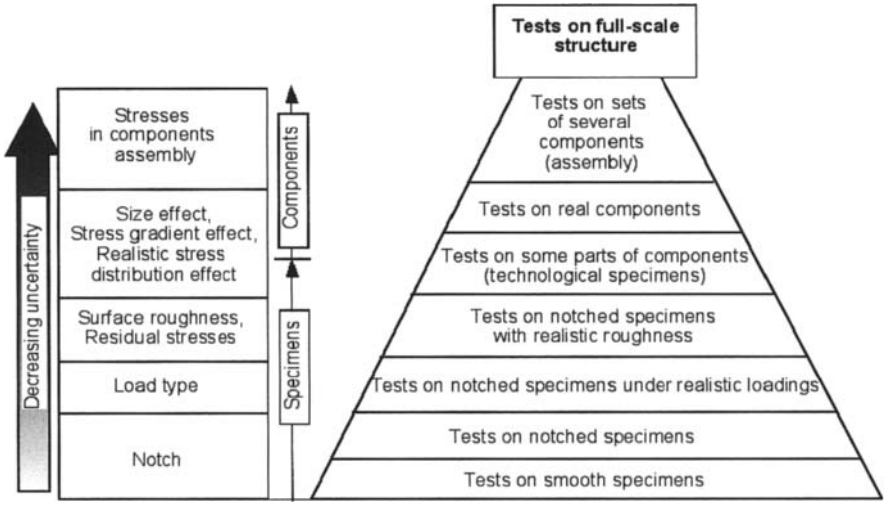

Figure 12.2. *Evolution of the representativeness of fatigue tests as a function of components tested (according to [SCH 94a])*

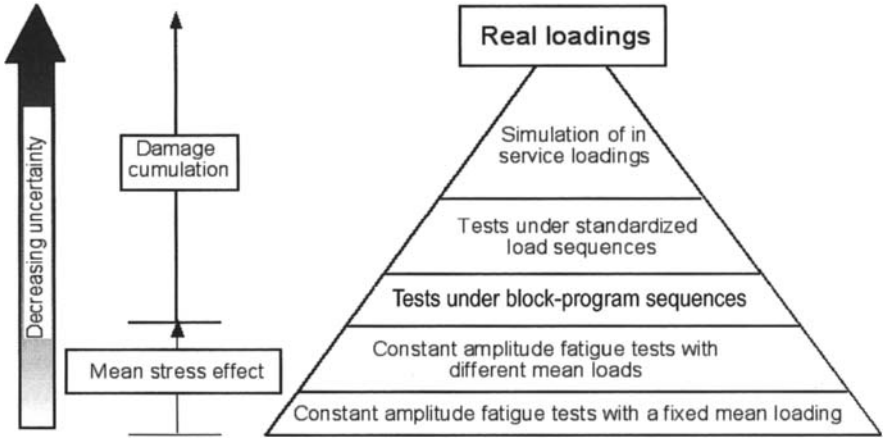

Figure 12.3. *Evolution of the representativeness of the tests as a function of loadings (according to [SCH 94a])*

This chapter focuses on the presentation of current ways of determining the lifetime of materials and structures by using simulation tests. The connections between the methods based on calculation and those based on digital simulation will be presented at the end of the chapter.

12.2. Variable amplitude loadings

12.2.1. *Why should we carry out fatigue tests under variable amplitude loadings?*

12.2.1.1. *Limitations of the Wöhler curve*

Wöhler first met the problem of fatigue on train axles at the end of the 19th century, which led him to devise a curve relating to fatigue (known as the "Wöhler curve" or "SN curve"[1]). This illustrates the experimental relationship between stress amplitude (or maximum stress) and the number cycles to fracture (or to the initiation of a crack of a specified size) for given external parameters, such as:

- the mean stress or the loading ratio;
- the environment;
- the temperature;
- the theoretical stress concentration factor;
- etc.

This Wöhler curve remains closely connected to the notion of cycle (sine, triangle, and trapeze) and cannot be used to represent the relationship between the temporal evolution of the force applied on a structure under service conditions and its lifetime.

12.2.1.2. *Service loadings*

In most cases, the real loadings applied to the structures are not cyclic and do not have any constant amplitude and mean value; they are said to have variable or random amplitude, as shown in Figure 12.4. Therefore, the study of lifetime under fatigue conditions of a material or of a structure under cyclic loadings does not really represent the durability within a real environment. We will see that the present experimental testing systems allow us to load the mechanical components with recorded service loadings or standardized sequences representing the service. We will then talk about simulation tests.

---

1 SN stands for *stress-number of cycles*.

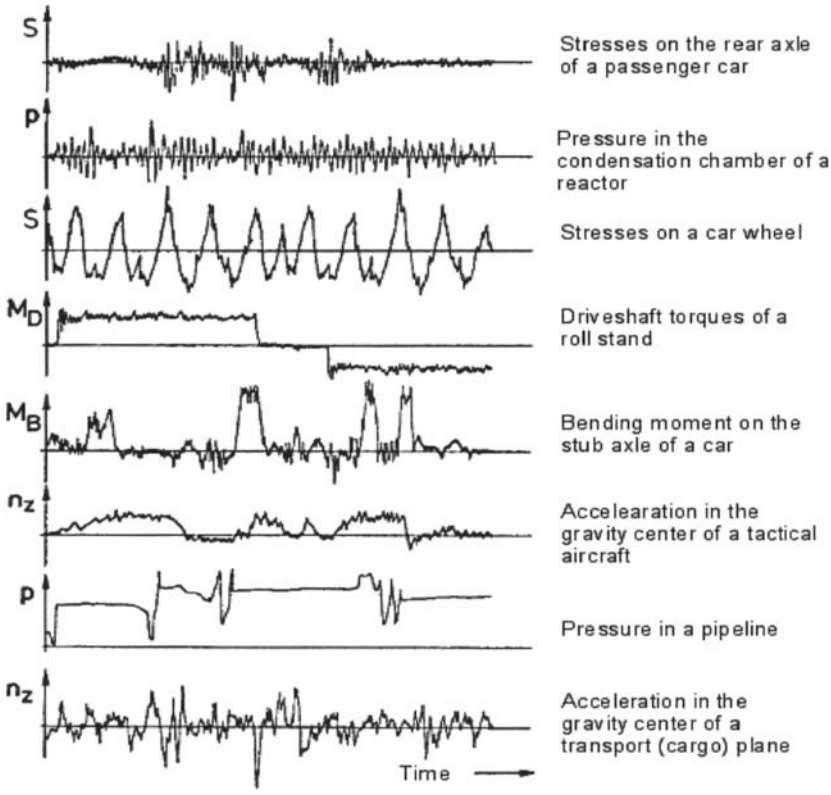

Figure 12.4. *Examples of variable amplitude loadings (according to [SON 07])*

12.2.1.3. *Concept of fatigue damage*

The first concept of fatigue damage under variable amplitude loadings is likely to be the one proposed by Palmgren in 1924 [PAL 24] and developed by Miner in 1945 [MIN 45]. The damage created by n_i stress cycles with an amplitude of $\sigma_{a,i}$ is supposed to be proportional to the work transferred to the material. Thus, with w_i being the work transferred to the material per loading cycle, Palmgren and Miner calculated the damage d_i created after n_i cycles as the transferred work ratio $n_i w_i$ on the whole work accepted by the material $N_i w_i$, where N_i is the lifetime corresponding to $\sigma_{a,i}$ on the Wöhler curve:

$$d_i = \frac{n_i w_i}{N_i w_i} \Leftrightarrow d_i = \frac{n_i}{N_i} \qquad [12.1]$$

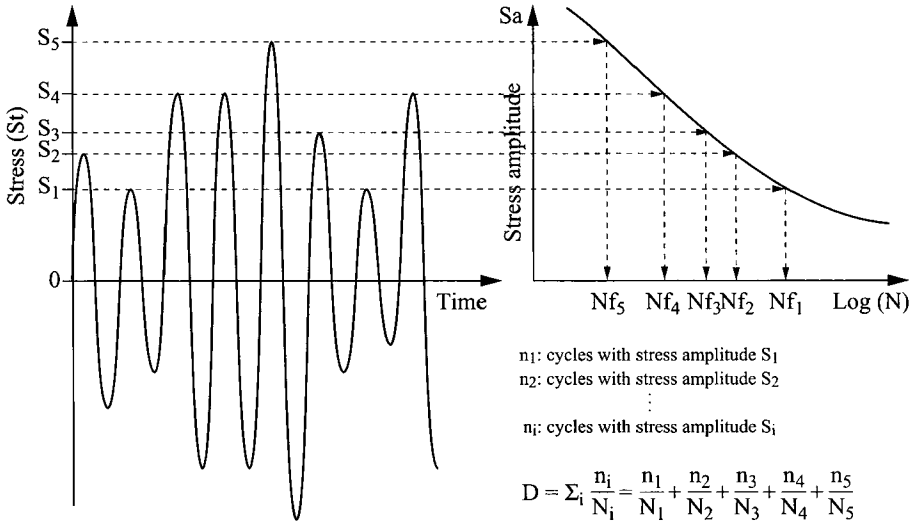

Figure 12.5. *Principle of linear damage accumulation according to Palmgren-Miner (example of cycles with zero mean stress)*

This simple law supposes that damage accumulation is a phenomenon that is linear with the number of cycles. It has been shown in the literature that under variable amplitude loadings, this law can be discarded when certain signs of overloading can be observed, for instance within the domain of low cycle fatigue followed by cycles with low intensity (within the high-cycle fatigue domain) or *vice versa*. In this instance, we then consider history effect [FAT 98, SCH 03].

Miner's rule is still used in industry, however, to estimate the lifetime of structures under service loadings. Nevertheless, the weaknesses of this model often lead the engineers to modify the cumulative damage law or to be cautious for two main reasons:

– the Wöhler curve of the material has to be used to determine the lifetime N_i related to each stress level $\sigma_{a,i}$. To consider the damaging effect of small cycles below the fatigue limit, several SN curve models are used: original Miner, modified Miner and elementary Miner (see Figure 12.6);

– the threshold value of the sum of critical damage; i.e. the total damage that represents the failure (fracture or technical crack initiation) is often considered as equal to the unit, whereas many tests show that this value is spread out and is usually lower than one [BER 02, SON 07].

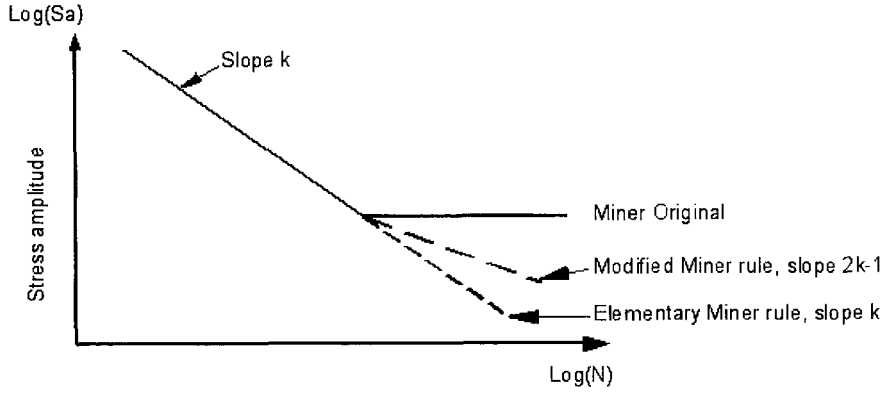

Figure 12.6. *Different modifications of the Wöhler curve used in practice (according to [BER 02, SCH 03, SON 07])*

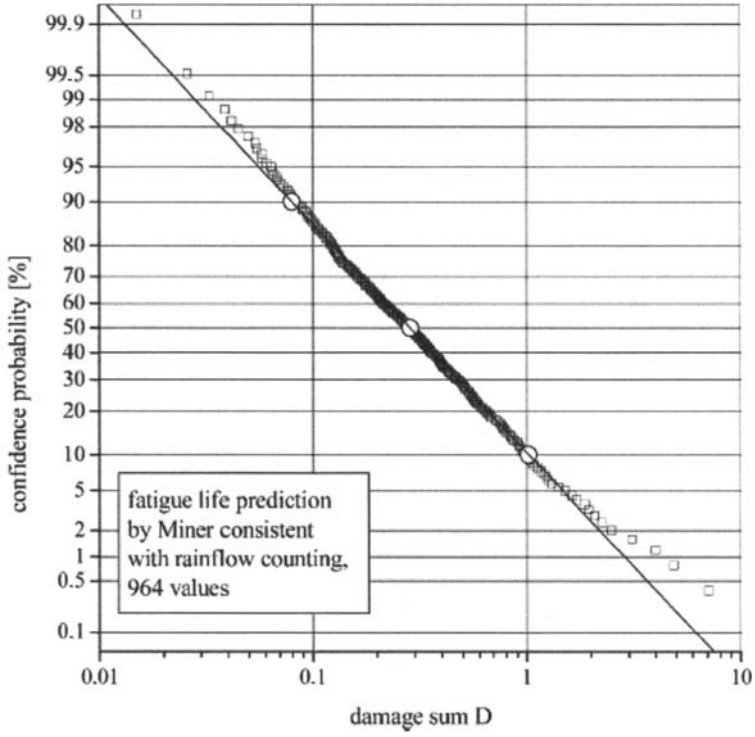

Figure 12.7. *Miner sum of experimental damage (according to [BER 02])*

Like many cumulative damage laws under fatigue conditions [FAT 98], Miner's rule uses the concept of damage per cycle (we will focus on this phenomenon at the end of this chapter). The cycles then have to be identified within a random loading signal; which is basically what the cycle counting methods were made for. The significant variations in total damage at failure (calculated according to Miner, see Figure 12.7) make the simulation tests under fatigue necessary. Even if some improvements have been achieved in the calculation methods of lifetime since the proposition of this model, as yet there is no method that is satisfactory for industrial structures[2].

12.2.2. *Characterization of loading signals and terminology*

12.2.2.1. *Random processes*

The simulation tests, which are still called tests under loading spectra, are carried out in order to get as close as possible to the loadings the structure will undergo during its life. In tests under sinusoidal loading with a constant amplitude or block-program variable amplitude, the time evolution of the forces or applied moments is deterministic. This means that it can be defined using an explicit mathematical equation. In reality, the force or strain records on a component of a structure often show that the loadings are *random* or "stochastic": their temporal evolution cannot be predicted, it is not defined by an explicit mathematical equation. Nevertheless, in order to perform simulation tests that can be repeated, the loadings are assumed to follow certain stationary random processes.

12.2.2.2. *Stationary and ergodicity conditions*

A random signal (or process) is said to be "stationary" if its probability structure is not affected by a change of the time origin. We can then say that its statistical properties (mean value, variance, etc.) do not depend on time [BLA 06]. Thus, most of the time, the loadings used for simulation tests and for the calculation of lifetimes under variable amplitude loadings, come from the service recordings, which are thought to represent the loadings a structure will bear during its life. We are therefore looking for the number of sequences that the component will be able to bear before its failure, each sequence representing a certain number of kilometers, flying hours or working hours.

A random process is said to be "ergodic" if the statistical and time mean values are the same, which means that the mean calculated on n samples of the signal (n

2 It shows that we have to work with cumulative damage models but also with the fatigue life assessment methodology of the structures.

times the process) has the same value as the one calculated on a single sample[3]. The "ergodicity" property therefore allows us to replace the global mean values with some time averages estimated from a single occurrence of the process.

The fatigue tests with loading spectra are usually performed assuming that signals are both ergodic and stationary.

12.2.2.3. *Irregularity factor, peak factor and band width*

The irregularity factor I of a random sequence is defined as the ratio of the number of times it is equal to the mean value with a positive slope N_0^+ on the mean number of maxima of the signal by time unit N_e:

$$I = N_0^+ / N_e \qquad [12.2]$$

When the irregularity factor is close to one, each extreme value is systematically followed by a zero. The spectra is then said to be with a "narrow band". If the irregularity factor is close to zero, the spectrum is said to be a "large band", i.e. there are many fluctuations of the signal on both sides of its mean value.

A signal presents a narrow band if its irregularity factor I is close to one (there are almost as many maximums as cycles). It presents a large band if I is close to zero. For instance, if $I = 0.99$ for the signal in Figure 12.8a, whereas $I = 0.74$ for Figure 12.8b, the band width is sometimes quantified by the parameter $(1-I^2)$.

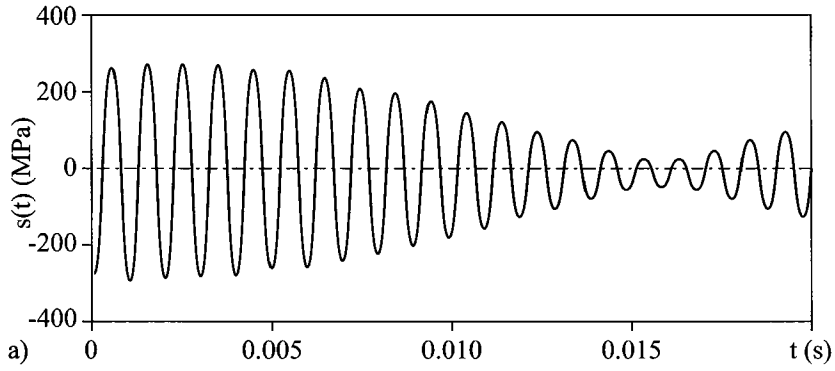

Figure 12.8a. *Example of signals in a narrow band (according to [PIT 01])*

3 For instance, for a racing car the recording of the strain within a single direction of a suspension arm during a circuit tour is a sample.

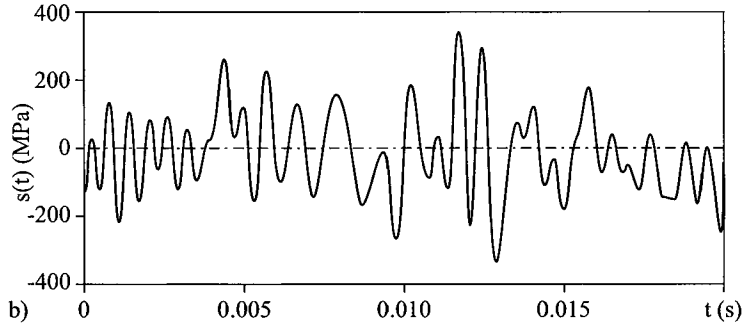

Figure 12.8b. *Example of signals in a large band (according to [PIT 01])*

12.2.2.4. *Power spectral density*

The power spectral density (PSD) is a frequency decomposition of the quadratic mean value of the process [BLA 06].

We should keep in mind that when we represent a random process by its single PSD this is an incomplete representation. Indeed, a PSD does not contain any information on the phase – only the real part is described. The time history of a signal cannot be built by its own PSD; there is no bijection between a PSD and a time signal.

To generate a time signal from a PSD, some hypotheses have to be made on the distribution of the phases. For instance, for some "Gaussian stationary ergodic" signals, the phase is uniformly distributed between $-\pi$ and $+\pi$ radians. The algorithm usually used to artificially generate time signals from a given PSD is based on the "fast Fourier transform" (or FFT) and on the Monte-Carlo method regarding the drawing of random numbers used for the phase [PRE 94a, WIR 95].

12.2.2.5. *Different types of variable amplitude fatigue tests*

Fatigue tests under variable amplitude loadings can be split into two main families: (i) cumulative or sequential loadings; and (ii) random loadings; each of these families containing several sub-groups presented in Table 12.1. Since the 1970s the evolution of the control systems of servo-hydraulic test benches, especially thanks to the advances of the controlling computers, have enabled the development of fatigue tests under random loadings. Before this time, tests were often limited to block-program or cyclic variable amplitude tests [GAS 39, GAS 77, GRÉ 81]. We will focus on these block program and cyclic variable amplitude tests in section 12.3.

There are also some variable amplitude fatigue tests whose loadings are not defined within the time domain but within the frequency domain by their PSD. These tests are especially useful in aeronautics and in the aerospace industry. We often talk about "vibration fatigue" here but this is just another term as we are still dealing with mechanical loadings evolving over time and leading to the initiation of fatigue cracks and to their possible propagation.

Loading sequence		Random loadings	
Programmed test		Spectra	
By blocks	By cycles	Representative	Real
- conventional program (8 blocks) - random sequence	- standardized sequence	- random - stationary	- direct - modified

Table 12.1. *Different types of variable amplitude fatigue tests*

12.2.3. *From in service recordings to test spectra*

12.2.3.1. *About representative loadings*

For simulation tests to be representative of reality, all of the changes that the structure will undergo during its life have to be reproduced. This assumes that the different loadings that affect the fatigue of the structural element being considered have been identified. All the incidental or rare events that may occur during regular use (stepping on the sidewalk at a high speed, air turbulence, etc.) also have to be known. Knowing these real loadings is important for a reliable estimation on the lifetime of structures under fatigue loadings, being either an experimental or digital (with a fatigue damage model).

Many service failures are due to errors in the assessment of service loadings [SCH 92]. Figure 12.9 illustrates the global methodology of lifetime assessment based on simulation tests. The framed parts in dotted lines show the choices that have to be made in the design procedure. The quality of the final results depends on these choices.

To get to know the service loadings, service recordings of real loadings applied on the mechanical components have to be carried out. Various sensors (strain gauges, accelerometers, force or displacement sensors, etc.) are judiciously fixed on the structure; the signals they measure are then recorded and stored [LEE 05].

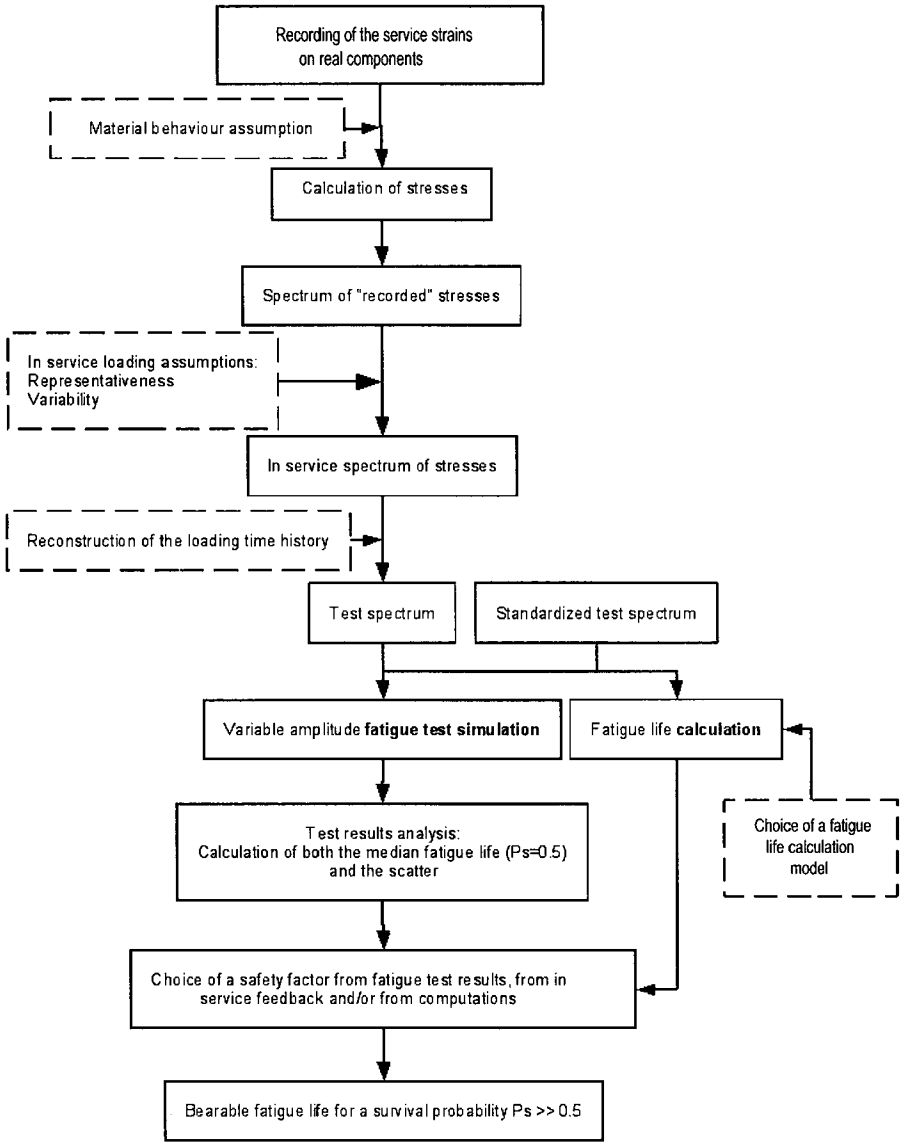

Figure 12.9. *General methodology of the fatigue lifetime assessment (according to [SCH 92])*

The recording conditions have to be adapted to the frequency of the physical signals. The sampling frequency of the signals has to be at least twice as high as the frequency of the highest ranked harmonic, which can be found within the frequency

spectrum of the signals. A low pass analog filtering before digitization (with a cutoff frequency equal to half the sampling frequency) avoids the spectrum aliasing problems that can occur during frequency analysis of the signals after their recording [BLA 06]. In any case, we have to make sure that the recording and digitization conditions do not lead to a deterioration in the real signals.

12.2.3.2. *Cycle counting methods*

12.2.3.2.1. Why should we count the cycles?

The first fatigue tests under variable amplitude loadings were carried out in Darmstadt in Germany at the FhG-LBF institute (*Fraunhofer-Institut für Betriebsfestigkeit*) with test devices that could only load the specimens or structures with sinusoidal signals [GAS 39]. To approach real loadings, tests were then performed by applying a sequence of sinusoidal loading blocks with different amplitudes from one block to another (eight-block-program method [GAS 39, GRÉ 81]). In addition, up to 10 years ago, the methods used to assess the lifetime of a structure used the concept of damage per loading cycle. This is why we tried to recognize (or extract) some cycles within real random signals in order to "simplify" them. At the end of this chapter, we will briefly see that the latest improvements are getting closer to incremental methods to assess the lifetime of components (without counting any cycles) because the concept of cycle under non-proportional and multiaxial random loadings is still not well defined[4].

12.2.3.2.2. Different cycle counting techniques

Cycle counting techniques are used to extract (recognize) the cycles within a "random" evolution of the stresses or strains. These methods can only be applied to a single scalar variable as they were initially developed for simple loadings (tension, bending, torsion). The six main counting methods cited in the literature are presented below and illustrated in Figure 12.10.

– *Peak count*: this method only uses the peaks and the valleys of the signal [AST 85]. A loading cycle is built after a series of a peak and a valley. Thus, the cycle with the widest area is the one made of the highest peak and the lowest valley (regardless of the time they appear within the original signal). Whole cycles are counted according to peaks with a decreasing order and to connected valleys with an increasing order. A similar technique allows us to avoid counting every small oscillation: we then only consider the *mean peak count*.

4 There is no cycle counting method approved by the scientific community for this kind of multiaxial loading. Wang and Brown [WAN 96a, WAN 96b] propose a cycle counting method relying on the stresses and strains of time history. Dressler *et al.* [DRE 92] propose a method relying on the time history of the applied forces.

– *Time count*: this technique does not use the notion of cycle and is based on the estimation of the probability density of the signal. The counted statistical event is the number of times the signal becomes equal to a certain value. This method cannot be applied once the original signal follows a peak-valley pattern. For a sequence lasting T'' the probability density of a level A_i is given by:

$$p(A_i) = \lim_{A_i \to 0} \left(\frac{\Sigma_j \Delta t_j}{A_i T} \right) \qquad [12.3]$$

– S*imple range count*: in this technique, the event counted is the area defined as the difference between the two local extremes of the signal. There are two different cases that can be seen: (i) when the first extreme is a valley, the area will be positive; (ii) when the first extreme is a peak, the area will be negative. Depending on the case being analyzed, some positive areas will be counted, or some negative areas, or both positive and negative areas. When the positive (or negative) areas are counted, each area defines a cycle. If the positive and negative areas are counted, each one of them defines a half-cycle.

– *Range-pair counting*: only the peaks and valleys of the signal are used by this counting technique. A cycle consists of a pair of consecutive areas (a peak followed by a valley and a valley followed by a peak or *vice versa*) with the same size and with opposite signs. Counting is carried out if the area e_{i+1} is higher or equal to the area e_i; the points forming area e_i are then removed from the sequence and counting resumes from zero.

– *Level crossing counting*: this counting algorithm comes from the one dealing with the time count. Two different level crossing cycle counting techniques exist [AST 85, GRÉ 88]. For instance, according to the American Society for Testing of Materials (ASTM) [AST 85], a cycle is counted each time the signal crosses a reference level (the mean value of the sequence for instance) with a positive slope. When the signal is below the reference level, a cycle is counted each time the signal crosses the amplitude class with a negative slope. The use of a reference level makes this technique unsuitable for loadings whose mean values vary a lot (e.g. lifting machines, driving parts of automotive vehicles during the sudden change of direction, slowing down, etc.).

– *Rainflow counting (Association Française de Normalisation and ASTM)*: this technique is based on the range-pair technique and is now the most frequently used [AFN 93, AST 85]. The rainflow techniques consider a cycle with analogy to the area of a hysteresis loop within a stress-strain diagram. From the result obtained with the rainflow method, we can calculate the result of the extremes method, the level crossing method, the ranges and range-pair method. Even if it has not yet been standardized, a rainflow counting technique has been published for multiaxial loadings [DRE 92].

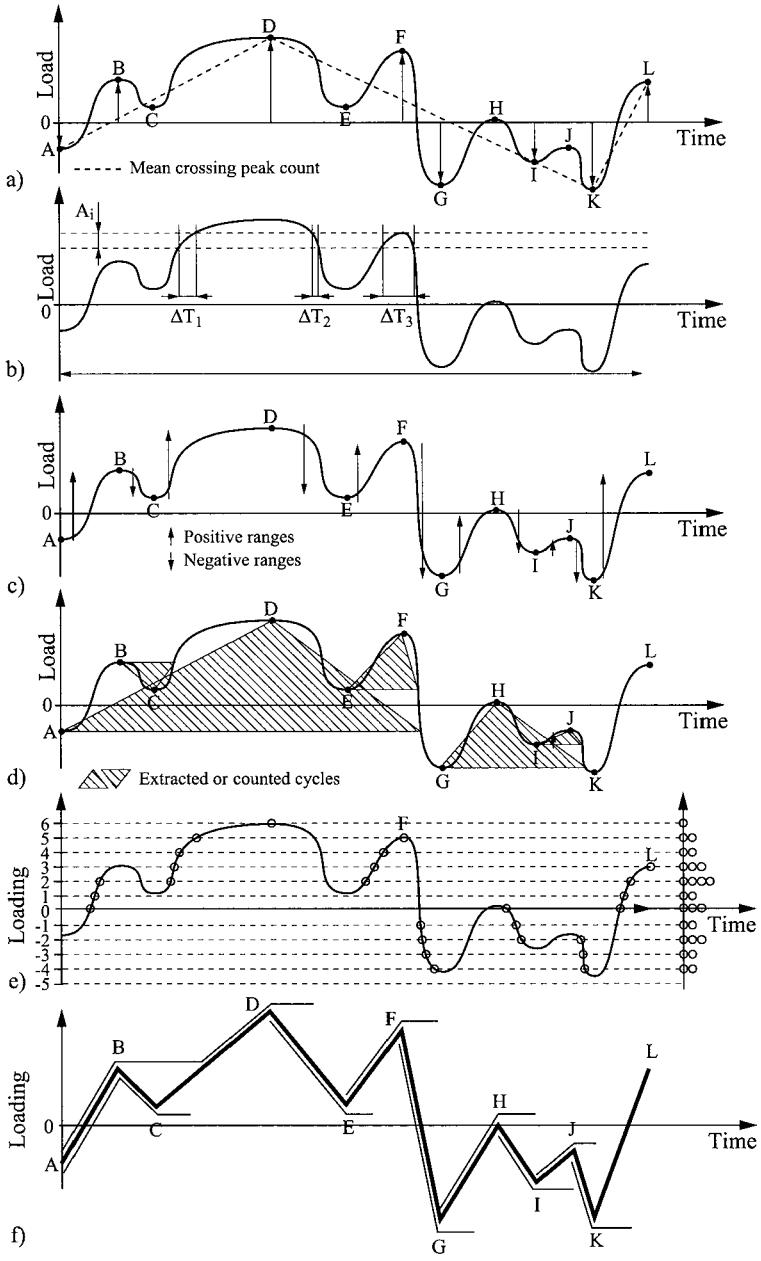

Figure 12.10. *Illustration of the six main cycle-counting methods: a) extrema; b) time count; c) simple range; d) range-pair; e) level crossing; and f) rainflow*

In the case of non-proportional multiaxial loading (or stress states), a given cycle-counting method is usually applied on an equivalent scalar variable. The choice of this equivalent variable (usually similar to a stress or strain) is not yet well defined. Wang and Brown, for instance, apply the rainflow counting method to the von Mises equivalent strain [WAN 96a, WAN 96b].

12.2.3.2.3. Comparative discussion

The only aim of a counting method is to discretize the loading time history into significant statistical events. To use the result from counting in a simulation test (or in a fatigue life assessment method), we must try to build stress cycles from the event counted. For instance, if the extremes are counted, the most significant stress cycle is made up of the highest peak followed by the lowest valley. Several authors [GRÉ 88, DOW 83] have compared some accumulated areas of loading cycles, built from one of the counting methods. For instance, in Figure 12.11, for the same loading recorded on an automotive vehicle Grégoire [GRÉ 88] compares the cumulated distribution of the stress cycle ranges obtained from the level crossing method and the range-pair method. In that case, counting using the level crossing technique allowed us to build some cycles with a higher amplitude than counting using the range-pair method.

The methods that do not count the same statistical event do not record the same number of events. This is because the definition of the stress cycle is not the same. The stress cycle defined by the rainflow method is actually approved (under proportional loadings). This is why the rainflow counting methods are the most commonly used in industry [FLA 94].

Several counting algorithms have been proposed, based on the rainflow method. They are different due to their way of considering the residue (the points remaining at the end of direct application of the counting algorithm). As the result contains the biggest areas of the signal, thus the most damaging cycles, this difference can have a significant impact on lifetime simulated during the test or during calculations. If the loading sequence starts and ends at the highest peak or lowest valley, there is no residue and all of the rainflow methods count the same cycles [AST 85].

There is no cycle-counting method that considers the order of appearance of events. Several authors ([LEM 88, SCH 03] for example) and the ASTM [AST 85], however, say that the application of the cycles can affect the cumulated damage for some materials and under certain loading conditions. This aspect is particularly noticeable on tests where some cycle levels correspond to the low-cycle fatigue domain. In this case, the cyclic hardening or softening of the material can be different, depending on the order of appearance of stress levels. Nevertheless, within the endurance and limited endurance domains, the history effect remains less obvious [PAL 96].

In addition, besides the time count, there is no counting method that considers the shape of the loading cycle (sine, triangle and trapeze) as the sequence is reduced to a succession of peaks and valleys. In tension, Mielke [MIE 80] showed by experiments on some steels that the shape of the cycle has no influence on the fatigue limit. Some Centre Technique des Industries Mécaniques tests, however, show that this shape has a slight influence on lifetime under limited endurance conditions [BRA 92].

Some biaxial fatigue tests under combined tension and internal pressure carried out on a steel by Dietmann *et al.* [DIE 89] and Mc Diarmind [MCD 89] show that the shape of the loading cycle has significant effects under non-proportional load paths. As you will see later on, this observation leads us to take precautions with the servo-control of fatigue tests under non-proportional multiaxial loadings.

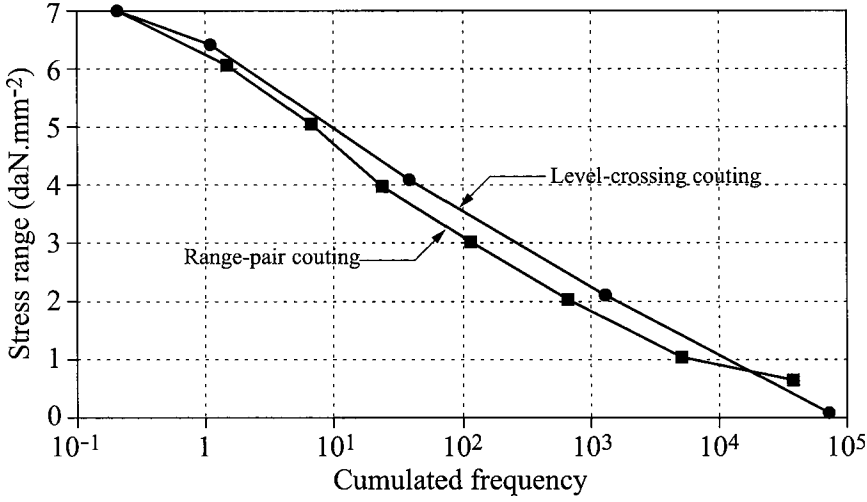

Figure 12.11. *Difference between the cumulated loadings obtained on the same signal by the range-pair (1) and level crossing (2) counting methods [GRÉ 88]*

12.2.3.3. *Cumulative frequency distribution*

The result of a cycle counting method is often graphically illustrated by a cumulative diagram. It represents the stress level as a function of the number of cumulated cycles (see Figure 12.12). Its shape represents the type of loading (highway, mountain road, rough road, etc.). It is necessary to follow certain rules to get results closer to the service loadings.

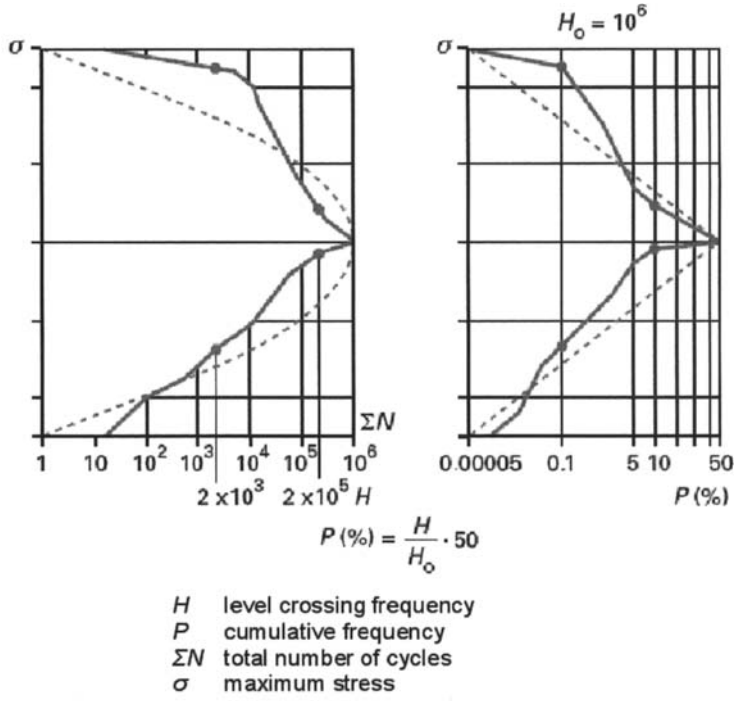

Figure 12.12. *Comparison of a real loading spectrum (vehicles driving on a metal bridge, full lines) with a Gaussian spectrum (dotted lines) [RAB 03]*

12.2.3.4. *Representativeness of a test sequence*

The representativeness of all of the service recordings used to build loading spectra or test sequences can only be obtained if we know the statistically relative part of each type of signal within the global lifetime of a structure. For instance, for a car:

– 30% of a rough road with holes;

– 29% of a country road in good shape;

– 14% of a country road in bad shape;

– 23% in town; and

– 4% on a highway [SCH 90];

with different loading conditions (empty, half loaded, entirely loaded) and for different speed ranges. The knowledge gained by the feedback from service loadings

remains significant in the reliability we can expect from fatigue simulation tests under variable amplitude loadings.

If the loading sequence is long (10^6 cycles and more) rare events usually occur (from 1 to 10 for a million cycles). However, some artificial modifications have to be performed for shorter service recordings that we wish to use to experimentally identify the loading spectra to be applied in the test ring or to be considered in computation of fatigue life. Indeed, the simulation tests or calculation of lifetime have to consider a few events that are unlikely to occur [LEE 05]. We have to extrapolate the highest level of the rarer signals (see Figure 12.13), for instance. Nevertheless, we have to ensure that we do not go over the physical limits imposed by the working conditions of the mechanical system because beyond it a sudden fracture would occur.

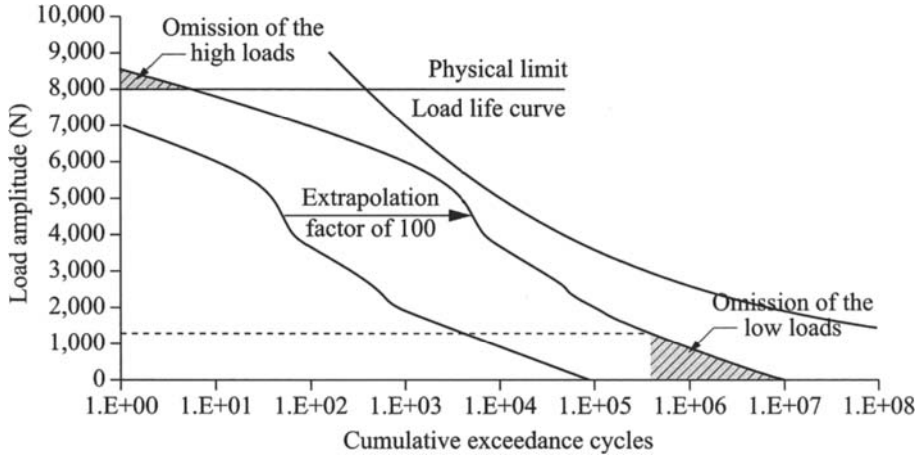

Figure 12.13. *Modification of a spectrum by extrapolating rarer events [LEE 05]*

12.2.3.5. *Standardized load sequences*

The first fatigue tests under variable amplitude loading spectra were performed in Germany by Gassner in 1939 using the eight-block program technique [GAS 39]. At the time of testing, due to the limitations of the technology, fatigue tests under random loading were not possible. Since the 1960s the servo-hydraulic systems have enabled us to apply random signals to the structures. In addition, many standard spectra have been developed in various industries to get results closer to real loadings; a list is given in Table 12.2 for uniaxial loadings and in Table 12.3 for multiaxial loadings.

All of these spectra have enabled several laboratories to compare the durability of various mechanical components under the same variable amplitude loadings. The use of the spectra also allows the laboratories to compare technological solutions. These spectra are presented without any dimensions $\sigma_{\max} / \sigma_{mean}$.

The aerospace industry was the first to set up standardized spectra (see Figure 12.14). Twist and Falstaff deals with bending forces applied to the wings of some transport and fighter aircraft, respectively, under service loading. A twist sequence represents 4,000 flights and a Falstaff sequence represents 200 flights. In the case of helicopters, helix and felix represent the impact of 140 flights on rotor blades (articulated and fixed respectively). In the aerospace industry, temperature influences Enstaff (Falstaff version including the temperature fluctuations).

Name	Year	Industrial domain
Eight-block program	1939	General
Twist	1973	Aeronautics (wing of a transport aircraft)
Gaussian	1974	General
Falstaff	1975	Aeronautics (fighter aircraft)
Mini twist	1979	Twist short version
Helix, felix	1984	Helicopters
Cold turbistan	1985	Engine disc of tactical aircraft
Wisper	1988	Wind turbine
Wash	1989	Offshore structures
Wawesta	1990	Steel mill drive
Carlos	1990	Car loading standard (front suspension parts)

Table 12.2. *List of the standardized sequences of uniaxial loadings (according to [BER 02, HEU 05, SON 07])*

Name	Year	Industrial domain
Eurocycle I	1981	Wheel of cars
Eurocycle II	1983	Truck wheel
Enstaff	1987	Falstaff and temperature
Hot turbistan	1989	Turbistan and temperature
Carlos multi	1994	Car loading standard (multiaxial)
Carlos PTM	1997	Car power train (manual shift)
Carlos PTA	2002	Car power train (automatic transmission)
Carlos TC	2003	Trailer coupling hook for car

Table 12.3. *List of the standardized sequences of multiaxial loadings (according to [BER 02, SON 07])*

In the offshore sector, wash spectrum deals with the effects of swell, wind and stream on the structures of oil platforms (in the North Sea or undergoing similar loadings).

The Carlos spectra were created by several European car manufacturers gathered in the FhG-LBF) and in the IABG (Industrieanlagen-Betriebsgesellschaft). They are related to parts of the front wheel axle-unit in automotive vehicles. The uniaxial version [SCH 90] presents three sequences related to vertical, lateral and longitudinal forces (see Figure 12.15). The multiaxial version [SCH 94b] deals with the forces applied in four directions: longitudinal, vertical and lateral to the tire/road contact and longitudinal to the rotation axis of the wheel.

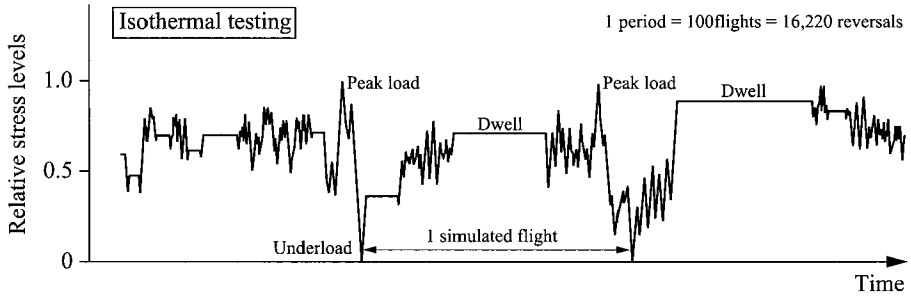

Figure 12.14. *Different parts of the hot turbistan sequence (according to [HEU 05])*

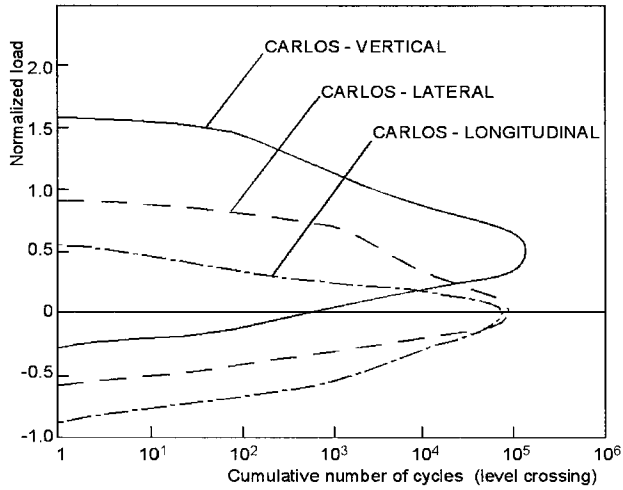

Figure 12.15. *Uniaxial Carlos spectra without considering small cycles [SCH 90]*

12.3. Fatigue tests under variable amplitude loadings

12.3.1. *General methodology of the simulation tests*

Depending on what we can rely on and what we are aiming for, the fatigue test can be more or less complex. The different types of tests are listed below starting, with the least complex one:

– block program;

– sequences of programmed random cycles;

– standardized load sequences;

– real signals.

During variable amplitude fatigue tests, the test sequence is reproduced until a final criterion is reached (initiation of a crack with a given size, stiffness loss or failure of the component in several parts). The load sequence has to be applied at least 5 to 10 times for the tests to be representative [SON 07].

12.3.2. *Test benches*

Since the end of the 1980s, the improvements in informatics tools, and especially of the digital servo-control of the servo-hydraulic test benches, has allowed engineers to perform tests under loading signals very close to the service signals recorded.

The current servo-hydraulic testing systems are usually controlled by microcontroller cards that communicate with a computer. This computer generates the test files (sine, block-program, peaks and valleys, real signals), defines the test and control condition (phase difference, time difference, mean value, tolerance on the controlled variables), as well as the safety limits and threshold values above which the test has to be stopped. Finally, the controlled variables and measured variables can be recorded and stored in digital files.

12.3.3. *Block-program tests*

The technique of block-program tests is the oldest; it was proposed by Gassner at the FhG-LBF institute in 1939 [GAS 39, GAS 77]. It consists of reproducing, as accurately as possible, a loading spectrum by a succession of sinusoidal loading blocks with the same mean load. The usual method consists of eight different loading (or stress) levels. For practical and technical reasons, the blocks are applied

in order of increasing amplitude, from the lowest to the highest, and then in decreasing order (see Figure 12.16).

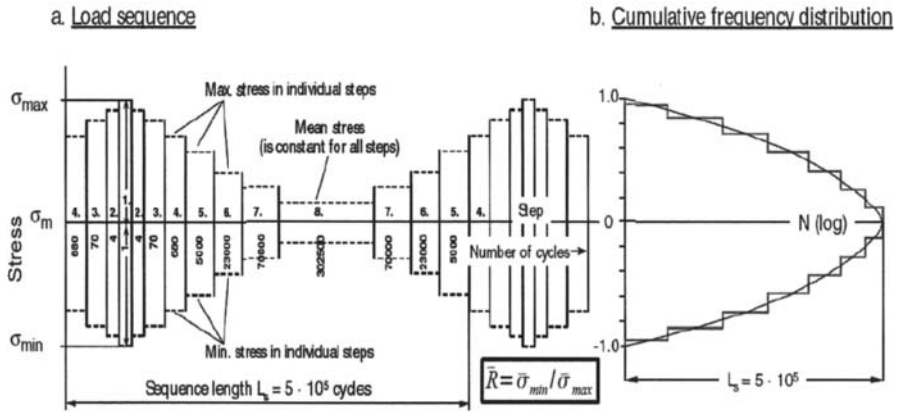

Figure 12.16. *Gassner's eight-block-program sequence (according to [SON 07])*

According to this test method, the usual distribution is Gaussian but several different cumulative frequency distributions can still be simulated if the distribution is deformed (see Figure 12.17). The shape of the cumulative frequency distribution can be defined by the factor v according to the following equation:

$$\ln H_i = \left[1 - \left(Sa_i / Sa_{max}\right)^v\right] \ln H_0 \qquad [12.4]$$

where:

– H_i represents the cumulative appearance frequency of the stress amplitude Sa_i;

– H_0 the size of the block (number of counted cycles); and

– Sa_{max} the highest amplitude of the spectrum.

For a Gaussian distribution $v = 2$, whereas v tends towards infinity for a uniform distribution (i.e. towards a constant amplitude loading), see Table 12.4). The distributions whose v is lower than two represent loads that are not always stationary. They are obtained by Gaussian spectra superposition with different maximum stress amplitudes [SCH 92].

ν	Type of loading
∞	constant amplitude
4	road bridge
2	stationary Gaussian signal
1	typical loading due to the roughness of the road
0.8	typical loading due to water swell or to the wind

Table 12.4. *Different values of ν according to the type of loading*

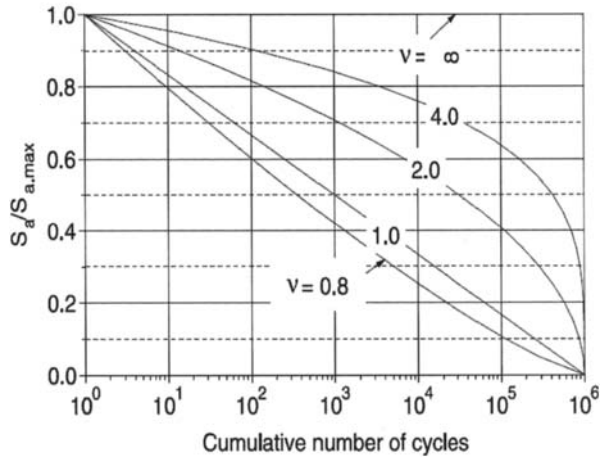

Figure 12.17. *Different types of load amplitude spectra (according to [HEU 05])*

12.3.4. *Variable amplitude fatigue tests and spectra*

12.3.4.1. *Sequences of random programmed cycles*

Usually, during fatigue tests using the block-program method, the mean stress does not vary. To vary the stress, Haibach *et al.* [HAI 76] proposed storing the signal using a reduced Markov matrix (or transition matrix). In the squared matrix (with a diagonal equal to zero), each line or column is relative to a type of stress (most of the time 32 or 64). For example from the maximum level σ_{max} to the minimum level σ_{min}. In Figure 12.18, the value of the square a_{ij} located above the diagonal represents the transition frequency that appears in the signal to get from the minimum $\sigma_{min,i}$ to the maximum $\sigma_{max,j}$ (and *vice versa* for the square a_{ji} located below the diagonal). To generate a signal from a Markov matrix, the starting square within the matrix is chosen randomly, for instance line i. The related transition frequencies are located within the partial line containing T_α elements (see Figure 12.18).

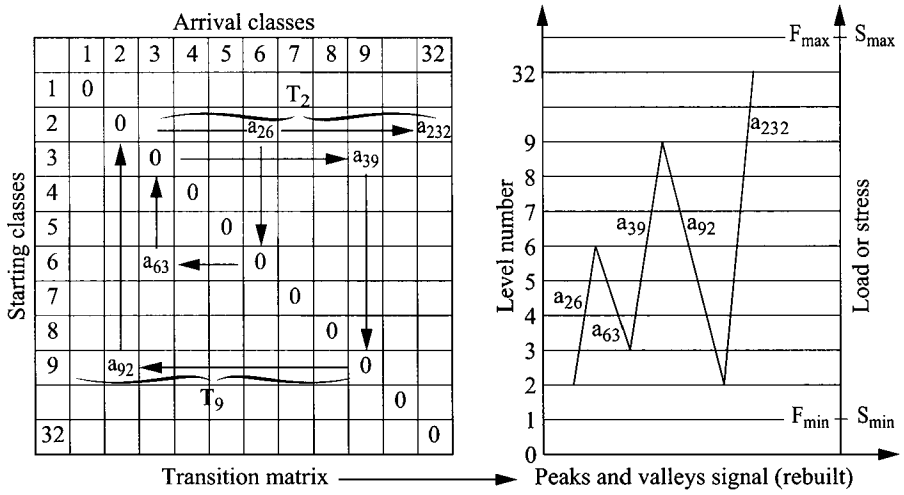

Figure 12.18. *Procedure to generate a variable amplitude signal (peaks and valleys) according to a transition matrix*

12.3.4.2. *Standardized loading sequences*

In standardized loading sequences, the order in which extremes (peaks and valleys) appear is set. The extremes were selected at random while they were created. The use of one of these sequences on specimens or different components enables us to compare their obtained lifetimes easily, thus the adopted technological solutions.

12.3.4.3. *Characteristics of non-proportional multiaxial loadings*

During variable amplitude fatigue tests under non-proportional multiaxial loadings, the load path is complex (the frame of the principal stresses is not fixed compared to the material and the principal stresses do not proportionally change between each other). In these conditions, studies [DIE 89] showed that fatigue lifetime depends on the shape of the load path. In order to test a specimen or a component under this type of loading, we have to make sure that the time evolution of the different forces applied complies with the command signals throughout the test.

Indeed, some systems do not control the time evolution of every force, but only the value of the applied forces, regardless of the time. In this case, the extremes of the signals (peaks and valleys) are considered well but not the non-proportionality of the loading. We have to be extremely cautious during long or very long tests (of

several weeks), otherwise the results will not be truly representative of the conditions chosen.

12.3.5. *Tests under random loading*

12.3.5.1. *Test spectra from a PSD*

Service loadings are not always known within the time domain (recordings of the signals as a function of time). For instance, in the aerospace industry, vibration loadings are often known by their PSD (see section 12.2.2.4) and possibly by their phase spectrum.

12.3.5.2. *Generation of loading signals*

Some fatigue tests can be carried out from a given PSD. Two solutions are then possible (see Figure 12.19):

– before the test, a loading sequence can be prepared in the time domain with a reconstruction algorithm;

– the loading can be built in the real time domain (using a generator of random signal during the fatigue test).

In the first case, the test consists of repeating a temporal load sequence. We then have a configuration similar to that of standardized tests. In the second case, the loading (time history) changes in real time (there is no sequence repetition).

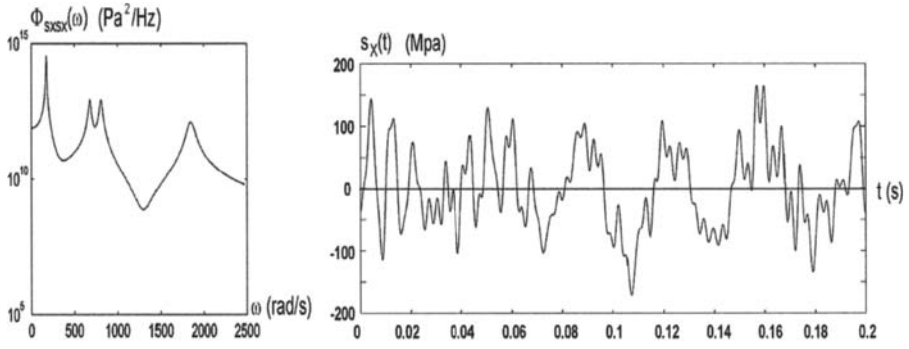

Figure 12.19. *Generation of a loading signal $S_X(t)$ according to its PSD [PIT 01]*

12.3.6. *Representation of the test results*

12.3.6.1. *Gassner curve or pseudo Wöhler curve*

Under real loading or spectrum, the Gassner curve is used to illustrate the equivalent of the Wöhler curve under constant amplitude loading (see Figure 12.20). The Gassner curve is a pseudo Wöhler curve representing the maximum stress of the spectrum as a function of lifetime. This kind of curve depends then on the considered loading spectrum (basically, the shape of the spectrum). As for the Wöhler curve, this curve also depends on the component (or specimen) tested and on the environment.

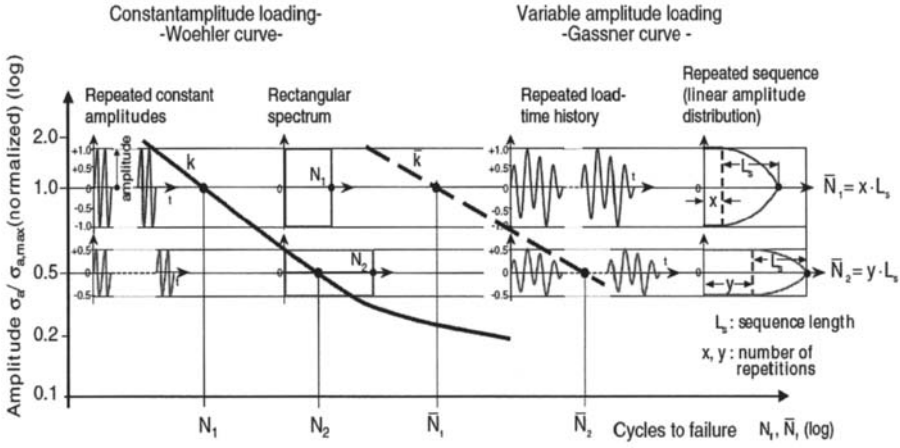

Figure 12.20. *Principle of the simulation tests under constant or variable amplitude loadings [SON 07]*

12.3.6.2. *Test report and details*

In order to compare the results of variable amplitude fatigue tests, results have to be given with as many details as possible.

The test spectrum is characterized by:

– the length of the sequence L_s;

– its stress ratio $R = \sigma_{min} / \sigma_{max}$ or loading ratio $\overline{R} = F_{min} / F_{max}$;

– its irregularity factor I;

– its peak factor;

– its rainflow matrix;

– its shape (its cumulative frequency distribution, depending on the level crossing method and the range-pair method[5]).

The extremes (peaks and valleys) of the signal are also necessary in order to carry out another test under the same conditions.

Finally, the test frequency has to be given if it remains constant throughout the entire test. The stopping criterion of the test and the number of sequences when the test stops have to be indicated as well as the environment, which can strongly influence the fatigue lifetime of the structure (air, saline smog, temperature, etc.).

In the statements we must also mention the type of control used (extreme of the signal, constant or variable frequency, or control of the shape of the signal). This last property is significant for tests under multiaxial loading.

The test results make sense if the reason why the test ended is known. The criteria are usually: stiffness loss of the structure, initiation of a crack with a given size or total failure of the component.

The environment in which the tests were carried out has to be described: temperature, humidity (especially in the case of composite materials with an organic matrix), corrosive environment, etc.

During tests on structures with non-linear behavior (vehicle suspension, for instance), the PSD of the signals has to be mentioned. If the loadings are multiaxial, the PSD of all of the forces involved has to be described in addition to the previous details for each force. The temporal recordings of any force also need to be kept in order to precisely know the load path (see Figure 12.21). Controlling the phase shift between each force is really important in ensuring that the proportionality (or not) of the load path will remain constant from one sequence to another. This non-proportionality can be illustrated with diagrams where the evolution of a force is plotted as a function of another one (see Figure 12.22).

Some authors mention in the literature the first statistical moments of the signals (mean value, rood mean square (RMS) value) or an equivalent stress. We should bear in mind that these indications can complete the previous measurements but are not enough. For instance, various different signals may have the same RMS value but lead to different fatigue lives [SON 89].

---

5 The comparison of the shape of cumulative frequency distributions for the same signal obtained with the level crossing and range-pair methods shows us whether the mean value of the signal varies or not [SON 05].

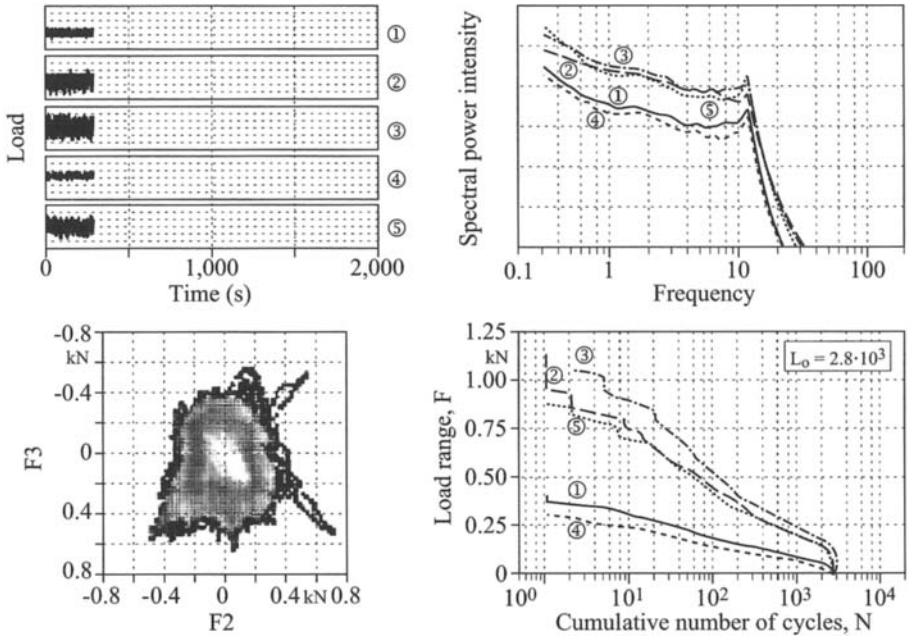

Figure 12.21. *Example of a variable amplitude multiaxial test [SON 07]*

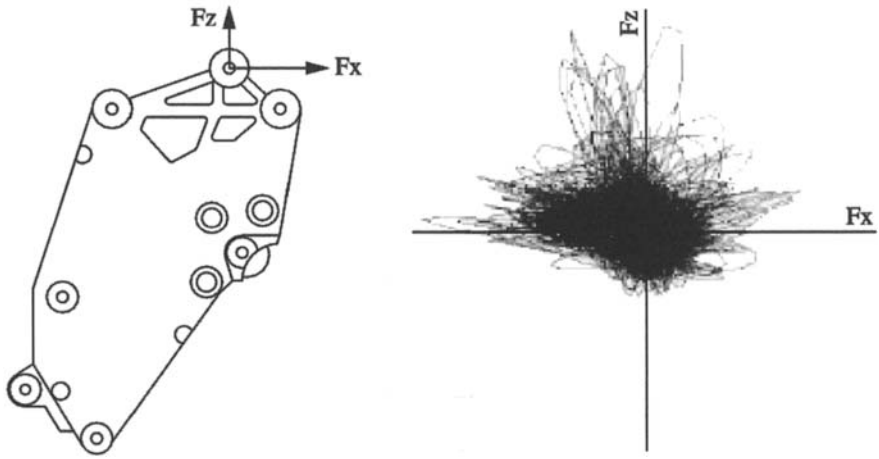

Figure 12.22. *Non-proportional multiaxial loading on a car engine (according to [LIU 04])*

12.3.6.3. *Scatter of the results*

The test results in the literature show that the scatter of fatigue lifetime of a structure under variable amplitude loading is usually smaller than that under a constant amplitude loading [BER 02]. This can usually be explained by the fact that the cycles with the highest amplitude activate many crack initiation sites; the cycles with lower amplitude then propagate the previously initiated cracks.

The asymptotic tendency of the Wöhler curve under constant amplitude loading is not present in the Gassner curve under variable amplitude loading. This is due to the "small cycles" (see section 12.4.8). The scatter of the test results, given as lifetimes, is almost constant as a function of the median lifetime. This is not the case under constant amplitude loading, where the scatter increases when we get towards long lifetimes (10^6 or 10^7 cycles).

12.4. Factors influencing the test results under variable amplitude loading

The test conditions of the simulations may influence the lifetime of a structure in real conditions.

Carrying out simulation tests under variable amplitude loading means that the various factors influencing fatigue life have to be known in order to be able to transfer the results obtained with a simulation test to a component under service conditions. These effects also have to be known when we need to compare several technological solutions tested in conditions that are not always the same.

12.4.1. *Counting method used to build the sequence*

It has been shown in section 12.2.3.2 that various cycle counting methods could be used to turn a random signal into a cumulative frequency distribution. Each method counts different cycles (number, amplitude and mean value). Le Pautremat *et al.* [LE 94] studied the propagation of fatigue cracks using five different cycle counting methods. Some tests under Gaussian loading sequences with three irregularity factors ($I = 0.3$, 0.7 and 0.99) and five counting methods show that, for large band sequences ($I = 0.3$ and 0.7), lifetime strongly depends on the counting technique chosen.

12.4.2. *Number of loading levels*

The block-program method (see section 12.3.3) is usually applied with eight different stress levels but its application is possible with any number [BRA 92, GAS 39, GRÉ 81]. The same goes for the number of levels used to approximate

cumulative frequency distribution. If the number of levels is reduced, the effect of the blocks of higher amplitude compared to low level ones (risk of overloading/underloading effect) has to be considered. For instance, this effect can be significant in tests where the duration of fatigue crack propagation is non-negligible [BAS 82].

12.4.3. *Application order of the loading levels*

The effect of application order of the loading levels often occurs in the block-program method when it is applied to few different stress levels (four for instance instead of the usual eight). For standardized loading spectra, or with service recordings, the high number of loading levels and significant number of repetitions of the sequence before crack initiation allows us to avoid the effect of the application order of the levels. For some block-programs with four levels, however, several authors [BAS 82] have observed that lifetime depends on the application order of the blocks (lifetime is reduced if the blocks are applied when stress levels are decreasing, and increased when stress levels are increasing).

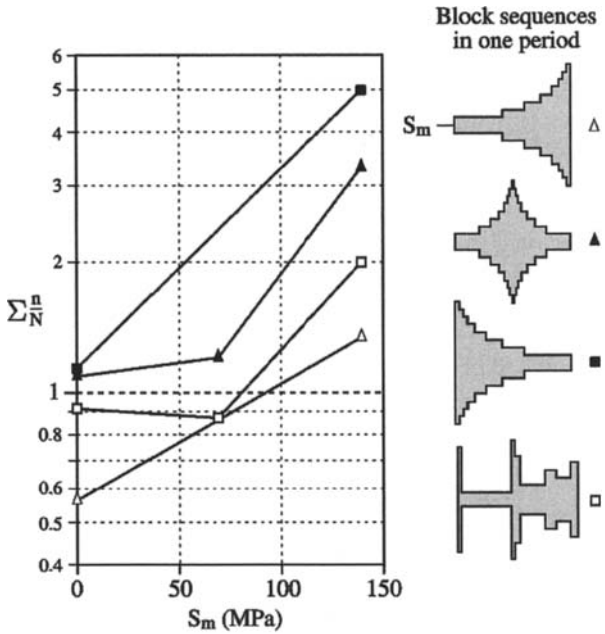

Figure 12.23. *Effect of the application order of some loading levels on the crack propagation of metal sheets made of 2024-T3 [SCH 03]*

The effect of the order of loading levels is also significant in crack propagation tests (see Figure 12.23) [SCH 91, SCH 03], and during crack initiation tests when the highest loading cycles correspond to the low-cycle fatigue domain. The study of the fatigue of structures under loading involving both low-cycle fatigue and high-cycle fatigue is ongoing.

12.4.4. *Loading frequency*

Usually loading frequency on metallic materials has no effect on fatigue life for the initiation of cracks if the test frequency remains lower than about 250 Hz [BRA 92]. Nevertheless, this statement is not always true, depending on the material being considered. Indeed, on ductile or semi-ductile materials, the temperature of the specimen, or of the structure, can be increased by several dozen degrees for a loading frequency of about 100 Hz. During the test (for instance using thermo-couples or an infrared camera), the temperature of the component (or specimen) has to be measured to check it does not increase by more than a few degrees and to be sure there is no self-heating phenomenon that might lead to modification of the fatigue characteristics of the material.

12.4.5. *Limitation of the signals under high stresses*

The maximum stress level reached during a variable amplitude fatigue test is a significant characteristic of the test. Indeed, on notched structures the highest loading cycles can affect lifetime because of the residual stresses and cyclic hardening (or softening) induced by the local plasticity of the material at the notch tip during the overloading.

Within the propagation domain of the cracks, the high cycles can also affect the propagation curve due to overloading for the same reasons.

We therefore have to be cautious when we extrapolate the spectra towards high stress levels in order to reduce the duration of the simulation tests. The physical phenomena involved during simulation tests should not be taken beyond the stress-strain domain where the material will be cycled in real service conditions (i.e. the level of macroscopic plastic strains).

12.4.6. *Irregularity factor*

During tests under narrow band loading, the variations in irregularity factor, I, do not really affect the lifetime for crack initiation or the propagation phase. According to Gassner [GAS 76] this is true as long as the irregularity factor ranges from one to

0.85. This has been confirmed by [LE 94]. However, for large band signals (meaning for low values of I) lifespan depends mainly on the irregularity factor.

This can be explained by the less damaging effect of the low-amplitude cycles (whose number increases when I becomes smaller) and by the effect of the mean value of these cycles. This mean value varies a lot within the large band signals (see Figure 12.8, section 12.2.2.3). Thus, between several signals with the same RMS value, Jacoby [JAC 70] suggested choosing the narrow band signals during the validation tests in order to be within a discriminating (or safe) configuration.

12.4.7. *Type of spectrum*

The shape of the loading spectrum strongly influences lifetime, as shown by the example in Figure 12.24 for welded joints made of steel E36. Figure 12.25 illustrates this effect under a rectangular (i.e. constant amplitude) spectrum, a Gaussian and a linear one. For the same maximum stress, lifetime varies with a factor of 200. This can be explained because, within a linear spectrum, the number of cycles with a low amplitude (therefore causing small damage) is much higher than within a Gaussian spectrum.

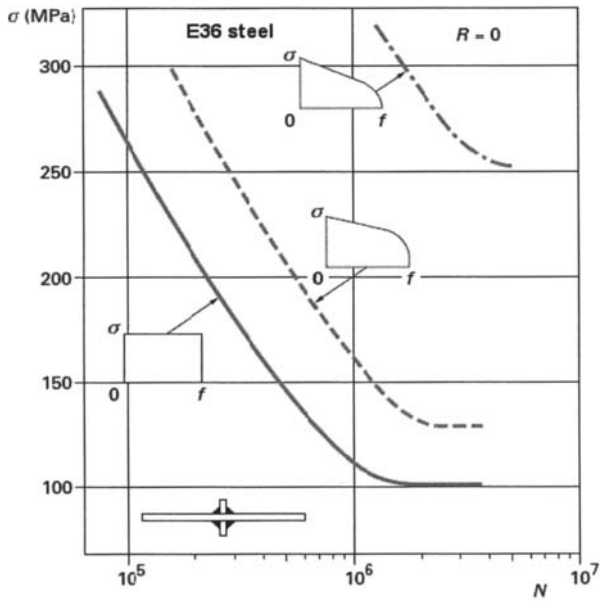

Figure 12.24. *Effect of the shape of the spectrum on the lifetime of welded joints made of steel E36 (according to [RAB 03])*

This can lead to significant consequences regarding the lightening of a structure. For instance, in Figure 12.25, to guarantee a lifetime of 10^8 cycles, the resisting section of a rod supporting a same variable axial load will be much smaller under a linear spectrum (1.9 times for this example) than under a constant amplitude loading. The choice of the spectrum (according to the service loadings) used in simulation tests or in the calculation of lifetime is therefore essential for designing against fatigue under variable amplitude loading.

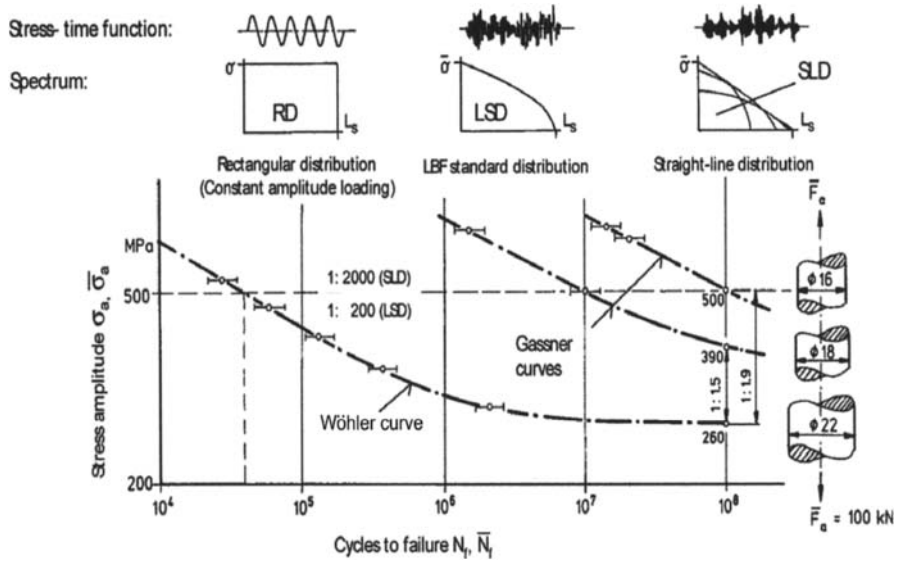

Figure 12.25. *Influence of the shape of the loading spectrum on lifetime (according to [BER 02])*

12.4.8. *"Small cycles" or cycles with low amplitude*

The tests under spectra contain a more or less significant number of cycles with low amplitude (or "small cycles") compared to the fatigue limit of the material. The damage due to these small cycles seems to be negligible, at least to some extent. We tend to reduce the length of a spectrum by removing some of these cycles. This is one of the aspects of accelerated fatigue tests.

12.4.9. *Accelerated fatigue tests*

Due to the duration of some fatigue tests under variable amplitude loadings, which is sometimes very long (from a day to several weeks), engineers have tried to

reduce the duration of such tests. Several methods are possible, but we have to be cautious with regard to the representativeness of the reductions. Feedback remains essential for assessing the fatigue life of industrial components from fatigue test simulations or for a validation procedure.

12.4.9.1. *Issues and goals of these tests*

When we want to reduce the duration of fatigue tests under variable amplitude loadings, we also wish to accurately determine the relationship between the lifetime of the structure under a real loading compared to the lifetime obtained during simulation tests on a test bench (which is shorter).

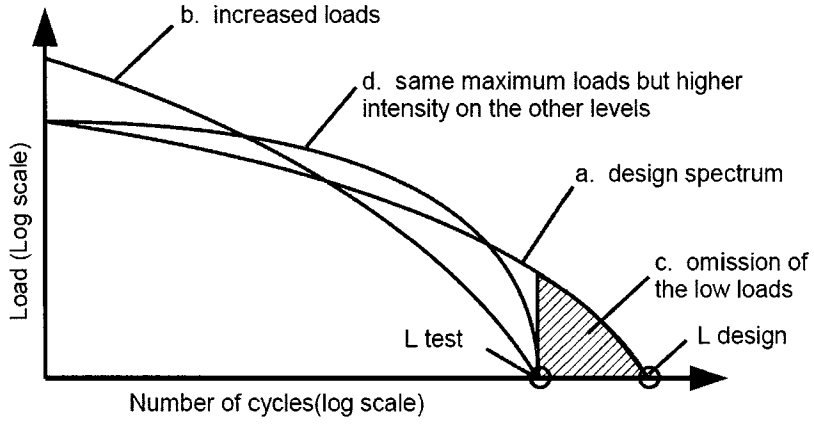

Figure 12.26. *Different ways to reduce the lifetime L of the tests according to [BER 02]. (L test – life under accelerated fatigue tests; L design – life under the original spectrum)*

The damages involved have to be identical, the fracture surfaces of the tested components also have to be similar, and the materials have to be loaded within the same stress-strain domain. To sum up, we can:

– increase the test frequency;

– modify the loading spectrum:

- by increasing the level of the highest cycles (Figure 12.26b),
- by removing some small cycles (Figure 12.26c),
- by magnifying the spectrum with constant maximum loads (Figure 12.26d).

12.4.9.2. *Increase the test frequency*

If the phenomena involved are similar to those under real loading, the tests can be carried out by increasing the loading frequency of the low amplitude cycles. However, the maximum frequency cannot be higher than the frequency from which the lifetime under constant amplitude loading changes. In addition, if the transfer function of the whole set (test bench, tested structure) is non-linear, we have to make sure that the accuracy of the control system is not affected by the increase in frequency [SON 07].

12.4.9.3. *Filtering the signals and omission of the "small cycles"*

In order to make the tests under loading spectrum shorter, the shape of the spectrum is nowadays modified by removing the small cycles (which are supposed to be slightly damaging). In the literature, we come across several values for the filtering threshold, the most common values range from 30% to 50% of the fatigue limit under fully reversed tension conditions [LAG 00, LAG 01]. For simulation tests on structures from the laboratory, a filtering threshold is often directly applied to the force signal[7]. We can then consider the threshold to be 15% of the maximum stress of the spectrum [LEE 05].

Recently, Banvillet *et al.* [BAN 06] proposed an original technique dealing with the reduction of the length of multiaxial fatigue tests under variable amplitude loadings. It relies on the concept of a threshold stress amplitude, σ^*, which is lower than the conventional fatigue limit and is specific to each material. According to this approach, some cycles with a stress amplitude lower than σ^* do not damage the material, whereas some cycles higher than this threshold take part in the propagation of mesoscopic damage if they are mixed with higher amplitudes. The fatigue limit is then considered to be a non-propagating limit of macrocrack (typically a technical crack of 1 mm). The threshold σ^* is seen as a mesoscopic non-cracking limit.

Through the strain work density given to the material per loading cycle, this threshold can be transposed to a multiaxial stress state. With this technique, the number of repetitions of the loading spectrum is the same with the modified signal as it was with the original one. The length of the test is reduced as the loading spectrum is shorter, but the shape of the spectrum is changed (see Figure 12.27), without any arbitrary choice in filtering and without any increase in maximum stresses. In addition, we have to mention that this technique does not use any cycle counting techniques; therefore its results do not depend on the choice of any counting technique.

7 This is an empirical practical rule.

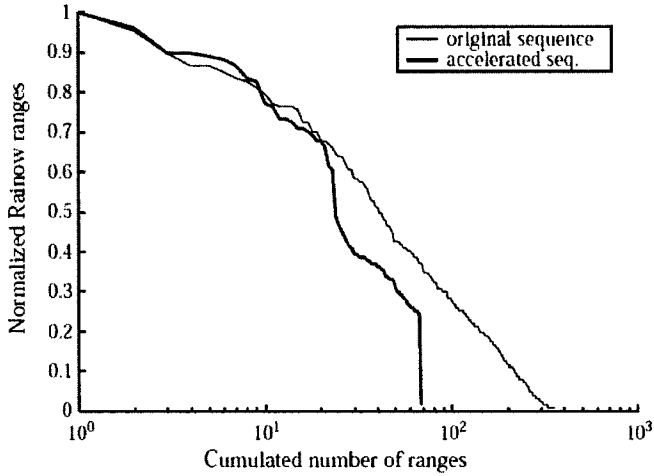

Figure 12.27. *Example of the modification of the loading spectrum according to [BAN 06]*

12.5. Fatigue lifetime assessment under variable amplitude loading

The aim of this section is not to present the different calculation methods of the lifetime in multiaxial fatigue under variable amplitude loading. A chapter of this book deals with this topic, which is still being analyzed today. There is no approved global method. This section simply presents the general methodology used by many methods dealing with the estimation of lifetime. The reader will find several notions there that have already been presented in this chapter.

12.5.1. *Main methodology*

The calculation methods of fatigue lifetime under multiaxial variable amplitude loadings usually rely on the following elements:

– a cycle counting method;

– a fatigue criterion;

– a cumulative fatigue damage rule;

– a Wöhler curve (or a S-N curve).

The cycle counting method allows us to turn the "random" evolution of all the stress (and/or strain) tensor terms into a sequence of different sinusoidal cycles (each with a mean value and amplitude).

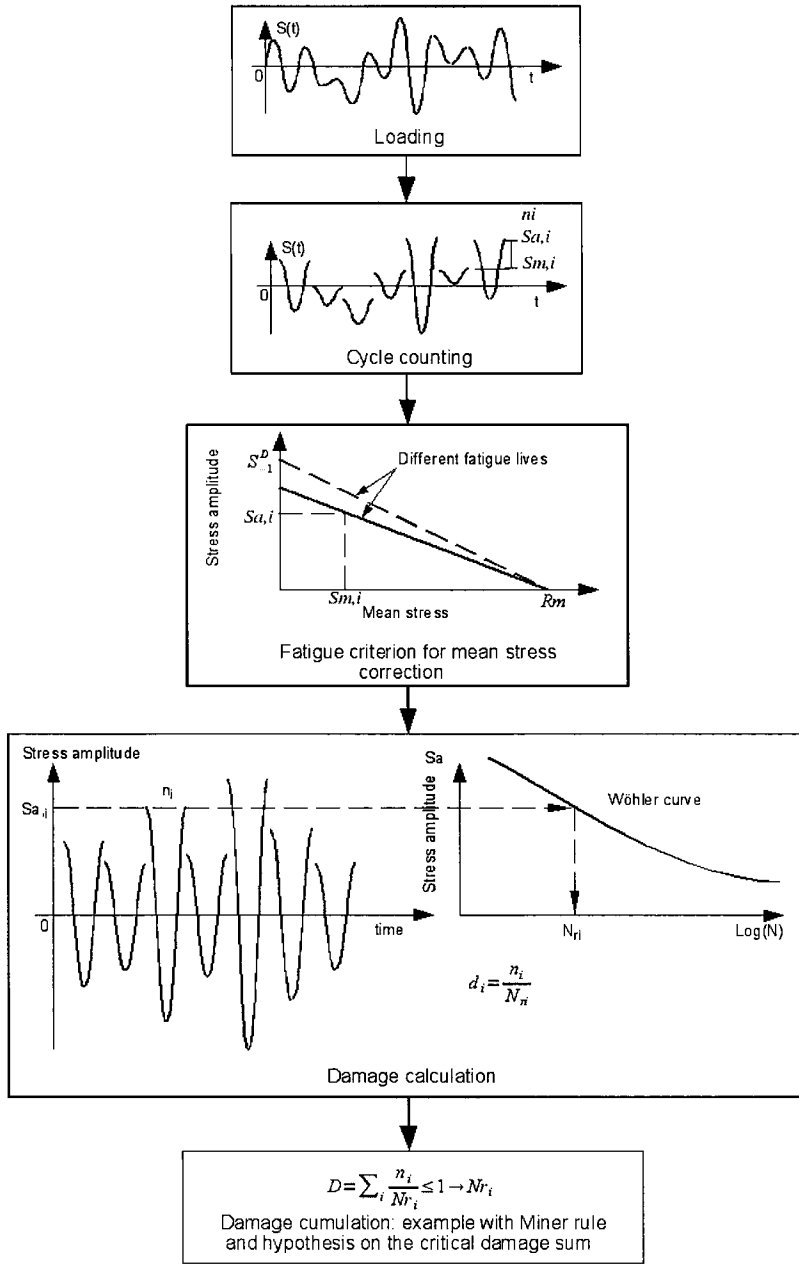

Figure 12.28. *Main steps of fatigue life calculation methodology under variable amplitude loading*

After counting the cycles (using the rainflow method, for example), the damage due to each cycle i (with an amplitude $\sigma_{a,i}$ and a mean value $\sigma_{m,i}$) is calculated. To do this, the easiest method[8] is the Palmgreen-Miner one [MIN 45, PAL 24]. Its application supposes that for each couple ($\sigma_{a,i}$, $\sigma_{m,i}$) the number of associated cycles N_i on the corresponding SN curve is known. As the S-N curves are not all known, a fatigue criterion (Goodman or Gerber, for instance) enables us to make *a mean stress correction.* For each cycle with a non-zero mean stress, an equivalent fully reversed cycle is calculated. The damage due to each cycle is then computed, for instance according to Miner, $d_i = 1/N_i$. This entire method is presented in Figure 12.28.

12.5.2. *Characteristics of multiaxial loading*

The methodology previously illustrated becomes more complex when the stress state is multiaxial (when several principal stresses are not equal to zero). If all of the principal stresses change proportionally with time, compared to each other, and if the principal coordinate system remains fixed compared to the material, the loading path is then said to be *proportional.* If the principal stresses are not proportional compared to each other at any time or if the principal directions of stresses turn around the material, the loading path is said to be *non-proportional.*

12.5.2.1. *Proportional loading*

Under proportional loading, cycle counting can be performed on any term of the stress tensor because all of the terms change proportionally at the same time. The methodology previously presented can be applied if a multiaxial fatigue criterion (Crossland, Findley, Papadopoulos, etc.) is used in order to carry out the mean stress correction.

12.5.2.2. *Non-proportional loading*

With non-proportional loading, the notion of cycle is difficult to define. Many authors have chosen to count cycles through a counting variable. It is actually a scalar variable (an equivalent stress, the stress normal to a material plane, an energy based quantity, etc.).

When the stress (and/or strain) cycles are extracted, the associated elementary damage is computed. Each cumulative damage method then uses a damage variable and a special cumulative damage rule [FAT 98, SCH 03].

---

8 Different cumulative fatigue damage rules were proposed in [FAT 98], for instance.

12.5.3. *Towards no cycle counting*

12.5.3.1. *Principle of the incremental methods*

Over the past 15 years, several new fatigue life assessment methods have been developed without using any cycle counting techniques. The principle of these methods is to follow the evolution of a damaging variable (let's say X) in time. The evolution of this cumulated variable between the start of the loading at $t = 0$ and at time t is given by: $X_c(t) = \int_{t=0}^{t} dx(t)$. These methods then follow the infinitesimal (or incremental) evolution of a variable to determine its cumulated value. This variable can for example be the mesoscopic plastic strain, as in the Papadopoulos [PAP 94] or the Morel [MOR 00] methods.

With these kinds of methods, defining the notion of cycle under non-proportional loading is not longer necessary. The result of the calculation method of the lifetime no longer depends upon the choice of counting technique. We should point out that in the main methodology previously described (see Figure 12.28), as all cycle counting methods count different cycles, the choice of counting technique influences the calculated lifetime. As a consequence, the current studies focus on such approaches without counting any cycle.

12.5.3.2. *Principle of the frequency methods*

As we saw previously, the variable amplitude loadings are not always known within the time domain but only within the frequency domain. In such cases, we do not have any typical recordings of the evolution of loading as a function of time, only the PSDs are known and used in the calculation. In this case, we then talk about "spectral methods" of lifetime assessment.

The principle of these methods is to estimate the damaging variable used within the frequency domain. This can be, for instance, the von Mises equivalent stress $\sigma_{eq,VM}$ [PRE 94b]. To move from the non-sensitivity of this equivalent stress to the hydrostatic one (whose influence can be observed under fatigue conditions), Pitoiset recently proposed a frequency method based on the Crossland criterion [PIT 00a, PIT 00b]. Using statistical tools to study the signal [LAR 91, WIR 80], cycle counting can be approximately done within the frequency domain. The frequency methods allow us to determine the lifetime of a component using the mean power (according to the signal analysis), the variance of the signal or a special statistical moment.

These techniques are approximations – within the frequency domain – of some models developed within the time domain. So far, they can only be applied if the time evolution of the equivalent stress chosen is a stationary phenomenon with a

mean value equal to zero. These methods are based in a model (Rayleigh distribution) of the cumulative frequency distribution of cycles extracted by the rainflow cycle counting method, followed by a linear cumulative damage rule (Miner). They have only been developed within the high-cycle fatigue regime. Studies have still to be carried out in order to estimate the lifetime of certain structures under non-proportional loadings within the frequency domain.

12.6. Conclusion

The fatigue of materials and structures under variable amplitude multiaxial loading remains a complex domain where many factors interact (loading, mechanical behavior of the material, geometry of the structure, roughness of the surface, residual stresses, temperature, environment, etc.).

Assessing the lifetime of the structures in real conditions or in service conditions is still impossible without the use of experiments.

The fatigue simulation tests under multiaxial variable amplitude loadings were significantly improved during the second half of the twentieth century. Today, we can assess multiaxial loadings representing the life of a structure. For these tests, which are used to validate the design of a structure before it is launched on the market and to improve the results of digital simulations, we have to:

– analyze, beforehand, every loading that might be applied to the structure being studied during its life;

– rely on service recordings of certain loadings, representing real loadings, or to rely on standardized loading spectra (taken from service recordings from a given industry, for example off-shore, automotive industry, aerospace industry, etc.);

– reproduce the loadings and efficiently control them so they can be carried out again;

– make sure the loading spectra are not modified, in order to reduce the amount of time tests take. The only thing that has to be taken care of is the representativeness of modifications made and of their consequences on the experimental lifetime obtained compared to real conditions.

Although they are complex, long and costly, multiaxial fatigue tests under variable amplitude loadings present many advantages that cannot yet be reached with computations. Multiaxial fatigue tests under variable amplitude loadings:

– locate the fatigue crack initiation areas and consider the external factors, especially the ones related to the geometry of the structure, the manufacturing

processes, the interactions between the components when they make up a whole mechanical system (front wheel-axle unit, gear box, fuselage of an aircraft, etc.);

– consider the over- or underloading effects;

– compare technological solutions (for various manufacturing processes, for instance) in order to perform the same tests on the structure but in different ways;

– quantify the distribution of service lifetimes representing reality in order to avoid excessive over-sizing;

– optimize (to reduce) the design of a component compared to a design under multiaxial loadings with constant amplitude (which is far from reality);

– validate a design in order to get it certified (in the aeronautic industry, for instance).

A predictive design against fatigue under variable amplitude loading has to consider the simulation calculation, simulation tests and the feedback (especially with the study of service failure) from customers. Indeed, to predict the durability of materials and structures, we have to consider:

– the geometry of the components;

– the manufacturing processes;

– the properties of the materials; and

– the loading characteristics (mechanical, thermal, environmental, etc.) [BER 02, GRÉ 88].

Significant progress in the study of the durability of mechanical structures will come from connections between experimental and digital simulations.

12.7. Bibliography

[AFN 93] AFNOR, *Fatigue sous sollicitations d'amplitude variable. Méthode Rainflow de comptage,* NF A 03-406, 1-32, AFNOR, 1993.

[AST 85] ASTM, "Standard practices for cycle fatigue counting in fatigue analysis. Designation E 1049-85", *Metal Test Methods and Analytical Procedure*, vol. 3, no. 1, p. 836-848, 1985.

[BAN 06] A. Banvillet, T. Palin-Luc, J.F. Vittori, "How to reduce the duration of multiaxial fatigue test under proportional service loadings", *Int. J. Fatigue*, vol. 28, p. 554-563, 2006.

[BAS 82] F. Bastenaire, H.P. Lieurade, "Programme fatigue. Influence of load sequence on number of cycles to failure", *Sciences et Techniques de l'Armement*, vol. 56, p. 467-487, 1982.

[BER 02] C. Berger, K.G. Eulitz, P. Heuler, K.L. Kotte, H. Naundorf, W. Schuetz, C.M. Sonsino, A. Wimmer, H. Zenner, "Betriebsfestigkeit in Germany - an overview", *Int J Fatigue*, vol. 24, p. 603-625, 2002.

[BLA 06] G. Blanchet, M. Charbit, *Traitement Mumérique du Signal*, Techniques de l'Ingénieur, vol. E 3 087, p. 1-30, 2006.

[BRA 92] A. Brand, J.F. Flavenot, R. Gregoire, C. Tournier, *Recueil de Données Technologiques sur la Fatigue*, 3rd edition, CETIM, Senlis, France, 1992.

[DIE 89] H. Dietmann, T. Bonghibhat, A. Schmid, "Multiaxial fatigue behavior of steels under in-phase and out-of-phase loading including different wave forms and frequencies", *3rd International Conference on Biaxial/Multiaxial Fatigue*, vol. 61, p. 1-17, Stuttgart, April 1989.

[DOW 83] N. Dowling, "Fatigue life prediction for complex load versus time histories", *Transactions of the ASME*, vol. 105, p. 206-214, 1983.

[DRE 92] K. Dressler, R. Carmine, R. Krüger, "The multiaxial rainflow method", in Rie K. (ed.), *Low Cycle Fatigue and Elasto-plastic Behaviour of Materials 3*, Elsevier, Amsterdam, p. 325-330, 1992.

[FAT 98] A. Fatemi, Y. Yang, "Cumulative fatigue damage and life prediction theories: a survey of state of the art for homogeneous materials", *Int J Fatigue*, vol. 20, no. 1, p. 9-34, 1998.

[FLA 94] J.F. Flavenot, "Predicting of the fatigue life of mechanical structure", in Amzallag C. (Ed.), *Automation in Fatigue and Fracture: Testing and Analysis*, 1231, ASTM STP, ASTM, Philadelphia, p. 493-507, 1994.

[GAS 39] E. Gassner, "Festigkeitversuche mit viederholter Beanspruchung im Flugzeugbau. (Strength tests under reapeated loading for aeronautical engineering)", *Luftwissen*, vol. 6, p. 61-64, 1939.

[GAS 76] E. Gassner, H. Lowak, D. Schütz, Bedeutung der unregelmässigkeit Gauss'scher zufallsfolgen für die bestrigfestigkeit, Report No. FB-124, FhG-LBF, 1976, English version, 1907, October 1976.

[GAS 77] E. Gassner, "Fatigue resistance of various materials under random loading", *9th ICAF symposium LBF - TR - 136*, vol. S.3.5, p. 1.34, 1977.

[GRÉ 81] R. Grégoire, "La fatigue sous charge programmée", *Note Technique* no. 20, 1981.

[GRÉ 88] R. Grégoire, "La prévision de durée de vie en service des structures travaillant en fatigue", *Review Française de Mécanique*, vol. 1, p. 29-41, 1988.

[HAI 76] E. Haibach, R. Fisher, W. Schutz, W. Huck, "A standard random load sequence of gaussian type recommended for general application in fatigue testing ; its mathematical background and digital generation", in Bathgate R. (ed.), *Fatigue Testing and Design,* The Society of Environmental Engineers, London, 1976.

[HEU 05] P. Heuler, H. Klatschke, "Generation and use of standardized load spectra and load-time histories", *Int J Fatigue*, vol. 27, p. 974-990, 2005.

[JAC 70] G. Jacoby, "Contribution to the comparison of the information value of program and random tests (Aircraft design fatigue life and cumulation damage problems, discussing information value of programmed load and random tests)", *Zeitschrift für Flugwissenschaften*, vol. 18, p. 253-258, 1970.

[LAG 00] T. Lagoda, E. Macha, A. Nieslony, A. Muller, "Fatigue life of cast irons GGG40, GGG60 and GTS45 under combined random tension with torsion", in Fuentes M.E., Martin-Meizoso A. (Ed.), *Fracture Mechanics: Applications and Challenges*, Elsevier, p. 256 (CD ROM p. 56), San Sebastian, Spain, ECF 13, 2000.

[LAG 01] T. Lagoda, E. Macha, R. Pawliczek, "The influence of mean stress on fatigue life of 10HNAP steel under random loading", *Int J Fatigue*, vol. 23, p. 283-291, 2001.

[LAR 91] C. Larsen, L. Lutes, "Predicting the life of Offshore structures by the single moment spectral method", *Probabilistic Engineering Mechanics*, vol. 6, 2, 96-108, 1991.

[LE 94] E.L. Le Pautremat, M. Olagnon, A. Bignonnet, "Sensitivity of equivalent load crack propagation life assessment to cycle-counting technique", in Amzallag C. (ed.), *Automation in Fatigue and Fracture: Testing and Analysis*, 1231, ASTM STP, p. 353-366, 1994.

[LEE 05] Y.L. Lee, J. Pan, R. Hathaway, *Fatigue Testing and Analysis: Theory and Practice*, Elsevier, Butterworth-Heinemann, 2005.

[LEM 88] J. Lemaitre, J.L. Chaboche, *Mécanique des Matériaux Solides*, Bordas, Paris, 1988.

[LIU 04] J. Liu, "Lifetime prediction under multi-axial variable amplitude loading – Further development of the shear stress intensity hypothesis", *7th Int Conf Biaxial Multi-axial Fatigue Fracture*, Berlin, ESIS, June 28–July 1, p. 40-408, 2004.

[MCD 89] D. Mc Diarmind, "The effect of mean stress on biaxial fatigue where the stresses are out of phase and at different frequencies", in Brown M.W., Miller K.J. (ed.), *Biaxial and Multiaxial Fatigue*, Mechanical Engineering Publications, London, EGF 3, p. 605-619, 1989.

[MIE 80] S. Mielke, Festigkeitsverhalten metallischer werkstoffe unter zweiachsigschwingender beanspruchung mit verschiedenen spannungszeitverlaufen, PhD Thesis, Aix-la-Chapelle, 1980.

[MIN 45] M. Miner, "Cumulative damage in fatigue", *J Appl Mech Trans ASME*, vol. 12, p. 159-164, 1945.

[MOR 00] F. Morel, "A critical plane approach for life prediction of high cycle fatigue under multiaxial variable amplitude loading", *Int J Fatigue*, vol. 22, p. 101-119, 2000.

[PAL 24] A. Palmgren, "Die Lebensdauer von Kugellagern", *VDI-Zeitschrift*, vol. 58, p. 339-341, 1924.

[PAL 96] T. Palin-Luc, S. Lasserre, C. Froustey, J.Y. Berard, "Experimental approach of damage cumulation in high cycle fatigue with random loadings in blocks", in *11th European Conference on Fracture*, vol. 2, Poitiers-Futuroscope, France, ESIS, 3-6 September, p. 1337-1342 1996.

[PAP 94] I. Papadopoulos, "A new criterion of fatigue strength for out-of-phase bending and torsion of hard metals", *Int J Fatigue*, vol. 16, no. 6, p. 377-384, 1994.

[PIT 00a] X. Pitoiset, A. Preumont, "Méthodes spectrales pour une analyse des structures métalliques en fatigue aléatoire", *Revue Française Mécanique*, vol. 1, p. 3-11, 2000.

[PIT 00b] X. Pitoiset, A. Preumont, "Spectral methods for multiaxial random fatigue analysis of metallic structures", *Int J Fatigue*, vol. 22, p. 541-550, 2000.

[PIT 01] X. Pitoiset, Méthodes spectrales pour une analyse en fatigue des structures métalliques sous chargements aléatoires multiaxiaux, PhD Thesis, Université libre de Bruxelles, 2001.

[PRE 94a] A. Preumont, *Random Vibration and Spectral Analysis*, Kluwer Academic Publisher, Dordrecht, 1994.

[PRE 94b] A. Preumont, V. Piefort, "Predicting high-cycle fatigue with finite elements", *Journal of Vibration and Acoustics*, vol. 116, p. 245-248, 1994.

[RAB 03] P. Rabbe, H.P. Lieurade, A. Galtier, "Prise en compte des sollicitations d'amplitude variable", *Essais de Fatigue*, vol. M4 171, p. 13-21, 2003.

[SCH 90] D. Schutz, H. Klatschke, H. Steinhilber, P. Heuler, W. Schutz, "Standardized load sequences for car wheel suspension components – CARLOS", *FhG-LBF FB-191 report, ABG TF-2695*, FhG-LBF and ABG, 1990.

[SCH 91] J. Schijve, "Predictions on fatigue", *JSME International Journal*, vol. 34, no. 3, p. 269-280, 1991.

[SCH 92] W. Schutz, "The significance of service load data for fatigue life analysis", *Fatigue Design*, vol. 1, p. 11-35, 1992.

[SCH 94a] D. Schutz, P. Heuler, "The significance of variable amplitude fatigue testing", in Amzallag C. (ed.), *Automation in Fatigue and Fracture: Testing and Analysis*, 1231, ASTM STP, p. 201-220, 1994.

[SCH 94b] D. Schutz, H. Klatschke, P. Heuler, "Standardized multi-axial load sequences for car wheel suspension components - CARLOS multi", *FB-201, FhG-LBF report*, FhG-LBF and ABG, 1994.

[SCH 03] J. Schijve, "Fatigue of structures and materials in the 20th century and the state of the art", *Int J Fatigue*, vol. 23, no. 8, p. 679-702, 2003.

[SON 89] C. Sonsino, "Limitations in the use of RMS values and equivalent stresses in variable amplitude loading", *Int J Fatigue*, vol. 11, no. 3, p. 142-152, 1989.

[SON 05] C. Sonsino, "Principles of variable amplitude fatigue design, testing and analysis under variable amplitude loading conditions", in Mc. Keighan P.C., Ranganathan N. (eds.), *Fatigue Testing and Analysis Under Variable Amplitude Loading Conditions*, 1439, ASTM STP, p. 3-23, 2005.

[SON 07] C. Sonsino, "Fatigue testing under variable amplitude loading", *Int J Fatigue*, vol. 29, p. 1080-1089, 2007.

[WAN 96a] C. Wang, M. Brown, "Fatigue under multi-axial variable amplitude loading", *Nuclear Eng Design*, vol. 162, no. 1, p. 75-84, 1996.

[WAN 96b] C. Wang, M. Brown, "Multi-axial random load fatigue: life predictions techniques and experiments", in A. Pineau, G. Cailletaud, T.C. Lindley (eds.), *Multi-axial Fatigue and Design*, Mechanical Engineering Publications, London, ESIS 21, p. 513-527, 1996.

[WIR 80] P. Wirsching, M. Light, "Fatigue under wide band random stresses", *Journal of the Structural Division*, vol. ST7, p. 1593-1607, 1980.

[WIR 95] P. Wirshing, T. Paez, H. Ortiz, *Random Vibrations*, Wiley-Interscience, New York, 1995.

List of Authors

Louis ANQUEZ
Dassault Aviation
Saint-Cloud
France

Jean-Paul BAÏLON
Département génie mécanique
Ecole polytechnique
Montréal
Canada

Claude BATHIAS
Université Paris X
Ville d'Avray
France

John-Ivan DICKSON
Département génie mécanique
Ecole polytechnique
Montréal
Canada

Jean-Marc GENKIN
Department of Materials Science and
Engineering
MIT
Cambridge, Massachusetts
USA

Henri-Paul LIEURADE
CETIM
Senlis
France

Jacques MASOUNAVE
Département génie mécanique
ETS University of Québec
Montréal
Canada

Thierry PALIN-LUC
LAMEF
ENSAM
Bordeaux
France

Régis PELLOUX
Department of Materials Science and
Engineering
MIT
Cambridge, Massachusetts
USA

Jean PETIT
LMPM
ENSMA
Futuroscope
Chasseneuil
France

André PINEAU
Centre des matériaux
ENSMP
Evry
France

Sylvie POMMIER
LMT
Ecole normale supérieure Cachan
France

Paul RABBE
Ancien directeur de l'IRSID
ARCELOR Research
Saint-Étienne
France

Christine SARRAZIN-BAUDOUX
LMPM
ENSMA
Futuroscope
Chasseneuil
France

Yves VERREMAN
Département génie mécanique
Ecole polytechnique
Montréal
Canada

INDEX

D

Index Terms	Links		
L			
Laplace-Gauss	29		
integral	29		
law	9	12–13	28
	37	39	98
	110	121	130–133
	145	165	182
	222	224	232
	245–246	249	251
	296	306	318
	333	352–354	357–359
	367	369–374	378
	382	385–386	416–417
	427	443	446
	462		
lead	4	6	11
	28	34	54
	61–62	69	75
	83	117	120–121
	133	141	152
	157	161	167–168
	184	209–210	255
	276	287	290
	293	298	300
	315	340–341	347
	355	373	387
	403–406	409	426
	429–431	434–435	439–440